Radio & Infrared Observations of the W3/W4/W5 Star-forming Regions

Thesis

Radio & Infrared Observations of the W3/W4/W5 Star-forming Regions

Kiz Natt, M.Phys

A Thesis submitted for the degree of Doctor of Philosophy

28th of February 2015

Physics & Astronomy Department / The Open University

Space Science & Technology Department / Rutherford Appleton Laboratory

Acknowledgments

It is a pleasure to thank those who helped me during the course of this thesis. First and foremost, I would like to express my sincere appreciation to my academic supervisor Professor Glenn J. White who made this thesis possible, providing me with important teaching, excellent guidance, invaluable knowledge and a great source of encouragement and suggestions during the course of this project. I am very grateful to all of the LOFAR team of commissioning scientists and engineers based at Groningen, and in particular Dr. Sarod Yatawatta and Dr. Raymond Oonk of ASTRON and Dr. Cyril Tasse (l'Observatoire de Paris) who made possible an important part of this thesis with useful instructions and suggestions on the calibration the LOFAR diffuse maps and radio recombination lines; close collaboration was essential during this experimental and early developmental phase of the array where this work was a important part of the telescope's commissioning.

I am very thankful to Dr. Chris Pearson for his suggestions and guidance with photometry using AKARI data. I am very grateful to Dr. Derek McKay-Bukowski and Dr. Stefan Wjinholds and Dr. Ben Mort, Dr. Fred Dulwich and Dr. Stefano Salvini of The University of Oxford's e-Research Centre (OERC) who provided constructive guidance and invaluable advice during my work with LOFAR single-station calibration. Computational resources were provided by ASTRON, the Netherlands Institute for Radio Astronomy, without which the experimentation and development of our calibration pipelines would not have been possible.

I would like to give special thanks to the University of Oxford who have hosted me during my PhD and to all of the members and visitors of the Department of Astrophysics at the Open University, the Rutherford Appleton Laboratory and the University of Oxford, for support, advice

and social interaction. A number of fellow academics encountered at conferences were also useful and deserve credit, particularly our collaborators, who provided their results to be contained in this very thesis. Funding was provided by the Open University and the Rutherford Appleton Laboratory (Science and Technology Facilities Council).

Finally, a special thank you to my wonderful Mum for her love, inspiration and motivation to follow my dreams. I have deep gratitude to my continually encouraging sister, my family and my dear friends for all their help, support and rays of light.

"I noticed, but only to avoid them, great clouds of dust, huge as constellations, eclipsing the star-streams; and tracts of palely glowing gas, shining sometimes by their own light, sometimes by the reflected light of stars. Often these nacreous cloud-continents had secreted within them a number of vague pearls of light...

. . . . . .

The heart of the nebula was now condensing into a smaller bulk, more clearly defined. It was a huge, congested globe of brilliance. Here and there throughout the disc knots and lumps of light were the embryonic star-clusters."

— Olaf Stapledon, *Star Maker*

Abstract

As part of the Low Frequency Array (LOFAR) Surveys KSP, targeted observations of H II regions close to high mass star-forming regions in the Galactic plane have been conducted, as part of the telescope's commissioning. This thesis details the calibration and analysis of one particular commissioning field, the prominent Galactic star-forming W3/W4/W5 complex and 2 supernova remnants (SNRs) HB3 and 3C 58, at unprecedented low radio frequencies ~ 30–76 MHz (§ 1). This part of the radio spectrum contains large-scale filaments, arcs, bubbles and shells which would be interesting to detail in new parameter space, both spatially and spectrally. A LOFAR calibration pipeline was developed as part of this work (§ 3) resulting in unique continuum maps ~10 deg^2 that detail extended diffuse emission of W3/W4/W5 at unprecedented sensitivity and angular resolution at low frequencies. Our final full bandwidth image (at ~ 53.5 MHz) reaches a final resolution of between ~ 62–85″ and noise level of 4.78 mJy/beam, making it the deepest image obtained in this frequency range. Spectral index maps (§ 4) made from 35.2 MHz, 54.7 MHz and 69.9 MHz continuum images give strong evidence of radio emission by thermal Bremsstrahlung with some localised regions demonstrating free-free self-absorption (§ 2), although we suspect a complete turnover of the H II regions outside of our observed range < 30 MHz. We obtain a spectral index of α ~ -0.03±0.02 for 3C 58 and observe a possible plateau in the emission of HB3 near ~ 55 MHz. High spectral resolution data was also analysed for the possibility of a carbon RRL detection in absorption < 100 MHz in the direction of W3 (§ 5). An initial all-sky image was also made during the commissioning of the Chilbolton LOFAR single station (§ 3); the wide FoV gave an overview of the large-scale diffuse Galactic synchrotron emissivity with the intention of measuring the spectral index < 100 MHz.

High mass star formation is an important area of research in modern astrophysics and triggers of this process along with many of the aspects of early stellar evolution including the onset of maser emission being poorly understood. Stars form out of large gas and dust clouds, detected through: (i) thermal dust continuum emission and (ii) line emission of organic molecules traced through masers. Hence, ancillary observations of W3 were made using the Onsala 20m radio

telescope for maser source detection and a point source catalogue of ~ 1300 sources at far-IR wavelengths of predominantly cold proto-stars was made from the newest AKARI maps (§ 6).

Finally, in addition to the Galactic diffuse radio emission, ~ 300 extragalactic point sources were captured in the background of the FoV with LOFAR. Their extracted fluxes were catalogued and over ~ 50 % provided a rich sample of spectral index information to constrain turnover of synchrotron < 100 MHz. We observed strong and moderate SED flattening attributed to free-free absorption processes at the source for ~ 3.2 % and ~ 19.1 % of sources respectively which is consistent with Rafferty et al. (2013).

Contents

Chapter 1

Introduction & Aims

1.1 The Interstellar Medium: An Overview

The space between the stars in the Milky Way galaxy does not entirely consist of a vacuum, but instead contains tenuous material, 99% the mass of which is made up of gas (in neutral, ionised and molecular form), and the rest in dust and cosmic rays; this material is called the *interstellar medium (ISM*). Stars form within molecular clouds (the densest regions of the ISM), and replenish the ISM with the release of matter and energy through *planetary nebulae*, *stellar winds*, and *supernovae*. This creates thermal instabilities within the ISM resulting in clouds of various temperatures, densities and compositions containing many embedded structures, which are dispersed in an inhomogeneous manner across the Galactic plane. We can study the radiation resulting from the absorption and re-emission of stellar energy by the ISM, and deduce its diverse physical properties (Spitzer 1998). Table 2.1 gives an overview of the properties of various components of the ISM.

As a result of primordial nucleosynthesis, gas in the ISM is made up of approximately 90.8% by number (70.4% by mass) of hydrogen and 9.1% (28.1%) of helium (Ferrière 2001). The remaining 0.12% (1.5%) consists of heavier elements resulting primarily from nuclear fusion during stellar evolution. Since hydrogen is the principal ingredient of interstellar gas, a region in the ISM is characterised as to whether its hydrogen is atomic (H I), ionised (H II) or molecular (H_2).

A nebula is an interstellar cloud of ionised gas and dust, and its various structures include *dark clouds* (detectable as a cool extinction medium in front of a radiating background along our

line of sight), *reflection nebulae* (detectable by reflection of mainly optical light from cold gas and dust) and *emission nebulae*. The latter category contains objects displaying a wide variety of conditions and chemical compositions, resulting from processes in thermal plasma, and in turn consists of 3 main emission types:

(1) *Star Formation Region nebulae*: the photo-ionised gaseous ISM surrounding new stars. Ionised elements include hydrogen (which is well known for the optical appearance of bright nebulae constituting H II regions), helium and carbon (found in the Warm Ionised Medium).

(2) *Planetary (Stellar Remnant) nebulae:* where a newly exposed hot core ionises an expanding shell of expanding gas expelled from the outer layers of a dying central star (Gordon & Sorochenko 1990).

(3) *Supernovae Remnant (SNR) nebulae:* the shell of gas expelled from a star by a supernova event (Downes & Wilson 1974). As well as some thermal radiation from the shock-heated plasma, the emission from SNRs is predominantly synchrotron in origin at lower frequencies, a result of relativistic electrons trapped in magnetic fields (see Lee et al. 2012 for an example of a SNR broadband spectrum).

Whilst planetary nebulae are comparatively smaller discrete, compact structures, most SNR and star-forming nebulae are large extended diffuse regions with poorly defined boundaries. We focus on the latter for this project by taking advantage of LOFAR's coverage at short baselines (§ 3.2.1), which maximises sensitivity to diffuse emission.

1.2 Stellar Feedback Processes & Super-bubbles

It was understood from the 1970s mm-wave CO (carbon monoxide) observations, that molecular clouds are the birthplaces of most new stars (Lord & Young 1990). These large diffuse nebulae have typical sizes between 20 - 200 pc, with individual molecular cloud masses ranging from $\sim 10^4$ $M_\odot$ – 2×10^6 $M_\odot$ (Solomon et al. 1987). They are complex and disordered structures, evident from large CO spectral line widths that indicate the presence of turbulent, as well as systematic motions within the gas (Solomon et al. 1987).

Gravity works to collapse the molecular cloud, and internal pressure forces, primarily from the gas (thermal pressure) as well as embedded magnetic fields (Li et al. 2009), work to keep the cloud from collapsing. Angular momentum can also hinder collapse (Larson 2010). Initially the gravitational and pressure forces are in balance. When these forces become unequal and gravitational forces dominate, the cloud begins to collapse and fragment into smaller components, the smallest of which can contract and accrete to form spatially coherent structures, leading to the birth of self-gravitating proto-stars (Dopita & Sutherland 2001). After a proto-star has either assimilated or expelled all the gas in its initial core, according to the *gravitational collapse model* (e.g. Shu et al. 1987) it may continue accreting from its parent clump although it will not accrete enough to change its mass substantially (Krumholz et al. 2005). The *accretion theory* (e.g. Bonnell et al. 1998) is a competitive model, and suggests that at birth all stars are much smaller than typical stellar mass, at ~ $0.5M_{\odot}$, and that the final stellar mass after the initial core is consumed, is a result of subsequent accretion of unbound gas from the clump; this is substantially larger than the proto-stellar mass. Whilst accretion may play a small role in star-formation, recent studies such as Krumholz et al. (2005) show strong evidence in support of the gravitational collapse model.

Gravitational collapse occurs due to the turbulence in dense molecular clouds which generates the distribution of density structures through *density fluctuations* providing the seeds for gravitational instabilities and fragmentation (Reipurth et al. 2007). The resulting massive fragments can manifest as *dense filaments* which are structures possibly containing embedded *clumps* of smaller clouds and spherical pre-stellar *cores* (Krumholz et al. 2005). We explore such cores with our *water maser* (§ 1.3.3) far-IR studies in § 7. It should be noted that filamentary structures are abundant in molecular clouds, and can be both actively star forming and quiescent (e.g. Arzoumanian et al. 2011 and Kirk et al. 2013). The following mechanisms are generally accepted for triggering star-formation in molecular clouds:

(1) A *density-wave shock front* via adjacent molecular cloud-cloud collisions (Lord & Young 1990).

(2) An *ionisation-wave shock front* at the edges of expanding H II regions (Yankulova 1969) driven by *ionised jets* and *outflows* arising from young stellar objects (YSOs). H II regions also expand independently due to UV photo-ionisation from OB stars and heating of surrounding gases, resulting in regions of overpressure in surroundings of lower pressure (Doptia & Sutherland 2001).

(3) Interstellar *supernova shock fronts* provided from nearby supernova explosions (Herbst & Assousa 1977).

(4) Triggered gravitational instabilities can also propagate through a spiral arm of the galaxy through large-scale spiral density waves (Dopita & Sutherland 2001).

The 4 examples above demonstrate how external disturbances can *compress* molecular clouds triggering star formation. In particular we are interested in the effects of (2) i.e. stellar feedback processes on molecular clouds. Spontaneous star formation can also occur in molecular clouds in a latent environment i.e. an environment with no external disturbances (Niwa et al. 2009), although this is not the focus for our study.

A simplified model of star formation based on gravitational contraction and collapse within molecular clouds predicts much higher star-formation rates than those observed in the galaxy (Zuckerman & Evans 1974). One explanation is that the role of turbulence in star-formation is complex and just as it can lead to spatially coherent structures, it can also it can *counter* local collapse. For example Dale et al. (2013) detail the destructive feedback effects of massive stars on star-formation within the dense filaments. Also Whitworth (1979) suggests that feedback processes decrease star formation efficiency by expelling gas from molecular clouds before it is able to collapse or be accreted.

Therefore, the *structure* and *dynamics* of the cloud turbulence, which control important properties of star formation, must be better understood. Low radio frequency studies of emission spectra will detail new parameter space for diagnosing their dynamics. This is what we hope to do with the study of emission spectra at low radio frequencies from W3/W4/W5 (§ 1.4), an altogether turbulent diffuse complex located in the Perseus spiral arm of the Galaxy at a distance of ~ 2.3 kpc from Earth (Massey et al. 1995). W3 (Westerhout 3) is possibly the most active region of current star-formation within the local Milky Way and extends 30 pc along the edge of a ~ 5×10^4 $M_\odot$ Giant Molecular Cloud (GMC) (Feigelson & Townsley 2008).

Stars of spectral type O and early B are usually formed in clusters (caused by triggering), called OB associations which are generally ~ few million years or less. The massive O stars have strong stellar winds, and all of these stars are short-lived, exploding as supernovae at the ends of their lives. Multiple (1) stellar winds and (2) supernovae can help power the creation and

expansion of a huge cavity into the ISM (some ~100's pc across), known as a *superbubble* (Ferrière 2001):

(1) Stellar winds can produce *stellar wind bubbles* with typical radii of 30 pc (Castor et al. 1975). The strongest stellar winds release 10^{51} ergs of kinetic energy over the lifetime of a star, which is comparable to a supernova explosion (Dopita & Sutherland 2001). The stars inside OB associations are close enough that their individual wind bubbles can merge to form a giant bubble.

(2) When these stars die, their supernova explosions drive shock waves within the cavity created by the stellar wind bubbles expanding them to even greater sizes, with expansion velocities reaching hundreds of km s^{-1}. This sequential expansion helps to explain super-bubbles with radii 200 ~ 1000 pc (Tomisaka et al. 1980).

Eventually the interstellar gas transported by the super-bubble will typically cool to form a dense cool *shell* around the cavity and were first observed with the H I 21cm emission line (Dopita & Sutherland 2001). Deharveng et al. (2010) give a thorough review of a sample of 102 bubbles and their associated shells where present. *Super-shells* are larger older objects, and are found around the cavities of several merged super-bubbles.

1.3 Active Star Formation Regions & Stellar Evolution

1.3.1 Pre-stellar Infrared Dark Cloud (IRDC) Cores

As explained in § 1.2, *molecular clouds* are the main sites of Galactic star formation and represent the coldest and densest form of the ISM. They form isolated structures which range from *Bok globules* (1 – 100 $M_\odot$; Clemens & Barvainis 1988), to *dark clouds* (10^3 – 10^4 $M_\odot$) to GMCs (10^5 – 10^6 $M_\odot$), the latter of which holds most of the Galactic molecular material (Weliachew & Lucas 1988) and ~1 % of the Galactic total mass (see Table 2.1).

Early studies (Carey et al. 1998, 2000 and Simon et al. 2006a,b) showed that the embryonic environment in star forming *dark* clouds is often dense (>10^5 cm^{-3}) and cold (< 25 K), with high molecular column ($N_{H2} > 10^{23}$ cm^{-2}) and volume ($n_{H2} > 10^4$ cm^{-3}) densities. GMCs are larger, warmer, and more massive and have higher velocity dispersions than dark clouds (see Table 1.1; Wilking 1996). Dark clouds are less highly excited star-formation regions and examples such as

G34.43_0.24 (Rathborne et al. 2005) and G11.11_0.12 (Carey et al. 2000; Pillai et al. 2006a) mark the sites of embedded proto-stars (§1.3.2) where the *maser phase* (a possible marker of star-formation activity; § 1.3.3) is often seen (Pillai et al. 2006b, Sridharan et al. 2002 and Chambers et al. 2007, 2008).

	Dark cloud complexes	GMCs
Mass	10^3–10^4 $M_\odot$	10^5–10^6 $M_\odot$
Size	10–20 pc	50–100 pc
Temp.	10-25 K	10-50 K
Velocity dispersions	1–2 km s^{-1}	2–4 km s^{-1}
	Dark cloud cores	**GMC cores**
Mass	0.3–10 $M_\odot$	5-500 $M_\odot$
Size	0.05–0.2 pc	0.1–1 pc
Density	10^4–10^5 cm^{-3}	10^4–10^6 cm^{-3}
Temp.	10 K	10–20 K
Velocity dispersions	0.2–0.4 km s^{-1}	0.6–2.5 km s^{-1}

Table 1.1: Molecular Cloud properties (Wilking 1996)

Clumps (§ 1.2) of dust and gas with typical masses of about 10^3 - 10^4 $M_\odot$ in regions extending ~ 2–5 pc across for GMCs (Sargent 1977, Evans 1978, Blitz 1978, Rowan-Robinson 1979) are located within molecular clouds and are distributed along larger filaments. Typically within GMCs clumps are very dense GMC *cores,* with typical sizes of ~ 0.1–1 pc, temperatures ~ 10–20 K and masses of ~ 5–500 $M_\odot$ (Table 1.1; Wilking 1996). In comparison, infrared dark cloud (IRDC) cores are smaller (~ 0.05-0.2 pc), cooler (~ 10 K), and less massive (~ 0.3–10 $M_\odot$) (Table 1.1; Wilking 1996). Pre-stellar cores emit almost all of their radiation in the far-IR/sub-mm/mm regimes (André et al. 2000) and the 800 μm study by Ward-Thompson et al. (1994) demonstrated that pre-stellar cores do not have single scale-free power law density profiles but rather flat inner radial density profiles, suggestive of magnetically-supported cores *contracting* by the still poorly understood mechanism of *ambipolar diffusion* (see Mouschovias 1995).

IRDC cores are *candidates* for active star formation (Deharveng et al. 2005) since not all IRDC cores have been seen to host the earliest stages of high-mass star formation in studies of molecular and *H_2O maser surveys* (§ 1.3.3) toward Northern (Vadaretto et al. 2001) and Southern (Vasyuina et al. 2009) star-formation regions. Hence an association with IRDC cores alone is not sufficient to guarantee whether or not maser emission will have started. Some cores rest in the pre-stellar stage (identified in observations by Bacmann et al. 2001 using the Infrared Space

Observatory, ISO) whilst others are in the proto-stellar phase before nuclear fusion ignites the core, enabling fully-fledged self-luminous YSOs. Properties of proto-stellar cores can differ, affecting high or low mass star formation (Myers 1986) and represent the *initial conditions* of star formation, the knowledge of which remains surprisingly poorly understood (Beuther et al. 2007 and Zinnecker & Yorke 2007), with details of *when* the interstellar masing phase first 'switches on' being almost completely unknown. There have been comparatively low maser detection rates towards many IRDCs (and 'starless' cores) from previous studies implying that these may mark an earlier stage of star-forming evolution *before* the switch-on of maser emission. In § 7 we investigate further how maser activity, an indicator of star formation, is connected to stellar evolution (see aims in § 7.1).

1.3.2 Proto-stellar Evolution & YSO Classification

Proto-stars are the embryonic first stages of star formation, enshrouded by hot dusty *envelopes* of gas and dust (which appear as diffuse 'blobs' as the dense molecular clouds collapse; § 1.2) and are numerous at far-IR wavelengths (indicative of their characteristic cold spectra; Dobashi et al. 1994). We conduct a census of these dusty envelopes (their distribution and properties of their dust components) in the W3/W4/W5 complex (§ 1.4) at far-IR wavelengths and locate the young proto-stars inside (§ 7) to probe the structure and distribution of active star forming sites and their relationship to their surroundings including subsequent ionisation of the surrounding diffuse gas which can in turn trigger (§ 1.2) further high and low mass star formation. Low mass stars are able to form in isolation (e.g. Herbig 1962), although it has been thought that they could go onto forming high mass stars in the process of *bimodal star formation* (see Shu et al. 1987). In comparison high mass stars from almost exclusively in *clusters* embedded in their parent GMCs (Lada & Lada 2003). The W3 GMC (see § 1.4 & § 7.4.2) in particular is a prime target for the study of the *early* stages of triggered high and low mass star-formation.

André et al. (2000) detail the classification criteria of proto-stars and YSOs from *Class 0* to *Class III* which can be distinguished based on the spectral index (the slope of their spectral energy, α distributions or SEDs in logarithmic scale; § 2.3.5) between wavelengths 2.2 μm and 10–25 μm:

$$\alpha = \frac{d\log(\lambda S_\lambda)}{d\log(\lambda)} \tag{1.1}$$

where λ is the wavelength and S_λ is the flux density at that wavelength. The boundaries were established by Lada (1987) as: $0 < \alpha \sim < 3$ for Class I, $-2 < \alpha \sim < 0$ for Class II and $-3 < \alpha \sim < -2$ for Class III. These criteria are explained by Lada & Wilking (1984) and Lada (1987) in terms of a proto-stellar evolutionary sequence where proto-stars represent the main accretion phase during which the central object builds up its mass, M_* from a surrounding in-falling envelope of mass $M_{\rm env}$ and/or an accretion disk of mass $M_{\rm disk}$, while progressively increasing in temperature.

Indirect evidence for a central YSO through detection of either a compact cm radio continuum source, a collimated CO molecular outflow, or an internal heating source distinguishes Class 0 proto-stars from pre-stellar cores which have no such compact radio continuum sources at their centres (Bontemps 1996 and Yun et al. 1996). The dominant mechanism for such radio emission is likely to be *thermal free-free Bremsstrahlung* (§ 2.2), although this remains to be investigated further (Scaife 2012); this is expanded in relation to our study in § 4.1.1. Radio emission is a reliable method for the detection of very young low luminosity YSOs (Class 0/I) where the source may be heavily embedded in its natal dust envelope (Scaife 2012).

Bolometric temperature

The *bolometric luminosity,* $L_{\rm bol}$ and *bolometric temperature*, $T_{\rm bol}$ of YSOs can be used to classify the evolutionary sequence of YSOs where the latter is a measure of the circumstellar obscuration and evolutionary development of the YSO (Myers & Ladd 1993). $T_{\rm bol}$ is defined as the temperature of a black-body with the same mean frequency as the source's observed SED:

$$T_{bol} \equiv [\zeta(4)/4\zeta(5)]\, h\nu/\, k = 1.25 \times 10^{-11} \langle \nu \rangle \; KHz^{-1} \tag{1.2}$$

where ζ(n) is the Riemann zeta function of argument n, h is Planck's constant, k is Boltzmann's constant, $\langle \nu \rangle$ is the mean frequency (defined in Eq. 1.3 below), S_ν is the flux density measured at frequency ν (Myers & Ladd 1993).

$$\langle \nu \rangle = \frac{\int \nu S_\nu \, d\nu}{\int S_\nu \, d\nu} \tag{1.3}$$

Chen et al. (1997) showed the distinctive ranges of T_{bol} for each YSO class with T_{bol} < 70 K for Class 0, T_{bol} = 70 – 650 K for Class I, T_{bol} = 650 – 2880 K for Class II, and T_{bol} > 2880 K for Class III.

The ratio between L_{submm} and L_{bol}

A more direct way to track the circumstellar evolution of YSOs is to use the circumstellar mass, $M_{c\star}$ (defined as the sum of M_{env} and M_{disk}) which can be derived from *submm continuum observations* of optically thin dust emission (André et al. 2000). Whilst being extremely faint in the optical and near-IR, Class 0 YSOs emit a significant amount of extended submm continuum emission and are characterised by a high ratio of submm luminosity, L_{submm} (measured long-ward of 350 μm) to bolometric luminosity, L_{bol} where $L_{submm}/L_{bol} > 5 \times 10^{-3}$ (André et al. 1993). Several condensations detected in submm dust continuum maps of molecular clouds appear to be associated with established Class 0 proto-stars (André et al. 1993). This indicates the presence of a circumstellar dust envelope whose mass *exceeds* that of the central stellar mass (André et al. 2000). Overall, the L_{submm}/L_{bol} ratio should roughly track the ratio M_{env}/M_{*} of envelope to stellar mass (as shown by André et al. 1993), and may be used as an evolutionary indicator for YSOs with $M_{env} \gg M_{*}$ for the youngest proto-stars Class 0/Class I (e.g. Terebey et al. 1993), decreasing with time by a factor ~ 5–10 on average from one YSO class to the next (André et al. 1994) for low-luminosity ($L_{bol} \lesssim 50\ L_{\odot}$) embedded YSOs (André et al. 2000).

L_{bol} is calculated by integrating over the full observed SED:

$$L_{bol} = \int_0^{\infty} 4\pi d^2 S_v dv \tag{1.4}$$

where d is the distance to the source (André et al. 1993). The submm luminosity is calculated by integrating over the observed SED for $\lambda \geq 350$ μm (André et al. 1993):

$$L_{submm} = \int_0^{v=c/350\ \mu m} 4\pi d^2 S_v dv \tag{1.5}$$

Young & Evans (2005) suggested the following boundaries for classifying protostars: L_{bol}/L_{submm} = 35 between prestellar cores and Class 0 YSOs, L_{bol}/L_{submm} = 175 between Class 0 and Class I YSOs, and $L_{bol}/L_{submm} \sim 2000$ between Class I and Class II.

The $L_{submm} - L_{bol}$ (and equivalent $M_{env} - L_{bol}$) diagram has been proposed by Saraceno et al. (1996) as an alternative method of monitoring the evolution of self-embedded YSOs. Reipurth et al. (1993) for example, showed how L_{submm} and M_{env} are well correlated with L_{bol} for the majority of embedded YSOs and essentially the ratio L_{bol}/M_{env} can also be used to constrain the evolution of YSOs.

Class I sources are relatively more evolved embedded sources compared with Class 0 sources, surrounded by *both* circumstellar *disks* and diffuse envelopes of substellar ($\lesssim$ 0.1–0.3 $M_{\odot}$) mass (Whitney & Hartmann 1993 and Lucas & Roche 1997). Whilst also being almost undetectable at optical wavelengths, Class I sources have SEDs that peak at mid-IR to far-IR wavelengths (André et al. 2000) since the density of their circumstellar envelopes are smaller compared to Class 0 sources, allowing much more stellar radiation to be observed. Class II YSOs are classical *T-Tauri* stars and have significant circumstellar disks where the whole envelope is usually dispersed with strong emission lines and substantial IR or UV radiation (André et al. 2000). Class III sources are weak T-Tauri stars and have weak or no emission lines since they are no longer accreting significant amounts of matter; they only have a very thin disk allowing their SEDs to look very similar from all viewing angles.

YSOs interact with their natal molecular cores through (i) mergers (ii) outflows believed to arise from all YSOs at the beginning of their lives (e.g. Lada 1985); and (iii) shocks (Bally & Zinnecker 2005) which are mentioned in § 1.2. The outflows from YSOs are believed to carry away the excess angular momentum of the in-falling matter (André et al. 2000) and their opening angles evolve from highly collimated (typically $\leq$ 0.5 rad for Class 0) to less collimated (Class I) finally reaching a wide-angle outflow from Class II objects (Scaife 2012).

1.3.3 Current Water Maser Surveys: Potential Indicators of Stellar Evolution

H_2O masers can provide a diagnostic to the evolutionary status of star-forming regions by

indicating their level of activity and are commonly observed towards massive star formation sites typically associated with and traced by radio continuum emission. Extensive pre-existing surveys of H_2O masers strongly link the maser phase to massive YSOs and H II regions and suggest a *threshold* below which maser activity may not yet have switched on. The *MOPRA HOPS* survey (Walsh et al. 2008) maps an unbiased selection of the southern Galactic plane for the presence of H_2O masers and other molecular tracers including OH masers. There is also the RMS survey of H_2O maser detection towards massive YSOs and compact H II regions (Urquhart et al. 2009), Bok globules (6 detections out of 207 positions in 6 clouds; Gomez et al. 2006), IRDCs (17 detections out of 140 clouds; Wang et al. 2006), and ATLASGAL sub-mm selected samples. Masers are *strongly* seen to be associated with *ultra-compact* (UC) H II regions, which are found around young massive stars (~ 2% of O stars are believed to spend their early lifetime in the UC H II region; Casassus et al. 2000) and have relatively short lifespans (~ a few 10^4 yr) before they become giant H II regions. Please refer to Scaife (2013) for the distinctive physical parameters (typical size, density and emission measure) of hyper-compact, ultra-compact, compact and classical H II regions. Observations toward 38 IRDCs with 140 compact cores, revealed an H_2O maser detection rate of 12% (Wang et al. 2006), compared to 67% toward UC H II regions (Churchwell et al. 1990), 43% towards high mass proto-stellar objects (Sridharan et al. 2002) and 27% from the RMS survey of massive young proto-stars (Urquhart et al. 2009). Extending to YSOs where the proto-stellar phase is more established, Furuya et al. (2001) showed H_2O maser detection rates towards *low-mass* Class I YSOs is ~ 40%, decreasing for Class II YSOs to only a few %, further signifying that the detection rate of masers may be an indicator of proto-stellar evolution.

In order to better understand the maser process (their point of switch-on, detection rates etc. in relation to the evolution of star formation sites) and characterise their relationship with radio/sub-mm sources and associated stellar-phenomena (e.g. outflows and dense gas cores*;* § 1.3.2) the latter of which can create conditions favourable to their emission (see § 7.2), it is necessary to search for their presence across a *wide range* of star formation environments (§ 7.3).

1.4 Introducing the W3/W4/W5 Complex

1.4.1 H II regions

As mentioned, emission nebulae associated with star formation are present near young O and B stars in the Galactic disk. These stars are immensely hot, emitting intense ultraviolet (UV) radiation, which ionise the surrounding material resulting in a photo-ionised plasma which is a source of electromagnetic (EM) emission as photons are re-emitted across a variety of frequencies, appearing as both compact or more extended sources that may have line and continuum spectra. H II regions directly surround the hot O and B stars which emit high-energy photons that ionise the H I, and so these *compact* plasmas have electron temperatures of typically 7,000 - 10,000 K (Kassim 1989).

As well as the H II regions which exist in the Hot Ionised Medium (HIM), the *Warm Ionised Medium (WIM)* is a region of the diffuse ionised ISM which is also associated with massive star formation regions. The WIM material is less dense than in classical H II clouds, and cooler since they are further away from the associated young hot ionising stars (Haffner 2010). The WIM is normally part of what is known as a *Photon Dominated Region (PDR),* since this medium is also irradiated by the photons from the hot massive stars. However these Far Ultraviolet (FUV) photons are lower in energy after managing to escape the inner hotter H II regions. The periphery of H II regions found in the PDR is more typically associated with ionised carbon, which has a lower ionisation potential than hydrogen (see § 2.4).

The W3, W4 as well as the nearby W5 regions, constitute a chain of giant H II regions running from West to East (Figure 1.1) and are visible at optical wavelengths by their associated ionising star clusters catalogued as IC 1795, IC 1805, and IC 1848. They were first observed by Westerhout in the 1950s during a survey of major Galactic radio sources; a survey which was able to uncover major H II regions and SNRs previously obscured by massive dust clouds at optical wavelengths (Westerhout 1958). These strong radio frequency generating regions are associated with the 'Heart and Soul' nebulae in the outer galaxy; suitably named because of their appearance at visual frequencies.

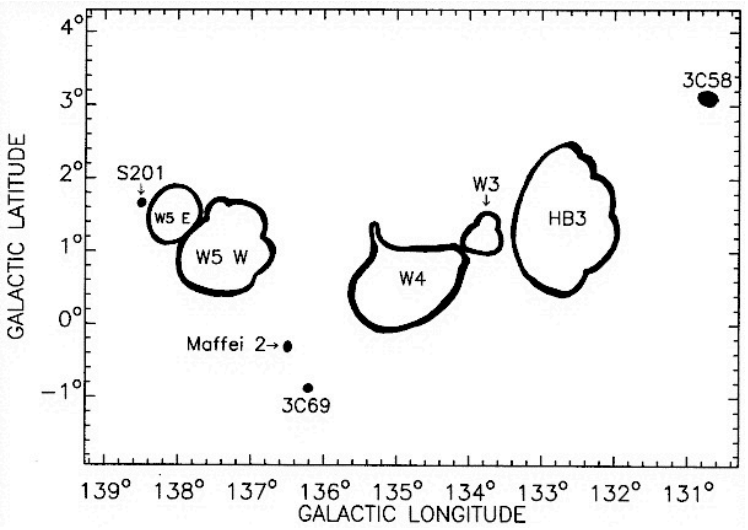

Figure 1.1: Sketch of the W3/W4/W5 complex and SNR HB3 with the main regions of continuum emission outlined. SNR 3C 58 and 2 strong extra-galactic sources 3C 69, and Maffei 2 are also shown (Normandeau et al. 2007).

W3/W4/W5 is understood to be a region where nearby star clusters can influence the causal triggering of the formation of newer massive star clusters (Ballantyne, Kerton, & Martin 2000). In fact, this region is believed to a three-generation system of hierarchical triggered star-formation by the shock waves of super-bubbles and mechanical feedback from massive stars (Oey et al. 2005). The succession started with clouds of initially cold neutral gas, fragmenting and condensing in numerous areas, giving rise to clusters of bright young ionising stars collectively known as the Cas OB6 association. The oldest clusters first formed in IC 1805 (embedded within in the heart of W4), which is one of the best-studied clusters in the Milky Way (Massey et al. 1995; Sung & Lee 1995). It contains 10 main sequence stars with masses between ~ 20−85 $M_{\odot}$ that were formed in the last 1−3 Myr (Mirabel et al. 2004) which have provided a continuous source of pressure from ionisation fronts and possibly stellar winds (Lada et al. 1978). However, the HR diagram of Massey et al. (1995) provides the possibility of an older population of stars in IC 1805, with ages ~10−20 Myr, although it is has not been established whether these stars belong to IC 1805 or to a foreground population.

The bright UV-radiating O and B type giants of Cas OB6 illuminate the chain of several giant molecular clouds (GMCs) (Oey et al. 2005). Observations at optical wavelengths centred on IC 1805 show a massive shell-like cavity of excavated gas, with an outer diameter of ~53 pc across, (Vallee et al 1979) which is the result of associated stellar winds from the comparatively older stars of IC 1805 which forced W4's expansion into the neighbouring smaller W3 region (~20pc in diameter; Oey et al 2005), initiating the most recent burst of young OB star formation there only

100,000 years ago (Dickel 1980; Thronson et al. 1985) and is the youngest of the 3 H II regions. This is an example of triggered star-formation at an ionisation shock front, as described earlier. IC 1795 represents these intermediate, second generation stars (Oey et al. 2005).

The W3 and W4 nebulae are physically connected by what seems like a large loop of diffuse emission ~1° in size (Kraemer et al. 2003). This 'bridge' between IC 1795 and IC 1805 is very clear in radio observations by Ballantyne, Kerton, & Martin (2000) as seen in Figure 1.2 and has been suggested to be the base of the well-known Perseus 'Chimney' (Normandeau et al. 1997).

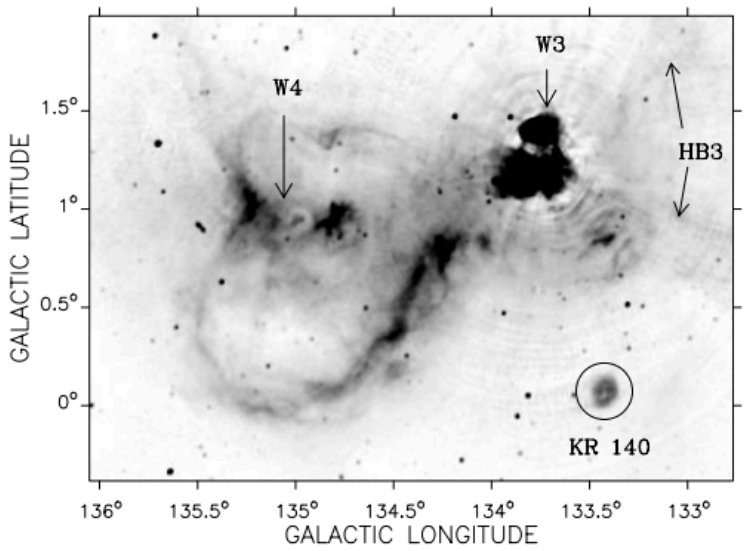

Figure 1.2: 1420 MHz continuum image of the W3/4 star-forming region and the HB3 supernova remnant (Ballantyne, Kerton & Martin 2000).

However, as mentioned above, this structure is also representative of a superbubble which is believed to have been blown out by generations of massive stars within W4 (Feigelson & Townsley 2008). It would be interesting to detail the structure and physical emission and absorption processes (§ 2.2.2 & § 2.2.4) within this W4 loop at frequencies < 100 MHz as well as at far-IR, to shed light on how young ionising stars physically interact with the ISM (see § 4.2.3 and § 7.6.1).

IC 1795 is small compared to neighbouring star clusters and borders one of the most massive molecular clouds known in the outer Milky Way (Heyer et al. 1998); this is the W3 molecular super-bubble (Oey et al. 2005). A *Spitzer* channel 4 mosaic of the W3 GMC featured in Rivera-Ingraham et al. (2011) details several IRDCs and filaments (§ 1.3.1) in the region. Studying molecular clouds themselves can prove to be difficult since their main constituent of H_2 is difficult to detect in the general ISM as the first rotationally excited state, $\Delta E \equiv E(J=2) - E(J=0) \sim 7.5 \times 10^{21}$ J corresponds to an excitation temperature of ~ 540 K. This is greatly in excess of the average ISM

temperature ~ 10 - 40 K (Donahue et al. 2011 & Dopita et al. 2001). However, the otherwise invisible, dense W3 molecular cloud was detected in CO radio emission; it has a CO mass of ~10^5 $M_\odot$ spread over a ~60 pc region determined by measurements of CO column density in radio frequency observations by Lada et al. (1978). More recent observations determine its mass at ~ 5 × 10^4 to 4 × 10^5 $M_\odot$ (Feigelson & Townsley 2008 and Polychroni et al. 2012). Ionised carbon in the WIM is a particularly important transition layer (as mentioned earlier) between fully ionised H II regions and the surrounding neutral molecular clouds (§ 2.4.3; Figure 2.14) and mapping the spatial distribution of its discrete emisison at low frequencies will help to better understand the dynamics of its parent molecular cloud, of which it closely matches (Kantharia & Anantharamaiah 2008). Essentially, the CO environment of the bubble envelope provides information about the molecular environment, the 3-dimentional morphology and column density of the material surrounding the bubbles (Deharveng et al. 2010).

Thermally excited carbon Radio Recombination Lines (RRLs) are numerous in the low frequency spectral band and particularly sensitive to the poorly understood PDR environment of which we are interested in (see § 2.4.4). A better PDR model can better understand the interaction of young high mass stars embedded within H II regions with the surrounding low density FUV-irradiated ISM. W3 has been studied well for its RRLs, and includes line surveys to determine electron temperatures of the H II regions (e.g. Wilson et al. 1979 and Kantharia et al. 1998) where a mean electron temperature of ~8000 K has been determined (Roelfsema & Goss 1991). Carbon lines have been detected towards W3 at a number of frequencies (indicating the presence of an associated C II region) and has allowed detailed models of the WIM/ Partially Ionised Medium (PIM) near W3 (e.g. Pankonin et al. 1977), although RRLs < 100 MHz remain unexplored. We attempt a low frequency carbon RRL (§ 2.4) detection with LOFAR in the direction of W3 and find that progress of our investigation is connected to LOFAR's continuing improvement in instrumentation and sensitivity (§ 5).

It is understood that the formation of IC 1795 in W3 created an ionisation shock front which compressed ambient molecular material in the W3 GMC creating gravitational instabilities in the post shocked gas. This in turn triggered the recent third-generation star-forming events which are embedded in regions W3-North, W3-Main (which is a combination of W3-West and the more

diffuse W3-East), and W3-OH to the south-east. These dominant bulges of ultra-compact H II regions are strong *thermal* radio sources (Oey et al. 2005) and are shown in Figure 1.3. The central part of W3 contains OH and H_2O masers (e.g. Harvey-Smith & Cohen 2006) which are potential diagnostics for star-formation activity; masers in the region are investigated in § 7.

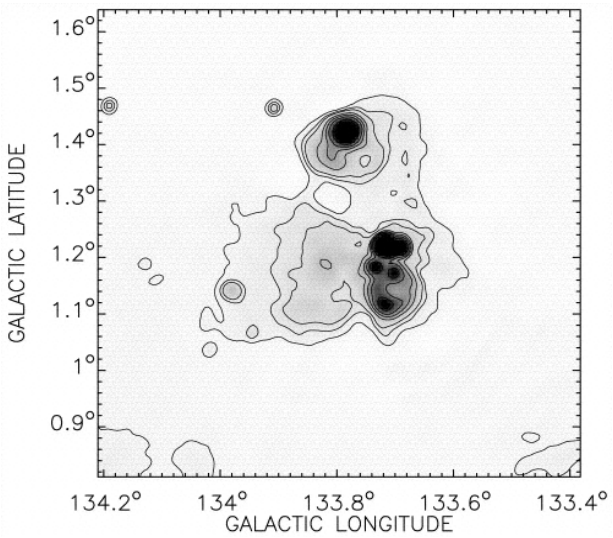

Figure 1.3: The W3 region at 1420 MHz with contrasts adjusted to enhance the structure, with the compact source in the north (W3-North) and group of bright sources in the south which constitute W3-main. W3-East contains more diffuse, extended emission (Normandeau et al. 1997).

The W5 nebula is more isolated and shows indications of triggered star formation on a smaller scale (Kaar & Martin 2003). LOFAR's large FoV should also be able to capture the W5 nebula, which has an elongated H II region extending 10 pc. W5-East is the eastern part of the W5 H II region (Figure 1.1) and is excited by the centrally located O7 V star BD+590578 (Niwa et al 2009). W5-West also constitutes the H II region to the west, and is ionised by four O stars, BD +590552, BD +590553, BD +590562, and BD +600586 (Kaar & Martin 2003). The expanding H II region strongly affects the morphology of the surrounding molecular clouds compressing them in regions observed as bright rims (Niwa et al. 2009). Kaar & Martin (2003) found that the timescale of interaction between the W5 H II region and molecular clouds was 0.5 – 1 Myr.

1.4.2 SNRs

The Galactic pulsar-powered supernova remnant SNR 3C 58, (originally classified as a pulsar wind nebula; Camilo et al. 2002) is also contained within our field. 3C 58 had been presumed to be the remnant of SN 1181, however Bietenholz (2006) negates this since the expansion rate of the radio nebula (a synchrotron bubble) corresponds to a relatively low speed of 630 ± 70kms^{-1} along the major axis; if 3C 58 was a remnant of SN1181, it would have been strongly decelerated, which is

unlikely given the absence of emissions from the supernova shell (Bietenholz 2006). Bright radio emission would be expected if the supernova ejecta had been decelerated. Such emission had not been observed in the 1.4 GHz VLA observations which are the highest quality radio images of this object to date (Bietenholz 2006). Alternatively this suggests, according to Bietenholz, that 3C 58 is far older at ~ several thousand years. We investigate the continuum emission and spectral index maps of 3C 58 in § 4.2.6.

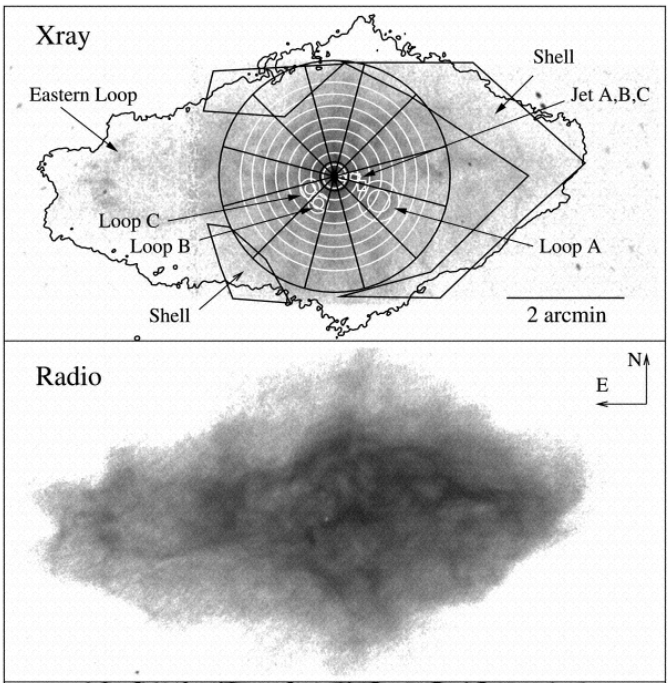

Figure 1.4: The top image is by the Chandra X-Ray Observatory of 3C 58 with the outermost radio contour overlaid. The bottom image is the VLA image (Reynolds & Aller, 1988). Virtually all of the filamentary structures observed in the X-ray image have counterparts in the radio image (Slane et al. 2004).

The pulsar of 3C 58, PSR J0205+6449, has been detected in X-rays with the Chandra X-ray telescope, as a central point-like source; a rapidly rotating neutron star (rotation period = 65.67895 ± 0.00001 ms) embedded in a compact cloud of high-energy particles, shown as an elongated torus with a curved jet erupting westwards (Murray et al. 2002). Additional intricate filamentary x-ray rings and loops are found in the SNR interior (Figure 1.4) which are the result of radiation from relativistic particles in a complex magnetic field. The comparison of the Chandra image with a radio image by Slane et al. (2004) as shown in Figure 1.4 revealed that the radio structures do coincide with each of the X-ray loops.

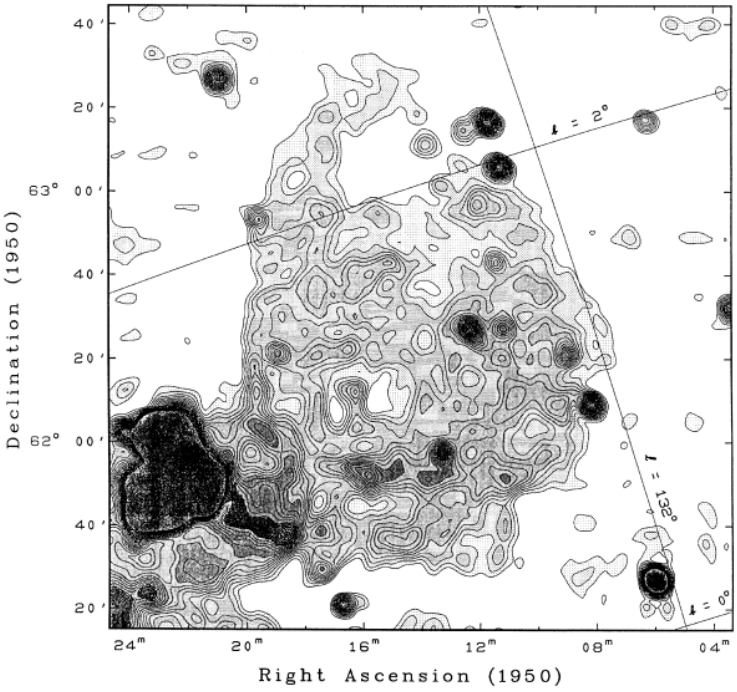

Figure 1.5: A 408 MHz emission map of HB3 in the centre and W3 in the lower left. Contours are 65 to 160 K in steps of 5 K (Landecker et al. 1987)

Located Northwest of W3, the large-scale shell-type SNR HB3 (G132.7+1.3) centred at RA 2h14m Dec 62°25′, has dimensions of 90 x 123 arcmin EW x NS as measured by Landecker et al. (1987). Assigning it a distance of 2.7 ± 0.3kpc (Goudis 1979) gives it a physical size of 71 x 97 pc; this large physical size for the irregular scalloped shell structure suggests a long evolution time at ~1.7×10^6 yr (Landecker et al. 1987). The non-thermal emission of HB3 made it a prominent radio source in the early long-wavelength radio surveys. Previously a difficult target due to its close proximity to W3, a very strong thermal source, new observations with adequate resolution and sensitivity allowed Landecker et al. (1987) to make better determinations of the extent of the large, irregular and comparatively low-level SNR at 408 MHz with the Dominion Radio Astrophysical Observatory (DRAO). Since it has been hard to separate HB3 from the W3 complex, estimating the background emission level in order to obtain an accurate integrated flux density of HB3 for a reliable spectral index (established as 0.60) has not been trivial. Tian & Leahy (2005) determined the spectral index as ~ -0.6, confirming previous studies e.g. Landecker et al. (1987) found -0.60 ± 0.04 and Fesen et al. (1995) found -0.64 ± 0.01.

We are interested in the interaction of the SNR shock waves with the ISM, and its subsequent evolution. HB3 interacts with the molecular gas in which W3 is embedded. Whilst some studies have found that HB3 is brighter on the side facing W3, there is no evidence for a direct interaction (Tian & Leahy 2005). Landecker et al. (1987) also studied a possible connection between HB3 and

W3 (Figure 1.5) although inadequate dynamic range made it challenging to separate thermal and non-thermal emission in the field. Normandeau et al. (1997) presented improved images of the field with mosaicked fields of the region also with the DRAO at 408 MHz, similar to Landecker et al. (1987), but with greater sensitivity (by overlapping several fields), revealing weaker emission features. 1420 MHz images were also created, constituting the highest resolution radio continuum observation to date of this SNR. LOFAR has the potential to reveal new details of a possible interaction between W3 and HB3 at very low radio frequencies (§ 1.4) and we examine this in §§ 4.2.4 & 4.2.5.

1.5 Advantages of Low Radio Frequency Studies

The use of low radio frequency observations of the ISM offers many unique opportunities compared to other regions of the EM spectrum, which drive our current scientific objectives as shall be explained in this section.

The Earth's atmosphere acts as a barrier to large section of the EM spectrum. LOFAR, the LOw Frequency Array is a large next-generation software-driven ground-based distributed radio telescope developed by ASTRON in the Netherlands (Best 2007), which capitalises on the 'atmospheric window' of permissible radio frequencies which can reach the Earth. For frequencies < 30 MHz, the ionosphere becomes increasingly impenetrable and < 10 MHz waves are reflected off the ionosphere which is effectively opaque (Wijnholds 2010). The highest range of radio frequencies are permissible before absorption effects become significant for shorter wavelengths. The details of LOFAR's unique instrumentation are presented in § 3.2 and examples of the core and international stations are shown in Figures 1.6 and 1.7. "Essentially LOFAR currently detects low radio frequencies between ~ 15 – 240 MHz, offering unprecedented angular resolution at these frequencies, and a sensitivity 2 – 3 orders of magnitude better than existing telescopes (§ 1.6) because of its large total effective collecting area reaching ~ 1 square km at its lowest frequencies (Röttgering et al. 2012).

Another advantage of low radio frequency studies is that a wide range of radio frequencies suffer no dust extinction (a combined effect of absorption and scattering of photons) during

propagation across the entire Galactic 30 kpc diameter, along the line of sight (LOS). In comparison optical wavelengths suffer extinction after approximately 1 – 2 kpc (Terzian et al. 2005). Please refer to Gordon et al. (2003) for a quantitative study of the Milky Way dust extinction curve (extinction coefficient as a function of wavelength). Absorption and scattering is most effective at wavelengths close to the size of the interstellar dust grains (typically ~ 100 nm) and therefore is most pronounced for UV radiation and negligible for comparatively longer radio wavelengths. Therefore, radio frequencies are an essential probe of dust-shrouded environments, particularly the Galactic centre and star-forming regions providing critical information on a Galactic scale.

Low radio frequency studies particularly offer powerful new diagnostics and unique insight into the ionised ISM (H II and WIM regions) allowing essential properties to be deduced which are not possible at higher frequencies, allowing radiation mechanisms related specifically to the scientific objects of interest for this project to be probed:

(i) Continuum spectra: H II regions and Cosmic Rays (CRs) emit radiation primarily by thermal free-free Bremsstrahlung and non-thermal synchrotron radiation, respectively, which can to first order, be inferred from their SEDs. Specifically free-free radio emission is generally not well observed at low frequencies < 10 GHz (please refer to Figure 2.10) in contrast to synchrotron radiation, which has a spectrum increasingly toward low RFs. It is also understood that *free-free absorption* (§ 2.3.9) by classical hot H II regions becomes more pronounced at low radio frequencies < 100 MHz; a mechanism we hope to probe.

(ii) Discrete Spectra: Radio Recombination Lines (RRLs) are numerous in the low frequency spectral band and originate from loosely bound electrons of Rydberg atoms (§ 2.4.2). Low frequency carbon RRLs (arising from atoms with very high principle quantum numbers) are sensitive to the poorly understood inhomogeneous PDR environment of which we are interested (see § 2.4). Below 120 MHz they turnover into absorption (see § 2.4.3) and the broadening of their features increases with higher principle quantum numbers, increasing accuracy of the diagnosis of their environment (please refer to Figure 5.1).

Finally, the lower range of the radio frequency spectrum is one the few spectral windows that still remain to be explored (Röttgering et al. 2012). LOFAR's unique design allows spectral flexibility and an instantaneous field of view of many tens of square degrees. This coupled with its unprecedented sensitivity and increased angular resolution at these low frequencies dramatically opens the territory of unexplored parameter space. As well as gaining unique insight into the parameter space of conditions within star forming regions allowing for critical properties to be deduced, serendipitous detection of new sources and phenomena are expected that perhaps may not have been possible at higher radio frequencies (Röttgering et al. 2010). These could include the discovery of new classes of rare extreme-spectrum sources and low-frequency spectral and temporal variables as well as mapping additional details of the structures of SNRs giving a better understanding of their underlying physics (Röttgering et al. 2010).

Figure 1.6: The Superterp core station in the Netherlands. Image from http://blog.lofar-uk.org/

Figure 1.7: The Chilbolton outstation capturing the Low Band Array (LBA) which collects 30 MHz < radio frequencies < 80 MHz and High Band Array (HBA) in the background which collects 120 MHz < radio frequencies < 240 MHz (de Vos et al. 2009). See § 3.2 for more information on instrumentation. Image from http://blog.lofar-uk.org/

1.6 Background of Low Frequency Galactic Plane Surveys

Karl Jansky first discovered extra-terrestrial radio waves accidently in 1932, when investigating a troublesome source of radio static described as '…a steady hiss type static of unknown origin' (Jansky 1933). In the 1940s, Grote Reber continued from Jansky's experiment creating the first prototype radio telescope dish to collect these waves. Consequently, Reber explored the sky at 160 MHz and found the direction of Sagittarius, Cygnus and Cassiopeia, to be the major emission regions (Figure 1.8). Since these two pioneers, numerous all-sky surveys have provided information about the distribution of radio intensity across the sky.

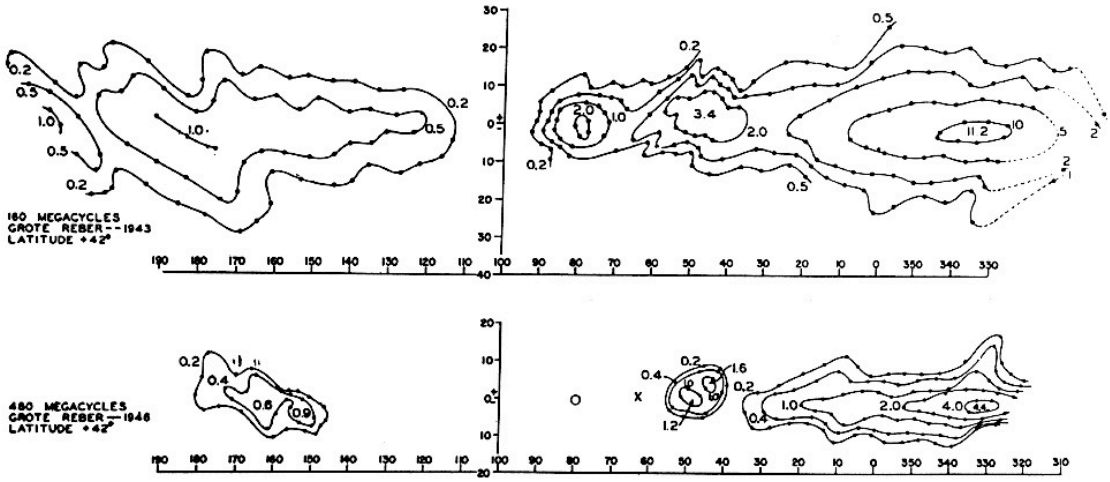

Figure 1.8: Reber's pioneering maps of our Galaxy capturing a large Field of View (FoV) of contours of constant intensity at 160 MHz (above) and 480 MHz (below) plotted in Galactic coordinates with the Galactic equator running horizontally. This was an important initial overview of Galactic emission (Reber 1949).

The 1950s provided many low radio frequency surveys between 100 - 400 MHz and the very first all-sky map was created at 200 MHz by Dröge & Priester (1956) combining Northern and Southern sky data. However, these early surveys were usually made with a poor angular resolution between 10º – 20º and had low sensitivity (Wielebinski 2003). They gave enough information to deduce that the highest intensity emission was emerging from the Galactic centre, as well as distinguishing emission along the plane.

The 1960s saw an improved angular resolution reaching ~ 1º due to availability of larger antennas. Galactic plane surveys were produced with a better dynamic range as a result of wider frequency coverage and better receiver sensitivity (Wielebinski 2003). These surveys emphasised

how absorption of synchrotron emission by H II regions becomes more pronounced at low frequencies (see § 2.3.9). The most recent investigation with radio frequencies < 100 MHz is principally from the VLA Low Frequency Sky Survey (VLSS) at 74 MHz (Nord et al. 2006) and the 8C survey from early Cambridge studies using the Cambridge Low-Frequency Synthesis Telescope (CLFST) at 38 MHz (Hales et al. 1995). Nord et al. (2006) explain how whilst sub-arc-minute resolution is possible with the VLSS, the surface brightness sensitivity is insufficient to detect H II regions in absorption (see § 2.3.9) on size scales much larger than a few arc-minutes, which *is theoretically* achievable using LOFAR (Kassim et al. 2004). Even though the VLA was not initially designed to operate at frequencies as low as 74 MHz, it did demonstrate the effectiveness of self-calibration techniques (§ 3.4.5) for lifting the constraints on poor angular resolution and consequently confusion-limited sensitivities on long-wavelength astronomy (Pihlström 2006). According to Kassim et al. (2004) the development of self-calibration has led to a quiet revolution in low-frequency radio interferometry, by finally allowing correction to previously intractable ionospheric phase distortions.

Inspired by the success of the VLSS at breaking through low radio frequency ionospheric effects through self-calibration, LOFAR was designed to reach more ambitious science goals where sub-milli-Janksy sensitivities and sub-arcsecond resolutions are advantageous (van Haarlem et al. 2013). LOFAR's potential collecting area of $\sim 10^6$ m^2 at its lowest operating frequencies and very long baselines ~ 1000s km, give this array a possible 2 - 3 orders of magnitude improvement than both the VLSS and 8C surveys in both sensitivity and angular resolution over confusion effects (Röttgering et al. 2011). Please see § 3.2 for the more technical details of LOFAR. The VLSS at 74 MHz reached at best a sensitivity ~30 mJy/beam and angular resolution of ~25″ with its modest collecting area of $\sim 10^3$ m^2. In comparison, LOFAR *could* reach sensitivities of < 1 mJy at 15 MHz and < 300 μJy at 150 MHz and resolutions of 8″ at 15 MHz and 0.8″ at 150 MHz (Kassim et al. 2004).

Such technical specifications allow the deepest all-sky radio source surveys at unprecedented low frequencies and constitute one of the LOFAR key science projects*:* the LOFAR Surveys Key science program (Best 2007). This particular project focuses on the collection and analysis of data from the first LOFAR surveys of the Galactic Northern radio sky at low radio frequencies < 100

MHz, targeting specific supernova remnants (SNRs) and H II regions embedded within high mass star forming regions (Röttgering et al. 2010) to achieve our scientific aims. These surveys were part of the commissioning process where on-going technical research helped obtain maps close to theoretical noise levels (Röttgering et al. 2012).

Chapter 2

The Fundamental Physics

2.1 Radiation Mechanisms of Accelerated Charges

This chapter describes the primary mechanisms of EM emission from Galactic regions relevant to this study. We can detect either the continuum or discrete spectra that result; these terms will be explained in the forthcoming §§ 2.2 and 2.3. Such spectra provide powerful diagnostics at low frequencies. The radiation mechanisms are either: (i) *thermal,* where energy from stars with high surface brightness temperatures thermally excite electrons in the surrounding nebulae and photo-ionise them, or (ii) *non-thermal,* e.g. the interaction of CR electrons with magnetic field regions.

2.1.1 Larmor's Formula: The Non-Relativistic Case

Maxwell's equations establish through careful treatment of retarded potentials, that the key to EM radiation production is the acceleration of electric charge. The classical treatment by Thompson (1906) (later revived by Longair 2011) also gives the same outcome, resulting in *Larmor's formula.* This formula provides the angular distribution of radiation intensity and shows the total power P, of emitted radiation in relation to acceleration $\dot{\boldsymbol{V}}$ of a single point charge, q (measured in elementary charge $e = 1.60217657 \times 10^{-19}$ C):

$$P = \frac{dE}{dt} = \frac{q^2 \dot{\boldsymbol{V}}^2}{4\pi c^3} \int \sin\theta^2 \, d\Omega = \frac{2q^2 \dot{\boldsymbol{V}}^2}{3c^3} \tag{2.1}$$

where c is the speed of light. Please refer to Rybicki & Lightman (1979) and Longair (2011) for more detailed derivations of this equation. It is also shown that the power (change in energy, dE per unit time, dt), per unit solid angle, $d\Omega$ is characteristic of a dipole pattern $\propto \sin\theta^2$: it follows no radiation is emitted along the direction of acceleration and the maximum is emitted perpendicular to the acceleration. It is important to note that (Eq. 2.1) does not take into account (i) relativistic effects (Larmor's formula is only valid in classical frames where $|\boldsymbol{V}| \ll c$ with respect to the radiating particle), and (ii) quantum mechanical effects (the equation incorrectly predicts that an electron would radiate away all of its kinetic energy and fall into nucleus) (Rybicki & Lightman 1979).

Since the force, $\boldsymbol{F}$ required to produce an acceleration of a particle of mass, m is $\boldsymbol{F} = m\dot{\boldsymbol{V}}$, by substituting acceleration $\dot{\boldsymbol{V}} = \boldsymbol{F}/m$ into (Eq. 2.1) it follows that the radiated power from an accelerated charge per unit solid angle varies with $\sim 1/m^2$. As a result, radiation from electrons is typically $\sim (m_P/m_e)^2 = 4$ x 10^6 stronger than radiation from protons, which are $\sim 2 \times 10^3$ times more massive. Therefore for radio emission, we generally assume electrons are the *only* particles important for emission (Shu 1991).

2.1.2 Larmor's Formula: The Relativistic Case

To calculate the total power of radiation emitted by a charged particle moving at nearly the speed of light with respect to the observer's frame, Larmor's formula is first used to calculate the power of radiation in the *particle's rest frame, P′*. This result is then relativistically corrected to the observer's frame using the Lorentz transformations (Rybicki & Lightman 1979), where the Lorentz factor, γ is:

$$\gamma = \frac{1}{\sqrt{1-\frac{\boldsymbol{V}^2}{c^2}}} \tag{2.2}$$

Acceleration, $\dot{\boldsymbol{V}}$ can be written in terms of components parallel and perpendicular to the velocity, $\dot{\boldsymbol{V}}_{\parallel}$ and $\dot{\boldsymbol{V}}_{\perp}$ respectively (please refer to Shu 1991 for more details). The final result is:

$$P = \frac{2q^2}{3c^3}\gamma^4(\dot{v}_\perp^2 + \gamma^2 \dot{v}_\parallel^2) \tag{2.3}$$

Whilst the exact form of the angular distribution of radiation is complex in the relativistic case, the essential detail is that the radiation will be strongly beamed in the forward direction into a cone of opening angle $\sim 1/\gamma$ and *the faster the particle travels*, the more the radiation is beamed in the forward direction (Rybicki & Lightman 1979). This is will be demonstrated further in § 2.3.2.

Whether relativistic or non-relativistic, Larmor's formula fundamentally demonstrates how accelerating charges radiate energy and is the basis for understanding the mechanisms of *free-free* and *synchrotron* emission from astrophysical sources. The difference in the energy, ΔE, gained or lost by the accelerated charge, results in the absorption or emission of a corresponding photon of frequency ν, and energy:

$$E_{Photon} = h\nu = E_f - E_i = \Delta E \tag{2.4}$$

where E_f is the final energy and E_i is the initial energy of the charge and h is Planck's constant (6.62606957×10^{-34} joule.second).

2.2 Continuum Spectra: Thermal Free-Free Bremsstrahlung

Plasmas are hot ionised gases and constitute the fourth state of matter after solids, liquids and gases. They exist at relatively high temperatures where the atoms have enough thermal kinetic energy for collisions between their components to result in electron loss i.e. ionisation. These free electrons are deflected electrostatically by the Coulomb force when encountering the numerous, positive ions, which are much more massive, hence relatively immobile. The force, $\boldsymbol{F}$ on an electron in the electrostatic field, $\boldsymbol{E}$ of one ion of charge Z, is:

$$\boldsymbol{F} = q\,\boldsymbol{E} \sim \frac{Ze^2}{\boldsymbol{X}^2} \tag{2.5}$$

where **X** is the distance between the electron and the ion. Taking the simple case of ions of singular protons (in the case of H II plasma), $\boldsymbol{F}$ varies $\sim e^2/\boldsymbol{X}^2$.

The resultant accelerated charges generate *free-free* or *thermal Bremsstrahlung* (braking) radiation according to Larmor's formula (Eq.s 2.1 & 2.2). To understand Bremsstrahlung, it is necessary to first use classical electromagnetics to obtain the overall behaviour by making use of Larmor's formula in the *dipole approximation.* Then quantum mechanics must be taken into account since photons of energies comparable to that of the emitting particle can be produced. This is done by introducing a correction or *Gaunt factor* into the classical formulae (Rybicki & Lightman 1979).

2.2.1 A Single Electron-Ion Encounter

The *dipole approximation* is valid for electron-proton Bremsstrahlung which is essentially the most significant interaction. The electrons and protons also have homologous interactions i.e. electron-electron and proton-proton, but do not emit radiation significantly since the dipole moment is proportional to the centre of mass giving an electric dipole of zero (if we consider each interaction as a isolated system, as detailed by Shu 1991). The accelerations of the 2 identical particles are equal in magnitude but opposite in direction, effectively cancelling out their respective radiated electric fields at large distances. The dipole approximation is detailed further by Rybicki & Lightman (1979).

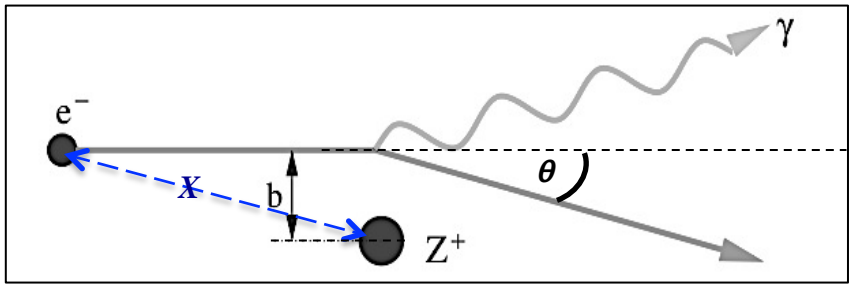

Figure 2.1. Electrostatic deflection of a free electron at a specific velocity by the Coulomb field of the heavier positive ion of charge resulting in Bremsstrahlung radiation (after Shu 1991).

Figure 2.1 shows the deviation of the straight-line path of an electron of specific velocity, $\boldsymbol{V}$, upon encounter of ion charge, Z by an angle, θ. Its acceleration (which results in radiation according to Larmor's formula, Eq. 2.1) depends on the electron's position vector $\boldsymbol{X}$ with respect to the ion, Z and $\boldsymbol{V}$. The impact parameter is $\boldsymbol{b}$ and is the distance of the closest approach of the encounter: it is related to $\boldsymbol{X}$ at time, t by:

$$\boldsymbol{X} = (\boldsymbol{b}^2 + \boldsymbol{V}^2 t^2)^{1/2} \qquad (2.6)$$

Equating the Coulomb force (Eq. 2.5) to $\boldsymbol{F} = m_e\dot{\boldsymbol{V}}$ where m_e is the electron mass and substituting $\boldsymbol{X}$ with (Eq. 2.6) gives the acceleration as a function of $\boldsymbol{b}$, $\boldsymbol{V}$ and Z:

$$\dot{\boldsymbol{V}} = \frac{Ze^2}{m_e(\boldsymbol{b}^2 + \boldsymbol{V}^2t^2)} \tag{2.7}$$

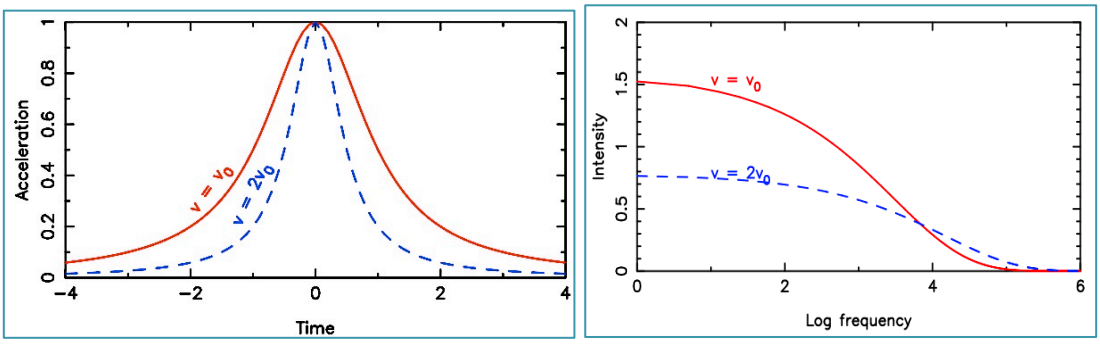

Figure 2.2. Bremsstrahlung: a single electron is accelerated by an ion (after Shu 1991).

The interaction between the electron and ion is a function of time (left graph of Figure 2.2) and is very short, lasting $\Delta t \sim 2\,\boldsymbol{b}/\boldsymbol{V}$. If we consider $\boldsymbol{X} \sim \boldsymbol{b}$ and Larmor's formula (Eq. 2.1), the total emitted energy in a single interaction becomes:

$$P\Delta t = \frac{2e^2}{3c^3}\left(\frac{Ze^2}{\mathrm{m}_e\boldsymbol{X}^2}\right)^2\frac{2\boldsymbol{b}}{\boldsymbol{V}} = \frac{4}{3}\frac{Z^2e^6}{c^3\mathrm{m}_e{}^2}\frac{1}{\boldsymbol{b}^3\boldsymbol{V}} \tag{2.8}$$

Hence radiation comes in pulses of duration, Δt and the spectral line profile is slightly asymmetric due to the decrease of the electron's velocity. This spectral distribution of radiated energy of the pulse can be obtained via the Fourier Transform (Parseval's Theorem), shown by the graph on the right of Figure 2.2. Since the time of the interaction is $\Delta t \sim 2\,\boldsymbol{b}/\boldsymbol{V}$, the highest frequencies in the spectrum are:

$$v_{max} \simeq \frac{1}{\Delta t} \approx \frac{\boldsymbol{V}}{2\boldsymbol{b}} \tag{2.9}$$

The intensity of the spectrum is flat up until this frequency, which is related to the kinetic energy of the electrons (Figure 2.3). This maximum frequency, v_{max} (or thermal cut-off) is much higher than radio frequencies and typically corresponds to infrared radiation. There is exponential decay in the intensity beyond v_{max}.

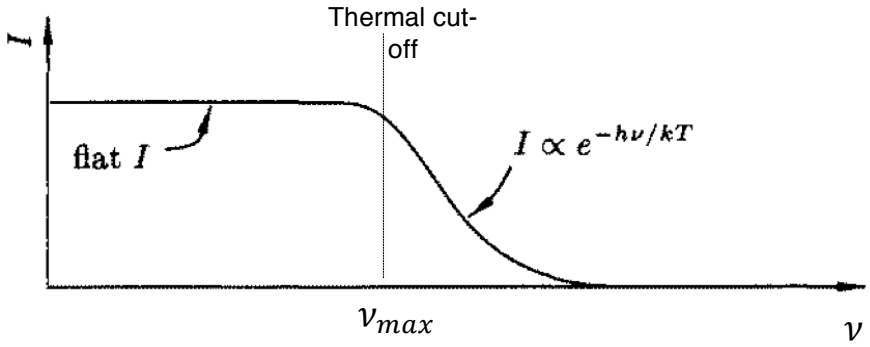

Figure 2.3. Behavior of thermal Bremsstrahlung intensity, I with variations of radiation frequency, ν. The spectrum is approximately flat at low frequencies, with a cutoff at $h\nu \approx kT$, where T is temperature, k is the Boltzmann constant and h is the Planck constant (after Shu 1991).

The radiated energy per unit frequency (assuming a flat spectrum where $\nu < \nu_{max}$) from a single event can be written as:

$$\frac{P\Delta t}{\Delta\nu} \approx \frac{P\Delta t}{\nu_{max}} = P(\Delta t)^2 \simeq \frac{8}{3}\frac{Z^2e^6}{c^3{m_e}^2}\frac{1}{\boldsymbol{b^2V^2}} \approx \frac{1}{\boldsymbol{b^2V^2}} \qquad (2.10)$$

Each acceleration produces a broad-spectrum radiation pattern along its direction of motion, *perpendicular* to its acceleration. A wide range of photons can be detected in continuum power spectra, from optical to radio wavelengths. Radio emission is due to relatively gentle, distant collisions of electrons with ions and in this weak scattering, the velocity vector, $\boldsymbol{V}$ changes little. In contrast, X-rays indicate head-on energetic collisions. Sources of Bremsstrahlung include H II regions (where $T \sim 10^4$ K) and accretion disks (around evolved stars and black holes). Bremsstrahlung is the main cooling process for plasmas at very high T ($> 10^7$ K) e.g. galactic hot-coronae and intergalactic gas in clusters and groups. Other sources of *radio* Bremsstrahlung radiation in particular, are *ionised winds and jets* (e.g. Gibb 1999) and powerful molecular *outflows* (Scaife 2012) arising from YSOs and are of relevance to our study (see § 4.1.1).

2.2.2 Considering Multiple Interactions

So far, only single electron-ion interactions have been considered. In reality the plasma has a number of ions of number density, n_i and free electrons of number density, n_e resulting in multiple interactions. In a unit time, each electron experiences a number of collisions with an impact

parameter between $\boldsymbol{b}$ and $\boldsymbol{b} + d\boldsymbol{b}$; this gives an area element around the ion of $2\pi\boldsymbol{b}\, d\boldsymbol{b}$. Therefore the total number of collisions, N between the ions and electrons within an increment of radius $d\boldsymbol{b}$ with respect to the ion is:

$$N = 2\pi n_e n_i \boldsymbol{V}\, \boldsymbol{b}\, d\boldsymbol{b} \tag{2.11}$$

Emissivity is the energy emitted, dE in time, dt, from volume, $d\mathbb{V}$, with a frequency interval, $d\nu$. To arrive at the total emissivity from the plasma (assuming all electrons are at the same velocity, $\boldsymbol{V}$), emitting via Bremsstrahlung, it is necessary to integrate (Eq. 2.11) over the range of impact parameters $\boldsymbol{b}$ (which in effect considers the multiplicity of ions):

$$\begin{aligned} J(\boldsymbol{V},\nu) = \frac{dE}{d\nu\, d\mathbb{V} dt} &= 2\pi n_e n_i \boldsymbol{V} \int_{b_{min}}^{b_{max}} \frac{8}{3} \frac{Z^2 e^6}{c^3 {m_e}^2} \frac{1}{\boldsymbol{b}^2 \boldsymbol{V}^2}\, \boldsymbol{b}\, d\boldsymbol{b} \\ &= \frac{16\pi e^6}{3c^3 {m_e}^2} \frac{1}{\boldsymbol{V}} n_e n_i Z^2\, ln\left(\frac{b_{max}}{b_{min}}\right) \\ &= \frac{16\pi e^6}{3c^3 {m_e}^2} \frac{1}{\boldsymbol{V}} n_e n_i\, Z^2\, \frac{\pi}{3^{\frac{1}{2}}} g_{ff} \end{aligned} \tag{2.12}$$

where the *Gaunt factor* for free-free transitions, $g_{\mathrm{ff}}(\nu, T, Z)$ is introduced as:

$$g_{\mathrm{ff}}(\nu, T, Z) = \frac{3^{\frac{1}{2}}}{\pi} ln\left(\frac{b_{max}}{b_{min}}\right) \tag{2.13}$$

This factor is a slowly varying function of the energy of the electron and of the frequency of the emission (Shu 1991). The *Gaunt factor* typically ranges from ~ 1 – 10 in the radio domain; essentially it characterises the distribution and energy cut-off for scattering in the thermal plasma (Scaife 2012). The physics is determined by setting b_{min} and b_{max} (see Rybicki & Lightman 1979 for more details). Typically, for any emission, there is a reasonable maximum impact parameter, where $b_{max} = \boldsymbol{V}/\nu$. For radio emission (where the collision energy is relatively low), the minimum impact parameter can be taken as for a 90° deflection, which occurs for $b_{min} = 4Ze^2/\pi m_e \boldsymbol{V}^2$. For higher-energy emission (i.e. X-rays, with head-on collisions), a smaller impact parameter should be taken (Rybicki & Lightman 1979).

(Eq. 2.12) considers multiple ions involved in each electron-ion encounter. The final step is to integrate the emissivity over a population of electrons, with a spread of velocities. In most cases for radio emission, this spread is taken to follow the thermal or *non-relativistic* Maxwellian distribution $f(\boldsymbol{V})$ which is a consequence of Local Thermal Equilibrium (LTE) (Spitzer 1998). This probability density function describes the probability per unit speed, of a particle of a gas (electron in this case), being within the velocity range from $\boldsymbol{V}$ to $\boldsymbol{V} + d\boldsymbol{V}$ and follows:

$$f(\boldsymbol{V})d\boldsymbol{V} = \left(\frac{m_e \boldsymbol{V}^2}{2kT}\right)^{\frac{3}{2}} e^{-\left(\frac{m_e \boldsymbol{V}^2}{2kT}\right)} 4\pi \boldsymbol{V}^2 d\boldsymbol{V} \tag{2.14}$$

where T is temperature measured in Kelvin, k is the Boltzmann constant and the factor of $4\pi d\boldsymbol{V}$ accounts for the entire solid angle, Ω. (Eq. 2.12) must be integrated over the electron velocity distribution to arrive at the total emissivity. We can place a lower limit for the velocity distribution, since in order to emit a photon of energy, $h\nu$ an electron needs a kinetic energy of at least:

$$\frac{1}{2} m_{\mathrm{e}} \boldsymbol{V}^2 \gg h\nu \quad \Longrightarrow \quad \boldsymbol{V}_{min} = \left(\frac{2h\nu}{m_{\mathrm{e}}}\right)^{1/2} \tag{2.15}$$

Taking (Eq. 2.12), n_e can then be replaced with $n_e(\boldsymbol{V}) = n_e f(\boldsymbol{V}) d\boldsymbol{V}$ and then integrated for a velocity range from $\boldsymbol{V}_{min}$ to ∞. This gives the total emissivity or emission coefficient of free-free transitions, J of electrons of density n_e interacting with ions of charge Ze and density n_i (Kwok 2007):

$$J(T,\nu) = \frac{dE}{d\upsilon \, d\mathbb{V} dt} = \int_{V_{min}}^{\infty} J(\boldsymbol{V},\upsilon) \, f(\boldsymbol{V}) d\boldsymbol{V}$$

$$= \frac{2^5 \pi e^6}{3 m_e c^3} \left(\frac{2\pi}{3k m_{\mathrm{e}}}\right)^{\frac{1}{2}} T^{-\frac{1}{2}} Z^2 n_e n_i e^{-\frac{h\nu}{kT}} \langle g_{ff} \rangle$$

$$= 6.8\times10^{-38} T^{-\frac{1}{2}} Z^2 n_e n_i e^{-\frac{h\nu}{kT}} \langle g_{ff} \rangle \; erg \; cm^{-3} S^{-1} Hz^{-1} \tag{2.16}$$

Here $\langle g_{ff}(T,\nu) \rangle$ is the *velocity averaged Gaunt* factor. The factor $T^{-1/2}$ comes from the fact that $dE/dvd\mathbb{V}dt \propto 1/\boldsymbol{V}$ (Eq. 2.12) and the temperature, T approximately follows the electron energy $\langle \boldsymbol{V} \rangle \propto T^{1/2}$ (see Rybicki & Lightman 1979).

The total emissivity, ε_{ff} is the total amount of energy radiated in Bremsstrahlung free-free transitions per second per cm^3 and is obtained by integrating (Eq. 2.16) over the whole frequency spectrum (Rybicki & Lightman 1979):

$$\varepsilon_{\text{ff}} = \frac{dE}{dt\, d\mathbb{V}} = \left(\frac{2\pi kT}{3m_e}\right)^{\frac{1}{2}} \frac{2^5\pi e^6}{3hm_e c^3} Z^2 n_e n_i \langle g_{ff}\rangle$$

$$= 1.426 \times 10^{-27} Z^2 n_e n_i T^{\frac{1}{2}} \langle g_{ff}\rangle \ erg\ cm^{-3} S^{-1} \qquad (2.17)$$

2.2.3 Relativistic Bremsstrahlung

When Bremsstrahlung is emitted in *relativistic* situations, ε_{ff} becomes:

$$\varepsilon_{\text{ff}} = \frac{dE}{dt\, d\mathbb{V}} = 1.426 \times 10^{-27} Z^2 n_e n_i T^{\frac{1}{2}} \langle g_{ff}\rangle\, (1 + 4.4 \times 10^{-10} T)\ erg\ cm^{-3} S^{-1} \qquad (2.18)$$

The second term bracketed is the relativistic correction to (Eq. 2.17) and the derivation is detailed by Rybicki & Lightman (1979). Situations where relativistic Bremsstrahlung can arise are solar flares for example (Dermer & Ramaty 1986).

2.2.4 Free-Free Self-Absorption

Just as there is an emissivity, J_ν in free-free transitions within the plasma, there is also a corresponding *absorption coefficient,* κ_ν where energy is absorbed by the free moving electrons. This is Kirchoff's Law which assumes a *black-body* model; an idealised medium in which all incident EM radiation is absorbed. At *thermal equilibrium,* TE (constant temperature), the black-body also emits all absorbed radiation at every frequency according to Planck's Law (Eq. 2.19) i.e. the spectrum shape is determined by temperature alone (and is independent of the material composition or shape of the body). B_ν is the spectral radiance of a black-body at frequency, ν and absolute kinetic temperature, T of the gas at thermodynamic equilibrium (Spitzer 1998):

$$B_\nu(T) = \frac{2h\nu^3}{c^2} \frac{1}{e^{h\nu/kT} - 1} \qquad (2.19)$$

where c is the speed of light, k is the Boltzmann constant. Continuing from Kirchoff's Law, the ratio of the coefficient of emission to the coefficient of absorption is equal to the Planck Function i.e.

$$J_\nu {}^*/_{\kappa_\nu} {}^* = B_\nu(T). \tag{2.20}$$

These coefficients are asterisked to denote their qualities are valid at Equivalent Thermodynamic Equilibrium (ETE), which is a state of TE occurring when collisions dominate interactions (please see Spitzer 1998 for more details). To arrive at κ_ν for radio waves, the emission coefficient (Eq. 2.16) and Planck black-body function (Eq. 2.19) substituted into (Eq. 2.20) gives the *absorption coefficient* κ_ν measured in cm^{-1}:

$$\begin{aligned}\kappa_\nu = \frac{J_\nu}{B_\nu(T)} &= \frac{4e^6}{3chm_e}\left(\frac{2\pi}{3km_e}\right)^{\frac{1}{2}} T^{-\frac{1}{2}} Z^2 n_e n_i \nu^{-3}\left(1 - e^{-h\nu/kT}\right)\langle g_{ff}\rangle \\ &= 3.7\times 10^8\, T^{-1/2} Z^2 n_e n_i \nu^{-3}\left(1 - e^{-h\nu/kT}\right)\langle g_{ff}\rangle\end{aligned} \tag{2.21}$$

κ_ν is measured in units of m^{-1} and is the fraction of intensity lost per unit distance. Plasmas such as H II regions, are typically described as optically thin (see definition below) for *high* frequencies, when $h\nu \gg kT$, creating a negligible exponential and $\kappa_\nu \propto \nu^{-3}$.

However, at *low* frequencies (typically radio frequencies) where $h\nu \ll kT$, such plasmas are *optically thick* (see definition below) and the spectral radiance, B_ν (Eq. 2.19) can be validly approximated by the *Rayleigh-Jeans law* (Spitzer 1998):

$$B_\nu(T) = \frac{2\nu^2 kT}{c^2} \tag{2.22}$$

and (Eq. 2.21) approximates to $\kappa_\nu \propto \nu^{-2}$ and numerically (Rybicki & Lightman 1979):

$$\kappa_\nu = 0.018\, T^{-3/2} Z^2 n_e n_i \nu^{-2}\langle g_{ff}\rangle \tag{2.23}$$

The radiative transfer equation is (Rybicki & Lightman 1979):

$$dI_\nu/_{ds} = -\kappa_\nu I_\nu + J_\nu \tag{2.24}$$

The emission coefficient represents the gain in intensity, dI_v and the absorption coefficient represents the loss in intensity as the beam travels distance ds. The optical depth, τ_ν is defined as (Rybicki & Lightman 1979):

$$d\tau_v = \kappa_\nu ds$$

$$\tau_v(s) = \int_{s_0}^{s} \kappa_\nu(s')ds' \tag{2.25}$$

A medium is optically thick (opaque) when $\tau_v > 1$ and optically thin (transparent) when $\tau_v < 1$. Therefore the intensity of a free-free emitting plasma with a specific optical depth can be described as:

$$I_v(\tau_v) = \frac{J_v}{k_v} + e^{-\tau_v}\left(I_v(0) - \frac{J_v}{k_v}\right) \tag{2.26}$$

It is common to represent (Eq. 2.26) above in terms of the source function, S_v:

$$S_v = \frac{J_v}{k_v} \tag{2.27}$$

If $I_v > J_v/k_v$ then I_v decreases along the ray and if $I_v < J_v/k_v$ then I_v increases along the ray. The intensity is trying to approach the value J_v/k_v and does successfully if it is given enough optical depth. In optically thick regions, the *Rosseland mean opacity* (Rybicki & Lightman 1979) of the free-free self-absorption coefficient, κ_{R} is defined by:

$$\left[\int dv \frac{dB_\nu}{dT}\right]\frac{1}{\kappa_{\mathrm{R}}} = \left[\int dv \frac{1}{\kappa_\nu}\frac{dB_\nu}{dT}\right] \tag{2.28}$$

which gives (in CGS units):

$$\kappa_{\mathrm{R}} = 1.7 \times 10^{-25} T^{-7/2} Z^2 n_e n_i \nu^{-2} \langle g_{ff} \rangle \tag{2.29}$$

The derivation of the pre-factor is detailed by Rybicki and Lightman (1979). The result $\kappa_{\mathrm{R}} \propto T^{-7/2}$ is known as *Kramer's Law*.

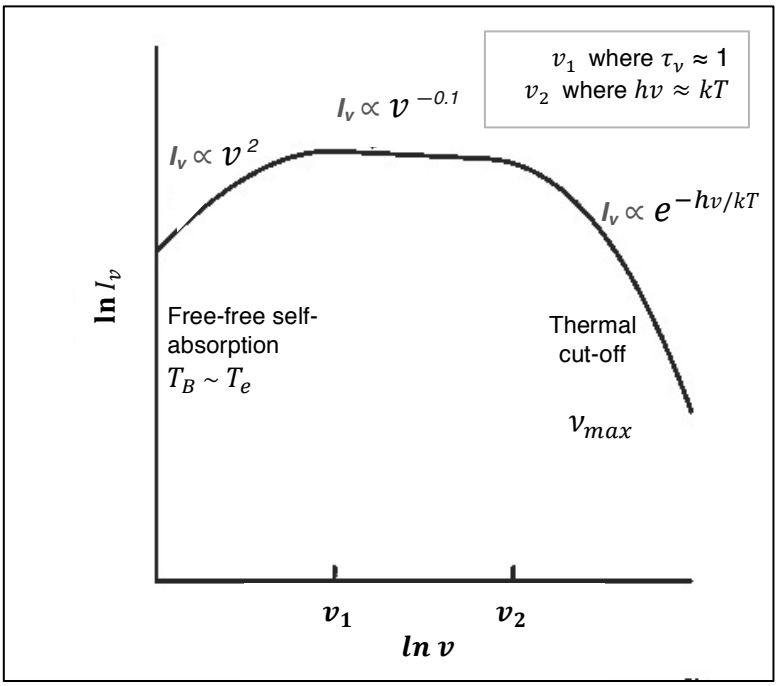

Figure 2.3: The free-free SED in the optically thin and optically thick regimes (after Longair 2011).

In summary, at low frequencies, $\tau_\nu \gg 1$ which gives $I_\nu \propto B_\nu(T_e) \propto \nu^2$ where T_e is the effective electron temperature (see § 2.2.1) and the spectrum is effectively black-body. With increasing frequency, the absorptivity and hence emissivity decrease approximately as $I_\nu \propto \nu^{-2}$. This situation eventually counteracts the ν^2 dependence of the Rayleigh-Jeans law (Eq 2.22), and thus the spectrum becomes *almost flat* and $\tau_\nu \ll 1$ which gives $I_\nu \propto \tau_\nu B_\nu(T_e) \propto \nu^{-0.1}$ (Scaife 2012) until ν_{max} is reached (Figure 2.3).

The radio emission from the Galactic ionised planetary nebula, *NGC7027* (Thompson 1974) of Figure 2.10 gives a real spectral example of free-free thermal Bremsstrahlung. At the low frequency end after ~10 GHz the nebula is opaque to its own radiation and is self-absorbed (Thompson, Moran, & Swenson 1991). Spectral turnover occurs when $\tau_\nu \approx 1$ and is ~1 GHz for the *Great Orion Nebula (NGC1976, M42)*, a well-studied H II region (Subrahmanyan et al. 2001).

2.3 Continuum Spectra: Non-Thermal Synchrotron

Despite the number of thermally radiating sources, the origin of most radiation in our Galaxy is actually non-thermal and produced by mechanisms independent of the temperature of the ISM components i.e. when relativistic charged particles from CRs encounter magnetic fields. We will concentrate on CR electrons, as it far easier for them to attain large values of γ, than for CR protons (Shu 1991). The magnetic field, **B** accelerates these free electrons in an analogous way to the deflection of the electrons by Coulomb electric fields of ions (free-free Bremsstrahlung). The result is *synchrotron* or *magneto-Bremsstrahlung* radiation.

2.3.1 Gyro-Emission & the Motion of the Electron

The Lorentz force is fully expressed as:

$$\boldsymbol{F} = q\boldsymbol{E} + (q/c)\,\boldsymbol{V} \times \boldsymbol{B} \tag{2.30}$$

Looking at the magnetic part of the Lorentz force only for a CR electron in a uniform magnetic field, **B**, with velocity, $\boldsymbol{V}$, and considering the relativistic equation of motion (Rybicki & Lightman 1979) we have:

$$\frac{d\boldsymbol{\rho}}{dt} = \frac{d\gamma m_e \boldsymbol{V}}{dt} = \frac{e}{c}\,\boldsymbol{V} \times \boldsymbol{B} \tag{2.31}$$

where the relativistic momentum is $\boldsymbol{\rho} = \gamma m_e \boldsymbol{V}$. Since $\boldsymbol{V}$ x $\boldsymbol{B}$ is in the plane perpendicular to both $\boldsymbol{V}$ and $\boldsymbol{B}$, so is the electron's acceleration. Hence:

$$\frac{d\boldsymbol{V}_{\parallel}}{dt} = 0 \qquad \frac{d\boldsymbol{V}_{\perp}}{dt} = \dot{\boldsymbol{V}_{\perp}} = \frac{e}{\gamma m_e c}\boldsymbol{V}_{\perp} \times \boldsymbol{B} \tag{2.32}$$

The constant perpendicular force means the CR electrons will move in a circular or helix path (if uniform forward propagation is present), around the magnetic lines of force (Figure 2.4).

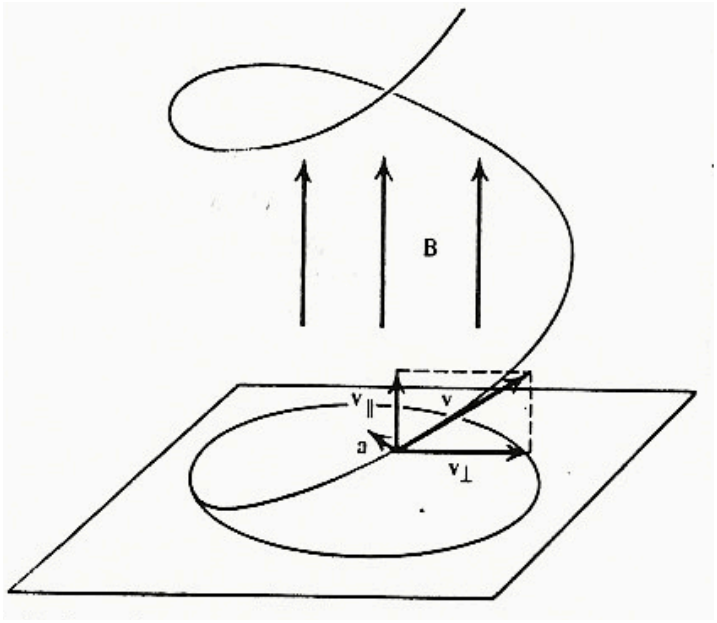

Figure 2.4. Deflection of a CR electron by the Galactic magnetic field, B results in emission of EM radiation. The velocity of the charged particle, **V** can be separated into parallel and perpendicular components, $V_{\|}$ and $V_{\perp}$ which in the relativistic case follow Eq. 2.3 (Rybicki & Lightman 1979*)*.

From the relativistic Larmor formula (Eq. 2.3) the power radiated will be:

$$P = \frac{2q^2\dot{\boldsymbol{V}}^2}{3c^3} = \left(\frac{2e^2}{3c^3}\right)\gamma^4\left(\frac{B^2e^2}{\gamma^2 m_e{}^2c^2}\right)\boldsymbol{V}_\perp{}^2 \qquad (2.33)$$

When the charged particle's velocity is much lower than the speed of light ($\boldsymbol{V} \ll$ c), the result is *cyclotron radiation*. In this case the frequency of emission, is merely the frequency of *gyration* of the rotational helical motion in the magnetic field or *Larmor frequency*, ω_L and is independent of the electron velocity, which is:

$$\dot{\boldsymbol{V}}_\perp = \omega_L \boldsymbol{V}_\perp = \omega_L \boldsymbol{V} sin\varphi \qquad (2.34)$$

where φ is the angle between $\boldsymbol{V}$ and **B.** The Larmor frequency depends only on the magnetic field strength where:

$$\omega_L = 2\pi\, \upsilon_L = \frac{\boldsymbol{B}e}{m_e c} \qquad (|\boldsymbol{V}| \ll c) \qquad (2.35)$$

When viewed from afar, the sinusoidal radiated power (following the Larmor formula of Eq. 2.1) from a single electron has a fixed gyro-frequency of:

$$\upsilon_L = \frac{\boldsymbol{B}e}{2\pi m_e c} = 2.8 \text{ x } 10^6\, \boldsymbol{B} \text{ Hz} \qquad (2.36)$$

which measures as one peak in the SED.

2.3.2 Radiation Beaming From Relativistic Motion

Only when the charged particles are ultra-relativistic ($|\boldsymbol{V}|$~ c), they emit a much stronger form of cyclotron of gyration frequency, ω_B when they encounter magnetic fields in the Milky Way:

$$\omega_B = \frac{\omega_L}{\gamma} = \frac{\boldsymbol{B}e}{\gamma m_e c} \tag{2.37}$$

The relativistic effect comes in and changes the Larmor sinusoidal dipole pattern to an asymmetric shape, the severity of which depends on how close $|\boldsymbol{V}|$ is to c. A good overview of this effect is given by Dulk (1985), which includes *gyro-resonance* and *gyro-synchrotron radiation* at slight and mild relativistic speeds respectively. In the case of *synchrotron radiation,* the highly relativistic speeds cause the forward lobe to become a narrow beam of emission following a cone of opening angle $\Delta\theta \sim 1/\gamma$ (Figure 2.5). Due to these relativistic beaming effects, the emitted synchrotron radiation is strongly beamed along the direction of motion, as described in § 2.1.

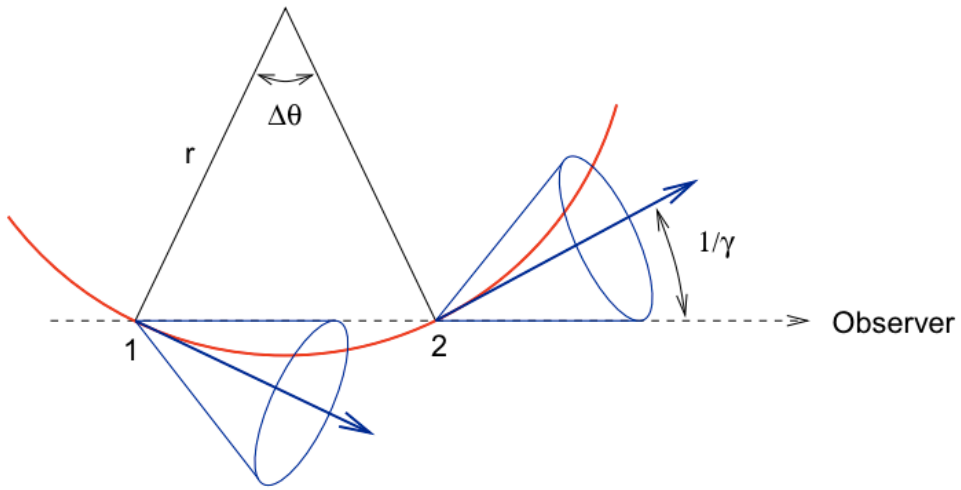

Figure 2.5. Beaming of radiation: the observer detects the cones of emission at points 1 and 2 arising from the circular trajectory of an ultra relativistic electron accelerated by a magnetic field pointing into the plane of the paper (Rybicki & Lightman 1979).

2.3.3 The Doppler Effect for Synchrotron Radiation

From the observer's frame, the Doppler effect takes place since the electron is closer at point 2, than point 1 (Figure 2.5) during the time interval Δt. Hence, the observed pulse duration, $\mathbb{T}$, from the observer's frame is:

$$\mathbb{T} = \left(1 - \frac{\boldsymbol{V}}{c}\right)\Delta t = (1 - \beta)\Delta t \tag{2.38}$$

where $\beta = \boldsymbol{V}/c$. In the *electron's frame of rest*, the beam passes observer during time:

$$\Delta t = \frac{\Delta\theta}{\omega_B} = \frac{\gamma m_e c}{\boldsymbol{B}e}\frac{2}{\gamma} = \frac{2}{\omega_L} \tag{2.39}$$

For more details of the geometry of (Eq. 2.39) please refer to Rybicki & Lightman (1979). At ultra-relativistic speeds, using the limit $|\boldsymbol{V}| \rightarrow c$, and $\beta = \boldsymbol{V}/c \sim 1$, $\mathbb{T}$ becomes:

$$\mathbb{T} = \left(1 - \frac{\boldsymbol{V}}{c}\right)\Delta t = \left(1 - \frac{\boldsymbol{V}}{c}\right)\frac{1+\boldsymbol{V}/c}{1+\boldsymbol{V}/c}\Delta t = \frac{1-\boldsymbol{V}^2/c^2}{1+\beta}\Delta t \approx \frac{1}{2\,\gamma^2}\Delta t = \frac{1}{\gamma^2\omega_L} \tag{2.40}$$

Hence, the Doppler effect causes a further 'sharpening' of the received pulses by a factor of γ^{-2} in the time domain and the characteristic frequency of synchrotron radiation, ω_{Sync} is given by:

$$\omega_{Sync} = \gamma^2\omega_L = \gamma^3\omega_B = \frac{\boldsymbol{B}e}{m_e c}\left(\frac{\boldsymbol{E}}{m_e c^2}\right)^2 \qquad (|\boldsymbol{V}| \sim c) \tag{2.41}$$

As a consequence, the observer detects narrow gyration pulses of emission from points 1 and 2 of Figure 2.5 along the particle's path. *Each pulse* lasts a short duration of $\Delta t \ll \Delta t_L$, where $\Delta t_L = 2\pi/\omega_L$ is merely the cyclotron period at the rest frame of the electron. The difference is by a factor of γ^2 (or a factor of γ^3 from the beamed time interval, $t_B = 2\pi/\omega_B$ as shown in Figure 2.6). The very short pulses result in a more complex and broadband frequency spectrum, spreading to many times the cyclotron frequency υ_L, which is the highest frequency in the regime. This is an essential feature of synchrotron radiation. In effect, the synchrotron pulse containing countless harmonics of the cyclotron line υ_L (Eq. 2.36) (Rybicki & Lightman 1979).

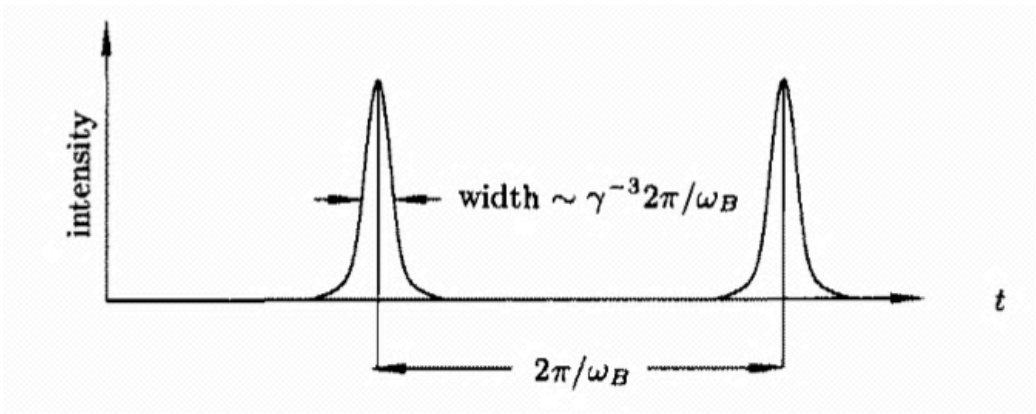

Figure 2.6. The temporal structure of received pulses: The effects seen are (1) angular relativistic beaming of synchrotron radiation and (2) Doppler effect on the time interval of the pulses from the rest frame of the electron, Δt and that of the observer, $\mathbb{T}$ (Shu 1991).

2.3.4 Radiated Power

Working from Larmor's formula (Eq. 2.1) and the assumption of an isotropic mono-energetic velocity distribution of the relativistic CR electrons, Rybicki & Lightman (1979) detail the derivation of the *average emitted power,* $\langle P \rangle$ of a single electron in a B-field, by averaging Larmor's formula over all angles, at any given Lorentz factor γ, or speed $\beta = \boldsymbol{V}/c$:

$$\langle P_\nu(\gamma) \rangle = \frac{4}{3}\beta^2\gamma^2 c\sigma_T U_B \emptyset_\nu(\gamma) \tag{2.42}$$

where the magnetic field density is $U_B = B^2/8\pi$, the Thompson cross-section is $\sigma_T = 8\pi e^2/(3m_e^2c^4)$ and $\emptyset_\nu(\gamma)$ represents the frequency distribution. This is essentially a spectral energy distribution (SED), P_ν of a single electron of total energy, $E = \gamma m_e c^2$. Substituting this into (Eq. 2.42) yields that $\langle P \rangle \propto E^2 U_B$. Also, since $\langle P \rangle \propto \sigma_T \propto {m_e}^2$, there is further proof that synchrotron radiation from charged particles with larger mass, such as protons, is negligible.

The spectral *shape* of the above SED is described by the frequency distribution of received radiation from a collection of electrons with a single value of γ is:

$$\int \emptyset_\nu(\gamma)\, d\nu = 1 \tag{2.43}$$

which is the normalisiation condition.

2.3.5 Integration Over the Electron Distribution

There is however a distribution of electrons of various energies, where $n(\gamma)$ is the number electron density with energies between γ and $d\gamma$. The emitted spectrum is found by properly weighting the contributions of these different electron energies, which in the case on non-thermal synchrotron radiation, follows the power-law distribution:

$$n(\gamma)\, d\gamma = n_0 \gamma^{-p} d\gamma \tag{2.44}$$

where p is the particle (electron) exponent or spectral power law index. This value determines the electron energy spectrum distribution and is typically ~ 2.5 (Shu 1991). Since $E = \gamma m_e c^2$ (Eq. 2.44) can also be written as:

$$n(E)\, d\gamma = n_0 E^{-p} dE \tag{2.45}$$

where $n(E)$ is the number electron density with energies between E and dE. Hence the spectrum or total emitted power at frequency, ν is merely the superposition of the contributions of various electrons each emitting its own individual electron spectra:

$$P_\nu = \int_1^\infty \langle P_\nu(\gamma) \rangle\, n(\gamma) d\gamma = 1 \tag{2.46}$$

Following the careful derivation by Shu, (1991), of (Eq. 2.46) in the ultra-relativistic limit $\boldsymbol{V} \rightarrow c$, and $\beta = \boldsymbol{V}/c \sim 1$, the following is attained:

$$P_\nu = \frac{2}{3} c \sigma_T \frac{U_B}{\nu_L} \left(\frac{\nu}{\nu_L}\right)^{-(p-1)/2} \tag{2.47}$$

This spectrum follows a power-law demonstrated in Figure 2.7 (Shu 1991) where the spectral index of the observed radiation, α is $\alpha = -(p-1)/2$. Usually α ~ -0.7 − -0.8 at GHz frequencies which implies p ~2.5 − 2.6 at GeV (Miley 1980). This spectral index is typical for many radio synchrotron sources that are *optically thin* (please refer to § 2.2.4*)*. Hence (Eq. 2.47) can be simplified to:

$$P(v) \propto v^\alpha \tag{2.48}$$

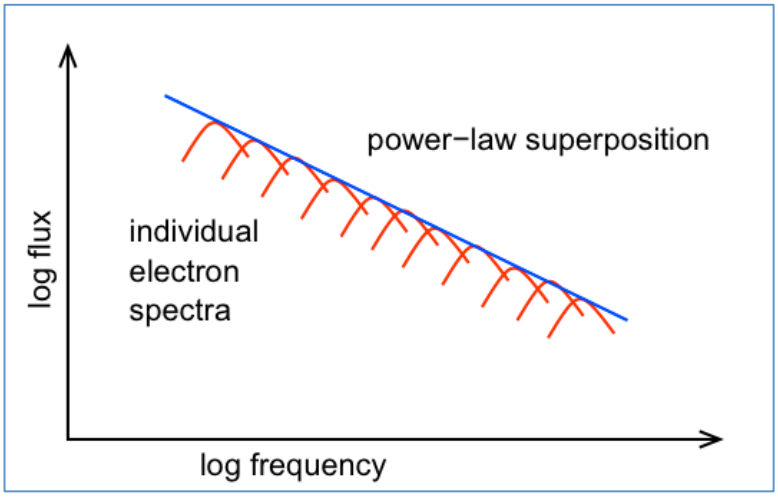

Figure 2.7: The spectrum has a spectral index of $-(\mathrm{p}-1)/2$ which depends on the superposition of individual electron spectra. The energy distribution of each electron follows the power-law $\gamma^{-\mathrm{p}}$ with a Lorentz factor γ (after Shu 1991).

2.3.6 Energetics of a Radio Source

The energetics of radio sources are important and relate to both the source-production mechanism (as detailed earlier) as well as the how radio sources are held together or confined within a volume, $\mathbb{V}$ (Miley 1980). Overall the presence of Galactic synchrotron radiation is indicative of CR electrons with a particular energy density, U_e in the presence of a particular interstellar magnetic field strength, $\boldsymbol{B}$ whose energy density, U_B is contained within a source volume, $\mathbb{V}$.

Following from (Eq. 2.47) the measured intensity of monochromatic *Synchrotron Volume Emissivity, I* at a particular frequency, ν approximately follows:

$$I_\nu \sim N_e \boldsymbol{B}_{\perp tot}{}^{(p+1)/2} \nu^{-(p-1)/2} \tag{2.49}$$

This emissivity formula essentially gives the power emitted from a unit volume, $\mathbb{V}$, per unit frequency interval and per unit solid angle where $\boldsymbol{B}_{\perp tot}$ is the *total transverse* magnetic field i.e. the strength of the total Galactic magnetic field component in the sky plane perpendicular to the line of sight (LOS; Giovannini 2004). The total magnetic field energy contained in the source volume is given by:

$$E_{B\,tot} = U_B F \mathbb{V} = \frac{\boldsymbol{B}^2}{8\pi} F \mathbb{V} \tag{2.50}$$

where F is the fraction of the source volume occupied by the magnetic field (filling factor). Determination of the strength of $\boldsymbol{B}_{\perp tot}$ from the measured synchrotron intensity, I requires reliable data about the number density of the CR electrons, N_e which can be gathered via

their gamma-ray Bremsstrahlung emission with interstellar hydrogen nuclei or alternatively X-ray emission by inverse Compton scattering (Beck 2005). The gamma-ray emissivity depends on N_e and also the interstellar hydrogen density, whilst synchrotron radio emissivity depends on the same N_e and $\boldsymbol{B}_{\perp tot}$. Using measurements from low energy *gamma-ray* data and comparing it with low frequency radio data, would give a reliant and *independent* value for the CR electron density. From this, we could solve for $\boldsymbol{B}_{\perp tot}$ (and also hydrogen density) (Jones & Weiler 1995). Direct measurements of the CR energy density, U_{CR} (which is the sum of the energy densities in electrons, U_e and protons, U_p) exist directly outside the Earth's atmosphere, from measurements by the *Voyager* and *Pioneer* spacecraft.

If such data are absent, an assumption about the relation between CR electrons and magnetic fields has to be made (Beck 2005). The most commonly used approach is to set the total energy density, U_{tot} of the synchrotron source at a minimum, where $U_{tot} = U_{CR} + U_B = U_e + U_p + U_B$. 'Invisible'" protons and heavier ions may emit negligible synchrotron power but they still contribute to the CR particle energy with U_p. The ion/electron energy ratio is denoted as K (Longair 2011). Therefore $U_{CR} = (1 + K)\, U_e$ and the total energy density of both CRs and magnetic fields is:

$$U_{tot} = (1 + K)\, U_e + U_B \tag{2.51}$$

At the condition of minimum energy, the ratio of relativistic cosmic-ray particle energy to magnetic field energy is

$$U_{CR}/U_B = (1 + K)\, U_e/U_B = 4/3 \tag{2.52}$$

and implies *near equipartition* of the contributions of the magnetic field and the relativistic particles to the energy. The classical derivation of this assumption is carefully detailed by Pacholczyk (1970) and Longair (2011). This assumption gives a practical estimate for the strength of $\boldsymbol{B}_{\perp tot}$ without a-priori knowledge of U_{CR}. For a region in a synchrotron radio source the minimum magnetic field density energy density can be written as (Miley 1980):

$$U_{B_{min}} = \left(\frac{7}{3}\right)\left(\frac{B_{min}^2}{8\pi}\right) = 0.0928\, B_{min}^2\ erg\ cm^{-3} \tag{2.53}$$

The strength of the corresponding magnetic field is (Miley 1980):

$$B_{min} = 5.69 \text{ x } 10^{-5} \left[\frac{1+K}{F} (1+\mathbb{Z})^{3-\alpha} \frac{1}{\vartheta_x \vartheta_y s \, sin^{3/2}\theta} \frac{\mathbb{F}_0}{v_0^{\alpha}} \frac{v_2^{\alpha+1/2} - v_1^{\alpha+1/2}}{\alpha+1/2} \right]^{2/7} gauss \qquad (2.54)$$

where K is the ratio of energy in the heavy particles to that in the electrons (it is usual to assume that heavy particles can be neglected, so that K = 1); F is the filling factor of the emitting regions (we assume that all of the volume is emitting radiation, in which case F=1); $\mathbb{Z}$ is the redshift; ϑ_x and ϑ_y (arcsec) corresponds to the source sizes or to the equivalent beam widths; s (kpc) is the path length through the source in the line of sight (LOS) (we usually assume cylindrical symmetry, so s is the same to the source width as projected onto the plane of the sky); θ is the pitch angle between the uniform magnetic field $\boldsymbol{B}$ and the LOS; $\mathbb{F}_{\mathbf{0}}$ (Jy or Jy per beam) is the flux density or brightness of the emitting region at frequency v_0 (GHz); v_1 and v_2 (GHz) are the assumed upper and lower cut off frequencies for the radio spectrum, and α is the spectral index of the radiation (Eq. 2.48) between for frequencies between v_1 and v_2 (Miley 1980).

However, this classical textbook approach to the minimum-energy formula (~ equipartition) does not always hold true. It has been shown to be inaccurate by Beck & Krause (2005) and empirically, Chi & Wolfendale (1993) show how whilst equipartition seems valid for the Milky Way, it does not hold true in Magellanic Clouds. Longair (2011) shows how the value for U_{CR} is determined by replacing the integral $E_{min} \rightarrow E_{max}$ with $v_{min} \rightarrow v_{max}$ which is typically 10 MHz → 10 GHz, in the range accessible to radio observations by using the relationship:

$$E_{max} = \left(\frac{v_{max}}{C\,\boldsymbol{B}}\right)^{1/2} \qquad E_{min} = \left(\frac{v_{min}}{C\,\boldsymbol{B}}\right)^{1/2} \qquad (2.55)$$

where the constant, C = 1.22 x 10^{10}/($m_e c^2$)^2. By doing so, an additional term is introduced that has dependence on $\boldsymbol{B}$. This means that the total energy density U_{tot} depends on a constant power of $\boldsymbol{B}$ and deriving the minimum U_{tot} leads to an inaccurate exponent dependence. Beck & Krause (2005) revised the formula for the equipartition of energy so that the CR energy spectrum would be integrated rather than the radio frequency spectrum.

Also the equipartition principle assumes particles and magnetic fields fill the source *homogeneously* with no preferred direction, and employs the use of the radio emissivity $L_v / \mathbb{V}$ which is the average luminosity, L_v over the source's volume, $\mathbb{V}$. However, the field strength, $\boldsymbol{B}$ could be inhomogeneous within the source, creating local variations. Beck and Krause (2005) proposed to replace this with $I_v \,/\, \ell$ where I_v is the *local* synchrotron intensity (surface brightness) and ℓ is the path length through the emitting medium, thus compensating for some local differences.

Finally, the accuracy of the derived magnetic field strength from the intensity of the total synchrotron emission is reliant on the CR proton/electron energy ratio, K. This classically assumes the ratio is $K \sim 100$ in the relevant energy range at radio wavelengths. Variations from this standard value by a factor of several are not serious (Beck 2009). However, CR electrons could lose a significant fraction of their energy in regions where there are strong magnetic fields or radiation fields or where the particles are far away from their places of origin so that the value of K could deviate to K'. In fact there is great uncertainty in determining K, which is why equipartition (minimum energy) field strengths are regarded as crude estimates for $\boldsymbol{B}$. In such cases, K may become very large, ($K > 100$) and the classical value of 100 *underestimates* $\boldsymbol{B}$ (Beck & Krause 2005).

2.3.7 Cosmic Rays

Interstellar Cosmic Rays (CRs) are an energetically important component of the ISM, comprised of charged particles (98% protons and atomic nuclei and 2% electrons) with the highest known kinetic energies, ranging from $\sim 10^7 - 10^{20}$ eV (Shapiro et al. 2001). Synchrotron emission is a possible indication of the presence of CR electrons and can arise in extreme energy environments such as: (1) Type II and 1b SNRs which are prominent Galactic sources (Rafferty et al. 2013) and; (2) active galactic nuclei (AGN) from radio galaxies and quasars which are prominent extragalactic sources possibly giving rise to energies beyond 10^{20} eV (Haswell et al. 1992).

Shock wave or Fermi acceleration from powerful supernovae has been predicted (Shklovskii 1953 and Ginzburg 1953) and confirmed with the observation of SN 1006 (Koyama et al. 1995) as

responsible for the high energies gained by GCR electrons. Particle acceleration is theorised to take place at either the shock front between the expanding shell type SNR and the ISM (expansion shock acceleration), or at the termination shock generated by the collision of the residual pulsar wind with the surrounding medium (wind shock acceleration) (Weinstein 2009).

However, the mechanism of channelling the energy from supernovae explosions into comparatively few high-energy particles $>10^{18}$ eV has been difficult to explain (Blandford & Eichler 1987). Hence it is believed that this is the maximum value GCRs (Butt 2009) and the origin of ultra-high energy (UHE) CRs (energies $E \geq 10^{18}$ eV) is likely to be Active Galactic Nuclei (AGN) accounting for the full energy spectrum (Shapiro et al. 2001). AGN are powerful jets of energy due to accretion of matter around super-massive black holes at the centres of galaxies giving rise to characterisitically strong continuum synchtrotron radiation.. Spectral shapes can reveal the nature of these active galaxies as will be discussed in § 4.1.2).

2.3.8 Galactic Synchrotron Background Radiation

Just as the coupling of Galactic magnetic fields and *Galactic* Cosmic Rays (GCRs) accelerates and confines GCRs to the Galactic disk (Ferrière 2001), it also deflects their motions and *randomises* their distribution to such a degree that their associated synchrotron photons may no longer point to their sources of origin in the Milky Way and hence their sources are unresolved. The result is *diffuse synchrotron background radiation*, which contributes to the overall radio background present uniformly and universally throughout the Milky Way (the other type of background radiation is thermal CMB). It was this non-thermal synchrotron background (which constitutes the majority of background radiation) that was first detected by Jansky in 1932 and can be Galactic or extra-galactic (Beck 2009). As a result, the origin of CRs has to be determined by indirect ways. As well as relativistic electrons gyrating in the magnetic field, an additional smaller contribution to diffuse Galactic synchrotron emission is observed from CR electrons accelerated by SNRs and pulsar wind nebulae situated in the Galactic plane (Sun et al. 2007).

Galactic magnetic fields, which were first proposed by Fermi, are ‘illuminated’ by the emission of synchrotron emission in the presence of CR electrons and are consequently observable;

an explanation given only in 1950 by Karl Otto Kiepenheuer (Beck 2009). Our detection of Galactic synchrotron emission is described in § 3.3. Essentially CR electron interaction with magnetic field lines traces presence of magnetic field and its direction and allows estimates of energy distribution of the particles (electrons).

The strongest concentration of non-thermal emission was clearly shown towards the Galactic plane, even in the earliest all-sky maps, such as that of Landecker and Wielebinski (1970) at 150 MHz with a low resolution of 2° x 2°. Figure 2.8 shows this as a single extended source, but subsequent maps with better resolution, resolved this as the very intense 3.5′ component (Sagittarius A*; Sgr A*) with several surrounding discrete sources superimposed onto the diffuse synchrotron background. Other gross properties show how whilst considerable emission is present over the entire sky, the distribution is far from uniform with the Galactic centre acting as an approximate centre of symmetry (Beck 2009). Milky Way Surveys of Galactic total emission yielded total equipartition magnetic field strengths of ~6 μG near the Sun and ~10 μG in the inner Galaxy (Wielebinski 2005). Figure 2.8 shows how emission along the plane is very irregular, where peaks may reach near the Galactic centre several 100 μG (Reich 1994).

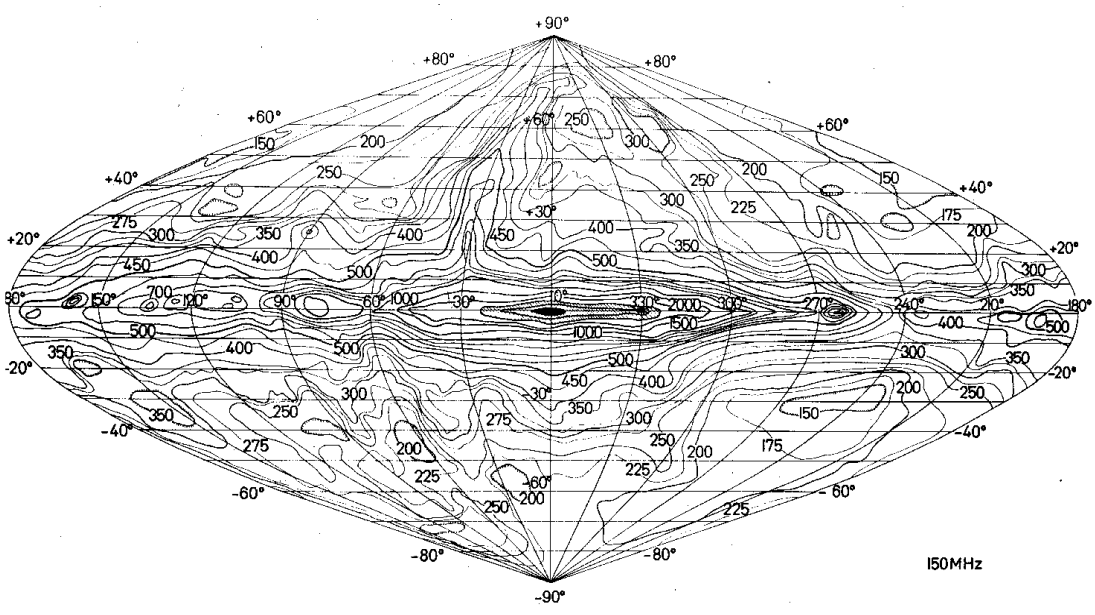

Figure 2.8: Early all-sky brightness map in Galactic coordinates of Northern sky data. Intensity of synchrotron background taken at 150 MHz, resolution ~ 2^{o} x 2^{o} degrees (Landecker & Wielebinski 1970).

2.3.9 Energy Losses

Several processes can modify the SED of a synchrotron source**.** This can include time-evolution, synchrotron self-absorption and free-free absorption.

Time evolution

Particles radiate with the expenditure of their kinetic energy. As a result, the energy distribution of the initial electron population of a synchrotron source, of volume, $\mathbb{V}$ fully filled by magnetised relativistic plasma *will* be lost with time unless somehow replenished e.g. a pulsar energises the Crab nebula (Aharonian et al. 2004). Consequently the radiation intensity dies out at higher frequencies due to this 'aging' effect. The search for this break in synchrotron spectrum at the high frequency cutoff, v_*(GHz) can be used to determine the age of the source, and unlikely to fall within the observable frequency range for this project. For an *isotropic* distribution of pitch angles, $\boldsymbol{\theta}$ the average age of a radiating synchrotron source, t_r is:

$$t_r = 0.82\ \mathbf{B}^{1/2}(\mathbf{B}^2 + \boldsymbol{B}_R^2)^{-1}(1+\mathbb{Z})^{-1/2} v_*^{-1/2}\ yr \tag{2.56}$$

where B (measured in gauss) is the magnetic field strength within the source, $B_R = 4 \times 10^{-6}(1 + \mathbb{Z})^2$ gauss is the equivalent magnetic field strength of the CMB (see Miley, 1980).

Synchrotron Self-Absorption

As mentioned in § 2.2.4, to every emission process there is a corresponding absorption process. In the case of synchrotron radiation, this is *synchrotron self-absorption* (SSA), an effect which occurs when the synchrotron-radiating electron population in the presence of a magnetic field reabsorb their very own low frequency (hence low energy) synchrotron photons, diminishing the detected emission. This absorption process occurs when the intensity of synchrotron within a source becomes bright enough, and gives rise to the optically thick regime.

At higher frequencies (giving rise to optically thin emission), the intensity of the synchrotron is as described in § 2.3.5 (Eq. 2.49) resulting in the following relation between flux density, S_v, spectral index, α and electron exponent, p:

$$S_v \propto v^{\alpha} = v^{-(p-1)/2} \tag{2.57}$$

If the source has the same physical size at all frequencies, following from the Rayleigh-Jeans Law (Eq. 2.22), its brightness temperature, T_B is (Longair 2011) is:

$$T_B = \frac{c^2}{2kv^2}\frac{S_v}{\Omega} \tag{2.58}$$

where Ω is the solid angle of the source with respect to the observer. In this case, T_B is proportional to $v^{-(2+\alpha)}$ and is the lower limit to the temperature of the region since thermodynamically no source can emit incoherent radiation with a greater intensity than that of a black-body at its thermodynamic temperature (Longair 2011).

At low enough frequencies, the brightness temperature, T_B of the radiation may approach (although can never exceed) the effective kinetic temperature of the source's radiating electrons, T_e. The relativistic formula relates the mean energy per electron to their effective temperature, T_e:

$$\gamma m_e c^2 = 3kT_e \tag{2.59}$$

The internal thermal energy density of a gas, u is $u = NkT/(\gamma_{SH} - 1)$, where N is the number density of electrons and γ_{SH} is the ratio of specific heat capacities. Setting γ_{SH}= 5/3 results in the classical $E = 3kT_e$ and setting γ_{SH} = 4/3 (for a relativistic gas), results in (Eq. 2.59) (Longair 2011). Following (Eq. 2.41) leads to $\gamma = \left(v_{Sync}/v_L\right)^{1/2}$ and therefore:

$$T_e = \left(\frac{m_e c^2}{3k}\right)\left(\frac{v_{Sync}}{v_L}\right)^{1/2} \tag{2.60}$$

For a self-absorbed source, $T_B \sim T_e$ and therefore, in the Rayleigh–Jeans limit, following (Eq. 2.57), (Eq. 2.59) and (Eq. 2.36), we have (Longair 2011):

$$S_v = \frac{2kv^2T_e}{c^2}\Omega = \frac{2m_e}{3}\Omega\frac{v^{5/2}}{{v_L}^{1/2}} \propto \frac{\theta^2 v^{5/2}}{B^{1/2}} \tag{2.61}$$

where the solid angle subtended by the source is $\Omega \approx \theta^2$ and θ is the angular size of the source. The break at higher energies is due to energy losses of the highest-energy electrons. Hence, SSA has a characteristic spectral distribution of:

$$S_v = \frac{J_v}{k_v} \propto I_v \propto v^{5/2} \tag{2.62}$$

This spectral index of 5/2 is independent of the spectrum of the emitting electrons with exponent, p so long as the magnetic field is uniform. Both optically thin and thick regimes (§ 2.2.4) are depicted in the synthetic SED of Figure 2.9. Turnover occurs at the low-frequency cut-off or critical frequency, v_c (Clemens et al. 2010).

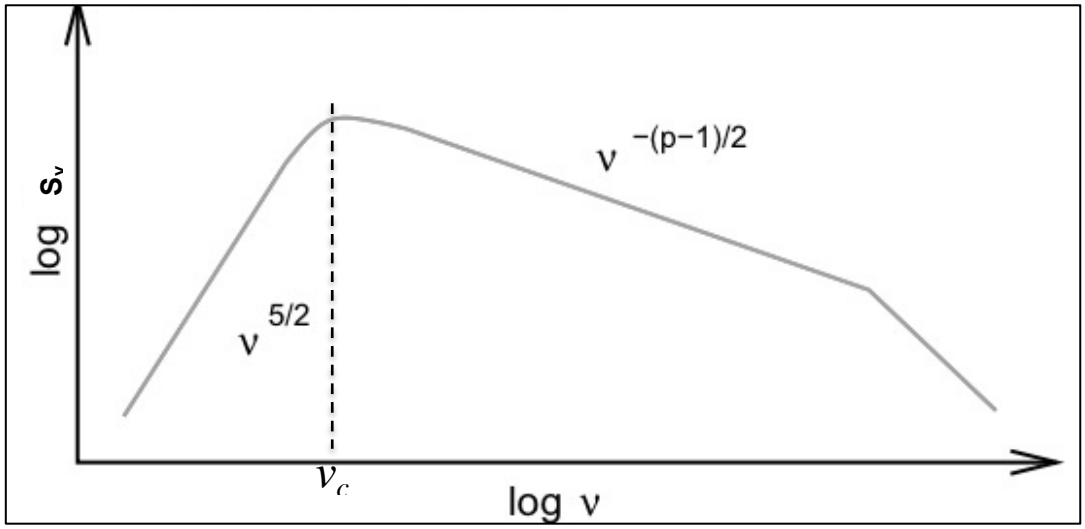

Figure 2.9: The Synchrotron SED of both optically thin and optically thick regimes (after Shu 1991)

The optically thick regime is typically found at radio λs ~ 10^{-2} – 10^{-3} m in *compact* radio sources such as extragalactic active galactic nuclei (AGN) and quasars (see § 4.1). Classically for a source observed at λ = 4 x 10^{-2}, parameters observed are θ ~ 1 milliarcsec, and flux density ~ 1 Jy. This gives the brightness temperature as $T_B \approx 10^{10}$ K, which is the lower limit for T_e (Longair 2011).

Figure 2.10 shows SEDs from 3 discrete radio sources. In general, more compact regions are optically thick, more extended regions are optically thin. In comparison, whilst free-free emission is generally not well observed at low frequencies < 10 GHz (Figure 2.10), demonstrated by the Galactic ionised planetary nebula, *NGC7027 (*as described in § 2.2.4), synchrotron emission typically dominates in the 1-10 GHz range (Clemens et al. 2010) until v_c is reached (see below) as

in the case of quasar *3C48*. SSA is demonstrated by quasar 3C48 (Kellermann & Pauliny-Toth 1969) which is a much more compact object than the radio galaxy *Cygnus A* (Conway et al. 1963), creating high enough electron density and magnetic field lines to produce self-absorption of the radiation at low frequencies (Thompson, Moran & Swenson 1991).

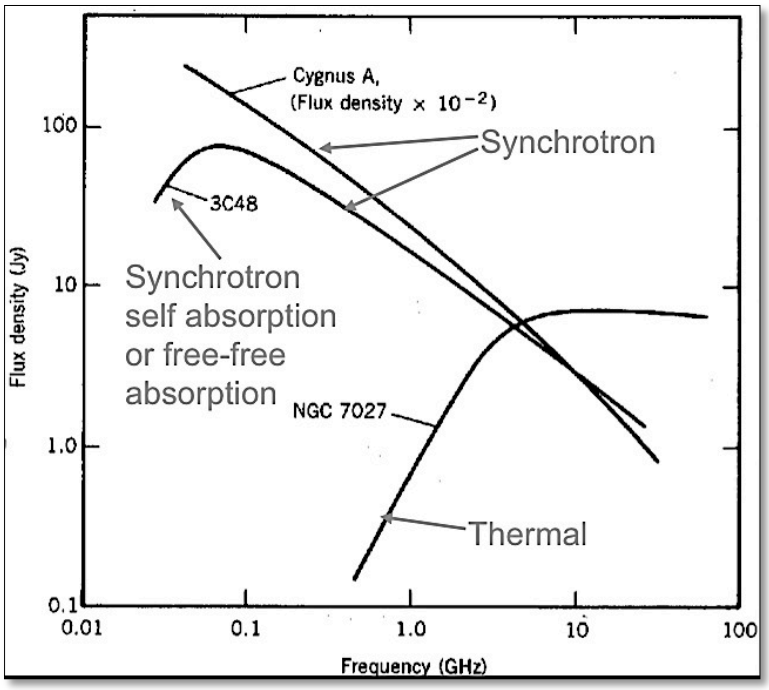

Figure 2.10. An overview and comparison of continuum radiation spectra. While the intensity of thermal radiation increases, the intensity of non-thermal synchrotron radiation usually decreases with increasing frequencies < 10 GHz (after Thompson, Moran & Swenson 1991).

Free-Free Thermal Absorption of Synchrotron

Synchrotron self-absorption (SSA) where absorption is *internal* to the generating source itself, if it is compact enough (Tingay et al. 1997) is a plausible absorption mechanism responsible for synchrotron turnover. The other is free-free absorption (FFA) of synchrotron radio radiation in an *external* screen of high-density ionised plasma (such as a H II region) that obscures the source (external FFA). Tingay & de Kool (2003) give a quantitative analysis of extrinsic FFA modeling and found necessity in considering a more complex inhomogeneous absorbing screen.

Free-free absorption could also be *intrinsic* to the synchrotron source, in thermal plasma that coexists with the relativistic electrons responsible for the synchrotron emission (internal FFA) (Tingay & de Kool 2003). Physically in the general case of FFA, when a free electron passes near

an ion in the plasma, just as an acceleration changes its kinetic energy, corresponding to the emission of a photon, it can also result in the absorption of a photon in the vicinity of the electron.

Whether extrinsic or intrinsic, in both cases of FFA the low frequency photons are less able to escape absorption associated with the two mentioned continuum emission processes. Whilst SSA requires extremely high brightness temperatures in order to be significant, in situations where this is not significant (such as diffuse gas) FFA is the defining mechanism of power absorption especially in plasmas at low frequencies, depending on the properties of the plasma (Clemens et al. 2010 and Peterson & Webber 2002). In FFA, this absorption takes place by a screen of thermally radiating ionised gas located along the line of sight (LOS) of the synchrotron-emitting region. These primary *Galactic* FFA regions have typical electron temperatures ~$10^{4.5}$ – 10^{7} K (Longair 2011) and are the Hot Interstellar Medium (HIM), the Warm Ionised Medium (WIM), halos of ionised gas around H II regions and H II regions themselves. The opacity of these thermal regions at low frequencies is determined by thermal electron temperature, T_e and thermal electron density, n_e of the ionised medium as shown in Table 2.1. The absorption coefficient that describes this attenuation has been given by (Eq. 2.23).

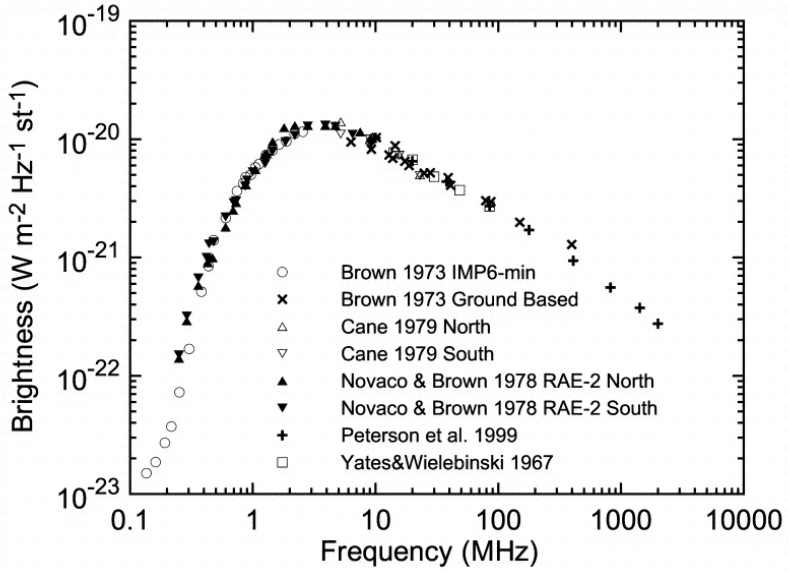

Figure 2.11: The data points represent various independent low radio frequency observations of the Galactic polar synchrotron background between ~ 0.1 – 500 MHz (Peterson & Webber 2002). Synchrotron spectral turnover is evident at 3 – 4 MHz.

Figure 2.11 graphs data points of low frequency Galactic polar radio synchrotron background radiation (produced almost entirely by CR electrons), showing a peak at ~3 – 4 MHz, and spectral index α ~ 0.5 – 0.7 between 10 – 100 MHz (optically thin regime; we make our own observations

using LOFAR of Galactic background radiation in § 3.3). In optically thick regimes, this background synchrotron is partially absorbed. The turnover frequency, ν_c is dependent on the particular parameters of the intervening thermal electrons of the absorbing region, and is generally below ~ 40 MHz (typically ~ 0.1 - 10 MHz) according to Peterson & Webber (2002) for the Galactic ionised gases. Greatest FFA (highest opacity) occurs within regions of *both* high n_e and high T_e e.g. H II regions (Table 2.1).

Hence observations of the background radio spectrum ~ 0.1 - 10 MHz are a probe of the Galactic height distribution of parameters n_e and T_e which can be obtained given some a priori knowledge or assumptions about the synchrotron emissivity spectrum (Peterson & Webber 2002). Independent measurements of n_e and T_e and synchrotron volume emissivity, I (Eq. 2.49), have been made with enough precision to establish acceptable limits for height distributions of their values. Please refer to Peterson & Webber (2002), on how suitable models can be established.

If we consider a large optically thick H II region with optical depth $\tau_\nu \gg 1$ i.e. virtually opaque for low radio frequency background synchrotron originating from behind, then in principal by observing low radio frequency continuum spectra in the direction of known H II regions, any detected emission would solely be the product of the volume emissivity of synchrotron radiation due to GCR electrons between the H II region and Earth (the foreground synchrotron) and thermal emission from the H II regions itself which can be estimated from higher frequency measurements and subtracted (Nord et al. 2006). The ratio of the observed intensity to the distance of an H II region gives the mean foreground synchrotron volume emissivity along the LOS. Such studies have been developed and detailed by Kassim (1990) for example in the 10 – 100 MHz regime and H II regions in absorption against the Galactic non-thermal synchrotron background have clearly been shown in surveys at low radio frequencies by Shain et al. (1961) at 19.7 MHz, Jones & Finlay (1974) at 29.9 MHz, and Roger et al. (1999) at 22 MHz.

Component/ Phase	T_e **Average Temperature (K)**	n_e **Density (cm^{-3})**	**Average Scale Height (pc)**	**% Volume of ISM**	**Ionisation fraction (x_e)**	**Most Common Location**
Molecular hot cores	100–300	>10^6			≤10^{-8}	Proto-stellar cores
Giant Molecular Clouds (GMCs)* e.g. H_2 regions	10 - 20 0-50	10^3– 10^5	~75	< 1%	10^{-7}-10^{-8}	Dense dark clouds primarily in the spiral arms and between 3.5 - 7.5 kpc from the centre of the galaxy
(Atomic) Cold Neutral Medium (CNM)	50 - 100	10-100	100- 300	1—5%	~10^{-3}	Diffuse atomic hydrogen clouds (H I regions); Detectable by H I 21 cm line *absorption*
Warm Neutral Medium	~ 3000 - 8000	~ 0.1 – 0.5	220	10—20%	0.1	Warmer neutral gas extends up to 220pc above the disk and down into the lower halo; Detectable by H I 21 cm line *emission*
Warm ionised medium (WIM)*	~ 8000 - 10000	>10	900	20—50%	1	Both in distinct H II clouds and diffuse component; clumps along mid-plane and diffuse gas extends to about 1 kpc away from disk
Normal H II regions *	~10000	> 50 - 10^5	70	< 1%		Found in the spiral arms associated with molecular clouds and active star forming regions; formed around young hot O and B stars
Hot interstellar medium (HIM) Coronal gas	~10^6 - 10^7	~ 0.003	1000 - 3000	30—70%	1	Fills most of the volume of the halo. Irregular distribution in disk.
* *Regions of significance to our studies*						

Table 2.1: The properties of the components of the neutral and ionised ISM. Values are highly variable and for this table came from Tielens (2005), Kassim (1989) and Ferrière (2001).

2.4 Discrete Spectra

2.4.1 Recombination Lines

The continuum emission from H II clouds results from the thermal energy and hence kinetic collisional energy between atoms detaching electrons creating complete ionisation (a *bound-free* transition). Thermal energy in the same way can also excite the electrons of atoms to higher energy states during collisions with other atoms, without complete ionisation (a *bound-bound* transition). Another process which raises electrons to higher states is *recombination,* when the formerly free electron is recaptured by the ion (a *free-bound* transition). These atoms radiate photons at various *discrete* frequencies as the electrons make energy level transitions on their descending cascade towards the ground state. These energy levels are predicted by Neils Bohr's highly accurate model for one-electron atomic systems, in particular the hydrogen atom. Certain situations allow other atoms to be simplified to the one-electron 'hydrogenic' system (see § 2.4.2). The natural state of hydrogen is for the lone electron to occupy the lowest ground energy state (principal quantum number, $n = 1$). During excitation, quantised higher energy levels are occupied. When the electron then drops back to its lower energy state (Figure 2.12), a photon of energy is released at a wavelength predicted by Bohr that is characteristic of that atom, creating a discrete 'line' on the observed EM spectrum. This is why this type of radiation is called spectral line or recombination line emission and its characteristic nature is exploited to identify major constituent atoms and molecules of an object or region (Osterbrock 1989).

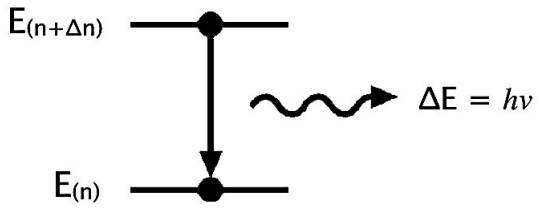

Figure 2.12: Recombination line generation: the electron in Bohr's model of an atom can fall from the level (n + Δn) to n, where Δn and n are integers.

Please refer to the Shu (1991) for detailed derivations of the following equations based on quantum mechanics. The electronic energy change, ΔE from an initial level, (n+Δn) to final level, n is equal to the energy, $h\nu$ of the emitted photon:

$$\Delta E = \left(\frac{m_e e^4}{2\hbar^2}\right)\left[\frac{1}{n^2} - \frac{1}{(n+\Delta n)^2}\right] = h\nu \tag{2.63}$$

The photon frequency of the recombination line, ν_n can be calculated using the appropriate n values:

$$\nu_n = \left(\frac{2\pi^2 m_e e^4}{h^3 c}\right) c\left[\frac{1}{n^2} - \frac{1}{(n+\Delta n)^2}\right] = R_H c\left[\frac{1}{n^2} - \frac{1}{(n+\Delta n)^2}\right] \tag{2.64}$$

where R_H is the Rydberg constant ~ 1.09737 x 10^7 m^{-1}.

Recombination lines are labelled by the chemical element involved, the final level number n, and successive Greek alphabetical letters to indicate the level change, Δn or line's order: α for $\Delta n = 1$, β for $\Delta n = 2$, γ for $\Delta n = 3$, etc. (Gallagher 2005). For example, the H91α recombination line is produced by the transition between the $n = 92$ and $n = 91$ levels of a hydrogen atom. This associated photon is observable at radio frequencies centred at 8.584 GHz, hence why this is a radio recombination line (RRL). Observations of this RRL have been of great importance for observing the planetary nebula NGC 324 (Rodríguez et al. 2010).

2.4.2 Rydberg atoms

An atom or molecule is said to be in a Rydberg state when one of the electrons have been excited to a very high principal quantum number orbital. Such highly excited states ($n > 100$) are typical of radio-emitting atoms in the ISM. Classically the radius of an orbital, R_n for an atom of hydrogen as deduced from Bohr theory (Gallagher 2005), is

$$R_n = 0.529(n^2/Z)\ \text{Å} \tag{2.65}$$

where Z is the atomic number. This leads to the dependence $R_n \propto n^2$, hence for n=100, $R_{100} \approx 10^{-4}$ cm (1μm). This project is focussed on low frequency RRLs which are associated with even larger principle quantum numbers e.g. carbon RRL (C RRL) observations towards the strong supernova remnant Cassiopeia A (Cas A) by Konovalenko, Stepkin & Shalunov (2002), detected a bound state of n ~ 868 near 20 MHz. At high values of n, most atoms can be considered 'hydrogenic', since the bound electrons in low energy levels effectively shield the outermost

electron from the nucleus (Gallagher 2005). This becomes significant for highly excited carbon as shall be seen, which has 6 electrons when in the neutral state.

Since low frequency RRL emission is associated with large *n*, such orbital dimensions are very large compared to the size of the nucleus, making the loosely bound electrons of these Rydberg atoms extremely sensitive to the external physical conditions in the ISM. In particular, they provide very unique diagnostics of local electron density and temperature, levels of ionisation, abundance ratios etc.in the partially ionised ISM at low radio frequencies (§ 2.4.3); Shaver (1975) shows theoretically how bound atoms with $n \sim 1500$ are expected to exist in *tenuous* media. Stepkin et al. (2007) report detection of a series of narrow weak RRLs in *absorption* at ~ 26 MHz (Figure 2.18) arising from the largest bound carbon atoms detected in space which are more than a *million* times larger than the ground state, in a *tenuous* cool medium towards the direction of Cas A.

2.4.3 Diagnostics from RRLs

RRLs from H II regions

Large compact H II regions have been extensively studied by their optical recombination lines since they emit a large fraction of their energy in this EM wavelength range. Examples include the Lagoon Nebula (NGC 6523) in the constellation Sagittarius which is one of the most prominent H II regions in the Galaxy (White et al. 1997) and the Orion Nebula (Blagrave et al. 2007). Detection of the recombination wavelength $\lambda = 656.3$ nm (the H2α line of the Balmer series), gives the thin hydrogen emission nebulae their distinctive red colour. In essence, these nebulae glow from the fluorescence of hydrogen atoms which are 'lit up' in the visible range because of UV radiation from nearby hot stars. The Hubble Space Telescope (HST) has been used to explore the properties of their twisted, turbulent features at optical wavelengths, which are caused by varying densities of the gas and dust and differences in temperature (Stecklum et al. 1998).

However, as stated earlier (§ 1.5), extinction by dust particles at optical wavelengths limits the use of optical lines such as the $\lambda = 656.3$ nm line to studies of nearby regions out to ~ 2 kpc since short recombination wavelengths are physically constrained by ISM dust extinction. So, whilst optical and near infrared (IR) spectroscopy can provide the physical properties of *nearby* emission nebulae, RRLs are the only means of providing this information on a Galactic scale, deep

into the plane. Terzian et al. (2005) for example, detail RRL observations at 5 GHz toward the compact H II region, *Sharpless 88 (Sh2-88)* with the Arecibo telescope, some 2.2 - 2.4 pc away.

RRLs from carbon regions

Since the ionisation potentials of hydrogen (13.6 eV) and helium (24.4 eV) are relatively high, these elements are ionised by the strong UV radiation very close to the O and B stars of effective temperatures greater than 20,000 K (White et al. 1997). By detecting H and He RRLs, we can trace the hot ionised regions, with electron temperature $T_e \sim$ 5,000 – 10,000 K (Kantharia & Anantharamaiah 2008). Figure 2.13 shows the main components of a H II region in which H is ionised to the *Strömgren radius,* R_H and He out to R_{He} (Roelfesma & Goss 1992). The exact quantitative derivation and equation for the Strömgren radius is found in Osterbrock (1989) and Spitzer (1998).

In comparison, carbon, which is the fourth most abundant element in the Galaxy, has much lower ionisation potentials with the first being 11.4 eV (and second being ~ 24 eV). Hence *singly-ionised* carbon (C II) is mainly found in cooler regions on the periphery of H II regions and samples very different environments compared with RRLs from ionised H and He (Terzian et al. 2005).

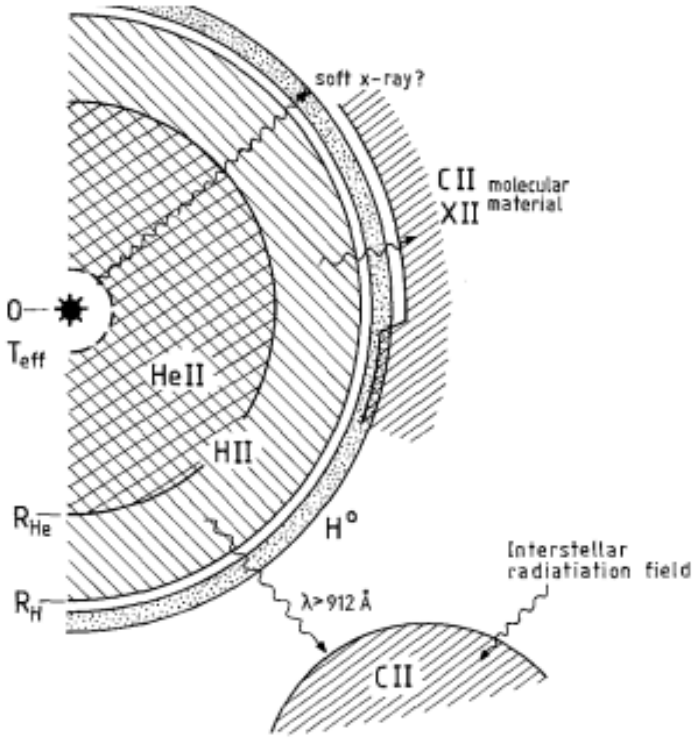

Figure 2.13: Schematic of H II and C II regions as summarised by Roelfesma & Goss (1992). H II regions directly surround the young star. Ionised helium is also found in this region, because of its high ionisation potential. The Warm Ionised Medium (WIM) is located outside of the regions of completely ionised gas forming an interface between the H II region and surrounding ionised cloud. From this region, emission from ionised carbon can result.

Photo-Dissociation or Photon-Dominated Regions (PDRs) are expanses of the ISM dominated by radiated Far Ultraviolet (FUV) photons from hot O and B stars which provide the sole source of heat (Hollenbach & Tielens 1999). PDRs are found in what is known as the 'ultraviolet ISM' and are cold enough (less than a few hundred K) so that the majority of the atoms and molecules (hydrogen, helium and oxygen) remain largely neutral albeit lower ionisation potential elements such as carbon, which can then be singly-ionised by the escaping low energy photons of energy E < 13.6 eV (Kantharia & Anantharamaiah 2008) corresponding to $\lambda > 912$ Å. These FUV photons have energies between 6 eV < $h\nu$ < 13.6 eV to be exact, (Mookerjea et al. 2006) and are known as 'hard photons' (Lehner et al. 2010) as they have managed to escape the H II regions which encase the hot stars.

Since ionised carbon (a C II region), is found at the immediate interface of the ionised H II regions such as W3 and NGC 2024 as confirmed by the RRL C109α detections by Palmer et al. (1967), it is an important transition layer between the fully ionised H II regions and surrounding neutral molecular clouds. Figure 2.14 shows how *classical* C II regions can form Strömgren spheres around H II regions (Kantharia & Anantharamaiah 2008); hence detection of C RRLs possibly traces the periphery of H II regions.

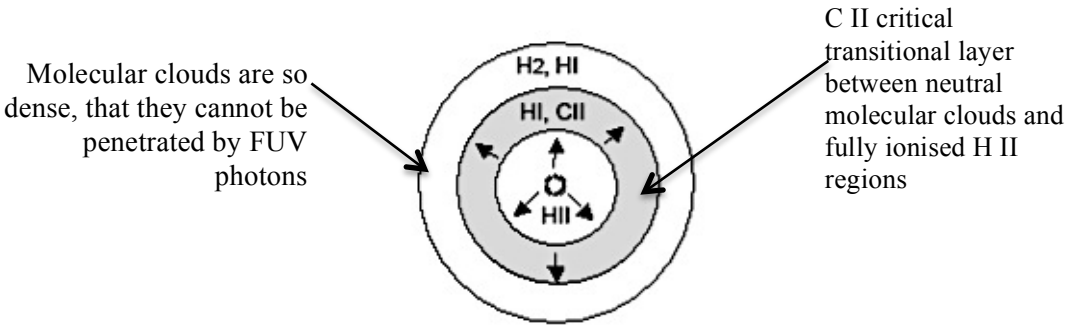

Figure 2.14**:** Characteristic of PDRs is a layered structure, with ionised elements out to Strömgren spheres of characteristic radii from the central young star. Carbon is almost completely ionised in the diffuse interstellar gas outside H II regions by FUV photons (912 Å < λ < 1100 Å). These photons are depicted travelling from the O and B stars by arrows (Konovalenko 2002).

RRLs from classical C II shell regions are narrow (4 − 10 kms^{-1}), indicative of a comparatively much cooler medium (< few 100 K). Hence, C RRLs characteristically reflect velocities closer to the surrounding molecular cloud than to the inner H II region (Pankonin 1980). Stimulated emission of the background continuum is likely to enhance C RRL emission intensity, sometimes

making them comparable in strength to H RRLs observed from the associated hot H II region (Kantharia & Anantharamaiah 2008).

Carbon plays a major role in thermostatic processes of H II regions and generally is an important *coolant* of atomic and molecular interstellar gas exposed to stellar ultraviolet (UV) photons in PDRs. Carbon Far-IR line emission, with fine structure at [C II] 158 μm is the *dominant* coolant in PDRs (Luhman et al. 2003). There are a variety of photons emitted at different wavelengths, but [C II] 158 μm carries relatively high emission intensity providing 0.1% − 1% of the total far-IR luminosity. This makes carbon a major reactant in gas-phase chemical reactions in the ISM, tracing the cooling transition zone (grey shell of Figure 2.14) from the hot ISM with $T_e > 10^6$ K to the warm ISM with $T_e < 2 \times 10^4$ K. The study of the C II interface would lead to a better understanding of energy transfer from the H II region 'stellar nursery' to the parent star forming molecular cloud (Lehner et al. 2010).

C RRLs from classical C II regions are generally observed in at frequencies $\nu \geq 1$ GHz, but none are currently known < 1 GHz (Kantharia & Anantharamaiah 2008). As well as classical, C II regions are *diffuse* and the C631α RRL line confirmed by Blake, Crutcher & Watson (1980) in the direction of Cas A had arisen from a cold region of $T_e \sim 50$ K and $N_e \sim 0.1$ cm^{-3} identified with diffuse neutral H I clouds. H RRLs are typically not seen below ~ 120 MHz, where C RRLs in emission turnover into absorption since the excitation temperature of the atoms approaches the typical kinetic temperature of the gas; this inverts the population levels (Anantharamaiah et al 1988 and Erickson, et al. 1995).

2.4.4. Analysis and diagnostics with carbon RRLs

Relative RRL intensity

The time-averaged radiated power, $\langle P \rangle$ for radio photons emitted by Rydberg atoms with $\Delta n >> 1$ transitions is given by the classical Larmor's equation for a dipole with dipole moment eR_n is (Shu 1991):

$$\langle P \rangle = \frac{2e^2}{3c^3}(2\pi v)^4 \frac{R_n^2}{2} \qquad (2.66)$$

Since RRLs are measured with respect to the free–free emission underlying their spectra, it is essential to characterise the intensity of continuum emission, I_C in order to interpret the spectral lines observations. Opacities are additive and the opacity, τ_ν of (Eq. 2.25) is the sum of linear and continuum opacities, τ_L and τ_C; therefore the intensity of the RRL itself, I_L is (Gordon & Sorochenko 2009):

$$I_L = I - I_C = B_\nu(T_e)e^{-\tau_C}(1 - e^{-\tau_L}) \approx B_\nu \tau_L \tag{2.67}$$

where I is total intensity, and B_ν (Eq. 2.22) is the spectral radiance. This occurs when τ_C and $\tau_L \ll 1$ which is typical in H II regions at $\lambda \sim 10^{-2}$ m. Under these conditions, $I_C \approx B_\nu \tau_C$ and the ratio of the line-to-continuum emission for the same object must be (Gordon & Sorochenko 2009):

$$\int_{line} \frac{I_L}{I_C} dv = \int_{line} \frac{\tau_L}{\tau_C} dv = \int_{line} \frac{\kappa_L}{\kappa_C} dv \tag{2.68}$$

where κ_L and κ_C are the line and continuum absorption coefficients. Please refer to Gordon & Sorochenko (2009) pp. 66 – 78, for more detailed quantification of these values.

RRL shift and broadening

The spectral *line-profile* is the *normalised* intensity as a function of frequency. It is principally determined from the Doppler equation relating the line rest frequency, v_0 to the observed frequency, v:

$$v \approx v_0 \left(1 - \frac{V_r}{c}\right) \tag{2.69}$$

The Doppler shift above reflects radial velocities, V_r in the non-relativistic limit ($v_r \ll c$), which can be the result of microscopic thermal motions or macroscopic turbulent motions. Overall, the observed line widths, Δv_L of a RRL Gaussian line-profile are influenced by several line *broadening* mechanisms:

- *Natural line widths:* these arise from the uncertainty principle, $\Delta E \, \Delta t \approx \hbar$ of the Rydberg states involved in the transition, where Δt are their typical lifetimes. This contribution is small for high n.
- *Microscopic Doppler-broadening:* due to the kinematic motions of atoms of a characteristic temperature. This thermal component of the line-profile is calculated using the Maxwellian velocity distribution (Eq. 2.14) assuming Local Thermodynamic Equilibrium (LTE), which causes a cumulative Doppler effect.
- *Collisional (impact pressure) broadening*: which is the result of collisions between the emitting atoms and becomes more pronounced with density. This becomes significant at high n, leading to a sharp increase in line widths at lower frequencies especially for observed C RRLs. This results in the necessity of non-LTE analysis for deriving the physical conditions in the gas (electron density, N_e and electron temperature, T_e) accurately at high n (see below).
- *Macroscopic Doppler-broadening:* energy transfers due to the kinematics of large-scale turbulence and ordered bulk motions such as outflows, expansions, contractions, rotations and shocks in the H II plasma.

Generally the broadening effects are greater for atoms excited to high principal quantum states n since they are very big and fragile making their loosely bound electrons more sensitive to the environment in which they reside. The width of the radio absorption lines in C II regions has been found to increase dramatically towards lower frequencies due to pressure, temperature, density, cloud turbulence and radiation broadening (Kantharia & Anantharamaiah 2008). These features help probe the complex and poorly understood environment of the cool partially ionised ISM (PDRs, where carbon is almost completely ionised) so that their physical conditions can be deduced (Onello & Phillips 1995; see § 5.1 for the motivations of our work).

Non-LTE analysis

A hydrogen atom, with an electron in principal quantum level n = 110, providing RRL H109α for Δn = 1, has a radius that is 12,000 times larger than at n = 1. Therefore its 'target area' is classically ~ 1.4 x 10^8 times larger with more opportunity to be influenced by external collisions i.e.

the likelihood of interaction between particles (the *collisional* cross-section) *increases* with n^4 (Verschuur & Kellermann 1974). Therefore, populations of atoms with very high quantum states will have excitation temperatures more indicative of the electron temperatures of the gas. Collisions have a decreasingly smaller effect on atomic electrons occupying smaller principle quantum states. Therefore departures from LTE must be made to account for the atoms in high Rydberg states, in what is known as *non-LTE analysis*. Effectively, widths of RRLs *broaden* as non-LTE effects increase with *n* depicted in Figure 2.15 (Stepkin et al. 2007). Goldberg (1966) showed non-LTE analysis was essential for RRL strengths from H II regions with large emission measures, Ɛ. RRLs initially observed from H II regions were assumed to be emitted in LTE, leading to straightforward deductions of N_e and T_e from observed line-profiles. However, such analysis was soon understood to have provided electron temperatures, T_e that were too small (Verschuur & Kellermann 1974).

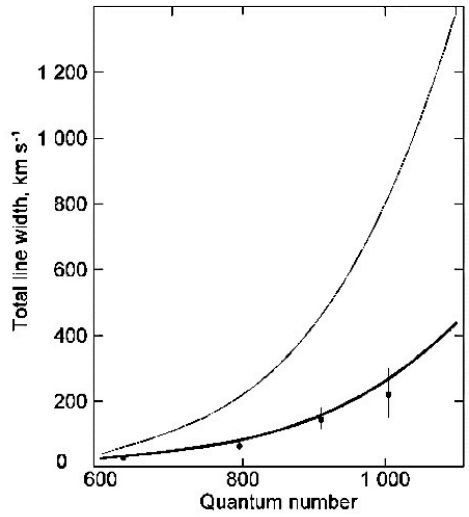

Figure 2.15: The dependence of line width against principle quantum number. The narrow line corresponds to the best previous model and the data reflects that the collisional broadening effects are much gentler than expected (Stepkin et al. 2007).

The values for the ratio of line-to-continuum brightness temperature T_L/T_c resulting from non-LTE analysis, as functions of principle quantum number, *n* were plotted by Sejnowski & Hjellming (1969) for values of the emission measure, Ɛ, from $10^4 - 10^{7.5}$ pc cm^{-6} (Figure 2.16). The plots demonstrate how variations in electron temperatures of T_e = 5,000, 7,500, and 10,000 K and electron densities $N_e = 10^2$, 10^3 and 10^4 cm^{-3} have significant impacts on the line-profiles. Non-LTE effects become increasingly important for higher *n* (confirming Figure 2.15) where there is greater departure from LTE solutions, shown as dashed curves in Figure 2.16. The plots also show non-LTE effects increase for increasing Ɛ, i.e. strengths of RRLs from nebulae with high emission are

most dependent on non-LTE using analysis modeling populations of the appropriate energy levels. Non-LTE effects also increase for decreasing T_e or decreasing N_e with the latter being the most critical (Anantharamaiah, Payne & Erickson 1988).

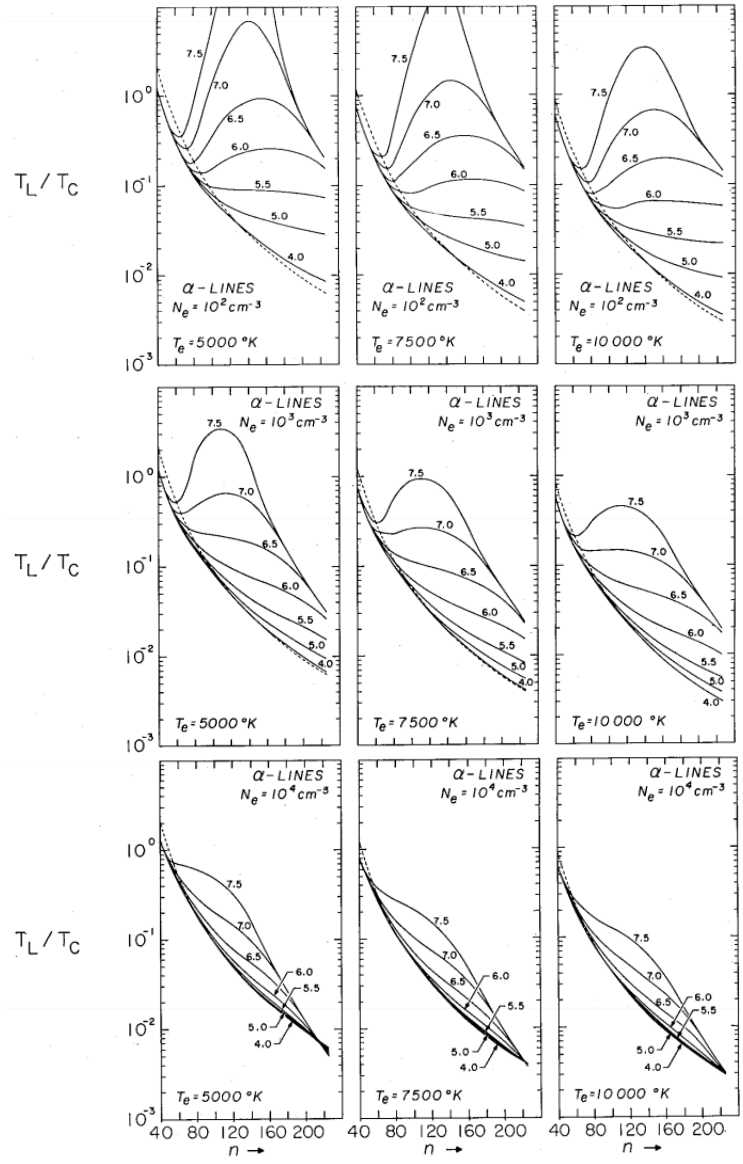

Figure 2.16 Plots of the ratio of line to continuum brightness temperature T_L/T_c with principle quantum number, n resulting from non-LTE analysis for T_e = 5000, 7500, and 10,000 K and N_e = 10^2, 10^3 and 10^4 cm^{-3}. In each plot are values of emission, Ɛ, for Ɛ = 10^4, 10^5, $10^{5.5}$, 10^6, $10^{6.5}$, 10^7 and $10^{7.5}$ pc cm^{-6}. The dashed curves indicate the LTE solutions (Hjellming, Andrews & Sejnowski 1969).

2.4.5. Observing carbon RRLs with LOFAR

Figure 2.17 shows RRLs from a prominent H II region (Quireza et al. 2006). Although this RRL emission spectra is in a frequency band higher than the range we are interested in at v < 100 MHz (hence these are emission RRLs), it demonstrates how the intensity of C RRLs in most bandwidths are weaker than H and He RRLs typically by 3 orders of magnitude (Konovalenko, Stepkin & Shalunov 2002). This is particularly the case in C RRLs originating from *diffuse* C II regions. As mentioned, C RRL intensities from classical C II regions can become stronger due to stimulated

emission of the background continuum.

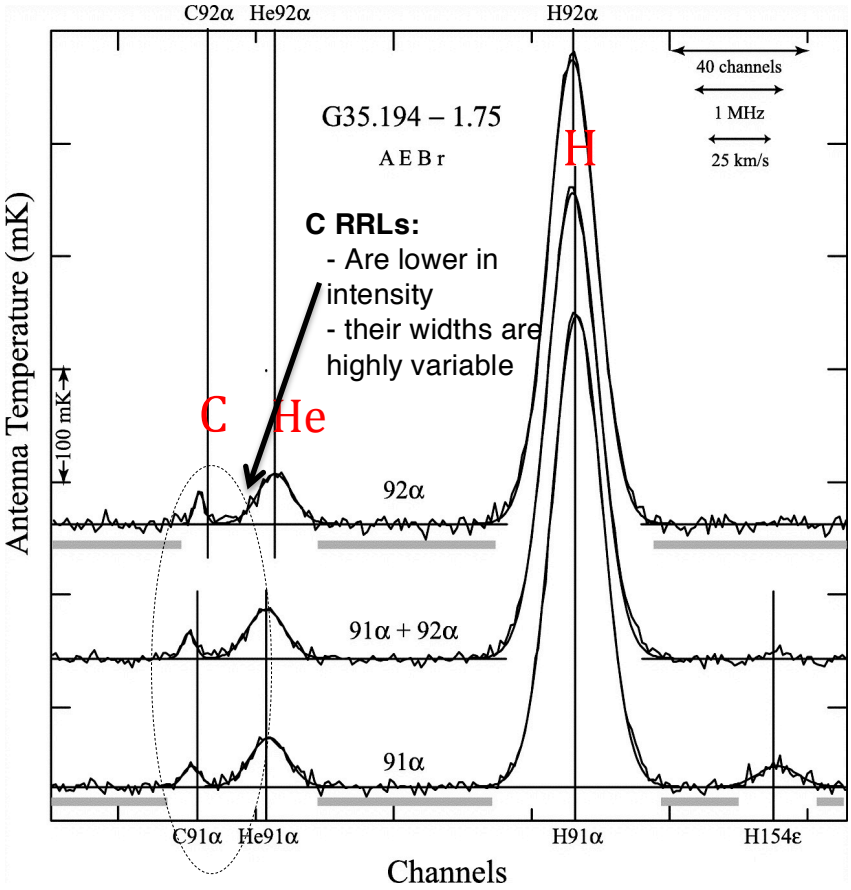

Figure 2.17: Spectra for the Galactic H II region G35.194-1.75 showing 91α (bottom spectrum) and 92α (top spectrum) transitions, together with their average (middle spectrum) (Quireza et al. 2006). C RRLs come from different gas components than H and He RRLs and therefore have different morphologies and their widths are highly variable.

C RRLs at v < 100 MHz arising in tenuous medium of cold clouds have been observed at the UTR-2 telescope in the Ukraine, (Konovalenko, Stepkin & Shalunov 2002), the Indian Gee-Tee telescope at 34.5 MHz (Onello & Phillips 1995), the NRAO, USA at 34 - 78 MHz (Quireza et al. 2006), the DKR-1000 telescope in Russia at 42 MHz and the Parkes 64-m telescope in Australia at 76.5 MHz (Stepkin et al. 2007). Of all these observations, the biggest low frequency instruments such as UTR-2 of the Ukraine were best at detecting the extremely *low frequency C RRLs in absorption* at 25 - 26 MHz, from delta transitions (n ~ 1009, Δn = 4) (Stepkin et al. 2007). Figure 2.18 shows the spectrum obtained with the relative intensity (ratio of line-to-continuum brightness temperature T_L / T_c). The α, β and γ lines appear approximately every 120 kHz with the general rule of spacing, Δv for α lines as $\Delta v \sim 3v/n$ demonstrating the need for adequate spectral resolution (Stepkin et al. 2007).

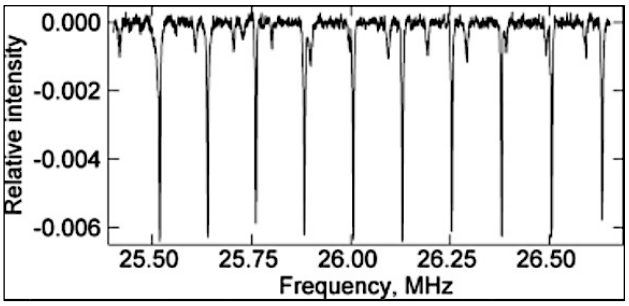

Figure 2.18: High resolution spectrum of Cas A showing multiple carbon RRLs; α lines appear ~ 120 kHz apart. (Stepkin et al. 2007)

LOFAR's design is advantageous for investigating these C RRLs at low radio frequencies with even better *spectral* resolution and sensitivity compared with previous interferometers (§ 3.2.3). The frequency of LOFAR's receivers (~ 15 – 240 MHz), corresponds to atoms with $n \sim 300 - 850$ allowing better detection and understanding of the PDR environment, effectively opening a new ISM phase for further exploration. We can further improve the sensitivity of C RRLs observations by removing the radio foreground such as radio frequency interference and ionospheric phase corruptions. Improving the signal-to-noise S/N ratio is important in any detection of RRLs. Please see § 5.3 for more methodology on attempts to increase sensitivity to improve C RRL detection with our datasets. This work followed from the progress and methods established by Asgekar, Oonk et al. (2013) where 5 C RRLs (α transitions) were detected in absorption between 40 – 50 MHz with LOFAR with an enhanced S/N ratio towards Cas A.

Deducing distances using Oort equations

Much of the total macroscopic Doppler-broadening of RRLs comes from *differential Galactic motion* contributing to the bulk kinematic effect (Verschuur & Kellermann 1974). Radial (along LOS) velocity is inferred by measuring the Doppler shifts of the RRL profile (Eq. 2.69) and gives the basis for conducting *Oort analysis* to determine distance.

Velocity determination

The different components of the Milky Way rotate around the centre, along the plane of the disk in almost circular orbits, where the inward force of gravitational attraction is balanced by centrifugal forces (Longair 2011). In 1927 Jan Oort conducted motion analysis and found that stars nearer the Galactic centre have faster orbital velocities. This difference in angular speeds of different parts of the Galactic disk is *differential rotation* (Verschuur & Kellermann 1974). Differential rotation

dictates that gas clouds closest to the Galactic centre are moving at the greatest angular speed or radial velocity and hence exhibit the greatest redshift (Figure 2.19).

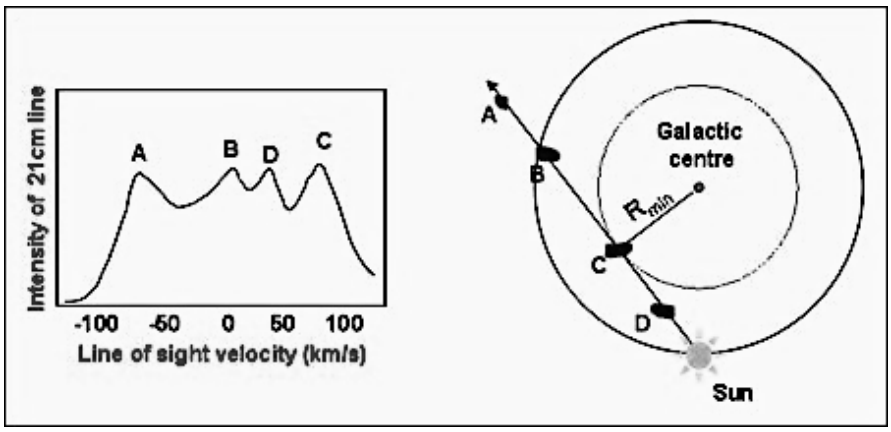

Figure 2.19: The presence of each H II cloud creates an intensity peak in the discrete line-profile detected along the LOS. Each peak has a narrow and well-defined Doppler shift, dependant on the LOS velocity of the H II cloud. A cloud which orbits at the same radius from the galactic centre as the sun (B) will move at the same angular speed and hence will exhibit a LOS velocity ~ 0. H II clouds closer to the Galactic centre orbit faster than the Sun and have positive LOS velocities (**D and C**), whilst clouds located further from the Galactic centre (**A**) orbit relatively slower and have negative LOS velocities (Longair 2011).

The Oort constants are empirically derived parameters that characterise the local rotational properties of our galaxy. Oort's constant A is the local shear rate and Oort's constant B is the local rotation rate (see Shu 1982). These constants are derived by plotting the cloud radial velocities, V_r against Galactic longitude, ℓ for nearby H II clouds for example (e.g. Feast & Whitelock 1997) in the case $r \ll R_0$ (the solar neighbourhood) where R_0 is distance between the Local Standard of Rest (LSR) taken to be the sun and Galactic centre, and r is distance between the LSR and RRL emitting object (H II cloud). The circular rotational velocity of the LSR is $V_0 = \mathrm{V}(R_0)$ and Oort's constants are defined as:

$$A = -\frac{1}{2} R_0 \left(\frac{\mathrm{d}\omega}{dR}\right)_0 \tag{2.70}$$

$$B = -\omega_0 - \frac{1}{2} R_0 \left(\frac{\mathrm{d}\omega}{dR}\right)_0 \tag{2.71}$$

where ω is the *mean angular velocity* of disk stars at distance R_0 from the centre:

$$\omega(R_0) = \frac{\mathrm{V}(R_0)}{R_0} \tag{2.72}$$

The subscript '0' indicates these values at the LSR. Once these constants are determined, the following Oort equations can be solved. The radial (along LOS) velocity, V_r and tangential (perpendicular to LOS) velocity, V_t which sum to the total velocity, V of the H II cloud, are given by:

$$V_r = \curlyvee A \sin(2\ell) \tag{2.73}$$

$$V_t = \curlyvee [A \cos(2\ell) + B] \tag{2.74}$$

Oort's constants also determine the Galactic orbital period, $\mathcal{P}$ *and* rotational velocity, V_0

$$\mathcal{P} = \frac{2\pi R_o}{V_o} = \frac{2\pi}{A - B} \tag{2.75}$$

$$V_o = R_o \times (A - B) \tag{2.76}$$

The local shear is defined as:

$$\left(\frac{\delta V}{\delta R}\right)_{R_o} = -(A + B) \tag{2.77}$$

One important diagnostic to this project will be the measurement of the Doppler shifts of RRLs (Eq. 2.69) from the H II clouds with respect to the LSR (of known V_0 and R_0) along a particular LOS in order to determine V_r. Using (Eq. 2.73) with known values of ℓ and determined Oort's constants, the distance, $\curlyvee$, of the H II region from the LSR can be determined.

Distance determination

A *rotation curve* is an established graph of the rotational velocity, V_ϕ (calculated from V_r and V_t; please see Bobylev & Bajkova 2013) of Galactic components vs. their distance from the Galactic

centre (Galactocentric distance), R_G. It is a very useful tool in estimating inferred V_ϕ of RRL peaks from emitting H II regions, into R_G and then r (Anderson & Bania 2009).

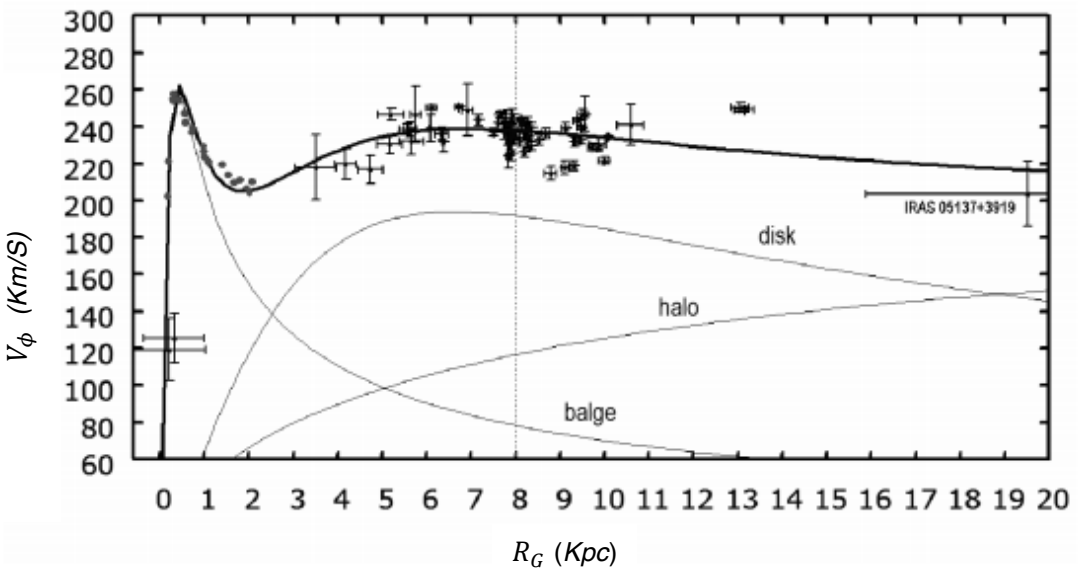

Figure 2.20: The Galactic rotation curve (thick line). The thin lines indicate the contribution from the bulge, disk, and halo to the rotation curve. The sun is located at the dotted line marks the position of the Sun, at ~8.4 Kpc (Bobylev & Bajkova 2013).

One problem with using rotation curves is that they all have some degree of error since they are just a simplification of a more complicated rotation pattern. Also velocities which depart from circular motion (due to streaming motions) will create errors in derived distance using the rotation curve (Anderson & Bania 2009). There is also increased uncertainty within R_G ~ 2.9Kpc, known as the inner Galaxy kinematic distance ambiguity, and it is unclear whether this is real or an artefact introduced by markedly non-circular motions of gas near the centre (Anderson & Bania 2009).

Figure 2.20 clearly shows that observed rotation curves do not match predicted Keplerian rotation speeds. Instead of reducing with large radii, V_ϕ values level out and remain steady at ~ 220 km s^{-1}. On the basis of detected Galactic mass, V_ϕ should decrease beyond the Solar Galactic radius R_o. However, V_ϕ does not decrease in the predicted manner and this discrepancy indicates extra matter (gas) must be present, which cannot be directly detected. We can only infer of its presence indirectly from its gravitational effects. This is the strongest evidence for dark matter.

Chapter 3

LOFAR Instrumentation & Methodology

3.1. Interferometry

Traditional radio telescopes are designed such that they collect and concentrate radio frequency waves for a receiver at the central focus by reflection from a parabolic shaped dish. The radio frequency waves induce a weak current in the conductor antenna, which is amplified by the receiver so that it is strong enough to measure and record; this is a *signal* (Chengalur et al. 2007). Larger dishes capture more photons and are therefore more *sensitive,* which is advantageous for studying very faint objects (see § 3.2.3 for a more quantitative description of sensitivity). They also provide better *angular resolution,* allowing better capability to resolve objects in the sky and ascertain small details from large distances. For our project, this is advantageous in allowing us to detect fine-scale structures of complex Galactic diffuse nebulae; a capability enabled by LOFAR **(**Röttgering et al. 2010). The achievable angular resolution on a telescope is largely governed by the diffraction limit of ~λ/D, where λ is the wavelength of the observed radiation and D is the aperture diameter of a telescope (Thompson, Moran & Swenson 1991). For example, for a 25 m dish, the resolution achievable for 21 cm radio radiation would be ~ 30′. To achieve arcsecond or sub-arcsecond resolution for the same wavelength, a dish greater than 43 km would be needed. However, there is a physical maximum size of filled-aperture telescopes that results from engineering and cost limitations.

3.1.1 Aperture Synthesis

To achieve higher angular resolution, 2 or more smaller, spatially distributed antenna elements can be combined together, using the technique of *interferometry*. The first basic 2-element radio interferometers were developed in the late 1940s by Ryle & Vonberg (1946) and McCready et al. (1947) and the detailed principles of multi-element aperture synthesis were detailed by Ryle & Hewish (1960). As mentioned, for a single dish the angular resolution, θ is dependent on the diameter of the aperture. For an array, this is the equivalent of the maximum baseline, $\vec{B}$ (the distance of projected separation between any two antenna components as seen from the radio source). The resulting angular resolution, θ in radians is (Taylor et al. 1999):

$$\theta = \frac{\lambda}{\vec{B}} \tag{3.1}$$

The power of an interferometer comes from its ability to image the measured 2-dimensional (2-D) angular brightness distribution of a radio source in the sky. The Fourier synthesis of the interferometer response pattern is the key to achieving this as will be described in this section (Edwards 2007). If the source emission is non-variable, then it is not necessary to catch the entire electromagnetic (EM) wavefront at any particular instant. Instead pairs of signals resulting from the incident wavefront can be combined; this is the basis of aperture synthesis. If there are n elements in the array, then there are n_B baselines or signal pairs to combine:

$$n_B = \frac{n^2 - n}{2} \tag{3.2}$$

3.1.2 Combining Antenna Pairs

Aperture synthesis is only possible if *both* the amplitude, and the phase of the EM wavefront are independently recorded at each array element, and then later *correlated* at a central processing facility. Correlation takes place by multiplying and time-averaging the pairs of antenna voltages. For LOFAR, this takes place at an IBM Blue Gene supercomputer located at The University of Groningen in the Netherlands.

Thompson (1999) details a 2-element interferometer response to radiation of a point source from direction, $\vec{s}$ and from a small solid angle, dΩ observed at a very narrow frequency band centred on frequency, v (approximately monochromatic) or angular frequency, $\omega = 2\pi v$. As shown, the correlated signal of the cosine correlator, R_C is independent of time, but is dependent on the time delay, T_g of the wavefront incident on antenna 1 and antenna 2:

$$R_C = \frac{[V_1 V_2 \cos(\omega T_g)]}{2} = \frac{[V_1 V_2 \cos(2\pi v \vec{B} \cdot \vec{s}/c)]}{2} \tag{3.3}$$

Since T_g is related to direction, it corresponds to the source brightness distribution on the sky, which can in effect be measured and imaged. The voltage of the signal, V, measured by one antenna is related to the source brightness or specific intensity I_v (measured in unit Jansky where 1 Jansky = 10^{-26} W m^{-2} Hz^{-1} sr^{-1}) by:

$$V \propto E \propto \sqrt{I_v} \tag{3.4}$$

It is essentially a record of the electric field component, E of the incident EM wave. Therefore the strength of the product of the combined pair of voltages, $V_1 V_2$ is directly proportional to the source intensity, I_v. To determine the dependence of the response over an *extended source* (neglecting any frequency dependence), the solid angle, $d\Omega$ is integrated over:

$$R_C = \iint I_v(\vec{s}) \cos(2\pi v \vec{B} \cdot \vec{s}/c) d\Omega \tag{3.5}$$

Please refer to Verschuur & Kellermann (1974) and Thompson, Moran & Swenson (1991) for detailed derivations of these equations. Since the vector $\vec{s}$ is a *function of direction*, the phase of the cosine function is determined by the arrival angle of the wavefront and consequently on source structure. This gives a relationship between the observable quantity (R_C, the interferometer response) and the quantity of interest (I_v, the source brightness on the sky). The cosine correlator effectively casts a cosinusoidal fringe pattern on the sky of angular spacing ~$\lambda/\vec{B}$ (this is the cosine term of Eq. 3.5). The correlator multiplies the source intensity distribution by this fringe pattern, and integrates the result over the sky. The cosine correlator response, R_C gives the even coherence

pattern. To obtain the odd coherence pattern, a sine correlator is used. Please refer to Thompson (1999) for the mathematical derivation of the sine correlator response R_S.

The orientation of this fringe pattern is determined by the orientation of the baselines and the fringe separation is determined by the baseline length, $\vec{B}$ and wavelength, λ i.e. long baselines give close packed fringes and extended sources average out to give highly resolved point sources. Alternatively, short baselines give widely separated fringes and flux from extended sources adds up with low resolution (Thompson, Moran & Swenson 1991).

3.1.3 The Visibility Function

The combination of the sine and cosine correlator responses from individual baselines gives the complex correlator response. This is essentially a series of interference fringes from which components of the complex *visibility function, VF* can be derived. It is essentially the correlated signal between average electric fields across the FoV of 2 antennas separated by a baseline (Yatawatta 2009). The VF of amplitude, A and phase, ϕ is defined as (Taylor et al. 1999):

$$VF = R_C - iR_S = A \cdot \exp(i\phi) \tag{3.7}$$

which results in the following:

$$VF = \iint I_\nu(\vec{s}) \exp(-i2\pi\vec{B} \cdot \vec{s}/\lambda) d\Omega \tag{3.8}$$

The visibility amplitude, A is defined as:

$$A = \sqrt{R_C^2 + R_S^2} \tag{3.9}$$

and the visibility phase, ϕ is:

$$\phi = \tan^{-1}(R_S / R_C) \tag{3.10}$$

3.1.4 Imaging Geometry and the (u, v) Plane

The projected baseline vector on the sky is defined as, $\vec{B} = (\Delta X, \Delta Y, \Delta Z)$ and is dependant on where the object is on the sky (hour angle, *HA* and declination, *dec*). The directions of dimensions (X, Y, Z) are such that, X pointing is to HA = 0h, Dec = 0^o; Y pointing is to HA = -6h, Dec = 0^o

and Z pointing is to Dec = 90°. The *spatial frequency* of the interference fringes of the correlator response are given by (Thompson 1999):

$$(u, v, w) = (1/\lambda)\ (\Delta X, \Delta Y, \Delta Z) = \vec{B}\ /\lambda \qquad (3.11)$$

where u, v and w are measured in wavelengths (cycles arcsec^{-1}) at the central frequency of the radio frequency signal band and correspond to the rate of sampling the X, Y and Z dimensions in the sky and follow directions towards East, North and the phase tracking centre of the source, respectively (Thompson 1999). For the simplistic case, we consider 2 dimensions u, v i.e. where the volume from which visibilities are measured is approximated to be a flat plane. This holds for a small angular FoV on the sky. Please see § 3.4.10 where for wide-field imaging**,** the w-term has to be considered in what is known as *w-projection.*

Coordinates on the sky are defined in *l* and *m*, which are directional cosines measured with respect to the u and v axes (Figure 3.1). The synthesised image in the *l, m* plane is a projection of the 3-D celestial sphere onto a 2-D tangent plane at the *l, m* origin. Distances in *l* and *m* are proportional to the sines of the angles measured from the origin (Thompson 1999). Since the unit vector $\vec{s}$ is defined by its projection onto the (u, v, w) axes (we continue in 2-D using only u and v), it follows that:

$$VF_v(\mathrm{u},\mathrm{v}) = \iint \frac{I_v(l,m)}{\sqrt{1-l^2-m^2}} \exp\left(-i2\pi(\mathrm{ul}+\mathrm{vm})\right) dl dm \qquad (3.12)$$

Hence the complex visibility function, $VF_v(\mathrm{u},\mathrm{v})$ *i*s the 2-D Fourier transform of the projected brightness distribution on the sky, $I_v(l,m)$. Following Thompson (1999), this Fourier transform can be inverted to give:

$$I_v(l,m) = \cos(\gamma) \iint V_v(\mathrm{u},\mathrm{v}) \exp\left(+i2\pi(\mathrm{ul}+\mathrm{vm})\right) du dv \qquad (3.13)$$

where γ is the angle between $\vec{s}$ and the w axis which points to the phase centre of the source. Therefore with enough measures of the VF (which is distinctive for each baseline) we can determine $I_v(l, m)$; an image of the sky.

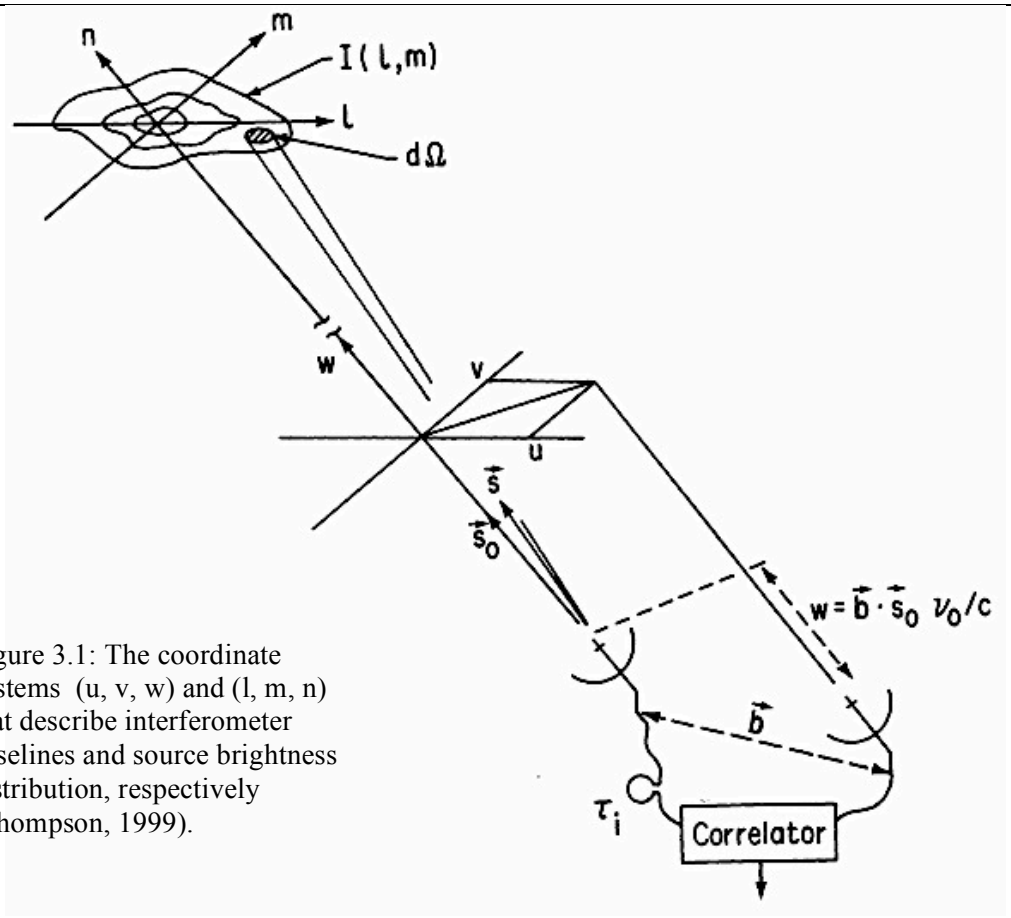

Figure 3.1: The coordinate systems (u, v, w) and (l, m, n) that describe interferometer baselines and source brightness distribution, respectively (Thompson, 1999).

Essentially the (u, v) plane is the Fourier-transform plane of the angular distribution of the source on the sky and describes the way in which the Fourier plane is sampled. (Eq. 3.13) presumes knowledge of $VF_\nu(u, v)$ for all values of u and v (requiring an infinite number of antenna pairs). However, at a single time slip a single baseline measurement only provides a single datum on the (u, v) plane and poor (u, v) coverage results in poor quality images. In order to produce a high quality image, as many different separations (baselines) as possible are required from the source's point of view between the different telescopes.

(Eq. 3.2) gives the number of *static* baselines, n_B for an array of *n* telescopes (Taylor et al. 1999). However, most aperture synthesis interferometers use the rotation of the Earth to increase the number of different baselines in an observation, which increases the number of (u, v) points (see Ryle & Neville 1962). Taking data at different times effectively provides different telescope separations and angles without the need of additional telescopes or moving them physically, as the rotation of the Earth moves the telescopes to new baselines orientations from the source's point of view. This is *Earth rotation aperture synthesis* and creates tracks in the (u, v) coverage as shown in Figure 3.2 (see Ryle 1962).

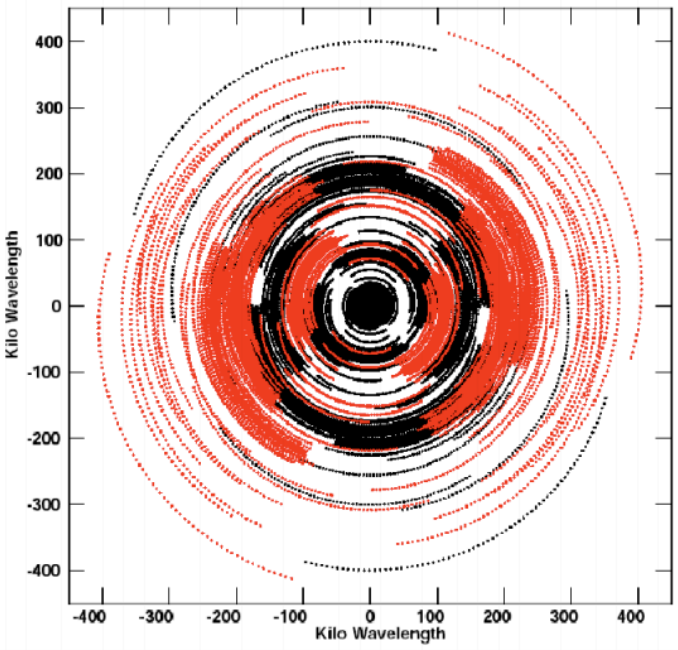

Figure 3.2: A simulation of the (u, v) coverage at 100 MHz provided by the Dutch and international LOFAR stations. Simulated baselines involving UK stations are shown in red. This demonstrates how potentially powerful VLBI (§ 3.2.2) is in improving (u, v) coverage (Best 2007). During the duration of an observation, tracks are traced out on the (u, v) plane. The number of tracks is equal to n_B.

In all, how well the (u, v) plane is sampled depends on: (i) the observatory parameters (number, n, diameter and configuration of antennas); (ii) where the object is in the sky (*HA* and *dec*) which affects projected $\vec{B}$; and (iii) duration of the observation (integration time) which affects Earth rotation aperture synthesis. *Multi-frequency synthesis* can also help to fill in the (u, v) plane and optimise sensitivity (§ 3.4.12).

The synthesised antenna beam will have *side-lobes* evident in raw 2-D images created directly from an interferometer due to gaps in the (u, v) plane. Thompson, Moran & Swenson (1991) refer to these as ring-lobe responses with profiles related to spatial sensitivity, represented as a series of circular delta functions. These instrumental image artefacts result from the 'dirty beam' (the point source response pattern or point spread function, PSF) by which the image is convolved and is in contrast to the ideal 'clean beam'. Convolving an astronomical source with the 'dirty beam' produces a dirty image as demonstrated by Figure 3.18 (in addition to uncalibrated ionospheric effects). The extent of the side-lobes can be reduced and the resultant beam tip enhanced by increasing the sampling of the (u, v) plane with the listed methods above.

Data-reduction and *imaging synthesis* algorithms such as CLEAN (Högbom 1974) can approximate the ideal single dish image given the dirty image and the dirty beam (Cornwell, Braun & Briggs 1999). A 'clean beam' is classically created by fitting a 2-D Gaussian to the primary lobe of the 'dirty beam'. The CLEAN algorithm works principally on the basis that most sources in the sky are point-like, and identifies these point sources and then scales and subtracts off their

'dirty beams'. In reality, many sources are diffuse, but the approach of treating the brightest areas in the image as point-source responses is still a valid approximation producing good results (Thompson, Moran & Swenson 1991). At each subtraction, the position and flux subtracted are recorded, until the map from which the 'dirty beams' have been subtracted (the residual map) comprises only of noise. At this stage, the subtracted fluxes are convolved with a restoring beam selected by the user and added back into the field of noise to give a final clean map from which the side-lobes (particularly negative) of the 'dirty beam' have been removed (Högbom 1974). In all, the CLEAN procedure breaks down the intensity distribution into point-source responses, and replaces their 'dirty beams' with 'clean beams' free from side-lobes (Högbom 1974). Please see § 3.4.9 for more details on CLEAN and the imaging process for our data.

3.2 LOFAR

3.2.1 Hardware

LOFAR *currently* operates between ~ 15–240 MHz and employs the use of 2 antenna types: Low Band Antennas (LBAs) and High Band Antennas (HBAs). Our observation was carried out during the commissioning of the array, before the telescope came properly into data production. At that time, the LBAs were optimised for detecting frequencies between 30–80 MHz and HBAs were optimised for frequencies between 120–240 MHz (de Vos et al. 2009). Frequencies 80–120 MHz were avoided since they are prominent Radio Frequency Interference (RFI) regions e.g. the FM radio band (87–108 MHz) was clearly visible in this range on LOFAR frequency spectra (Bentum et al. 2010). However, RFI suppression capabilities have improved since, as detailed by van Haarlem et al. (2013); for the present LBA, either a 10-MHz or 30-MHz high-pass filter can be inserted to suppress the strong RFI often encountered below 20 MHz (van Haarlem et al. 2013). Hence the sensitivity at the lowest frequency capability of the LBA has improved from ~ 30 MHz (at the time of our observation) down to the current 15 MHz, and is *designed* to go as low as 10 MHz (Wijnholds 2010). Kondratiev et al. (2013) describes how the implementation of a full-core single-clock in 2013, would result in a fourfold increase in sensitivity. Unfortunately this capability was *not* something we could take advantage of in 2011 and clock issues are discussed in

§ 3.4.13.

LOFAR consists of three station types: *core*, *remote* and *international,* the key features, and *current* performance capabilities of which are summarised in Table 3.1 and the schematics of which are demonstrated in Figures 3.3, 3.4 and 3.5 (Nijboer et al. 2009). The central core of radius 2 km is densely filled with antennas forming what is known as *Superterp* as shown in an aerial photograph in Figure 1.6, the purpose of which allows more effective calibration of the telescope and optimises sensitivity (Wijnholds 2010). These core stations create very short baselines whilst the remote stations are spread out further over 100 km within the Netherlands. The number of stations applicable to our observation (§ 3.4.1), which utilised the array during its commissioning before it properly came into data production, are also included and contrasted in Table 3.1.

Station Configurations	**Current Number of Stations**	**LBA dipoles per station**	**HBA tiles per station**	**Signal Paths per station**	**Min. base-line (m)**	**Max. baseline (km)**
Superterp	6 (Also 6 for our observation)	2x48	2x24	96	68	0.24 (Also 0.24 for our observation)
NL Core Stations (incl. the 6 of Superterp)	24 (19 at the time of our observation)	2x48	2x24	96	68	3.5 (~2.8 for our observation)
NL Remote Stations	16 (9 at the time of our observation)	2x48	48	96	68	121 (~82.7 for our observation)
International Stations	8 (0: we did not use international stations during our observation; see (§ 3.4.1)	96	96	192	68	1158 (N/A for our observation)

Table 3.1: Summary of the key features (LBA antennas and HBA tiles) according to the station type (van Haarlem et al. 2013). These numbers are not applicable to the time of our observation (§ 3.4.1), which was taken during commissioning in 2011, before the telescope came properly into data production; the exact numbers as they were when our data were taken, are given in brackets.

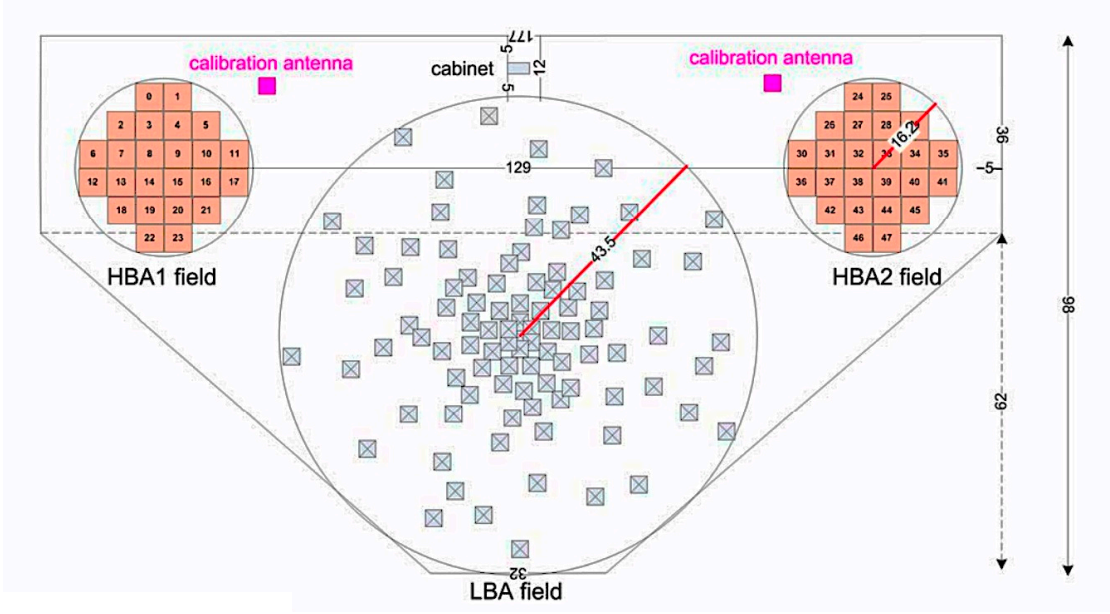

Figure 3.3: Plan view of a core station. The LBA is in the centre with a spare pseudo-random configuration, and the HBA sections on either side, each consisting of 24 tiles (Nijboer et al. 2009).

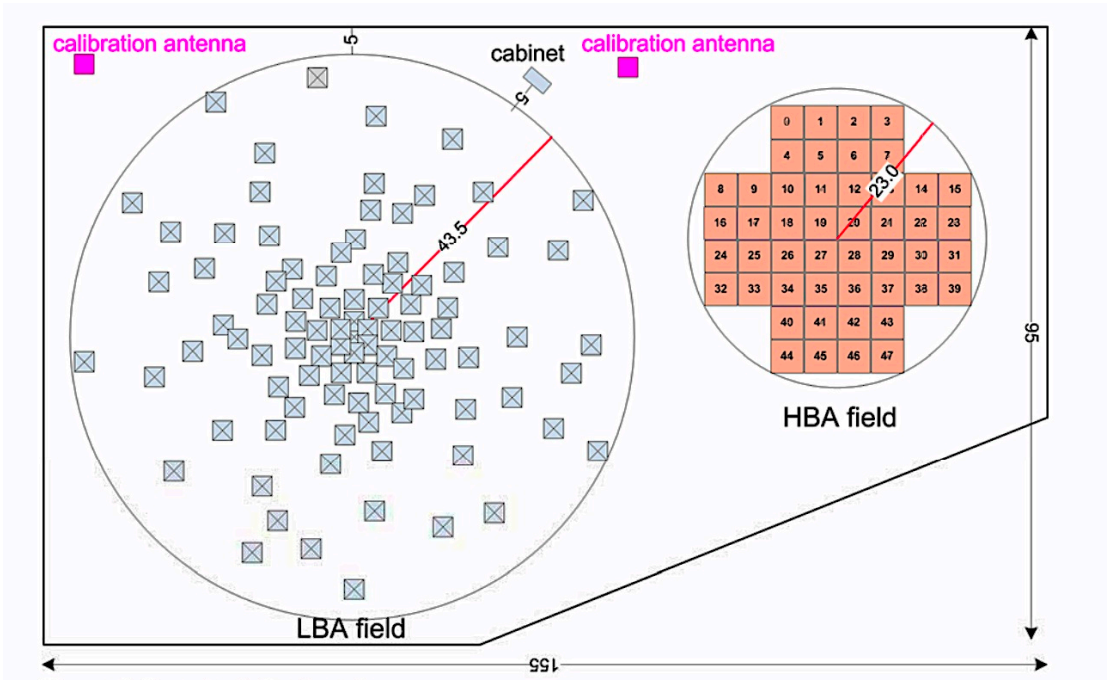

Figure 3.4: Plan view of a remote station.
The 48 HBA tiles are grouped together (Nijboer et al. 2009).

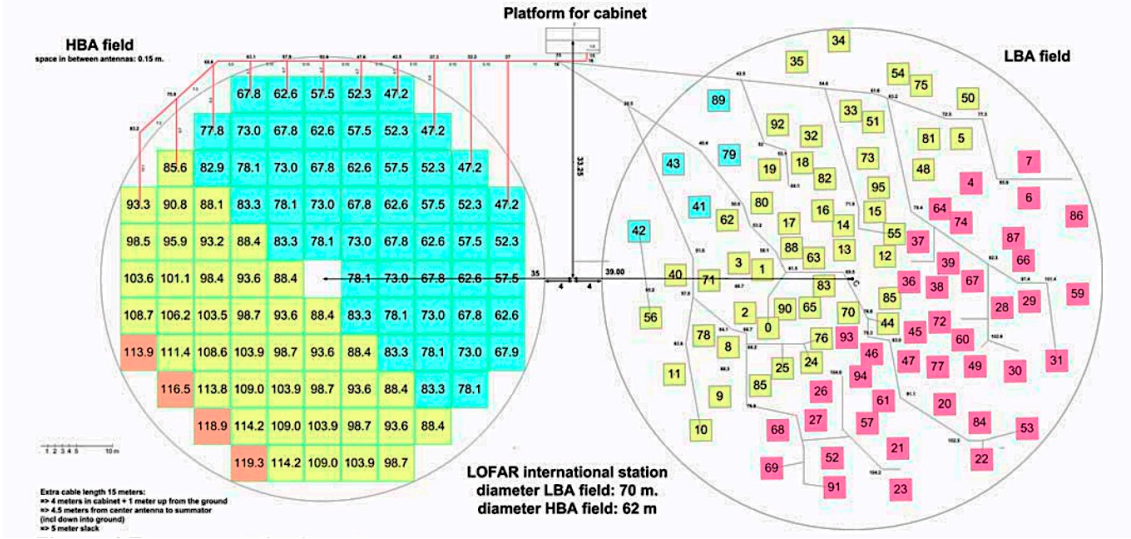

Figure 3.5: Plan view of an international station. There are 96 HBA tiles (twice that for core and remote stations.) Each HBA tile comprises of 16 HBA dipoles (Nijboer et al. 2009).

3.2.2 LOFAR's Angular Spatial Resolution

LOFAR collects low RFs, so 1 repeating unit of the EM radiation is very large e.g. at 30 MHz, the unit λ is 10m. Such low frequencies would result in poor images of resolutions of arc-minutes if the array were not very extensive (Eq. 3.1). Therefore, baselines are appropriately long to determine decent resolution. LOFAR makes use of Very Long Baseline Interferometry (VLBI) by linking international stations separated by 1000s of km, spread over Northern Europe (Table 3.1) which dramatically and sufficiently improves resolution relative to having remote and core stations only. This allows radio sources to be accurately positioned and identified at low frequencies and compared to counterparts detected in other wavebands (such as optical) (Best 2007). The LOFAR angular resolution, θ_{res} in radians is calculated using (Nijboer et al. 2009):

$$\theta_{res} = \alpha_2 \frac{\lambda}{\vec{B}} \tag{3.14}$$

where α_2 depends on the array size and configuration and spatial taper function i.e. imaging weighting scheme (Wijnholds & van der Veen 2008) (§ 3.4.9). $\alpha_2 \approx 0.8$ for uniform weighted images using the Dutch array only (Nijboer et al. 2009).

Van Haarlem et al. (2013) detail improvement in LOFAR angular resolution for various baseline lengths as a function of frequency (Figure 3.6).

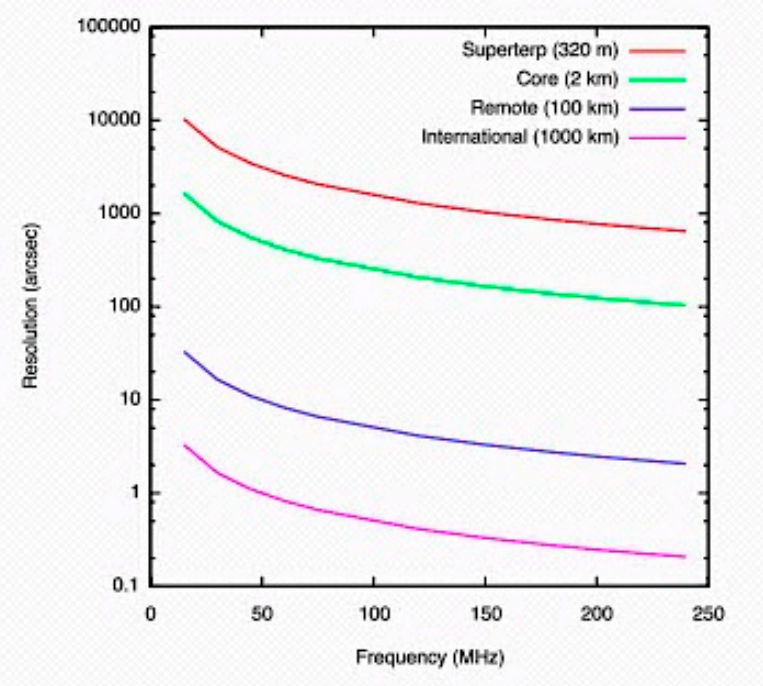

Figure 3.6: Angular resolution as a function of frequency for different configurations of LOFAR (van Haarlem et al. 2013).

International stations were not included in our observation as detailed in § 3.4.1 and remote stations constituted the longest baselines. Hence according to Figure 3.6 the best level of achievable resolution is in the range ~ 10–50″ for the LBA. This was sufficient to resolve numerous extra-galactic sources in the FoV (see § 4.1.1).

The LBA Station Configuration

The Dutch LOFAR stations each are capable of processing 48 dual polarisation (X and Y) signal paths; for International stations, this is 96. The Dutch stations have 48 Receiver Unit Boards (RCUs), so that for the 96 single LBA dipoles, only 48 can be selected for any single observation. For the International stations, there are 96 RCUs, so LBA selection is not required and all 96 antennas can be used simultaneously (Nijboer et al. 2009). Therefore, due to limited RCUs, the Dutch stations employ the use of different LBA selections (inner, outer, sparse, X and Y). In the inner configuration, both polarisations from the innermost 48 LBAs are used. In the outer configuration, the outer 48 LBA dipoles are used, also in dual polarisation. The sparse configuration uses 48 LBA dipoles from different parts of the LBA field in dual polarisation. The X configuration uses only the X polarisation of all of the 96 LBA dipoles, and the Y mode does the same for the Y polarisation (Nijboer et al. 2009).

3.2.3 LOFAR's Sensitivity

As seen, (Eq. 3.4) shows how the strength of the product of the combined pair of voltages V_1V_2 is directly proportional to the source intensity, I_ν. The product strength also depends on antenna electronic *gain factors*, which can vary with temperature and time. These can be corrected for, using coefficients related to the time varying system temperature, which can be monitored continuously (Edwards 2007). For LOFAR, the variability of antenna gains are recorded and corrected every 24 hours in single-station calibration allowing for a more stable instrument (see § 3.3.2).

The collecting areas of the antennas also affect the strength of V_1V_2. As mentioned, arrays are much less sensitive than a single 'filled aperture' telescopes since many photons are lost to the ground between the collective dishes; this is revealed by the large gaps in the (u, v) plane. Hence, the sensitivity of a radio telescope is directly proportional to its collecting area. For a phased array like LOFAR (§ 3.2.4), the useful observing area of the station is the sum of the individual dipole collecting areas. This collection area, A_e is the effectiveness of the dipole at converting the incident EM radiation of wavelength, λ into an electric current (van Cappellen et al. 2005):

$$A_e = \frac{\lambda^2}{4\pi} G \tag{3.15}$$

where G is the antenna gain. This in turn is related to directivity D, by $G = \eta D$ where η is the radiation efficiency of the antenna (assumed to be 1 if antenna losses are neglected). D can be estimated geometrically from normalised antenna patterns (van Cappellen et al. 2005) and accounts for projection effects (which can reduce A_e) depending on the direction of pointing.

From (Eq. 3.15) it follows that the inner and outer LBA usage schemes depend on the observing frequency: for radio frequencies < 40MHz, outer is used, and for radio frequencies > 40MHz, inner is used (de Vos et al. 2009). This is because for dipoles placed close together (as in the core of the LBA), for lower observing frequencies their effective areas can significantly overlap, resulting in a reduction of the effective area of the station. Therefore the outer LBA configuration is advisable for these frequencies. Wijnholds (2007) visually demonstrates the inner and outer usage schemes and the effective areas of the dipoles at two contrasting frequencies and

their corresponding (u, v) coverage.

The system sensitivity, S_{sys} is defined as:

$$S_{sys} = \frac{2\eta k}{A_e} T_{sys} \tag{3.16}$$

where k is Boltzmann's constant, and T_{sys} is the system noise temperature (please see Taylor et al. 1999) which itself consists of 2 components: sky brightness temperature, T_{sky} and instrumental noise temperature, T_{instr} (Nijboer et al. 2009):

$$T_{sys} = T_{sky} + T_{instr} \tag{3.17}$$

For LOFAR frequencies, T_{sky} is dominated by the Galactic radiation which is determined by the wavelength of observation:

$$T_{sky} = T_{s0}\lambda^{2.55} \tag{3.18}$$

where T_{s0} = 60 ± 20 K, for Galactic latitudes between 10 – 90º (Bregman 1999). T_{instr} is determined from measurements or simulations and Figure 3.7 shows T_{instr} for a LOFAR LBA dipole based on measurements in the field (Nijboer et al. 2009). The peak between 50–60 MHz is LOFAR's most sensitive observing range for LBA.

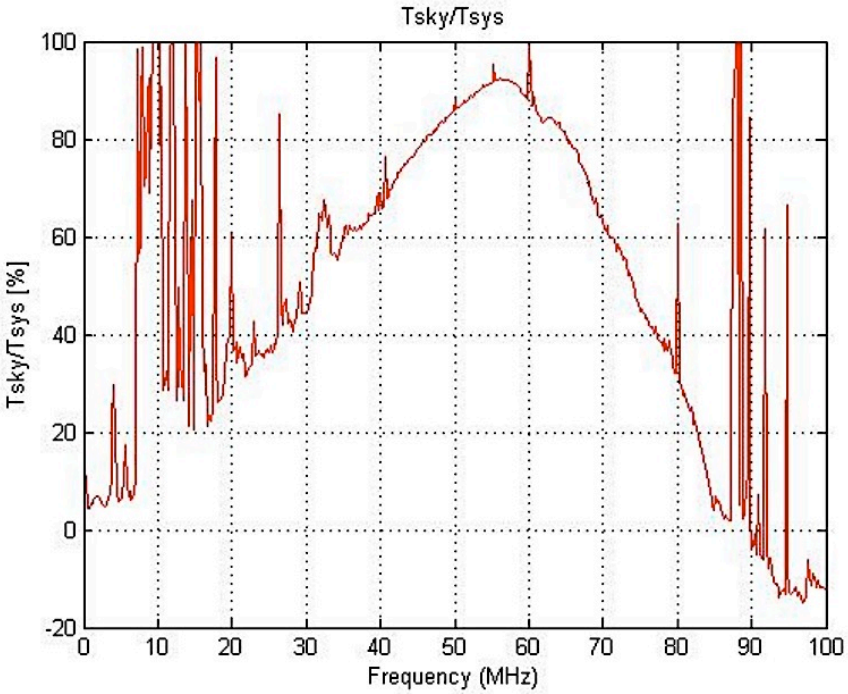

Figure 3.7: measured T_{sky}/T_{sys} for a LOFAR LBA antenna averaged over 48 dipoles (Nijboer et al. 2009).

3.2.4 Hierarchical Beam Structure & Beam-Forming

With the planned 24 core stations and 16 remote stations, the full Dutch LOFAR array alone has approximately 30720 HBAs and 3840 LBAs (as anticipated by Wijnholds 2010) although these numbers would be smaller for our observation due to fewer stations available (Table 3.1; § 3.4.1). It would be far too costly to sample and process every signal from every individual antenna. Therefore LOFAR employs the use of a hierarchy of beams with increasingly smaller FoV but higher sensitivity to decrease the amount of signal paths at each level by order 100 (Wijnholds 2010). The first level of the LBA hierarchy is the antenna or element beam pattern, which is combined with other antenna beam patterns by the station beam former to form the station beam. Multiple signals from other stations can be combined to form the LOFAR array beam. The station beam can be considered as that from a classical single dish radio telescopes but it much more flexible as it does not form the base of the beam forming hierarchy (Wijnholds 2010). Since LOFAR's components are not made up of single dish parabolic reflectors but of omni-directional antennas, this has allowed unprecedented flexibility of observational frequency as well as multiple beam direction with independent sky coverage. Pointing direction is carried out electronically by combining signals from the antennas (LBA or HBA) with specified set of time delays in the beam-forming process (Wijnholds 2010). This phasing of the antennas by specific delays makes LOFAR a *phased-array* which does not need moving parts for specific pointings of the sky. The LOFAR beam configuration utilised for our observation of the W3/W4/W5 complex is shown in Figure 3.13 and further information on the array observation is detailed in § 3.4.1.

3.3 LOFAR Single-Station Observation & Reduction

3.3.1. Aims & Observation

The international LOFAR stations are very sensitive telescopes in their own right and can be used *independently* from the LOFAR array. In the low-band, the primary beam diameter can reach as much as ~ 20º at 30 MHz using the inner LBA configuration (Nijboer et al. 2009). This allows huge FoVs to be observed with high sensitivity (the 8 international HBA and LBA Stations of 70 m and 62 m diameter respectively, alone account for ~ 30% of LOFAR's total collecting area) and very fast sampling of the incoming radiation, make them very useful stand-alone arrays (Best 2007 and Wjinholds 2010). We took advantage of single-station imaging for this project to capture the large-scale, irregular patches of Galactic diffuse synchrotron emission at low frequencies with short baselines spanning only a few λs of observed radiation.

Both thermal radiation and synchrotron emission contribute to diffuse Galactic emission, the fraction of which depends on observing frequency and varies as a function of Galactic coordinates (please refer to the all-sky surveys section of the German Long Wavelength consortium paper in Brüggen et al. 2005). We anticipate that at LOFAR frequencies, thermal emission will be optically thick and synchrotron emission will dominate (§ 2.3.5). If the quality of our maps is sufficient then we may see evidence of FFA (§ 2.3.9) by ionised H II regions (e.g. Shain et al. 1961) which is anticipated to be most prevalent near the Galactic centre at a Galactic latitude < 10º and a Galactic longitude of 40–60º (based on observations by Cane 1977 at 10 MHz). Very low radio frequency observations have already been conducted of the Galactic background using various low frequency telescopes, and early results taken in directions toward the Galactic centre, the anti-centre, and the North Galactic Pole all show a peak brightness near ~ 3 MHz (Alexander et al. 1970) confirmed in SED analysis by Peterson & Webber (2002) (§ 2.3.9). From Figure 2.11 we predict that we will see a negative spectral index between our observed frequencies, although this value could *vary spatially* with some degree of flattening according to the magnetic field structures of the Milky Way traced out by low energy cosmic ray electrons (§ 2.3). All-sky radio emission and spectral index information across a whole frequency range from a variety of telescopes (which comes with its own technical challenges), together with the magnetic field structure derived from radio polarisation data, will help construction of a 3-D model of the Galactic cosmic rays (Brüggen et al.

2005). A better understanding of the diffuse radio synchrotron foreground will also be advantageous for extragalactic and Epoch of Reionisation (EoR) LOFAR KSP groups who are keen to remove these effects (see Best 2007). A spectral index map has been made between 408 – 1420 MHz (Reich & Reich 1988) and at the very low radio frequencies between 14.7 – 25 MHz (Vasilenko 2007) with the UTR-2 radio telescope; we hope to make the first spectral index map between ~ 35 – 75 MHz.

With the time of year of the observation in mind, the direction of Sgr A* (the approximate centre of the Milky Way) was predicted to cross the meridian at 13.39 UTC and was rising and falling between ~ 09.35 - 18.00 UTC. Hence data was collected using the Chilbolton international station on 7th November 2011 between 11.36 – 17.43 UTC. The LBA correlator observes the range 0–100 MHz which is split into 512 sub-bands (SBs; see § 3.4.1) of ~ 195kHz each. Approximately 43 scans were captured as binary accumulation (acc) datasets with 1-second integration per SB.

3.3.2. Relative Self-Calibration Pipeline

In order to increase the sensitivity of observations, we must calibrate our data to mitigate (i) instrumental and (ii) ionospheric effects (§ 3.4.3). The difference between calibration at the array (§ 3.4) and single-station level is that ionopheric refraction effects are less extreme for the latter since there are no long baselines and all antennas see the same part of the atmosphere (see § 3.4.3).

Calibration of single stations is carried out routinely to mitigate against small but significant biases in calibration factors that repeat after 24 hours including (i) gain and phase differences between antennas and (ii) unmodelled systematic effects such as mutual coupling of closely spaced antennas, ionospheric scintillation and broadband Radio Frequency Inference, RFI (see Wijnholds 2011b and § 3.4.6). A stable instrument with a predictable nominal station beam is paramount for calibration at the station and array level. This is achieved by the construction of a *station calibration table* of complex beam-formed weights of frequency independent gain factors and frequency dependent phase factors at each SB. This corrects geometric gain, phase and time delays between signal paths taking care of the baseline effects, dipole and cable variation etc. (Wijnholds 2011b). This is detailed for LBA observations by Wijnholds (2011a) using the *StationCal* package

written by Stefan J. Wijnholds, which operates within the MATLAB software environment and makes use of *Cramer–Rao lower bound (CRB) analysis* (detailed in Wijnholds 2010). For array observations, these calibration tables are automated and applied to the data at the station level, but for our single-station observation this table was created manually following Wijnholds' work in a method of self-calibration (§ 3.4.5) before being imaged.

Wijnholds' pipeline, which solves for an adapted version of the Measurement Equation (Eq. 3.20), involves: (i) applying a bandpass filter to leave 10–90 MHz useful range; (ii) flagging RFI which is strong in a number of SBs particularly $v < 25$ MHz and $v > 88$ MHz; (iii) flagging short baseline effects such as electrical crosstalk (see Subrahmanyan & Deshpande 2004 and Wijnholds 2010); (iv) inspecting time-frequency planes for phase solutions of a few antenna elements to check the quality of the solutions (see Figure 3.8); (v) correction of the gain differences between antennas for each signal path using an amplitude model (including direction dependent gains towards specified sources which involves the application of the sky model of the 5 celestial sources in the northern hemisphere: Cas A, Cyg A, Tau A, Vir A and the Sun); and (vi) correction of direction dependent phase differences between antennas (modeled by a linear frequency dependent ionospheric phase screen model applicable for *short* baselines; see § 3.4.3) (Wijnholds 2010). Steps (v) and (vi) need an antenna configuration file which gives information on the position and orientation of the antenna in the field and an initial global sky model (which self-calibration relies upon; § 3.4.5) as well as the observational parameters (time, duration etc.) and longitude and latitude of the station.

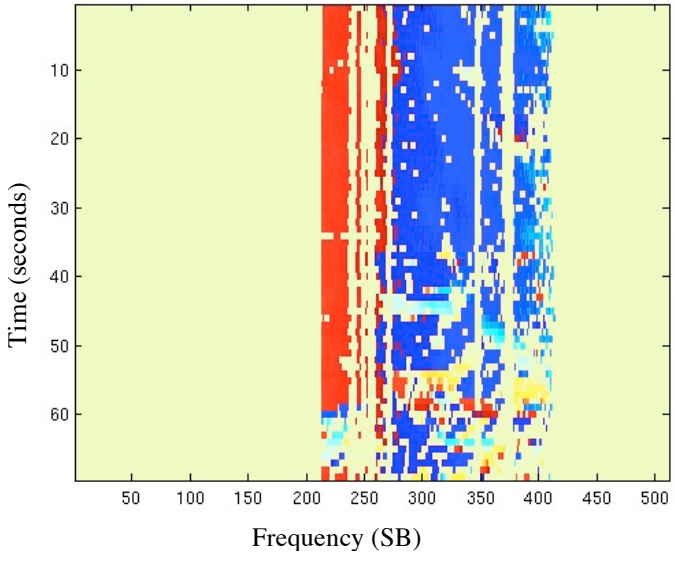

Figure 3.8: plot of a time-frequency plane of phase solutions during a test trial of our data observing at a bandwidth 39 MHz – 84 MHz for a single element. The data should be smooth over time and vary slowly over frequency and not too severely flagged (evident as gaps). No fringing patterns or phase gradients over frequency should be evident.

Meqtrees self-calibration techniques (Noordam & Smirnov 2010) can also be used to correct for instrumental effects between signal paths and generate complex gain solutions and is an alternate method of station calibration to Wijnholds' self-calibration technique as has been explored by the Oxford e-Research Centre (OeRC) although it was not directly used for our observation. Both self-calibration techniques take a modified application of the 'Least Squares' approach (§ 3.4.5).

3.3.3. Imaging of Calibrated Data

Wijnholds' imaging MATLAB algorithm was used for widefield all-sky imaging of the calibrated correlations. The images created are essentially 1-second snapshots of single-frequency observations of the sky projected onto the *l*-*m* plane (§ 3.1.4). The large FoV is captured with North at the top and East to the left of our *test* dataset taken a month earlier as shown in Figure 3.9. The large-scale structure of the Galactic plane is clearly visible and *dynamic range* (*DR*; § 3.4.8) of ~180 at 80 MHz is impressive, despite only collecting the data during 1 second, demonstrating the high sensitivity (albeit coarse resolution) of a single station. The 2 prominent bright spots are the noisy radio bright sources Cygnus A (Cyg A), near the centre and Cassiopeia A (Cas A) towards the North East. The Galactic plane passes these sources and extends to the South-West. The large cloud of Galactic radio emission evident as an arc-like feature at +30º, 0º starting from the Galactic centre in the South and extending towards the western horizon could possibly be the North Polar Spur (e.g. Salter 1983), but we would need deeper images with longer integration times to confirm this.

Time-lapse images were made mapping the sky as it rotates during the observing period at a particular frequency. This follows work by James Anderson of the Max Planck Institute for Radio Astronomy who created the first time-lapse movie for the Effelsberg single-station in Germany (van Haarlem et al. 2013). Time-lapse movies were also created with images ranging across the frequencies starting at ~ 30 MHz with each subsequent frame ~ 195 kHz higher, reaching ~ 85 MHz. As expected, the resolution of the images changes with frequency varying from ~ 7º at 35 MHz to ~ 4º at 80 MHz evident by the change in the apparent size of Cyg A and Cas A. Figure 3.9

shows how we can smooth the 80 MHz image to the same resolution as that at 35 MHz using the 2-D Gaussian PSF of the beam at the lowest frequency.

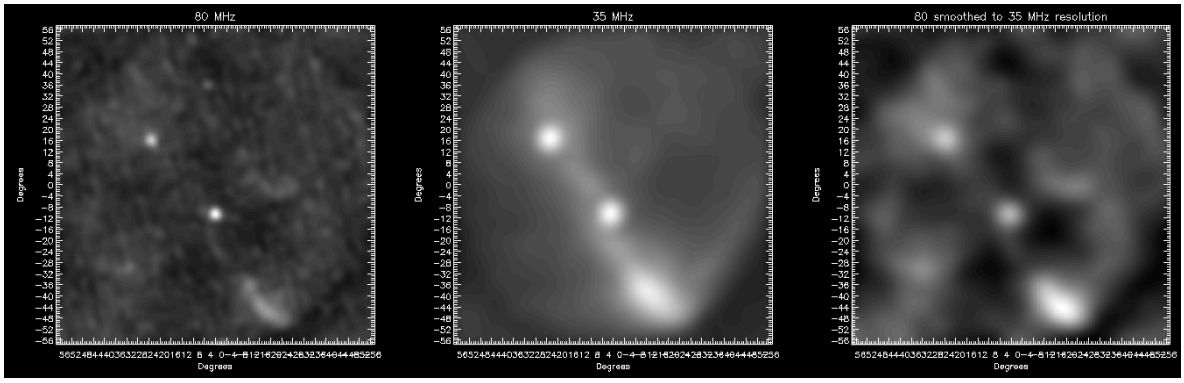

Figure 3.9: 80 MHz (left) and 35 MHz (middle) all-sky images made with Chilbolton made with our test observation. On the right is the 80 MHz image smoothed to the resolution of the 35 MHz image. Note that these images are *not* on the same brightness intensity scale.

3.3.4. Subtracting out the Sky Model (Cas A & Cyg A)

The problem with the all sky test images of Figure 3.9 is that Cas A and Cyg A and their respective large side-lobes dominate the all sky diffuse emission, which we are interested in. Therefore it is important to correct for and remove their effects. Taurus A (Tau A) is a weaker source and at the time of our observation it was below the horizon to have a significant impact on our image plane. Wijnholds' updated 2014 version of the StationCal algorithm does provide an estimate of the power of Cas A and Cyg A with *updated* sky models based on the input data and we used these to subtract out these sources post-calibration. This had the effect of leaving holes where they had been since the code does not consider the background emission and is a relatively crude method of source removal compared to the sophisticated techniques discussed in § 3.4.4 for array data. We also could not fully remove Cas A and Cyg A since they are very strong and the calibration using StationCal entangles them and their direction-dependent side lobes with the strong Galactic emission. In particular, there seems to be residual Cyg A emission at frequency ~ 57 MHz (Figure 3.10). We modified Wijnholds' code so that all images were displayed in Stokes I only by imaging $Vis_{Stokes\,I} = 0.5\times(Vis_{XX} + Vis_{YY})$ where $Vis_{Stokes\,I}$, Vis_{XX} and $+Vis_{YY}$ are visibilities in Stokes-I and linearly polarised feeds XX and YY respectively.

Figure 3.10 demonstrates how relative self-calibration removes much noise from the image and improves the relative ionospheric phase distortions whilst the removal of Cas A and Cyg A has the effect of brightening the emission along the Galactic plane. Relative phase calibration is

carried out with respect to the first source in the source list (Cas A) which stays at the unit flux of 1; Cyg A and Tau A (if included) are given initial fluxes of 0.7 and 0.5 respectively in Wijnholds' algorithm. The apparent flux ratios of the *relative* emission across the FoV are then updated with respect to Cas A (which remains at 1 unit flux). However, as shall be discussed, Cas A is generally not a reliable source to calibrate against at low radio frequencies (§ 3.3.5), as it is imprecise to assume it is stable.

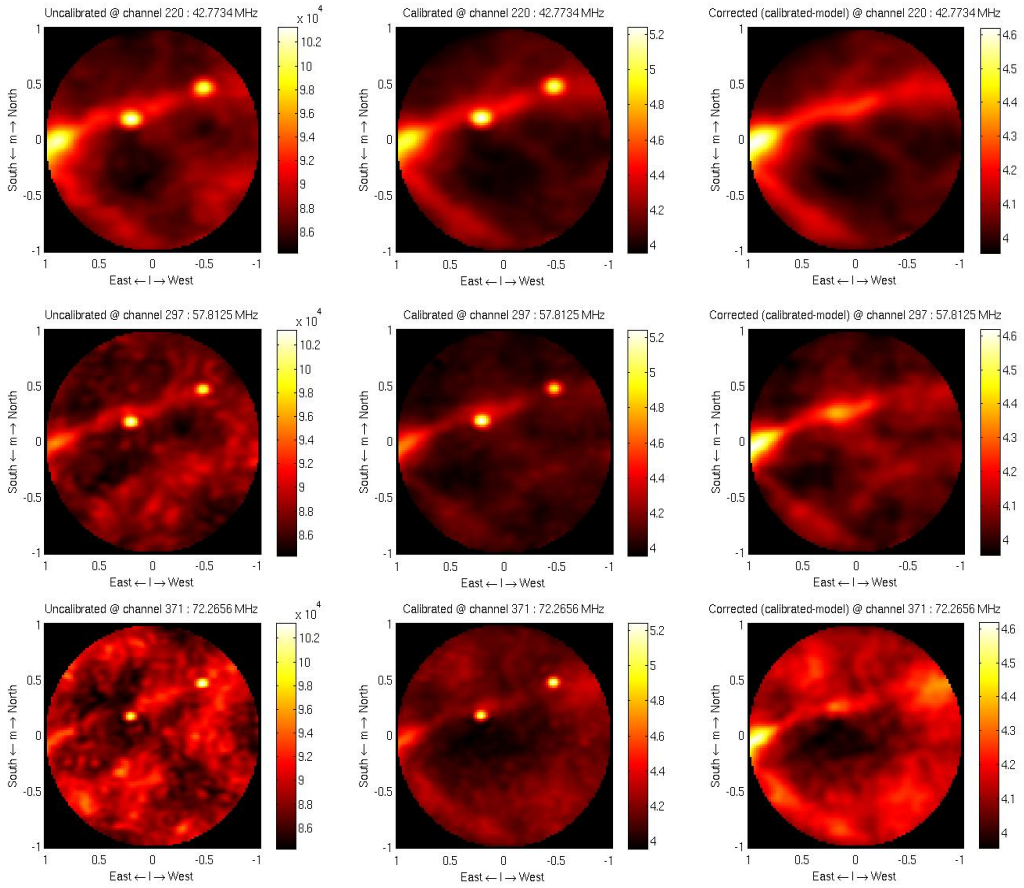

Figure 3.10: The images on the left are uncalibrated raw images; the centre images are the imaged visibilities calibrated with respect to Cas A and Cyg A and the images on the right are the calibrated images with Cas A and Cyg A removed. These images are all made in Stokes I, at ~42.7 MHz (top), ~57.8 MHz (middle) and ~72.3 MHz (bottom). Please note that these 2-D *l*-*m* image planes have *not* yet been smoothed to the same resolution.

Reliable relative flux *normalisation* was fundamental for evaluating a spectral index. As long as each image plane per frequency increment (SB), within each binary accumulation (acc) dataset was calibrated *consistently* with respect to each other, a fair comparison of the flux scaling across the SBs could be justified without the need for absolute calibration (§ 3.3.5); in essence this was a *relative* calibration scale. We experimented with ways to obtain calibration results that were normalised properly across frequency and chose to lock all apparent relative fluxes in the calibrated visibilities with respect to the first SB of the range. However, again whilst sidestepping the

challenges of setting the absolute calibration scale (as discussed below), we cannot be confident in the stability of Cas A which introduces caveats into these relatively calibrated results, the details of which are discussed below.

3.3.5. Discussion: Results, Considerations & Future Work

The calibrated images with Cas A and Cyg A removed (to first order), were exported from MATLAB as FITs images where they were then convolved to the same resolution as the lowest frequency in the Common Astronomy Software Applications package (CASA); a radio data reduction and imaging software (Jaeger 2007). The spectral index was then calculated using the 'SPIX' mode in the CASA function Immath (see methodology in § 4.1 for more details).

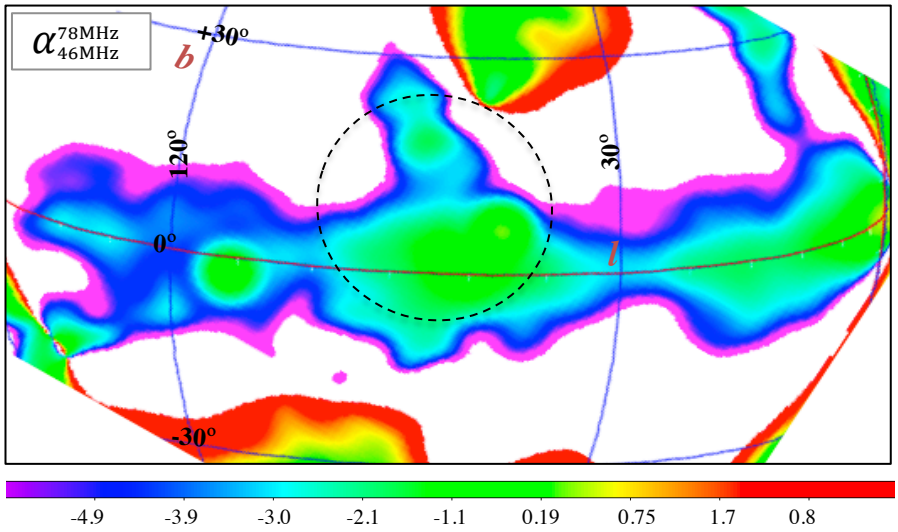

Figure 3.11: A first order attempt of a spectral index map with our LOFAR data viewed in Galactic spherical coordinates with ~ 6° resolution. This map could also be viewed as a Mollweide projection. The area within the dashed circle is an estimation of where the beam is flattest (see below).

Figure 3.11 shows our *first order* attempt of comparing relative emission between 46 – 78 MHz by means of a spectral index map. The spectral index values do look reasonable (values are negative as we suspect for synchrotron) and vary spatially over the Galactic plane (a consequence of the magnetic field and electron density; § 2.3). We may possibly see the emergence of the North Polar Spur at ~60°, +15° with the same features as that of the 408 MHz map of Haslam et al. (1982) which Bridle (1967) found has a lower spectral index than its surroundings between 13 – 404 MHz; we need would a more sensitive map to confirm this. We do not see evidence of flattening in the synchrotron emission between 46 – 78 MHz which is consistent with Alexander et al. (1970) i.e. that the spectral index is negative and steep in this range. We cannot trust the spatial variation in the index outside of ~ 15° from HA = 0° (i.e. directly overhead where the beam is flattest) due to

the direction-dependence of the beam which will dominate measurements (see below). It is within this limited region (represented by the dashed circle of Figure 3.11) that the expected value of α = -0.7 falls within the range of values given by the map (specifically between -0.4 – -2.5). The initial spectral index map of Figure 3.11 is the best result we could attain within the limited time frame and resources. Residual Cas A and Cyg A flux remains and are not completely subtracted out from our data as is evident with the halo of Cas A at ~5º, 0º. Whilst the low resolution (~ 6º) could buffer some calibration inaccuracies, we are very cautious of our result for the following reasons, for which suggestions of improvement are given in future work:

(i) Poor dynamic range (DR): We did reach a DR of ~ 60 (with Cas A and Cyg A removed) although an increase of a factor of 10 would greatly improve the quality of the spectral index map. In order to improve the DR of each single-frequency image, multiple images at the same SB, taken from the chronological acc files could be stacked, increasing sensitivity to the diffuse Galactic background synchrotron (we demonstrate the success of this with the diffuse emission of our array observation using wideband imaging; § 3.4.8 & § 4.1). Stacking must take account of the 'moving' sky since it takes 512 seconds to sweep across all 512 SB increments of the frequency range. This also means that there are 180 seconds between frequencies 46 – 78 MHz. At the time of this work there was no way of observing on just a single SB but on scales of 180 seconds the sky only varies by ~ 0.75º making a very small difference to the position of structures on a Galactic level. We cannot improve the resolution significantly (since this is baseline dependent; Eq. 3.1). However, an improvement in DR would enhance sensitivity to finer diffuse structures in the FoV.

(ii) Relative Calibration: As mentioned, absolute calibration is not entirely necessary for a first-order attempt of a Galactic spectral index map, as long as all the flux scaling of the SBs within a acc dataset are consistent across the frequency range and locked or normalised relative to the first SB of the range, in order to allow a reliable comparison. However recovering fluxes after *absolute* gain calibration could be an aim for future work. We were not able to solve this in our time constraints and absolute calibration is an on-going issue for LOFAR. Prasad, Wijnholds et al. (2014) discuss the challenges of absolute flux calibration with the Amsterdam-ASTRON Radio Transients Facility and Analysis Center (AARTFAAC) with reference sources at these low frequencies primarily due to ionospheric amplitude scintillation.

Absolute calibration of the station would require (a) an element beam model of the station and (b) absolute fluxes of the calibrators (Cas A and/or Cyg A) at a given frequency, since our relative calibration is carried out with respect to this source. Scaife & Heald (2012) present broadband spectral models for 6 bright radio sources as an initial reference for conducting science using LOFAR; the main reason why they reject the brightest sources, Cas A and Cyg A as calibrators is due to their complex structure, and assume a 20" resolution limit. As a consequence 3C sources that are bright, well understood, compact and highly spread in RA are more suitable calibrators. This may hold for the LOFAR core, but a LOFAR station provides a much coarser resolution (evident from our maps). As a result, Cas A and Cyg A do not have structure as far as a single station is concerned and can be treated as point sources, just like the 3C calibrators investigated by Scaife & Heald (2012). Hence after applying an element beam correction, it was initially considered that the *absolute* flux scale *could theoretically* be achieved by set by bootstrapping the normalised fluxes to the point sky model of the calibration reference Cas A set to its known Baars et al. (1977) spectral flux index. However, as mentioned in Scaife & Heald (2012), below 300 MHz, the Baars et al. (1977) radio flux density scale is incomplete and so using this method is limited. In addition, there is a secular decrease in the flux density of Cas A < 100 MHz (see point iii below), which is not considered in the Baars et al. (1977) scale (see Rees 1990).

(iii) Relative calibration initial sky model: It may be necessary to improve the accuracy of the sky model to achieve a more scientifically viable result. As mentioned, the StationCal calibration code works by calibrating all relative fluxes against Cas A which may be a problematic calibrator especially at low radio frequencies within the range of LOFAR, since its flux is decaying at a rate of ~ 1–4 % over ~ 10 yr (Elshamouty et al. 2013 and Heinke & Ho 2010). Helmbolt & Kassim (2009) find the decrease of the flux density of Cas A at ~ 80 MHz occurs at a rate of 0.7 – 0.8% yr^{-1} and that this is consistent across all frequencies between 38 – 80 MHz. Hence until there is thorough low frequency monitoring campaign of Cas A as advised by Helmbolt & Kassim (2009), in order to be able to better predict the flux density of Cas A at any given epoch, its reliability as a low frequency calibrator remains poor. In addition to Cas A's secular decrease in the flux density, the calibration assumes that the flux of Cas A is always greater than Cyg A but the sources' apparent gains can change as they transit the primary beam according to the time and frequency of

the observation (Foster et al. 2014). This may not directly affect our results, but it does impact longer single-station observations.

(iv) Direction Dependent Effects: Whilst we have demonstrated that spectral index maps can be made, the inclusion of a element beam model is essential as its direction dependent effect could dominate the spectral index. Work is in progress to improve the current element beam model which changes with observing frequency (affecting the FoV), time (atmospheric seeing can modify the effective beam shape) and pointing direction (see § 3.4). At the time of this work, there were no reliable element beam models and simulation attempts of dipole patterns were deemed too inaccurate to allow a trustworthy improvement in the emission maps and hence spectral index. BBS (see § 3.4.3) does make use of a dipole model during calibration of array datasets which forms the base of the LOFAR beam hierarchy. However, BBS (§ 3.4.3) does not work on single-station binary acc data-files; a '*station data-to-measurement set'* converter would be a practical way forward in terms of software re-use (a measurement set is a tabular format of storing the LOFAR full-array visibilities and metadata). However, at the station level, dividing out the dipole beam model from an image is theoretically possible since it can be done as a multiplicative correction per pixel. It may therefore be easier to extract the required corrections from interpolation of a tabulated dipole beam model, which can be simulated. It is technically possible to conduct EM simulations of the LBA dipoles in Stokes I polarisation (Yatawatta 2008) and parameterised descriptions of these results of these simulations form the basis of the dipole beam model used in calibration of LOFAR data. By approximating the taper for a Stokes I beam model we must assume an ideal quarter-wavelength dipole at a given frequency (Kraus 1988).

Whilst we may not have arrived at a full-scale spectral index map of the low frequency sky, this work has been an important phase of on-going commissioning into the calibration and stability of single stations. The absolute flux density scale and accuracy of single-station beam corrections (measured vs. simulated) must be investigated further in the future which will not only benefit single-station observations, but also those of the full array since the beam hierarchy of the latter is dependant on the single-station beam.

3.4. LOFAR Array Observation & Reduction

3.4.1. Observation

Our observation was made with the LBA of 19 core and 9 remote stations located within the Netherlands (see Table 3.1 for the array parameters applicable to our *commissioning* observation). VLBI, as explained, is advantageous for resolving point like sources. However, such long baselines can be insensitive to extended structures due to *fringe washout* (please see Thompson, Moran & Swenson 1991, for the definition of the fringe washout function which provides the upper limit to the visibility of angular structures as a function of the array size). Since we are interested in large-scale structures, international baselines were not used and the longest baseline was ~ 82.7 km; this allowed an achievable resolution of 60 – 90″ (§ 3.4.8).

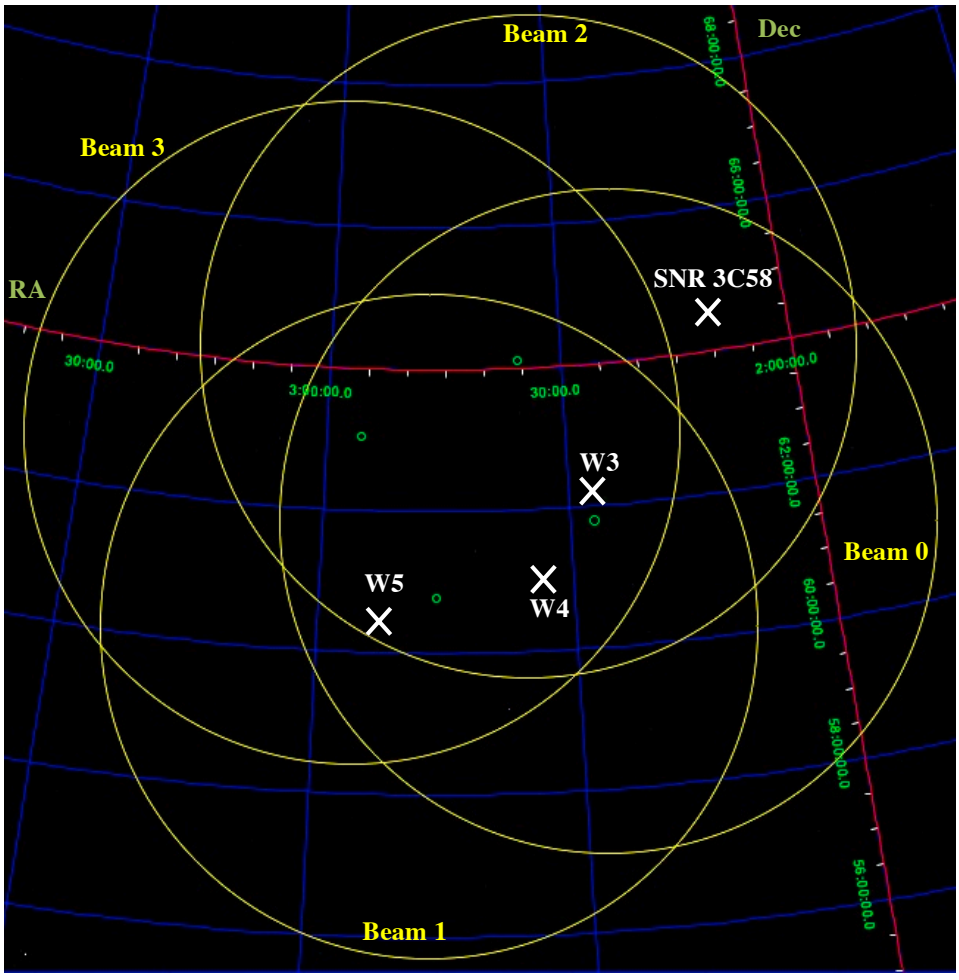

Figure 3.13: The yellow circles represent the 4 beams used for our LOFAR observation. The exact pointing positions represented in green were 02:27:17.04, +61.47.42.00 for Beam 0, 02:46:24.96, +60.48.21.60 for Beam 1, 02:35:33.60, +64.06.39.60 for Beam 2 and 02:55:51.60, +63.02.45.60 for Beam 3. The approximate centre for the field is taken to be 02:46:08.00, +61.22.07.00. The white crosses indicate the approximate centres of the W3, W4 and W5 nebulae.

In order to cover the entire W3/W4/W5 complex, the field was observed with 4 beams ~ 3.5° apart exploiting LOFAR's multi-beaming capabilities, with each pointing position represented as a small green circle in Figure 3.13. Each beam FWHM was ~ 4 – 5 ° across at the peak response of ~ 50 – 60 MHz (Figure 3.7) as represented by the yellow circles (although realistically these are ellipses). This gave a final mosaicked FoV of ~ 10° (Figure 4.1). The continuum datasets were taken with the inner LBA configuration (§ 3.2.2) at radio frequencies ~ 30 – 77 MHz giving a bandwidth of ~ 47 MHz, with 9.33 hours integration time on 30th October 2011 from 02:30:17 to 11:49:20 UTC. The output visibility dataset contained 4 linear polarisations (XX, XY, YX and YY complex correlations). The observation was written by the correlator as a set of 60 *sub-bands* for each beam. A sub-band (SB) is essentially a frequency slice in the observed bandwidth, with an increment of ~195 kHz, using a 200 MHz sample clock (de Vos et al. 2009). Each SB is sub-divided further into 256 channels; the benefit of such narrow channels is in the process of editing and flagging specific and narrow band RFI frequencies (§ 3.4.6).

3.4.2 Data Reduction

The quality and accuracy of the final synthesised images is dependent upon: (1) astrometry i.e. the accuracy of source absolute or relative positions (§ 4.1.1); (2) photometry i.e. the absolute or relative flux scale of these sources which determines the spectral energy distributions (§ 4.1.2) and; (3) the image quality (measured quantitatively by DR etc.) and image fidelity (§ 3.4.8).

Image accuracy is determined by deficiencies in the fringe visibility data, which can be polluted by: (1) limited (u, v) sampling producing instrument effects evident as a dirty beam in the final image; this beam can be improved by deconvolution (CLEAN) processes as discussed (§ 3.1) where the spatial response of the array is disentangled from the source structure; and (2) distortions from foregrounds resulting in errors in the measurements themselves. These must be removed prior to imaging, in order to detect any signals from the target; this is the essence of calibration as detailed below.

Calibration: Solving the Measurement Equation (M.E)

The resultant observation by LOFAR is the 'true sky' visibility, $V^{true}(t)$ distorted by: (i) instrumentation effects (station beam, clock drift, global bandpass, electronic gain etc.) and (ii) environmental effects (ionospheric refraction and Faraday rotation), the latter of which accounts for the delay error in signal propagation path (Yatawatta et al. 2009). The aim for calibration is to accurately compute the 'true sky' by removing these time-variable distortions prior to any imaging. The external influences of instrument and environment on the measured signal are described by the *measurement equation (ME)*. Please refer to Hamaker et al. (1996) and Hamaker (2000) for the development of this equation for an interferometer i.e. the radio interferometer measurement equation (RIME) or Hamaker-Bregman-Sault Measurement Equation (Sault & Cornwell 1999). Each direction-dependent effect (DDE), as well as direction-independent effect (e.g. electronic gains which differ from station to station), that alters the target electric field can be described by a separate Jones 2 × 2 matrix in the full matrix version of the ME (Hamaker et al. 1996). All radio interferometry calibration and imaging packages today, directly or indirectly implement some simplified and fixed form of the ME (Smirnov & Noordam 2006):

$$V_{ij}^{OBS}(t) = g_i(t)g_j{}^*(t)V^{true}(t) + \varepsilon_{ij}(t) \tag{3.20}$$

where $V_{ij}^{OBS}(t)$ is the observed visibility between antennas i and j, $g_i(t)$ is the complex gain of antenna i, $g_j(t)$ is the complex gain of antenna j and $\varepsilon_{ij}(t)$ is additive noise. Please refer to Tasse et al. (2012) for details of the version of the ME most applicable for LOFAR.

3.4.3 The Effects of the Ionosphere

For radio frequencies < 300 MHz, the ionosphere located at an altitude of ~50 –1000 km causes: (i) spatially variant (direction dependent) refractions, both large-scale and small-scale and (ii) time delays in the wavefront, which depend on the local electron density (Tasse et al. 2012) causing differential Faraday rotations. Both effects distort the EM wavefront before it reaches the array. Hence disturbances can vary with *time*, viewing *direction* and antenna location (Intema et al. 2009) corrupting true source positions, affecting subsequent astrometry. Lonsdale, (2005) illustrates the 4 different regimes of ionopheric calibration applicable for a low radio frequency array, with the

parameters of array size, A, the FoV at the specified height, H of the ionosphere, and the scale of ionospheric irregularities, S (Figure 3.14).

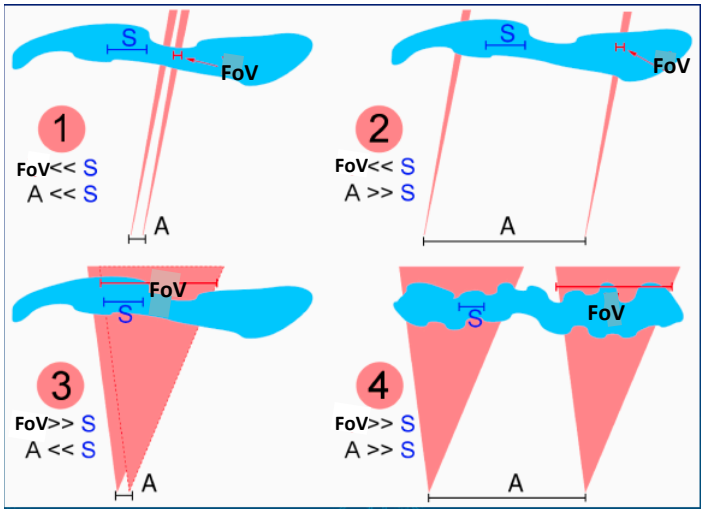

Figure 3.14: Ionospheric corruption varies with each aperture size and FoV: regime 1 (upper left) is a small array with small FoV; regime 2 (upper right) is a large array with a small FoV; regime 3 (bottom left) is a small array with a large FoV and regime 4 (bottom right) is a large array with a large FoV (after Lonsdale, 2005).

Whilst traditional interferometers like the VLA would have been affected by the same ionospheric distortions, S for observing radio frequencies < 300 MHz, the beam width is generally small compared to the angular scale of the ionospheric phase shift variation as demonstrated by regime 1 (Tasse et al. 2012) allowing phase coherence across the FoV to be preserved. In that case the ionosphere can be considered to be a direction-*independent* effect, and can be corrected with a single scalar multiplication of the antenna gains, using the phase (delay) *self-calibration* technique only (§ 3.4.5) possibly even for long baselines in regime 2 (Bemmel & Röttgering 2007). However this simple correction does not hold true for LOFAR due to its larger beam (Tasse et al. 2012) as shown in regimes 3 and 4 (Figure 3.14), which results in TEC (see definition below) variations across the FoV as detected by the antennas of the array (Intema et al. 2009).

The ionosphere is a plasma with a Total Electron Content, TEC which is the integrated electron density, N_e along the LOS. The variable plasma quantity, N_e can vary with the sun, causing a layer thickness change from day to night. This affects the TEC which introduces phase variability, $\Delta\phi$ of the radio frequency signal in direction and time (Thompson, Moran & Swenson 1991). This additional propagation delay due to excess path length for the EM ray is proportional to λ^2 hence the corresponding phase shift is proportional to λ:

$$\Delta\phi \approx -25\lambda\,\Delta TEC \tag{3.20}$$

As well as these large-scale ionospheric phase changes which increase linearly with increasing λ and increasing TEC, small-scale fluctuations of phase with time (order ~10 seconds) and space

(order ~ 10 km) are caused by Travelling Ionospheric Disturbances (TIDs) (van der Tol 2007). We can attempt to reduce phase instabilities caused by TIDs in ionospheric self-calibration. Scintillation also introduces quick phase fluctuations due to local changes in the atmosphere (i.e. pressure, temperature or water content). At a high level, phase variability can become erratic making phase correction almost impossible. At the latitude of LOFAR, scintillation occurs ~ 30% of the time at radio frequencies < 30 MHz which means that there is a diminished efficiency between 15 – 30 MHz (Weiler 2013).

Finally, phase corruption is worse for longer baselines (regimes 2 and 4 of Figure 3.14) since ionospheric thickness and structure varies more over longer distances. For shorter baselines (i.e. between LOFAR core stations or antennas within a single station demonstrated by regime 3 of Figure 3.14), phase coherence is preserved due to less ionospheric variability (van der Tol et al. 2007) and TEC variation across the array for a single viewing direction within the FoV is approximately a gradient (Intema et al. 2009; see § 3.3.2). For LOFAR remote stations at large distances apart (regime 4 of Figure 3.14), the ionosphere is more varied and 2 separate stations will 'see' entirely different sections of the ionosphere with no spatial coherence and the TEC variation across the array for a single viewing direction differs significantly from a gradient (Intema et al. 2009). This results in noise characterised by high amplitude variability over a small time range (van der Tol et al. 2007).

At LOFAR's low operating frequencies, the Earth's ionosphere behaves as a random refractive sheet which over the wide FoV 'seen' from the LOFAR stations and large aperture, induces source direction dependent effects (DDEs). These phase errors must be predicted and calibrated out by solving the ME by computing the Jones matrices as a function of station and direction (van der Tol et al. 2007). Field-based direction dependant calibration as described by Cotton et al. (2004) will work for regime 3. In order to calibrate the ionospheric phase variations of LOFAR's extended configuration (regime 4), a 2-D time-dependent phase screen at a specified height, H above the array and thickness, dH has been modeled by Intema et al. (2009) and van der Tol et al. (2009), at an observing radio frequency of 74 MHz and this has been extended in the Source Peeling and Atmospheric Modeling (SPAM) technique. Spatial variations are also considered in the model, which also incorporates TIDs (Bemmel & Röttgering 2007).

Current radio astronomy *self-calibration* (see § 3.4.5) algorithms used at higher frequencies by other radio astronomy instruments such as the VLA do not address direction dependence and will not work in the LOFAR environment (van der Tol et al. 2007). SAGECal and the BlackBoard Selfcal package (BBS; Pandey et al. 2009) which incorporates SPAM, are 2 software packages designed specifically for DDE calibration of a large distributed sensor array like LOFAR (see the pipeline in § 3.4.6).

3.4.4. Removal of Off-Axis Sources Outside the Main Beam

There are bright nuisance 'off-beam' sources in the low radio frequency sky (< 100 MHz) most notably Cygnus A (Cyg A), Cassiopeia A (Cas A), Virgo A (Vir A), Taurus A (Tau A), etc. collectively known as 'A-team sources' as well as the Sun and Jupiter. Even when located far from the field centre, one or a few 'A-team sources' can dominate the residual noise in the data at low RFs, modulated by the secondary lobes' time and frequency variations (Tasse et al. 2012) and this is evident as a 'beating effect' in the target visibilities (Figure 3.15). This PSF noise from A-team side-lobes can negatively affect subsequent calibration if not effectively removed reducing the sensitivity of the observation. Inspection of the elevations of the A-team from our target field during observation showed that only Cas A and Cyg A were high enough in elevation to be of influence, and almost equally bright with intensities of ~ 20000 Jy each at 50 MHz (Yatawatta et al. 2009). Tau A was also high in elevation, but is of a lower intrinsic brightness to be of significance.

These nuisance side (and grating) lobes can be improved in a variety of ways which are outlined in detail by Tasse et al. (2012). At the instrumental level, station rotation and tapering (Wijnholds et al. 2011) lowers the extent of these side-lobes. Averaging in time and frequency helps to smear out the contributions of off-beam sources on longer baselines (Scaife & Heald 2012). This step is incorporated into the NDPPP averaging step (§ 3.4.6). Due to the nature of our observation, the most appropriate algorithms for direction dependent gain correction and subtraction of off-axis emission from bright Galactic sources from target visibilities in the (u, v) plane, are: *peeling with BBS*, *Demixing*, and *SAGECal* the merits of which will be discussed below.

Peeling with BBS (Loose & Zweiten 2007) as outlined in detail by van der Tol et al. (2007) consists of carrying out simultaneous solving over different directions (including the target field and the 'A-team sources') to give accurate gain solutions in each different direction. Then the contamination from the 'A-team sources' can be subtracted one at a time from the observed visibilities. Solving this way has been proven to work well but is computationally very intensive (Tasse et al. 2012) compared to the *demixing* algorithm (see below) and is also directionally limited whereas *SAGECal* (see below) theoretically can calibrate along hundreds of directions handling thousands of sources.

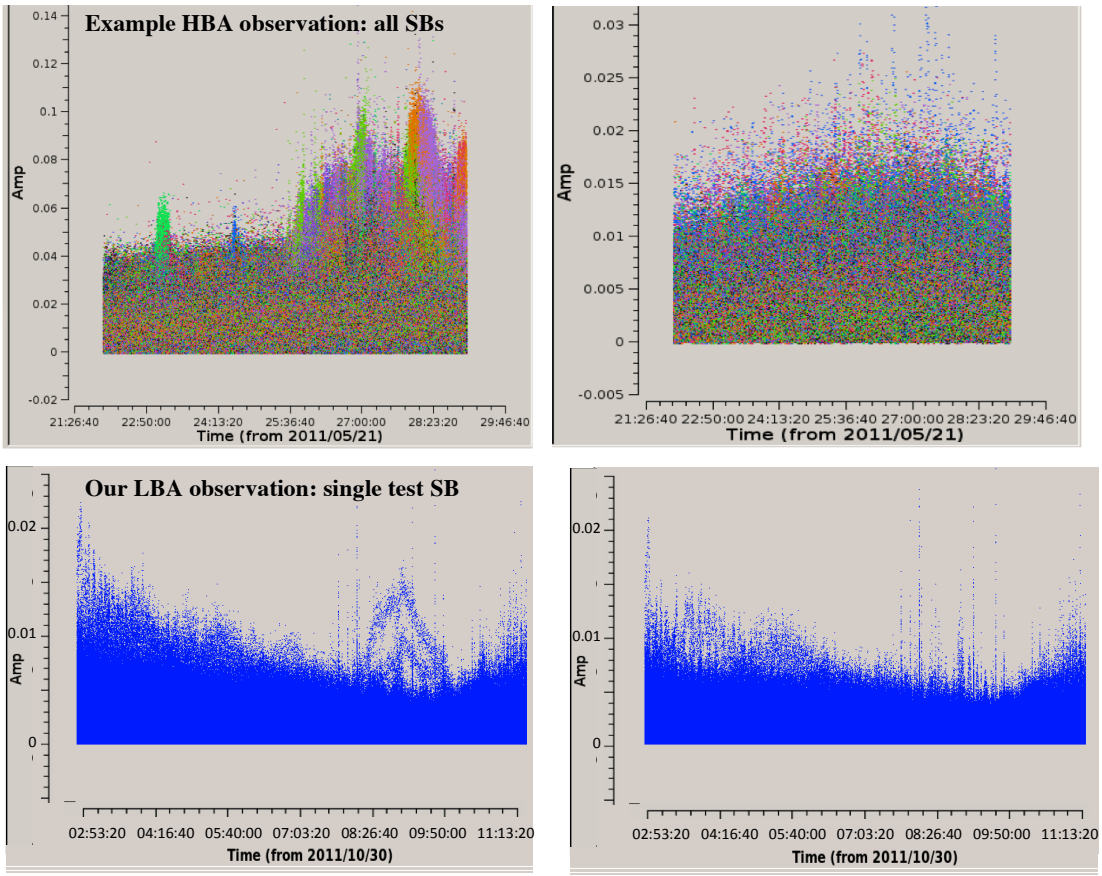

Figure 3.15: Plots of visibilities from target B1835+62 with amplitudes vs. time for all baselines (top). The combined 'beating' effect of the fringes of Cas A and Cyg A is shown on the left as a prominent bulge (Pizzo et al. 2014*)*. These 'A-team source' nuisance side-lobes are removed (right) using demixing which uses the assumption that the interfering sources are far from the field centre, so that their fringe rate is high with respect to the target. Below is a visibility plot of a *single test SB* of our observation centred at ~ 46 MHz before (left) and after (right) demixing Cas A and Cyg A.

The demixing step (van der Tol et al. 2007) is a procedure incorporated into the LOFAR pipeline (§ 3.4.6) which lessens the 'A-team source' effects with appropriate filtering applied on the phase variations over time and frequency of signals that are correlated between stations. This can suppress signals outside the FoV substantially (van der Tol et al. 2007). Figure 3.15 shows an

HBA observation centered on B1835+62 (Pizzo et al. 2014) and a *single* test SB of our data below, where the interference effects of Cas A and Cyg A (evident as a prominent bulge in the raw visibilities on the left) are demixed from the target visibilities (right).

SAGECal (The Space Alternating Generalized Expectation Maximization Calibration) is a self-calibration algorithm developed for radio interferometers by Fessler & Hero (1994) and adapted specifically for LOFAR by Yattawatta et al. (2009). SAGECal provides a faster alternative to demixing solving the 'effective' Jones matrices towards many sources; both these algorithms are currently being tested and directly compared by the LOFAR Radio Observatory for various observations. Yattawatta et al. (2009) describe the application of the *Expectation Maximization* algorithm (Dempster et al. 1977 and Feder & Weinstein 1988**)** by SAGECal as an iterative solution for the *maximum likelihood estimation* (Pearson & Readhead 1984) when the complete data is not observed. In contrast, the demixing calibration technique makes use of *Cramer–Rao lower bound (CRB) analysis* (detailed in Wijnholds 2010) to constrain signal models and van der Tol et al. (2007) define its limitations. Expectation Maximisation type algorithms like SAGECal have faster convergence and reduced computational costs (e.g. it does not require full spectral resolution like demixing) as well as providing better quality of calibration over existing algorithms (Yattawatta et al. 2009). Please refer to the LOFAR status meeting report by Bonafede & Orrù regarding extensive tests of peeling with BBS, demixing and SAGECal on an LBA dataset, where SAGECal was found most superior for 'A-team source' subtraction providing the best S/N solutions and taking < 5% the computing time of demixing (http://www.lofar.org/wiki).

As well as the advantages of speed, efficiency and accuracy, SAGECal was deemed the best 'A-team source' remover for our data for another reason. Issues manifested when images were made after BBS calibration (see § 3.4.6) with demixed data. It became apparent that the final image depended heavily on the *initial input sky model*, which is variable due to differing survey frequencies and array arrangements (see § 3.4.5 & § 3.4.7). The initial sky model seemed to be artificially *forced* onto the data by BBS, losing the intrinsic properties of real source structure. This was checked and verified by using a pseudo-model with a false bright source arbitrarily specified at RA ~ 2:14 and Dec ~ +63.08, which resulted in a new peak in the image shifted to these exact coordinates, with emission appearing nowhere else. It is possible that the forced

application of a sky model during self-calibration is a particular issue for LBA observations due to a wider station beam compared with the HBA (see § 3.4.3 for properties of differing ionospheric regimes) but this is something that will need to be investigated further (see 3.4.5). If the primary beam is larger than the coherence length of the ionosphere (as it could be in the LBA), then the effects of *non-isoplanticity* become more severe; the self-calibration algorithm minimises the differences between *model* and data by applying an averaged time-dependent correction to the field (§ 3.4.5) and will not be effective when the beam samples various isoplantic patches.

Testing during the LOFAR commissioning busy weeks has *also* shown that demixing has a detrimental effect on large-scale diffuse structures in particular which may help explain our poor calibration results post BBS (http://www.lofar.org/wiki). These commissioning tests on a simulated Gaussian structure showed that the severity of the negative effect of demixing is worse for larger and more complicated diffuse structures of lower flux densities which are closer to the 'A-team sources' whose visibility fringe rates (Figure 3.15) become indistinguishable from the target.

3.4.5 Self-Calibration Techniques

The traditional approach to calibration is to observe one or more external calibrators (known celestial objects; ideally discrete strong point sources which do not vary rapidly with time) in addition to the target field of interest. The ME can then be solved for the calibrator visibility measurements where *absolute* flux density, position and angular dimension are known. Consequently, the direction-independent instrumental effects can be estimated, and the gain solutions can then be applied for the target FoV. However, this method has proven to be limited due to discouragingly large experimental discrepancies where temporal and spatial variations in the atmosphere (troposphere and ionosphere) affecting the calibrator, may not be the same as for the target, observed at a different time, (frequency) or different region of the sky (Cornwell & Fomalont 1999). The station electronics may also be variable with time (an effect which can be mitigated against for LOFAR with single-station calibration tables as described in § 3.3).

Whilst the traditional method is good for astrometry and photometry of sources, results can then be improved using *self-calibration, w*here the observed sky itself is used for calibration i.e. the

target visibilities are used, and direction-independent antenna gains are allowed to be free parameters. There is no external calibrator and so both sky and instrument are unknowns (Cornwell & Wilkinson 1981 and Cornwell 1982). Refinement of the instrument and sky model is carried out *iteratively*, improving the quality of calibration i.e. image fidelity (see § 3.4.8) by orders of magnitude in comparison to using an external calibrator (Yatawatta et al. 2009). This technique allows iterative estimation and improvement in the *power*, *location* and *shape* of sources within the FoV which is initially unknown. As mentioned, whilst self-calibration is widely used for higher frequency synthesis arrays (Cornwell & Wilkinson 1981 and Pearson & Readhead 1984) it was unknown how well self-calibration techniques would work for an array like LOFAR with thousands of antennas spread over 10s to100s of kilometres and according to van der Tol (2007) neither the theoretical or practical bounds on calibration accuracy are well understood for arrays in the presence of strong ionospheric perturbation. Since we did not use international baselines, the longest baseline of ~ 82.7 km could justify self-calibration techniques as the prime technique of improvement of small-scale ionospheric corruption (§ 3.4.3) and quantitative improvement of this iterative approach is shown in (§ 3.4.8).

Cornwell (1982) outlines the main steps of self-calibration. This starts with an initial approximate model of source visibilities, ${V_{ij}}^{model}$ created typically from a pre-existing catalogue:

$$V_{ij}^{OBS}(t) = g_i(t){g_j}^*(t)V_{ij}^{model} + \varepsilon_{ij}(t) \tag{3.21}$$

The complex antenna gains, g_i and g_j can then be solved for, and applied to correct the observed data, $V_{ij}^{OBS}(t)$ to give the corrected visibility, $V_{ij}^{CORR}(t)$:

$$V_{ij}^{CORR}(t) = [g_i(t){g_j}^*(t)]^{-1}V_{ij}(t) \tag{3.22}$$

From the corrected data, a new model can be created, and the process is iterated (stabilising the ionospheric phase drifts) in combination with CLEAN deconovolution (which improves the side-lobes) until the current model is satisfactory. Please refer to Cornwell (1982) for the mathematics of this approach using a sum of "Least Squares" of residuals between observed visibilities and the product of gains and model visibilities, with some degree of minimisation through adjustment of the gains.

An initial sky-model

Initial sky models are *essential* for the self-calibration of LOFAR data and accurate sky models need accurate source models. The aim of the Multifrequency Snapshot Sky Survey (MSSS) observations (Heald 2013) is to produce an accurate and detailed low frequency Global Sky Model (GSM) catalogue, which will form the basis of future LOFAR image calibration. However, since there were no such models available when our data was collected and analysed, during the early developmental phase of the array, it was necessary to undergo a protracted set of analysis steps to determine a reliable model from the data itself. Even today, sky models are normally based on point sources, and there is very little from which to start with in achieving realistic sky models for *LBA* data; a frequency range that has remained largely unexplored.

Smirnov (2011) describes the advantages of using self-calibration on the field around 3C 147; there is no significant extended emission which has allowed very accurate sky models to be constructed. This is in contrast to our field, which has *extensive diffuse emission* and few surveys close to our frequency range from which to obtain an initial model. Different point source models were tested from an assortment of catalogues including the NRAO VLA Sky Survey (NVSS) at 1.4 GHz (Condon et al. 1998), the Cambridge 7C survey at 151 MHz (Hales et al. 2007) and Cambridge 8C survey at 38 MHz (Hales et al. 1995). The Westerbork Northern Sky Survey (WENSS) catalogue at 325 MHz (Rengelink et al. 1997) was decided most suitable due to its greater sensitivity to extended emission and resolution helping differentiation between diffuse and point structures (Verkhodanova et al. 2009). The VLA Low Frequency Survey (VLSS) at 74 MHz (Cohen et al. 2007) is close to our range but comparatively less sensitive and resolved out the diffuse structure evident in the WENSS image. It was important to create a simple yet *accurate* initial sky-model as this had repercussions on iterative self-calibration, as discussed in § 3.4.7.

Approximately only 8 of the very brightest points in the field were extracted from the WENSS map using the source extraction program, *Duchamp* (Whiting 2012; § 4.1.1). These points constituted the *very basic* initial point source model for the phase centre of the field. In order to calibrate the extended diffuse emission which we know a-priori exists in the field from the literature (§ 1.4), an initial model consisting *only* of a set of discrete sources was found to not be adequate. Initial experimentation with this model revealed no sign of any diffuse emission in the

image after the first iteration, even after combining multiple SBs in multi-frequency synthesis (§ 3.4.12); hence the diffuse regions also had to be accounted for.

From readings in the WENSS image, diffuse emission is ~ 1-10% the flux levels of the bright point sources nearby. Work by Yatawatta (2010) with a test observation taken by LOFAR has found that traditional pixel based image deconvolution places limitations for bringing out weak extended sources to suitable DR and fidelity in radio interferometry. *Shapelets* (Refregier 2003) help to overcome this limitation and there is on-going work to improve their performance and efficiency. Shapelets are an image decomposition technique developed in astronomy for modelling vague spatial objects with no 'crisp' boundaries (Zinn et al. 2007). In order to satisfactorily model the diffuse emission in the WENSS image it was divided into 4 main regions; modelling the entire region with just a single shapelet was not effective as faint diffuse emission was overshadowed by much brighter regions. Shapelets modelling was run after first subtracting out the point sources within each region using the *restore* script as described in Pizzo et al. (2014) (see Figure 3.20).

3.4.6 Our Adapted & Tailored Processing Pipeline for Commissioning Data

Figure 3.16 shows the *current* standardised LOFAR processing pipeline applied to the raw visibilities, where editing and calibration takes place before imaging. For its numerous advantages over demixing (as discussed in § 3.4.4), several commissioners are still in the process of incorporating SAGECal into the mainstream pipeline.

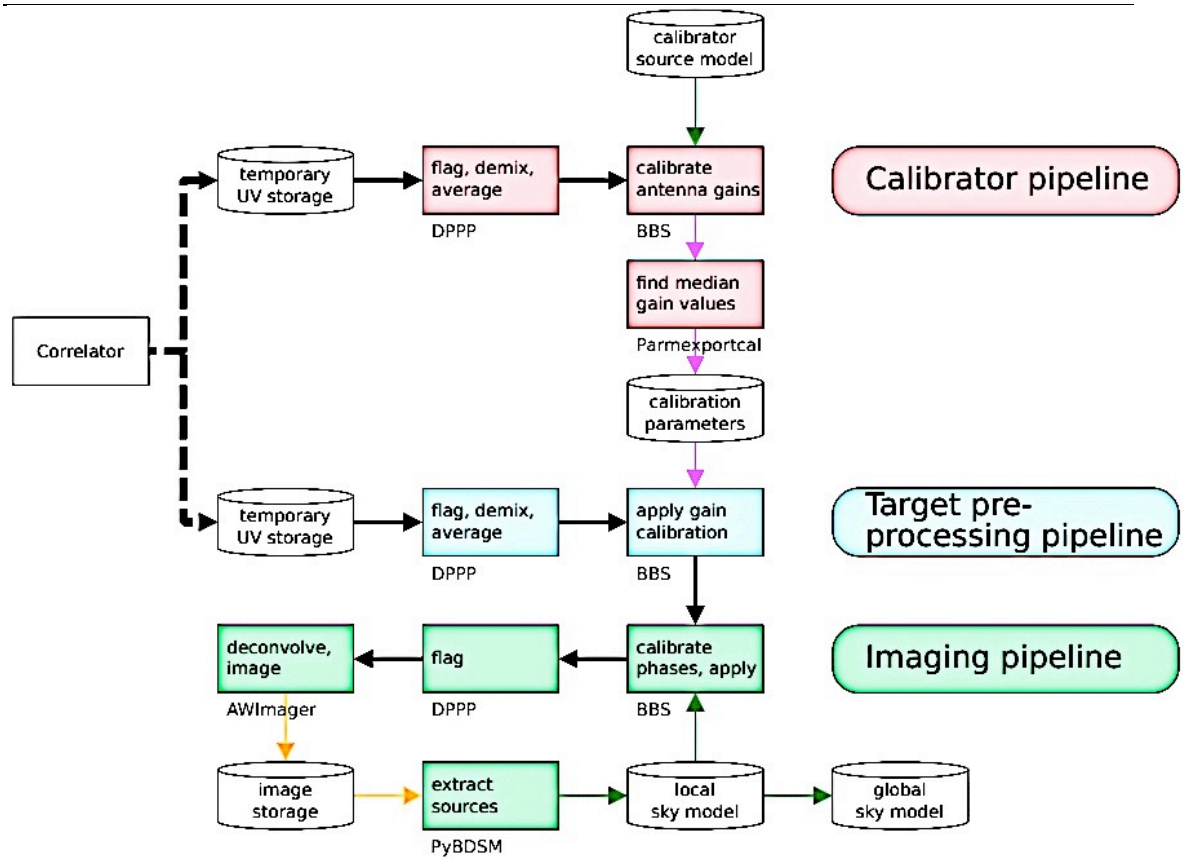

Figure 3.16: The standard LOFAR processing pipeline (Pizzo et al. 2014).

Important Note

It should be realised that during the time of this work there were no official observational pipelines implemented into the LOFAR standard pipeline (as they are now). Our observation was an early *commissioning* dataset taken in 2011, when the LOFAR processing pipeline was still *experimental* and the series of processing steps was dependant upon the science aims and nature of the target field i.e. point or diffuse structures; Galactic or extragalactic sources. Much of the progress with this work has been carried out by working closely with the LOFAR survey team who have developed algorithms to tackle problems associated with calibration (ionosphere, beam, etc.) and wide-field imaging during this critical commissioning phase (e.g. Tasse et al. 2012) of which this work has been a part of. Issues such as debugging, algorithm complexity and computation resources have been encountered during reduction, which is to be expected for huge early datasets. A suitable pipeline (Figure 3.17) was developed for our field, initially testing on 2 SBs from each beam centred on ~ 46 MHz, within the optimal frequency of LOFAR sensitivity (Figure 3.7),

before running on all available SBs individually and in parallel on the LOFAR computing machines (see Pizzo et al. 2014).

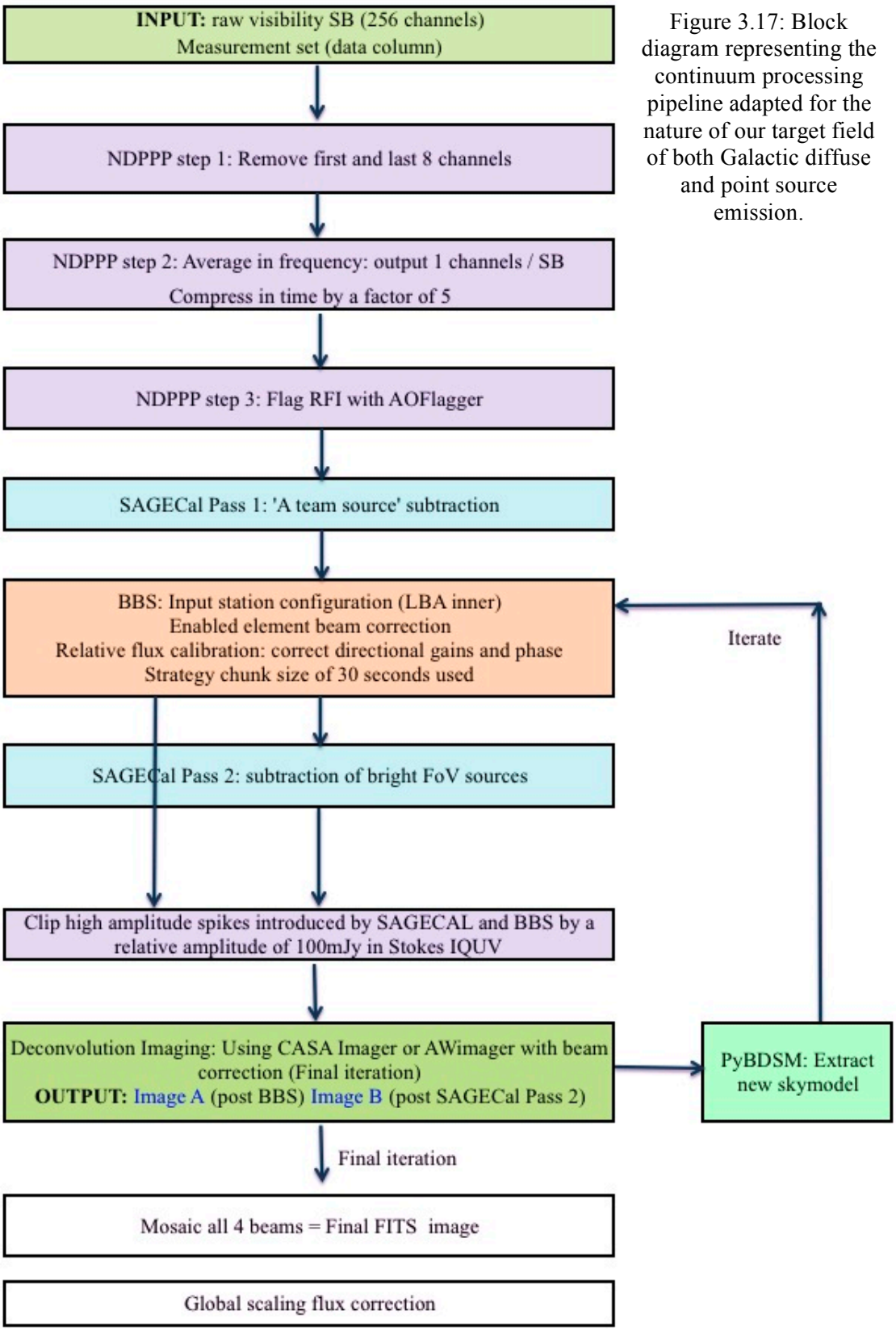

Figure 3.17: Block diagram representing the continuum processing pipeline adapted for the nature of our target field of both Galactic diffuse and point source emission.

Initial Dirty Map

An initial inspection of the raw uncalibrated visibilities was made in an initial 'dirty' map before any processing, to diagnose the data and characterise suitable steps. Side-lobes were clear from bright sources inside and outside of the FoV. When comparing the raw images at ~ 46MHz with the 151 MHz Cambridge 7C survey map of the same coordinates (Figure 3.18), it was clear that the arc-like structure (in contours) at the lower left, emerges as a corrupted projection of the bright source at its centre. With the same reasoning, a similar splash structure (in contours) appears smeared out from the collective flux of bright points of W3 at RA 02:26:05 and Dec +62.05.00 and other 'hot-spots' may show some correspondence with features we see.

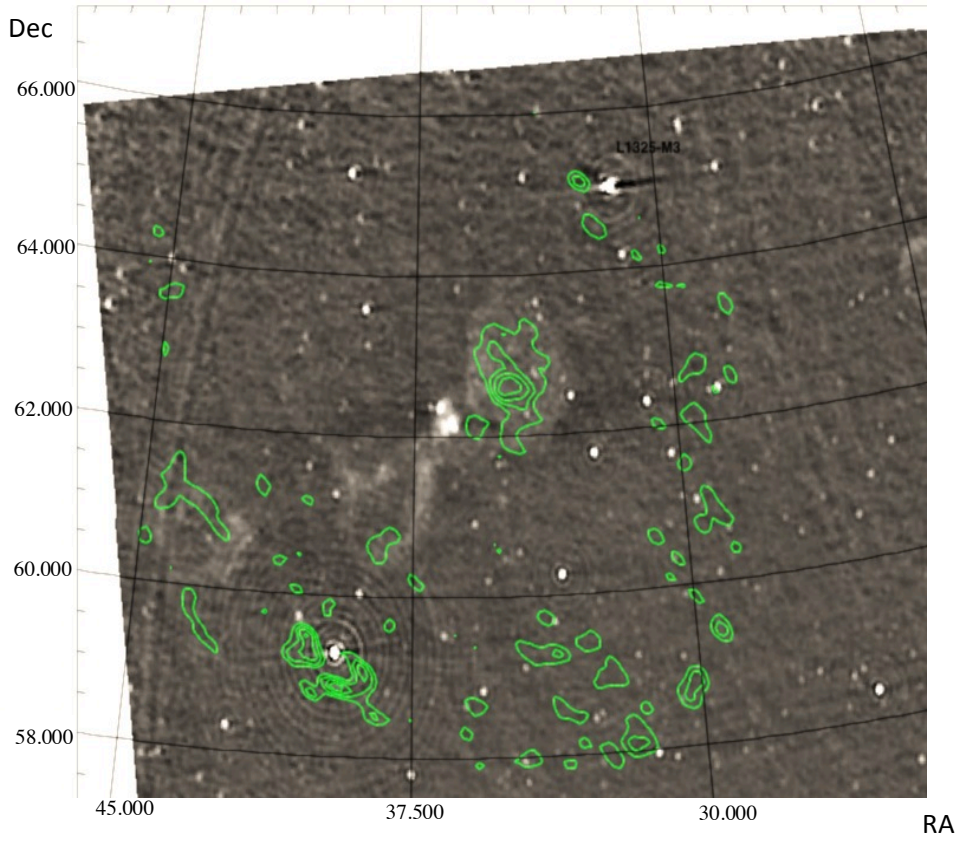

Figure 3.18: The brightest contours represent the raw uncalibrated LOFAR data from beam 1, centred at 45MHz, co-aligned and overlaid onto the 151 MHz map from the Cambridge 7C survey. The grid lines represent sky coordinates: RA and Dec.

Editing

Radio Frequency Inference, RFI originates from artificial signals generated within the antenna electronics or by external sources e.g. radio and TV stations, electronic devices, electric fences, lightning, power cables, vehicles and trains. This local noise adds to the total noise of the

observation, decreasing the sensitivity of signals from the 'true sky' reaching the correlator. Mitigation can be enabled by careful antenna design, electronic filters and shielding. The New Default Pre-Processing Pipeline or *NDPPP* is a LOFAR routine which flags prominent spikes in the visibilities using *AOFlagger* (Offringa et al. 2010), eliminating artificial RFI efficiently creating clean spectra for calibration. Also since the first and last channels of a raw LOFAR dataset are usually bad, NDPPP also excluded these (Figure 3.17). Lastly, by using data inspection tools such as *MSviewer* in CASA (Jaeger 2007), obvious instrumental problems and problematic baselines and stations (possibly due to variations in electronics etc.) were noted and also manually edited out.

Data Reduction Steps

The first pass of SAGECal solved for 3 directions as described by a *cluster file*, with the third direction accounting for the basic initial sky model for the target centre as described in § 3.4.5. It then subtracted the off-axis sources Cyg A and Cas A only (§ 3.4.4). Cyg A was represented by a point source model but for Cas A this was not adequate and it had to be modeled more accurately as a shapelet (provided from previous work by Sarod Yatawatta).

The residual data were then calibrated using BBS with only the centre described by the initial sky model (§ 3.4.5). The essence of BBS is the computation of simulated visibilities based on the sky model, and a feedback loop converging to some specified criteria i.e. the smallest difference between simulated and observed visibilities (Pizzo et al. 2014). BBS calibration essentially estimates parameters in the ME, outputting gain solutions which can be inspected afterwards for each baseline in an output instrument table (§ 5.2). BBS also requires a set of instructions described in a *parset file,* the parameters of which were investigated in detail including the *cell size time,* whose value determines the number of timeslots that are grouped together in a cell during calibration, affecting the resolution of the final image. From the observation records, the data was formed of 5.15 seconds integration per sample point; hence from sampling theory, the smallest time interval to solve for gains without under-sampling was every ~ 10 – 30 seconds provided the ionospheric phase was steady enough and there were no fast changes in the ionosphere i.e. due to scintillation (§ 3.4.3). However over-sampling would also result in a poor image since only these

time-dependent variations in the ionosphere would be represented. This was evident as artefacts in the final image which were improved with a larger sampling solution (30 seconds was judged best).

Prior to any imaging, the residual visibilities were clipped for any spikes (evident as very high amplitude events of relatively short duration spanning ~ 10s of seconds to a few minutes) introduced by calibration over a relative threshold of 100 mJy in Stokes parameters IQUV. Wide-field images (§ 3.4.11) were made with 'uniform', 'Briggs' and 'natural' weights (see § 3.4.9 for descriptions), with all available SBs from each Beam across the ~ 47 MHz bandwidth, to enhance the (u, v) coverage (defined in § 3.1); this was carried out with the aim of enhancing the faintest point sources (see § 3.4.12). For uniform-weighted images, point sources were extracted using PyBDSM (§ 4.1.1) and the sky-model was updated for *each* beam pointing direction (as shown in Figure 3.13), since the sensitivity of each beam peaks at different coordinates in the sky and drops off from the phase centre. Hence, new sources detected vary from beam to beam with some sources common to all beams at the field centre. The results were then improved iteratively by calibrating the raw data again in BBS using a sky model based on the data itself (self-calibration). This improvement can be seen visually on the top row of Figure 3.30 for Beam 0, and all mosaicked beams on the bottom row. The quantitative iterative improvement is detailed in Figures 3.27 and 3.28.

It could be verified we were on right path and that the initial sky model was valid (i.e. not being 'forced' onto the data) after the first iteration in two ways: (i) that the point sources provided in the original sky model did not agree exactly in flux magnitude, shape or position with the detected sources i.e. these output values were intrinsic to the true nature of the data; (ii) new fainter point sources appeared that are not in the original sky model, the astrometry of which were confirmed with existing NVSS, VLSS and WENSS catalogue overlays using *SAOImage DS9,* an astronomical imaging and data visualization application which supports FITS images (Figure 3.19). This helped to differentiate extracted point sources using PyBDSM (§ 4.1.1) from possible artefacts and diffuse emission. It is possible that a new source was detected that was not evident in pre-existing catalogues, but it was decided to take the most *conservative* route when extracting a sky model at each iteration and place constraints in model extraction in order to mitigate all possible artefacts.

The iterations were run until sky models could no longer be noticeably improved i.e. no new faint sources emerged that were not in the input model. With each iteration the diffuse emission in the maps became clearer as sensitivity improved (see § 3.4.8). A total of 3 iterations were run giving an RMS of < 10mJy/beam across the whole bandwidth for beam 0, 1 and 2, although further improvements to the sensitivity of the images may have been feasible had it not been for time constraints. It was decided this level was adequate for analysis to fulfill our science objectives.

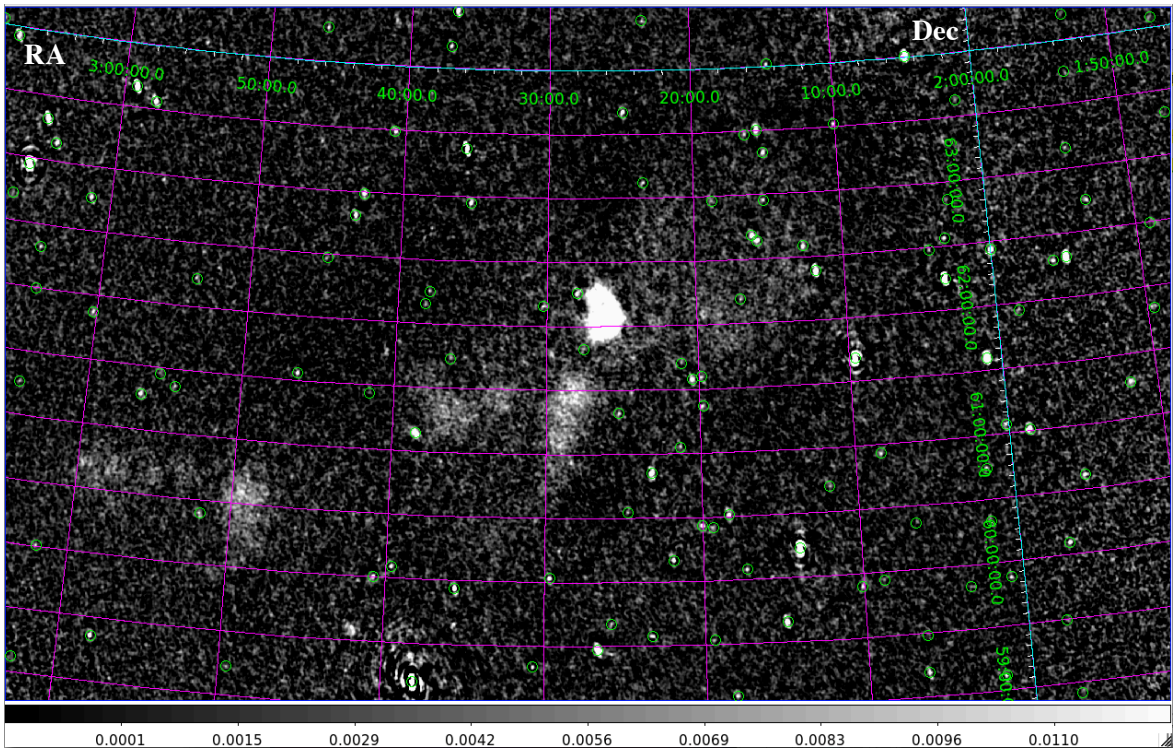

Figure 3.19: The VLSS overlay (source positions represented as small green circles) onto the full bandwidth uniform weighted image for beam 1 after the second iteration using AWimager (§ 3.4.11). This helped to verify the validity of the PyBDSM detected sources.

3.4.7 Issues During Iterative Self-Calibration

After the third iteration of self-calibration (attempt 1) through the pipeline as depicted in Figure 3.17, the initial sky model was only yielding mediocre results with prominent side-lobes around the central sources. This was because self-calibration relies fundamentally on an initial sky model that is simple yet *accurate* to the true nature of the field in order to bring out what is intrinsic within the data. This is a particular issue with amplitude and phase self-calibration, which can lead to erroneous results if the initial model is unsatisfactory. When one only has to solve for the phases (as in the case of an external calibrator where gain amplitudes can be transferred), there are fewer parameters to solve for, and hence the initial model accuracy is less critical.

The complex W3 region (located at the centre of our target field) had initially been modeled using a shapelet only and prior to that, as compact point sources only, with consequent calibration results post-BBS (Figure 3.17) that seemed 'forced' (§ 3.4.4). The 'golden rule' as mentioned in the LOFAR cookbook, is to always model the central compact structures as point sources only and shapelets are strictly for extended structures (Pizzo et al. 2014). Some level of a-priori knowledge was essential for an accurate interpretation of the complex structure of W3 in the WENSS map; it was difficult to differentiate point and diffuse emission otherwise. After numerous attempts, the best results followed very careful sky model construction as composite of both points in areas of brightest emission, surrounded by a shapelet representing the H II region. The threshold for pixel selection within Duchamp (see § 4.1.1) was incrementally lowered from 5.5 to 4.0 units of standard deviation above the mean, excluding the bright sections of the diffuse and picking up the point sources only, confirmed from previous studies such as Normandeau & et al. (2007) as represented in Figure 1.3, staying true to the structure of W3. This is demonstrated in Figure 3.20 below, with repercussions shown in Figure 3.21.

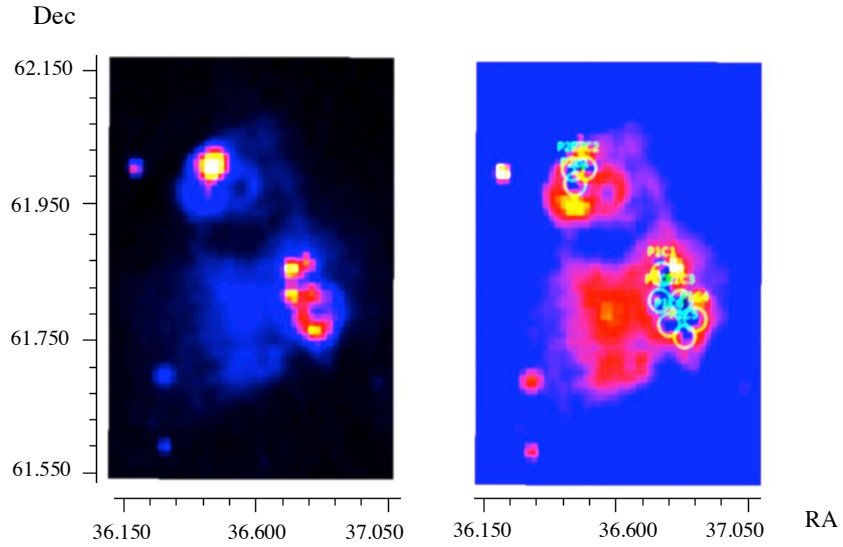

Figure 3.20: The WENSS image of W3 (which is located at the centre of our target field) on the left. The image on the right demonstrates the same image with the bright point sources subtracted out, after careful adjustment of the threshold for pixel selection within Duchamp; a shapelet was then created for this remaining nebula. The images are *not* on the same brightness scale.

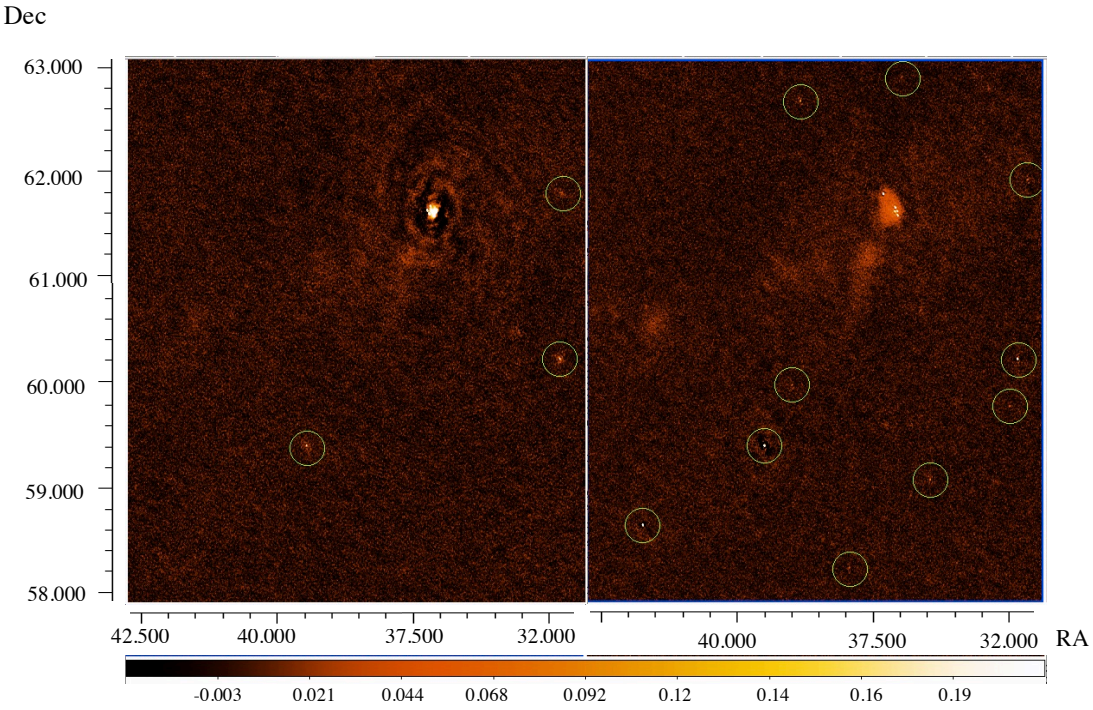

Figure 3.21: Beam 0 only (full bandwidth ~ 53.5 MHz), after the first iteration using an *inaccurate* initial sky model for W3 on the *left* and *improved* model for W3 on the *right* where more sources appear that were not included in the basic input model (highlighted in green circles).

Another demonstration of the importance of the extracted sky model accuracy was seen *between* iterations. An inaccurate extraction resulted in heavy side-lobes around the SNR 3C 58 and a *worse* image quality in iteration 2 than that of iteration 1 (left of Figure 3.23). Returning to the source model, the PyBDSM extracted regions were overlaid onto the FITS image (left of Figure 3.22). The extractor had inaccurately resolved the points of the SNR into double sources; hence parameters were adjusted for until the extracted regions focused in on the true bright points without 'blurring' with the diffuse emission (right of Figure 3.22). Consequently, the new extraction resulted in better image quality than that of the first iteration (right of Figure 3.23).

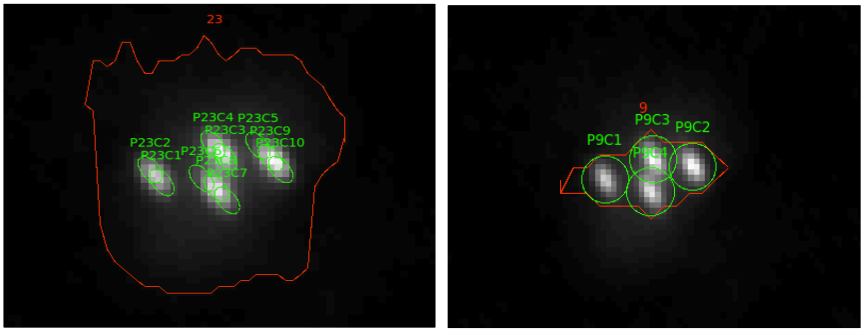

Figure 3.22: The source model for 3C 58 represented by the PyBDSM extracted regions (in green) overlaid onto the FITS image of iteration 1. Trial 1 (left) and trial 2 (right).

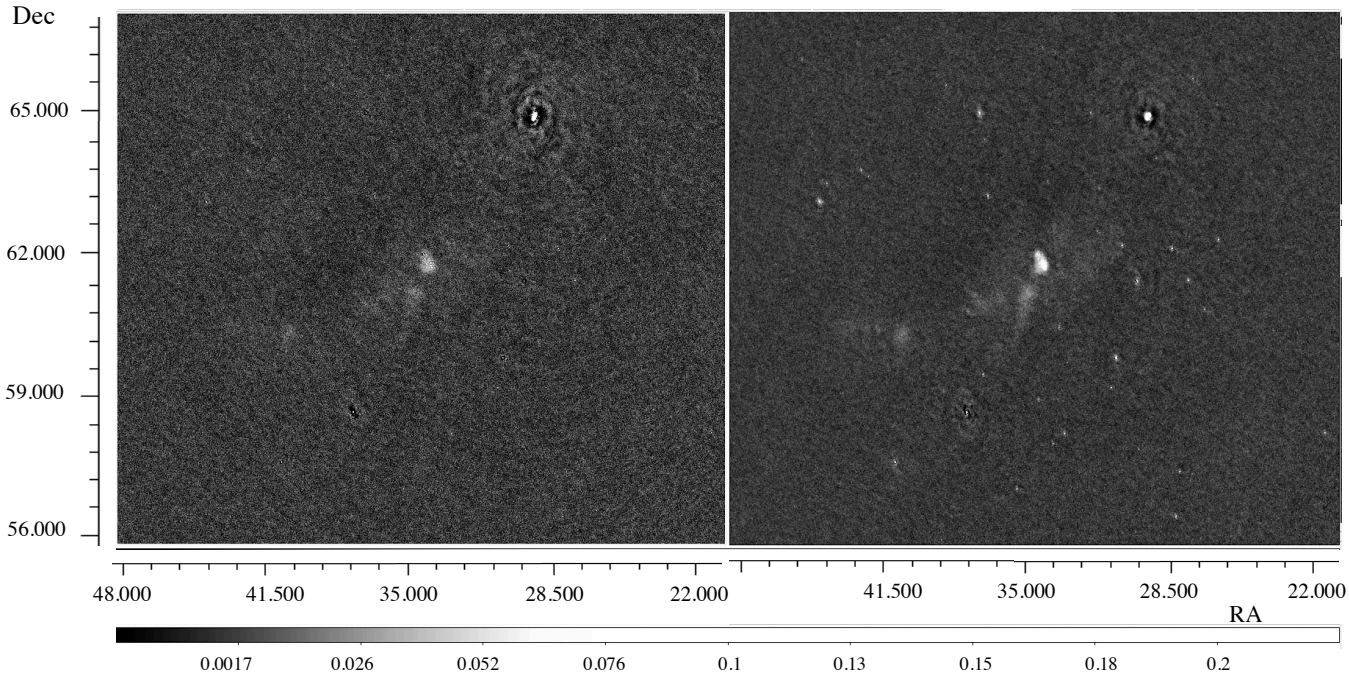

Figure 3.23: Output images of iteration 2 for Beam 0 (full Bandwidth ~ 53.5 MHz) with trial 1 (left) and trial 2 (right).

The second pass of SAGECal (Figure 3.17) was performed to reduce the side-lobes (caused by direction-dependent ionopheric and beam effects) from the brightest sources *within* the FoV (which had been calibrated for using BBS), in the same way the first pass of SAGECal had been used to subtract the 'A-team sources' outside the FoV from the target visibilities. It was run with the option of ignoring baselines shorter than 300 λ in order to protect the diffuse flux during subtraction. Sources within the FoV were clustered in various directions i.e. grouped such that the members of the same group (cluster) have similar DDEs according to their direction and proximity (please see Kaufman & Rousseeuw 1990, for more on the application of the clustering method). Theoretically only noise, diffuse structures and possibly further fainter sources should have remained in the resultant images. For the final image, the subtracted bright point sources were then *restored* (see Pizzo et al. 2014, for the 'restore' algorithm) to the residual image which was devoid of their side-lobes. This final image in practice was not proven to reveal fainter structures and the second pass of SAGECal seemed to have a *detrimental* effect on the S/N resulting in Figure 3.24 with possible over-subtraction. This image is worse than the input with *stronger* side-lobes introduced around the bright sources, interfering with the diffuse emission. The S/N could possibly have been improved when running the second pass of SAGECal by either: (i) using a larger solution interval (see commissioning tests on http://www.lofar.org/wiki); (ii) combining multiple

SBs *before* running SAGECal; (iii) reducing the number of directions solved for. Due to time constraints these routes of investigation were not explored and hence we did not carry out the second pass of SAGECal; this remains a possibility for further work.

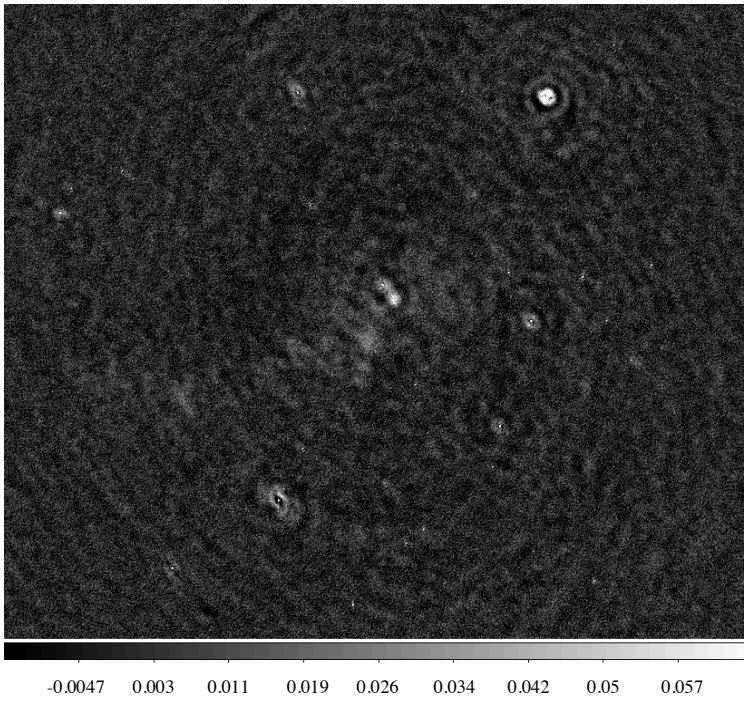

Figure 3.24: The output image of iteration 2 for Beam 0 after the second pass of SAGECal. Here the subtracted bright fluxes have not been restored and at this stage interest was on the residual diffuse extended structures (which were negatively affected).

3.4.8 Image quality

Image quality, determined by the array *sensitivity* and *resolution*, is judged by the measurable level of *RMS* background noise in the map and the *dynamic range (DR),* which is the power ratio between the peak flux in the image and the RMS noise. The quality of the overall image is determined by the achievable noise floor which can be raised by: (i) thermal system noise determined by receiver noise (in turn determined by the receiver collecting area itself) (Yatawatta et al. 2009); (ii) confusion noise; and (iii) calibration errors (Wijnholds & van der Veen 2008). Whilst the system noise is a fixed wall to achievable sensitivity, we can try to lower the noise floor by countering calibration and confusion (see Condon 1974) effects as much as possible. This is achieved by iteratively repeating self-calibration and updating the sky model hence improving the DR as well as *source fidelity* i.e. the likeness of the observed image to the true sky (Wright 1999). A more quantitative definition of fidelity based on information theory is the Landau-Pollak theorem (Landau & Pollak 1961).

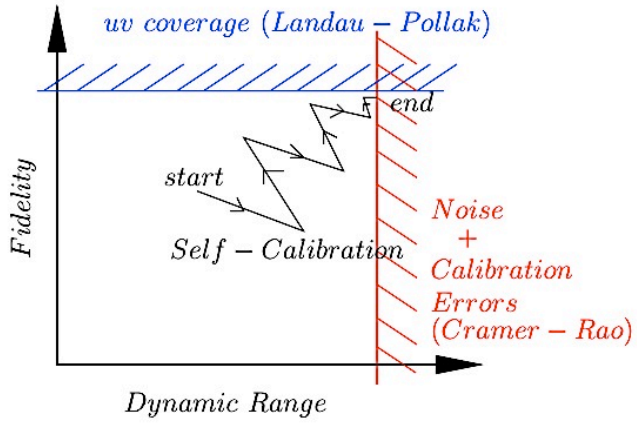

Figure 3.25: Fidelity-DR trade-off (Yatawatta, 2011b)

There is a complex relationship between image fidelity and DR as represented by Yatawatta (2011b) in Figure 3.25 which starts with an initial sky model and uncalibrated data. Each stage of calibration using an updated sky model, increases the DR and fidelity until there is a point beyond which there is no further image improvement i.e. the theoretical limits are reached and we cannot image 'deeper' (Yatawatta 2011b). Iterative improvement was measured using the image analysis tool *Imstat* in CASA on the final images made across the entire bandwidth (§ 3.4.12) for each of the 4 beams.

The theoretical LBA system sensitivity (Eq. 3.16) was calculated as 39.14 mJy/beam per SB for a single polarisation using the observational and array parameters and following Nijboer et al. (2009). The theoretical noise limit in a LOFAR image was calculated as 9.78 mJy/beam for a single SB. The actual RMS measured after the second iteration for one SB centred on 60 MHz was ~ 50.5 mJy/beam. Considering that the image weighting parameter may increase the calculated values by a factor of 1.3 – 2 (the images analysed were made with uniform weights), it was concluded that the data quality was quite close to the limitations of the instrument, although this could possibly have been improved further. Hence a third iteration of self-calibration was undertaken, and the RMS improved to 46.8 mJy/beam for the same SB. The contributions to the achievable noise floor from calibration errors and thermal noise scale inversely with the number of samples N in a snapshot observation, which is equal to the product of bandwidth and integration time (Wijnholds & van der Veen 2008). Hence the RMS and DR invariably improve with bandwidth which increases (u, v) coverage (Figures 3.27 & 3.28). The FoVs covered by Beam 1 and Beam 3 reached an RMS of 7.87 mJy/beam and 11.98 mJy/beam respectively across the entire bandwidth, after the 3rd iteration (Figure 3.28). Beam 3 has the poorest result due to 75% of

missing SBs across the ~ 47 MHz bandwidth compared to the other beams (an observational fault). By mosaicking all beams (as detailed in § 3.4.11) an impressive RMS of 3.62 mJy/beam could be achieved (Figure 3.28). Likewise the DR improved with iteration for all beams (Figure 3.27) reaching ~ 750 for Beam 1 and ~ 1004 for the mosaic. However, the DR is a highly variable diagnostic and depends strongly on the strength of the strongest source within the FoV and the RMS, which varies over the map (Wijnholds & van der Veen 2008).

Figure 3.29 shows the gradual improvement in average source size per iteration which allows more sources to be resolved, relating to the improvement in RMS. The measurements of major and minor axis width were outputted by PyBDSM (§ 4.1.1) from the uniformly weighted images. The iterations can be directly compared since they measure the same cross-correlated sources. There was no significant clustering of objects over the FoV and sources were evenly spread. Hence the average improvement of the objects' major and minor axis width is representative of the overall improvement of the average source size across the FoV on the whole. The mean major axis width improved from 101.26″ to 84.41″ and the mean minor axis width improved from 66.82″ to 61.63″. These values were approaching (although not quite at) the theorised resolution of ~ 10 – 50″ between ~ 10 – 60 MHz using remote stations only (§ 3.2.2; van Haarlem et al. 2013). Condon (1974) describes how at some point the number of detected sources becomes larger than the number of resolution elements in the image. This manifests as a "blur of sources" in the map and the maximum density of distinctive sources is the classical or instrumental *confusion limit,* relating to the resolution of the image. Hence it is possible that the confusion limits (which can often come ahead of the receiver noise limits) were reached by the 3rd iteration, due to no new sources becoming resolved at this point.

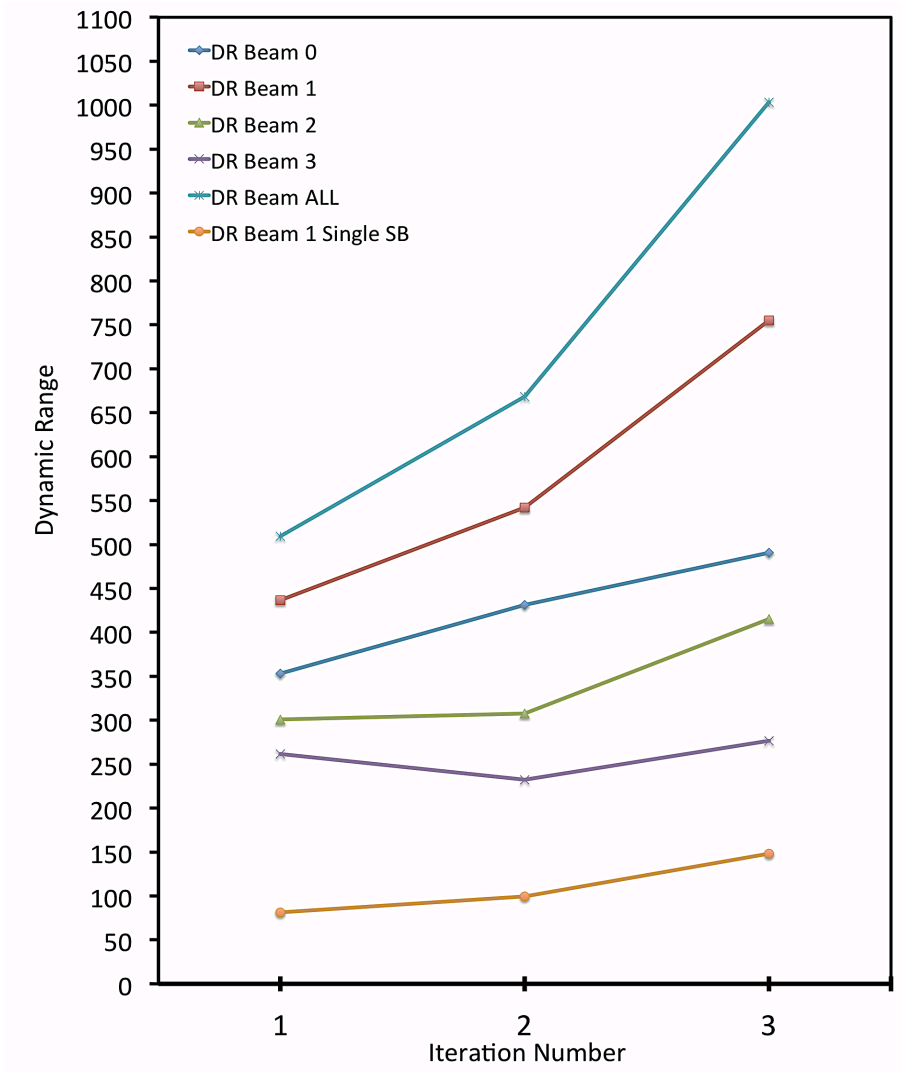

Figure 3.27: The improvement in DR per iteration for each beam across the full ~ 47 MHz bandwidth. This is also demonstrated for a single SB image, although the DR values are not as impressive. Clearly Beam 1 and Beam 0 show the best improvements. The values for the full mosaic are affected by the poorer values for Beam 3 on account of its higher RMS.

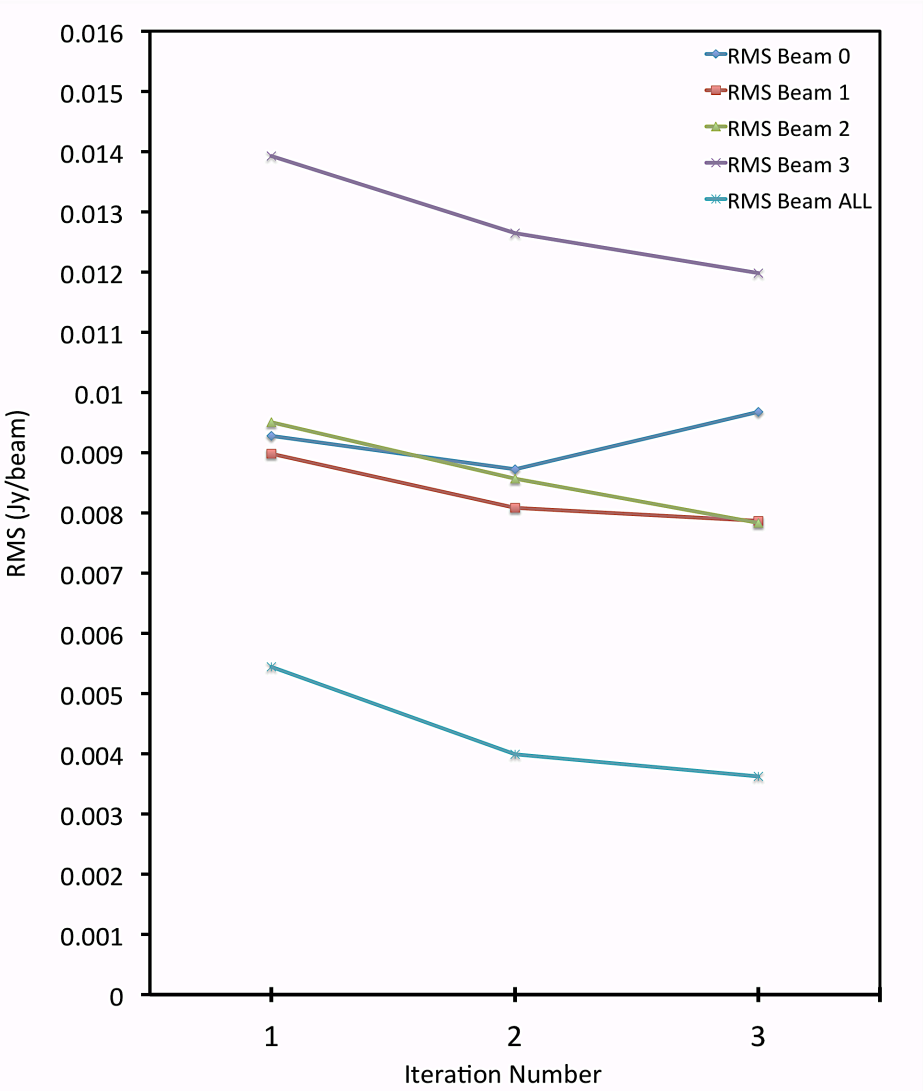

Figure 3.28: The improvement in RMS per iteration for each beam across the full ~ 47 MHz bandwidth. Beam 3 has the highest level of noise due to poorer (u, v) coverage. On the whole the level of noise for all beams improves with each iteration (although for Beam 0 it slightly increases between the 2nd and 3rd iteration). Iterating and mosaicking all beams allowed an RMS of 4.78 mJy.

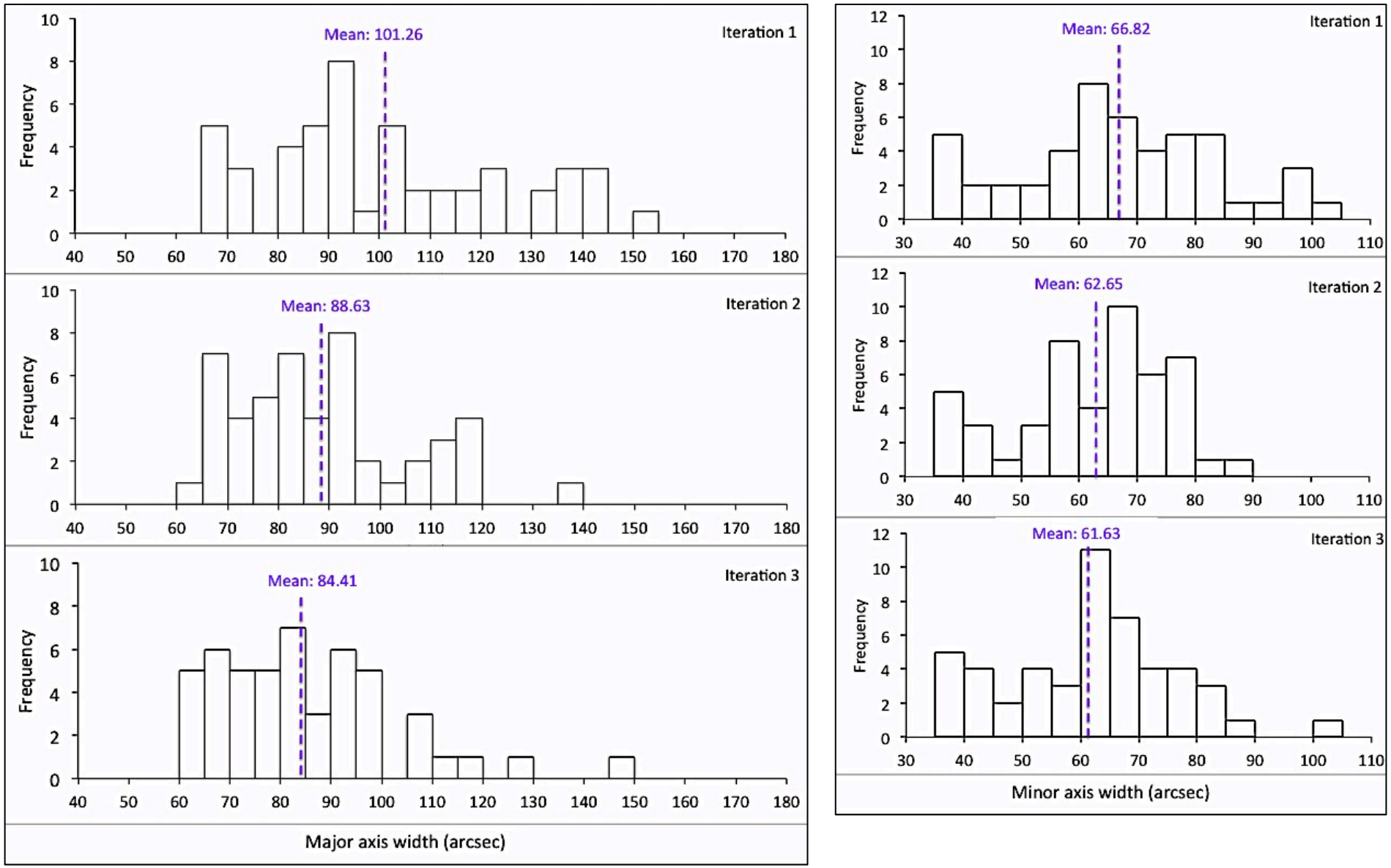

Figure 3.29: Histograms demonstrating the gradual improvement in resolution per iteration from mosaicked AWimages. There was no significant clustering of objects over the FoV and sources were evenly spread. Hence the average improvement of the objects' major and minor axis width is representative of the overall improvement of the resolution across the FoV on the whole.

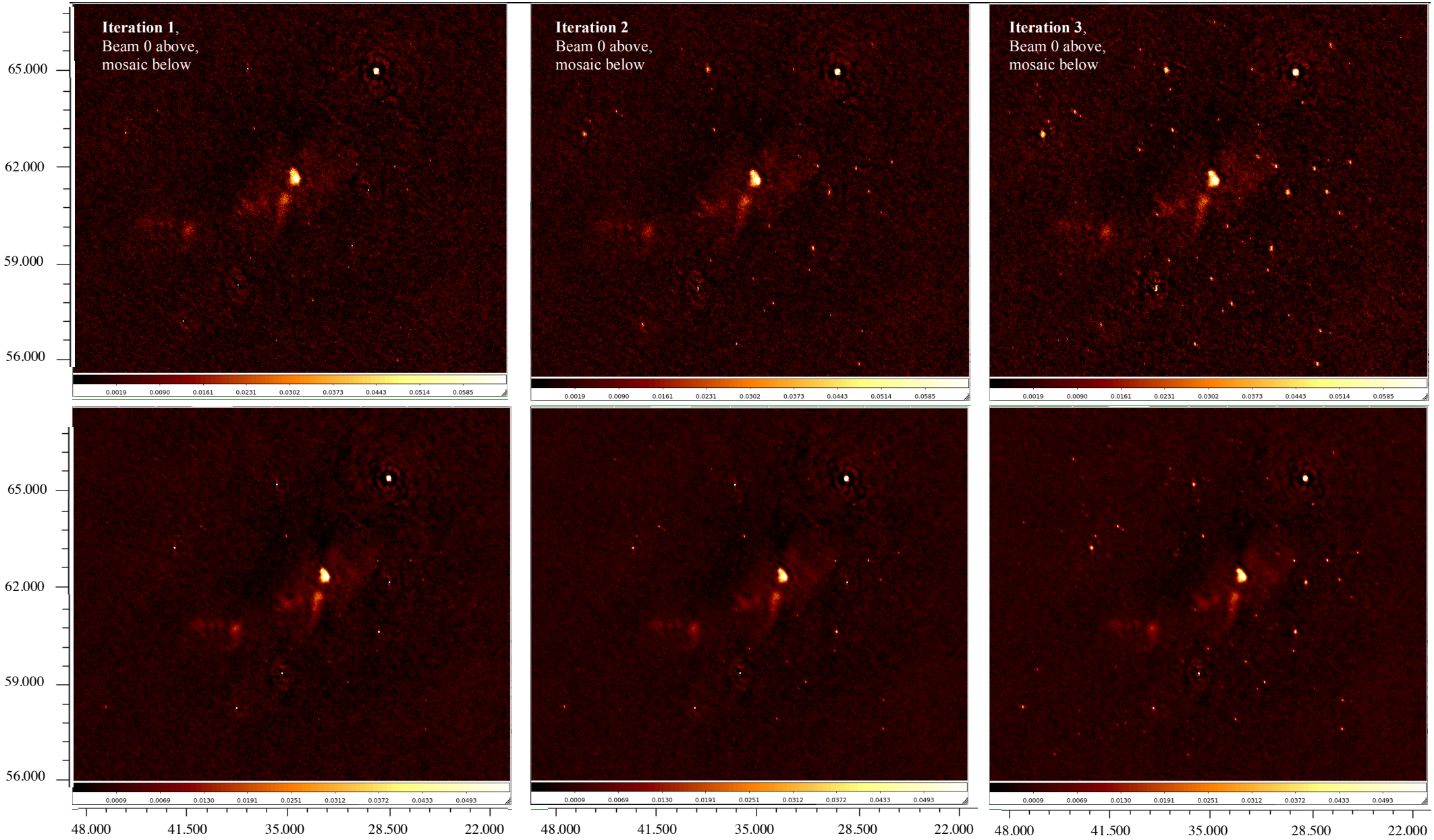

Figure 3.30: The iterative improvement in field images made with Beam 0 (above) and the full mosaic (below), full Bandwidth (~ 53.5 MHz). All images were made with the same parameters focusing on point source emission (i.e. uniform weighting) and full Stokes polarization within AWimager. Each Beam 0 image has been set with the same histogram intensity scale. The mosaics below have a separate histogram intensity scale consistent between each iteration. A visual improvement in noise can be seen, and the number of sources resolved increases as resolution improves.

3.4.9 Imaging

The CLEAN algorithm (Högbom 1974 and Clark 1980) was used to deconvolve and image the data, initially within CASA before moving onto AWimager software (§ 3.4.11). It is effectively a brute force deconvolution to disentangle source structure from the instrumental response PSF as explained in § 3.1, effectively reducing instrumental side-lobes in the image plane. This imaging function has 3 options for weighting visibilities, to alter the instrument's natural response function, which affects the sensitivity and spatial resolution. Please refer to Briggs et al. (1999), for the full development of these weighting schemes. The recorded data is in practice more concentrated towards the centre of the (u, v) plane (§ 3.1) and not uniformly distributed.

'Natural weighting' generally gives more weight to short baselines (low spatial frequencies) and provides the best signal-to-noise (S/N) in the final image (i.e. optimal point-source *sensitivity*) so this is advantageous for low level diffuse radiation. The weighting function is inversely proportional to the noise variance of the (u, v) cells. As a result the sampling function is more centrally concentrated, and its Fourier transform, (the synthesised dirty beam in the sky plane), is therefore more drawn-out; worse angular *resolution* results in the final map. Alternatively 'uniform weighting' gives more weight to long baselines (high spatial frequencies), so that the Fourier transform of the sampling function (and hence synthesised beam) is smaller, giving increased resolution at the expense of weighting down data at small u and v and degrading the S/N (sensitivity is lost). In this case the weighting function is inversely proportional to the local density of (u, v) points. A resultant improved beam with a minimised side-lobe level is advantageous for point sources. The Briggs or 'Robust weighting' creates a PSF that smoothly varies between 'uniform' and 'natural' weighting (Briggs 1995). It avoids giving too much weight to (u, v) cells with low natural weight; this form of visibility weighting is explored incrementally in Figure 3.31.

The shortest baseline determines the largest-scale structure that can be detected. However, it is also important to mitigate against instrumental short baseline effects, such as the mutual coupling and electrical crosstalk between closely spaced dipoles (Subrahmanyan & Deshpande 2004); hence imposing baseline restriction typically of $< 4\,\lambda$ is recommended by Wijnholds (2010). For our data, baselines were restricted from $< 40\,\lambda$, $< 20\,\lambda$, $< 10\,\lambda$ and $< 1\,\lambda$ and the $10\,\lambda$ restriction improved noise effects the most without a detrimental effect in recovering the large-scale structure.

Images were created at 3 distinctive frequencies: 35MHz, 55MHz, 70MHz (§ 4.1); in order to ensure that all had the same resolution, the maximum baseline was restricted to match the best possible theoretical resolution at the lowest frequency of ~15– 20″ (Eq. 3.14). The baseline taper was also experimented with, and enhancing the inner taper whilst restricting the outer did enhance the diffuse emission by decreasing the contributions of the longer BLs, but time constraints meant these parameters were not fine-tuned so default parameters were used: i.e. no taper. Evidently, it was challenging to enhance sensitivity to large-scale diffuse emission without degrading the angular resolution, which is useful for the kinematics of these structures as well as point source detection. Hence separate images were made with optimal parameters to enhance either point sources or the Galactic diffuse structures after careful experimentation.

Another important deconvolution parameter is choosing the image pixel size or CASA *cell size* in order to accurately sample the angular resolution element. One way is to make this of the same dimensions as the central spike in the dirty beam, which is the Fourier transform of the sampling function. Restoring the image with a CLEAN synthesised beam smaller than the fit of the main lobe of the dirty beam (the 'formal resolution') can be used in a process of *super-resolution* (please see Harris 1964), but with a risk of introducing incorrect structures in the map (e.g. Pearson and Readhead 1984). We calculated an optimal cell size of 15″ after experimentation and using Nijboer et al. (2009) for guidance which predicts a resolution of 13.8″ using a baseline of 80 m at 45 MHz. The FoV was also calculated using Nijboer et al. (2009) and was estimated at 4 – 5° across, towards the centre of our bandwidth (~50 MHz). The FoV is limited by the diffraction-limited response of the individual antennas and a greater bandwidth limits the FoV as coverage where all frequencies are in phase decreases. These edge effects result in unstable deconvolution and hence the edges were removed with an appropriate option in (please refer to § 3.4.11).

Robust Weighting 1.5 | Robust Weighting 1.0 | Robust Weighting 0.5 | Robust Weighting -0.5

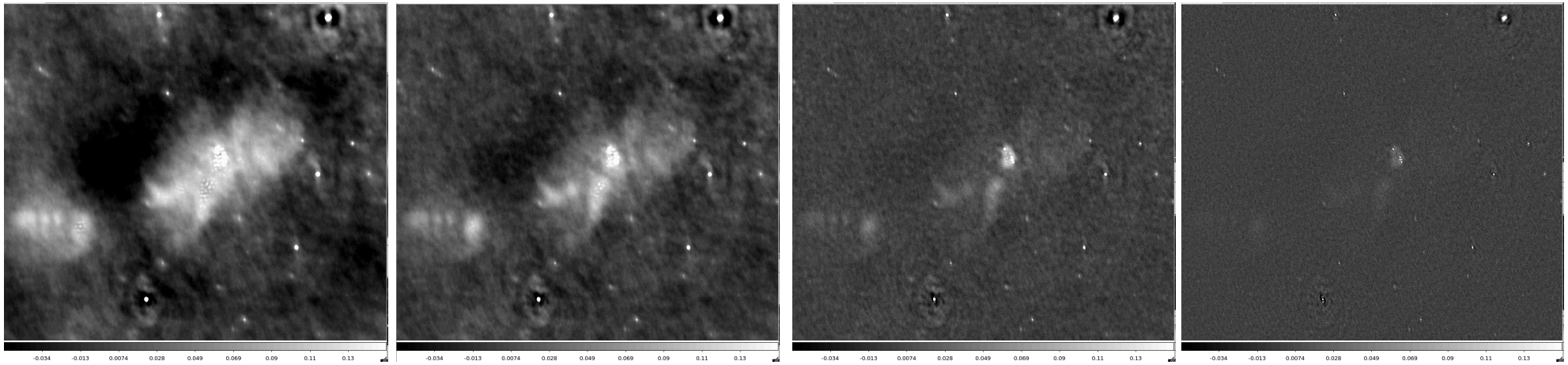

Robust Weighting 0.5, (u, v) >10 | Robust Weighting 0.5, (u, v) >20 | Robust Weighting 0.5, (u, v) >40

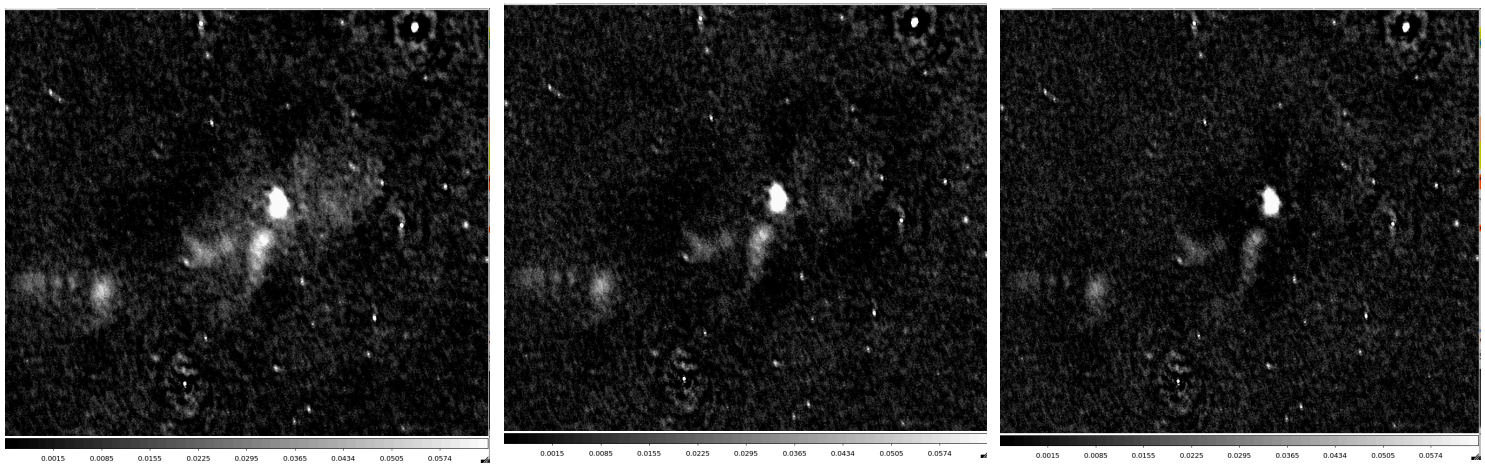

Figure 3.31: Experimenting with Beam 0 over the full bandwidth only using CASA imager. The Briggs Weighting was tested from -2 (almost uniform weighting) to + 2 (close to natural weighting) in the top row. A Briggs weighting of 0.5 was best for diffuse emission without too much detriment to the resolution. The bottom row explores the best minimum (u, v) parameter.

3.4.10 The Direction Dependent Effect Of Wide-Field Imaging

The 2-D (u, v) plane is a simplified assumption which cannot be applied to a wide FoV such as that covered by LOFAR, where the FoV surpasses the size of an isoplantic patch (Cornwell et al. 2008). In the low-band, the primary beam diameter can reach as much as ~ 20º at 30 MHz using the inner LBA configuration (Nijboer et al. 2009). This is a sufficiently large angular region to employ the use of the 'wide-field' imaging algorithm such as *w-projection*, which considers the DDE of a non-zero w-term introduced by sky curvature and non-coplanar baselines (Cornwell et al. 2008). As mentioned in § 3.1 such regions can no longer be approximated as a 2-D plane since iterative deconvolution algorithms such as CLEAN will produce distortions around sources, the severity of which increases with distance from the phase centre (Cornwell et al. 2008). W-projection is one of three methods to correct this w-term effect. The other 2 are *image-plane faceting* (Cornwell & Perley 1992) and (u, v)-*domain faceting* (Sault et al. 1999). In the case of our pipeline, the w-projection algorithm was used during imaging either as an option within CASA or to give the final images with AWimager, which is specially adapted to image wide FoVs.

3.4.11 The Direction Dependent Effect of the Beam

After successful calibration of the giant W3/W4/W5 Galactic star-forming complex, obtaining a beam corrected image to bring out more *accurate* values for the source fluxes was the next major objective. Low radio frequency interferometers such as LOFAR, have the common difficulty of having a beam that not only varies spatially and with frequency (§ 3.4.12), but also *time* (Tasse et al. 2013). One of the most important DDEs to calibrate for is the shape of the primary beam at the *station level*, which is carried out by finding the individual station beam Jones matrix as a function of pointing position and frequency (Tasse et al. 2013). Due to LOFAR's hierarchical beam structure (§ 3.2.4), the station beam requires an accurate estimation of the complex gains of each antenna element in the station array (van der Tol 2007). This level of instrumental calibration is covered in § 3.3 with the creation of a calibration table.

Station & Element Beam

The aperture-illumination-function (AIF) of each antenna within the array results in a direction-dependent complex gain that can vary with time (Thompson, Moran & Swenson 1991). For LOFAR, antenna AIF *does* vary with time, as well as direction and frequency. The resultant antenna power pattern or dipole projection is the *element beam* and is non-identical between antenna pairs. The element beam can be corrected in 2 ways: either (i) in the image-domain as a simple post-deconvolution step using an estimate of the average element beam or (ii) during calibration itself. This first method ignores the time-variable and baseline (direction) dependent element beam corrections which *can* be accounted for: (1) in the calibration step using BBS and; (2) using AWimager during gridding and deconvolving (Tasse et al. 2013). It is important to note that whilst both correct the same effect, AWimager can apply the correction for all directions accounting for the direction-dependent projection of the dipoles which slightly vary across the FoV, whilst BBS can only correct for a single direction, at the centre of the field.

AWimager accounts for dipole projection making use of *A-projection* (Bhatnagar et al. 2008) by computing gridding convolution functions for each baseline as the convolution of the complex conjugates of two antenna AIFs. This is an effective way of potentially taking all DDEs into account (including the non co-planarity of the array) in the deconvolution steps and is a specific adaptation of the traditional *w-projection* algorithm (§ 3.4.10). For this reason AWimager is advantageous over the CASA imager as a deconvolution package specifically for LOFAR data, as it includes the time-variable coupling between the antennas within stations to accurately model the LBA station beam which is valid even far from the primary lobe (Tasse et al. 2013). Hence this element beam correction allows AWimager to arrive at the more *accurate* relative flux values than CASA imager. Tasse et al. (2012) detail imaging of a field where the stark improvement of element and array (see below) beams with AWimager is showcased against an image made in CASA, which only considers the w-term (§ 3.4.3). Tasse et al. (2012) also demonstrate how fluxes converge to true underlying values and are well-recovered using deconvolution with AWimager.

Array beam

Once the 'final' self-calibrated image was acquired, it was corrected for the primary beam of the array. Traditionally this has been approximated as a Gaussian with a Full Width Half Maximum (FWHM) that gets smaller with the observing frequency (e.g. Normandeau et al. 1997 using the DRAO observations) and carried out in a simple corrective step using CASA. However, due to the complex and time-variant nature of the LOFAR beam, it needs to be modeled (Tasse et al. 2013). The theoretical beam model, which the commissioning teams have extensively been testing, was modeled in AWimager using the observational information (LBA selection, station configuration, date etc.) contained within the MS. This represented the array factor and station beams (ionospheric calibration regimes 3 and 4 of Figure 3.14), taking into account the ionospheric phase delays over the beam (van der Tol 2007). The correction itself took place during imaging but the most important step to normalise the residual image was as a post-deconvolution procedure, by dividing out the DDE of the primary beam of the array in a flat-noise correction (see below).

Mosaic

Once images were created (either narrow or wideband; § 3.4.12) for each of the 4 beam pointings, a mosaic was created using a script created by Cyril Tasse which took the individual field images and (i) regridded them to a common phase centre; and (ii) co-added them (i.e. summated and averaged) after weighting each with the individual field array primary beam (PB) profile (outputted as data products from AWimager; § 3.4.12) and the expected noise level, to improve accuracy of emission present in the overlapping regions, countering array primary beam attenuation. Essentially the script carried out a (1/Variance) averaged sum where the Variance follows ~ $1/(PB^2)$ for each field. The result was a single large and sensitive deep image (Figure 4.1).

3.4.12 Multi-Frequency Synthesis

Improving the sampling of the (u, v) plane is advantageous for high resolution and DR imaging. As mentioned in (§ 3.1) one way of filling the Fourier plane is to combine visibilities at multiple wavelengths in the process of *multi-frequency synthesis* or *MFS* (Thompson, Moran & Swenson 1991). This is demonstrated in Figure 3.32 below.

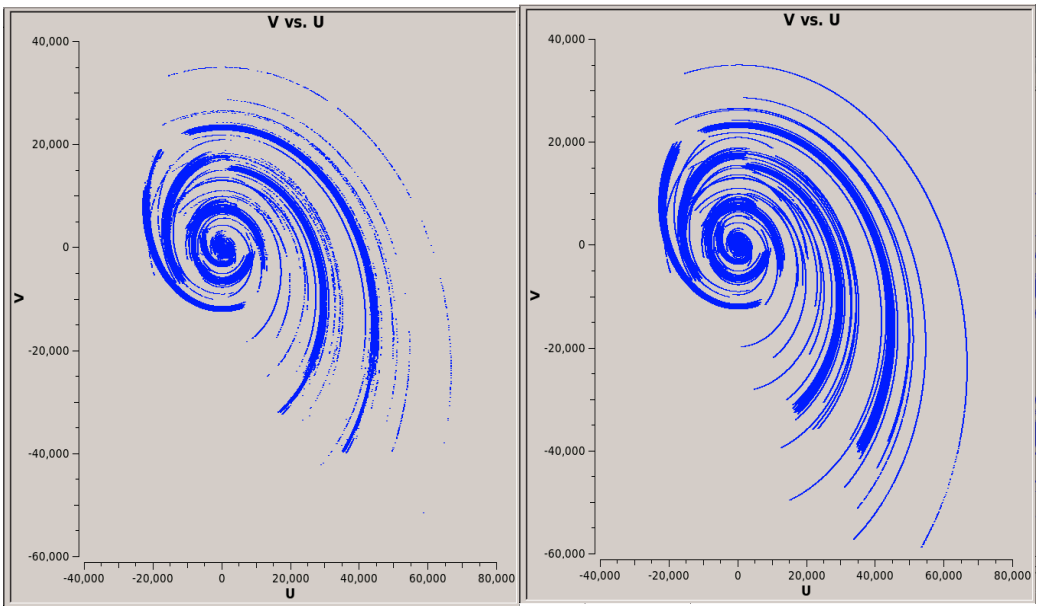

Figure 3.32: (u, v) coverage for a single SB at 74 MHz (left) and the entire frequency range 30-76 MHz (right). This is for Beam 0 only.

When combining frequencies across large bandwidths, one has to be careful of *bandwidth smearing* or *chromatic aberration* effects (Bridle & Schwab 1989). The angular size of the synthesized beam, θ_{PB} is larger at lower frequencies than higher frequencies and if this is not accurately corrected for, it can lead to distortions in the image of the source which worsens with distance from the beam phase centre, l and a reduction of the amplitude of the visibility by a factor of (Bridle & Schwab 1989):

$$\frac{\sin(\pi l \, \Delta \, v/v_0\theta_{PB})}{\pi l \, \Delta \, v/v_0\theta_{PB}} \tag{3.23}$$

where v_0 is the centre of the observing bandwidth, $\Delta \, v$ being correlated. Integrating the visibility data over $\Delta \, v$ inaccurately treats all data points as though they were all made at the singular frequency, v_0 and consequently the (u, v) coordinates and value of visibilities are only correct for

v_0 (Chengalur et al. 2007). Images made with CASA do not take the beam attenuation into account, spatially per SB, or across the bandwidth when combining SBs using a simple regridding and averaging script to give a mean image over all beams.

However, the recent version of AWimager commissioned in 2013 during this work (see below), does account for primary beam weighting correction at each SB increment within the frequency range. The final combined theoretical primary beam pattern over the entire bandwidth of input data was then generated from the array configuration and frequency range for a given observation and output by AWimager, as an image called '<imagename>.avgpb'; this is the averaged non-trivial non-Gaussian theoretical LOFAR primary beam profile over baseline, time and frequency which is used in the aforementioned mosaicking process and describes how the sensitivity of the beam profile varies with distance from the phase centre. The CASA mean image after the 3rd iteration was compared with the AWimager mosaic of the same input data; the latter is more superior as demonstrated in § 4.1.1 and source detection using the same threshold parameters revealed 122 source matches with the VLSSr for the CASA mean image whilst for the AWimager mosaic this was 226 (in all, 105, 135 and 226 sources had been matched with the VLSSr after the 1st, 2nd and 3rd iterations respectively demonstrating quantitatively the iterative increase in sensitivity; § 2.4.8).

For our data, a single SB image clearly did not have good (u, v) coverage and it was very difficult to detect any extended diffuse structures, the only evidence of which were the appearance of large scale waves in the image plane; an indication of poor (u, v) sampling which enhances side-lobes. Combining SBs across the entire ~ 47 MHz frequency range in *wideband MFS* allowed the best possible continuum image, averaging out the side-lobes and improving sensitivity especially to extended structures with enhancement of the faint point sources. This is demonstrated by the deep images of Figure 3.30 with statistics detailed in § 3.4.8.

However, whilst the DR, S/N ratio and angular resolution clearly increase, combining across the entire available frequency range may limit the *spectral* resolution as high and low frequencies originating from the same source could possibly cancel out (Conway, Cornwell, Wilkinson 1990). This may explain the general shift towards lower fluxes computed for the entire bandwidth compared in Figure 4.7 (§ 4.1.1). *Narrow-band MFS* is therefore advantageous in determining the

spectral index distribution with more accuracy and Thompson, Moran & Swenson (1991) recommend a frequency range of ~ ±15% of the mid-range. Hence, as well as the full bandwidth, images were also created for at 3 individual widely spread frequencies with 5 MHz bandwidth, these being ~35 MHz, ~55 MHz and ~70 MHz. Whilst these do not match the S/N or resolution values achieved with the full bandwidth images, they allowed extraction and comparison of the brightest sources on the SED plots at a finer frequency incrementation and spectral characteristics could be confirmed with greater detail (see § 4.1.2).

3.4.13 Final Image Quality Analysis

The advantages of using AWimager over CASA imager have been discussed (on account of its correction for the time, frequency and spatial non-Gaussian, non-trivial and baseline dependent correction of the LOFAR beam profile as well as its adaptation to wide FoVs and DDEs of the ionosphere). It was still in the final stages of development at the time of this work, and so it was important to work closely with the AWimager software developers, Cyril Tasse and Reinout Van Weeren to trouble-shoot initial problems. The final beam corrected mosaicked images across the entire bandwidth made with AWimager gave an RMS of 3.62 mJy/beam and DR of ~ 1004 (Figure 3.27) in comparison with CASA images which had an RMS of 7.29 mJy/beam and DR of ~ 668. Visually the AWimage appeared 'sharper' due to improved resolution allowing more fainter sources to be resolved (226 vs. CASA's 122 source matches with the VLSSr as mentioned in § 3.4.12). This improvement could possibley also be due to improved deconvolution with Awimager.

Residual Artefacts

Post calibration errors were evident in the images as artefacts of radial patterns 'ringing' around bright sources. These side-lobes left over by the CLEAN deconvolution process are remnant DDEs and side-lobe confusion refers to a reduction in the sharpness of the image which decreases the DR (Wijnholds & van der Veen 2008). These are noticeable in the images of Figure 3.30 particularly around W3 and 3C 69 (RA ~ 02:28 Dec ~ +59.10). We had attempted to reduce this by peeling away the brightest sources using SAGECal and a source model extracted from the previous iteration (§ 3.4.7). As well as side-lobes and grating rings, Normandeau et al. (1997)

refer to ‘spokes’ which are artefacts of processing strong, difficult-to-model sources and are to be expected for W3; this was also evident in our final images although to a lesser extent. According to Smirnov (2011), in the presence of a dominant source, self-calibration solutions will tend to incorporate all effects in the direction of that source. DDEs will then become apparent as artefacts around other off-axis sources within the FoV which are a certain distance from the dominant source which is usually placed at the pointing centre. Hence these DDE-related artefacts are also called off-axis artefacts (Smirnov 2011).

Braun & Walerbos (1985) describe the inefficiency and difficultly of 2-D mapping very extended objects adequately in the process of point-by-point deconvolution with the CLEAN algorithm (Hogbom 1974) as described in § 3.1. The instrumental PSF response tends to contain a ‘negative bowl’ due to missing (u, v) coverage and this results in large-scale inaccurate background variations when convolved with an extended brightness distribution (Braun & Walerbos 1985). CLEAN has been improved to increase its efficiency (Clark 1980) and reduce the extent of the ‘CLEAN ripples’ evident as fringes across extended objects (Cornwell 1983). A more appropriate adaptation of CLEAN for very extended objects is the ‘Multi-scale’ CLEAN algorithm where instead of points, the image is parameterised into a collection of inverted tapered paraboloids (Cornwell 2008). It was an option that was explored with the effect of reducing the ‘negative bowl’ and enhancing what seems to be very low flux emission around SNR 3C 58, improving DR around the SNR by ~ 6.8 %. However, this option resulted in poorer SNR elsewhere in the FoV and ultimately was not used.

LOFAR Calibration Challenges

Compared to existing telescopes, LOFAR calibration has the numerous instrumental and ionospheric complications which can manifest themselves as persistent artefacts in the final images (Smirnov 2011). Inaccurate single-station calibration tables due to imprecise antenna positions and clock drifts will do little to counter telescope instability; this is still an issue today, although more so during the collation of our commissioning data. LOFAR beams are complex and time variable and pointing errors are plausible (Smirnov 2011). Also there is no guarantee of complete ‘A-team source’ removal which can dominate in the station side-lobes over weak sources in the station main

lobe since each omnidirectional LOFAR antenna can see the full sky (van der Tol et al. 2007).

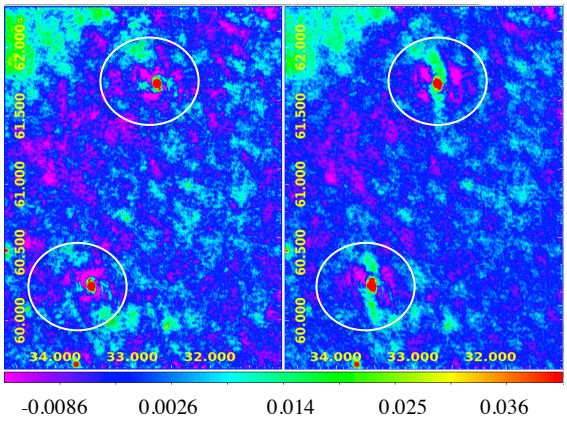

Figure 3.33: Point sources, before (right) and after (left) the time cut at 4000 samples. The comparison demonstrates ionospheric phase instability during the observation (highlighted by the white circles.

Furthermore the stability and behavior of the ionosphere is not completely predictable. We discovered that BBS phase solutions were not very stable after 2/3 of the total observation time. After ruling out that this was not an inherent fault of BBS (by re-running BBS with a larger solution time to increase the S/N), it is likely that the ionosphere became unstable after this time (due to bad weather or a higher level of scintillation). By restricting the data after the solutions become less stable, the images appear sharper (left of Figure 3.33). However this had the effect of losing some S/N due to data removal. There are advantages and trade-offs to both options, but for the following analysis, a high S/N was preferred.

Overall, there were numerous complications encountered during the calibration of this commissioning dataset; many were related to the technical difficulties of the incomplete array. There were also no pre-existing pipelines or source models within this low frequency range, making vigilant and lengthy experimentation essential during self-calibration. Even today, we still do not have a good methodology or pipeline that is able to properly deal particularly with *diffuse* emission, and this is subject of many on-going investigations.

Chapter 4

LOFAR Continuum Results & Analysis

After primary beam correction over the wide 47 MHz band and narrow 5 MHz band, the results are the following wide field maps presented in this section with imaging parameters fine-tuned to enhance point source (§ 4.1) and diffuse (§ 4.2) radiation respectively (Figure 4.1).

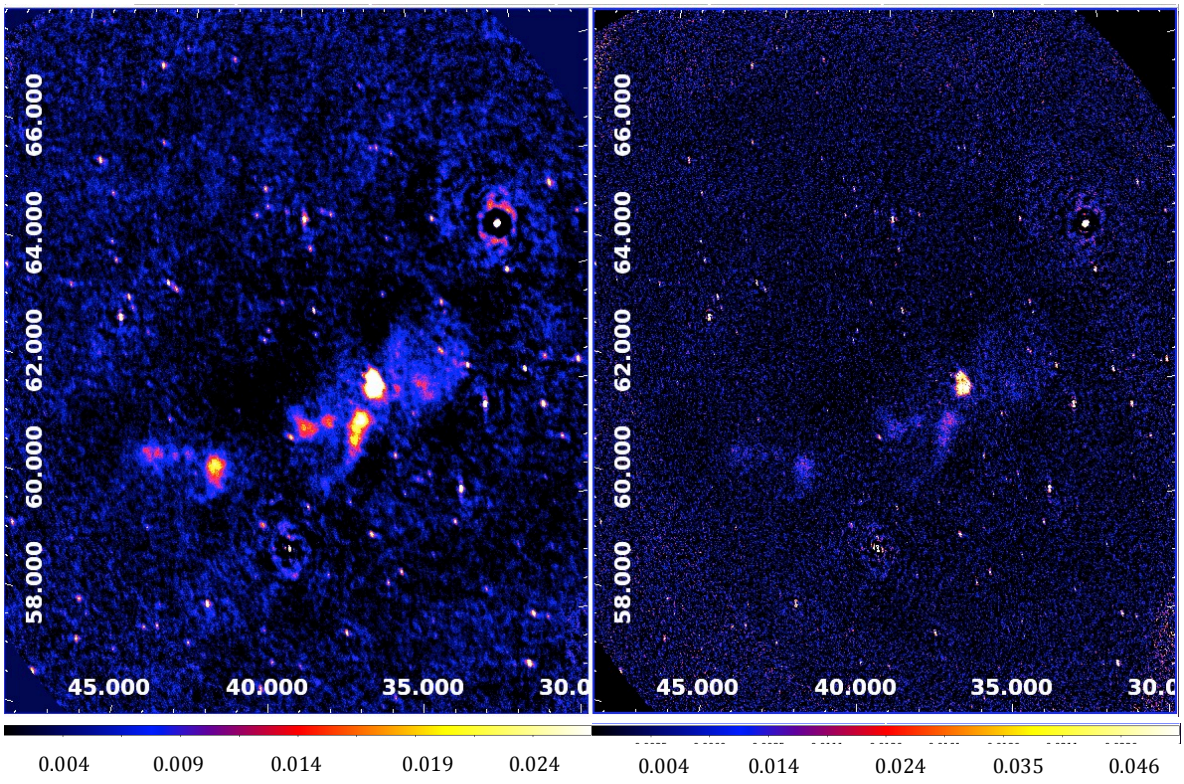

Figure 4.1: Enhanced diffuse emission (left) and enhanced point emission (right) using full bandwidth data.

4.1 Point sources

Aim: The ultimate aim of extraction of point sources from the final LOFAR images was to be able to determine their spectra over a wide range of frequencies, which requires combining and contrasting data from different radio-telescopes which is not trivial since they can differ widely in their characteristics (Verschuur & Kellermann 1974). These SED plots can ultimately give a more detailed picture of the underlying physical processes at the sources, the majority of which we suspect of being highly luminous AGN, radio-loud starburst galaxies and distant quasars, which as discussed in § 2.3.7 & § 2.3.9, are prominent sources of synchrotron < 30 GHz. SEDs can diagnose optically thin or thick emission, the latter of which is caused by free-free absorption processes (as will be justified in this chapter). Starburst galaxies are the dominant population at low radio fluxes (Condon 1992) and constraining their low radio frequency emission will also help to update models of the radio sky used in the design of future sensitive, low radio frequency telescopes such as the SKA (Rafferty et al. 2013).

4.1.1. Full Bandwidth Point Source Flux Recovery

The point sources were extracted with *Duchamp*, a source extractor written by Matthew Whiting (Whiting 2012). Strong correlations were seen with pre-existing radio catalogues specifying a 20″ search radius using a software called *TOPCAT* (Tool for OPerations on Catalogues And Tables) which allows analysis and manipulation of astronomical source catalogues. This established a *relative* correlation and coupled with the fact that the image quality was approaching theoretical noise levels (§ 3.4.8), confirmed that the LOFAR calibration was not too far out. However the *absolute* LOFAR fluxes expected at the bandwidth central frequency of ~ 53.5 MHz were lower by an order of magnitude when compared with the new VLA Low-Frequency Sky Survey Redux (VLSSr) at 74 MHz (Figure 4.4). WENSS fluxes at 325 MHz were brighter by a factor of ~ 2 which is not reasonable since we suspect many sources of extragalactic synchrotron with a spectrum that scales with $\alpha \sim -0.7 - -0.9$. For the same reasons we would expect LOFAR fluxes to be markedly brighter than the NVSS at 1.4 GHz but at this stage they followed each other ~1:1. Contrarily for the minority of sources which are Galactic (embedded in the H II regions), we would expect the thermal Bremsstrahlung spectrum to

scale between $\alpha \sim -0.1 - +2$ at radio frequencies (§ 2.2.4).

There were two main reasons for the LOFAR flux discrepancy with the VLSSr (and other catalogues). Firstly, due to the variable physical parameters and dimensions, the *resolution* can vary telescope to telescope. The VLSSr has a lower resolution at 80″ (Lane et al. 2012) so for the same source, LOFAR will have lower flux density if it is not a perfect point source. Secondly there is an issue of the *absolute flux scale*. All LOFAR calibration (SAGECal, BBS etc.) is carried out using a *relative* flux scale so there will be a *global scale difference* between the output fluxes and other surveys. The ongoing Multifrequency Snapshot Sky Survey (MSSS) observations (Heald 2013) take the traditional approach of transferring the amplitude gain solutions from the calibrator to the relatively calibrated target field (§ 3.4.5). Hence the flux scale is set from the calibrator itself whose intensity has already been determined on an 'absolute scale'. Scaife & Heald (2012) detail the broad-band spectral models for six 3C sources at low radio frequencies so that they can be established as standard calibrators for future LOFAR observations. These source models have also aided the VLA's recent VLSSr survey which operates at 74 MHz and has ~ 30 % more sources than the VLSS representing a major improvement over most of the sky (Lane et al. 2012). Our observations were taken during the early commissioning and science phase when LOFAR did not have established calibrators. The advantage of this meant that all available bandwidth was centred on the target field raising the sensitivity of the observation, as opposed to sharing a fraction of that bandwidth with an external calibrator. However, since we did not observe a calibrator, it was necessary to establish the *global scaling factor* for absolute error correction of the fluxes in the field (see below). We found the average linear scalar from the best LOFAR-VLSSr cross-correlated matches after selecting out the obvious Galactic sources (see below); this was essentially a bootstrap process using the VLSSr as a stop-gap solution.

Examining Calibration and the Spatial Correction of the Beam Profile

We would expect the correlation plots to improve after correction of the LOFAR beam profile (§ 3.4.11) and this is demonstrated in Figure 4.2. The sources from both beam corrected and uncorrected images have been cross-correlated (in TOPCAT), so that the same sources are plotted in both comparison graphs of Figures 4.15 and 4.16. Beam effects become more severe for off-axis sources with increasing distance from the radial centre as demonstrated by Figure 4.3 and this is more pronounced in the mean CASA image, which has no beam correction. Even the corrected AWimager mosaic is not completely 'flat' but does counter some beam attenuation so that is not as pronounced. An evident scatter over the entire range of radial distances still remains (an azimuthal dependence) due to limited accuracy of the LOFAR beam model and/or the calibration procedure.

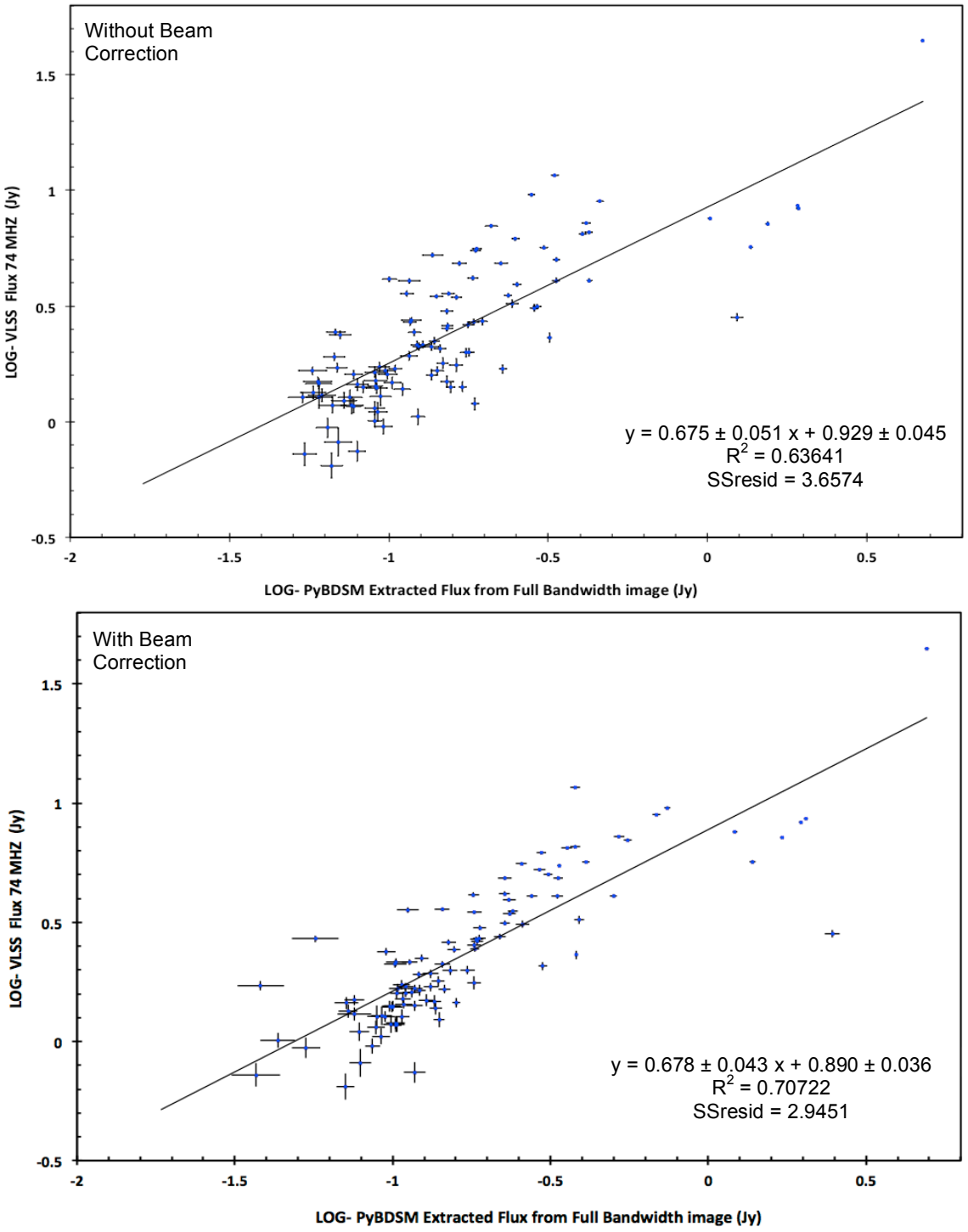

Figure 4.2: PyBDSM fluxes (using the same detection settings) extracted from CASA mean image over all beams (top) and AWimager mosaic (bottom) compared with VLSSr fluxes. There is more scatter in the uncorrected beam image (top). R^2 is the linear regression fit (coefficient of determination) indicating how well the data fits the model equation. SSresid is the residual sum of squares and is a measure of the discrepancy between the data and estimation model.

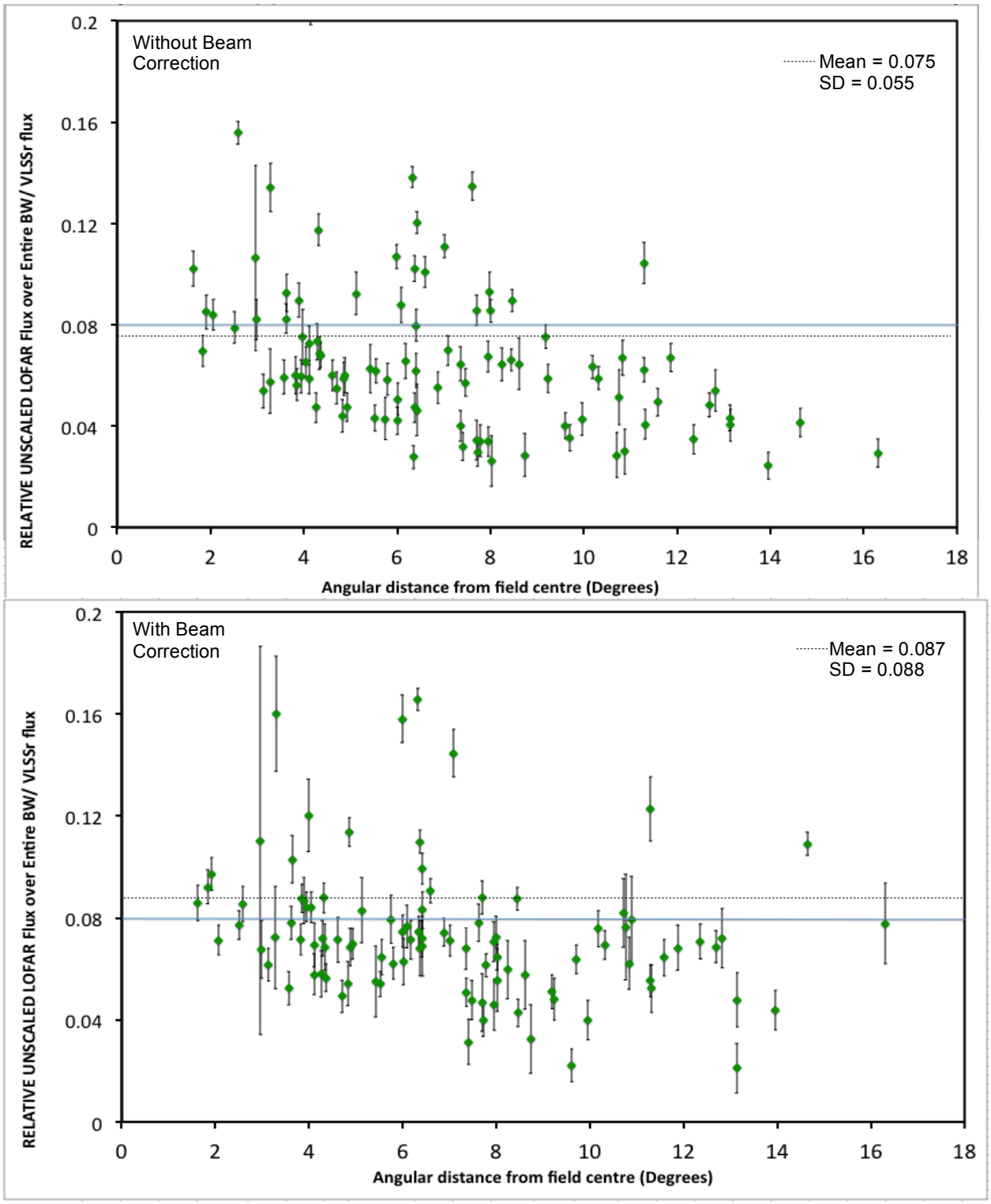

Figure 4.3: The ratio of flux of point sources between the *un-scaled* LOFAR fluxes and VLSSr fluxes as a function of their angular distance from the phase centre. A strong attenuation with angular distance is evident with the uncorrected beam image (top) compared with the beam corrected AWimager mosaic (bottom). The blue line is a mean of the flux ratios over *both* images (0.081) and helps to contrast the visual improvement across angular distance for both fields.

Testing the Source Extractor: PyBDSM vs. Duchamp

This final source extraction was carried out using *PyBDSM* (Python Blob Detection and Source Measurement), which gave better results than Duchamp (Figure 4.4), as it is an algorithm tested and adapted specifically for LOFAR; its improvement and accuracy is an ongoing process by the commissioning teams (please refer to PyBDSM test reports on http://www.lofar.org/wiki and Pizzo et al. 2014).

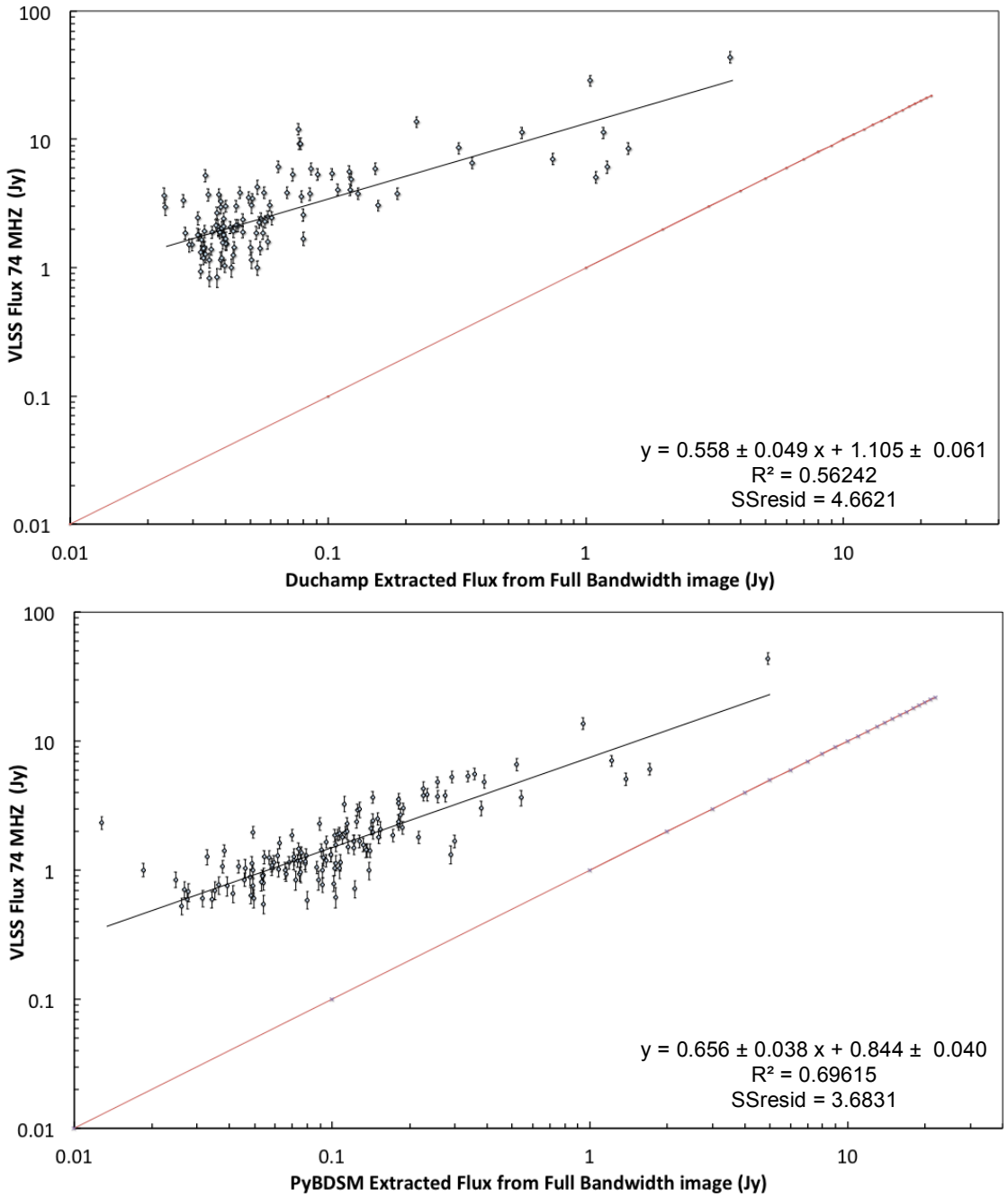

Figure 4.4: Fluxes extracted from the final full Bandwidth AWimager mosaic using Duchamp (Top) and PyBDSM (bottom). A log-log plot of LOFAR fluxes vs. the comparison VLSSr catalogue. The red line is x = y shown for comparison. The model equations of best fit later help determine out global scaling factors. It is clear there is a better model fit with the VLSSr using PyBDSM over Duchamp (a linear regression fit of ~0.696 vs. ~0.562)

PyBDSM works by fitting islands in areas of detection above a specified threshold and recovering the positions, integrated and peak fluxes, and shapes and sizes of these sources (Figure 4.5). Flux values are obtained by fitting Gaussians to the brightness distribution and the source finding settings were optimised after careful experimentation. This was a background RMS calculation in a box size of 20 by 20 pixels in steps of 10 pixels across the map; a threshold for the island boundary of 3 σ above the mean RMS which determined the extent of the island used for fitting; and a source detection threshold for the island peak of 5 σ above the mean RMS. The adaptive_rms_box parameter was also set to 'True', which had the effect of shrinking the box near bright sources where artefacts and noise are typically more significant (Pizzo et al. 2014).

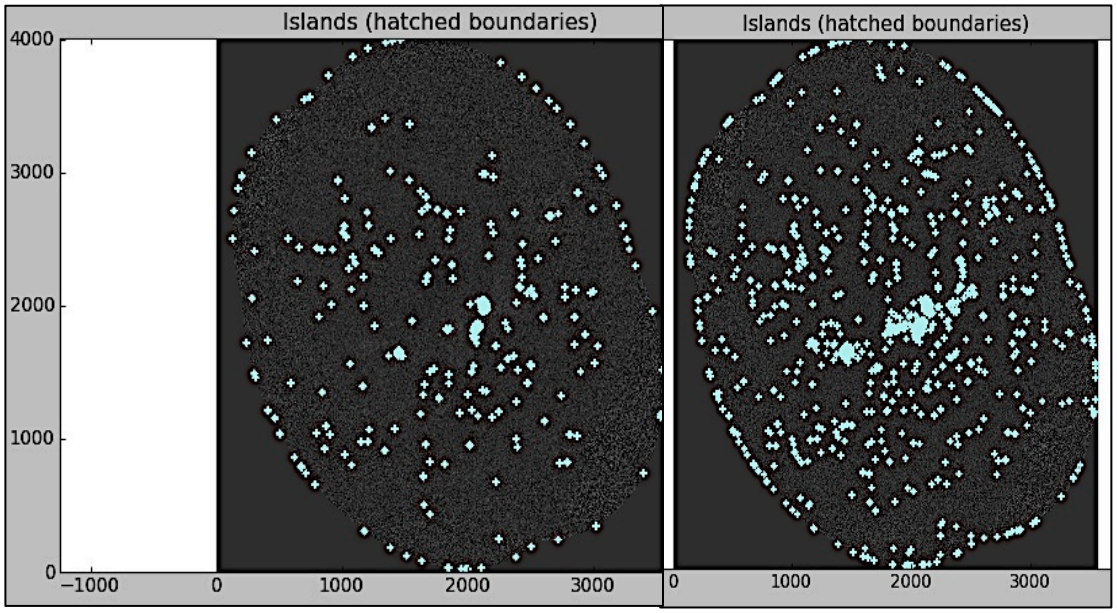

Figure 4.5: Varying the PyBDSM parameters to include all possible point sources using a source detection threshold for the island peak of 10 σ above the mean (left) and 5 σ above the mean (right). The latter inevitably picked up diffuse emission (which is as bright as the fainter sources) and artefacts, which had to be edited out manually (see below).

Quality Editing Of The Final Catalogue

§ 3.4.13 mentions how the quality of the final image was limited by: (i) remnant deconvolution artefacts; and (ii) ionospheric distortions. Both result in false detections and the task of editing them out manually could not be avoided. Real sources were verifed in cross matches with other radio catalogues using TOPCAT in addition to catalogue overlays (as shown in Figure 3.19) and 302 real sources were established. The catalogues at the narrow band 35.2 MHz 54.7 MHz and 69.9 MHz

frequencies, contain 61, 102, 69 sources respectively; these numbers reflect LOFAR's increased sensitivity between ~ 50 – 60 MHz (Figure 3.7). Each of our sources were also searched for in the *SIMBAD Astronomical Database* using coordinates of the NVSS cross-identified source name; this served as a secondary cross-check for real sources which were all identified and verified as an 'Astronomical radio source'.

Another factor to consider was that for point sources, the integrated flux should be greater than the peak flux as it integrated over the observed source distribution (Figure 4.6). It is only when you have an extended source that this changes; we cross-examined the PyBDSM extracted 'points' where the extended emission was greater than the peak and found that these originated from the bright gas of the Galactic H II regions. Such obvious extended Galactic sources could therefore be differentiated and removed from our analysis of points we were confident about being overwhelmingly extragalactic. Another reason why the integrated emission of a *real* point source could be less than peak emission is bias due to low S/N in the image. The general trend of our results in Figure 4.6 is a curve and the spread of deviation from the 1:1 trend (red line) gives a reflection of the quality of data (e.g. Tasse et al. 2006). This curvature is a reflection of the *Eddington bias* (Eddington 1913) where random measurement errors result in relatively more fainter sources being boosted into a higher flux density bin and relatively fewer bright sources to enter the fainter bin by having a measured flux density lower than the value. This increased effect or *Eddington shift* is far more obvious for fainter sources as evident Figure 4.6. There is a flattening in this curvature towards the lower frequencies, where we have reached the survey limits (see § 3.4.8) calculated at an absolute value of 9.78 mJy/beam in a full bandwidth LOFAR image.

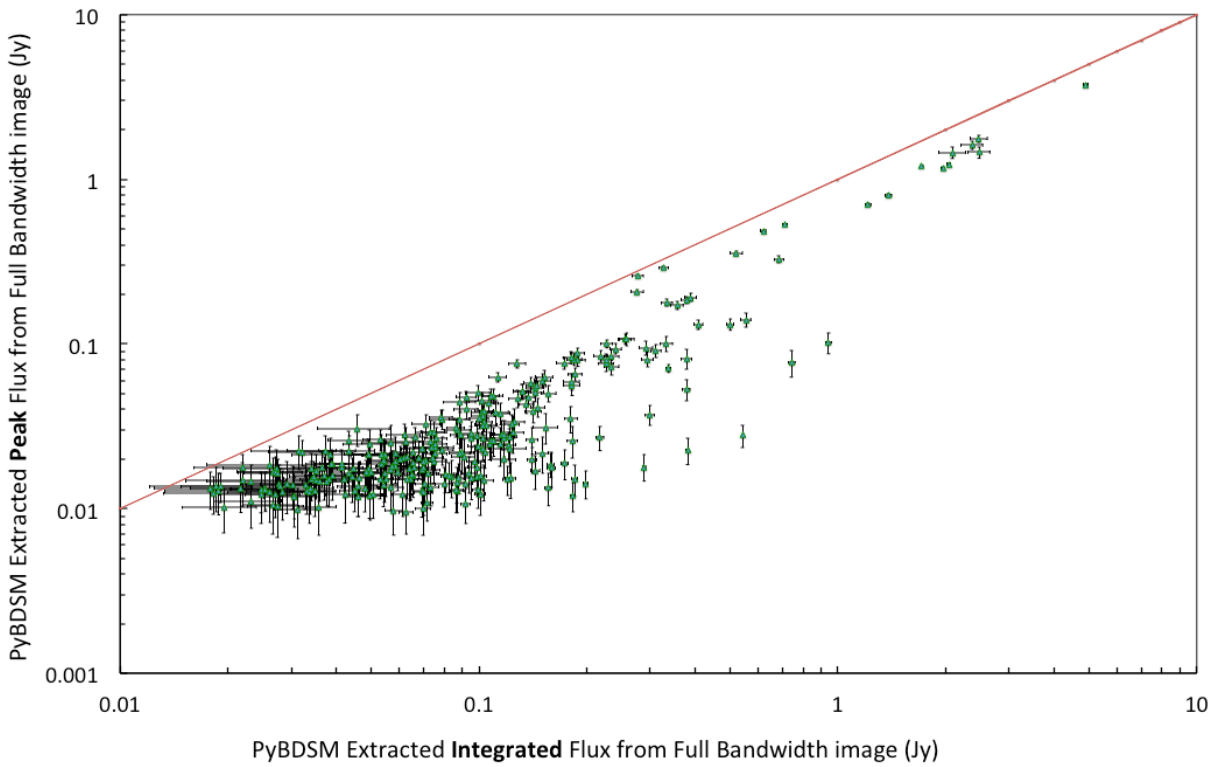

Figure 4.6: A comparison of un-scaled integrated and peak fluxes of our point source catalogue, after editing out the obvious Galactic sources. The red line represents y = x for comparison.

Establishing the global scaling factor

As mentioned, as well as containing the diffuse Galactic star-forming regions of W3/W4/W5 with embedded clusters of YSOs e.g. in the aforementioned W3 region (Figure 1.3) and the obvious SNR 3C 58, the FoV contains mostly discrete *extragalactic* compact sources. The main issue was discerning these from Galactic sources, to leave only the obvious extragalactic point sources from which to obtain the global scaling factor by cross-matching first to the NVSS and then to the to VLSSr. The latter was most suitable for extrapolating the global scaling factor since it is closer to our observed frequency range. Individual scaling factors were established on the beam corrected data at each narrow and full band frequency and Figure 4.7 shows the importance of this, and specifically how the scaling factor is affected by bandwidth of MFS possibly due to spectral turnover (§ 3.4.12).

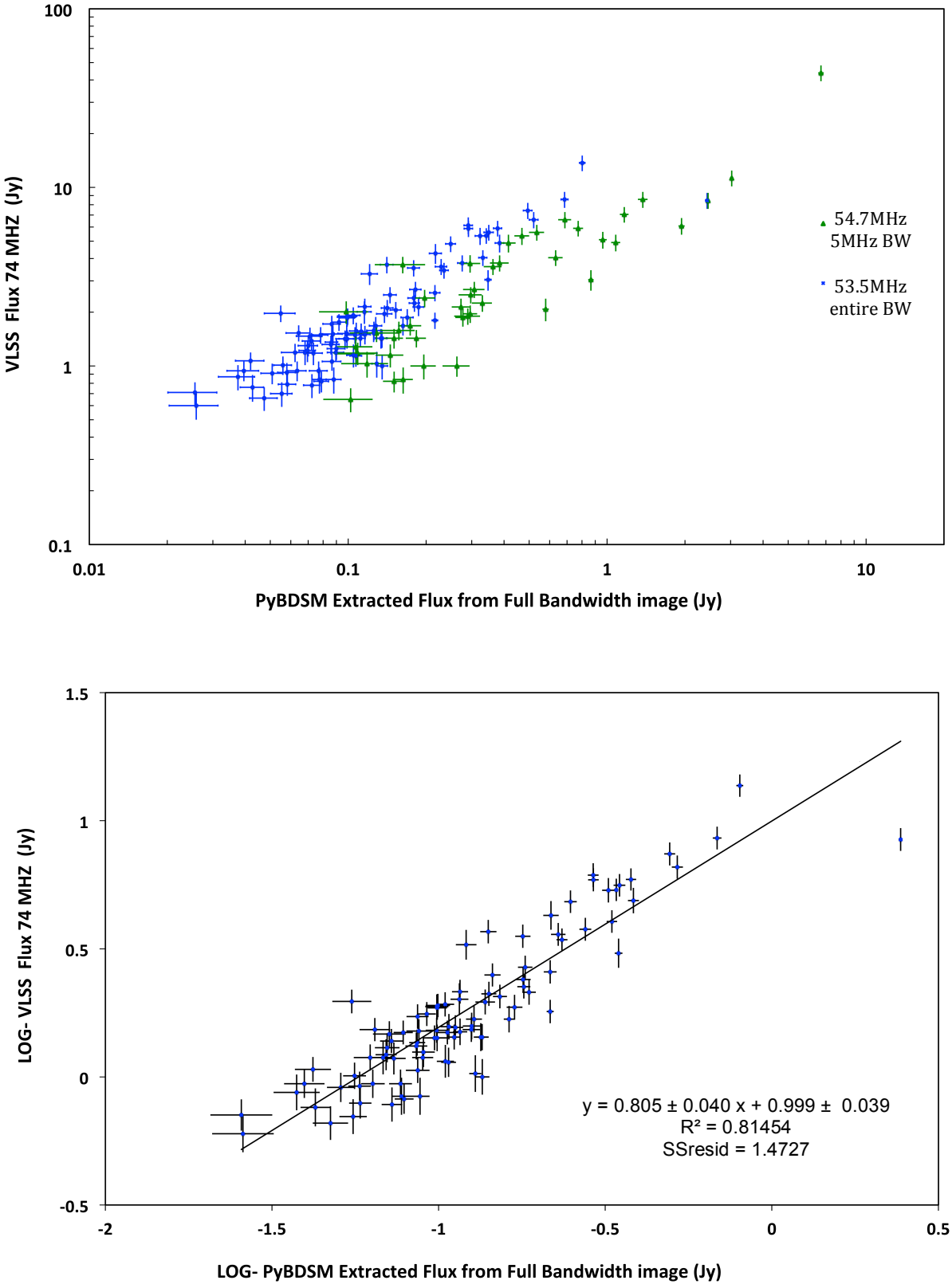

Figure 4.7: The top graph shows how the correlation is affected by wide and narrow MFS (as discussed in § 3.4.12). Hence the *individual* factors were established at each narrow-band frequency as well as the entire bandwidth available. The bottom graph is a log-log plot to establish the global scaling factor for the full bandwidth (bottom graph).

Spectral index correction

The spectral correction was then applied assuming an average spectral index, $\langle\alpha\rangle = -0.8$ (§ 2.3.5) which is also used in the flux correction method by Mauch et al. (2013) with results obtained with the Giant Metrewave Radio Telescope (GMRT). Following from (Eq. 2.48), or $S_v \propto v^{\alpha}$, frequencies which had been globally scaled to the 74 MHz using the VLSSr arriving at fluxes of S_v^{74MHz} were then spectrally corrected to the target frequency, v^{Target} (taken as the central frequency of each narrow band 35.2 MHz, 54.7 MHz and 69.9 MHz and wideband 53.5 MHz) as follows:

$$\langle\alpha\rangle = \frac{\log\left(S_v^{Target} / S_v^{74MHz}\right)}{\log(v^{Target}/74MHz)} = -0.8 \tag{4.1}$$

A final catalogue of 302 real point sources confirmed with matches in pre-existing catalogues was established and are included in csv format in Appendix D as well as 62, 103 and 70 real point sources in separate catalogues for the narrow bands 35.2 MHz, 54.7 MHz and 69.9 MHz respectively. The first 2 columns specify arbitrary point identification numbers from PyBDSM; columns 3-6, give the RA and DECs including the errors; Columns 7-10 give the Total (integrated) flux, Total (integrated) flux error, Peak flux, and Peak flux error. These values have been scaled globally (to match the equivalent at 74 MHz using the scalar given by VLSSr) and spectrally scaled in the way described above.

16.6 % of sources from the wideband catalogue had counterparts at the narrowband 35.2 MHz, and 27.5 % and 17.3 % had counterparts at the 54.7 MHz and 69.9 MHz catalogues respectively. 9.6 % of sources had matches across all 3 narrowband frequencies which was advantageous for providing finer spectral sampling allowing better confirmation of SED classification (§ 4.1.2).

The Radio K-Correction for Galaxies at High Red Shifts

The extragalactic sources observed in our sample, are likely to have different redshifts, $\mathbb{Z}$ with different rest-frame frequencies. To transform from our observed frame to the rest-frame, we must apply a *K-correction,* $K(\mathbb{Z})$ to the measured extragalactic flux (apparent magnitude, $S_{v,obs}$), which allows an accurate measurement of flux in the rest frame of the emitting source (absolute magnitude) by an

according shift in the spectrum. The emitted monochromatic luminosity, $L_{v,em}$ is given as (Bourne et al. 2011):

$$L_{v,em} = 4\pi d_L^2 S_{v,obs} K(\mathbb{Z})[1+\mathbb{Z}]^{-1} \quad (4.2)$$

where d_L is the luminosity distance to the source and $[1+\mathbb{Z}]^{-1}$ is a further bandwidth correction which accounts for the stretching of the spectrum in relation to the bandwidth of the receiver (Bourne et al. 2011). The K–correction to a monochromatic flux with a power law spectrum (Eq. 2.48) is given by $K(\mathbb{Z}) = [1+\mathbb{Z}]^{-\alpha}$ which is independent of the filter transmission function (see Bourne et al. 2011). Hence (Eq. 4.2) assumes that we have knowledge of the spectral index, α of the source and the shape of its spectrum within our observed bandwidth, which is precisely what we are trying to determine. Therefore for the extragalactic sources of our field, it has not been possible to apply the K-correction.

4.1.2 SED Analysis

The LOFAR catalogue was then cross-matched primarily to the NVSS catalogue in TOPCAT (using a search radius of 20″). To ensure that our sample was not biased against sources that did not have counterparts in the NVSS (88 % did), the final catalogue was also cross-matched with the VLSSr and WENSS catalogues which gave 73 % and 87 % of matches respectively. The pre-existing catalogue source identifier was then used in SPECFINDv2.0 which is a data-mining tool for pre-existing radio catalogues and enables cross-identification and data homogenisation of radio continuum spectra across 20 of the largest radio source catalogues contained within the VizieR database (Ochsenbein et al. 2000) of the Centre de Données astronomiques de Strasbourg (Vollmer et al. 2010).

Astrometric accuracy of source absolute and relative positions depends on phase (ionospheric) stability which for LOFAR has been shown to be problematic in § 3.4.13. The position of sources extracted from the fully calibrated and mosaicked image were compared with the NVSS and VLSSr (Figure 4.8) which have established positional accuracies of $< 1''$ (Condon et al. 1998) and $3 - 3.4''$ (Lane et al. 2012) for the brightest sources respectively.

The scatter in the measured shifted positions also reflects the accuracy of calibration, with fainter

sources < 15 σ on average having the highest degree of scatter from the zero offset. Van Weeren et al. (2014) also mentions how positional accuracy can also be dependent upon the level of local noise which is position dependent and affects Gaussian fitting by PyBDSM, or can be a result of the difference in source structure between higher frequency catalogues and LOFAR frequencies related to spectral index variations across the sources and/or differences in resolution. The mean offset is *close* to zero in both the NVSS and VLSSr comparisons of Figure 4.8 which account for the *cosec delta* factor (with actual mean offset values of ΔRA ~ 0.07″, ΔDec ~ 0.06″ and ΔRA~ 0.14″, ΔDec ~ 0.09″ respectively), which indicates no additional position offsets have appeared in the final mosaicking and cataloguing process.

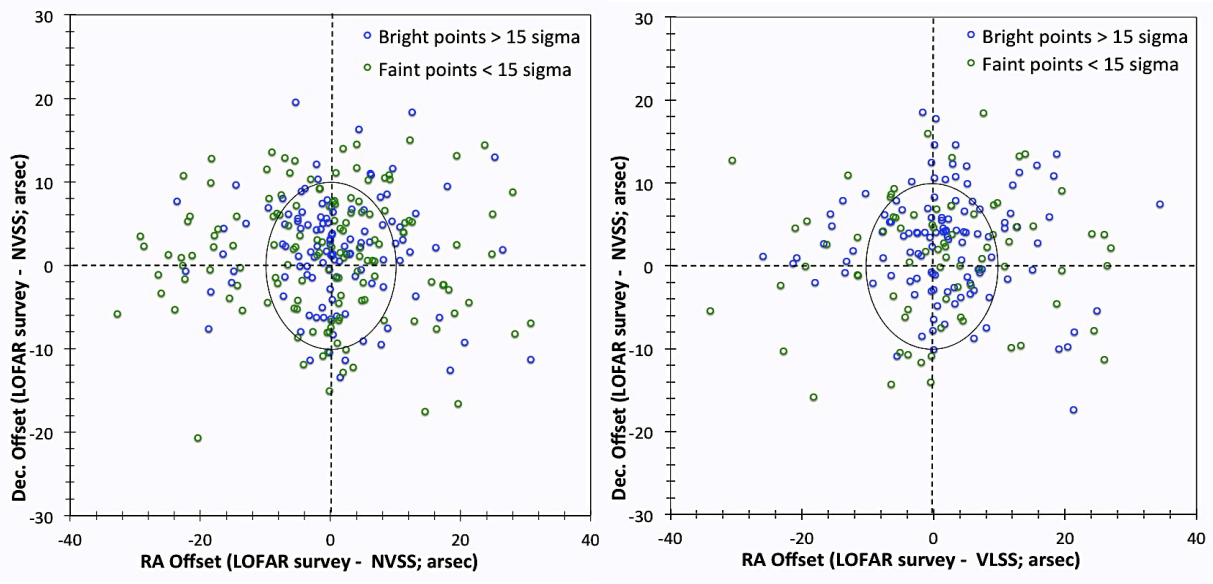

Figure 4.8: The positional offset error between LOFAR fluxes and the NVSS (left) and VLSSr (right). The oval represents the 10″ error in ΔRA and ΔDec.

The cross-identification of radio sources observed with different radio instruments operating in widely different frequency bands can be a challenge due to variations in sensitivity and resolution in addition to non-simultaneous observations of variable sources. SPECFINDv2.0 (Vollmer et al. 2010) is advantageous and provides the most reliable radio continuum catalogue to date because it takes into account the angular resolution of the individual observations, the source size and the flux densities observed at a given frequency allowing uniformisation and homogenisation of heterogeneous catalogue data. It is a successor of the SPECFIND v1.0 tool presented by Vollmer et al. (2005). Please refer to

Vollmer et al. (2010) for a table which summarises the surveys used in SPECFINDv2.0 for our analysis spanning from the 8C catalogue at 38 MHz to the Green Bank GB6 survey at 4850 MHz. The SPECFINDv2.0 algorithm also ensures that a radio source cannot be assigned to more than one physical object and assumes the power-law shape of radio spectra which can have a break if more than two independent frequency points contribute to each of two spectral slopes (Vollmer et al. 2010).

The astrometry has to match across instruments in order to provide an accurate radio continuum catalogue. SPECFINDv2.0 cross-correlates the large radio source catalogues with other published radio source catalogues of higher resolution at different frequencies to determine the positional accuracy, these being the TeXas Survey of discrete radio sources (TXS, Douglas et al. 1996) and the Green Bank 4850 MHz survey (GB6, Gregory et al. 1996) Vollmer et al. (2005).

In order to provide a common absolute flux scaling, SPECFINDv2.0 revises the points of catalogues < 325 MHz onto the Roger et al. (1973; RCB) scale. Whilst this affects WENSS fluxes, this does not affect the VLSSr fluxes (and consequently the LOFAR fluxes to which they are scaled), which are already on the Roger et al. (1973) scale based on source models presented by Scaife & Heald (2012) (Lane et al. 2012). Scaife & Heald (2012) list correction factors for catalogues such as WENSS (which is already scaled to Baars et al. 1977) to normalise them to the Roger et al. (1973; RCB) scale as a pre-requisite for spectral fitting. Like the VLSSr (and its predecessor, the VLSS; Cohen et al. 2007), the 6C (Baldwin et al. 1985), 8C (Hales et al. 1995) and MIYUN (Zhang et al. 1997) surveys are also calibrated on the RCB scale in their original form (Scaife & Heald 2012) and are utilised in SPECFINDv2.0.

A script was created with IDL to fit the Curvature Equation to the spectra in order to give the spectral indices of individual sources, and estimate the degree of turnover. A spectral model of the form (Scaife & Heald 2012 and Pizzo et al. 2014):

$$\log_{10} S_\nu = \log_{10}(S_0) + c_1 \log_{10}\left(\frac{\nu}{\nu_0}\right) + c_2\left[\log_{10}\left(\frac{\nu}{\nu_0}\right)\right]^2 + \ldots + c_n\left[\log_{10}\left(\frac{\nu}{\nu_0}\right)\right]^n \qquad (4.3)$$

was used where v_0 is the reference frequency of the field, c_1 is the spectral index, c_2 is the curvature, and $c_3, \ldots, c_n$ are higher order curvature terms. Polynomials were generated and superimposed to data points, taking account of the 1st, 2nd and 3rd order curvature terms of the curvature equation alongside their chi-squared, χ^2 statistics. The fits of each polynomial to the data points were judged by eye in each case. In some cases, a linear fit was best, in others the 2nd polynomial was more appropriate and in a handful of cases, the 3rd polynomials were best (see Figure 4.9). The χ^2 coefficients also gave a statistical objective way of judging the goodness of each 1D polynomial fit to the data directly and were a quantitative way of determining a believable turnover. This value invariably improved with more parameters fitted, and so at least a 10 % improvement in the χ^2 value between each order of polynomial model or more, generally reflected a good degree of improvement in model fit (Figure 4.9).

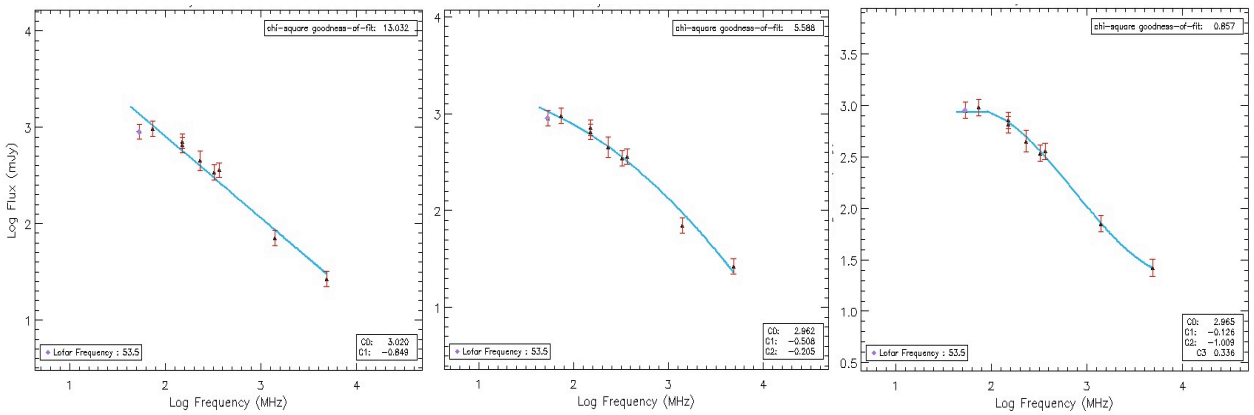

Figure 4.9: Source (identified as NVSS J022326+642303), which demonstrates the improvement in the fit of the polynomial model from linear or 1st order (left), 2nd order (centre) and 3rd order (right). Quantitatively χ^2 improved by ~57 % from 1st → 2nd order and ~84% from 2nd to 3rd order which confirms the improvement we see by eye.

Classification of Extragalactic Point Sources

Once the polynomial fit (to the 1st, 2nd or 3rd degree) was determined, each SED was placed into a category:

1) SEDs where the LOFAR fluxes poorly fit the trend (Figure 4.10). This was typically for the lower flux sources < 50 mJy (~ 10 σ) at LOFAR radio frequencies, where the S/N is poorer. Since the reliability of these SED coefficients were low, they were removed from our sample.

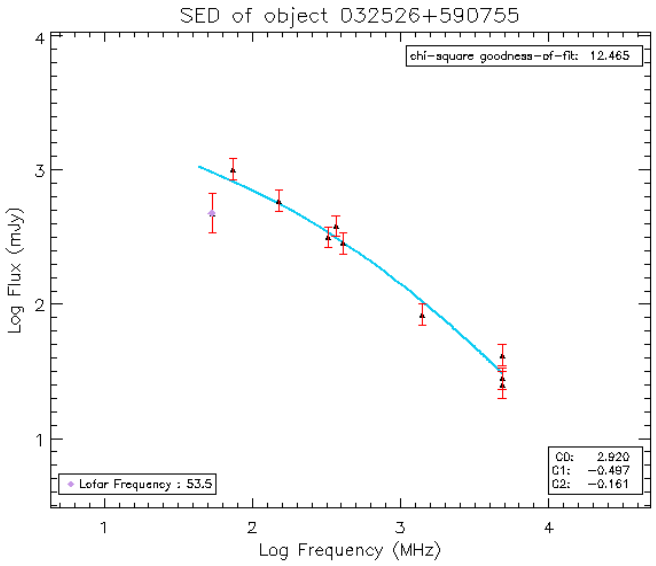

Figure 4.10: A poor fit to the SED trend by the LOFAR data point. It was found that this was typical for LOFAR fluxes < 50 mJy.

2) Complex multi-component sources which were either (i) extended (ii) complex or (iii) physical double sources (i.e. the double radio lobes of an AGN, which often differ in flux density, size, and spectrum) with sizes below confusion limits of the majority of surveys used in the SED Vollmer et al. 2010). Vollmer et al. (2005) caution against 'a blind use' of the SPECFINDv1.0 catalogue for this reason, where more than one source is given at observations of higher resolution which can resolve two sources where previous surveys had only detected one (Figure 4.11).

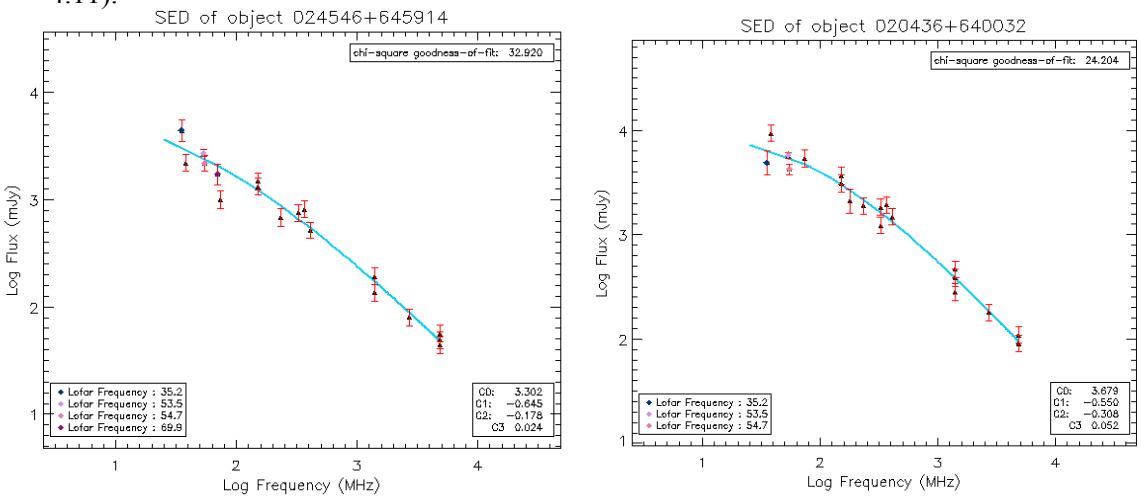

Figure 4.11: Examples of possible physical double sources where higher resolution surveys like the NVSS can resolve double components. There is a greater spread in the data of such SEDs.

3) Possible Variability: We see possible variability at radio frequencies < 100 MHz for ~ 5.8 % of sources as demonstrated in Figures 4.12 and 4.13 and where there is a discrepancy between the 8C fluxes at (Hales et al. 1995) and our LOFAR fluxes (taken in 2011). This *could* imply a possible variability at low radio frequencies over ~ 20 year time interval.

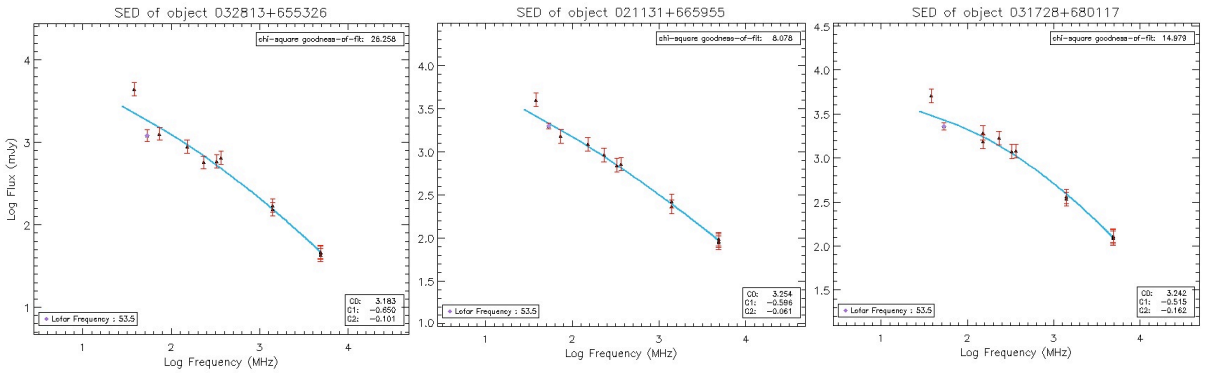

Figure 4.12: sources of possible variability at low radio frequencies. In these cases the LOFAR fluxes confirm the SED trend we see at higher radio frequencies. The 8C flux at 38 MHz seems to be an outlier. In particular, the SED on the far left has obvious flattening which our LOFAR results confirm.

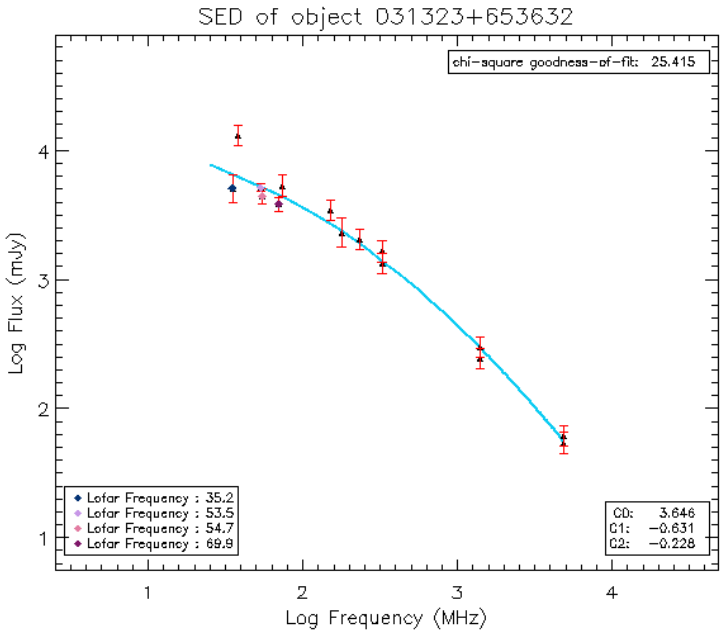

Figure 4.13: An example of a source where LOFAR narrow bandwidth frequency observations give a finer spectral resolution in addition to the full bandwidth to confirm the flattening trend that we see starting at higher frequencies.

Tingay & de Kool (2003) give a possible explanation for low-frequency flux variability of AGN due to the structure of an external free-free absorbing inhomogeneous screen becoming variable if it mechanically interacts with the radio jet that powers the source. The free-free opacity of large clouds which obscure the source can increase when dispersed into smaller clouds, increasing the percentage of the synchrotron source obscured perpendicular to the LOS

(Tingay & de Kool 2003). The resultant shocks may also produce energetic photons that ionise the clouds increasing their free-free opacity further (Bicknell et al. 1997). This would explain the decreasing flux-density confirmed with LOFAR in Figures 4.12 and 4.13. The contrary is true in cases of flux at low radio frequency flux increasing over time.

Tingay & de Kool (2003) also mention variability in dense plasma within the source (which can influence intrinsic or extrinsic FFA; see § 2.3.9) and variability in intrinsic SSA, the latter of which can occur for a number of reasons. The optically thin part of the spectrum is determined by the relativistic electron distribution only (§ 2.3.5) determined by particle injection and energy loss, predominantly by synchrotron cooling. The optically thick part is determined by a combination of the geometry of the source and the shape of the relativistic electron distribution (§ 2.3.9). Tingay & de Kool (2003) conclude that synchrotron cooling would be applicable in any variability in the gigahertz-peaked spectrum (GPS) in the AGN of the nearby radio galaxy PKS 1718-649 observed over a timescale of 2 years. Finally we cannot rule out the fact that the discrepancy in flux between that given by LOFAR and the 8C catalogue taken by the CLFST at 38 MHz is due to an instrumental improvement in sensitivity which had been anticipated in § 1.6. Our mosaicked full bandwidth images reached an RMS of ~ 5 mJy/beam which is an improvement in the sensitivity levels reported for the 8C which has a typical limiting flux density of about 1 Jy/beam (Cohen et al. 2007). Therefore we have reason to trust the reliability of LOFAR fluxes over those of the 8C.

4) Well-determined polynomials: The vast proportion (over ~ 50%) of our LOFAR fluxes supported well the trends determined by the complimentary catalogues of SPECFINDV2.0 (for example Figure 4.14). A selection of these well-determined fits are included in Appendix B.

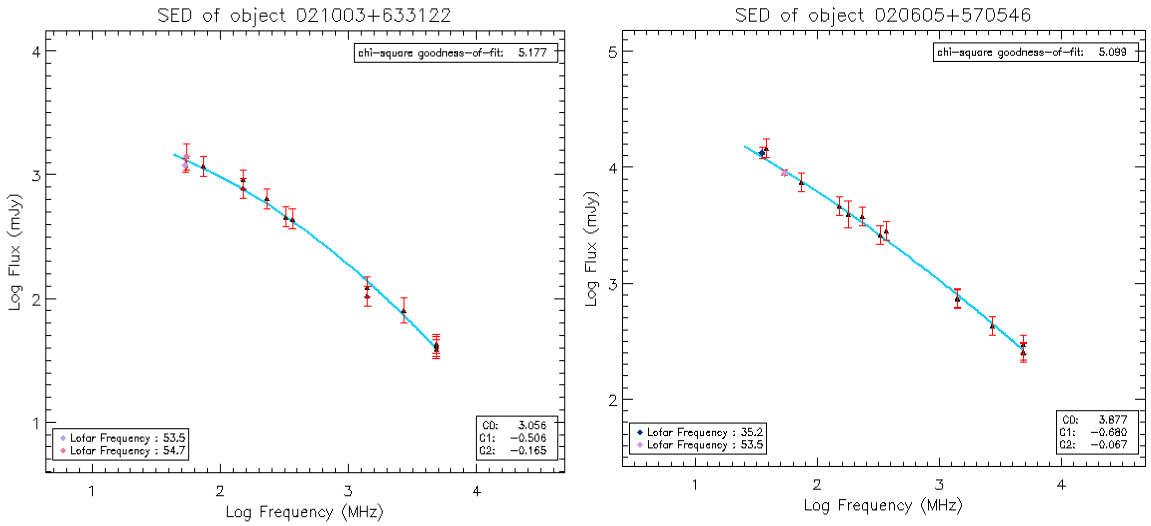

Figure 4.14: In the case of the source identified as NVSS J021003+633122, the narrow band flux centred at 54.7 MHz is likely to be slightly more accurate than the broadband flux centred at 53.5 MHz due to MFS bandwidth effects (see § 3.4.12 & Figure 4.7).

A percentage of the resulting spectra that could be fitted with the simple linear polynomial and are referred to as *Class S* by Verschuur & Kellerman (1974). Sources with SEDs that have a negative second derivatives such that the spectrum is steeper at short wavelengths are classified as *Class C*- spectra (Verschuur & Kellerman 1974). Almost all of our sources were either Class S or C- spectra.

For completion, we include the result from a source displaying increased (positive) curvature i.e. the SED rises more steeply at lower frequencies and are classified as *Class* C_I+ spectra by Verschuur & Kellerman (1974). We omit this *single* source from our analysis below; such spectra are typically found in sources located in rich clusters of galaxies (Verschuur & Kellerman 1974). Van Weeren et al. (2012) investigate the cluster Abell 2256 at LOFAR frequencies ~ 63 MHz, within which they find low-frequency spectral steepening of a source between 63 – 153 MHz which could possibly be explained by re-acceleration of the emitting particles by some mechanism which needs further investigation. Whilst we can start to see some steepening for our source (Figure 4.15) from 151 MHz (6C survey; Baldwin et al. 1985 and Hales et al. 1993), additional flux density measurements are needed to better determine and confirm this low-frequency trend.

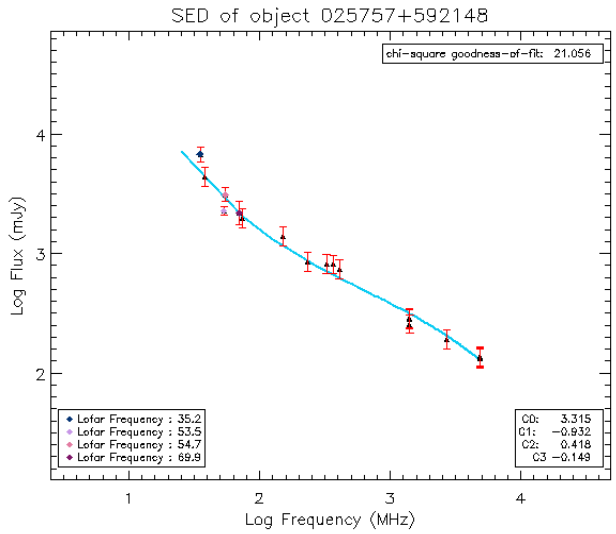

Figure 4.15: A SED with positive curvature towards lower frequencies and is classified as C_I+ spectra by Verschuur & Kellerman (1974).

Overall, for our analysis, as mentioned we removed all faint sources (category 1), due to their high uncertainty. We were cautious to include results from category 2 and 3 in addition to the well-determined polynomials of category 4; these sources were included if the discrepancy between the LOFAR and 3C flux or the spread of duplicate fluxes of complex sources was not significant enough to affect the overall polynomial trend.

Constraints on the Degree of Spectral Turnover

Rafferty et al. (2013) quantify the degree of flattening in their spectra by calculating the flux decrement between the flux measured at 60 MHz or 74 MHz and the flux extrapolated from a simple power-law fit. In their case, negative values of this decrement imply a flattening at low frequencies. For our data, in all cases where we trusted the polynomial fit (either simple linear, or 2nd or 3rd order), the measure of curvature was taken as the 2nd order curvature term, c_2 of (Eq. 4.3).

In Figure 4.16 we show the cumulative percentage of sources with decreasing level of curvature. The more negative the number, the higher the measure of curvature. Some examples of strong and moderate curvature are shown in Figure 4.17.

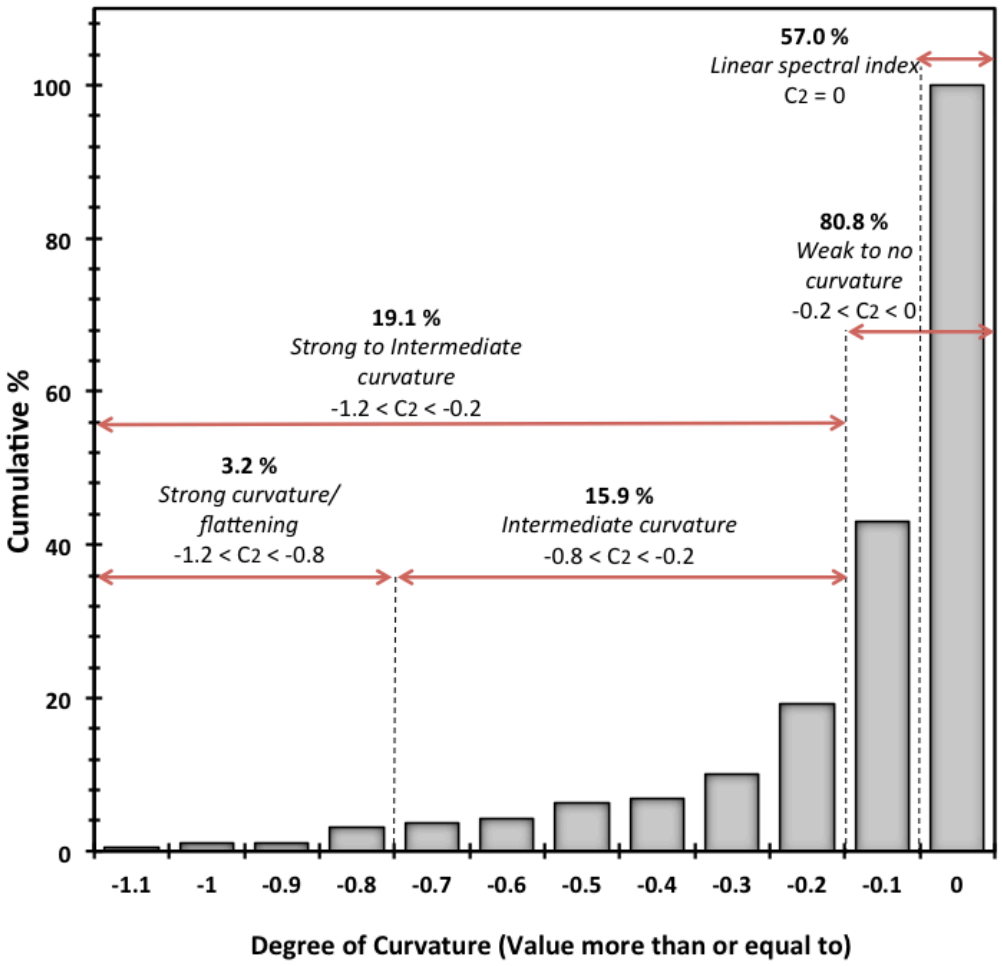

Figure 4.16: The cumulative percentage of sources with decreasing level of curvature (between 35/38 MHz and 325 MHz).

We find ~ 3.2 % of sources show evidence for a turnover or strong flattening in their SEDs down to at least ~ 53.5 MHz (Figure 4.17). This is consistent with Rafferty et al. (2013) who concluded that only a minority of their starburst galaxy sample show the same characteristics and specifically, they find ~ 20 % of their sample show some evidence of curvature in their spectra down to at least ~ 60 MHz. Our observations are consistent and we found that ~ 19.1 % of our sources show strong to immediate curvature, where -1.2 < c_2 < -0.2 (Figure 4.17). Rafferty et al. (2013) also found that the fraction of curvature was *not dependent* on the source total IR luminosity; we did not carry out IR selection constraints on our flux-limited sample to investigate this due to time limitations, but this could be a possibility for future work. Specifically we could separate sources cross-matched with the mid-IR sources of NASA's Wide-field Infrared Survey Explorer (WISE; Wright et al. 2010) in the method described by Rafferty et al. (2013). Mid-IR wavelengths are reliable indicators of IR-luminous

AGN activity (Donley et al. 2012) and a correlation between the 10 μm mid-IR and 1415 MHz radio luminosities of: (1) the *nuclei* of Seyfert galaxies was discovered by van der Kruit (1971) and (2) the *nuclei* of normal spiral galaxies (van der Kruit 1973). The WISE catalogue contains a high spatial density of mid-IR sources which could potentially give rise to a large percentage of false cross-matches (we observed this with an initial search using TOPCAT and a small search radius of only 5″). Hence the Sutherland & Sauders (1992) likelihood ratio cross matching technique would be advised in future work, alongside using the AGN selection criteria of Jarrett et al. (2011); this is incorporated into the meticulous selection technique of Rafferty et al. (2013).

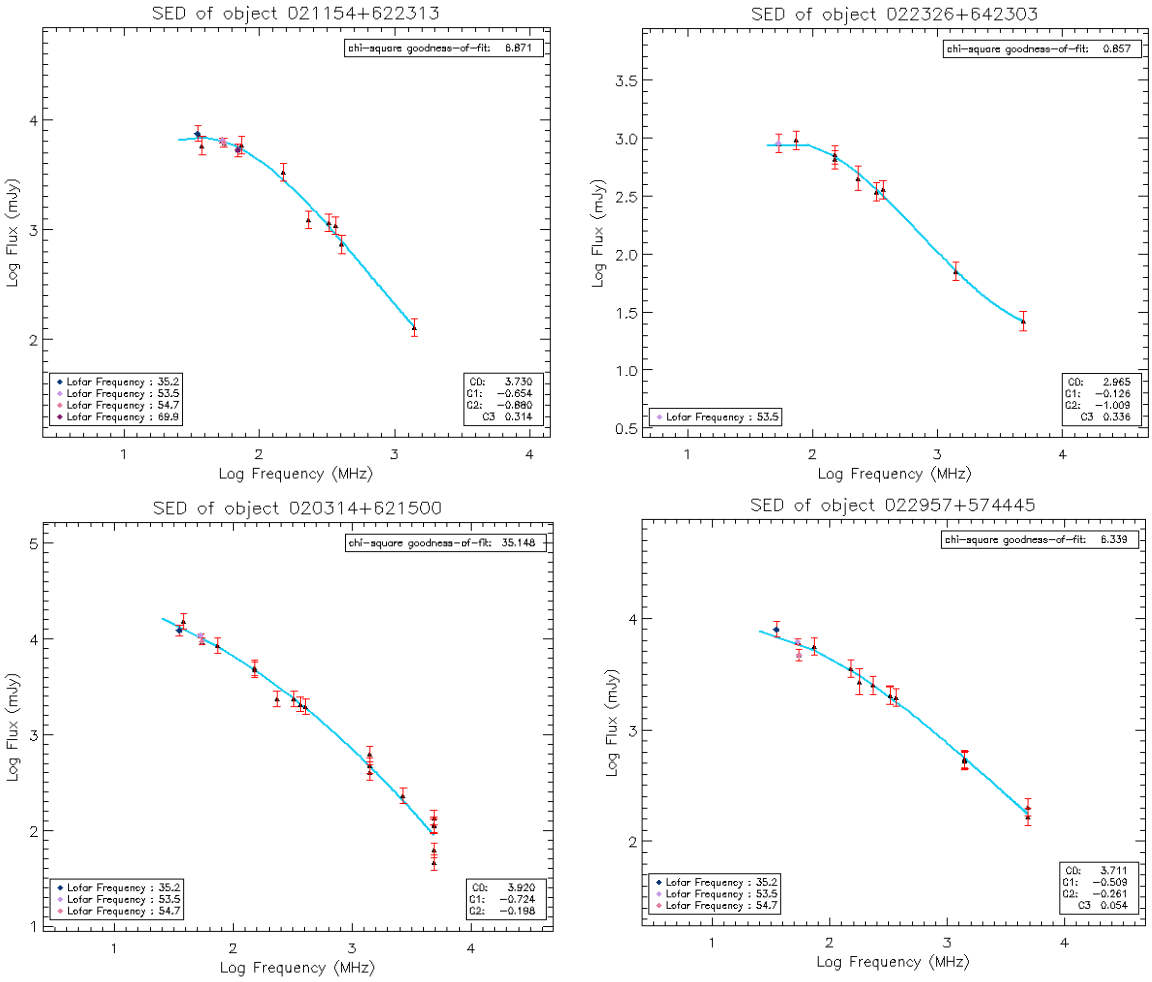

Figure 4.17: Examples of sources with turnover. We take a curvature of -0.8 or less as an indication of strong curvature and flattening at low radio frequencies (as represented by the top 2 sources). We take values of curvature between -0.2 - -0.7 as moderate curvature.

This theoretically would leave the starburst galaxies whose star-forming properties we would hope to probe in the future. Condon (1992) details reasons for *far*-IR and radio correlations of these normal disk-dominated galaxies and that far-IR arises from thermal re-radiation from dusty H II regions in starburst galaxies, while radio luminosities arise primarily from synchrotron from relativistic electrons accelerated in SNRs from the *same* population of massive stars that heat and ionise the H II regions (Harwit & Pacini 1975).

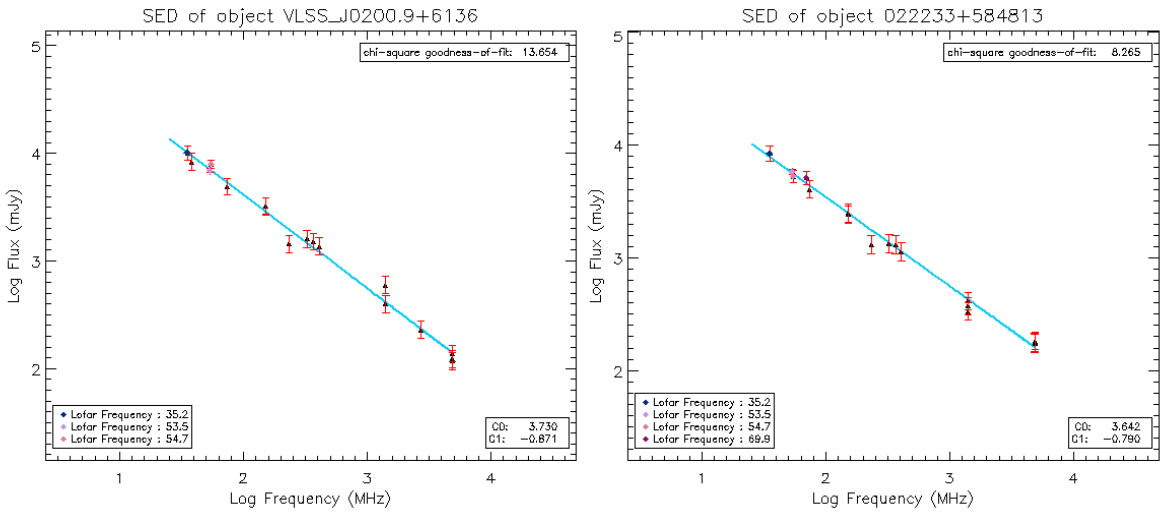

Figure 4.18: sources that are optically thin at all plotted frequencies

Rafferty et al. (2013) also found ~ 60–70 %, of sources had little to no curvature and we find this a little higher at ~ 80.1 % of our sample. We find that ~ 57.0 % of sources show no curvature at all (i.e. optically thin as shown in Figure 4.18). These sources have straight Class S spectra with indices ~ -0.8 which is typical for star-forming galaxies (Condon 1992) although steeper indices can occur in the AGN-dominated sources (Ibar et al. 2009). Nearly all Class S sources are the range $-1.3 < \alpha < -0.6$ (Verschuur & Kellerman 1974). The histogram of Figure 4.19 shows the distribution of established spectral indices given by the curvature term c_1 (Eq. 4.3) over the entire spectrum from 35/38 – 4850 MHz. The distribution median peaks at $\alpha \approx$ -0.75 suggesting that the majority of our sources are starburst (radio luminous) galaxies (Condon 1992) dominated by *optically thin* synchrotron emission.

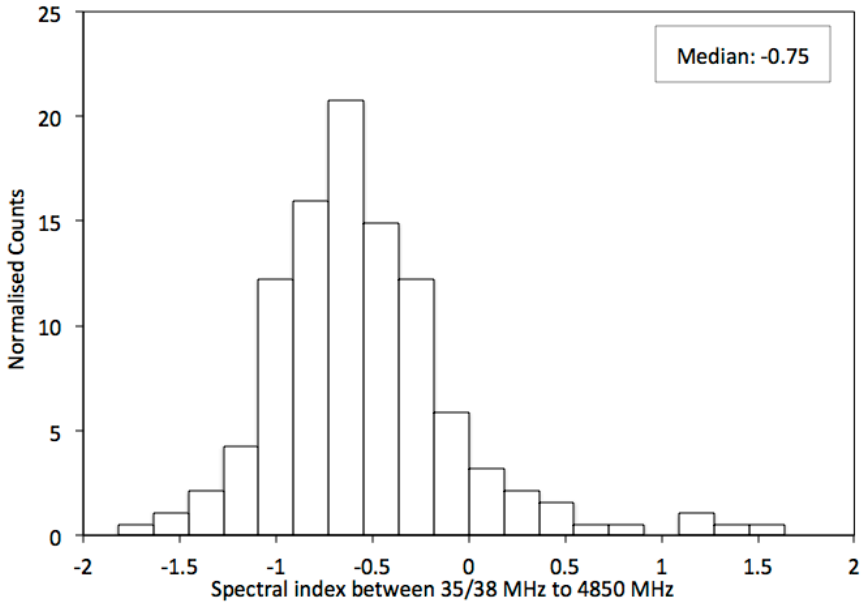

Figure 4.19: Spectral index calculated between 35/38 MHz - 4850 MHz.for all sources. There is a wide distribution of indices about a median of ~ -0.75. The steepest value of the index observed for these sources is ~ -1.8. Very few sources, however, have indices steeper than ~ -1.3.

Figure 4.20 gives the distribution of spectral indices at the upper and lower frequency range. For Class S sources with simple power law spectra, the spectral index is trivial (the gradient of the linear polynomial). For 2nd and 3rd order polynomials, the spectral index may be defined at any frequency as the tangent to the curve on the $\log S_\nu - \log \nu$ plot (Verschuur & Kellermann 1974). The histograms show a shift towards positive spectral indices with decreasing frequency range, caused by the flattening of the spectrum at low radio frequencies. According to Verschuur & Kellermann (1974) the typical region of curvature for a Class C- source extends over approximately a decade of wavelength whilst for wavelengths considerably removed from the maximum curvature there are two well-defined power laws with indices differing by ~ 0.5 (Verschuur & Kellermann 1974).

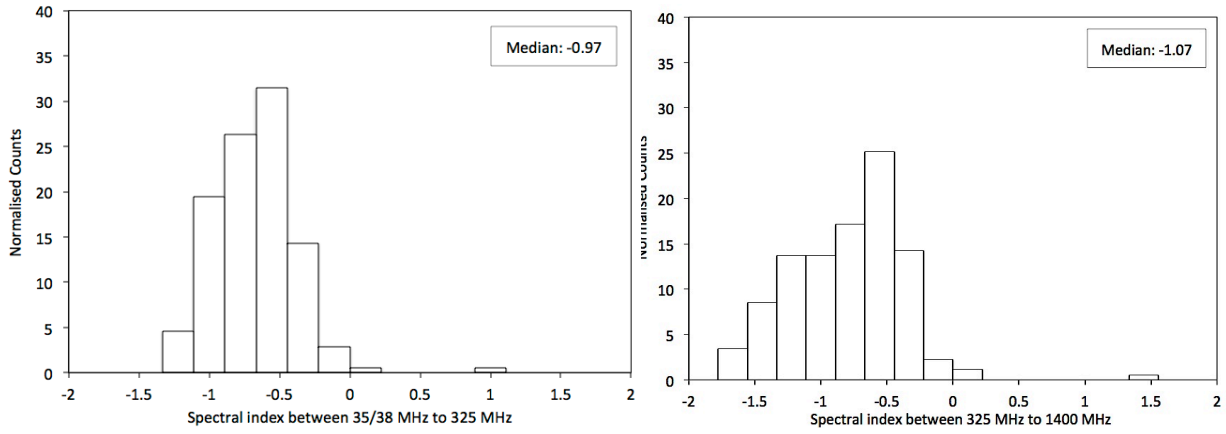

Figure 4.20: Spectral index between 35/38 - 325 MHz (left) and 35/38 - 1400 MHz (right). These are average values for a straight-line fit. Where the spectra were fit with a curve, a constraint was set and the value was taken as the tangent of the curve in the middle of the frequency range.

Whilst Tingay & de Kool (2003) conclude that SSA is the significant cause of turnover in their observed Gigahertz-Peaked-Spectrum (GPS) source (after exploring FFA models), our observed turnovers occur between 35/38 – 300 MHz and FFA processes (by ionised gas either intrinsic or extrinsic to the source) are more likely to modify low-energy photons (observed at lower radio frequencies) of starburst spectra (assuming the source size does not change with frequency) (Rafferty et al. 2013 and Clemens et al. 2010). In essence, the brightness temperatures of our sources are not high enough for SSA to be important (Clemens et al. 2010; see § 2.3.9 for the theory and properties of SSA). It was important to rule out any possible correspondence of the degree of SED curvature to Galactic foreground H I column density along the LOS to the source. The composite Neutral H I (N_{HI}) column density map (units of atoms cm^{-2}) of Dickey & Lockman (1990) from the Leiden/Dwingeloo Galactic H I survey was used which measured the 21.11 cm (1420 MHz) line profile from neutral hydrogen atoms in H I regions giving an estimation of the distribution of this phase of the interstellar gas.

Figure 4.21 shows that there is no correlation between intervening LOS H I column density and turnover of our sources, revealing there is no evidence that the intervening cold gas material of *Galactic* H I is responsible for extrinsic FFA of synchrotron (a possibility of synchrotron energy loss at

low radio frequencies as discussed in § 2.3.9). It is likely instead that FFA, possibly from H I regions directly surrounding the AGN of the extragalactic sources, is responsible.

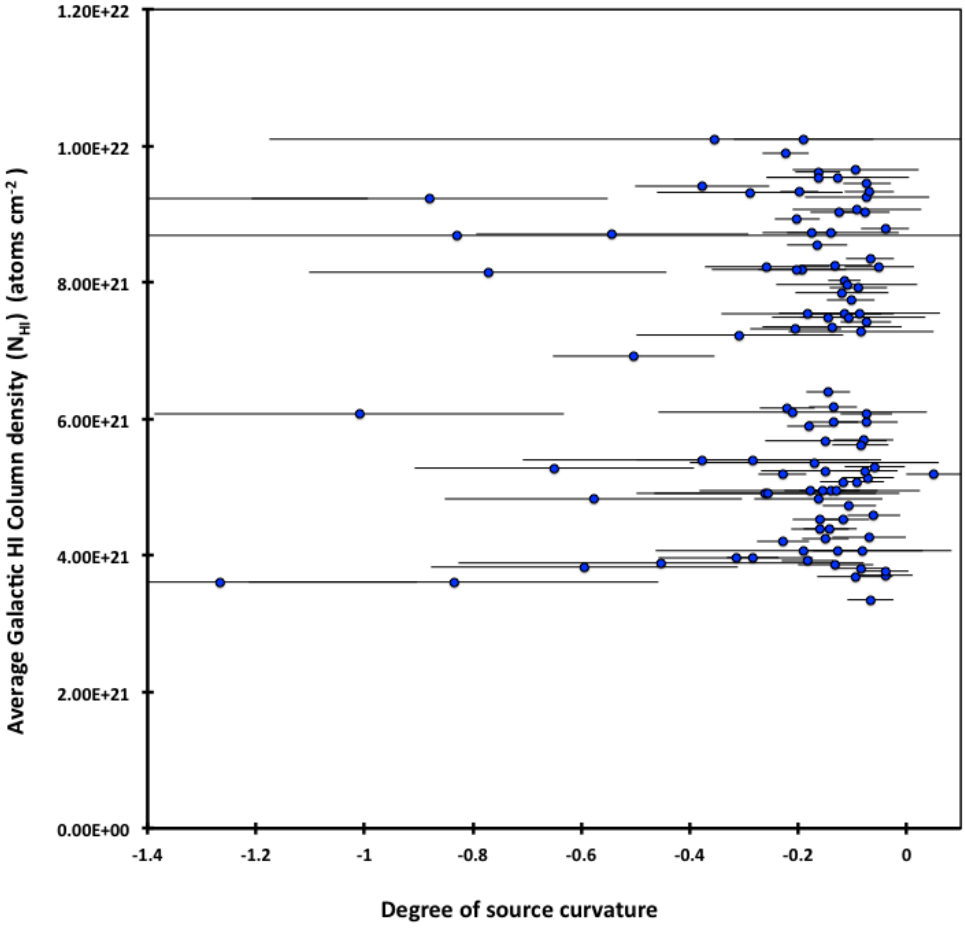

Figure 4.21: Relationship of the degree of individual source curvature at low frequencies vs. intervening average Galactic H I column density along LOS.

4.1.3. Summary & Future work

Examining the degree to which absorption at low radio frequencies is present is the key to understanding starburst radio-luminous galaxies (Rafferty et al. 2013) and LOFAR has provided useful data below ~ 100 MHz to better establish and constrain the SEDs of these sources. We observed strong and moderate SED flattening (attributed to free-free absorption processes at the source) for ~ 3.2 % and ~ 19.1 % of sources respectively which is consistent with Rafferty et al. (2013).

We do not see a correlation with Galactic H I column density along the LOS which rules out extrinsic FFA effects within our own Milky Way. However, FFA effects could be occurring within the

extragalactic source itself. For example Israel & Mahoney (1990) found evidence for flattening of spectra in a fraction of their sample of normal spiral galaxies at 57.5 MHz. They found that the degree of flattening correlated with the *galaxy axial ratio*, which affected FFA of non-thermal synchrotron emission along the LOS, which increased with the increasing tilt of disk-dominated spiral galaxies.

Clemens et al. (2010) state that the shape of the *low-frequency* spectrum depends, almost entirely on the quantity and distribution of ionised gas with respect to the source of synchrotron emission. Following from (Eq. 2.23) and (Eq. 2.25), the optical depth of an absorbing medium is (Clemens et al. (2010):

$$\tau_v(s) \propto N_e^2 \ell v^{-2.1} \tag{4.4}$$

where N_e is the electron density, v is the frequency and ℓ is the path length along the LOS; turnover in radio spectra occurs at $\tau_v = 1$. Israel & Mahoney (1990) argue that the FFA effects cannot be caused by discrete classical H II regions but rather by a widespread clumpy low-density medium, with a small filling factor. It would be interesting to detail whether our sources have a high axial ratios and whether this corresponds with the degree of curvature we observe.

Also, as mentioned, we did not separate out luminous mid-IR sources (possible sources of AGN) using counterparts in the WISE catalogue using the meticulous technique of Rafferty et al. (2013), which could possibly leave only a sample of starburst galaxies. We could further our understanding of the *evolution* of starburst radio-luminous galaxies by investigating possible far-IR-luminosity correlation of the resultant sample in the future to deduce the area over which star formation occurs and see how this relates to the rate of supernova (a possible source of the synchrotron) (Condon 1992). The parent population (which we have analysed) contains possible AGN sources of synchrotron which makes constraining the evolution of starbursts difficult at this stage.

4.2 Diffuse Maps

Aims & Strategy

Limiting the maximum baseline in AWimager as described in § 3.4.9 was not effective in bringing all images to the same resolution. Therefore the 54.7 MHz and 69.9 MHz as well as the full bandwidth images were convolved to the same resolution as that of the lowest frequency at 35.2 MHz using the *Imsmooth* function in CASA allowing direct comparisons to be made e.g. Figure 4.23. The resolution of the images (major and minor axis and position angle) were checked across all frequencies using PyBDSM (§ 4.2.1) on 10 of the brightest sources along with beam information contained within the image header. We then attempted to correct the absolute flux using scaling factors determined in § 4.2.1 with the CASA function *Immath*. However, these were derived from point sources images and were not applicable to the diffuse images because the fluxes in both were slightly different, possibly due to using differing imaging parameters which may have impacted the flux distribution (§ 3.4.9). Therefore to be cautious, we used un-scaled diffuse images since we are interested in the *relative* flux modification between frequencies; as long as the relative flux scale is consistent across the bandwidth, it is possible to derive spectral index maps. Global scaling factors could be derived in the future from extracted fluxes using Gaussians fitted to discrete sources in the diffuse images; a globally scaled map would be important to compare the *absolute* intensity of diffuse emission with WENSS etc. Finally, spectral index maps were calculated by taking the ratio of the logarithm of the fluxes and frequencies of the 2 LOFAR (beam-matched) image inputs using the SPIX mode in Immath.

4.1.1. W3

W3 is contrasted across all 3 frequencies in Figure 4.23 after scaling and smoothing to the same resolution. Different features become more prominent at each frequency and it is clear that at 35.2 MHz, the relative intensity decreases possibly due to *some* contribution from free-free self-absorption effects (§ 2.2.4). This is what we would expect for a H II region at such low radio frequencies although we do not see complete self-absorption which suggests we have not yet reached the critical

turnover frequency and there also may possibly be foreground Galactic synchrotron emission which has not been subtracted since we do not have *accurate* estimates at these low radio frequencies (§3.3.1).

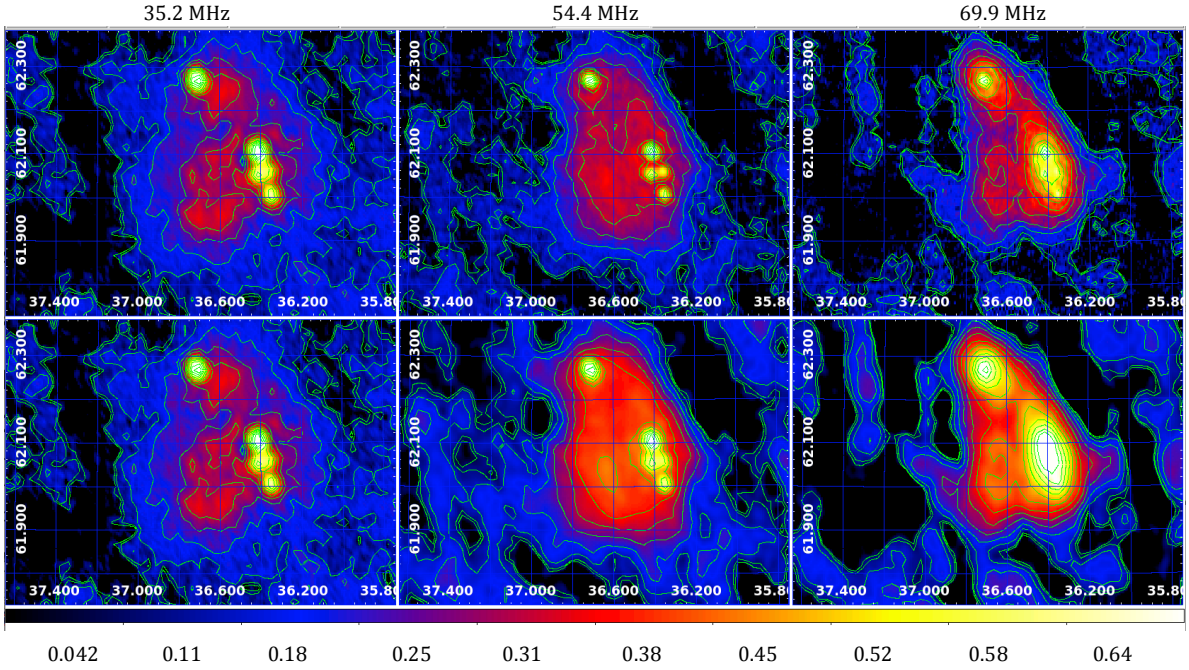

Figure 4.23: W3 maps at 35.2 MHz, 54.4 MHz and 69.9 MHz from right to left. The angular resolution at 35.2 MHz, 54.4 MHz and 69.9 MHz (major x minor axis) is 130″ x 110″, 96″ x 93″ and 95″ x 83″ respectively. The bottom row displays the same data convolved to a common angular resolution of 130″ x 110″ (PA = 9◦). Map units are in Jy/beam. Contours are plotted from -0.025 to 0.613 Jy/beam in 14 linear levels. The same intensity scale is used such that the intense emission from W3 is saturated in the display at 69.9 MHz.

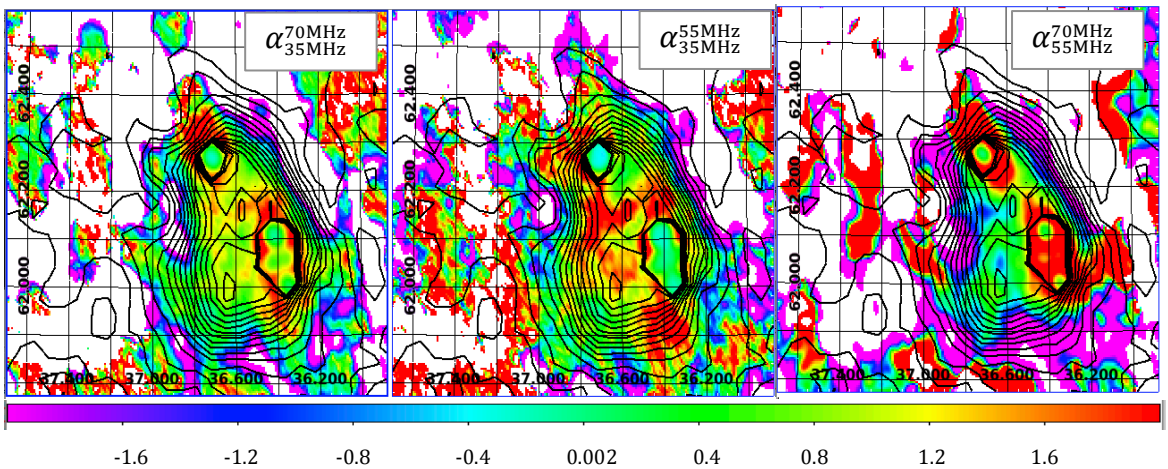

Figure 4.24: Beam matched observations of Figure 4.2 used to calculate spectral index maps. The contours indicate the full bandwidth radio emission centred at 53.5 MHz (beam smoothed to that at 35.2 MHz) at 16 levels from 180 mJy to 2200 mJy/beam.

Figure 4.24 gives an indication of the spectral index which ranges from $\alpha_{35\mathrm{MHz}}^{55\mathrm{MHz}} \sim 0$ to $\alpha_{55\mathrm{MHz}}^{70\mathrm{MHz}} \sim 2$ *around* the compact sources and this flattening towards lower frequencies is typical of thermal radio Bremsstrahlung (§ 2.2.4). The literature indicates that H II regions do become self-absorbed typically < 20 MHz (e.g. Shain et al. 1961, Roger et al. 1999 and Kassim 1990; § 2.3.9) and it would be interesting to detail emission from W3 below this frequency in future observations with LOFAR. The LBA low frequency limit was 30 MHz at time of our observation (de Vos et al. 2009; see § 3.2.1) and is *currently* 15 MHz (van Haarlem et al. 2013; § 1.5) reflecting LOFAR's improving instrumentation and sensitivity, which would make this possible.

W3 has *compact regions* of bright continuum emission (Figure 4.25) from which we have extracted fluxes from our resolved *point source* images; these fluxes *have been* globally scaled (§ 4.2.1) for SED analysis giving rise to Figure 4.26. W3-Main (within which our locations for SED analysis, arbitrarily numbered 3, 4, 5 & 6 of Figure 4.25) has been extensively studied at IR frequencies (Jaffe et al. 1983 and Richardson, White et al. 1989) and radio (e.g. Schwartz et al. 1989). The spectral indices of our low radio frequency SEDs are varied and possibly demonstrate the complex nature of W3 which can only be explained as an assortment of locally free-free emitting (e.g. Richardson, White et al. 1989) *and* free-free absorbing regions (evident in the diffuse surrounding regions of Figure 4.24). Wynn-Williams (1971) details radio maps of ultra-compact *condensations* of ionised gas with electron densities one or more orders of magnitude greater than the surrounding diffuse material of the W3 region; these are associated with regions of molecular activity (§ 1.2), which correspond to the high radio continuum flux locations of Figure 4.25 (see also § 4.1.5). W3 does not have any known non-thermal radio components (Ogura & Ishida 1976); therefore we suspect that strong radio Bremsstrahlung (please refer to Scaife 2012) is *mainly* responsible for the brightness in the continuum emission possibly arising from the ionised winds and jets (Tieftrunk et al. 1997; § 2.2.1) in clusters of Young Stellar Objects (YSOs) identified at these positions, which have been formed by triggered star-formation in the W3 molecular cloud (see § 1.4). Please refer to § 7.5 for more on the ultra-compact H II regions of W3 at far infrared (far-IR) wavelengths and Rivera-Ingraham et al.

(2013). *However*, we must also note, the weaknesses in the data which may explain the spread in the data beyond the error bars of Figure 4.26 and in particular, the relationship of the extracted fluxes to the subtraction on the background; the effects of the background could explain the artificially steep spectra in locations 4 and 6 of Figure 4.26. When there is extended emission that fills a significant portion of the image (as in the case for the region of W3), the background RMS is likely to be biased to a higher value, affecting island determination during PyBDSM flux extraction (Pizzo et al. 2014). This could have been avoided by forcing PyBDSM to use a constant mean and RMS value across the whole image. Since we have a large uncertainty in the island determination and in the background subtraction (both factors resulting in greater uncertainty in the flux values themselves), these influences should have been better reflected in the error bars and could possibly have been determined by comparing the PyBDSM fluxes before and after using a constant mean and RMS value.

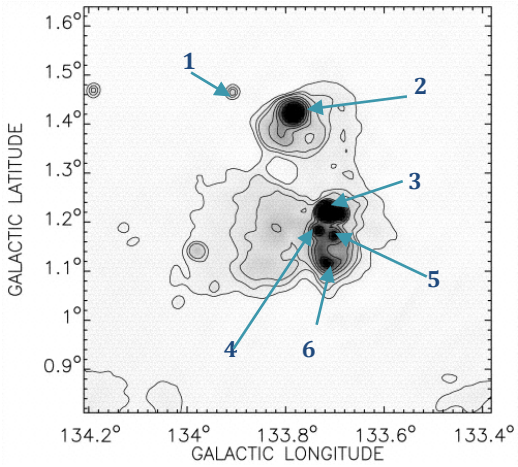

Figure 4.25: The W3 region as shown in Figure 1.3 (1420MHz continuum map; Normandeau et al. 1997) with numbers to represent the positions of our source extraction for SED analysis below.

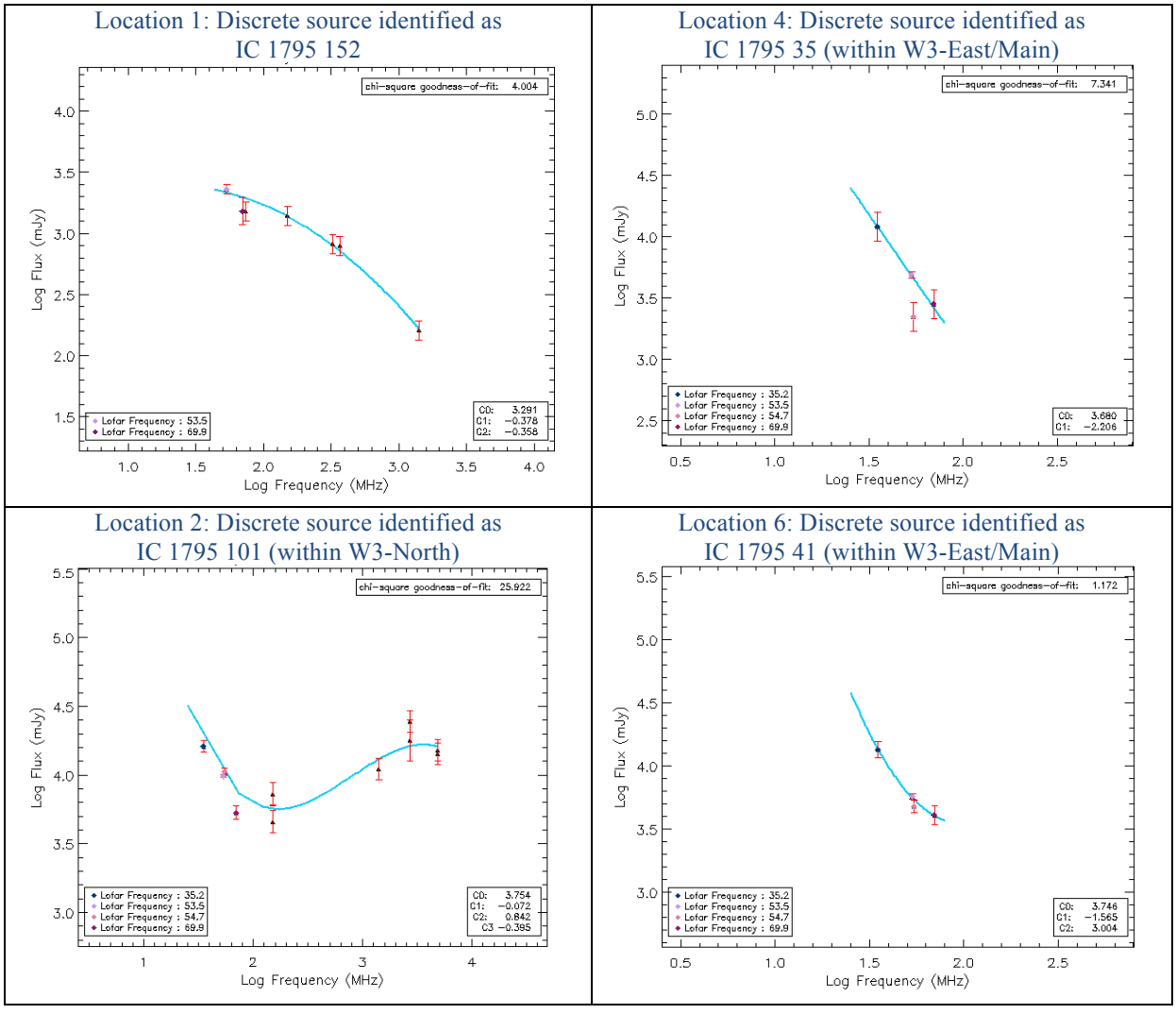

Figure 4.26: The discrete sources identified as stellar clusters within the W3 H II regions, which are loud at radio frequencies. Fluxes extracted from locations 3 and 5 were not reasonably resolved for SED analysis. There were no cross matches in SPECFIND with from locations 4 and 6. There are however IR matches for locations 3, 4 and 6 from Spitzer photometry in the W3 molecular cloud (Ruch et al. 2007).

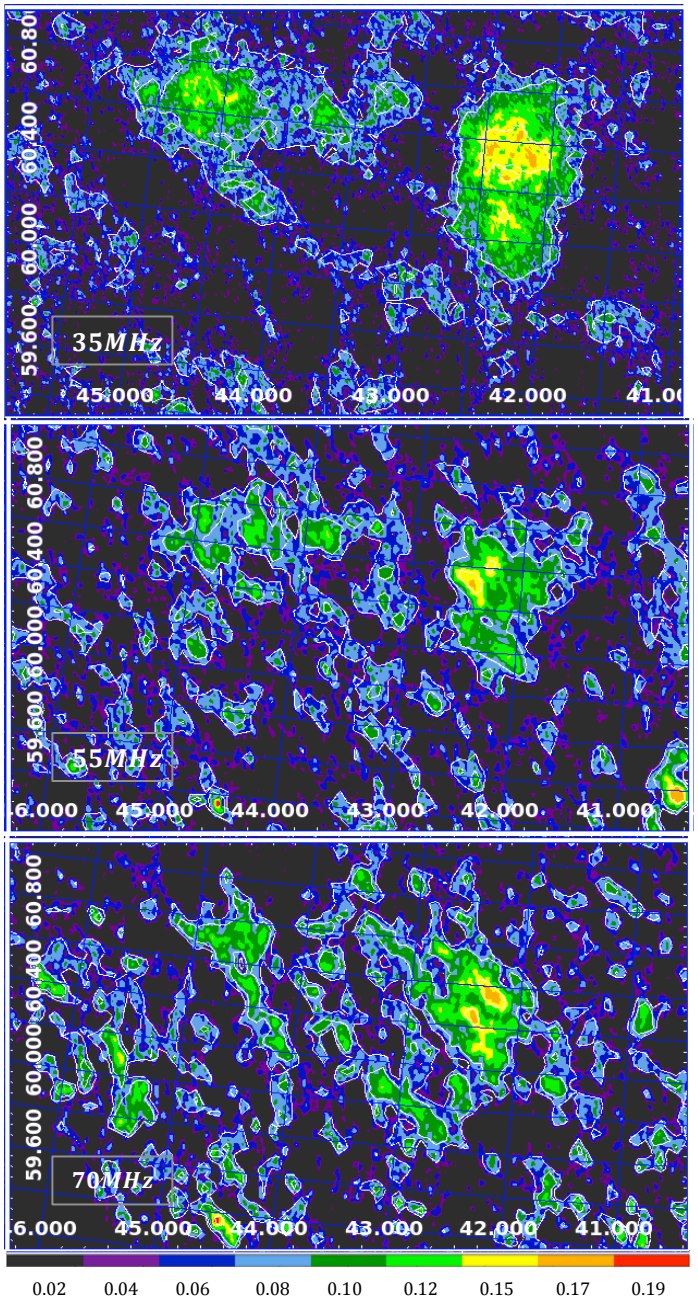

Figure 4.27: Beam matched observations (130″ x 110″ PA = 9◦) at 35.2 MHz, 54.4 MHz and 69.9 MHz from top to bottom. Map units are in Jy/beam. Contours plotted from 0.01 to 0.54 Jy/beam in 13 levels.

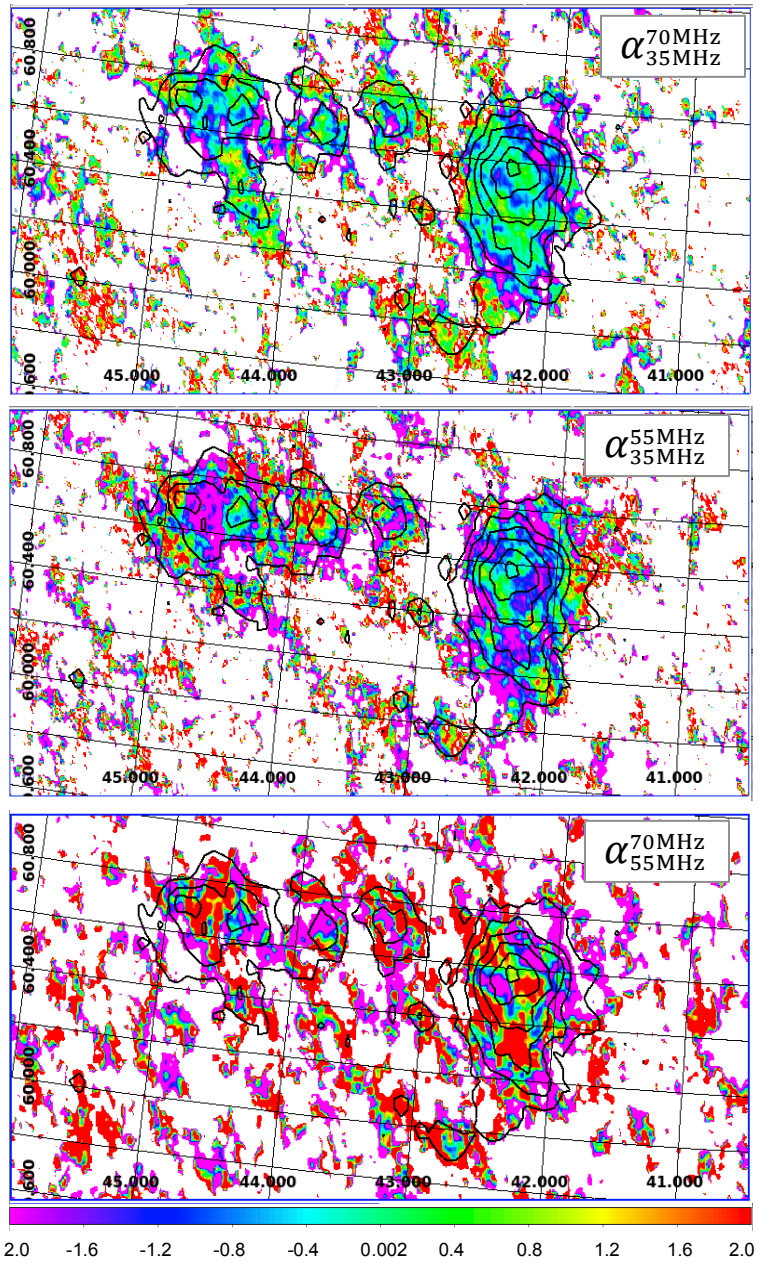

Figure 4.28: Beam matched observations used to calculate spectral index maps. The contours indicate the full bandwidth radio emission centred at 53.5MHz (beam smoothed to that at 35.2 MHz) at 16 levels from 180 mJy to 2200 mJy/beam.

4.2.2. W5

Figures 4.27 and 4.28 give an overview of the structure of the W5 H II region from which the relative emission appears most intense at 35.2 MHz, although we must bear in mind the reducing FoV at higher frequencies which may affect the flux towards the edges where W5 is located, unlike W3 which was our target; this can be an issue *even* after beam correction which itself has residual attenuation effects (§ 4.1.1; Figure 4.3). The eastern, spherical shell (W5 E) and a western more extended and amorphous region (W5 W) as described by Normandeau et al. (1997) can clearly be seen. A lower loop structure appears most prominent at 69.9 MHz and is likely to trace the rim of a partial shell as described by Kaar & Martin (2003) which appears bright because of limb-brightening. The spectral index between 35.2 – 69.9 MHz is predominantly flat in W5 E (Figure 4.28) as expected for a thermally emitting H II region.

4.2.3. W4

Both the W4 and W5 regions exhibit structures of what seem like large loops of diffuse emission ~ 0.5–1 ° in size (Figures 4.27 & 4.29) suggestive of limb-brightened shells (see Terebey 2003). The 'loop' structure connecting W3 to W4 is described in § 1.4.1 where it was suggested to be the base of the Perseus 'Chimney', although Normandeau (2000) describes the recent debate over this structure being more of a superbubble due to its shell-like morphology. We find its relative intensity seems reduced at 54.7 MHz, compared with 35.2 MHz and 69.9 MHz (Figure 4.29) and *could* be suggestive of free-free self-absorption at this frequency.

Normandeau et al. (1996) have suggested that the W4 superbubble/chimney is a powered by ionisation from the massive star cluster OCl 352 or IC 1805 (which contains ~ 145 stars, 11 of which are O type; Strobel 1992 and Massey et al. 1995), visible as a bright bulge at RA ~38.5° Dec ~+61.4° on our full bandwidth results (Figure 4.33). We find supportive evidence of W4 being a superbubble with our diffuse far-IR AKARI maps in § 7.5.1. The W4 superbubble/chimney itself seems to exhibit a complicated spectral index gradient from 35.2 – 69.9 MHz and 35.2 – 54.7 MHz (Figure 4.30) which

gradually increases as declination increases to having a relatively flat index nearest W3, characteristic of thermal emission. The spatial variations in the spectral index are suggestive of an inhomogeneous medium; Terebey et al. (2003) also found the W4 region to be highly inhomogeneous due to the local column density varying by a factor of 2-3, with over-dense regions (~20 cm^{-3}) present in the bottom half of the *patchy* thin shell (which we can confirm with our far-IR AKARI column density maps; § 7.5.1) extending 40 pc below the massive star cluster OCl 352 trapping many of the ionising photons from the cluster (~ 20%) and retarding the expansion of the shell in this direction (Terebey et al. 2003). Dust absorption of both ionising starlight (originating from the OCl 352 cluster) and also of non-ionising photons, contributes to increased luminosity at far-IR wavelengths along the shell's ionised inner edge. Terebey et al. (2003) found this emission was diminished when contrasted with radio images; we cannot confirm this since this difference is not so obvious in our LOFAR comparison with the IRAS far-IR 100 μm image (Figure 4.33). However, we can confirm increased thermal dust emission from our far-IR AKARI map along W4's inner edge in § 7.5.1. We find there are patches of negative spectral index ~ -0.3 – -1.5 predominantly below Dec ~61.2° (Figure 4.30) suggestive of synchrotron emission and West et al. (2007) have estimated that a magnetic field line of sight (LOS) component of 3-5 μG exists in the lower shell. The upper 'chimney' of W4 extending from RA ~37.0° Dec ~61.4° to RA ~37.5° Dec ~61.0°, appears spatially larger with more emission from the region at LOFAR frequencies compared to IRAS and WENSS (Figure 4.33) where it appears to exhibit more of a finer 'filament-like' structure. Contrarily the lower portion of the shell is less pronounced at LOFAR frequencies and is visible only at 54.7 MHz in our observations (Figure 4.29). This lower loop curves up and to the left in what appears as a faint 'wisp-like' structure, clear in IRAS and WENSS (Figure 4.33). However there seems to be no emission here in the LOFAR full and narrow bandwidth images (RA~39.0° Dec~60.4°) possibly due to complete free-free self-absorption (§ 2.2.4) of this region which may be optically thick at LOFAR frequencies.

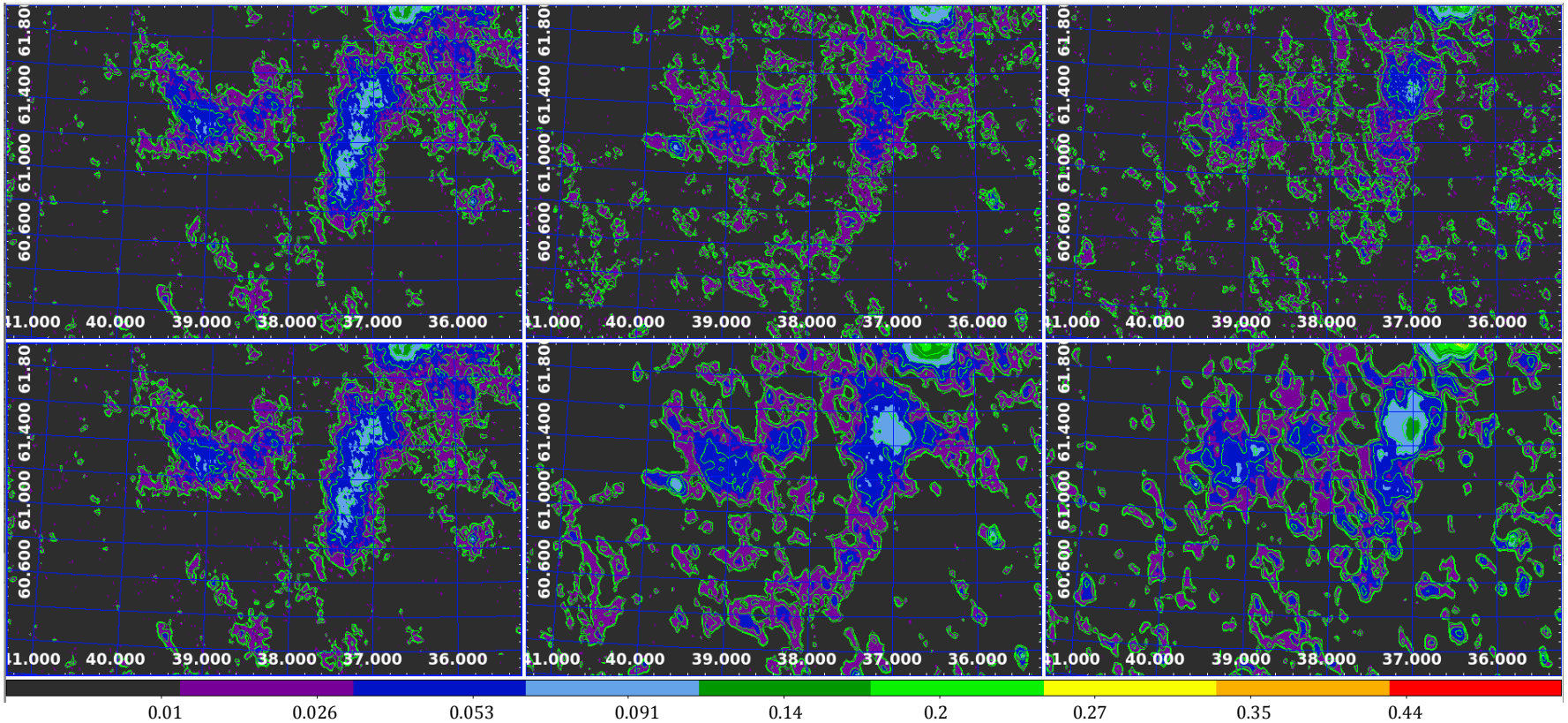

Figure 4.29: Individual observations (top) and beam matched observations (lower images) of W4 at 35.2 MHz, 54.7 and 69.9 MHz from left to right. Map units are in Jy/beam. Contours are plotted from -0.025, to 0.613 Jy/beam in 14 linear levels.

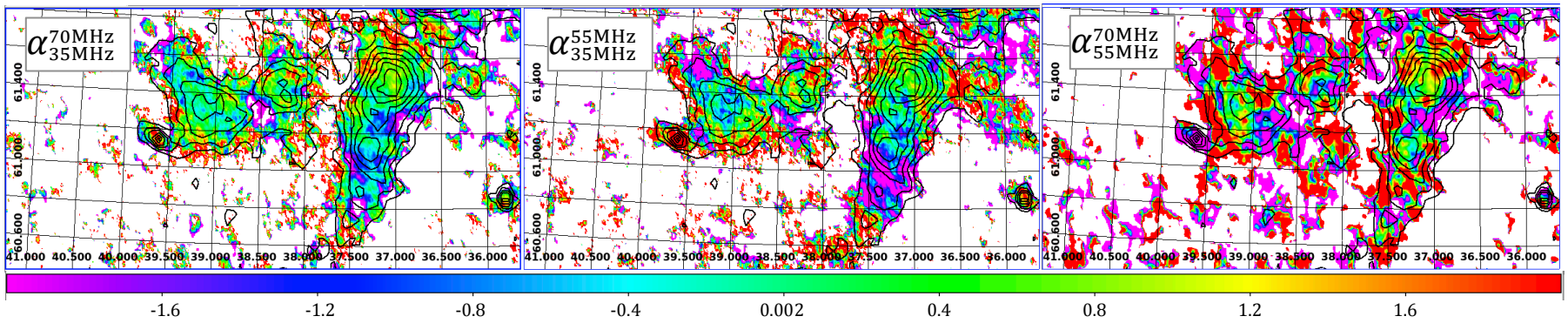

Figure 4.30: Spectral index maps of W4. Left: spectral index from 35.2 – 69.9 MHz; middle: spectral index from 35.2 – 54.7 MHz and Right: spectral index from 54.7 – 69.9 MHz. The histogram colour scale of all 3 images is consistent for a direct comparison. All maps are smoothed to a resolution of 130″ x 110″ (PA = 9◦) FWHM. The contours indicate the full bandwidth radio emission centred at 53.5MHz (beam smoothed to that at 35.2 MHz) at 16 levels from 180 – 2200 mJy/beam.

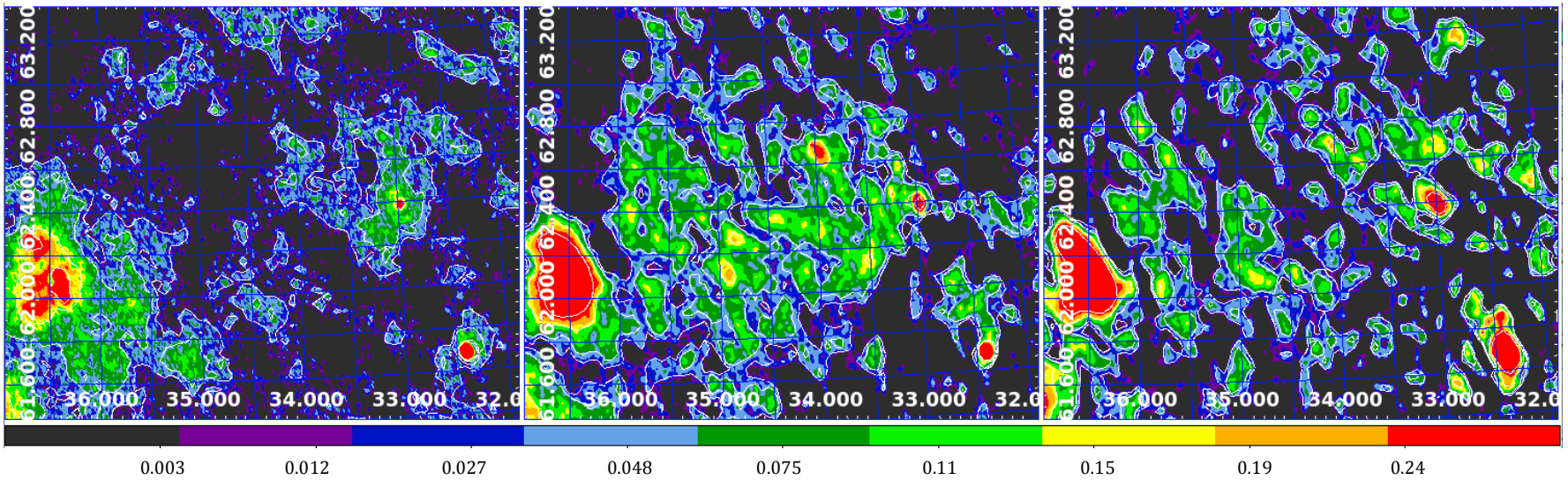

Figure 4.31: Beam matched observations of HB3 at 35.2 MHz, 54.7 and 69.9 MHz from left to right. Map units are in Jy/beam. Contours are plotted from -0.025, to 0.613 Jy/beam in 14 linear levels.

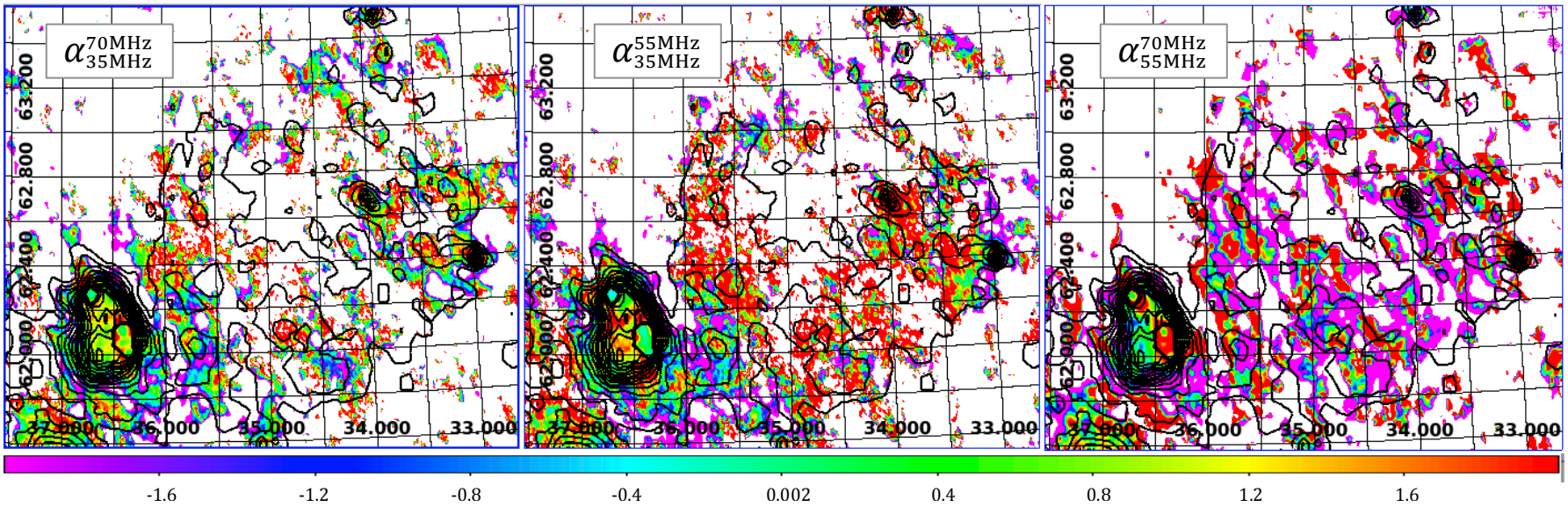

Figure 4.32: Spectral index maps of HB3. Left: spectral index from 35.2 – 69.9 MHz; middle: spectral index from 35.2 – 54.7 MHz and Right: spectral index from 54.7 – 69.9 MHz. The histogram colour scale of all 3 images is consistent for a direct comparison. All maps are smoothed to a resolution of 130″ x 110″ (PA = 9◦) FWHM. The contours indicate the full bandwidth radio emission centred at 53.5MHz (beam smoothed to that at 35.2 MHz) at 16 levels from 180 – 2200 mJy/beam.

4.2.4. SNR HB3

The spectral index maps of Figures 4.24, 4.28 and 4.30 produced with a beam of 130″ x 110″ (PA = 9◦) FWHM give an indication of the structure of the diffuse emission of the prominent H II regions. Often partially confused with the thermal emission from W3, the SNR HB3 has an established spectral index averaging ~ -0.6 from 408 – 1420 MHz (Tian & Leahy 2005) although our maps do not provide sufficient detail to confirm this at lower radio frequencies (Figure 4.32). What is evident is that the *relative* intensity of HB3 is particularly bright at LOFAR radio frequencies as predicted for diffuse synchrotron radio sources (Röttgering et al. 2012) in comparison with WENSS when viewed with the same histogram intensity scale (although the flux of the LOFAR image is not *absolutely* scaled). In Figure 4.33 the HB3 'Southern Shell' (Routledge et al. 1991) is most prominent in LOFAR compared with WENSS possibly giving indication of a stronger magnetic field structure in this region. Contrarily the HB3 'Northern Loop' (Routledge et al. 1991) is evident in WENSS but is diminished at LOFAR frequencies and does not appear at all in IRAS (as to be expected synchrotron at far-IR).

The structure of the shell-type cavity of HB3 is detailed in Figure 4.31 and emission seems most prominent at 54.7 MHz. It is interesting to note that the SED result of HB3 by Kothes et al. (2006) also shows a *possible* plateau near 50 MHz although a turnover must be confirmed with further narrow band low radio frequency studies < 60 MHz in the future. A plausible explanation is that thermal Bremsstrahlung emission associated with W3 *coexists* in HB3 in addition to the synchrotron component as discussed by Uroševic et al. (2007). This follows work by Kassim (1989) and Dulk & Slee (1975) and Brogan et al. (2003) who detail how associated free-free absorption from ionised gas along the LOS can be responsible for low radio frequency turnover in some SNRs < 100 MHz.

Uroševic et al. (2007) estimate properties of the thermal Bremsstrahlung component of HB3 by comparing electron density estimates from 3 regions and argue that the radio thermal Bremsstrahlung emission is emitted from the thin shell enclosing HB3 where the density distribution of ambient material is at its maximum, possibly indicating that HB3 is interacting with the adjacent W3 molecular cloud. It is evident from Figure 4.31, that different components of this shell become more pronounced at each of the 3 frequencies due to a spatially varying spectral index; this could be there result of a

spatially variable magnetic field and relativistic electron distribution (which would affect the synchrotron emission component) and possibly, as Uroševic et al. (2007) suggest, thermal electron content (which would affect the Bremsstrahlung absorption component). Routledge et al. (1991) describe the detection of a molecular bar feature partially surrounded by continuum emission from HB3 through CO observations, suggesting that HB3 is indeed interacting with the W3 molecular cloud (see below).

4.2.5. Comparing CO Velocity With Continuum Radio Emission.

The first complete low-resolution CO map of the Milky Way integrated over all velocities was carried out by Dame et al. (1987). A more recent spatial integrated velocity CO survey by Dame et al. (2001) using the CfA 1.2 m Millimetre-wave Telescope is shown in the comparison of Figures 4.34 and 4.35 with our continuum full bandwidth map. This survey of the stable diatomic molecule carbon monoxide gives an overview of the distribution of dense, star-forming GMCs and is an indication of molecular cloud activity (Dame et al. 2001).

Routledge et al. (1991) looked at integrated CO emission associated with HB3 and saw a strong correlation between the appearance of the SNR and the form of the CO in the velocity interval -39.3 to -45.9 km s^{-1} in the targeted ^{12}CO survey conducted by Huang & Thaddeus (1986). The 'CO bar' described by Routledge et al. (1991) is evident in our comparison in the range -20 to -40 km s^{-1} in the Dame et al. (2001) CO survey (Figures 4.34 and 4.35) as a prominent 'C' shape, the top of which overlaps the base of HB3. This confirms a possible interaction between HB3 and molecular material which Routledge et al. (1991) determined. Dickel (1980) found the velocity of the molecular material around W3 is -40.5 km s^{-1}, and the highest velocity of this material is evident as a peak in intensity in the W3 region in our comparison of Figure 4.34, between ~ -35 to -40 km s^{-1}. Routlege et al. (1991) also found this to be the location of ^{12}CO maximum velocity which follows W3 as the progenitor of a molecular superbubble (Oey 2005). It is believed that HB3 is *behind* this material (Routledge et al. 1991). We also see a secondary peak in the velocity map at ~ +134.25º, +0.70º (Figure 4.35) outside W3 located towards the upper W4 superbubble/chimney, which was also seen by Bieging & Peters

(2011) who found a correspondence with this region and maximum main beam brightness temperature for the CO J = 2–1 line in the velocity range -25 to -60 km s^{-1}; this is the location of the *AFGL 333* H II region (Carpenter et al. 2000) which, like W3, is a prominent star-forming reigon associated with the massive W3 GMC. The theory put forth by Roelfsema et al. (1987), is that the H II region of W3 is breaking out from the molecular cloud, into more tenuous areas; the high associated CO velocity ranges could be associated with this 'break-away.' They could also be associated with the gravitational instabilities which compress the W3 GMC and result from the passage of the ionisation shock front as described in § 1.4.1 and § 4.2.3. Our comparison of the W3 and W4 H II and star-forming regions is studied further in § 7.

Overall it is clear from Figures 4.32 and 4.33 that there is a relation between the distribution of the CO molecular cloud complexes and H II region of W3 (and possibly the top of W5) and this is also seen in the map produced by Digel et al. (1996) who determined large interconnected molecular clouds in the Perseus arm associated with W3, W4 and W5.

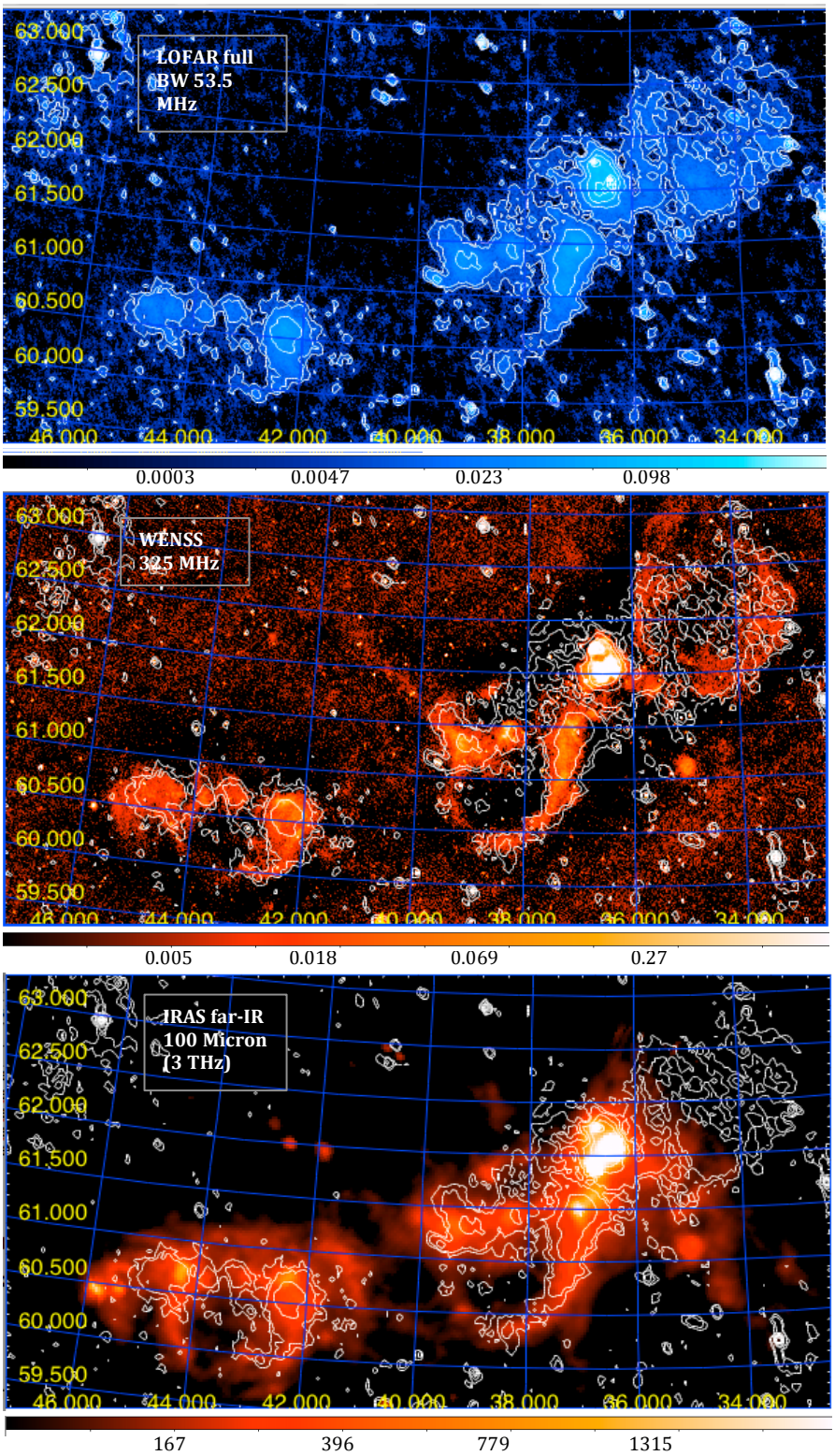

Figure 4.33: Comparison with previous surveys. Our processed LOFAR image (top), WENSS image (middle) and IRAS image (bottom). All images have varying beam size and display levels have been set independently to emphasise the features of W3/W4/W5. The LOFAR contours are superimposed and seem to agree with the WENSS peaks on the shells around W4 and W5.

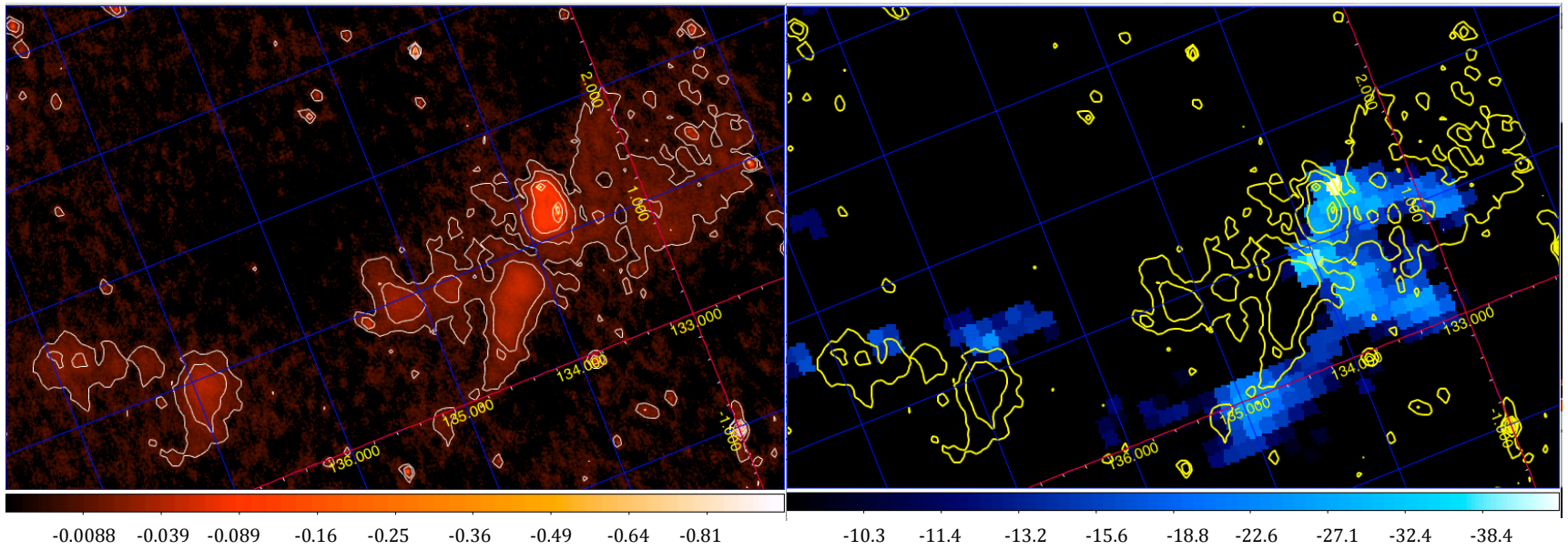

Figure 4.34: Full Bandwidth LOFAR image, with 8 linear contours from 0.01 – 0.45 Jy/beam (left). These contours are overlaid onto the CO integrated velocity intensity map (Dame et al. 2001) represented between -10 to -45 km s^{-1}.

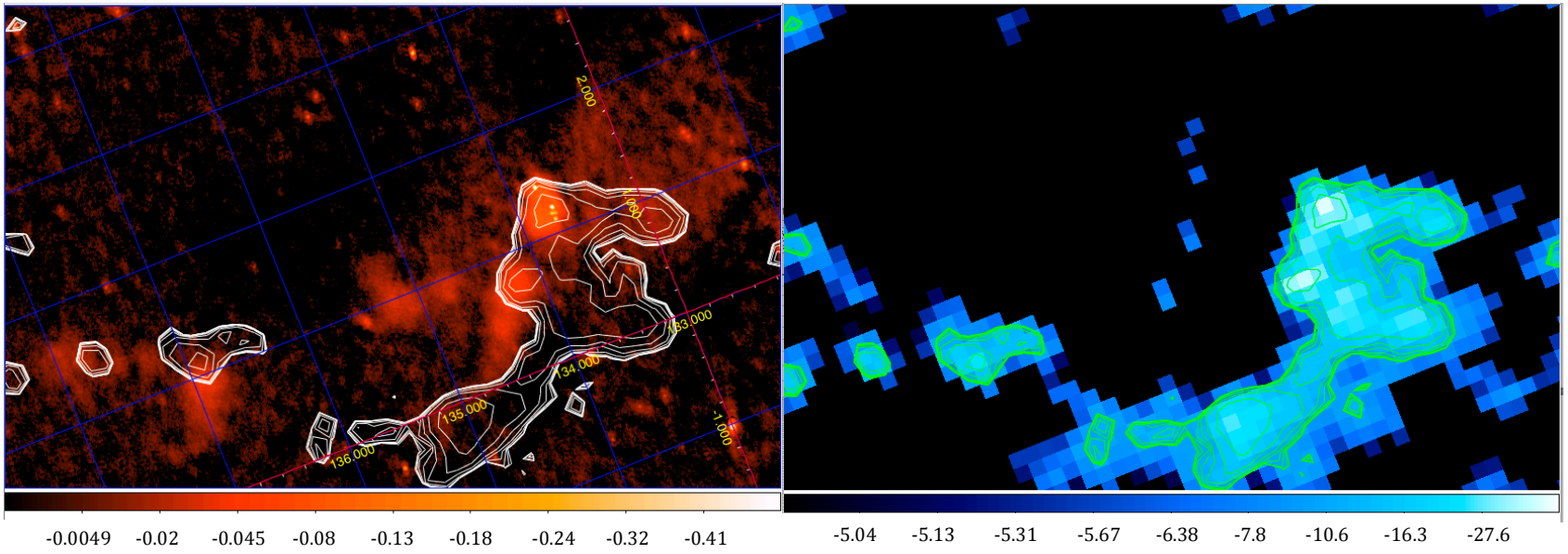

Figure 4.35: CO integrated velocity map (Dame et al. 2001) between -5 to -50 km s^{-1} with 10 linear contours from -10 to -50 km s^{-1} (right). These contours are superimposed onto the full bandwidth LOFAR image (left).

4.2.6. SNR 3C 58

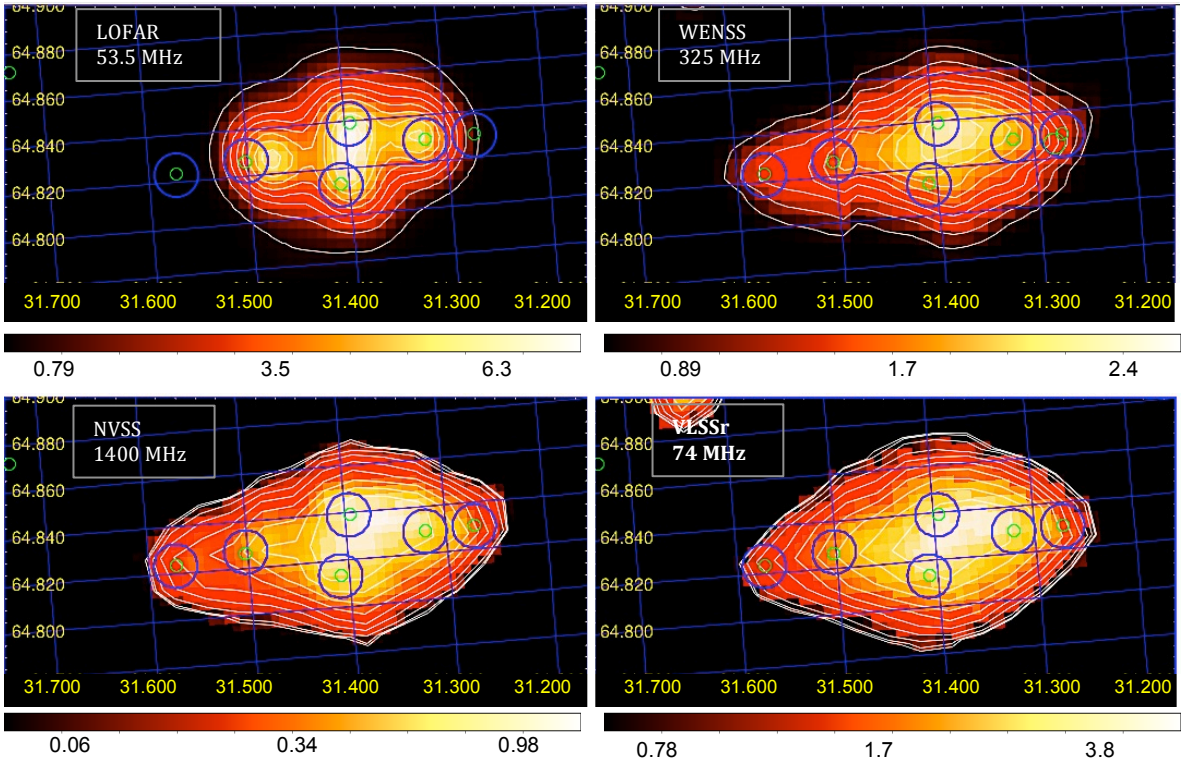

Figure 4.36: SNR 3C 58 in 4 surveys: LOFAR at ~ 62 - 85″ (upper left), NVSS at 45″ (lower left), WENSS at 54″ cosec(dec) (upper right) and VLSSr at 75″ (lower right). 11 linear levels of contours are plotted every 200 mJy/beam. The circles show locations from the NVSS point source catalogue.

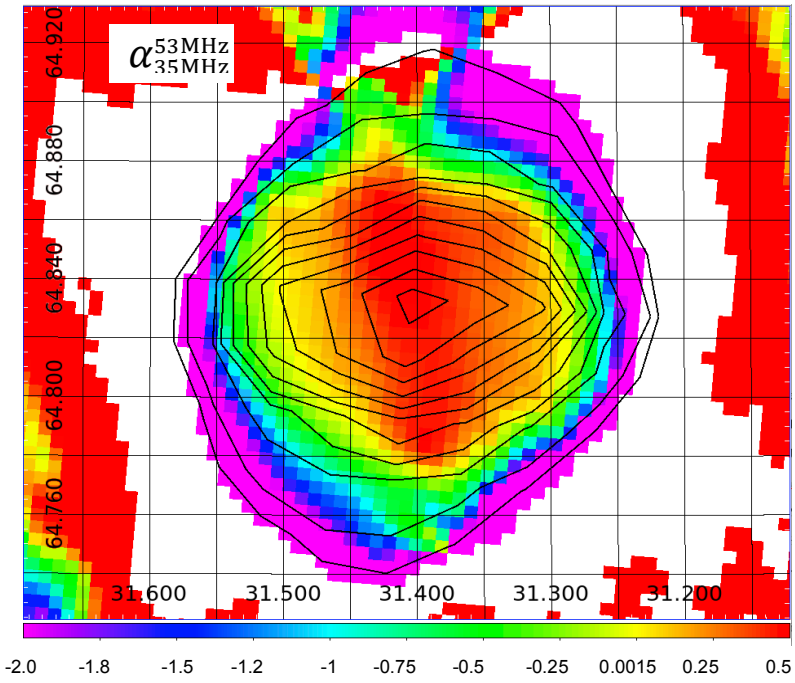

Figure 4.37: Spectral index map of SNR 3C 58 from 35.2 – 53.5 MHz made from continuum images enhancing diffuse emission. 11 levels of contours are superimposed from the LOFAR full bandwidth image (53.3 MHz) from 180 – 28510 mJy/beam.

The structure of SNR 3C 58 from the LOFAR map is contrasted with previous surveys (Figure 4.36). WENSS and the NVSS show a more elongated shape towards higher RA at ~ 31.60° which physically supports the location of the elongated torus and curved jet erupting westwards as described by Murray et al. (2002) (see § 1.4.2). At LOFAR and VLSSr frequencies there is more symmetry in the SNR. This overall geometry of the SNR is reflective of centre-filled morphology, typical of a plerion-type type II SNR (Weiler 1983). Whilst we are nearing the resolution limits of the telescope, 4 of the 6 NVSS point sources are traced distinctively by the contours of LOFAR for this multi-component SNR in Figure 4.36.

Figure 4.37 shows how the spectral index varies between 35.2–53.5 MHz (a comparison could not be made at 69.9 MHz, since the SNR lay outside the FoV of the final beam-corrected AWimage). The spectral index varies between ~ -0.75 – 0.25 over much of the SNR. There is a spectral gradient steepening towards the *edge* of the nebula from the centre where we know lies the pulsar PSR J0205+6449, a strong X-ray source (§ 1.4.2). As well as strong synchrotron emission, Gotthelf et al. (2006) confirmed the existence of an embedded *thermal* X-ray shell surrounding the pulsar. We observe that the spectral index starts off as flat towards the centre (*possibly* indicative of a thermal component) and becomes more negative with distance from the centre with an index typically originating from a synchrotron source.

We can confirm the absence of *large-scale* emission which may be indicative of an expanding shell, from our low radio frequencies at ~ 53.5 MHz of SNR 3C 58; this is in keeping with the observations of Bietenholtz (2006) at 1.4 GHz (see § 1.4.2). As shown in Figure 4.36, there is no sign of an *extensive* synchrotron halo or shell which is expected for relatively young SNRs with higher expansion velocities (generated by a supernova shock wave) and we do not measure emission above 0.305 Jy/beam beyond ~8 pc. As Bietenholtz (2006) suggests, if 3C 58 is the remnant of SN 1181 (to which it has been widely associated e.g. Clark & Stephenson 1977), it would have been strongly decelerated (previous observations indicate expansion speeds of only 630 ± 70 km s^{-1}; Bietenholtz 2006); strong deceleration is unlikely given the absence of emission from the supernova shell. We measure a size of ~7.3 - 7.7 pc along the linear axis of 3C 58 at ~53.5 MHz; with reference to Padmanabhan (2001) and the distance of ~2.6 kpc (Bietenholz et al.

2001) this places the SNR at order ~10^4 yr. This supports Bietenholtz's evidence that 3C 58 is far older than the historical supernova event of 1181 A.D at ~ several thousand years.

Castelletti et al. (2011) also found a localised spectral index flattening towards the centre of SNR IC443, which was concluded to be caused by free-free thermal absorption at 74 MHz along the LOS (where the free-free optical depth, τ_{74} reaches up to ~ 0.3). As mentioned extrinsic FFA by ionised gas along the LOS has long been speculated for the spectral flattening in SNRs by Dulk & Slee (1975) and Kassim (1989) and we have found some evidence of this with SNR HB3. The FFA for IC 443 was attributed to strong shock/molecular cloud interaction close to the expanding rim (White et al. 1987) where the passage of a fast J-type shock across an interacting molecular cloud was believed to be responsible for dissociating the molecules and ionising the post-shocked gas (Castelletti et al. 2011).

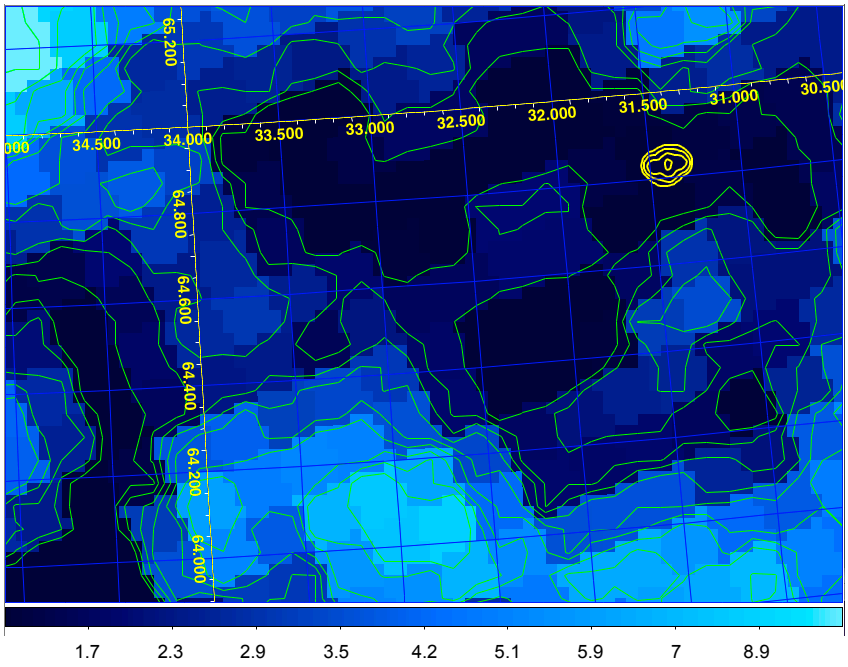

Figure 4.38: Contours represent the emission from 3C 58 from 1.3 – 12.4 Jy/beam in 5 linear levels and are overlaid onto the CO integrated velocity intensity map (Dame et al. 2001) represented between -1.3 to -12.4 km s^{-1}.

We see that the strongest synchrotron emission is towards the centre of SNR 3C 58; this is also where we see the flattest part of the spectrum at $\alpha_{35\mathrm{MHz}}^{53\mathrm{MHz}} \sim$ 0.25 – 0.5 (Figure 4.37). Figure 4.38 shows CO integrated velocity intensity map (Dame et al. 2001) with most prominent emission between -5.1 to -12.4 km s^{-1}. There seems to be no prominent CO directly in the location of SNR 3C 58 which may rule out any possible shock/molecular cloud interaction *along the LOS* that Castelletti et al. (2011) saw with SNR IC443. It may be more likely that the embedded *thermal* X-ray shell surrounding the pulsar PSR J0205+6449 (Gotthelf et al. 2006) is responsible for some

FFA effects towards the centre between 35 – 53 MHz.

Figure 4.38 shows how the CO emission takes a form *around* the SNR which may explain the steepening in spectral index towards the edges with $\alpha_{35\mathrm{MHz}}^{53\mathrm{MHz}}$ ~ -1.5 to -2.0. This was seen in the Eastern shell of SNR IC443 as presented by Castelletti et al. (2011) with values $\alpha_{74\mathrm{MHz}}^{330\mathrm{MHz}}$ between ~ -0.6 to -0.85 consistent with those expected under *linear diffusive shock acceleration processes* which is a model for weak shocks with low Mach numbers (Reynolds & Ellison 1992; Anderson & Rudnick 1993). There *may* be molecular cloud interaction towards the Northern and Southern regions of the SNR (Figure 4.38).

Following Castelletti et al. (2011) who obtain an emission measure (EM) between approximately 2.8 × 10^3 and 5.0 × 10^3 cm^{-6} pc for the eastern shell of SNR IC443, we can also attempt to calculate this towards the edges SNR 3C 58 where we observe spectral steepening. At radio wavelengths, the emission measure (EM) is given by (Castelletti et al. 2011):

$$EM = 6.086\times10^{-6} g_{\mathrm{f}}(T_e, v)^{-1} v^{2.1} \tau_v T_e^{1.35} cm^{-6} pc \qquad (4.5)$$

where $g_{\mathrm{f}}(T_e, v)$ is the Gaunt factor assumed to be 1 following Castelletti et al. (2011) at radio frequencies, for the range of astrophysical quantities involved in these calculations; v is the frequency in MHz; τ_v is the free-free optical depth and T_e is the electron temperature in K. A Type II SNR such as 3C 58 typically expands and cools adiabatically reaching a critical temperature of ~ 10^6 K (Shu 1992). Given our speculated age for the plerion SNR at several thousand years, we assume that T_e of post-shocked gas is at ~ 10^4 K (with reference to the evolution and physics of remnants detailed by Padmanabhan 2001). With evidence of a small thermal component within SNR 3C 58, we crudely estimate that τ_{35} ~ 0.1–0.3 of the intervening ionised gas along the LOS, with reference to Castelletti et al. (2011) who examine a low frequency range close to that of our observation and with reference to the integrated fluxes of SNR 3C 58 at 35 MHz and 53 MHz of 40.594 Jy and 32.684 Jy respectively and our value (see below) of the spectral index of α ~ -0.03±0.02. Hence working from (Eq. 4.5), we arrive at an EM between 3.0 × 10^3 and 9.1× 10^3 cm^{-6} pc towards 3C 58 at 35 MHz.

Figure 4.38 shows the SED of 3C 58; it was resolved into 4 bright components using

PyBDSM and these points were *globally scaled* (as described in § 4.1.1) after which we used SPECFINDv2.0 to cross-correlate the VizieR database with our LOFAR results; the location of one of our bright flux regions cross-matched successfully (Figure 4.38). We arrive at the spectral index result of -0.03±0.02 and whilst this confirms the result of Green (1986), that the spectrum of 3C 58 is flatter than the crab nebula at -0.26±0.01 (Baars & Hartsuijker 1972), which is a similar SNR in terms of filled-centre structure, age and expansion speed (Green 1986), it suggests a flatter spectrum than 0.09±0.02 found by Wilson & Weiler (1976) and -0.10±0.02 found by Green (1986) between 40 MHz - 15 GHz. It is however within the range of Bietenholtz et al. (2001) of 0.07±0.05 between 74 – 327 MHz which is arguably a more appropriate radio frequency range to make comparisons.

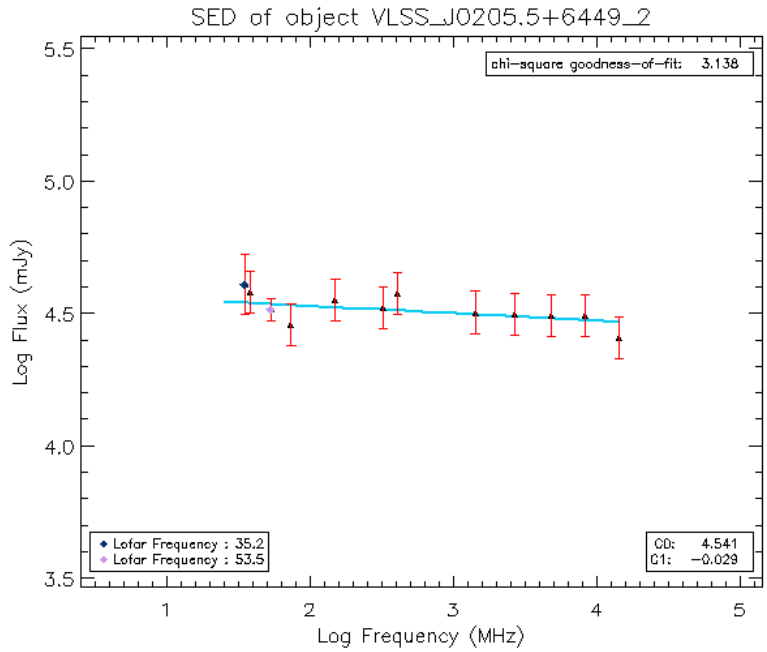

Figure 4.38: The SED of 3C 58 which averages as almost flat with a spectral index result of α -0.03±0.02.

Green (1986) discusses the difficulty in determining the spectral index for this object, which is highly dependent on extreme values of flux density and the contribution of low frequency values from any steep-spectrum compact *component* of 3C 58. Following Green (1986), the results included in a search by SPECFINDv2.0 from the 3C (159 MHz), 3CR (178 MHz) and 4C (178 MHz) catalogues were omitted in this case because of their unreliability due to the uncertainty in the correction for the partial resolution of 3C 58 which has a complex multicomponent structure (evident in Figure 4.37). Vollmer et al. (2005), as mentioned in § 4.1.2, also caution the user for results of *complex* sources where the SPECFINDv2.0 algorithm can give multiple entries per

frequency. Such sources are flagged in SPECFINDv2.0 and are the same low radio frequency sources Green (1986) cautions against. It was this unreliability at low radio frequencies that Green (1986) was trying to counter with a new result at 151 MHz which has been included above. The addition of 2 new LOFAR frequency points (35.2 MHz and 53.5 MHz) allows us to better confirm the trend at low radio frequencies with unprecedented precision. 3C 58 fell outside the smaller FoV at the higher narrow-band frequencies 54.7 MHz and 69.9 MHz, and hence no flux information could be extracted at these radio frequencies, but perhaps this object could be the target of observations with LOFAR in the future.

Chapter 5

RRL Detection with LOFAR in W3

5.1 Objective

The aim was to attempt to detect a carbon radio recombination line (C RRL) in absorption from the diffuse ISM surrounding the H II region, W3 with LOFAR (following previous work as mentioned in § 2.4.5). Surveys of these lines trace the diffuse low-density cold medium; the phase of the ISM which we are interested in and otherwise difficult to observe (§ 2.4.3). We know that carbon exists along the LOS *towards* the 'core' of W3 where RRLs have been observed by Roelfsema & Goss (1991) and C RRLs in emission have been detected in a number of radio frequencies near W3 (e.g. Pankonin et al. 1977, Palmer et al. 1967 and Roelfsema et al. 1987 found an enhancement in line-to-continuum strength of C168α towards the North-West of W3A; see § 1.4.1) which has allowed detailed modelling of the partially ionised medium. At LBA frequencies we anticipate carbon lines in absorption from the diffuse PDR region close to W3 (§ 2.4.3 & § 2.4.5) which could potentially give insight into the dynamics between the parent molecular cloud and W3 H II region (Roelfsema et al. 1987). Figure 5.1 (Payne et al. 1994) demonstrates how low frequency photons originating from high quantum or Rydberg states (where $\Delta n << n$) give rise to detections with increased optical depths (see § 2.4) and are plentiful in the LBA compared with higher frequencies. C RRLs are particularly sensitive to the environment of PDRs and § 2.4.4 details their spectral profile dependency on electron temperature, T_e and density, N_e. By developing a better model for PDRs via the features of C RRLs, direct

understanding would be shed on how the FUV *radiation-induced* feedback mechanisms at ionisation wave shock fronts (§ 1.2) drive the density perturbations of the GMCs, which ultimately lead to their collapse and the formation of stars (Mookerjea et al. 2006).

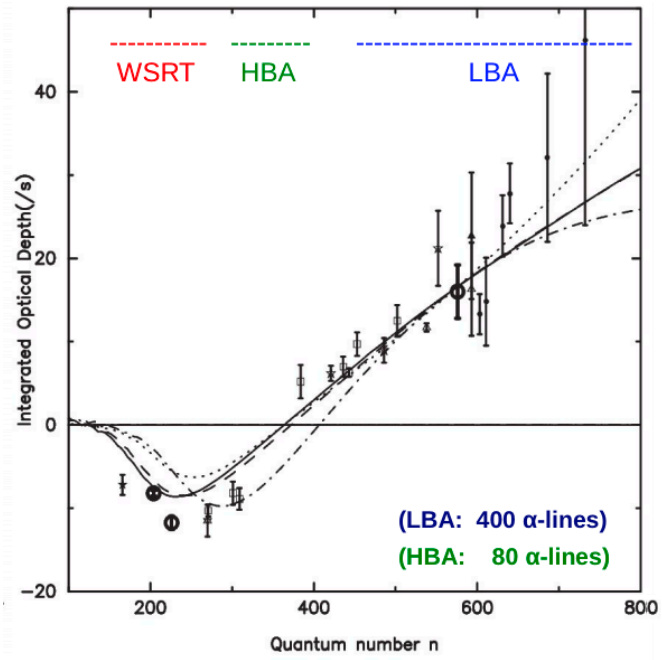

Figure 5.1: Modelling the RRL gas properties (curved lines) which are a function of N_e and T_e (after Payne et al. 1994). The integrated optical depths, τ_{peak} of real observations are compared. It is evident that the integrated optical depths of observations increases with quantum number (specifically after n = 500) which gives rise to low frequency RRLs detectable in the LBA.

5.2 Methodology

We had successfully calibrated the continuum datasets by this stage (which had been compressed to 1 channel/SB). We investigated RRL detection with a test SB which was un-archived from the LOFAR Long Term Archive (LTA; van Haarlem et al. 2013) and uncompressed had 256 channels/SB; this high spectral resolution was critical to resolving any possible narrow Galactic RRL features. From a-priori knowledge, we ensured that this test SB was centred on a frequency range known to have C RRLs alpha lines (Δn = 1) in absorption (please refer to the NRAO's *splatalogue database*, Markwick-Kemper et al. 2006 and Gordon & Sorochenko 2009) and that this frequency range was close to the LOFAR LBA continuum peak response ~ 50 – 60 MHz (§ 3.2.3) since we wanted to optimise S/N for any possible detection. Hence we chose SB093 from Beam 1 which has a central frequency of ~ 56.05 MHz and is known to contain a C RRL (C489α) within its ~ 195 kHz bandwidth range. The following steps were then carried out to attempt a detection of this line towards W3:

(i) We first processed the uncompressed raw dataset using the pipeline script already created for

the continuum datasets (see § 3.4.6). The NDPPP steps were applied as in Figure 3.17, with compression in time by a factor of 5, (but no compression in frequency) followed by SAGECal 'A team source' removal. However, BBS (§ 3.4.3) itself was not carried out in the same way as for the continuum datasets since it could take a time scale of a few hundred hours to run on a full spectrum dataset. Instead we *transferred* solutions from the 3rd iteration of the processed continuum SB093 to the post-SAGECal corrected data of *each channel* of the full spectrum dataset SB093. These (relative) amplitude and phase solutions (stored in the 'instrument table' folder of the measurement set) were first inspected using the LOFAR tool *parmdbm* (Pizzo et al. 2014). Possible ionospheric instability after 2/3 of the observation time (§ 3.13; Figure 3.34) was evident as very spikey relative amplitude solutions in parmdb, and hence we clipped these solutions (and our dataset) at 4000 time samples (see § 5.3) specifically for RRL processing. In essence, we were carrying out a basic continuum calibration, correcting for the amplitude and phase per SB by a multiplicative factor which was a *function of time* only. No frequency dependent calibration was carried out as this could change the spectrum and introduce artificial features. Also the full un-averaged dataset is very large and so this theoretically would take very long timescales.

(ii) Creating an image cube of the resultant phase and flux calibrated dataset consisting of 240 (the first and last 8 channels are removed due to noise; see § 3.17) 2-D *l, m* image planes (§ 3.1) for each remaining processed channel was then carried out (where the z-axis of the cube was the channel/frequency increment of the SB bandwidth). This 3D image cube was created using a customised script written by Raymond Oonk, which split off each channel from the full dataset, imaged each channel individually, *convolved* all images to the same resolution (which is essential since the beam is frequency dependent, affecting the statistics of each channel slightly) and then 'stitched' all 2-D images planes per channel together. Imaging was carried out with CASA imager (using Briggs weighting with a robust value of 0.0; Briggs et al. 1999) factoring for w-projection (§ 3.4.10), and a first-order correction of the LOFAR beam model. We did not use AWimager (a superior imager as far as beam correction is concerned; § 3.4.11); however, since we were only focusing on the centre of the FoV, on the target W3, erratic lateral fluctuation of spectra, which can result at the edges of an

uncorrected field, were not a concern. We decreased the number of clean iterations for each channel of the single SB, as less bandwidth requires less in depth cleaning compared with continuum imaging.

(iii) Once we had a stable image-cube, another script (Oonk et al. 2014) then took the generated channel maps of an area ~ 1 x 1 deg^2, and extracted spectral plots. We created profiles focused around the brightest diffuse regions toward the centre of the FoV (around W3).

(iv) In order to account for and correct the bandpass, it is necessary to observe (with the same frequency setup) a strong calibrator source with a known bandpass either simultaneously or shortly before/after the observation; for the LBA, this is typically calibrator 3C196. Fortunately for LOFAR, the bandpass is made via digital filters that have a very flat response over 80 % of a SB central frequency range (van Haarlem et al. 2013). Combining this response with the fact that Galactic lines are relatively narrow (typically < 50 km s^{-1}) means that it is possible to correct the bandpass after imaging, by fitting a low-order polynomial to the extracted spectrum. However, at the time of our commissioning observation, such calibrators were not available (see § 4.1.1) and we were not able to make an appropriate bandpass correction. The absence of a calibrator observation in the LBA was actually one of the main reasons for this data set being very difficult to calibrate.

5.3 Improving Quality & Sensitivity of the Data

Assessing the quality of the data was critical for determining the probability of credible detection of RRLs with our data. The statistics of the processed continuum images are found in § 3.4.8 and after the 3rd iteration we reached an RMS level of 7.87 mJy/beam for the entire bandwidth of Beam 1 and for a *single* SB around the LOFAR peak response (~ 58 MHz) this had been 46.6 mJy/beam. Also the DR reached was ~ 750 for the entire bandwidth of Beam 1 and for a single SB this had been ~ 150 around ~ 58 MHz. These values were deemed very impressive for the age of the data (it had been taken during the commissioning phase in late 2011) and so we decided to continue our investigation of a possible C RRL detection with this dataset.

As expected, the image quality of the planes generated per channel in the image cube step were worse than those of the continuum version which was averaged over all channels (increasing the S/N).

The image quality also varied channel-to-channel with RMS ranging between ~ 85 - 200 mJy/beam. The resolution of a single channel was also quite poor, and W3 appeared as a 'blob-like region' whereas with more bandwidth the multi-component structures are resolved. We attempted to improve the spectral quality and sensitivity in a number of ways with the following additional steps specific for RRL detection in hope of increasing the chance of detection against the bright continuum source:

- As mentioned, we cut the data after time 4000 time samples. Whilst this had the effect of sharpening the images at the *cost* of slight degradation in sensitivity of approximately ~ 5% (the latter of which had been preferred for continuum analysis; § 3.4.13), we found that this improved our image cube since resultant spectral profiles consequently recovered slightly more flux. Hence we gained more optical depth, τ_{peak} (§ 5.4).
- We verified there were no bad stations with poor calibration solutions that were degrading the signal using parmdb (we had initially ruled out bad stations during the initial quality check of the data; § 3.4.6). We then focused on the core stations only (all verified as good) and created an image cube with core stations only vs. core stations *and* remote stations. The reason for this was that some drifting with clock offsets were possible at the time of observation (§ 3.4.13); an issue more prominent for remote stations. We found this alone did not improve the S/N or have any impact on the possible detection of a line profile (although we did see more diffuse in the images as expected and decreased sensitivity) and hence we included the remote stations.
- Compared with continuum analysis, we flagged our RRL dataset more severely since strict flagging is fundamental to acquiring 'good' spectra (Asgekar, Oonk et al. 2013). More specifically, we flagged the BBS solutions that we were transferring more ruthlessly (assessing this by eye in each case) since these amplitudes throughout the observation were on the whole quite 'spikey' (although not as much as after 4000 time samples). We found this to be effective in improving the resolution of our image planes. We also tried smoothing the BBS amplitudes (to give average temporal amplitudes and counter some of the random fluctuations BBS can introduce) and retransferring the new solutions, after which we reimaged the cube. This technique had worked well with previous LOFAR datasets in the upper frequency range of the HBA (please

refer to tests by R. J. van Weeren on http://www.lofar.org/wiki) although this did not result in a significant improvement for our data. This has also been observed for other LBA commissioning tests, where this technique so far has not brought the improvements seen for higher frequencies.

5.4 Preliminary Results

The Doppler Shift Correction

LOFAR does not support Doppler tracking so we have to account for this motion (§ 2.2.4, Eq. 2.69) offline. We calculated the expected Doppler shift based on (i) the date and duration of the observation; (ii) the direction of our target, W3 (RA & Dec); and (iii) the latitude and longitude of LOFAR using the V_{LSR} algorithm written by M. A. Gordon (Meeks 1976). This gave a radial velocity of -11 km s^{-1} in direction of W3 which translates to a frequency shift of ~ 2.06 kHz. We were careful of whether this shift was in a positive or negative direction by considering W3's relative motion with respect to the local standard of rest (LST). We found this shift is to higher frequencies by the magnitude calculated (~ 2.06 kHz) with respect to the laboratory (i.e. rest) frequency, v_0 of the C489α line at 56.0955 MHz **(**Markwick-Kemper et al. 2006) and that this corresponds to where we observe the feature in Figure 5.2.

A Possible Feature & Processing Challenges

With 240 channels, the velocity resolution of our spectra is ~ 5 km s^{-1} or ~ 0.9 kHz $channel^{-1}$. An artificial slope of the average spectra exists across the SB bandwidth, which should otherwise be flat and could be a residing calibration issue. Even with the slope, we can still measure the RMS since in principle it should be conserved around the median; we estimate that the spectral RMS is ~ 150-200 arbitrary flux units, which corresponds to ~ 4.8 x 10^{-3} – 6.4 x 10^{-3}. The midline of the feature we observe has a peak optical depth, τ_{peak} ~ 9.5 x 10^{-3} which corresponds to ~ 1.5–2 σ, and the optical depth seems to have increased after the additional flagging by 32 %.

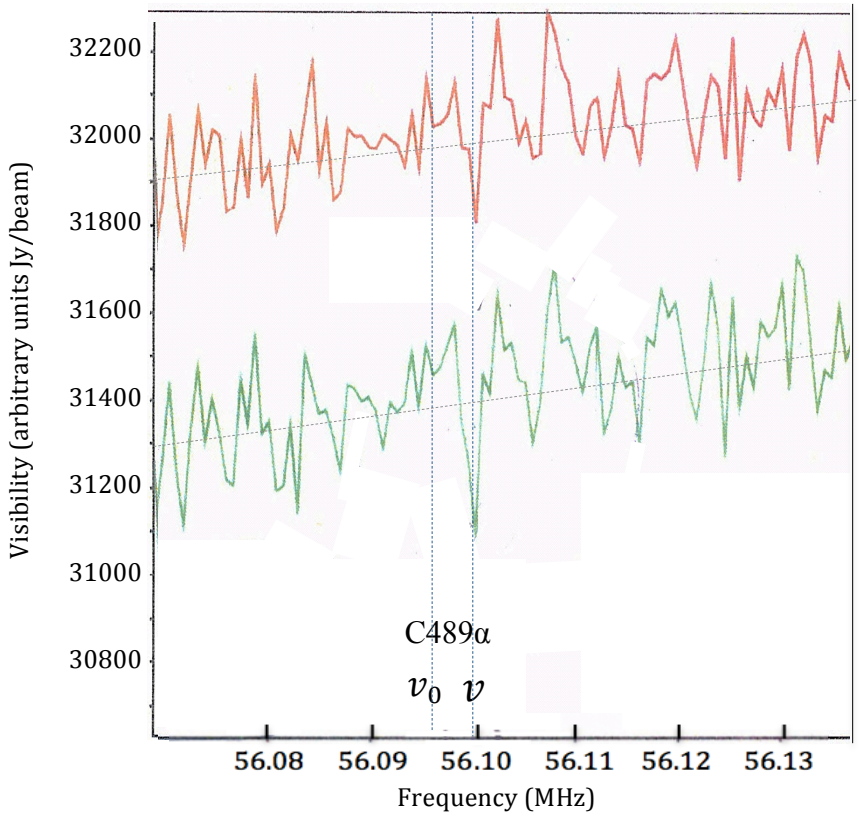

Figure 5.2: Scripts were run on a completely raw uncompressed SB093. This is the resulting spectrum of a *possible* detection of RRL C489α, which has a rest frequency, v_0 of 56.0955 MHz (Markwick-Kemper et al. 2006). The red spectrum represents data before flagging and in green is the spectrum after *additional* flagging which does deepen the relative optical depth, τ_{peak} of this feature by ~ 30 %. We cannot trust the units of intensity (due to global scaling factors which were not applied at this stage; § 4.2.1) and so we measure flux in *relative arbitrary units*. This translates to a spectral RMS of ~ 4.8 x 10^{-3} – 6.4 x 10^{-3} with respect to the median signal.

Overall, the feature we see in Figure 5.2 shows a *possible* detection of a very faint absorption line in the spectra of SB093, at the velocity or Doppler-shifted frequency we would anticipate, and the intensity of the peak (τ_{peak} ~ 9.5 x 10^{-3}) and spectral RMS (~ 4.8 x 10^{-3} – 6.4 x 10^{-3}) is in the order of magnitude we would expect given the quality of the dataset and the brightness of W3 (see below). Our work warrants further investigation in the future (§ 5.5) since the peak optical depth of this feature is relatively very weak against the RMS and at ~ 1.5–2 σ is rather modest to give us the confidence that is real. We also remain extremely cautious since our statistics must take flagging into account for each frequency channel. The green spectrum of Figure 5.2 is the result of additional flagging of RFI (using AOFlagger; Offringa et al. 2010), which reduces the total signal slightly (with the median signal dropping by ~ 1.88 %). Flagging is channel and time dependent and the process does not conserve the

total number of samples per channel. The resultant time-dependent spectrum of Figure 5.2 is the median of the dynamic range (DR) and flagging can move this median down. Hence the additional flagging of channels can introduce artificial signatures which we can only rule out by inspecting each channel that has been flagged and see if the frequencies are consistent with the feature we see by use of the 'RFI Gui' (Pizzo et al. 2014) which displays the dynamic spectrum (time vs. frequency) of the post-flagged dataset (van Haarlem et al. 2013).

Overall, we have encountered a range of challenges in our attempt of a C RRL detection:

(i) The data processing has been very time consuming since we have to work on every individual frequency channel from correlator. We can decrease the volume of the datasets by averaging further in time by a factor of 3 for low frequency spectral line work. However, averaging does leave spectra more vulnerable to interference spikes, and phase instability (van Haarlem et al. 2013).

(ii) Spectral line observations will always be affected by some continuum emission, which should optimally be subtracted (§ 2.4.4). The continuum emission can be close in magnitude to that of the spectral line, in which case, the final spectral images could possibly be dominated by the continuum and its associated errors (artefacts and sidelobes resulting from deconvolution and calibration errors, etc.) (Sault 1994). This could reduce the final dynamic range (DR) of the image possibly obscuring weak spectral features (Sault 1994). Consequently it is usually best to subtract the continuum from the data. The median flux of the continuum emission can be fitted with a simplified linear function and this can be divided out of the spectra (after which we would subtract 1) to give the final on-source SB spectra in units of optical depth, i.e. $\tau_\nu = (F_{\nu,\,obs}/F_{\nu,\,cont}) - 1$ (Oonk et al. 2014) where $F_{\nu,\,obs}$ is the observed flux and $F_{\nu,\,cont}$ is the continuum flux.

However, for our current stage of progress, the continuum subtraction was not the ultimate factor for improving detection of our observed feature, since it essentially serves as a background mean signal that can be removed. In the low frequency radio regime, the continuum background does not fluctuate a lot as function of frequency over a narrow bandwidth (~ 195 kHz for an LBA SB) and hence in the radio, the continuum is much better approximated by simple low-order polynomial or power-law functions as compared to for example the optical regime.

(iii) Even though we were cautiously optimistic to proceed with the search for an RRL judging by the image quality of our continuum images (§ 5.3), the data quality of our dataset taken in 2011 during the commissioning phase of LOFAR is generally rather low and thus difficult to calibrate. Even for the t = 0-4000 sample range, the BBS solutions remain at a relatively low S/N which leads to additional noise in the spectral data in addition to the low S/N inherent to the data itself.

(iv) Even with a better quality dataset, it may be hard to detect any RRLs (which are inherently weak at low frequencies originating from the PDR) due to the weak intensity of the target itself; therefore stimulated emission by the background emission will do little to enhance C RRL visibility in this case (essential for lines which have a peak optical depth at the ~ 10^{-3} optical depth units level originating from the cool and low-dense PDR explained in § 2.4.3; the C II region of W3 has a density of only N_e ~ 30cm^{-3} and T_e ~ 100 K; Pankonin et al. 1977 and Roelfsema & Goss 1991). The advantage and success of LBA detection of Galactic C RRLs in the direction of Cas A (Asgekar, Oonk et al. 2013) and Cyg A (Oonk et al. 2014) is in part due to these being the brightest continuum sources in the sky (e.g. Lazio et al. 2006); this is not the case with W3 which is not a particularly bright source at low frequencies. The intensity of W3 over our observing frequency range reached a maximum integrated flux of ~ 4 – 11 Jy/beam after global scaling of our continuum full bandwidth images; this is too weak in the LBA for us to be sensitive to find significant line emission easily against the source. For 8 hour observations with LOFAR, one needs a bright background source of at least ~ 50 – 100 Jy at 60 MHz to get to reasonable optical depths for sensitive RRL detection; specifically a 5 σ detection of a 10^{-3} (optical depth units) line peak would require 10 stacked lines (see § 5.5) where each line has a FWHM width of ~ 10 km s^{-1}. There would be more chance for detection with the HBA, which only requires a source flux of 5 – 10 Jy/beam for the same detection limits. There is unfortunately no published reference for this but follows work by commissioning teams; please refer to reports on RRL processing on http://www.lofar.org/wiki. However, the drawback with detection in the HBA is that the intrinsic RRL intensity will also be lower as demonstrated by Figure 5.1. Carbon RRLs in the LBA are more sensitive to the PDR environment (§ 2.4.5) and this has been the motivation for our work.

5.5 Future Work

Overall, we cannot claim to have made a C RRL detection towards W3 at this stage. We see a hint of an absorption feature with a peak optical depth, τ_{peak} ~ 9.5 x 10^{-3} or ~ 1.5–2 σ, that remains to be clarified in the future. Since this is not a detection, formally the 3 σ upper limit for the peak optical depth would be ~ 14.4 x 10^{-2}. Stacking would certainly help to increase the sensitivity of detection by decreasing the noise, which roughly scales with the square root of the number of stacked spectra (Oonk et al. 2014). This has been successful for C RRL detection in the bright extragalactic source, Cyg A by Oonk et al. (2014) at LBA frequencies. Hence, stacking ~ 10 SBs (retrieved from the LTA) from the same beam around the peak response frequency range (54–62 MHz) (after NDPPP, SAGECAL and BBS solution transfer steps) should increase the S/N of the resultant average line profile by a factor of ~ 3. It is essential that stacking is carried out accurately with the centres of each line precisely aligned and avoiding noise peaks which requires accurate radial Doppler velocity information and high spectral resolution. We reached a spectral RMS between 4.8 x 10^{-3} – 6.4 x 10^{-3}, which means that for 8–10 SBs we could reach ~ 1 x 10^{-3} – 2 x 10^{-3} at most; a level which may allow for a detection, but it is also close to where the expected signal would be. Therefore going a factor 2–4 deeper would be preferable which would mean processing at least 40 SBs. Unfortunately it proved impossible, for computing and time reasons, to process more data during the present work, but this will form part of the follow-up work over the coming months.

We must also bear in mind, that the combination of the poor data quality and the relative weak continuum of W3 at LBA frequencies means that it will be very difficult to obtain statistically significant CRRL detections towards this source from this single ~ 10 hour data set. Hence, a more recent targeted observation could provide the quality and sensitivity we need and a longer integration time would increase the integrated optical depth, τ_v. Also, now that calibrators have been established in the LBA, we could also simultaneously carry out a calibrator observation in addition to the target, which would aid the bandpass correction and increase the quality of the spectra.

Only when a detection is confirmed, a spectral profile could be fitted in the way described by Oonk et al. (2014) and possible broadening mechanisms in the PDR gas (§ 2.4.4) could be investigated.

Chapter 6

Constructing a New AKARI Catalogue

6.1 AKARI: An Overview

AKARI is a Japanese satellite telescope launched in February 2006 (Murakami et al. 2007) and is equipped with 2 instruments: the Far Infrared Surveyor (FIS) (Kawada et al. 2007) and the Infrared Camera (IRC) (Onaka et al. 2007). The AKARI FIS (Kawada et al. 2007; Verdugo et al. 2007) has observed all-sky surveys between May 2006 and August 2007 at 4 infrared wavelengths centred at 65 μm (band N60), 90 μm (band WIDE-S), 140 μm (band WIDE-L) and 160 μm (band N160). N60 and N160 span narrow frequency bands whilst WIDE-S and WIDE-L span wide frequency bands. These infrared all-sky surveys were the first since the Infrared Astronomical Satellite (IRAS) mission launched in 1983 which also made all-sky surveys centred at 12 μm, 25 μm, 60 μm and 100 μm (Wheelock et al. 1997). However the AKARI FIS maps covering the entire Galactic plane have an improved sensitivity, spatial resolution, coverage and fidelity than that of IRAS survey (as shown by work carried out by Etxaluze 2010 and Arimatsu et al. 2014) and also cover a wider wavelength range which is advantageous for constraining SED fitting (§ 6.3.4 & § 7.4) to our detected sources (§ 6.3.1).

6.2 New AKARI Maps: Aims

From the FIS all-sky data the AKARI far-IR Bright Source Catalogue (BSC) has already been released (Yamamura et al. 2010). Since 2010, the archived data of the AKARI Galactic surveys have been

reprocessed to enhance fainter diffuse emission and reduce instrumental artefacts resulting in new maps (Doi et al. 2012), which we have used for our analysis. The sensitivity of the old AKARI data maps in the 90 μm band was ~ 0.55 Jy (Yamamura et al. 2010). The new AKARI intensity maps used for our analysis cover ~30 x 30 degrees and are part of the Gould Belt surveys of nearby star-forming regions (including the W3/W4/W5 complex) and were anticipated to have improved sensitivity which should enable us to detect an increased number of fainter point sources (as well as more diffuse emission). We found that using the 90 μm maps we were able to extract sources down to ~ 0.4 Jy (Figure 6.1).

We went back to the AKARI data and used the new maps to conduct photometry with the aim of: (i) detecting the same sources as the AKARI FIS BSC (Yamamura et al. 2010) with a more accurate measurement for flux density and (ii) extracting new fainter sources by detecting deeper than the BSC. The objective was to separate out the properties of these discrete sources from the surrounding diffuse emission originating from interstellar gas and dust within the region, which absorb and re-emit radiation from nearby stars; the diffuse emission was of interest in its own right and we look at this in § 7.5.1. Far infrared (far-IR) wavelengths (such as those of the AKARI FIS maps) probe this thermal diffuse emission as well as that arising from the young stars themselves, and is less likely to be absorbed by intervening dust (due to its longer wavelength) allowing us to look inside deep the dense clouds (including the ionised shells and super-bubbles of W3/W4/W5; § 1.2) which are impenetrable at optical wavelengths (Spitzer 1998). With our new improved point source catalogue we hope to conduct analysis of new fainter point sources, by fitting black-body and grey-body models to constrain their temperatures, masses and luminosities (§ 6.3.4 & § 7.4; Figure 7.3).

6.3 Point source analysis from new AKARI maps

The input intensity map sky-brightness images (~9 in total for each band) had brightness scale units of MJy/sr. These images were analysed within the Herschel Interactive Processing Environment (HIPE) software package with a script which accounted for the input brightness scale units and the beam area (calculated from the FWHM), converting image units to Jy/beam, before any source extraction took

place (which subsequently outputted fluxes in mJy/beam) (Pearson et al. 2014). Evidently aperture photometry was dependent on the value of the FWHM which was waveband dependent as listed in Yamamura et al. (2010). The beam shapes were not perfectly spherical but elliptical Gaussians. Values were tested from the maximum in-scan FWHM to minimum cross-scan FWHM for WIDE-S, including the geometric mean FWHM. The fluxes resulting from the in-scan FWHM gave the best correlation with the established AKARI BSC. Hence the in-scan FWHM was also *consistently* used for the 3 ancillary bands during photometry and the correlations with the AKARI BSC are examined in (§ 6.3.3).

6.3.1. Source Extraction

Source extraction and subsequent photometry was carried out in HIPE using the SUSSEXtractor algorithm (abbreviated SXT; Savage & Oliver 2007) developed for the AKARI FIS All-Sky Survey by the team in University of Sussex. The algorithm applies Bayesian statistics in the source detection process (Yamamura et al. 2010) the details of which are described in Savage & Oliver (2007).

The detection threshold parameter was lowered incrementally to pick up as many realistic faint sources as possible: the optimal value for this was at 10 σ above the local background RMS (Figure 6.5) which picked up the fewest artefacts without excluding real sources. Inevitably much diffuse emission (particularly bright diffuse 'blobs') was also extracted, as well as partial bright spots along instrumental artefacts (evident as prominent stripes across some of the images in the scan direction). There is a destriping code to counter these stripes (Etxaluze 2010) but it was not applied to these particular datasets during calibration. There is also a way to apply the destriping filter post-processing, but this requires fine-tuning for the new maps and we decided it was safer to edit out spurious sources manually in HIPE by overlaying the extracted sources over the image frames (Figures 6.2 – 6.4) and inspecting the results by eye. Admittedly in a few cases it was challenging to differentiate between diffuse blobs and real faint sources, but a statistical improvement by subjective editing of these spurious sources seemed the best next necessary step (after optimal parameterisation of the SXT algorithm for maximum realistic faint source detection as demonstrated in Figure 6.5). Also a source

detected in WIDE-S, evident across all wavebands confirmed its authenticity (although this was not a general rule to check if the source was real). The outcome was a new catalogue of as many realistic point sources as possible (numbering 1298), with listed fluxes, errors and coordinates (please refer to Appendix E). Using this source list and taking all WIDE-S 1290 source positions, we used a liberal search radius of 60″ in the TOPCAT software (§ 4.2.1) to account for the full extent of AKARI's pointing errors and found only 910 source matches with the BSC. WIDE-S, WIDE-L, N60 and N160 bands have 5 σ detection limits of 0.55, 1.4, 2.4 and 6.3 Jy respectively (Kawada et al. 2007) hence the careful method of source extraction was first carried out on the 90 μm WIDE-S images (Table 6.1) constituting the most sensitive statistical faint source survey from which to base the input source list for photometry on the remaining 3 ancillary bands. The source count function i.e. the number of sources as a function of their flux, is demonstrated in the *log N- log S* plot of Figure 6.1 where *N* is the confirmed source count in the WIDE-S band and *S* is the flux density in Jy; this plot can be compared to that of Yamamura et al. (2010) for the BSC. Assuming that this source count function does not change significantly in the AKARI flux range, the drop in number count at the faint end is a result of the instrumental detection limit (Yamamura et al. 2010). The peak flux for WIDE-S in the log N-log S plot of Yamamura et al. (2010) was found to be 0.55 Jy; for comparison, our peak flux is 0.8 Jy which could therefore be regarded as the as the detection limit of our current catalogue. A smaller peak is seen at 0.4 Jy in Figure 6.1, and we detect 1.55 % of the total sources below 0.4 Jy and 15.7 % below 0.8 Jy which reflects a significant fraction of faint sources.

Frame/ image number	Number of realistic point sources extracted by SXT
366	131
367	155
368	132
390	215
391	112
392	131
409	174
410	137
411	151

Table 6.1: Listed frame numbers for WIDE-S with the total number of realistic sources extracted for each frame.

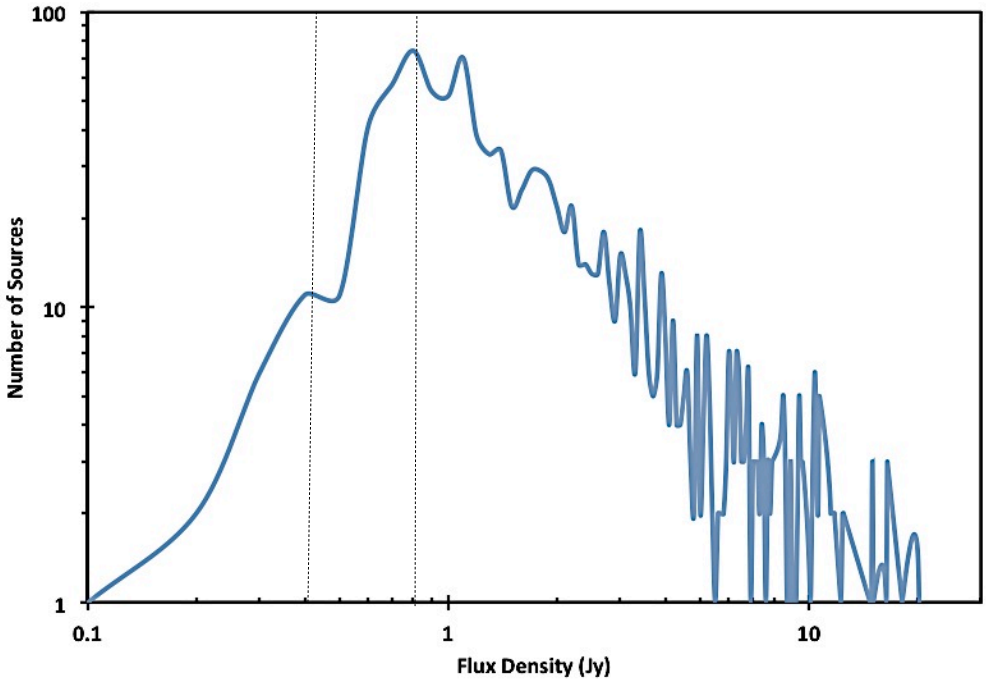

Figure 6.1: A *log N − log S* plot of all 1298 sources detected in WIDE-S from our new catalogue (sampled every 0.1 Jy). The 1st peak is at 0.4 Jy and the 2nd is at 0.8 Jy.

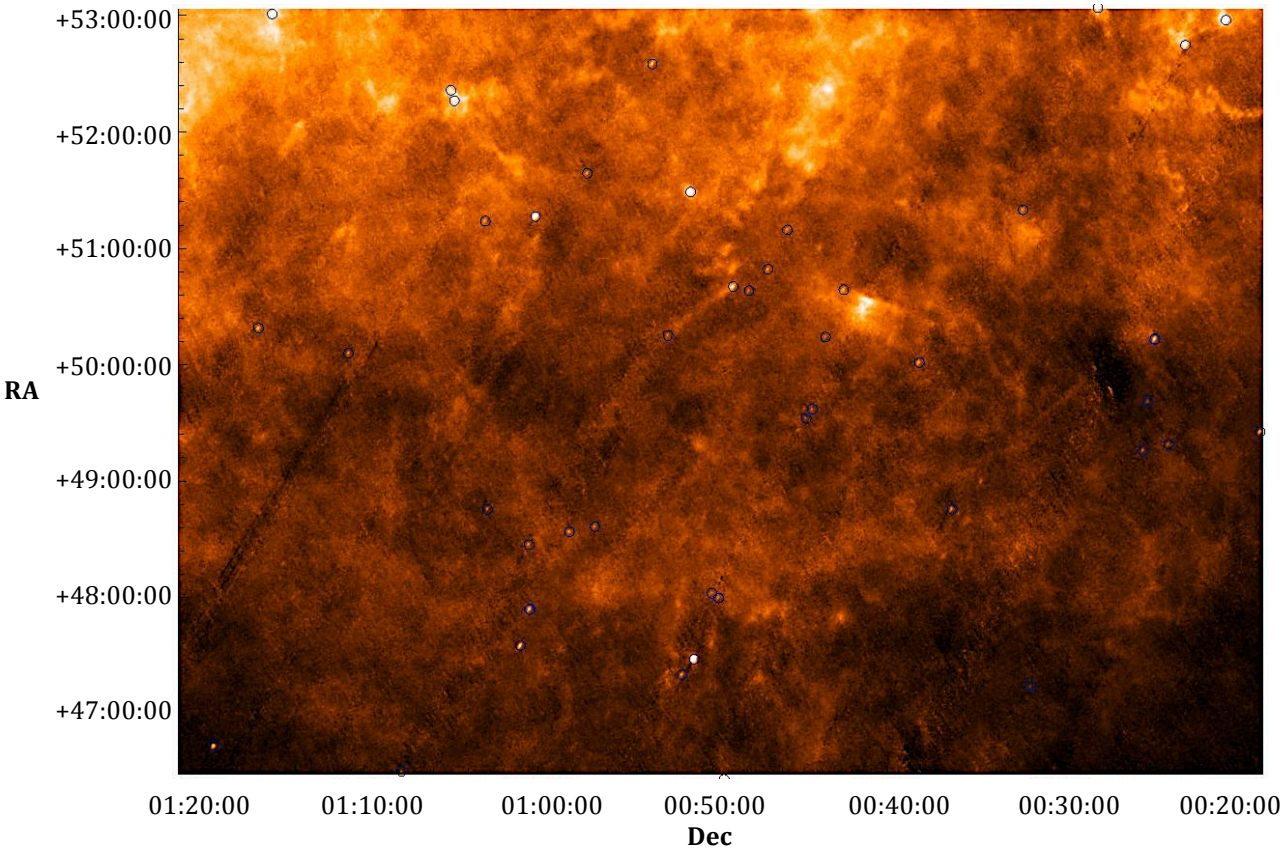

Figure 6.2: Frame 366 of band WIDE-S. Instrumental artefacts evident as striping on the left of the image as well as the widespread diffuse emission made point source extraction challenging. The final edited catalogue of realistic source locations is overlaid (represented as blue circles).

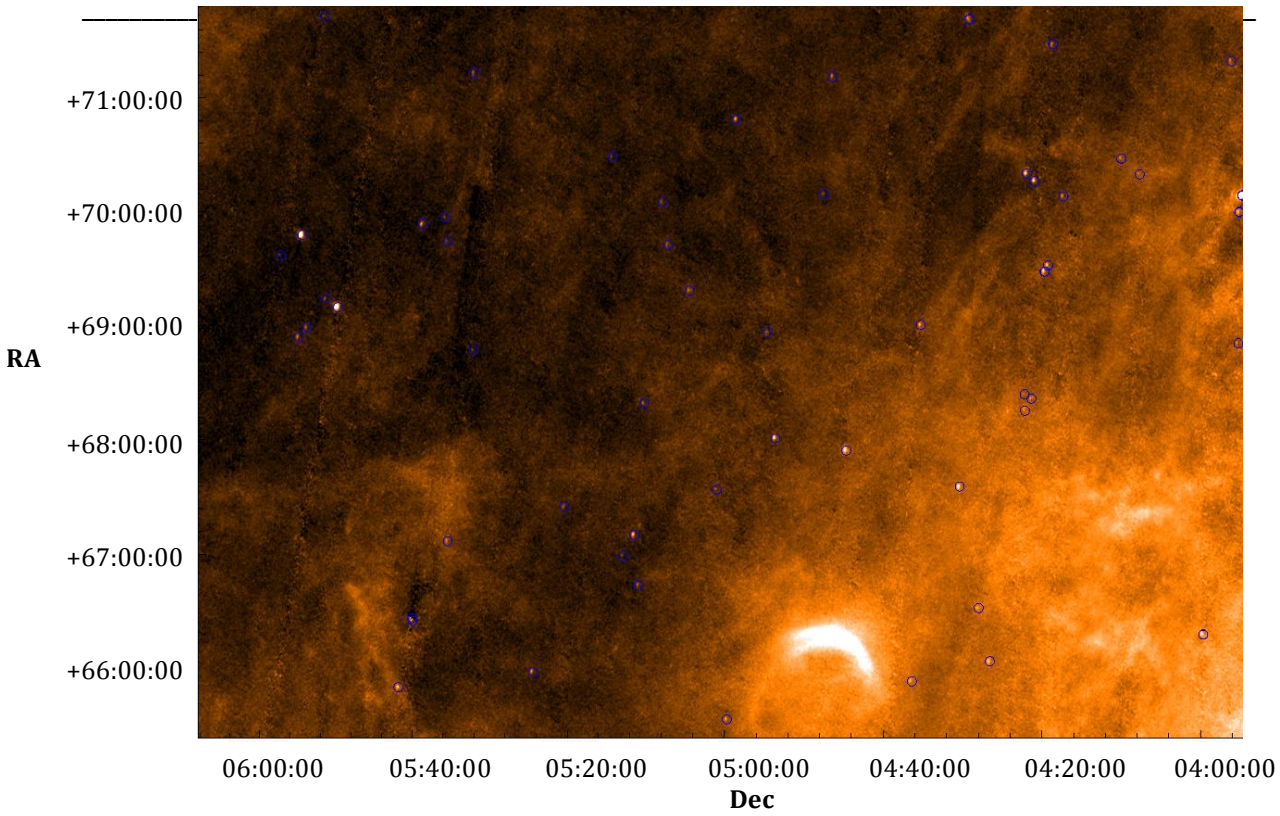

Figure 6.3: Frame 411 of band WIDE-S. The final edited catalogue of realistic source locations is overlaid (represented as blue circles).

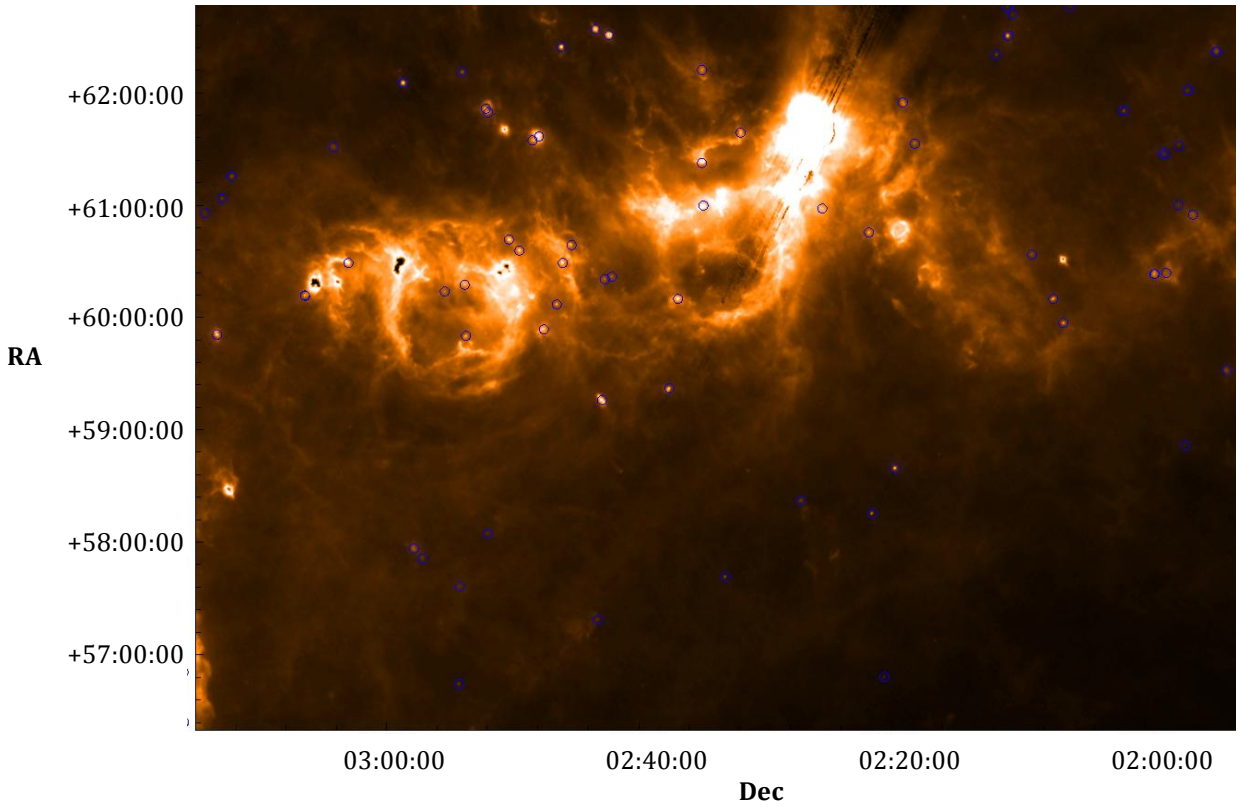

Figure 6.4: Frame 391 of band WIDE-S centred on the familiar W3/W4/W5 star forming complex.

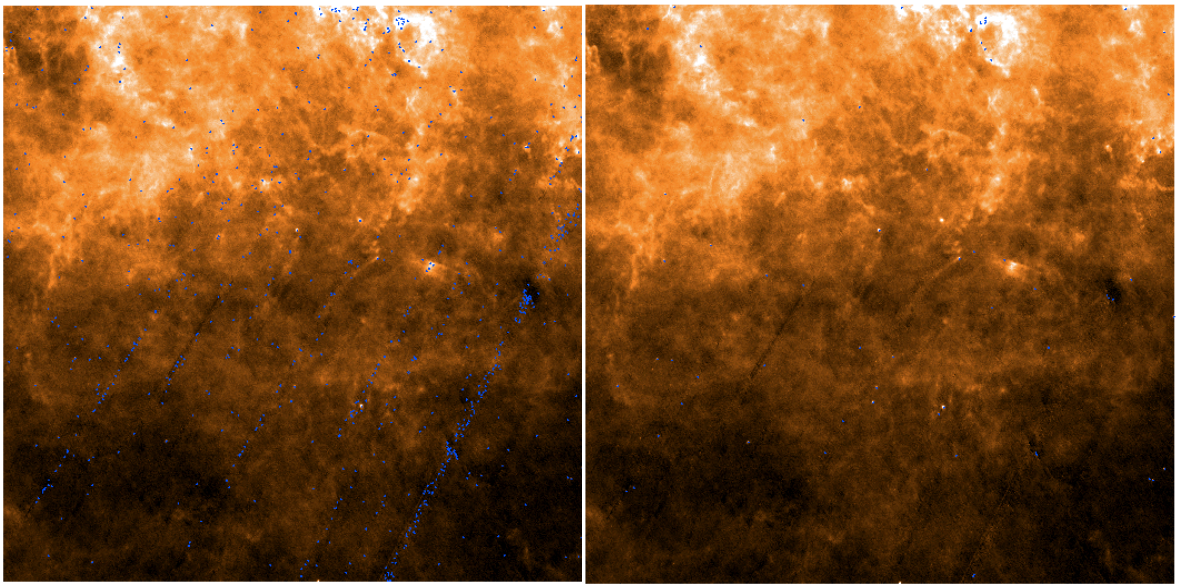

Figure 6.5: A close up of frame 366 with an overlay of detected sources using SXT. A detection threshold of 5 σ on the left picked up much of the instrumental artefacts evident in the striping effect towards the bottom left. On the right, 10 σ was used, which inevitably still picked up much bright diffuse emission at the top.

6.3.2. Flux Comparison with the AKARI Bright Source Catalogue

The TOPCAT software (§ 4.2.1) was used to compare and examine the correlation between the SXT fluxes and the AKARI BSC using a search radius of 5″. Before any official flux measurement, fluxes were extracted for all frames at each wavelength in a quick analysis to verify that there was no significant frame-to-frame variation which would have introduced a *random* error to the absolute flux values. With no evidence of random error, the next check was to examine whether the fluxes of the maps were off by a *constant* offset when compared to the BSC and if a justifiable scaling factor was needed (perhaps due to a systematic fault for example). A ~1:1 correlation signified that the new AKARI catalogue fluxes were in the same ballpark as the established BSC, supporting the fact that calibration and flux measurement of the new maps was sufficiently accurate: an important verification as we were still in the testing stage for these data.

Another initial test was to check which source extractor gave the best quality results for our data. The fluxes obtained with the DAOPHOT extractor (Stetson 1987) gave a poorer agreement with the BSC after optimal parameterisation for faint source detection as described for SXT. In comparison SXT fluxes have a tighter correlation as shown in Figure 6.6. This may be due to the different way the

algorithms deal with the bright diffuse background. SXT was more sophisticated in this respect: the option of 'Fit Background' was set as true allowing simultaneous estimation of local background flux as well as source flux, when fitting the Gaussian point response function to the source. This consideration of the background was also advantageous for detection of the fainter sources which could possibly be obscured. DAOPHOT did seem to miss a lot of these fainter sources even with a low detection threshold. There were options in DAOPHOT to account for the inner and outer sky annulus around each source, allowing photometry within the source aperture, and then subtraction of flux within the sky annulus assuming this is the background. The default values seemed too small causing too much subtraction from the source flux and larger values were optimised and used in the comparison of Figure 6.6. In all of the following correlation plots (Figures 6.6 to 6.10), the AKARI BSC flux uncertainty is ~15% of the absolute value (Y-axis error bars) for all bands (Yamamura et al. 2010). We do not show the X-axis error bars (SXT and DAOPHOT extracted sources) for clarity but they are of order 1-5 % of the total magnitude for the majority of sources across all bands. The red Y=X trend-line is shown to compare the scatter of fluxes around the optimal correlation.

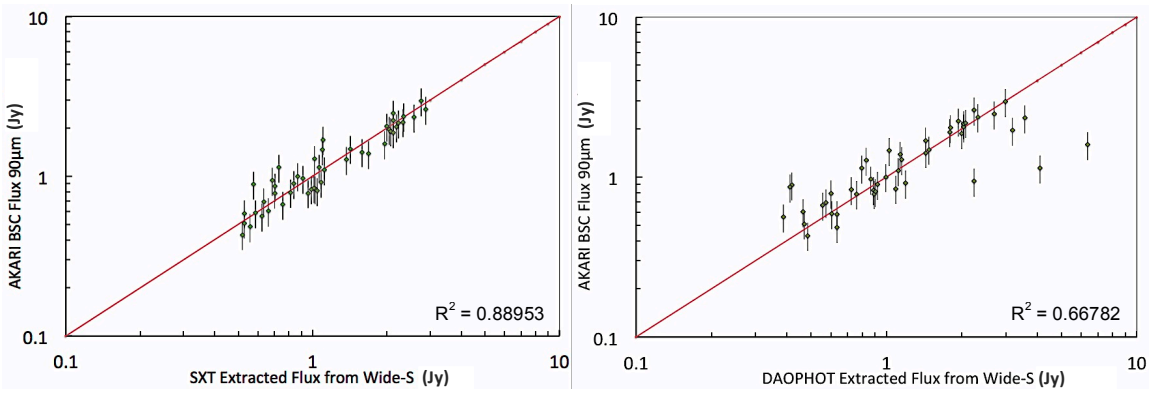

Figure 6.6: Fluxes extracted from frame 366 of WIDE-S. The results obtained with SXT on the left give a better correlation with the AKARI BSC than DAOPHOT on the right. The red line represents a 1:1 correlation X = Y.

6.3.3. Photometry & Band-Merging

After photometry was conducted for the remaining 3 filters at the WIDE-S source list positions, a final band-merged catalogue was produced (Appendix E). Further editing was carried out where a flux detected in WIDE-S was not 'seen' in an ancillary band (evident as a null value) probably due to

sensitivity limits of the detectors, particular the high limit of N160 (as detailed by Etxaluze 2010) which is left out completely from investigations by Arimatsu et al. (2014). WIDE-S as expected shows the best correlation with the BSC (Figure 6.7) although the brighter fluxes are more scattered from the general correlation from ~20 mJy. Missing fluxes from AKARI FIS ancillary bands (primarily from N160 at the longest wavelength of 160 μm) does limit analysis in § 6.3.4 particularly when constraining the black-body curves for colder proto-stellar objects and very cold pre-stellar cores where the star formation processes are taking place (Etxaluze 2010).

The relationship between the WIDE-S, WIDE-L and N160 fluxes and the BSC fluxes is more or less 1:1 within the errors. The scatter in WIDE-L could be explained by the severe contamination by the background emission for fluxes of standard stars which are relatively low (Arimatsu et al. 2014). As anticipated, N60 and N160 were much noisier which explains the large scatter in the fluxes below ~1 Jy which is due to instrumental noise (Kawada 2007). This was why there was a 3.2 Jy cut off in the BSC and a 12 $MJysr^{-1}$ cut off in the All-Sky maps for the N60 band (Yamamura et al. 2010). Of all the bands, N60 band had the worst correlation and the fluxes also seem to be off by a systematic offset (Figure 6.10). A caveat could have been used to correct the overestimation of the fluxes in N60 compared to the BSC but was not deemed necessary since the correction is between 1 – 10 Jy which would manifest as only a small percentage correction, and we preferred to keep the methodology of all the bands as *consistent* with each other as possible. Perhaps this is something to investigate in future work to improve the accuracy of the current catalogue.

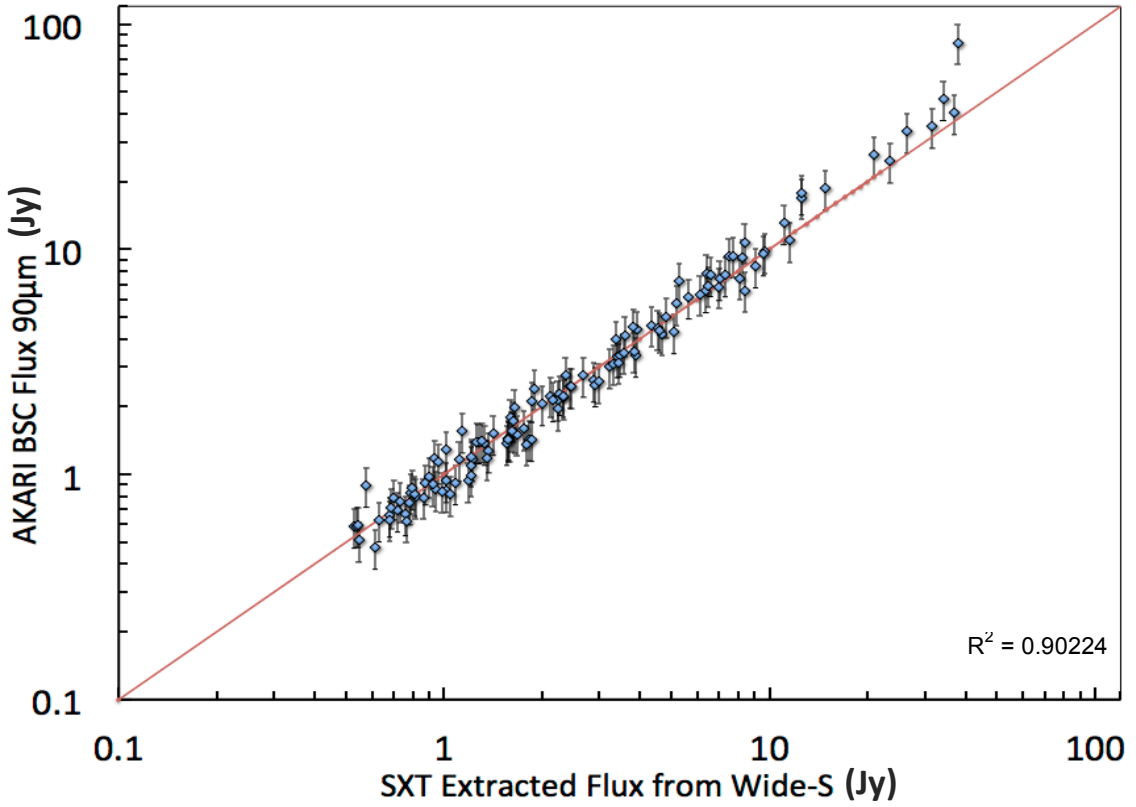

Figure 6.7: WIDE-S fluxes derived from all frames using the in-scan FWHM 93″ in SXT compared with AKARI BSC fluxes.

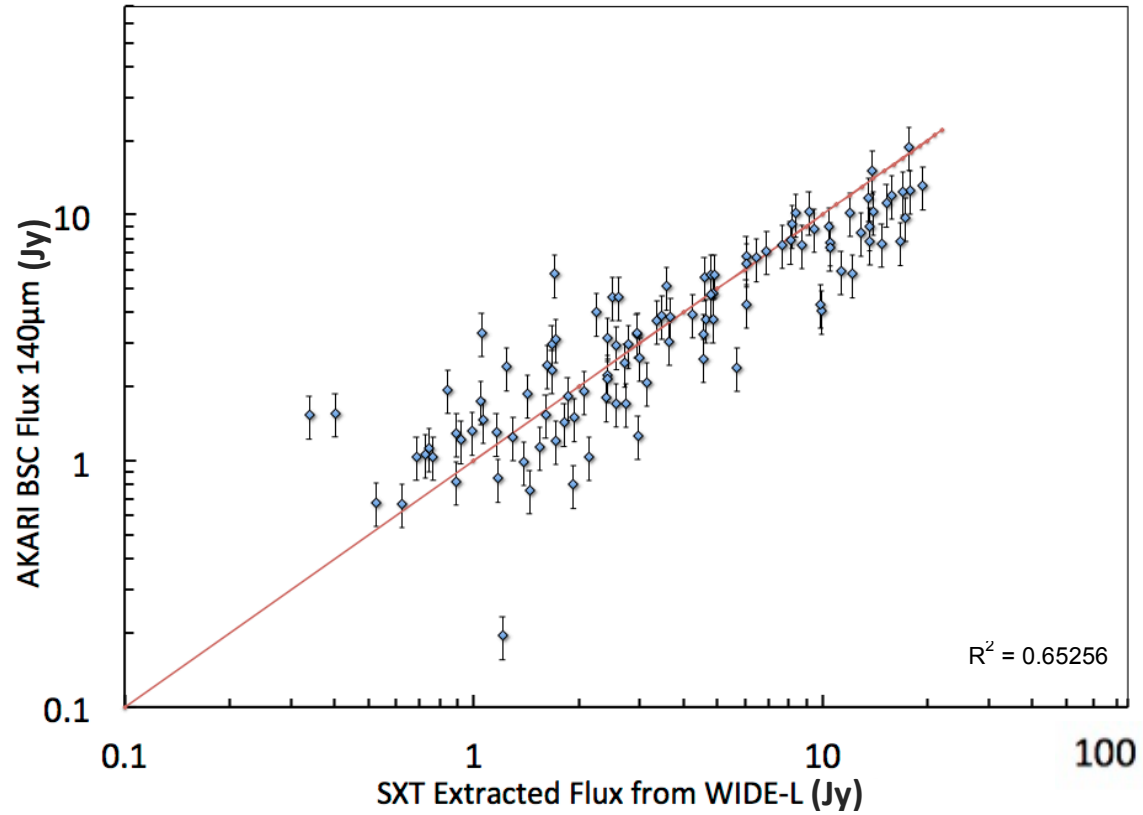

Figure 6.8: WIDE-L fluxes derived from all frames using the in-scan FWHM 107 ″ in SXT compared with AKARI BSC fluxes.

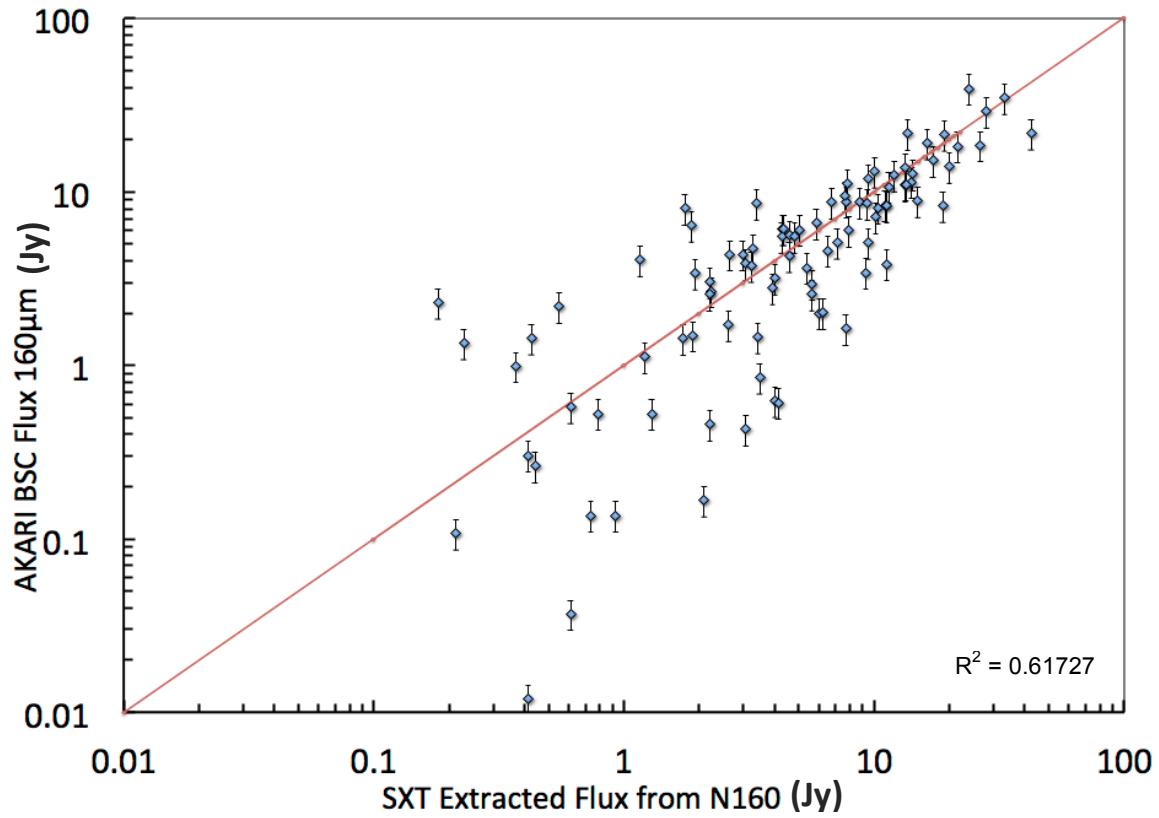

Figure 6.9: N160 fluxes derived from all frames using the in-scan FWHM 94 ″ in SXT compared with AKARI BSC fluxes.

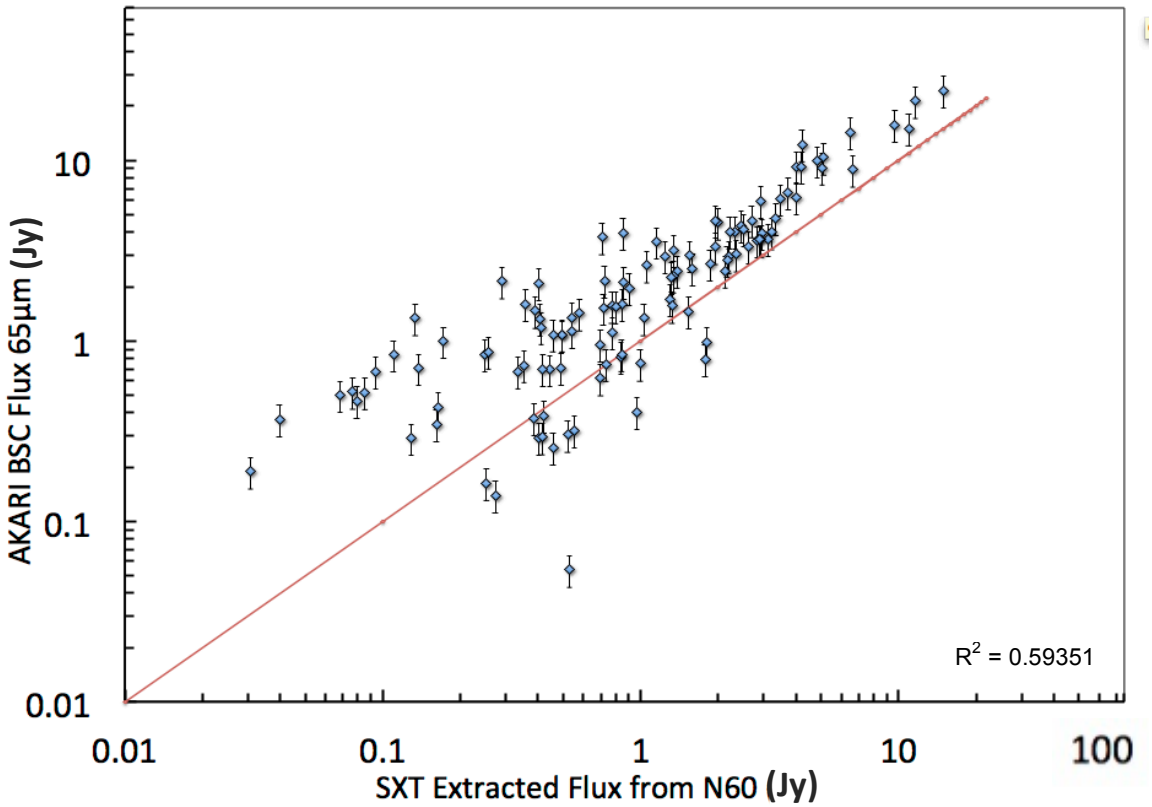

Figure 6.10: N60 fluxes derived from all frames using the in-scan FWHM 74 ″ in SXT compared with AKARI BSC fluxes.

6.3.4. Initial AKARI Point Source Analysis

Please refer to § 7.4, where we attempt to conduct black-body and grey-body analysis for our AKARI sources. For many of our AKARI FIS sources, it was difficult to constrain the grey-body fits especially in cases where a flux had not been detected at all of the wavebands in the far-IR wavelength range. Images made with the Spectral and Photometric Imaging Receiver (SPIRE) located on the HERSCHEL space observatory launched in 2009, were obtained to give complementary flux information towards sub-mm wavelengths at 250 μm (PSW band), 350 μm (PMW band) and 500 μm (PLW band) in the hope of confirming the trends seen at FIS wavelengths. We used complimentary maps taken from the *HERSCHEL science archive* and HERSCHEL data is also analysed independently in § 7.4.2. In the same way as with the new AKARI maps, the SXT algorithm was used within HIPE to carry out photometry at the established WIDE-S source list. Since AKARI is a 0.67 m telescope, and HERSCHEL is a 3.5 m telescope, this results in drastically different beam-sizes reflected by the FWHM values listed at each SPIRE observing band by Valtchanov (2014), which were used for the photometry. However, conducting photometry with the SPIRE maps was not trivial. One issue arose with the SXT algorithm, which took the AKARI locations and if the exact RA and Dec were not in the SPIRE frame, it would wrap around and extract a flux at a random location. The second issue was that the total areas of the 8 SPIRE frames do not cover the entire region of AKARI continuously on account of being targeted observations of specific star-forming regions. To try to get as many accurate source matches as possible, the AKARI locations (represented as small cyan circles in Figures 6.11 & 6.12) were overlaid on the PSW images using HIPE. TOPCAT was used to cross match the SPIRE SXT fluxes with the AKARI catalogue and these was also overlaid (represented as larger green circles). Each frame was examined to make sure no AKARI locations were missed in the SPIRE matches, whilst avoiding any SXT randomly generated flux. This meant experimenting with the matching error within TOPCAT which varied between 40″ – 60″. This value was high due to the combination of positional errors for both the AKARI and HERSCHEL telescopes; of these AKARI has greatest positional uncertainty (Etxaluze 2010). In total there were only ~90 matches (out of ~ 1300 sources) in the cross-matched catalogue due to the smaller sky coverage of the SPIRE maps.

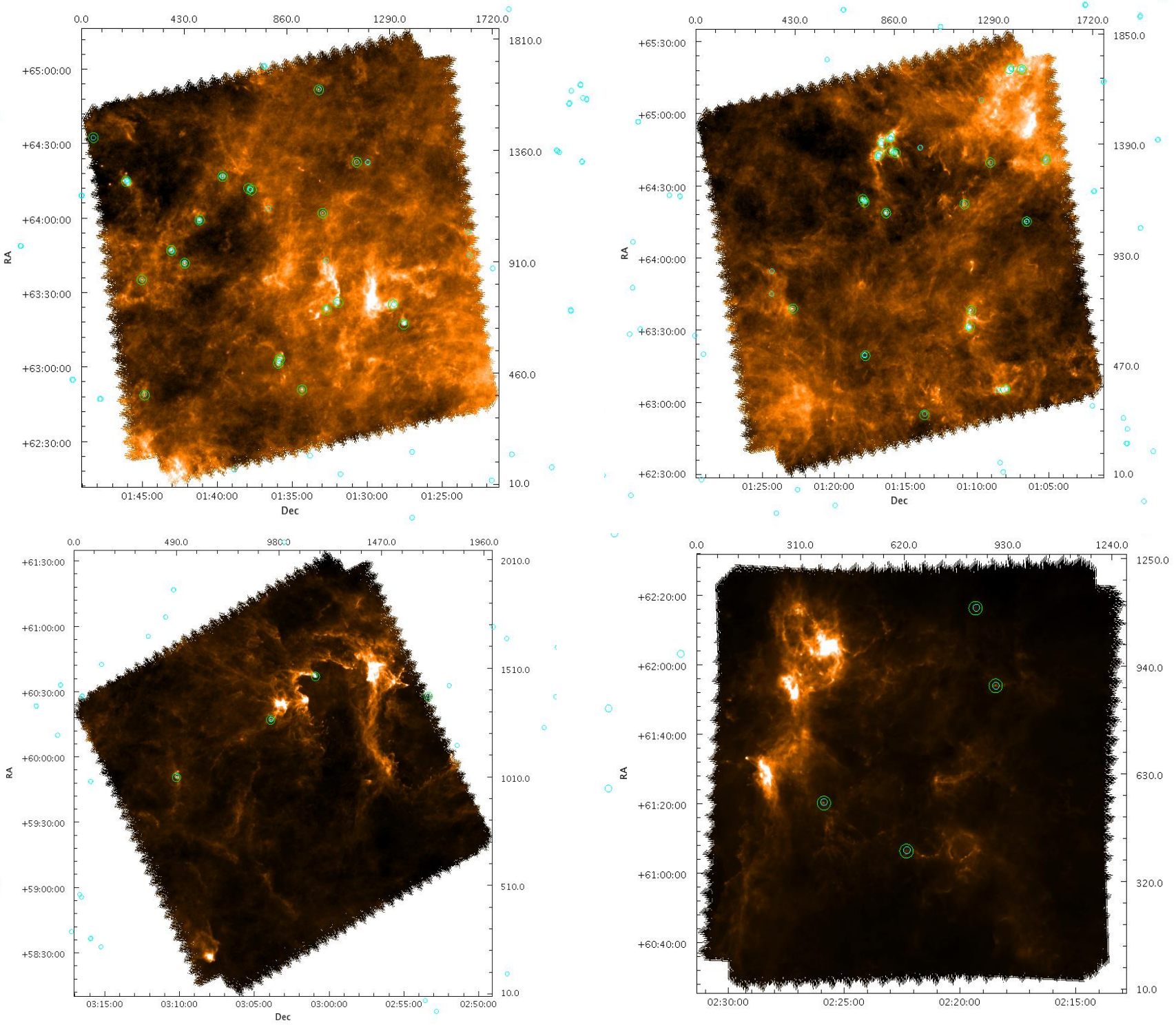

Figure 6.11: Photometry using locations of faint source detection in AKARI FIS (represented as green circles) maps on HERSHAL frames.

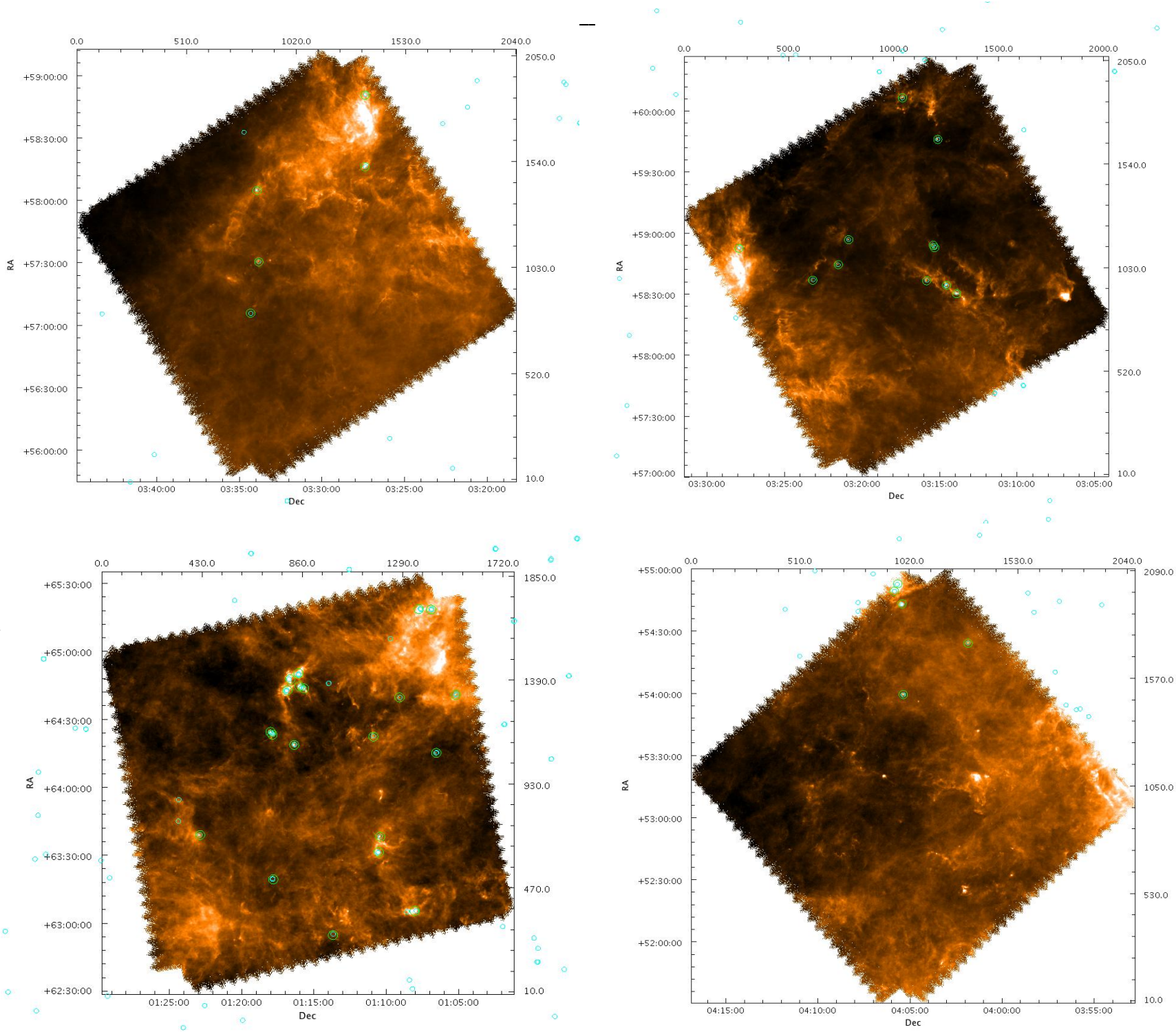

Figure 6.12: Photometry using locations of faint source detection in AKARI FIS (represented as green circles) maps on HERSHAL frames.

Correlations Between our AKARI Point Source Catalogue & Radio Catalogues

We cross-matched our new AKARI catalogue of 1298 point sources with our LOFAR point source catalogue (§ 4.1), to see if we could better identify extragalactic sources particularly in the W3/W4/W5 region. However, this resulted in 0 matches using a search radius of 20″ in TOPCAT. We then used the same search radius and found 6 matches with the VLSSr radio catalogue and 166 matches with WENSS radio catalogue. The correlations with WENSS are shown in Figures 6.13 and 6.14 for the AKARI WIDE-S 90 μm band and the AKARI WIDE-L 140 μm band respectively. The dotted lines are the equations of these trends: $S_{Radio}^{92cm} = (11.1 \pm 0.8) \times 10^{-3} S_{\mathrm{far-IR}}^{90\mu m}$ and $S_{Radio}^{92cm} = (5.6 \pm 0.6) \times 10^{-3} S_{\mathrm{far-IR}}^{140\mu m}$. Given the spread of the data (reflected by the large error bars of these correlations), these trends are only approximations and whilst the great majority of our AKARI catalogue sources do not match with the radio catalogues, ~ 12.8 % of the sources do; these matches are expected to be extragalactic in origin since the 325 MHz WENSS survey is likely to sample the radio-loud AGN and radio starburst galaxies and distant quasars (§ 2.3.7 & § 2.3.9) which emit by synchrotron radiation.

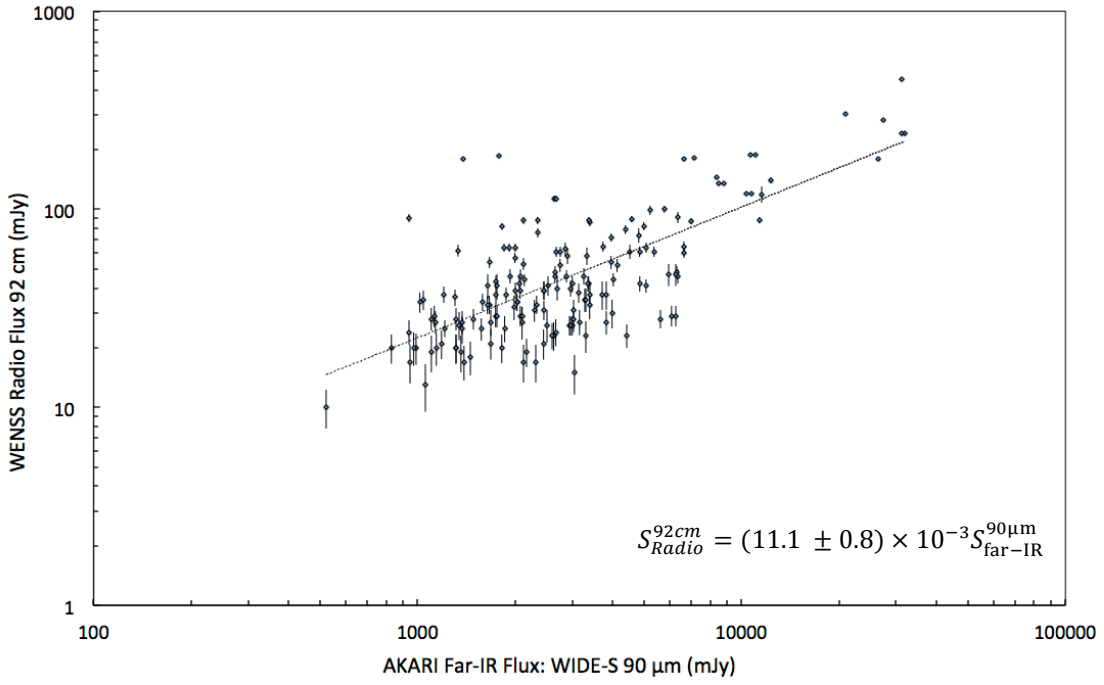

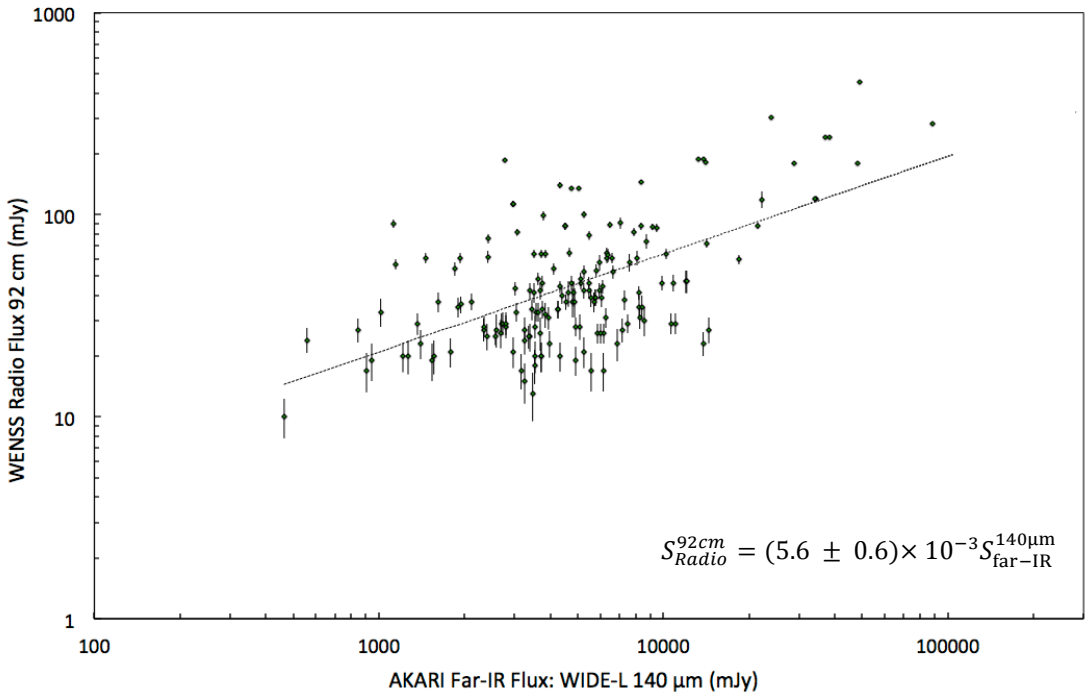

Figure 6.14: Figure 6.13: The correlation of the source matches between our AKARI catalogue (WIDE-L 140 µm band) and the WENSS radio catalogue.

Chapter 7

Water Maser & Far-IR Survey of W3/W4/W5

7.1 Aims

To support the radio observations of the W3/W4/W5 regions, we have carried out a survey to search for H_2O maser sources at the positions of far-IR sources in the field. In addition to (i) re-observing already known maser sources, the objective is to (ii) carry out a more *thorough* sampling of far-IR sources across a high mass star forming region and (iii) to search for *low-luminosity* H_2O masers. Our sample focuses on *very low luminosity* AKARI and HERSCHEL objects in W3/W4/W5 to explore the link between pre-stellar cores (§ 1.3.1) where the H_2O maser detection rates are low, and Class 0 proto-stars (§ 1.3.2), where the H_2O maser detection rates are likely to be high. Therefore AKARI and HERSCHEL sources can be used to define a well specified (and accurately positioned) sample of: (i) young proto-stars with low temperatures; and (ii) low luminosity point-like proto-stars with bolometric luminosity, $L_{bol} < 1\ L_{\odot}$. The far-IR source properties are determined from SED fitting which can allow careful selection of sources that mark the earliest stages of the self-luminous phase of young, *cold* proto-stars (see § 1.3). Interpreting the detection rates of H_2O masers has been complicated by (i) *statistical incompleteness* in the various surveys to date, and (ii) the lack of sufficient sensitivity in the large-scale targeted H_2O surveys. We hope to address these 2 factors

with (i) our large sample (§ 7.3) and (ii) the high sensitivity of the Onsala Space Observatory (OSO), a 20m radio telescope dish located in Onsala, Sweden which provides sufficient sensitivity to be able to detect faint spectral lines of low luminosity masers down to ~60–70 mJy (§ 7.2).

7.2. The Luminosity Relation between L_{H_2O} & L_{bol}

The characteristics of H_2O maser sources and their association to YSOs in star forming regions is well established (Valdettaro et al. 2001) with a strong correlation demonstrated by Figure 7.1 between H_2O maser luminosity vs. associated bolometric luminosity of all published water masers published up to 2012.

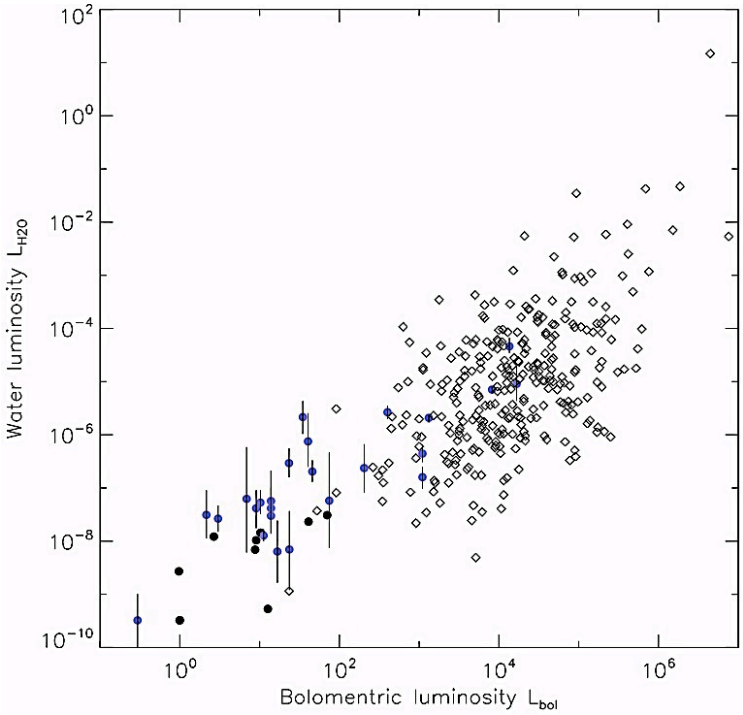

Figure 7.1: A *sample* of all published water masers up to 2012, which demonstrates how the luminosity of the associated far-IR source, and that of their H_2O masers is well correlated. Lower luminosity masers are less-determined owing to their greater variability, reflected by the large error bars (see § 7.3). Beige circles represent previous H_2O maser surveys but is primarily from Urquhart et al. (2011) and the blue circles represent the H_2O maser survey by Furuya et al. (2003) where the luminosities have been corrected as described by Furuya et al. (2007). The black circles represent the maser luminosities for the sources that have been detected only once during the monitoring by Furuya et al. (2007).

Depending on the *luminosity* of the associated star-formation regions, the maser luminosity, L_{H_2O} appears to correlate well with the YSO luminosity at far-IR wavelengths, $L_{\mathrm{far-IR}}$. This relation is $L_{H_2O}^{upper} = 6.37 \times 10^{-8} L_{\mathrm{far-IR}}^{0.81\pm0.07}$ according to Brand et al. (2003, 2005) and Valdettaro et al. (2001) where $L_{H_2O}^{upper}$ is the *maximum* luminosity the maser source can have. Furuya et al. (2007) found this relation to be $L_{H_2O} = 2.58 \times 10^{-8} L_{\mathrm{far-IR}}$ for the *mean* of the water/bolometric luminosity plot (please refer to § 7.7; Figure 7.24 for more details).

For proto-stellar sources at *high* luminosities (where $L_{bol} > 100\ L_{\odot}$) previous surveys have reported high H_2O maser detection rates (up to $\geq 50\%$). In contrast, numerous surveys published to date appear to indicate a minimum bolometric luminosity, L_{bol} (where $L_{bol} \sim 25\ L_{\odot}$) below which H_2O maser emission is detectable for *only* 30% of the masing phase (Persi et al. 1994 and Claussen et al. 1994). There is also an additional uncertainty in the apparent link between L_{bol} of YSOs and that of their collapsing envelopes; Kenyon et al. (1990) show the *liberated accretion luminosity* may be up to 10 times brighter than that of the proto-stellar photosphere.

The effects of the interaction between YSOs and their natal molecular cores (see end of § 1.3.2) on masers is not well-defined although masers are known to be *amplified* in the presence of (1) proto-stellar jets (evident by an apparent relationship between the H_2O and 6 cm radio luminosities given by $L_{H_2O} = 2.74 \times 10^{-19}\ L_{6cm}^{1.48}$) and (2) abundant high-density gas (i.e. a dense envelope). Hence, these particular phenomena could amplify low luminosity H_2O masers (associated with declining proto-stellar bolometric luminosities); this low bolometric luminosity phase remains scarce, due to limitations on the sensitivities of pre-existing surveys. Taking advantage of the sensitivity of the OSO telescope enables the current study of this data range for a large sample of objects with the aim of better defining their relation to their associated very low luminosity proto-stars; we also have the unique advantage of using the latest AKARI and HERSCHEL proto-star surveys to efficiently guide our source selection. Previous attempts to correlate far-IR colours (§ 7.8) with H_2O masers have achieved limited success (Palagi et al. 1993), with the bolometric luminosity of proto-stars and their associated H_2O masers and showing only a *weak* correlation (Wilking et al. 1994) down to H_2O luminosities $\sim 10^{-9}\ L_{\odot}$ (Furuya et al. 2001, 2003, 2007). The OSO telescope was used to target the low end of the far-IR luminosity function (focussing on low luminosity IR sources of $L_{bol} = 0.1 - 50\ L_{\odot}$). The aim was to search for evidence of associated low luminosity H_2O masers (with fluxes between ~60–70 mJy which OSO would have the sensitivity to detect) in the nearest star-formation regions (Gomez et al. 2006 and Wang et al. 2006) in a large sample of unprecedented size (§ 7.3). This work is part of a larger study (outside the scope of this thesis), which will bring together the results of this programme with other

surveys to explore not only this low luminosity regime, but also how other factors such as radiation, ionisation and shocks may influence the maser emission.

7.3. Our Sample & Methodology

Furuya et al. (2001, 2003) used the NRO 45 m telescope and detected H_2O masers towards ~ 40% of their sample of *low luminosity Class* 0 sources (where $L_{\text{far-IR}} < 10^2\ L_{\odot}$) which is a very high detection rate compared to star-formation regions believed to be at *an earlier stage* of their evolution (e.g. Bok globules; § 1.3.1). Low luminosity YSOs can be efficiently identified from sub-mm or far-IR surveys (§ 1.3.3) by telescopes such as the Infrared Space Observatory (ISO), the Midcourse Space Experiment (MSX), AKARI and HERSCHEL.

Surrounding gas and dust in the molecular clouds absorbs and re-emits proto-stellar radiation at long wavelengths with a specific spectral profile (§ 7.4.1) reflecting the properties of the region (e.g. Adams & Shu 1986, Adams et al. 1987 and Myers et al. 1987). Only during the later stages of star formation can the proto-star can be observed at UV and visible wavelengths, when it is hot enough for its radiation to expel and evaporate most of the surrounding material. Hence IR observations allow the studies of the main processes that trigger the star formation inside very dense clouds. Some of these proto-stellar sources were *too cold* to be detected in previous surveys by the Infrared Astronomical Satellite (IRAS) since they do not contain a substantial quantity of warm dust. The AKARI and HERSCHEL surveys detect sources in the 65–500 mm wavelength region with 5 σ detection levels 0.05–0.5 Jy and positional accuracies of about 4″.

Low luminosity YSOs are believed to be associated with *low luminosity* maser sources (§ 7.2), which may be more episodic/variable (reflected in the large error bars of low luminosity sources in Figure 7.1) in comparison with more stable H_2O maser sources associated with more luminous YSOs. This has been established by historical monitoring observations (e.g. White 1979, White & Macdonald 1977, Little, White & Riley 1977 and Brand et al. 2005). Therefore, single epoch surveys have been found to be statistically incomplete, as the time variable H_2O masers associated with the low luminosity proto-stars can sometimes give non-detections (i.e. a fraction of masers may be in a 'switched off' state at the time of observations, or simply are not beamed

towards the observer). Therefore *either (i) a* large sample is needed to *statistically* determine the overall properties of the population, or (ii) monitoring observations over long periods of time would be required. This study favours the former by observing a very large sample of targets which will mitigate against the possibility that the masers are 'switched-off' on the basis that a fraction of the sources will *statistically* be observed to be in the 'on-state'; we do not currently know that fraction with any precision although it has been suggested to be ~30% (Persi et al. 1994 and Claussen et al. 1994); see § 7.2. The steps in our study are the following:

(a) In order to characterise the environment of nearby star formation regions (including the W3/W4/W5 complex; our region of interest), a large sample of H_2O maser emission was conducted (which falls outside the scope of this thesis), with a search using the Onsala 20 metre telescope. A catalogue of 2650 H_2O masers was constructed, which lists the locations targeted during observations, using *all known* masers published to date in the literature, as well as by private communication from a number of observers about sources not yet published, that they have detected including Sunada et al. (2009 *in press*).

(b) The locations of the masers were then checked against the far-IR sources of the AKARI Bright Source catalogue (BSC; Yamamura et al. 2010), which was used for the initial target selection. Since the time of our maser observations (§ 7.6) we have an improved far-IR source catalogue from our recently updated (although not yet published) AKARI catalogue (§ 6 and § 7.4.1) and (currently proprietary) catalogue of the HERSCHEL HOBYS (§ 7.4.2) survey the latter of which provided more detailed positions of far-IR sources (see § 7.4.2) for the W3 region in particular; these catalogues cover proto-stars and envelopes with a wide range of luminosities, from a large census of 123 targeted far-IR cores which will help in our understanding of possible luminosity threshold for water masers.

(c) Distance determination helps in the estimation of *luminosities* of proto-stars themselves and is aided by associating the IR sources with nearby star formation regions of known distances; in the case of targeted W3 sources, this assumes that objects are all associated with the distance-determined W3 star formation region. These distance estimates in conjunction with the SED template tool (see § 7.4), which allows black-body and grey-body fitting for all available proto-star far-IR fluxes, can allow our estimation of source luminosities. This enables our sample to focus on

very young gaseous proto-stellar envelopes and objects (typically young Class 0/I or earlier) with *low bolometric luminosities* of ~ 0.2–10 $L_{\odot}$, which would correspond to *average* H_2O luminosities > 10^{-10} – 10^{-8} $L_{\odot}$ (please refer to Furuya et al. 2001 and Felli et al. 1992, where L_{H_2O} = 3.96 x 10^{12} $L_{bol}^{0.8}$; see also Wilking et al. 1994 for the contrast with high luminosity sources).

(d) Finally, the H_2O maser detection rate will be correlated with L_{bol} from this sample of low luminosity sources (like Figure 7.1), and we aim to search for and determine possible *threshold* conditions in the surrounding gaseous environment when maser emission first switches 'on'. These threshold conditions are weakly defined, although they are predicted in models such as those of Elitzur et al. (1989) and Kaufmann & Neufeld (1996). The OSO telescope used to conduct the water maser search has the sensitivity needed to explore this faint luminosity range (§ 7.2) to measure the *onset* of maser emission and to compare against the associated environmental properties.

7.4. Far-IR Source Detections

7.4.1. AKARI Data

The AKARI data was analysed to search for proto-stellar objects (as described in § 6), on the basis of the AKARI 65-160 μm photometry taken from the AKARI plates (Table 6.1). The spectral pass-bands are shown in Figure 7.2 where it is evident that the AKARI data are best suited to constraining the SEDs of sources which peak close to *100 μm,* which is appropriate for cold *proto-stellar* sources (with typical peaks between ~100 – 200 μm; Dobashi et al. 1994), but less so for *cloud cores* where the proto-star has not yet developed i.e. very cold pre-stellar cores (which peak typically towards ~250 μm; Stamatellos & Whitworth 2004) in which case the wavelength range of HERSCHEL (§ 7.4.2) is more suitable.

Grey-body Fitting to a Proto-stellar Source Sample

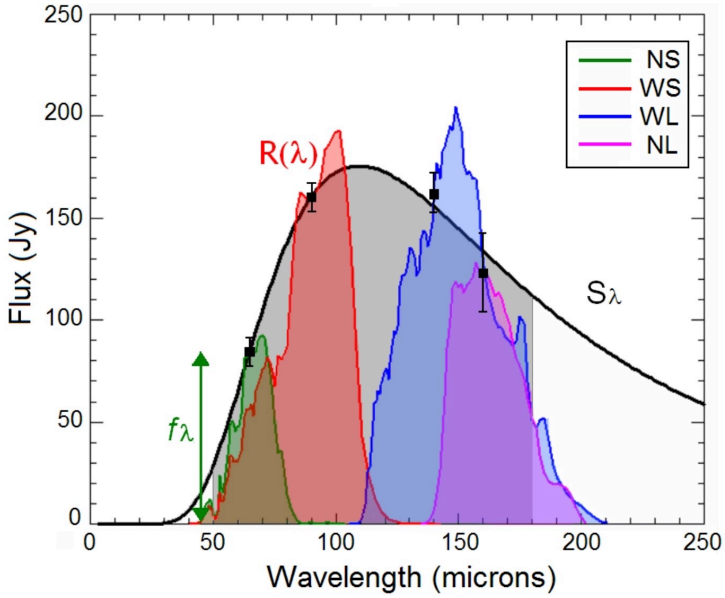

Figure 7.2: Spectral pass-bands of the 4 AKARI filters at 65 (NS), 90 (WS), 140 (WL) and 160 (NL) μm available from the AKARI far-infrared surveyor (FIS) instrument.

A typical SED fit to the data measured from the AKARI plates for a proto-stellar source is shown in Figure 7.3, along with a grey-body fit to the data:

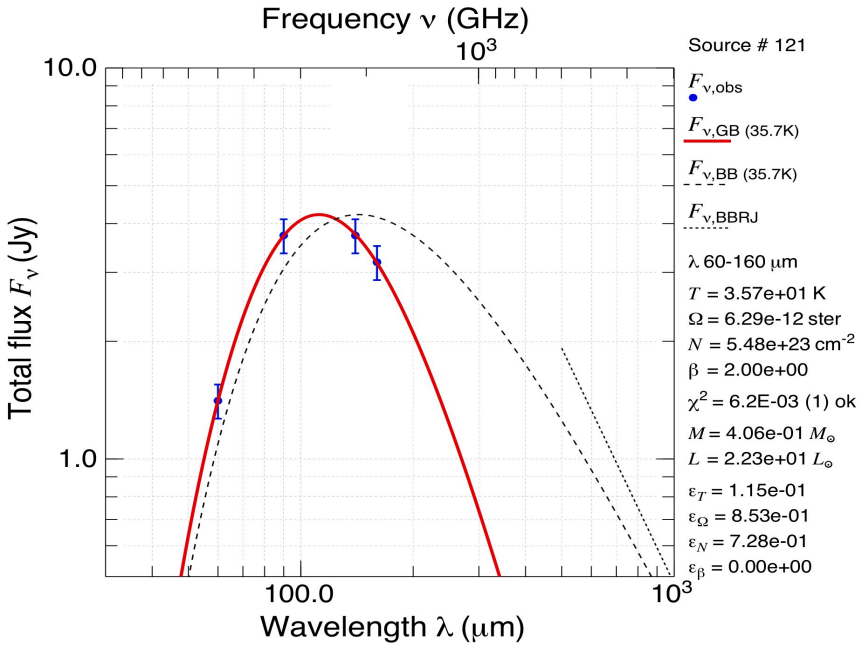

Figure 7.3: SED fit to AKARI data at wavelengths of 60, 95, 140 and 160 μm. The black dots with blue error bars are the data points, and the red line is the best grey-body fit to the data, shown along with a number of derived parameters.

Of the initial AKARI catalogue of ~1300 sources (§ 6.3.1), 1189 were located within ~ 20° of the extensive W3/W4/W5 cloud complex; out of these 1189, 189 sources were found to provide acceptable grey-body fits to proto-stellar sources peaking close to 100 μm based on their χ^2 values. Many more sources had rising spectra that peaked at a wavelength greater than 100 μm, and were

more likely to be trace cool material whose properties are better constrained using the longer wavelength HERSCHEL data; for these sources AKARI data alone would not be able to uniquely constrain grey-body fits. We attempt to look for HERSCHEL matches with our AKARI catalogue in § 6.3.4; however, this was only possible for ~ 90 matches (some of which are amongst the 189 acceptable grey-body fits to sources in the vicinity of W3/W4/W5). For the present study we also analyse HERSCHEL data separately, as a complete set of HERSCHEL data is only available for the W3 region (originally published in Rivera-Ingraham et al. 2013); we examine the properties of the HERSCHEL W3 proto-stellar sources further in § 7.4.2).

The Extended W3/W4/W5 Complex

The AKARI data are used here to trace the compact proto-stellar population of the W3/W4/W5 cloud complex *as a whole*, which is not available from the HERSCHEL data. A plot showing the bolometric luminosities vs. proto-stellar envelope masses of compact sources in the W3/W4/W5 regions and associated molecular clouds is shown below (deduced from the grey-body analysis as described above), along with evolutionary tracks for proto-stars between 0.6 – 20 $M_{\odot}$ taken from André et al. (2008).

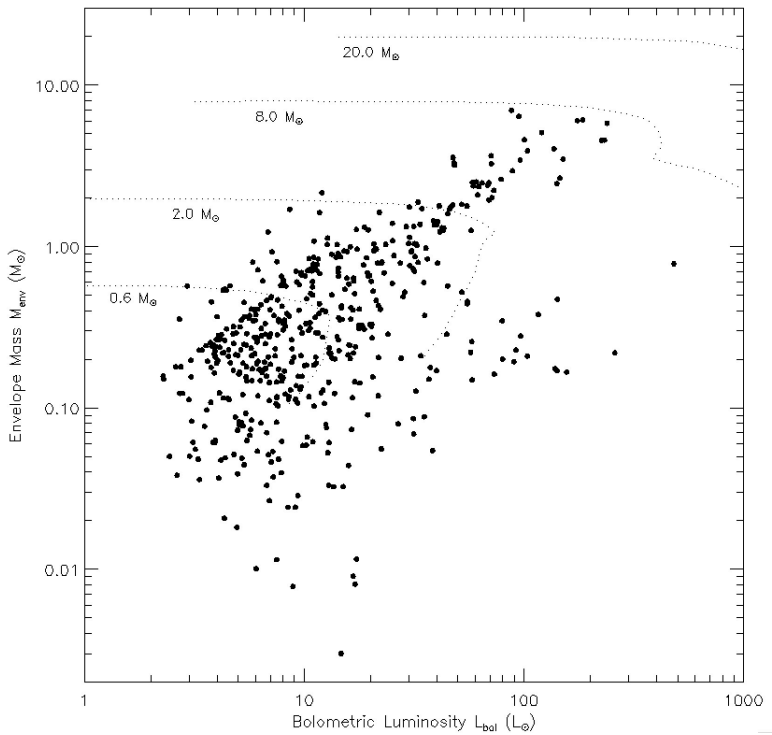

Figure 7.4: Proto-stellar bolometric luminosity vs. envelope mass plot from the AKARI data of the 189 compact sources in the W3/W4/W5 regions and associated molecular clouds, over-plotted with the proto-stellar evolutionary tracks from André et al. (2008) which give some indication of where we would expect a proto-star with a particular mass.

Low mass proto-stars are typically less than a 2 $M_{\odot}$ and high mass proto-stars are typically

between 8 – 20 $M_{\odot}$. Figure 7.4 indicates that we have a few proto-stars approaching the high mass range, lying between 2 – 8 $M_{\odot}$ and that the great majority are low mass proto-stars below 2 $M_{\odot}$. It is likely these proto-stars are the result of triggered star-formation from the radiation and ionisation shockwaves (§ 1.2) of high mass stars.

7.4.2. HERSCHEL HOBYS Data

HERSCHEL data with the Photoconductor Array Camera and Spectrometer (PACS) at 70, 100 and 160 μm and the Spectral and Photometric Imaging Receiver (SPIRE) at 250, 350 and 500 μm are advantageous over AKARI for filling the far-IR continuum towards sub-millimeter wavelengths, allowing the detection of *colder* proto-stellar objects and pre-stellar material providing a better knowledge of the high mass star formation process during its *earliest* stages.

Also, after an initial look at far-IR sources in the W3/W4/W5 complex with AKARI (§ 7.4.1) the new processed HERSCHEL data (see below), were found to have a higher sensitivity (which was advantageous for sources with low bolometric luminosities) and a smaller beam (allowing better discernment of sources in crowded regions). Typically we found that the HERSCHEL survey detected ~ 2 orders more sources than AKARI within a given field.

The W3 GMC

Moore et al. (2007) studied the star forming regions within the W3 GMC (§ 1.4.1) with their 0.9 deg^2 survey using SCUBA at 850 μm, and observed a sample of dense clumps in the mass range 13–2500 $M_{\odot}$, finding evidence of an interaction between the W3 GMC and the W4 shell. Specifically they found that the feedback from fast stellar winds generated by the previous generation of stars in the *W4 OB association* (IC 1805) work to compress one side of the W3 GMC triggering further star-formation (this scenario is briefly described in § 1.4.1). Moore et al. (2007) analyse the mass distribution and fraction of these dense clumps and find an increased fraction towards the *compressed region* of the GMC, compared to the diffuse cloud; their work supports enhanced star-formation efficiency in compressed post-shocked gas. They found their *clump mass spectrum* (which has a lower limit of ~ 13 $M_{\odot}$) does not obey a simple power law but instead shows

an apparent slope reversal at ~ 60 $M_{\odot}$; Moore et al. (2007) suggests this may be an artefact of confusion caused by *source clumping*.

Rivera-Ingraham et al. (2013) found from their examination of luminosity, mass, temperature, column density and stellar content of the W3 GMC, that W3 East, W3 West, and W3-OH which is a young UC H II region rich in OH masers (Dreher & Welch 1981) (as described in § 1.4.1) are the most massive, luminous and highest column density regions of the entire GMC. These regions constitute very dense clumps (typically of ~ 0.4 pc) hosting on-going *high-mass* star formation. Specifically Rivera-Ingraham et al. (2013) carried out their work using HERSCHEL data from the High Mass Star Formation HOBYS keys fields (the same data that we are analysing; detailed below) to identify the 'extreme' properties of this large sample of clumps and cores by probing *column density* and *temperature maps* and corresponding this with the high-mass stellar content; in essence they were constraining the star-formation processes specifically of high mass objects. They concluded, like Moore et al. (2007), that there is material in motion in the W3 GMC which allows the build-up of mass (due to accretion, compression, and confinement of material) during the earliest stages of massive proto-stellar formation. Specifically, Rivera-Ingraham et al. (2013) found that instead of stellar feedback countering the efficiency on-going star-formation (as has been proposed by Dale et al. 2013 and Whitworth 1979 for example; see § 1.2) they favoured 'convergent constructive feedback' where further star-formation can be triggered and enhanced towards the *centres of massive clumps*, resulting in inner younger regions versus an outer older population within the clumps of the W3 region. This is the *dynamical formation* of massive stars (e.g. Motte et al. 2007). At the same time, Rivera-Ingraham et al. (2013) *also* suggest *sequential formation* of high-mass stars in W3 main (confirming Tieftrunk et al. 1997) which are initiated at the *boundaries* of the high column density structures; this would explain the younger stellar populations towards the *outermost* regions of the clusters of W3.

W3 HOBYS survey: Source Extraction

The HOBYS HERSCHEL surveys (observed by Pilbratt et al. 2010) were specifically designed to address the major outstanding issues in high-mass star formation observing regions with high-mass stars at a maximum distance of ~3 kpc, performing a census of massive YSOs. As mentioned, this

was examined for the W3 GMC by Rivera-Ingraham et al. (2013) and we examine these data further; see Figure 7.5 for the W3 molecular cloud at 120 μm and 250 μm and Figure 10 of Rivera-Ingraham et al. (2013) for the same region at also 70 μm, 160 μm, 350 μm and 500 μm.

The W3 source catalogue of Rivera-Ingraham et al. (2013) was not published at the time of our work and was provided in private communication**.** It is likely that these data may be modified before formal publication following updates of more recent versions of the *HERSCHEL HIPE* extraction software (§ 6), although this is anticipated to bring only a *slight* change in the data. Hence the pre-publication data of the Rivera-Ingraham et al. (2013) extraction has been used to estimate the *envelope mass* and *bolometric luminosities* for sources in W3 only, as shown in Figures 7.6 and 7.7 below. We follow the technique previously described by Fallscheer et al. (2013) for determining masses and luminosities of these envelopes to determine the *mass-luminosity function* (see the analysis section below).

Specifically the catalogue of Rivera-Ingraham et al. (2013) was extracted from the multi-resolution HOBYS maps by using the multi-scale, multi-wavelength source extraction algorithm *getsources* (as described by Men'shchikov et al. 2012). This routine works by separating emission across a wide range of angular scales (where each image is decomposed into finely-spaced single scales that are cleaned of noise and their background), using this information to identify sources as peaks relative to their local backgrounds. Objects are then extracted without imposing any parametrisation on either their structure, or on that of the diffuse background. *Getsources* then assigns a shape, size, peak flux, total flux and significance value to each source identified in each waveband. The *getsources* catalogue contained 1087 sources in the overlapped area common to the PACS and SPIRE data, of which, 995, 1043, 864, 829, 779 were detected at 70, 160, 250, 350 and 500 μm respectively. In total 69 of the sources with 70 μm detections in the overlap region had associated 500 μm emission, while approximately 98 and 99 of sources detected at 500 μm had associated 160 and 250 μm emission respectively. It therefore seems that this region contains a large fraction of (cool) sources whose spectra peak within the SPIRE wavebands, or at even longer wavelengths.

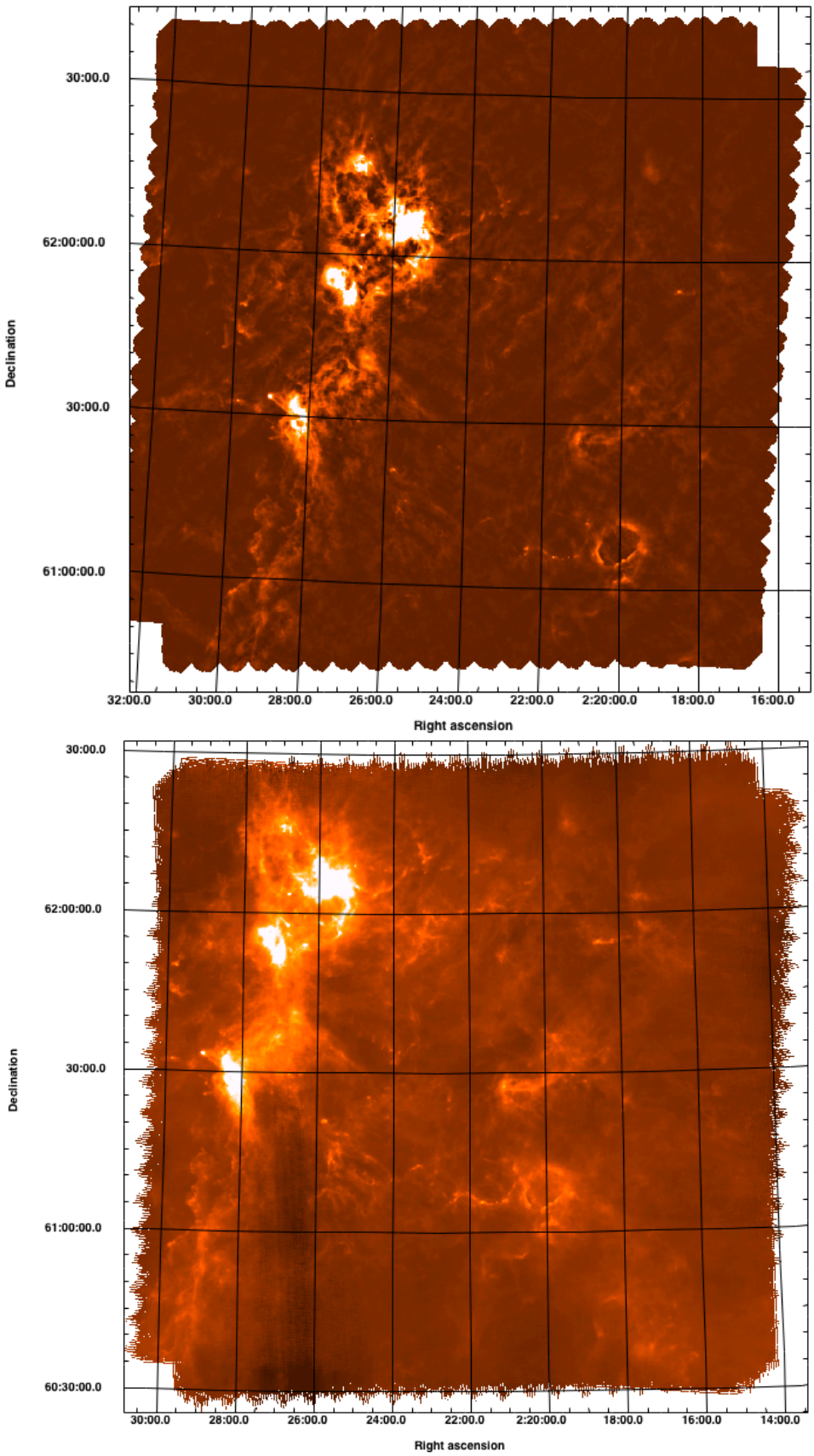

Figure 7.5: HERSCHEL images of W3. PACS 120 μm (top) and HERSCHEL SPIRE 250 μm (below). The PACS wavelengths are suitable for hotter regions, whilst SPIRE detectors are suitable for cooler material emitting at relatively longer wavelengths. Please note the above images are not on the same intensity scale.

W3 Source Analysis

The properties of *clumps* detected in the W3 HERSCHEL image were then examined. The individual luminosities themselves were estimated using the grey-body fitting described in § 7.4.1 and integrating under their grey-body curves extrapolated from 2–2000 μm (or the range involved) assuming an emissivity index of $\beta = 2$. The envelope *masses* were estimated by using the relationship described by Motte et al. (2010) and estimating the *ratio* of their sub-mm (350 μm) to HERSCHEL (70–500 μm) bolometric luminosities and using the 350 μm fluxes and source sizes, after applying the wavelength-dependent scaling correction proposed in that paper, and discussed in more detail by Reid et al. (2010) and Nguyn Lu'o'ng et al. (2011).

Only sources with multiple (≥ 4 wavebands) detections, with a combined S/N ratio of ≥7 σ and individual S/N ratios in each band of ≥5 σ have been included for the analysis. Since data were not included at wavelengths shorter than 70 μm, it is likely that some of the mass estimates for the envelopes of the Type I SED sources may be low. In total, *134* sources within W3 were identified as showing *Class I* SEDs and *137* showed *Class 0* SEDs (see classification criteria in § 1.3.3), of which *80* had envelope masses $M_{env} \geq 20\ M_{\odot}$ and $L/M_{env} \leq 1.0$ representing a *significant population* of massive *pre-stellar* clumps, and *298* sources had SEDs intermediate *between the two Classes*. Pre-stellar clumps provide an important link between the properties of newly formed proto-stars and the global processes that determine and regulate large-scale star-formation. The luminosity and mass data are shown as an *L vs.* M_{env} evolutionary diagram (Molinari et al 2008) in Figure 7.6, with the luminosities ranging across ~ 5 orders of magnitude, i.e. $0.1 \leq L \leq 20{,}000\ L_{\odot}$, and envelope masses spanning ~ 4 orders of magnitude, i.e. $0.3 \leq M_{env} \leq 3{,}000\ M_{\odot}$.

Figure 7.7 shows a substantial number of cores up to a few thousand solar luminosities, have a *distribution* similar to that seen in other high mass star forming regions (e.g. M16 & M17 - White et al. *in preparation*; NGC7538 - Fallscheer et al. 2013).

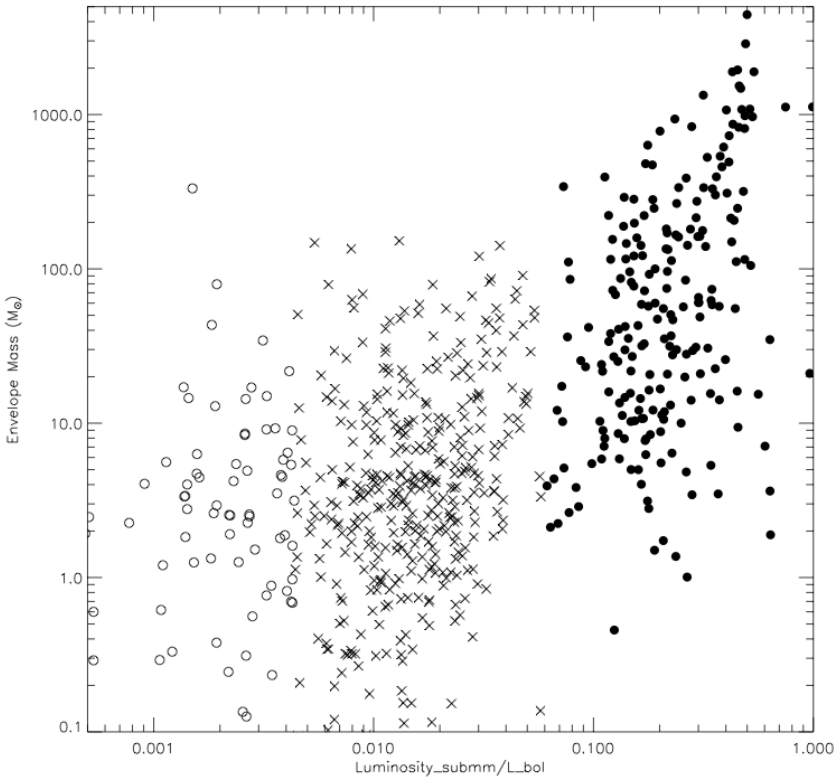

Figure 7.6: Using the W3 source catalogue of Rivera-Ingraham et al. (2013) to determine envelope *mass vs. the bolometric/submm luminosity ratio*. The black and white circles and the crosses represent the different classes of SEDS as described above i.e. Class 0, Class I and sources between the 2 respectively.

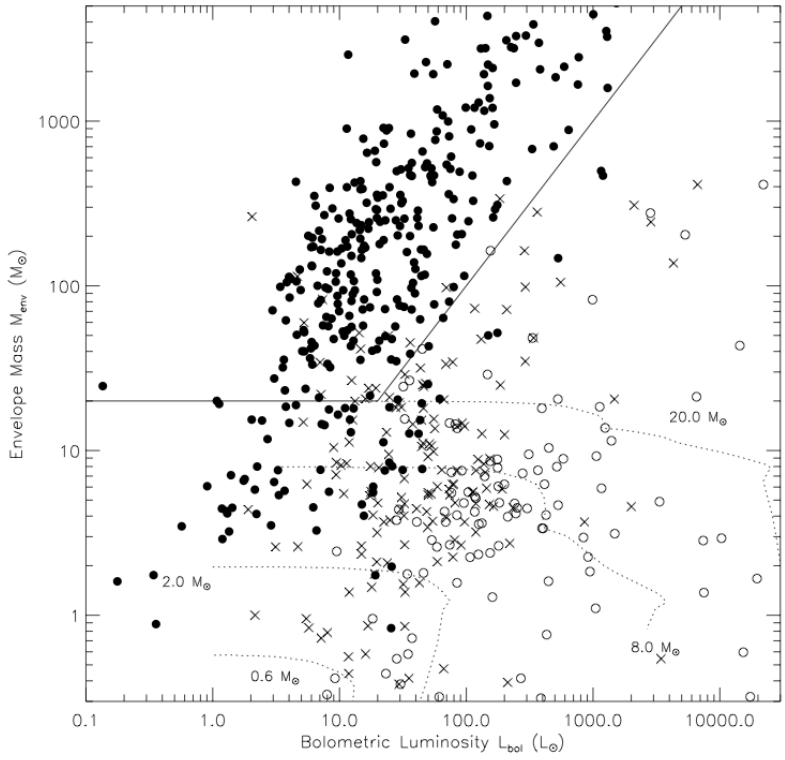

Figure 7.7: The envelope *mass-bolometric luminosity* function of W3 for *more luminous* sources with contours over-plotted from André et al. (2008) with the proto-stellar evolutionary tracks (as featured in Figure 7.4) which give some indication of where we would expect a proto-star with a particular mass. Compared to AKARI (Figure 7.4) which only sampled sources up to ~ 8 $M_{\odot}$ we see more massive pre-stellar clumps with masses $M_{\rm env} \geq 20\ M_{\odot}$

7.5 Diffuse Emission

7.5.1. AKARI Data

The W3/W4/W5 Complex Only

The pre-release data from the *AKARI* All-sky survey atlas (*AFASS;* Doi et al. 2015 *in press*) was used to make a *mosaic* of the W3/W4/W5 complex for the 60, 90, 140 and 160 μm far-IR bands (Figure 7.8) in order to look at the diffuse emission. The *AKARI* data, which is stored in Ecliptic coordinates, was image transformed and mosaicked to the J2000 FK5 system using the STARLINK WCSMOSAIC routines.

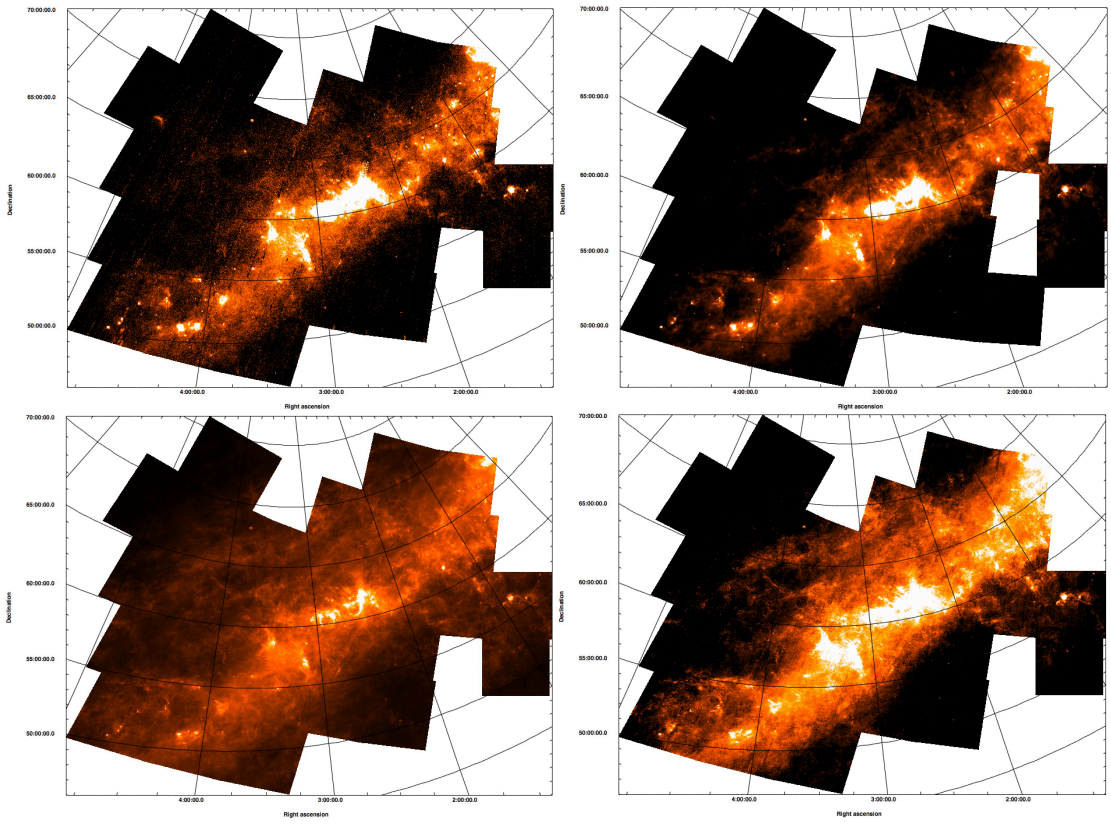

Figure 7.8: 60 μm (top left), 90 μm (top right), 140 μm (bottom left), 160 μm (bottom right). The scaling is arbitrary and aimed to emphasis the diffuse Galactic structure around the 3 H II regions.

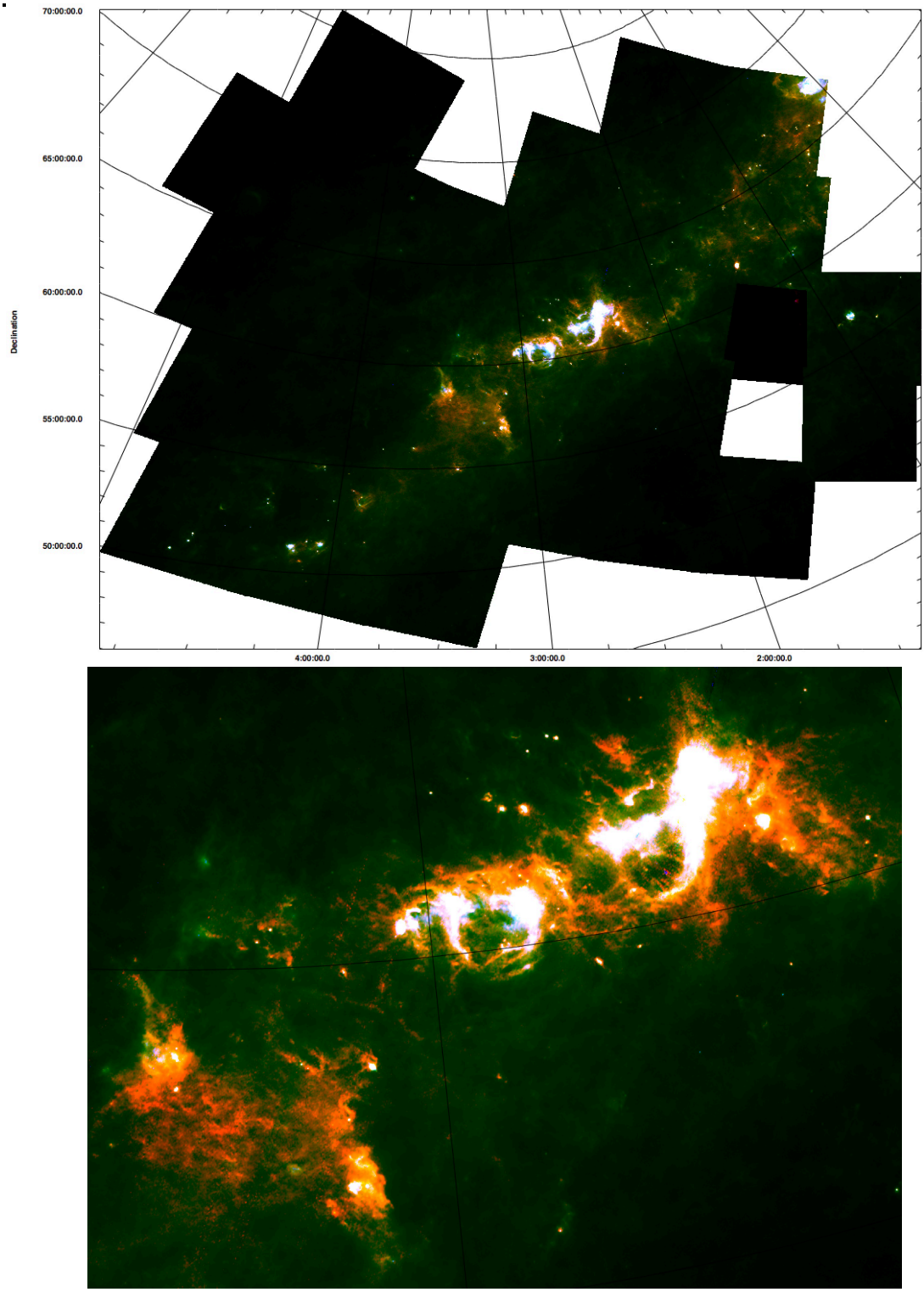

Figure 7.9: Top image: 3 colour (60 (blue) 90 (green) and 160 μm composite image. Bottom image: a zoom in on the W3/W4/W5 region. The scaling is arbitrary and meant to emphasis the warmer (bluer) and cooler (redder) Galactic structure around the three main complexes.

Temperature & Column Density

The AKARI diffuse all-sky atlas plates have been corrected to give an estimate of the absolute flux levels as described by Doi et al. (2015 *in press*). To derive the column density and dust temperature maps, AKARI sky flux plates were first convolved to the resolution at 140 μm, and

projected onto a common grid of 15″ (~ 0.15 pc at the distance of the W3 complex). The intensities at each pixel were fitted using the approximation:

$$I_\nu = (1 - e^{-\tau_\nu})\, B_\nu(T) \qquad (7.1)$$

where $B_\nu(T)$ is the Planck function for a dust temperature, *T*. This assumes that *T* remains constant along the LOS. The optical depth, τ_ν is taken from the widely adopted relationship: $\tau_\nu = \tau_{\nu_0}\,(\nu/\nu_0)^\beta$ where ν_0 is 1200 GHz (~250 mm) and β is the fixed dust emissivity index. The total H column density, N_H is then given by $N_H = \frac{\tau_\nu}{\sigma_\nu}$, where σ_ν is the opacity. Following Ingraham-Rivera et al. (2013), the dust emissivity index is assumed to have the value β = 2, and the opacity is as assumed in other HERSCHEL studies to have a value of 0.1 cm^2 gm^{-1} at 1000 GHz, which is equivalent to σ_o= 3.4 x 10^{-25} cm^2 H^{-1}, assuming that the mean atomic weight per nucleon is 1.4. Since the AKARI results are most directly comparable with those of Rivera-Ingraham et al. (2013), the present data have been scaled to use a factor of 2.33, rather than 2.8, for the mean atomic weight per molecule (see also Kauffmann et al. 2008) to convert to units of N_{H_2}. Since we wish to analyse the whole W3/W4/W5 complex, for which HERSCHEL data do not exist for many regions, that there limitations as to the ability of the AKARI data to recover column density and dust temperature maps. Notably: a) the present analysis uses only two far-IR wavebands, at 65 and 140 μm, and b) much of the cooler dust will not be sampled in the same way as is the case from use of HERSCHEL PACS and SPIRE bands together. Despite attempts to achieve better fits to the data using all four AKARI bands, the c^2 fits to the individual pixels were not sufficiently constrained to allow use of the multi-band data for the cooler region. Subject to the caveats above, the 65 and 140 μm images were used to estimate the column density and temperature of the diffuse dust across the whole W3/W4/W5 complex.

From the AKARI 60 and 140 μm data alone, the values for the column density and the dust temperature in the W3 region (as shown in Figures 7.10 & 7.11) provide a reasonably good match (with factors of ~ 2) as those estimated from HERSCHEL data by Rivera-Ingraham et al. (2013) which is impressive considering the latter has a much smaller beam, and much wider wavelength coverage.

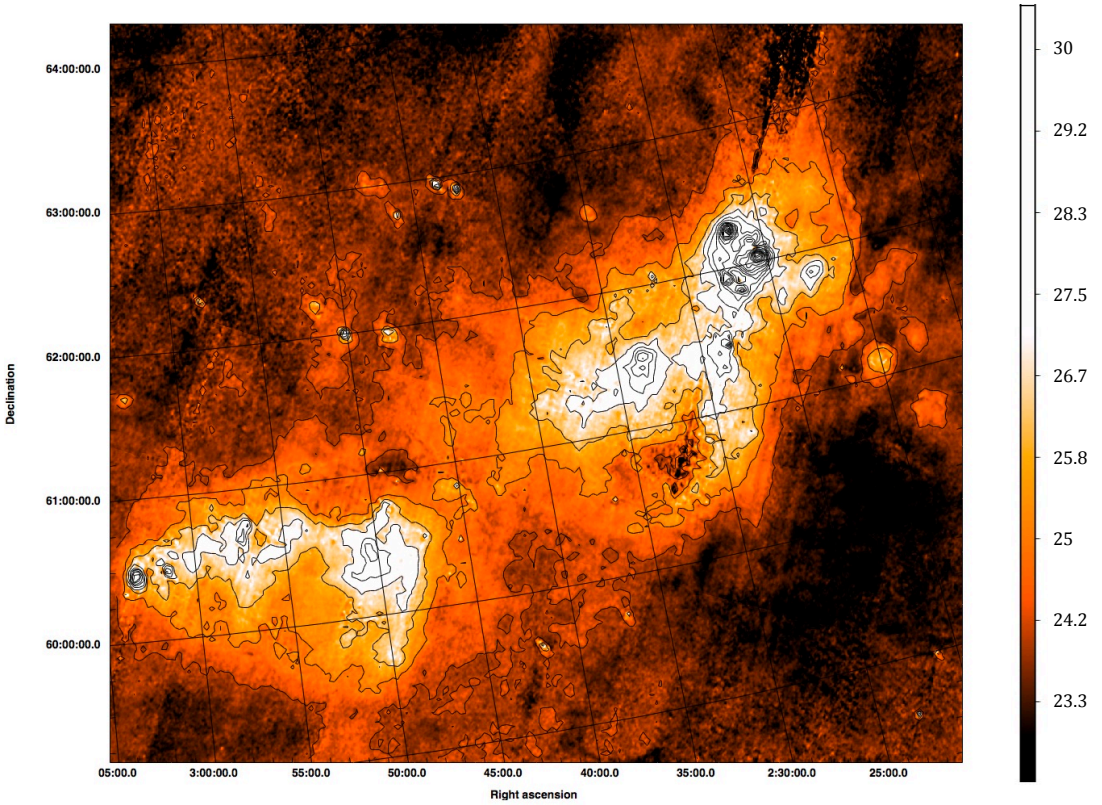

Figure 7.10: Dust Temperature Map of the W3/W4/W5 complex, derived using the AKARI 65 and 140 mm data. The lowest contour is at a dust temperature of 22 K, and subsequent contours increment in units of 1 K. The maximum value in the map is 43 K.

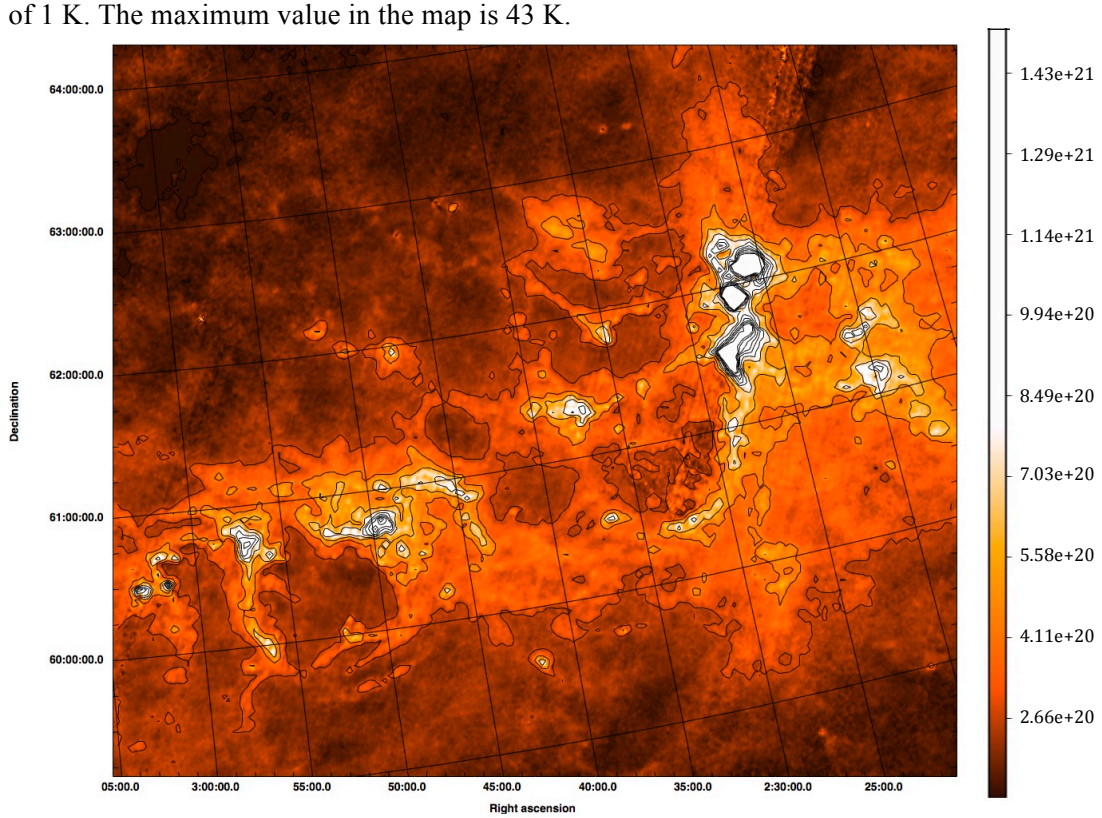

Figure 7.11: Column Density Map of the W3/W4/W5 complex, derived using the AKARI 65 and 140 mm data. The vertical axis is the column density N_{H_2} in units of cm^{-2}, with the lowest contour at 1.2×10^{19} cm^{-2}, and subsequent contours at intervals of 2.6×10^{20} cm^{-2}. The map has had a non-linear function applied for display purposes, as the maximum value in the map close to W3 IRS-5 has a column density of 2.0×10^{23} cm^{-2}.

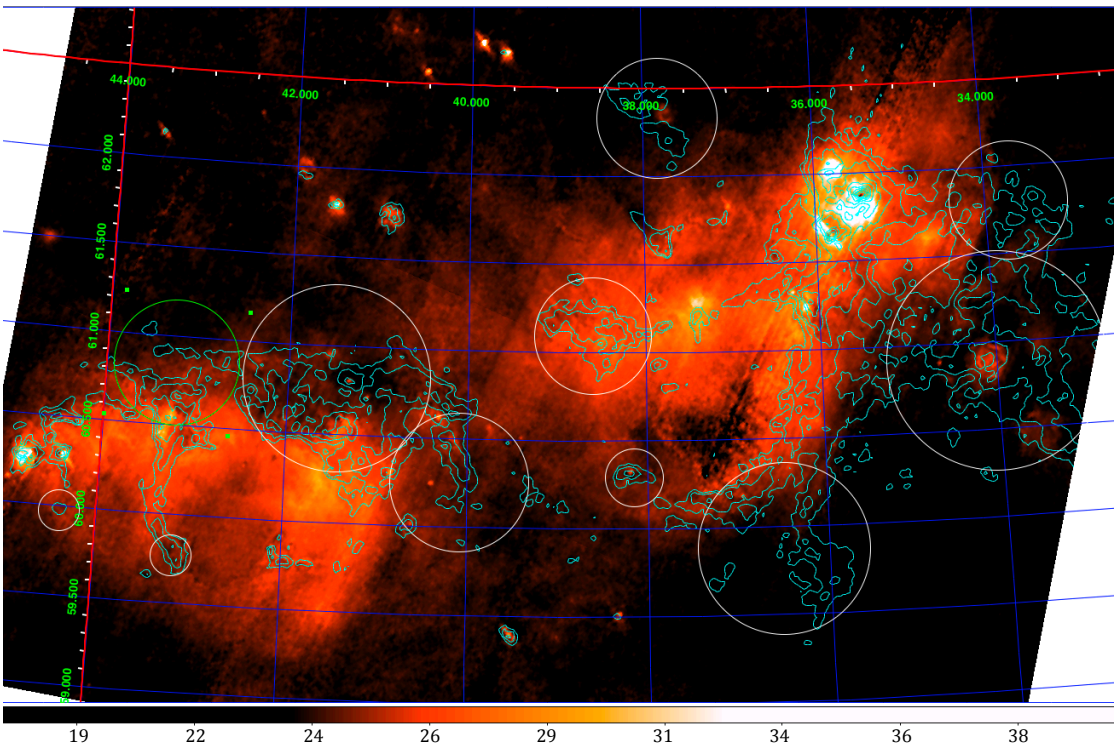

Figure 7.12: Investigating regions where there are peaks in LOS column density N_{H_2} but no dust temperature peaks (this is most prominent in the regions highlighted by the white circles). The map shows dust temperature in K, with column density contours superimposed from 4 x 10^{20} cm^{-2} to 1.24 x 10^{23} cm^{-2} at 11 linear levels.

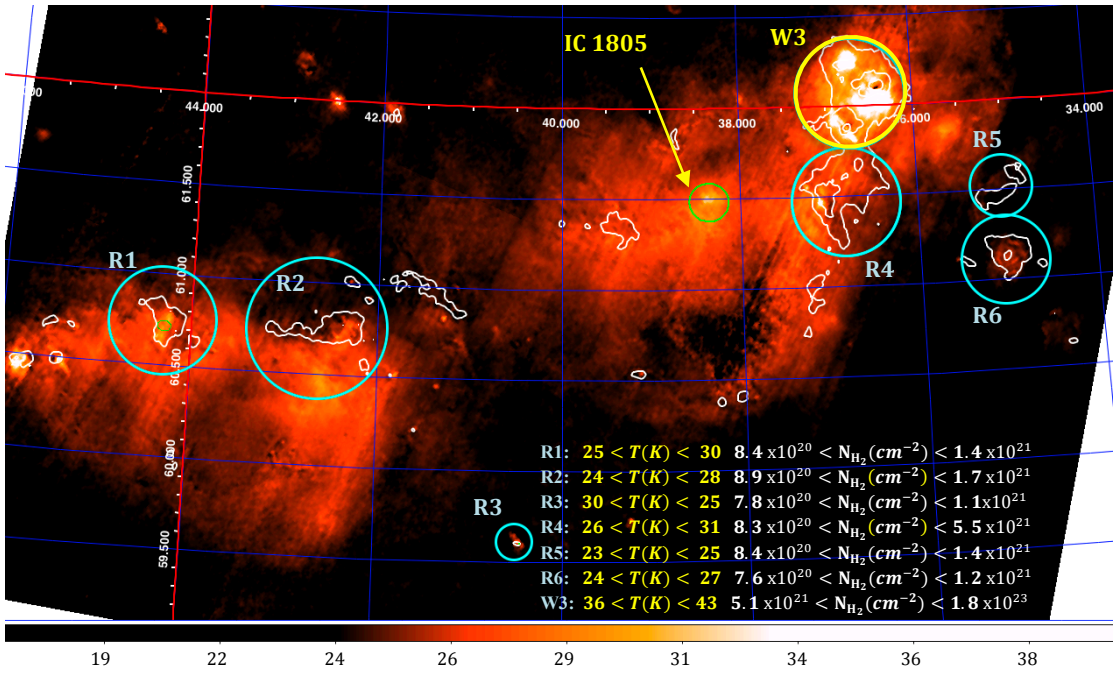

Figure 7.13: The map shows dust temperature in K, with column density contours superimposed from 7 x 10^{20} cm^{-2} to 1.24 x 10^{23} cm^{-2} at 4 linear levels. The regions (in blue) show peaks in the LOS column density (greater than 7.6 x 10^{20} cm^{-2}) but no dust temperature peaks (at less than 31 K); these are possible sites for pre-stellar core formation. W3 is also encircled in yellow but does not follow this trend (its regions W3-East, W3-West and W3-OH are simultaneously highly luminous and very dense as found by Rivera-Ingraham et al. 2013 which is confirmed by our AKARI maps).

Rivera-Ingraham et al. (2013) found a correlation between column density, N_{H_2} and dust temperature within the W3 region, with the hottest densest areas in W3-main and W3-OH; these regions as mentioned are associated with the youngest high-mass star-formation activity in W3 where there is more luminosity to heat the surrounding material. This is also confirmed in our AKARI maps (Figures 7.12 & 7.13) where the hottest region of W3, also corresponds with the densest column densities at the locations of W3-East, W3-West and W3-OH.

However, elsewhere, peaks in LOS column density N_{H_2} exist where there are no dust temperature peaks and these regions are highlighted in white circles (Figure 7.12). In Figure 7.13 the regions encircled in blue have peaks in the LOS column density ranging from 7.6 x 10^{20} to 5.5 x 10^{21} cm^{-2}, but no peak in temperature which remains relatively cool at 23-31 K. We anticipate these to be cool denser regions, which could hold cloud cores in the pre-stellar phase that *may* go onto produce self-luminous stars in the future. This is in contrast to W3 luminous peaks (located within the yellow circle of Figure 7.13) with column density N_{H_2} between 5.1 x 10^{21} – 1.8 x 10^{22} cm^{-2}, and dust temperatures of 36-43 K which are believed to host current on-going high-mass star-formation which heats the surrounding dust and are in the proto-stellar phase (Rivera-Ingraham et al. 2013).

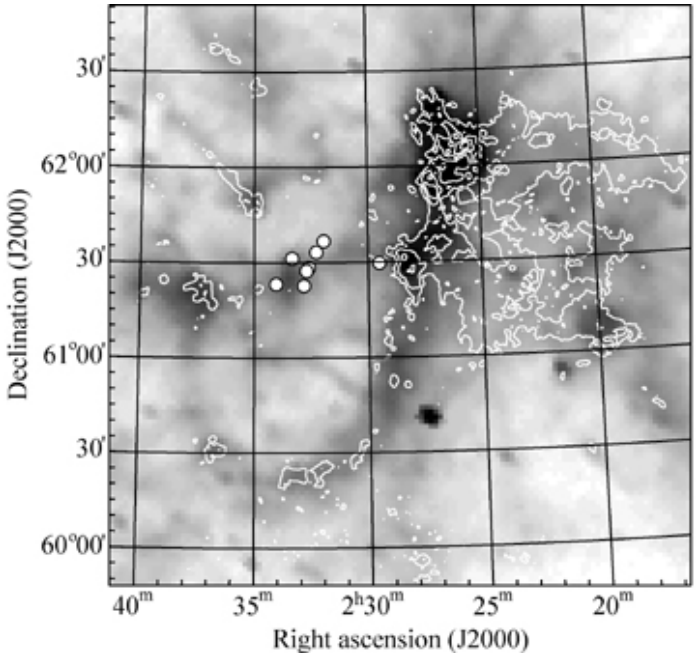

Figure 7.14: An overview of the W3 GMC from Moore et al. (2007), which compares MSX 8 μm emission (in grey-scale) against the integrated ^{12}CO *J*= 1–0 emission from the FCRAO Outer Galaxy Survey (Heyer et al. 1998) in white contours. The circles represent the O stars of the IC 1805 cluster (Massey et al. 1995).

Moore et al. (2007) compare MSX 8 μm emission with integrated ^{12}CO *J*= 1–0 emission from the FCRAO Outer Galaxy Survey (Figure 7.14) in much the same way, we conduct our

diffuse radio comparisons with the integrated velocity CO survey by Dame et al. (2001) in § 4.2.5. They observe the molecular material of the W3 GMC runs parallel to the Eastern edge of the W4 H II region (this is also clear in Figures 4.34 & 4.35 in CO comparisons with our low frequency continuum images). This layer of strong CO emission is referred to as the high density layer (HDL) by Lada et al. (1978) and is likely to have formed from compression of the cloud gas resulting from the expansion of W4 fuelled by the fast stellar winds from the of 11 O stars in the cluster IC 1805 (RA 2h32m Dec +61°27') W4 OB association which ionise and erode the surrounding molecular material (Moore et al. 2007).

The positions of the O stars of the IC 1805 cluster (Massey et al. 1995) are shown by the circles in Figure 7.14 (Moore et al. 2007) and their cluster is represented by the green circle in our AKARI & LOFAR maps of Figure 7.15.

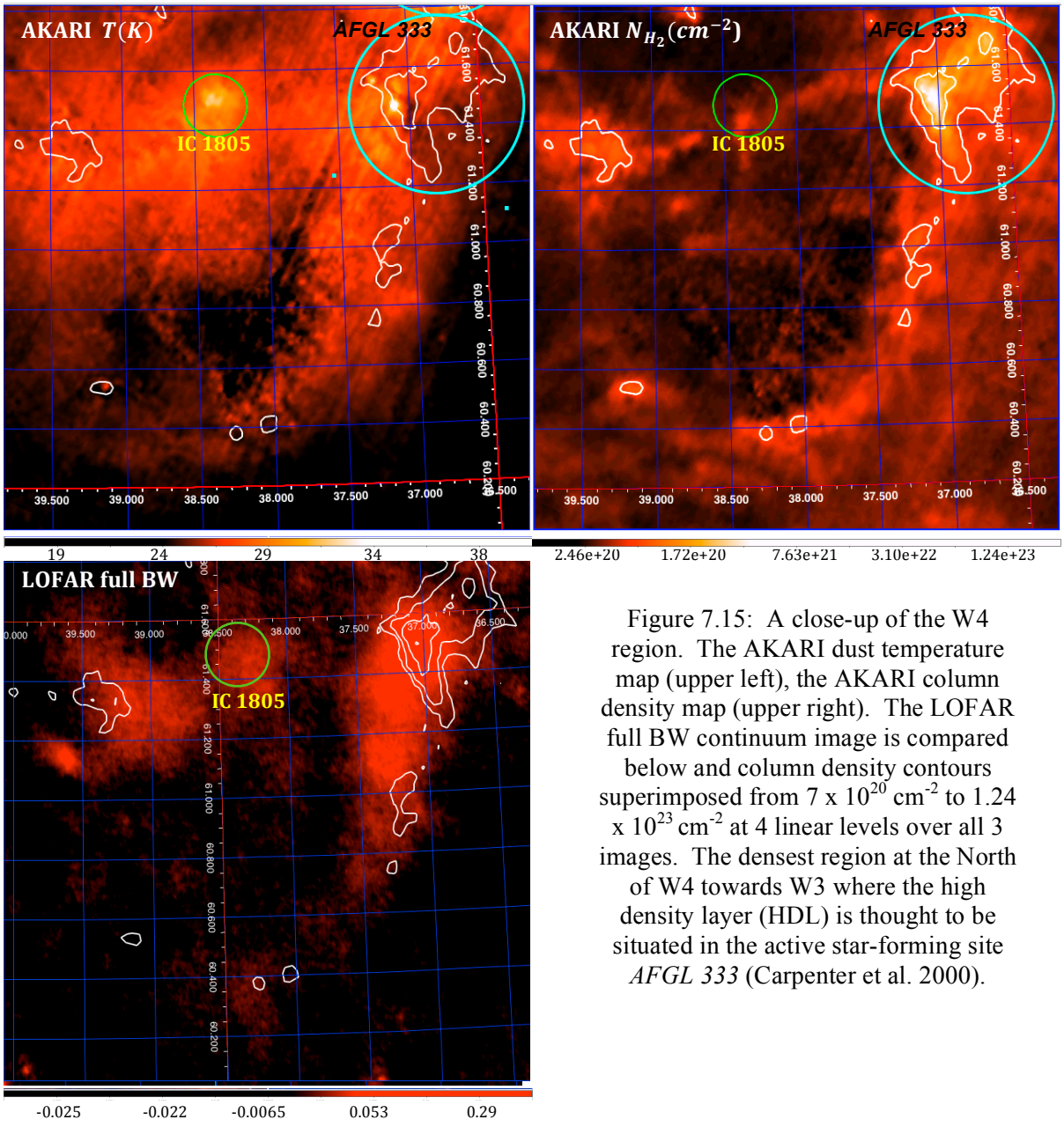

Figure 7.15: A close-up of the W4 region. The AKARI dust temperature map (upper left), the AKARI column density map (upper right). The LOFAR full BW continuum image is compared below and column density contours superimposed from 7 x 10^{20} cm^{-2} to 1.24 x 10^{23} cm^{-2} at 4 linear levels over all 3 images. The densest region at the North of W4 towards W3 where the high density layer (HDL) is thought to be situated in the active star-forming site *AFGL 333* (Carpenter et al. 2000).

Within the green circle of Figure 7.15 is situated the W4 OB association (IC 1805); its position is significant, as appears close to an equidistant radius from the W4 lower arc-like structure. §§ 1.4 & 4.2.3 presented the recent debate over the W4 structure being either a superbubble vs. the lower part of a chimney-structure which has blown out from the Galactic disk (please see Normandeau 2000); our column density maps seem to indicate a broken shell-like morphology with a variable structure along the LOS, at the centre of which falls the W4 OB association. This is strongly suggestive of a superbubble cavity being cast out of molecular material by the erosive and ionising effects of the cluster of O stars and supports the findings of Normandeau et al. (1997) and Moore et al. (2007). The inner shell of W4 has relatively higher thermal dust emission (varying between 26-27 K) and this reduces by 1-3 K to temperatures typical of the background (22-24 K) towards the outer regions and supports the fact this structure is an ionisation front re-emitting stellar radiation from the W4 OB association located at its centre; this supports Terebey et al. (2003) and this scenario is described in § 4.2.3. Our diffuse LOFAR radio continuum image clearly traces this ionisation front and emission is most significant towards the upper region towards AFGL 333 (as described in § 4.2.5) which is located in the eastern high density layer (HDL) with the least emission along the lower loop itself which contains active star-formation sites in addition to those within W3 itself (Oey et al. 2005).

Overall, the temperature and column density do not seem to be well correlated in the W4 shell region. The contours suggest material of highest density towards the *outer* shell where we also find the relatively cooler temperatures, suggestive of a shell of dense cool material formed from the compression of the molecular cloud by the radiation and ionisation shocks of IC 1805. The cool dense patches could represent regions that may condense to form self-luminous proto-stars inside in the future, triggered by activity of IC 1805. Presently there are not much evidence of local heating and no obvious signs of any strong IR sources in this region.

Figure 7.17 shows the masers in the region with the majority of new detections from our observation, located in the high-mass star-forming region of W3, strengthening their association to established ongoing star-forming and UC H II regions. The green circles show locations of HERSCHEL IR sources where we did not detect masers; these regions are found along the dense

filament structures in the GMC, and in particular the East loop, the West loop and KR 140-N; these are the W3 GMC pillars, structures and filaments referenced by Rivera-Ingraham et al. (2013).

7.6 Maser Observations with the Onsala OSO Telescope

7.6.1. Instrumentation & Observational Technique

During October 2012, March 2013 and May 2013, observations were made of the 6_{16}–5_{23} transition of the H_2O molecule (rest frequency, v_0 = 22235.080 MHz), which results in the presence of 1.35 cm water maser emission, using the 20 m antenna of the OSO telescope. A 1600-channel digital autocorrelation spectrometer was used to measure across a bandwidth of 20 MHz (an equivalent velocity width of 270 km s^{-1}), with a channel resolution of 12.2 kHz (0.16 km s^{-1}). During observations, the average system temperature varied between 90–130 K. At a frequency of 22 GHz, the aperture efficiency of the antenna was 17 Jy K^{-1} and the half-power beam width was 170″.

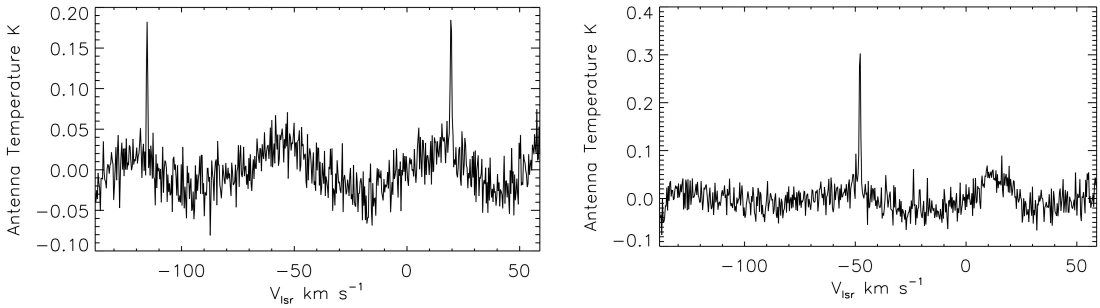

Figure 7.16: This is part of a raw spectrum from 1 minute of integration time as observed (left spectrum) with a frequency throw corresponding to +/- 67.4 km s^{-1}, before the two halves of the spectrum are folded and aligned with each other, and then (right spectrum) separately calibrated and weighted after applying a small correction for system temperature variations (typically less than a few percent) across the band, and finally intensity converted into Janskys. The resultant spectrum (on the right, taken on October 2013) was then fitted with a low order polynomial baseline to flatten the low order ripple on the baseline left as a consequence of the frequency switching mode that was used to improve the signal to noise of faint, narrow lines.

W3OH is a strong water-line source and its historical monitoring is reported in Little et al. (1977). A pointing check was carried out every 2 hours on this bright water maser, which has a well-determined position, and its flux of was also monitored and found not to vary significantly over several days. Observations were taken using *frequency switching*, where the target line was

switched across the observed band at 6.7 Hz, so that the line was continuously observed. The spectra were then divided into 2, and aligned to match the correct velocity scale. An example of a frequency switched spectrum as observed is shown in Figure 7.16.

7.6.2. Results of Targeted H_2O Maser Detections

Initial Target Selection: W3/W4/W5

The initial target selection for detecting the H_2O maser emission was based on data taken from the HERSCHEL HOBYS survey of W3 by Rivera-Ingraham et al. (2013). The targets for W4 and W5 were based on the inspection of *level 2.5* images from the *Herschel Science Archive*.

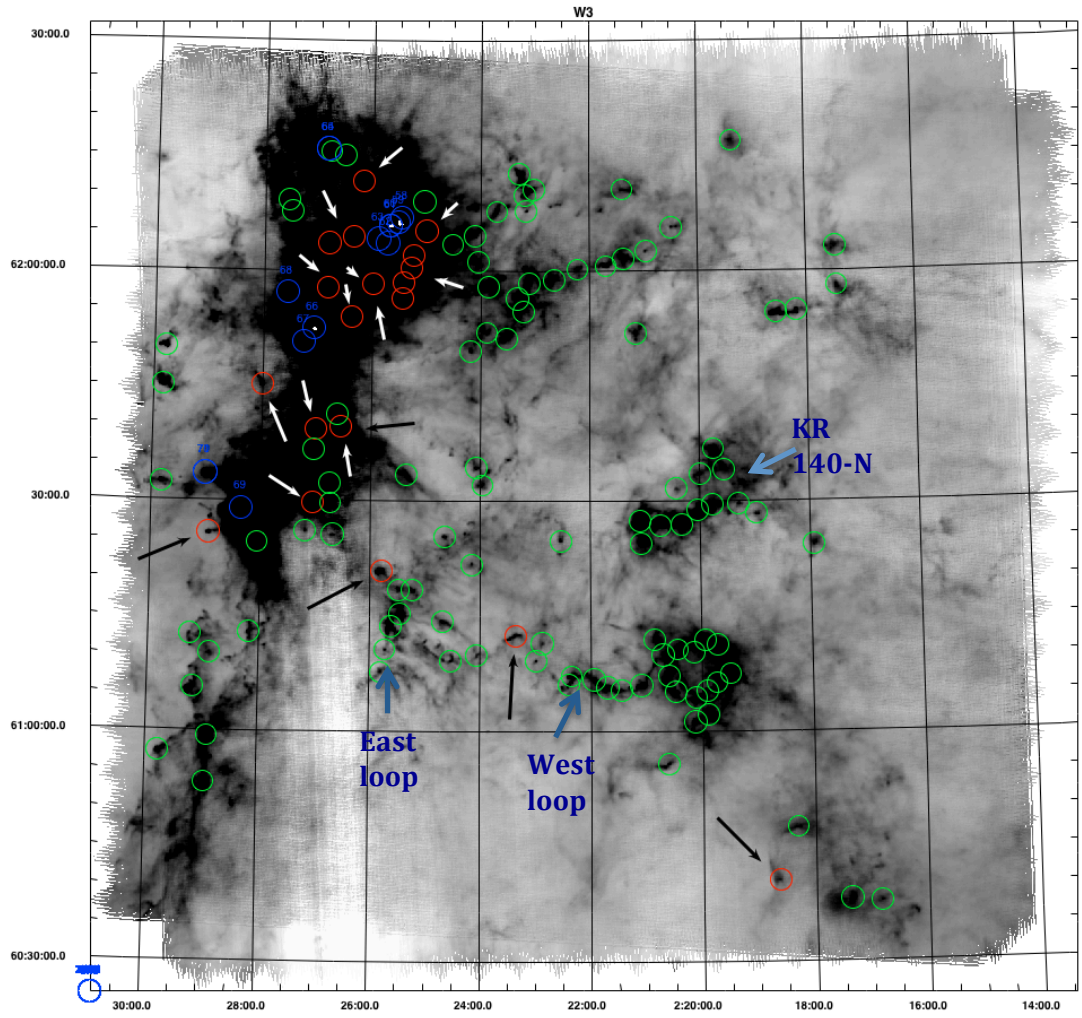

Figure 7.17: W3 maser sources (in circles) superimposed onto a HERSCHEL map of the molecular W3 cloud. The location of the prominent structures of the W3 GMC are labelled.

Figure 7.17 of the W3 region alone shows the positions searched for H_2O masers in the W3 complex, with no detection (green circles), previously known maser detections (blue circles), and

19 newly discovered H_2O masers (red circles with arrows pointing at them) from this survey. Please refer to Appendix C for all targeted far-IR locations in W3/W4/W5 and their associated water spectra.

In all, the H_2O observations of W3/W4/W5 surveyed a total of 123/41/203 HERSCHEL sources respectively, with the following source detections: W3 [1, 2, 3, 4, 5, 6, 7, 8, 9, 13, 17, 54, 64, 69], the latter may be the same as source 64, but seen at the edge of the beam at the source 69 position (see spectra of Figure 7.18); W4 [3, 9, 49, 56, 57] (see spectra of Figure 7.19); and W5 [2, 183] (see spectra of Figure 7.20). We noted a number of previously catalogued H_2O masers in all 3 sources which were not detected at any time during our survey observations, showing that they had gone into a low state; time variability is demonstrated in Figure 7.21. The spectra below show the *summation of all data* on the various sources over the entire observing period in 2012 and 2014, of all sources that had convincing detections in the W3 area.

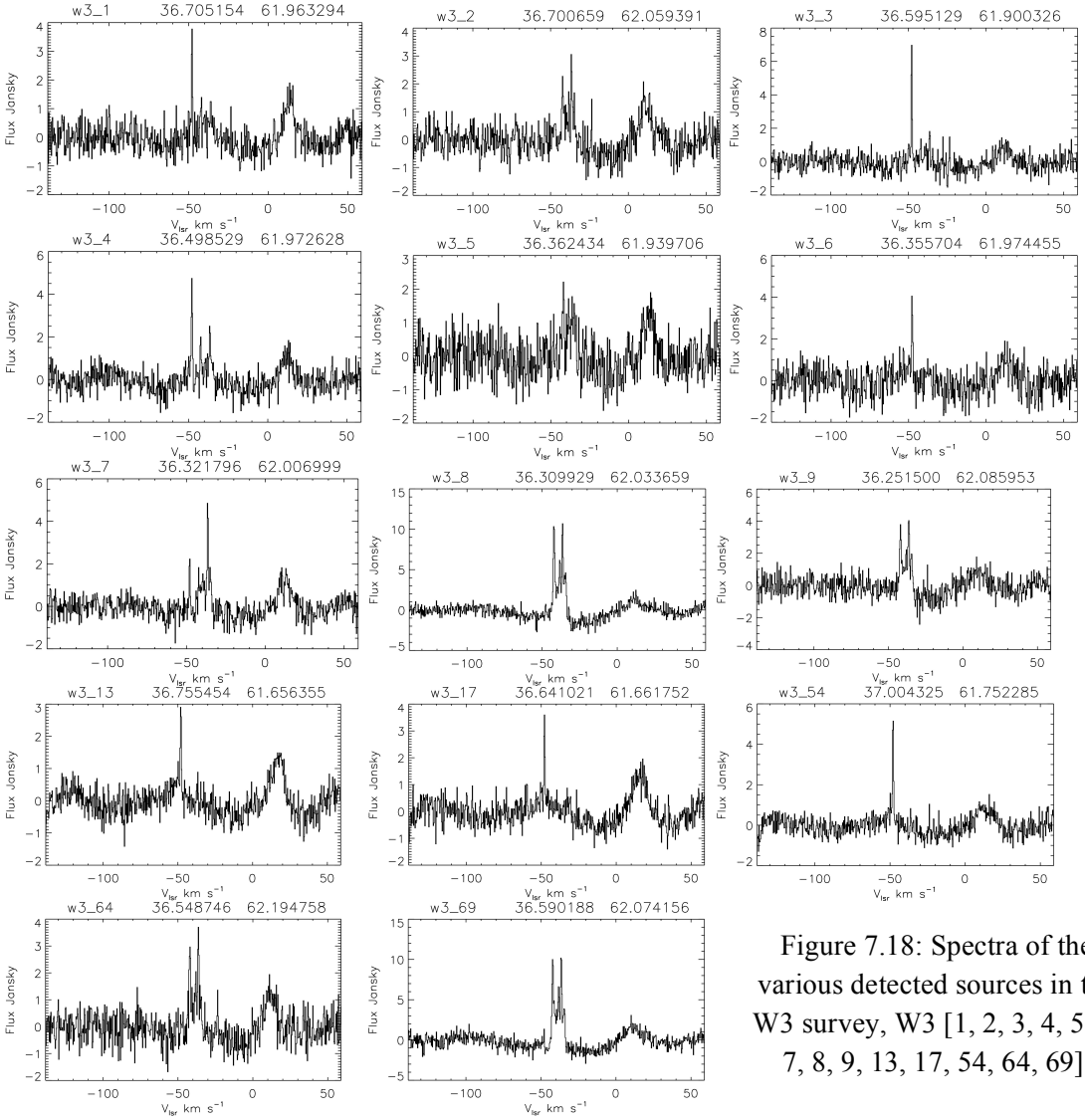

Figure 7.18: Spectra of the various detected sources in the W3 survey, W3 [1, 2, 3, 4, 5, 6, 7, 8, 9, 13, 17, 54, 64, 69].

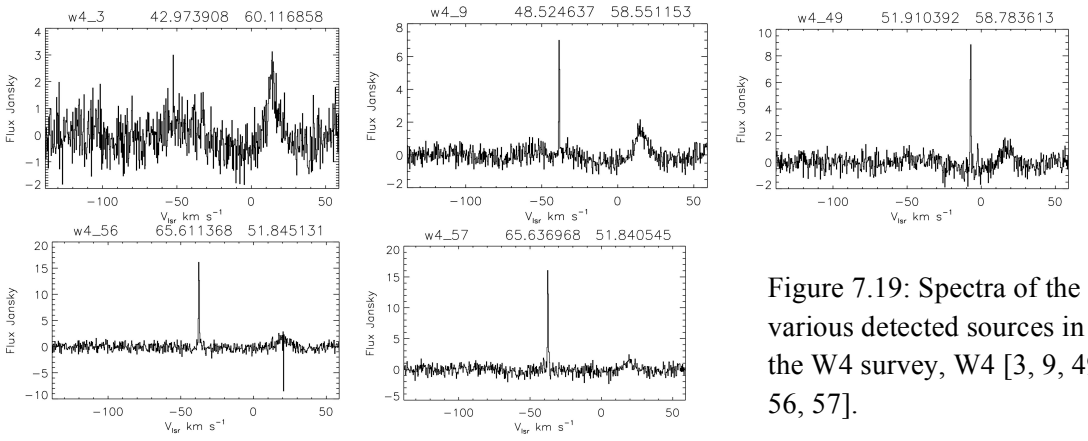

Figure 7.19: Spectra of the various detected sources in the W4 survey, W4 [3, 9, 49, 56, 57].

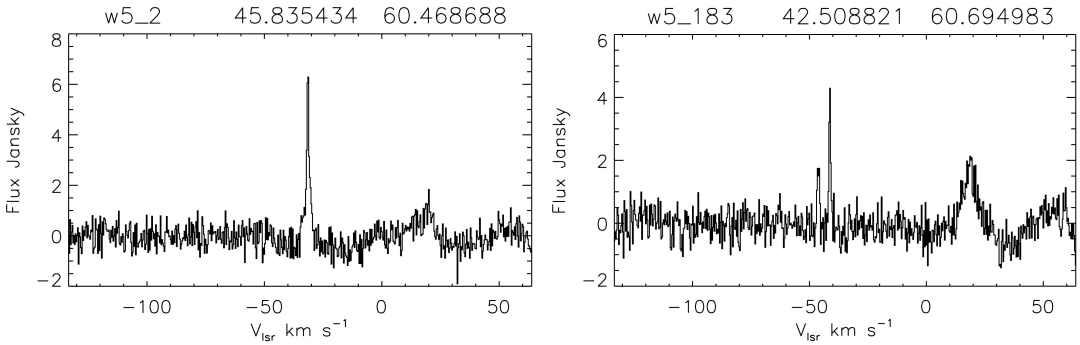

Figure 7.20: Spectra of the various detected sources in the W5 survey, W5 [2, 183].

Figure 7.21 below shows the *time variability* of the W3 water spectra observed as part of the survey, emphasising the need in detection studies for frequent revisits, even if emission is not seen first time around:

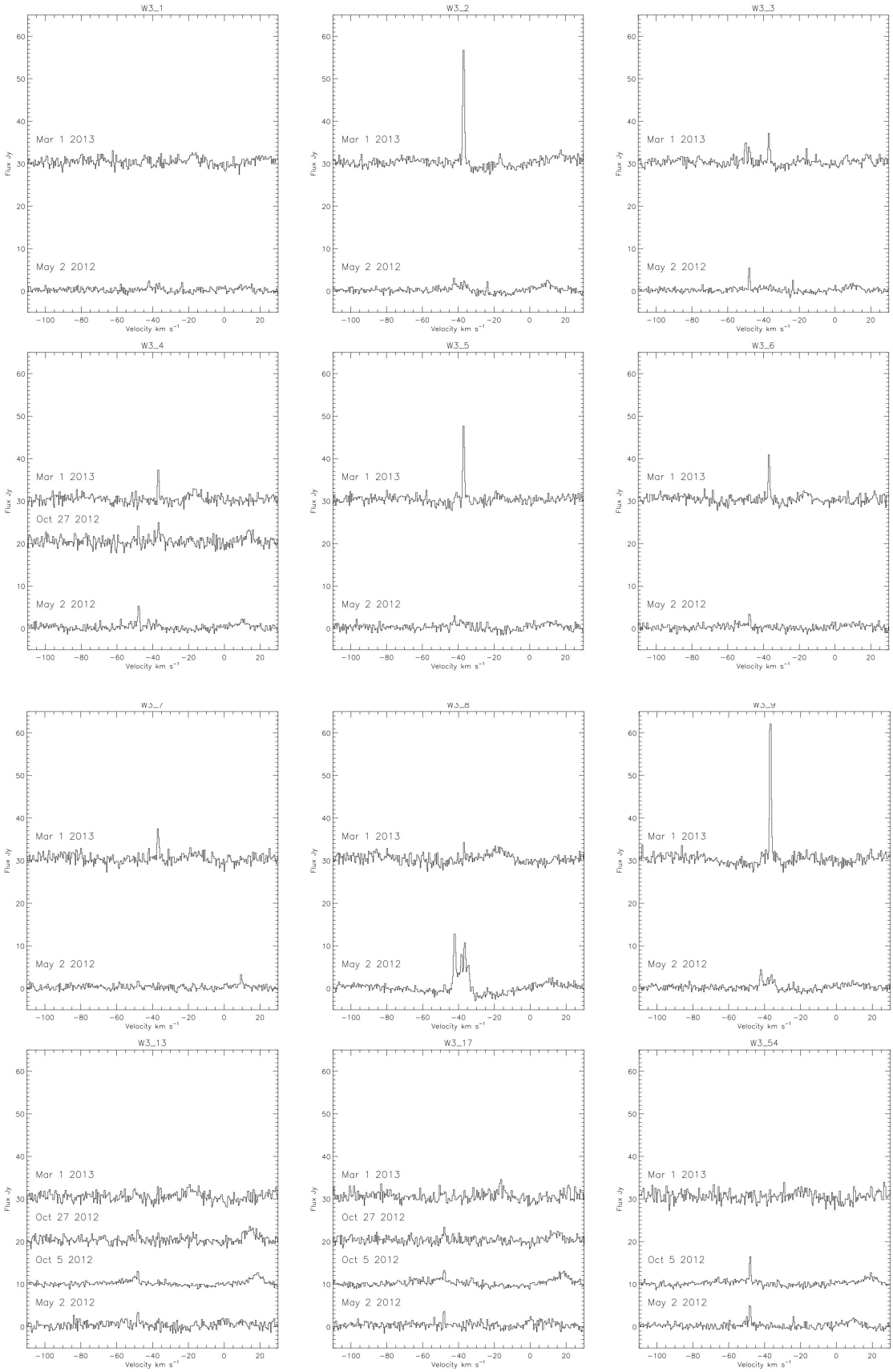

(continued next page)

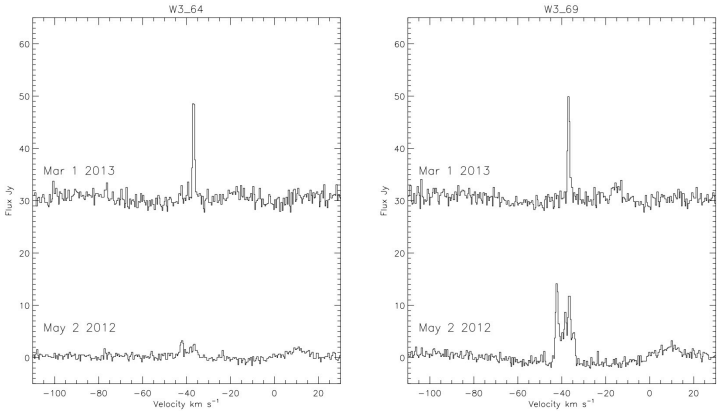

Figure 7.21: Water vapour spectra of sources in the W3 survey at different dates over the monitoring period.

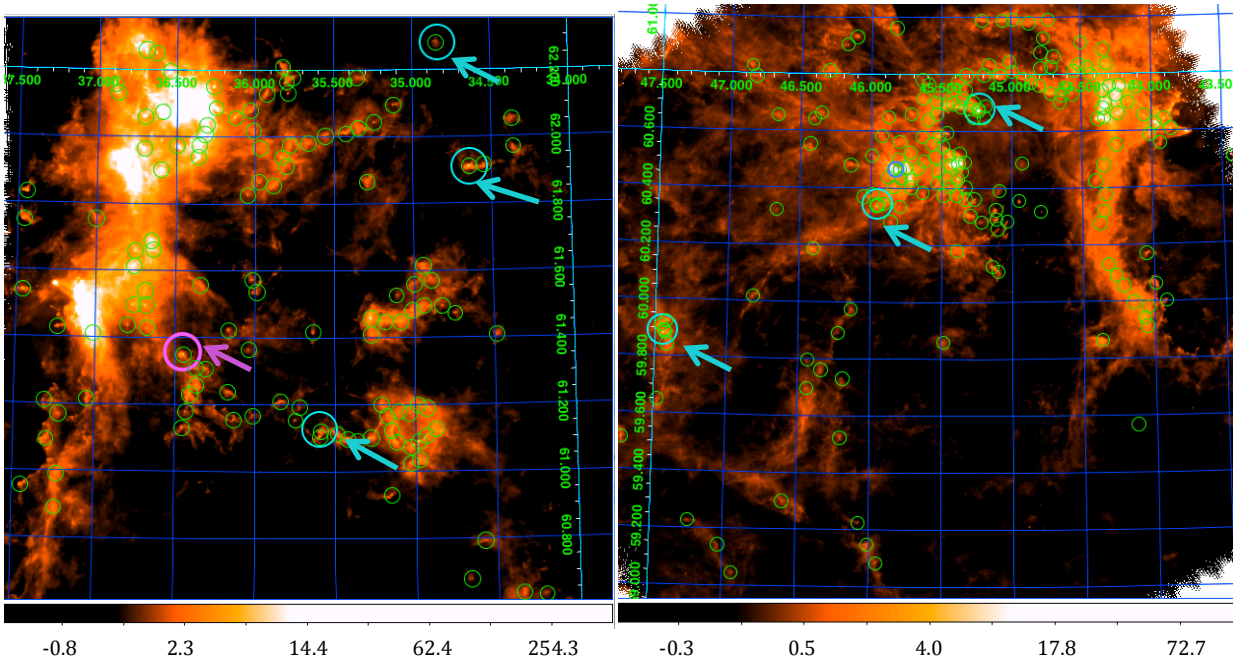

Figure 7.22: The HERSCHEL 250 μm images of *sections* of the W3 (left) and W5 (right) H II regions. The locations of targeted observations of water masers based on the HERSCHEL catalogue of Figure 7.17, as well as all known masers are over-plotted with small green circles. The larger blue circles with arrows are the AKARI source detections (§ 6), and these all correspond with the locations targeted (although not all these resulted in maser detections at the time of our observation; green circles of Figure 7.17). The pink circle in the W3 region corresponds with a new water maser detection (red circle of Figure 7.17).

Whilst not having the level of resolution and sensitivity as the HOBYS HERSCHEL survey (§ 7.4.2), Figure 7.22 shows AKARI detections (§ 6), which cover the whole expanse of W3/W4/W5, overlaid onto the smaller targeted HERSCHEL frames which only cover a few square degrees. Within the limited FoV, it is shown how all AKARI detections correspond with the locations of targeted water maser observations based on the initial HERSCHEL catalogue. One of the AKARI sources corresponds with a *new* water maser detection in W3 (pink circle of Figure 7.22) which is

likely to be an established proto-stellar region emitting at the relatively shorter (hotter) wavelengths of AKARI; we already know (§ 1.3.3) that masers are strongly associated with established YSOs. Hence, the AKARI sources tend to selectively pick out the hotter (and brighter sources), whereas the HERSCHEL data, better sample the cooler material emitting at the longer wavelengths, and hence, will identify more of the clumps and cloud fragments (Figure 7.7).

Bright Masers in W3

In searching for new water maser sources, it was important to check that new detections did not result from the very bright emission of these sources appearing at the edge of the relatively large Onsala 20 metre telescope beam, as they are up to several thousand times brighter than the weakest water masers observed. It was necessary to check that the new sources were not simply false detections of these bright sources observed at the edge of the telescope beam, the velocities of the new water masers were carefully checked to ensure that they appeared at slightly different velocities to the bright sources, or that the velocity profiles were significantly different.

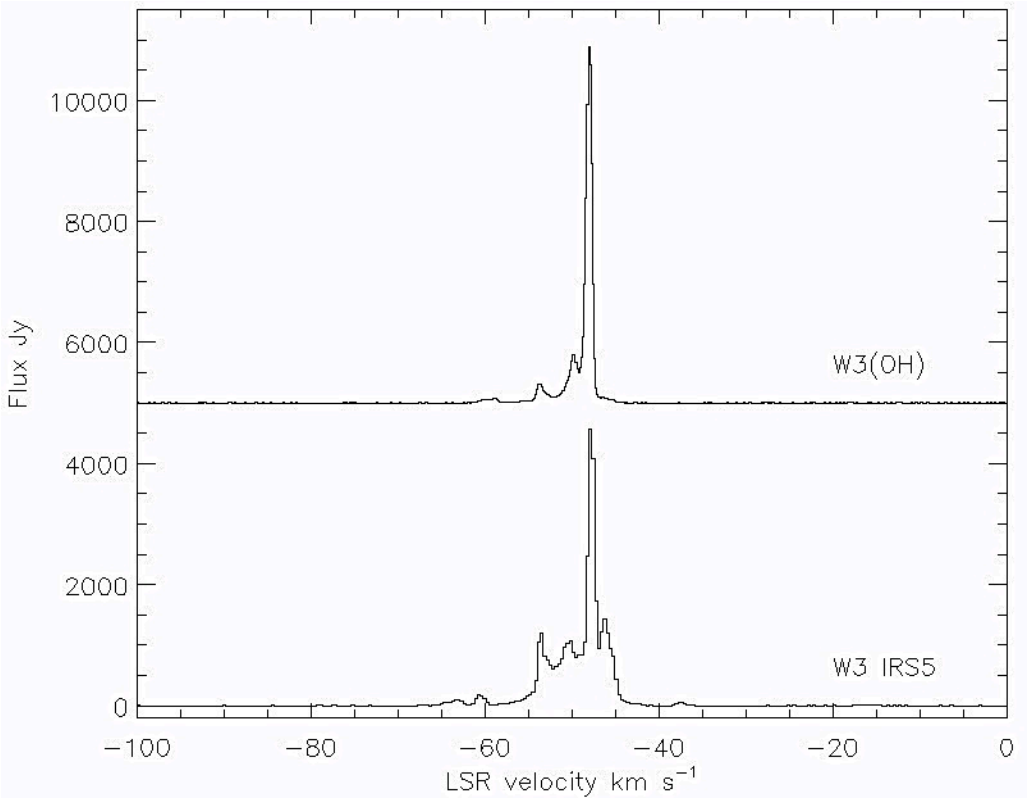

Figure 7.23: Spectra of the two bright water maser sources in the W3 region: W3 IRS-5 [RA J(2000 02:25:40.8 Dec (J2000) +62:05:51.2)] and W3(OH) [RA (J2000)02:27:04.7 Dec (J2000) +61:52:25.6].

The two very bright water masers in the W3 region were observed frequently (at least once a day) during the observing runs. The two dominant sources were associated with the well studied source bright water maser source associated with the H II region W3(OH), and the other with W3 IRS5 (Siparov, Samodurov & Laptev 2015). Spectra of both are shown in Figure 7.23. These were frequently measured during the observing periods to ensure that the new water maser detections were not confused as being detections of the much brighter bright sources, and their variability will be reported in a separate work at a later date.

7.7 The Luminosity Relation: Our Results

Water Luminosities

The luminosity of water maser sources can be calculated from the integrated antenna temperatures, $T_a^* \, dv$ (measured in K km s^{-1}) according to the formula:

$$L_{\mathrm{H_2O}} = 4\pi d^2 \frac{2k}{\eta_a A_p} \frac{v}{c} \int T_a^* \, dv \tag{7.1}$$

where d is the distance to the source (assumed to be at 2.3 kpc for the sources of the present survey associated with W3/W4/W5; Massey et al. 1995), k is Boltzmann's constant, η_a and A_p are the main beam efficiency and area of the aperture, v is the observing frequency and c is the velocity of light. If we adopt values for the telescope efficiency and aperture area from the Onsala 20 metre telescope handbook (Olofsson 2014) (Eq. 7.1) simplifies to:

$$L_{\mathrm{H_2O}} = 3.3 \times 10^{-7} \left(\frac{\int T_a^* \, dv}{1 \text{ K km s}^{-1}} \right) L_{\odot} \tag{7.2}$$

Palagi et al. (2003), Brand et al. (2003, 2005) and Felli et al. (2007) have found that monitoring water masers over an extended time period traces between the upper and lower envelopes of the maser emission, where the former is the *maximum* emission that the maser could produce if all the velocity components were switched on simultaneously and emitting at their maximum rate, and the latter is where masers may not be directed to the earth, or even just *switched off* (see also Little, White & Riley 1977 and Colom et al. 2015).

The studies also indicate masers of lower luminosity tend to be more *variable* (in terms of the ratio of maximum to minimum water flux). For masers of higher luminosity, the studies show that it is likely that a larger number of components may be simultaneously excited, which will have the effect of reducing the effect of time variability of and individual component, and suggest that the *upper limit* to the maser emission should correlate more closely with $L_{\text{far-IR}}$, as $L_{H_2O}^{upper} = 6.37 \times 10^{-8} L_{\text{far-IR}}^{0.81\pm0.07}$ (Brand et al. 2003, 2005).

The water maser survey and monitoring at Onsala was not taken over a long observational interval and so it is not possible to rule out that some of the non-detections might be detected as showing maser emission when observed at another time (i.e. due to variability or being in the switched off state). However, the best that can be done with the present data for the current analysis is to determine the *maximum* luminosity observed and then to examine how this scales with the $L_{\text{far-IR}}$. Table 7.1 gives the measured values from the present survey, as determined from the time monitoring spectra shown in Figure 7.21, the HERSCHEL estimated far-IR spectra (for W3), and the AKARI luminosities for W4 and W5. It should be noted that the luminosity estimates for the W3, and the W4/W5 sources are based on estimating the far-IR luminosities using different wavelength sampling, and that in particular the AKARI luminosities for W4/W5 sources are less sensitive to cooler dust.

Region	Source	RA (J2000)	Dec (J2000)	$\left(\frac{\int T_A^* \, dv}{1 \text{ K km s}^{-1}}\right)$	H_2O luminosity $L_\odot$	Far-IR luminosity $L_\odot$
W3	W3(OH)	02:27:04.7	61:52:25.6	414.6	1.3×10^{-4}	7.1×10^{4}
	W3 IRS5	02:25:40.8	62:05:51.2	733.8	2.4×10^{-4}	8.0×10^{4}
	W3_1	02:26:49.2	61:57:47.8	0.14	4.6×10^{-8}	21.1
	W3_2	02:26:48.2	62:03:33.8	0.51	1.7×10^{-7}	439.5
	W3_3	02:26:22.8	61:54:01.2	0.29	9.6×10^{-8}	18.
	W3_4	02:25:59.6	61:58:21.4	0.52	1.7×10^{-7}	58.5
	W3_5	02:25:27.0	61:56:23.0	0.09	3.0×10^{-8}	23.0
	W3_6	02:25:25.4	61:58:28.0	0.17	5.6×10^{-8}	45.1
	W3_7	02:25:17.2	62:00:25.2	0.72	2.4×10^{-7}	68.7
	W3_8	02:25:14.4	62:02:01.2	3.45	1.1×10^{-6}	82.
	W3_9	02:25:00.4	62:05:09.4	1.38	4.6×10^{-7}	47.6
	W3_13	02:27:01.3	61:39:22.9	0.18	5.9×10^{-8}	29.6
	W3_17	02:26:33.8	61:39:42.3	0.17	1.0×10^{-7}	36.
	W3_54	02:28:01.0	61:45:08.2	0.31	2.3×10^{-7}	10.8
	W3_64	02:26:11.7	62:11:41.1	0.69	9.8×10^{-7}	19.9
	W3_69	02:26:21.6	62:04:27.0	2.98	2.6×10^{-8}	20.2
W4	W4_3	02:51:53.7	60:07:00.7	0.08	2.4×10^{-7}	19.8
	W4_9	03:14:05.9	58:33:04.2	5.23	1.7×10^{-6}	103.6
	W4_49	03:27:38.5	58:47:01.0	0.41	1.4×10^{-7}	41.3
	W4_56	04:22:26.7	51:50:42.5	0.78	2.6×10^{-7}	71.2
W5	W5_2	03:03:20.5	60:28:07.3	0.75	2.5×10^{-7}	64.7
	W5_183	02:50:02.1	60:41:42.0	0.40	1.3×10^{-7}	43.6

Table 7.1: Measured properties of the H_2O masers detected in the W3/W4/W5 regions. The errors on the integrated fluxes are determined by the baseline fits and the absolute calibration, the latter of which dominates the error, and is estimated to be less than 6 %, based on the stability of the aperture efficiency of the dish, and the repeatability of measurement of the standard calibrator, W3(OH), which was monitored every few hours. The luminosities of W3(OH) and W3 IRS5 were taken from Hirsch et al. (2012) and van der Tak (2005) respectively. These luminosities have been calculated for a common assumed distance of 2.3 kpc (Massey et al. 1995). The W3(OH) luminosity may have been overestimated by a factor of ~ 25 % if the proper motion and parallax estimate of the distance is 2.04 kpc measured by Hachisuka et al. (2006) is correct.

Figure 7.24 below shows the final plot of the integrated water luminosity vs. the far-IR bolometric luminosity for a large sample of water masers (featured in Figure 7.1), including the new detections toward W3.

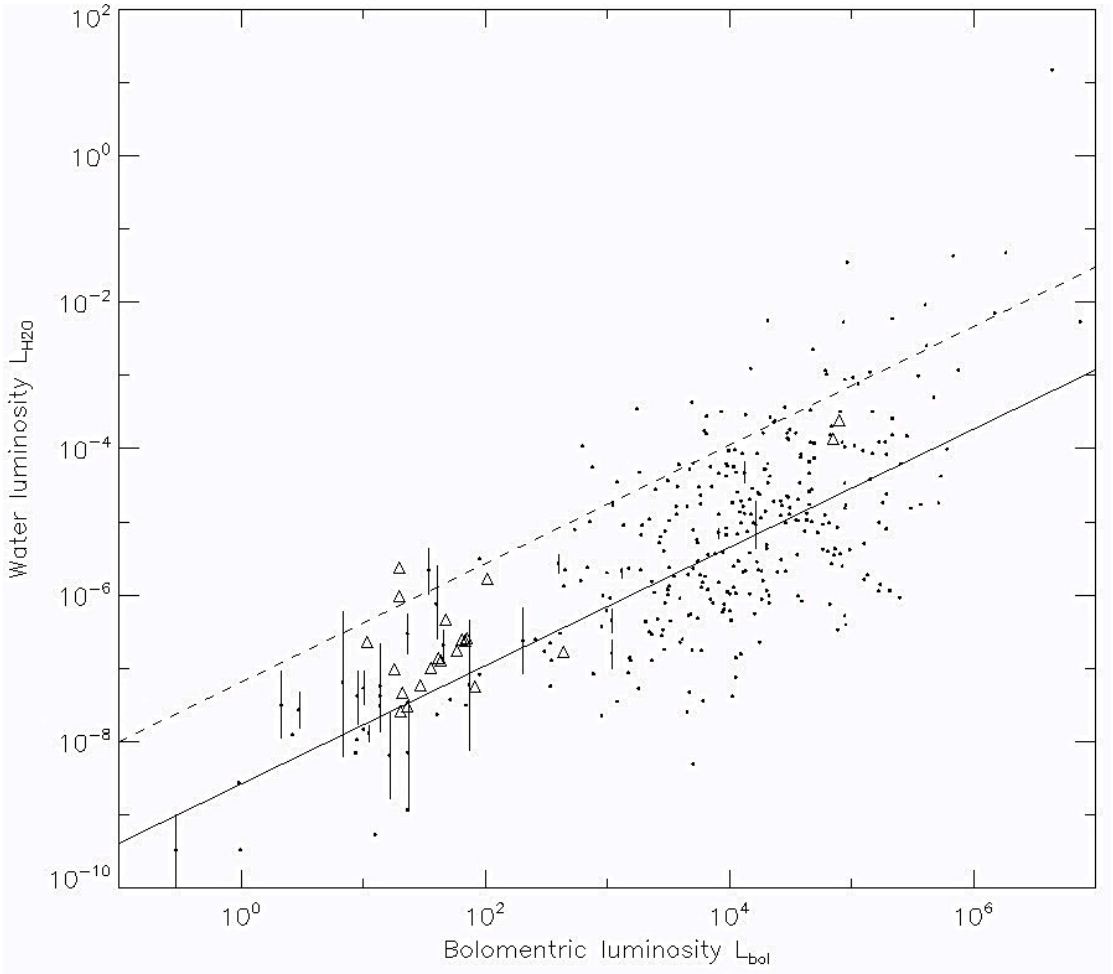

Figure 7.24: Plot of water luminosity against bolometric luminosity. The filled circles are data points taken from the literature, primarily from Urquhart et al. (2011); the filled circles with error bars are the low luminosity masers taken from the big survey paper of Furuya et al. (2003) where the luminosities have been corrected as described by Furuya et al. (2007), where the error bars represent the range of variability observed; the triangles represent the W3/W4/W5 results from the present work, where it can be seen that these preferentially (except for a couple of bright sources) sample the *low luminosity* part of the plot.

The *solid* line fit shown on Figure 7.24 is the relationship $L_{H_2O} = 2.58 \times 10^{-8} L_{\mathrm{far-IR}}$ suggested by Furuya et al. (2003, and corrected as described by Furuya et al. 2007). The *dashed* line shows the median of the fit based on an estimate of the *upper limit* to the luminosity that the maser could emit (from Brand et al. 2003). The new Onsala detections, indicated by triangles, are mainly located in the lower luminosity part of the plot, which has to date been poorly sampled, and are

consistent with both of these suggested relationships. To improve on the statistics, other observations obtained during the Onsala observing runs were focussed on considerably filling out and extending the sampling of this *lower* luminosity part of water/bolometric luminosity space, and results from this will be reported elsewhere.

7.8 Our Results: Far-IR Colour-Colour Diagrams

The far-IR data were examined to see whether the far-IR colours of the associated sources provide any indication as to whether or not water sources may be present. A colour-colour diagram (CCD) prepared using the 70, 160, 250 and 350 mm HERSCHEL fluxes of all sources in the HERSCHEL W3 catalogue (Rivera-Ingraham et al. 2013), and is shown below in Figure 7.25:

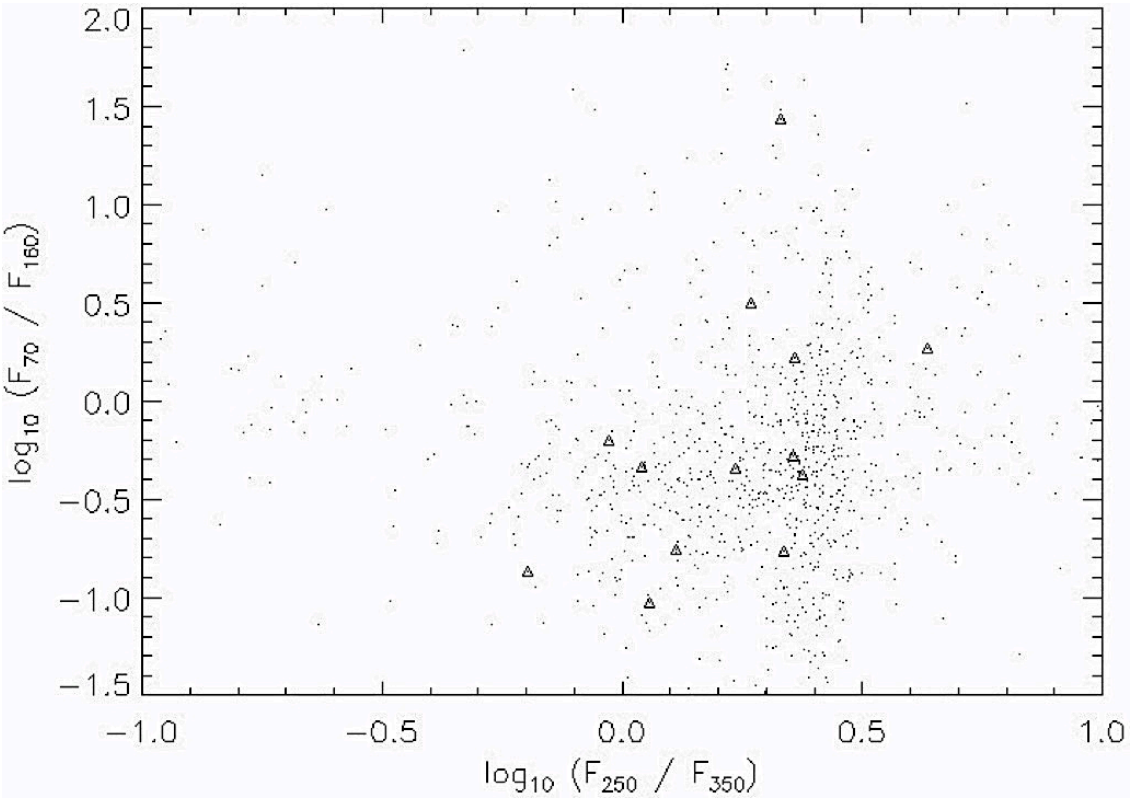

Figure 7.25: Plot of the far-IR colours of all HERSCHEL detected sources in the W3 area (*whether or not they have water masers associated with them*) from the catalogue by Rivera-Ingraham et al. (2013) represented as points. F_{xx} is the integrated flux at the wavelengths indicated. Those sources associated with the water masers (determined from the current study) are shown as triangles.

Figure 7.25 shows how our detected water masers are distributed across the entire range of other far-IR detections. Without any clear trend with HERSCHEL colour, it appears that the HERSCHEL colours *alone* do not provide a clear indicator of sources that show maser activity.

Due to the small statistical number, it was decided to *expand* the sample of water sources. A catalogue of *all known* water masers was built from data published in the Arcetri (Comoretto et al. 1990, Brand et al. 1994 and Valdettaro et al. 2001) and HOPS (Walsh et al. 2011) water maser surveys, as well as a number of other smaller studies. This catalogue was cross-correlated using the STARLINK utility TOPCAT (using positional matches within 10″), against a database of preliminary values of HERSCHEL fluxes from a pre-release analysis of survey tiles from the large-scale HERSCHEL HiGAL survey (White 2015 - work currently in preparation which forms part of a HERSCHEL HiGAL Consortium study). Working with this data, the results are shown below in Figure 7.26 for the *colours of HiGAL far-IR* sources that are associated *with known* water maser sources.

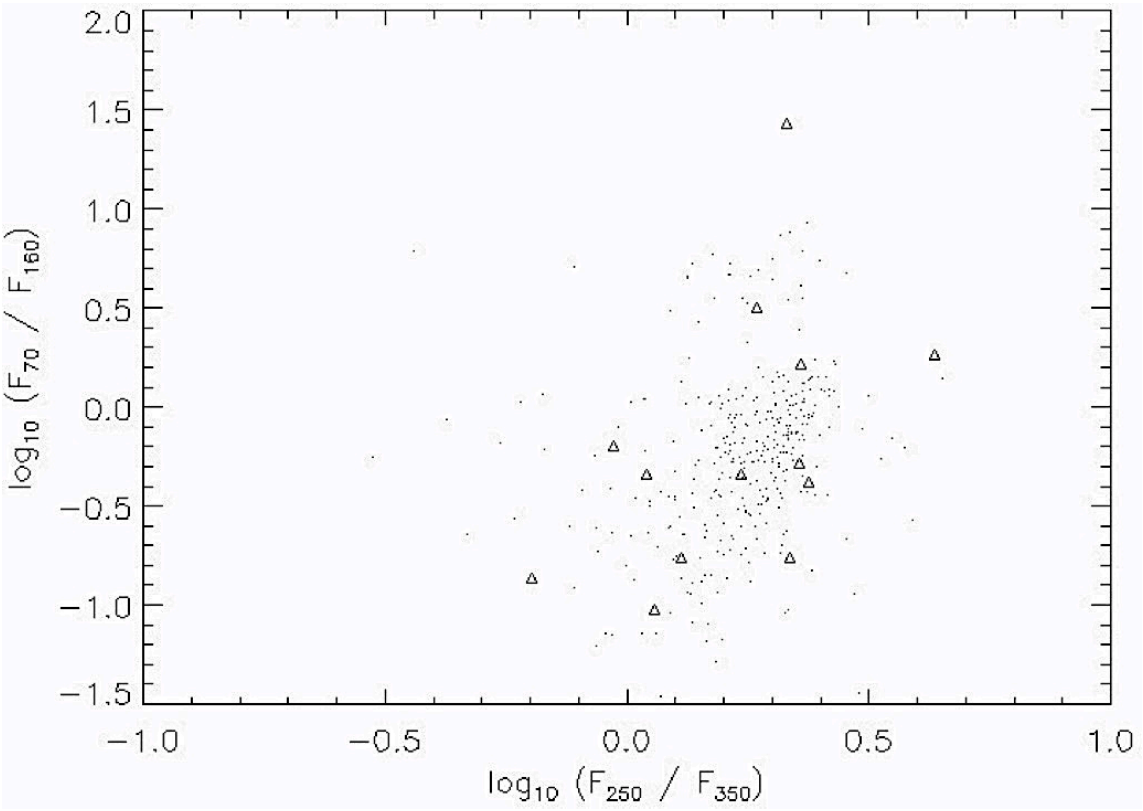

Figure 7.26: Plot of the *HiGAL far-IR* colours of all-known IR sources *associated with water masers* from the Arcetri and HOPS samples, as described in the text. The W3 water masers from the present study are again over-plotted as triangles.

Again, the plot shows no clear evidence for separation in colour-colour space between the populations far-IR sources associated *with* water sources, and those *not* having previously been associated with masers, and we conclude that on the basis of this small sample, the HERSCHEL colours alone do not provide a clear indication as the *whether or not* a water maser source is likely to be present. A *more detailed* analysis of whether near and far-IR colours can be used to indicate the likelihood of a water maser source will be made in future work when all of the analysis of a much larger sample of several thousand low luminosity HERSCHEL sources will be fully analysed.

Chapter 8

Conclusions & Future Work

This thesis describes the development of a pipeline as part of LOFAR's commissioning process, in order to calibrate diffuse maps between ~ 30–76 MHz of the high mass star-forming W3/W4/W5 regions and SNRs 3C 58 and HB3 in our unique continuum maps ~10 deg^2 where our final full bandwidth image (centred at ~ 53.5 MHz) is the deepest image of this FoV obtained at these frequencies with a final resolution of between ~ 62–85″ and noise level of 4.78 mJy/beam; a level approaching theoretical levels.

We have found the low radio frequency range to be a rewarding window of the electromagnetic spectrum detailing unique spatial characteristics of the arcs and shells of W4 and W5 as well as the UC H II regions of W3. The spectral maps show some degree of free-free self-absorption effects in the diffuse W3/W4/W5 H II regions, indicative of areas which are optically thick at low frequencies. This is in addition to the larger proportion of areas of free-free radio emission with characteristically flat spectral indices. W4 exhibits a complicated spectral gradient (indicative of an inhomogeneous medium) reaching a relatively flat index nearest W3 where there is also brightest radio emission in the star-forming region of AFGL 333. In addition to this area, the UC regions of W3 are highly luminous at LOFAR frequencies which is likely to be the result of radio Bremsstrahlung originating from clusters of YSOs. As well as confirming the simultaneously very hot and dense regions of W3-main and W3-OH which host ongoing star-formation, our diffuse AKARI dust temperature and column density maps give strong evidence of W4 being a

super-shell cast out by IC 1805 and we identify several dense yet relatively cool regions along the *outer* shell, which may host pre-stellar cores that may go on to host star-formation in the future.

Although we speculate a *possible* plateau in emission near 50 MHz (which could be explained by free-free absorption by thermal Bremsstrahlung associated with W3 coexisting in HB3 in addition to the synchrotron component, indicating an interaction), a turnover must be confirmed with further narrow band low radio frequency studies < 60 MHz in the future, with HB3 at the centre of the beam. We also anticipate from our findings (§ 4.2) and from the literature (§ 2.3.9) that a *complete* spectral turnover of free-free emission from the W3/W4/W5 H II regions will occur < 30 MHz. Such observations are likely to be possible in the future with the improving capability of LOFAR's lower frequency threshold from ~ 30 MHz (at the time of our observation) down to the current 15 MHz. The comparison with CO emission and our LOFAR diffuse maps also reveals a possible interaction between HB3 and the molecular material, with the highest velocity evident as a peak in intensity in the W3 and AFGL 333 H II regions; these regions are possibly breaking away from the W3 GMC.

We can confirm the absence of an *extensive* synchrotron halo from SNR 3C 58 at low radio frequencies ~ 53.5 MHz, with an age at order ~10^4 yr disproving its association to SN 1181 and is in keeping with Bietenholtz (2006). We obtain a near flat spectral index of α ~ -0.03±0.02 for SNR 3C 58. This object was not the target of our observation (which centred primarily on W3), and although we did correct for the LOFAR beam, this was without residual attenuation. Therefore it would be interesting to confirm our findings with LOFAR future observations specifically targeting SNR 3C 58, at the centre of the beam.

In order to investigate a possible threshold for the onset of water maser emission from star-forming regions, we expanded the sampling of the low luminosity of regime of water maser/ bolometric luminosity relation through our targeted OSO water maser surveys and correlated this with the derived luminosities from the recent HERSHEL HOBYS catalogue and our derived AKARI point source catalogue (which hosts 1298 sources). Our findings are in keeping with the previously determined luminosity functions of Furuya et al. (2007) and Brand et al. (2003). We did not find a clear distinction in colour-colour space between the populations of far-IR sources associated *with* water sources, and those *not* having previously been associated with masers, but this should be

made possible in future work, with a larger sample of several thousand low luminosity HERSCHEL sources.

Approximately ~ 300 extragalactic point sources were captured in the background of the FoV with LOFAR and over ~ 50 % provided a rich sample of spectral index information to constrain turnover of synchrotron < 100 MHz. We observed strong and moderate SED flattening attributed to free-free absorption processes at the source for ~ 3.2 % and ~ 19.1 % of sources respectively which is consistent with Rafferty et al. (2013). We could further our understanding of the *evolution* of starburst radio-luminous galaxies by investigating possible a far-IR-luminosity correlation of the resultant sample in future work to deduce the area over which star formation occurs and see how this relates to the rate of supernova (§ 4.1).

As we have seen, low frequency radio astronomy is challenging due to its inherently wide FoV (and associated DDEs), low resolution and vulnerability to the volatile ionosphere which can impact the quality of the data. From the challenges faced, observing an external calibrator is advised where possible in addition to the target, in future continuum and RRL observations. This may reduce the overall bandwidth on the target, but with LOFAR sensitivity anticipated to increase by a factor of 4 (§ 3.2.1), with the implementation of a full-core single-clock in 2013, lack of primary bandwidth is less likely to be an issue. There are several established 3C calibrators which now serve as standard calibrators for LOFAR which was not the case during early commissioning.

We have shown that the extensive challenges using the LBA without an external calibrator (in the method of complete self-calibration) can be overcome with *very* meticulous construction of the initial sky model and multiple cycles of self-calibration which iteratively and effectively reduced image noise and improved resolution. Future observations will benefit from the new LOFAR GSM catalogue populated by the on-going MSSS surveys which will help to produce initial sky models appropriate to the observed low frequency range. This was not available at the time of our data reduction and we carried out a number of protracted analysis steps which inevitably proved successful. For Galactic *diffuse* in particular, a basic point source model did not yield satisfactory results, regardless of the number of cycles of self-calibration. The use of shapelets is advised in regions where diffuse emission is anticipated. This technique was essential in the creation of an initial sky model *accurate* to the true nature of the source and for modelling

vague spatial objects with no 'crisp' boundaries. The shapelets technique has been subject to further adaptation and improvement by LOFAR commissioners since the writing of this thesis, and we have seen its effectiveness during its early implementation. Even today, there is still currently no 'set' technique or pipeline to calibrate Galactic diffuse emission in the *LBA* which remains a work in progress. We found that 'A-team' removal is essential for revealing weak large-scale diffuse structures, and SAGECal's performance is far superior over demixing for this purpose; for this reason, we recommend the implementation of SAGECal into the standardised pipeline.

The best calibration techniques will have little improvement if the quality of the observational data is poor. Our dataset was taken in late 2011 when LOFAR was far from complete. As a result numerous technical glitches (non-synchronous clocks etc.; § 3.4.13) reduced the inherent quality of data; this is less likely to be an issue today, given how far the array has improved in the intervening time with ongoing improvement in LOFAR's calibrated stations which allow more stable beams, and the addition of more remote and core stations which will allow better (u,v) coverage. Therefore, acquiring new LOFAR observations of W3/W4/W5 would be advised in the future with the improved instrumentation to verify and further the initial low frequency findings we make for this target.

For the *current data* stacking several subbands, after applying the processing steps in § 5 would increase the probability of C RRL detection in W3 (although it is advised to re-observe the FoV, with the addition of an external calibrator to aid bandpass calibration). A better estimate of foreground Galactic synchrotron emission in the future would also increase the accuracy of all Galactic and extragalactic LOFAR observations, which would benefit by subtracting out this emission. Our initial all-sky single station images (§ 3.3) and our *first order* attempt of comparing relative Galactic emission between 46 – 78 MHz by means of a spectral index map after successful subtraction of Cas A and Cyg A, highlighted factors for future work. We anticipate a full-scale spectral index map of the low frequency sky with better data quality in the near future due to improved relative calibration and stability of single station beams. Absolute station calibration is heavily dependent on an improved nominal element beam model, and an accurate flux model for the main calibrator (likely to be Cas A or possibly Cyg A). Countering more effectively the DDEs of the element beam will also inevitably benefit array observations.

Bibliography

Aharonian, F., et al., 2004, ApJ, 614, 897

Adams, F. C., Shu F. H., 1986, ApJ 308, 836

Adams, F. C., Lada C. J., Shu F. H., 1987, ApJ 312, 788

Alexander, J. K., Brown, L. W., Clark, T. A., & Stone, R. G. 1970, A&A, 6, 476

Anantharamaiah, K. R., Bhattacharya, D., 1986, Journal of Astrophysics & Astronomy, 7, 141–153

Anantharamaiah, K. R., Payne, H. E. & Erickson, W. C., 1988, MNRAS, 235, 151-160

Anantharamaiah, K.R., & Kantharia, N. G., 1999, New Perspectives on the Interstellar Medium, ASP Conference Series, eds. Taylor, A. R., Landecker, T. L., & Joncas, G., Astronomical Society of the Pacific, San Francisco, 168, 197-200

Anderson, M. C., & Rudnick, L. 1993, ApJ, 408, 514

Anderson, L. D., Bania, T. M., 2009, ApJ, 690, 706–719

André, P., Ward-Thompson, D., Barsony, M., 1993, Astrophys. J., 406, 122–141
André, P., Montmerle, T., 1994, Astrophys. J. 420, 837–862

André, P., Minier, V., Gallais, P., et al. 2008, AA, 490, L27

André, P., Ward-Thompson, D., & Barsony, M. 2000, In Protostars & Planets IV, eds. Mannings, V., Boss, A., Russell, S. (Tucson:Univ. Arizona), 59

Arimatsu, K., Doi, Y. et al. 2014, Publications of the Astronomical Society of Japan, 66 (2), 47

Arzoumanian, D., André, Ph., Didelon, P. et al., 2011, A&A, 529, L6

Asgekar, A., Oonk, J. B. R., Yatawatta, S., et al. 2013, A&A, 551, L11

Bacmann, A., André, P.; Ward-Thompson, D., 2001, ASP Conference Series, 243, 113

Ballantyne, D. R., Kerton, C. R., & Martin, P. G. 2000, ApJ, 539, 283

Baars, J. W. M., Genzel, R., Pauliny-Toth, I. I. K., & Witzel, A. 1977, A&AS, 61, 99

Baars, J. W. M & Hartsuijker, A. P., 1972, Astr. Astrophys., 17, 172

Baldwin, J.E., Boysen, R.C., Hales, S.E.G, et al., 1985, MNRAS, 217, 717

Beck, R., Shukurov, A., Sokoloff, D., Wielebinski, R., 2003, A&A, 411, 99-107

Beck, R., Krause, M., 2005, Astronomische Nachrichten, 326, 414-417

Beck, R., 2009, Proceedings of the International Astronomical Union, 4, 3-14

Beck, R., 2009, Astrophysics & Space Sciences Transactions, 5, 43–47

Best, P. N. & LOFAR-UK Consortium, 2007, 'LOFAR-UK White Paper: A science case for UK involvement in LOFAR', eprint arXiv:0802.1186

Beuther, H., Churchwell, E. B., McKee, C. F., & Tan, J. C. 2007, Protostars & Planets V, 165

Bentum, M. J, Boonstra, A. J., Millenaar, R. P., 2010, RFI mitigation workshop, PoS(RFI2010)006

Bhatnagar, S., Cornwell, T. J., Golap, K., & Uson, J. M. 2008, A&A, 487, 419

Bicknell, G. V., Dopita, M. A., & O'Dea, C. P. 1997, ApJ, 485, 112

Bieging, J. H. & Peters, W. L., 2011, The Astrophysical Journal Supplement Series, 196, 18

Bietenholz, M. F, 2006, ApJ, 645, 1180–1187

Bietenholz, M. F., Kassim, N. E., & Weiler, K. W. 2001, ApJ, 560, 772

Bally & Zinnecker, 2005, AJ, 129, 2281

Blagrave, K. P. M., Martin, P. G., Rubin, R. H. et al., 2007, ApJ, 655, 299

Blandford, R., Eichler, D., 1987, Physics Reports (Review Section of Physics Letters), 154, 1-75

Blake, D. H., Crutcher, R. M., Watson, W. D. 1980, Nature, 287, 707

Blitz, L. & Rosolowsky, E., 2006, ApJ, 650, 933-944

Blitz L., 1978, PhD Thesis, Columbia University

Bobylev V. V. & Bajkova, A. T., 2013, Astronomy Letters, 39, 809–818

Bourne, N., Dunne, L., Ivison, R. J., Maddox, S. J., Dickinson, M., Frayer, D. T., 2011, MNRAS, 410, 1155-1173

Bonnell, I. A., Bate, M. R. & Zinnecker, H., 1998, MNRAS, 298, 93–102

Bontemps, S., André, P., Terebey, S., Cabrit, S., 1996, Astron. Astrophys, 311, 858–872

Brand, J., Cesaroni, R., Caselli, P., et al. 1994, A&AS, 103, 541

Brand, J., Cesaroni, R., Comoretto, G., et al., 2005, Astrophysics & Space Science, 295(1-2), 133-141

Brand, J., et al. 2003, A&A, 407, 573-587

Braun, R. & Walterbos, R. A. M., 1985, A&A, 143, 307-312.

Bregman, J., 1999, Perspectives on Radio Astronomy – Technologies for Large Antenna Arrays, eds. Smolders, A.B. & van Haarlem, M. P., ASTRON, The Netherlands

Bridle, A. H., 1967, MNRAS, 136, 219

Bridle, A. H. & Schwab, F. R., Synthesis imaging in radio astronomy, A collection of Lectures, eds. Perley, R. A., Schwab, F. R., Bridle, A. H. Astronomical Society of the Pacific, 6, 247

Briggs, S. D., Schwab, F. R., Sramek, R. A., 1999, ASP Conference series, 180, 127-149

Briggs D. S., 1995, Ph.D. Thesis, New Mexico Institute of Mining Technology, Socorro, New Mexico, USA

Brogan, C. L., Devine, K. E., Lazio, T. J., Kassim, N. E., Tam, C. R., Brisken, W. F., Dyer, K. K., Roberts, M. S. E., 2004, Astronomical Journal, 127, 355-367

Brüggen, M., Falcke, H., Beck, R., & Enßlin, T., 2005, German LOFAR White paper, Technical report

Butt, Y., 2009, Nature, 460, 701

Camilo, F., Stairs, I. H., Lorimer, D. R. et al., 2002, ApJ, 571, L41

Cane, H. V., 1977, PhD Thesis, University of Tasmania

Carey et al. 1998, ApJ, 508, 721

Carey et al. 2000, ApJ, 543, L157

Carpenter, J. M., Heyer, M. H., & Snell, R. L. 2000, ApJS, 130, 381

Cassano, R., Brunetti, G., Röttgering, H. J. A., & Br uggen, M. 2010, A&A, 509, A68

Casassus, S., Bronfman, L., May, J., & Nyman, L.-Å., 2000, A&A, 358, 514-520

Castelletti, G., Dubner, G., Clarke, T., Kassim, N. E., 2011, A&A, 534, A21

Castor, J., McCray, R., Weaver, R., 1975, ApJ, 200, L107-L110.

Clemens, M. S., Scaife, A., Vega, O., Bressan, A., 2010, MNRAS, 405, 887-897

Clark, B. G., 1980, Astron. Astronphys. 89, 377

Chambers et al. 2007, BAAS, 38,197

Chambers et al. 2008, BAAS, 40, 197

Chi, X. & Wolfendale, A. W., 1993, Nature, 362, 610

Chen, H., Grenfell, T. G., Myers, P. C., Hughes, J. D., 1997, Astrophys. J., 478, 295–312

Churchwell et al, 1990, A&AS, 83, 119

Claussen M. J., Gaume R. A., Johnston K. J., Wilson T. L., 1994, ApJ 424, L41

Clemens, D. P. & Barvainis, R. 1988, ApJS, 68, 257

Clemens, M. S., Scaife, A., Vega, O., & Bressan, A. 2010, MNRAS, 405, 887

Cohen, A.S., Lane, W.M., Cotton, W.D. et al. 2007, AJ, 134, 1245

Colom et al., 2015, A&A, 575, A49

Comoretto, G., Palagi, F., Cesaroni, R., et al., 1990, A&AS, 84, 179

Condon, J. J., 1974, ApJ, 188, 279

Condon J. J., 1992, ARA&A, 30, 575

Condon J. J., Cotton W.D., Greisen E.W. et al., 1998, AJ, 115, 1693 (NVSS)

Cornwell, T., Braun R. & Briggs, D. S., 1999, 'Deconvolution', in Synthesis Imaging in Radio Astronomy II, ser. Astronomical Society of the Pacific Conference Series, eds. Taylor, G. B., Carilli, C. L. & Perley, R. A., 180, 151–170.

Cornwell, T. & Fomalont, E. B., 1999, ASP Conference Series, 180, 187-199.

Cornwell, T. J., Golap, K. & Bhatnagar, S., 2005, 'w-projection: A New Algorithm for Wide Field Imaging with Radio Synthesis Arrays' in ADASS XIV, Astronomical Society of the Pacific Conference Series, vol. 347

Cornwell, T. J. & Wilkinson, P. N., 1981, MNRAS, 196, 1067-1086
Cornwell, T., 1982, Synthesis Mapping, Proceedings of the NRAO-VLA Workshop held 21-25 June in Socorro, NM, eds. Thompson, A.R. & D'Addario, L.R., Green Bank: NRAO, p. 13
Cornwell, T. J., Golap, K., Bhatnagar, S., IEEE Journal of Selected Topics in Signal Processing, 2, 647-657
Cornwell, T. J., 1983, Astron. Astrophys. 121, 281
Cornwell, T. J. & Perley, R. A., 1992, A&A, 261, 353
Cotton, W.D., et al., 2004,'Beyond the isoplanatic patch in the VLA Low-frequency Sky Survey', Proc. SPIE, 5489, 180
Crocker, R. M., Jones, D., Protheroe, R. J., Ott, J., Ekers, R., Melia, F., Stanev, T., Green, A., 2007, Astrophysical Journal, 666, 934-948
Dale, J. E., Ercolano, B., & Bonnell, I. A. 2013, MNRAS, 431, 1062
Dame, T. M., Hartmann, D., & Thaddeus, P., 2001, ApJ, 547, 792
Dempster, A.P. Laird, N.M. & Rubin, D.B., 1977, Jnl. Royal Stat. Soc. Series B, 39, 1-38,
Dickel, H. 1980, ApJ, 238, 829
Dickey, J.M. & Lockman, F.J., 1990, ARA&A, 28, 215
Digel, S. W., Lyder, D. A., Philbrick, A. J., Puche, D., & Thaddeus, P., 1996, Astrophysical Journal, 458, 561
Deharveng, L., Zavagno, A., Caplan, J., 2005, A&A, 433, 565
Deharveng, L., Schuller,F., Anderson, L.D., Zavagno, A. et al., 2010, A&A, 523, 6
Dermer, C. D. & Ramaty, R., 1986, ApJ, 301, 962-974
De Vos, M., Gunst, A. W. & Nijboer, R., 2009, The LOFAR Telescope: System Architecture & Signal Processing, Proceedings of the IEEE, 97 (8), 1431-1437
Dobashi, K., Bernard, J.P., Yonekura, Y., Fukui, Y., 1994, ApJS, 95, 419
Doi, Y., Komugi, S., Kawada, M., Takita, S., Arimatsu, K., Ikeda, N., Kato, D., Kitamura, Y., Nakagawa, T., Ootsubo, T., Morishima, T., Hattori, M., Tanaka, M., White, G. J., Etxaluze, M., Shibai, H., 2012, Publications of The Korean Astronomical Society, 27(4), 111-116
Doi et al. 2015 in press
Donley, J. L., et al. 2012, ApJ, 748, 142
Donahue M., De Messières, G. E, O'Connell, R. W., Voit, G. M., Hoffer, A., McNamara B. R., Nulsen, P. l E. J., 2011, ApJ, 732, 40
Dopita, M. A., Sutherland, R. S., 2001, 'Diffuse Matter in the Universe', Physics-Monograph, Editorial W. Beiglböck, Springer-Verlag, Berlin- Heidelberg- New York
Downes, D., Wilson, T. L., 1974, A&A, 34, 133-139
Dreher, J. W., Welch Wm. J., 1981, ApJ 245, 857
Dröge, F. & Priester, W., 1956, Zeitschrift fur Astrophysik, 40, 236-248
Douglas J.N., Bash F.N., Bozyan F.A., Torrence G.W., & Wolfe C., 1996, AJ, 111, 1945 (TXS)
Dulk, G. A., 1985, IN: Annual review of Astronomy & Astrophysics (A86-14507 04-90). Palo Alto, CA, Annual Reviews, Inc., 23, 169-224
Dulk, G. A. & Slee, O. B., 1975, ApJ, 199(1), 61-68
Eddington, A. S., 1913, MNRAS, 73, 359
Edwards, P., 2007, Asian Radio Astronomy Winter School 2007 Textbook, Sokendai, NAOJ, NINS, EACOA, pp. 31-48
Eddy, J. A., 2009, 'The Sun, the Earth & Near-Earth Space: A Guide to the Sun-Earth System', Government Printing Office, 30 Nov 2009 - Science - 301 pages
Elshamouty, G., et al., 2013, The Astrophysical Journal, 777, 22
Elitzur, M., Hollenbach, D.J., McKee, C.F., 1989, ApJ 346, 983
Erickson, W. C., McConnell, D., & Anantharamaiah, K. R. 1995, ApJ, 454, 125
Etxaluze, M., 2010, PhD Thesis: 'Far Infrared Studies of the Galactic Plane', The Open University/ Rutherford Appleton Laboratory
Evans N. J., 1978, in "Protostars & Protoplanets", ed. T. Gehrels, p152, University of Arizona Press
Fallscheer, C. et al. 2013, ApJ, 773, 102
Feast, M. & Whitelock, P., 1997, MNRAS, 291, 683-693
Felli, M., et al., 1992, A&A, 255, 293

Feigelson E. D., & Townsley, L. K., 2008, ApJ, 673, 354-362,

Ferrière, K. M., 2001, 'The Interstellar Environment of our Galaxy', Reviews of Modern Physics, 73, 1031-1066

Fesen, R. A., Downes, R. A., Wallace, D., & Normandeau, M., 1995, AJ, 110, 2876

Fessler, J. A. & Hero, A. O., 1994, IEEE Explore, IEEE Tr. Info. Theory, 40(4), 1205-1210

Foster et al., 2014, MNRAS 439, 3180–3188

Furuya et al., 2001,ApJ, 559, L143

Furuya et al., 2003 ApJS, 144, 71-134

Furuya et al., 2007 ApJ, 659, L81

Gallagher, T. F., 2005, Cambrdge University Press, USA, New York, ISBN 0-521-38531-8

Ginzburg, V. L., 1953, Dokl. Akad. Nauk SSSR, 92, 1133−1136

Giovannini, M., 2004, Int.J.Mod.Phys., D13, 391-502

Gómez, J. F., de Gregorio-Monsalvo, I., Suárez, O., & Kuiper, T. B. H. 2006, ApJ, 132, 1322

Green, D. A., 1986, MNRAS, 218, 533

Gregory P.C., Scott W.K., Douglas K., & Condon J.J., 1996, ApJS, 103, 427 (GB6)

Goldberg, L., 1966, ApJ, 144, 1225-1231, 1968 in 'Interstellar Ionised Hydrogen', eds. Terzian, Y., W. A. Benjamin, Inc, New York

Gordon, M. A. & Sorochenko, R. L., 2002, 'Radio Recombination Lines: Their Physics & Astronomical Application', Astrophysics & Space Science Library, vol. 282, p. 110

Goudis, C., 1979, Astrophys. Space Sci., 61, 417

Gosachinskiĭ I. V., 1985, SvA, 29, 128

Gotthelf, E.V., Helfand, D.J., Newburgh, L., 2006, ApJ, 654, 267-272

Hachisuka, K., Brunthaler, A., Menten, K. M., et al. 2006, ApJ, 645, 337

Haffner, L. M., 2010, Astronomical Society of the Pacific Conference Series, 438, 179

Hales, S.E.G., Masson, C.R., Warner, P.J., Baldwin, J.E., Green, D.A.
1993, MNRAS, 262, 1057

Hales S.E.G., Waldram E.M., Rees Nick, Warner P.J., 1990, MNRAS, 244, 233

Hamaker, J.P., Bregman, J.D., Sault, R.J. 1996, A&AS, 117, 137

Hamaker, J.P., 2000, A&AS, 143, 515

Harris, J. L., 1964, J. Opt. Soc. Am., 54, 931-936

Harvey-Smith, L. & Cohen., R. J., 2006,
Proceedings of the International Astronomical Union, Symposium S237, 2, 422-422

Harwit, M. & Pacini, F., 1975, Ap. J. Lett. 200, L127-29

Haswell, C. A., Tajima, T., & Sakai, J.-I, 1992, ApJ, Part 1, 401(2), 495-507

Haslam, C. G. T., Salter, C. J., Stoffel, H., Wilson, W. E. 1982, A&AS, 47, 1

Helmboldt, J. F., & Kassim, N. E., 2009, AJ, 138, 838.

Heyer, M. H., Snell, R. L., Brunt, C., Howe, J., Schloerb, F. P., & Carpenter, J. M., 1998, ApJS, 115, 241

Heald, G. & LOFAR Collaboration. 2013, in American Astronomical Society Meeting Abstracts, American Astronomical Society Meeting, 221, 215.07

Heinke, C. O. & Ho, W. C. G., 2010, ApJ, 719, L167

Herbig G. H., 1962, Adv. Astron. Astrophys. 1, 47

Herbst, W., & Assousa, G. E. 1977, ApJ, 217, 473

Hirsch, L. et al., 2012, ApJ, 757(2), 113

Hjellming, R. M., Andrews, M. H., Sejnowski, T. J., 1969, Astrophysical letters, 3, 111-114

Hollenbach, D. J. & Tielens, A. G. G. M., 1999, Rev. Mod. Phys, 71, 173-230

Högbom J. A., 1974, A&AS, 15, 417

Huang Y. L. & Thaddeus P., 1986, ApJ, 309, 804

Ibar E., Ivison R. J., Best P. N., Coppin K., Pope A., Smail I., Dunlop J. S., 2009, MNRAS, 401, L53

Intema, H. T., van der Tol, S., Cotton, W. D., et al. 2009, A&A, 501, 1185

Israel, F. P., & Mahoney, M. J. 1990, ApJ, 352, 30

Jaeger, S., 2007, Proceedings of the conference held 23-26 September, 2007, in Kensington Town Hall, London, United Kingdom. eds Argyle, R. W., Bunclark, P. S., Lewis, J. R., 394, 623

Jaffe, D. T., Hildebrand, R. H., Keene, J., Whitcomb, S. E., 1983, ApJ, Part 2 - Letters to the

Editor, 273, L89-L93
Jansky, K. G., 1933, Proc. IRE, 20, 12
Jones, B. B., Finlay, E. A., 1974, Australian Journal of Physics, 27, 687-711.
Jones, D. L., Weiler, K. W., 1995, IAU, Working Group on Sky Surveys Newsletter, USA
Gordon, K. D., Clayton, G. C., Misselt, K. A., Landolt, A.U., Wolff, M. J., 2003, ApJ, 594, 279-293
Karr, J. L., Martin, P. G. 2003, ApJ, 595, 900
Kantharia, N. G., Anantharamaiah, K. R., Goss, W. M., 1998a, ApJ, 504, 375-389
Kantharia, N. G., Anantharamaiah, K. R., Payne, H. E. 1998b, ApJ, 506, 758
Kraemer, K. E., Shipman, R. F., Price, S. D., Mizuno, D. R., Kuchar & T., Carey, S. J., 2003, ApJ, 126, 1423–1450
Kassim, N. E., 1989, ApJ, 347, 915
Kassim, N. E., 1990, in 'Low Frequency Astrophysics from Space', eds. Kassim, N. E. & Weiler, K. W. (Berlin, Springer-Verlag), 144
Kassim, N. E., Lazio, T.J.W., Ray, P.S., et al., 2004, 52(15), 1343–1349
Kaufman, M., Neufeld, D., 1996, ApJ, 456, 611
Kaufman L., Rousseeuw P., 1990, Finding groups in data: An introduction to cluster analysis, Wiley Interscience, Wiley-Interscience, New York
Kawada, M. et al. 2007, Publ. Astron. Soc. Japan, 59, 389
Kenyon et al. 1990, AJ, 99, 869
Kiepenheuer, K. O. 1950, Phys. Rev. 79, 738
Kirk, H., Myers, P. C., Bourke, T. L., et al. 2013, ApJ, 766, 115
Kondratiev, V., Stappers, B. & LOFAR Pulsar Working Group, Proceedings of the International Astronomical Union, 291, 47-52
Konovalenko A.A., Stepkin S.V., Shalunov D.V., 2002, Proceedings of IAU Symposium, Pune, India, eds. Rao A. P., Swarup G., Gopal-Krishna, 199, 349-350
Konovalenko, A. A., 2002, Proceedings of IAU Symposium 199, Pune, India, eds. Rao A. P., Swarup G., Gopal-Krishna, 199, 327-334
Kothes, R., Dougherty, S. M., 2008, eds. Benaglia, P., Bosch, G. L. & Cappa, C. E., Revista Mexicana de Astronomía y Astrofisica (Serie de Conferencias), 33, 163-163
Kothes, R., Fedotov, K., Foster, T. J., Uyaniker., B., 2006, A&A, 457, 1018
Koyama, K., Petre, R, Gotthelf, E. V., Hwang, U., Matsuura, M., Ozaki, M., Holt, S. S., 1995, Nature, 378(6554), 255-258
Kraemer, K. E., Shipman, R. F., Price, S. D., Mizuno, D. R., Kuchar & T., Carey, S. J., 2003, ApJ, 126, 1423–1450
Kraus, J. D., 1988, 'Antennas', 2nd edition. New York, McGraw-Hill
Krumholz, M. R., McKee, C. F. & Klein, R. I., 2005, Nature, 438, 332-334
Kwok, S., Cambridge University Press, 'Organic Matter in the Universe', John Wiley & Sons, 27 Dec 2011, 300 pages
Lada, C.J., Wilking, B., 1984, Astrophys. J., 287, 610–621
Lada C. J., 1985, Annu. Rev. Astron. Astrophys. 23, 267
Lada, C.J., 1987, eds. Peimbert M., Jugaku, J., Proc. IAU Symp., 115, 1–18.
Lada, C. J., Elmegreen, B. G., Cong, H., & Thaddeus, P. 1978, ApJ, 226, L39
Lada C. J., Elmegreen B. G., Cong H., Thaddeus P., 1978, ApJ 411, 708
Lada, C. J. & Lada, E. A. 2003, ARA&A, 41, 57
Landau, H. J. & Pollak, H. O., 1961, Bell Syst. Tech. J., 40(2), 65–84
Landecker, T. L. & Wielebinski, R., 1970, Austrialian Journal of Physics Supplement, 16, 1
Landecker, T. L., Vaneldik, J. F., Dewdney, P. E., & Routledge, D. 1987, AJ, 94, 111
Lane, W. M., Cotton, W. D., Helmboldt, J. F., & Kassim, N. E., 2012, Radio Science, 47,
Larson, R. B., 2010, Rep. Prog. Phys., 73, 014901
Lazio, T. J. W., Cohen A. S., Kassim, N. E., Perley R. A., Erickson W. C., Carilli C. L., Crane, P. C., 2006, ApJ, 642, L33.
Lee, S-H., Ellison, D. C., Nagataki, S., 2012, The Astrophysical Journal, 750, 156
Lehner, N., Zech, W. F., Howk, J. C., Savage, B. D., 2010, ApJ, 727(1), 46

Li, H-b, Dowell, C. D, Goodman, A., Hildebrand, R. & Novak, G., Anchoring Magnetic Field in Turbulent Molecular Clouds, Astrophys. J., 704, 891-897, 2009
Little, L.T., White, G.J. & Riley, P.W. 1977, MNRAS, 180, 639
Longair, M. S., 2011, High Energy Astrophysics: Volume 1. Photons, Particles & their Detection, 3rd edition, 2011, Cambridge: Cambridge University Press
Lonsdale, C. J., 2005, ASP Conference Series 2005, eds. Kassim, N. E., Pérez, M. R., Junor, W., Henning, P. A., Vol. 345
Lord, S. D. & Young, J. S., 1990, ApJ, 356,135-148
Lucas, P. W., Roche, P. F., 1997, MNRAS, 286, 895–919
Luhman, M. L., Satyapal, S., Fischer, J., Wolfire, M. G., Sturm, E., Dudley, C. C., Lutz, D., Genzel, R., 2003, ApJ, 594, 758
Maran, S. P., 1991, 'The Astronomy & Astrophysics Encyclopaedia', John Wiley & Sons
Markwick-Kemper, Andrew J., Remijan, A. J., Fomalont, E., 2006,
American Astronomical Society Meeting 208, #51.01; Bulletin of the American Astronomical Society, 38, 130
Massey, P., Johnson, K. E., & DeGioia-Eastwood, K, 1995, ApJ, 454, 151
Mauch, T. et al., 2013, MNRAS, 435, 650
Mezger, P. G. & Henderson, A. P., 1967, ApJ, 147, 471
McIntosh, G., 2002, American Journal of Physics, 70(3), 285-287
McCready, L. L., Pawsey, J. L., & Payne-Scott, R., 1947, Proc. Roy. Soc. London, A190, 357-375.
Men'shchikov, A., André, P., & Didelon, P. et al. 2012, A&A, 542, A81
Miley, G., 1980, Ann. Rev. Astron. Astrophys. 18, 165-218
Mirabel, I. F., Rodrigues, I., Liu, Q. Z., 2004, Astronomy & Astrophysics, 422, L29-L32
Molinari, S., Brand, J., Cesaroni, R., Palla, F., & Palumbo, G. G. C. 1998a, A&A, 336, 339
Mookerjea, B., Kramer, C., Röllig, M., Masur, M., 2006, A&A, 456(1), 235-244
Moore, T. J. T., Bretherton, D. E., & Fujiyoshi, T. et al. 2007, MNRAS, 379, 663
Motte, F., Bontemps, S., & Schilke, P. et al., 2007, A&A, 476, 1243
Motte, F., et al., 2010, A&A, 518, L77
Mouschovias, T.Ch., 1995, 'Role of magnetic fields in the early stages of star formation' In 'The Physics of the Interstellar Medium & Intergalactic Medium', eds. Ferrara, A., McKee, C.F., Heiles, C., Shapiro, P.R., (San Francisco: ASP), 80, 184–217
Murray, S. S., Slane, P. O., Seward, F. D., Ransoml., S. M., 2002, ApJ, 568, 226-231
Murakami, H., et al., 2007, PASJ, 59, S369
Myers, P. C., 1986, in "Star Forming Regions, IAU Symp. No. 115", eds M. Peimbert, J. Jugaku
Myers, P. C., Fuller G. A., Mathieu R. D., Beichman C. A., Benson P. J., Schild R. E., Emerson J. P., 1987, ApJ 319, 340
Myers, P.C., Ladd, E.F., 1993, Astrophys. J. Lett. 413, L47-L50
Natta, A., Walmsley, C. M., Tielens, A. G. G. M., 1994, ApJ, Part 1, 428(1), 209-218
Nguyen Luong, Q., Motte, F., & Hennemann, M. et al., 2011, A&A, 535, A76
Njijboer, R. J., Pandey-Pommier, M., de Bruyn, A. G., 2009, SKA Memo 113
Niwa, T., Tachihara, K., Itoh, Y. et al., 2009 A&A, 500(3), 1119 - 1129
Normandeau, M., Taylor, A. R., & Dewdney, P. E., 1997, ApJS, 108, 279
Normandeau, M., 2000, ASP Conference Proceedings, eds. Alloin, D., Olsen, K. & Galaz., G., San Francisco: Astronomical Society of the Pacific, 221, 41
Nord, M. E., Henning, P.A., Rand, R.J., Joseph, T., Lazio, W., Kassim, N. E., 2006, Astronomical Journal, 132(1), 242-252
Ochsenbein, F., Bauer, P., & Marcout, J. 2000, A&AS, 143, 23
Oey, M. S., Watson, A. M., Kern, K., Walth, G. L., 2005, ApJ, 129, 393–401
Offringa, A. R., de Bruyn, A. G., Biehl, M., et al. 2010, MNRAS, 405, 155
Ogura, K., & Ishida, K., 1976, PASJ, 28, 651-664
Olofsson, A. O. H., 'The 20-m Telescope Handbook', Onsala Space Observatory, March 2014
Oonk, J. B. R., van Weeren, R. J., Salgado, F., et al., 2014, MNRAS, 437, 3506
Onello, J. S. & Phillips, J. A., 1995, ApJ, 448, 727-733
Onaka, T. et al., 2007, Publ. Astron. Soc. Japan, 59, S401-S410
Osterbrock, D. E., 1989 'Astrophysics of Gaseous Nebulae & Active Galactic Nuclei', Research

supported by the University of California, Mill Valley, CA, University Science Books
Pacholczyk, A. G., 1970, 'Radio Astrophysics', Freeman, San Francisco
Padmanabhan, T., 2001, Theoretical Astrophysics, Volume II: Stars & Stellar Systems, Cambridge University Press
Palla, F. et al., 1993, A&A, 280,599
Palagi, F. et al., 1993, A&AS, 101, 153
Palmer, P., Zuckerman, B., Penfield, H., Lilley, A. E., Mezger, P. G., 1967, Nature, 215(5096), 40-41
Pandey, V. N., van Zwieten, J. E., de Bruyn, A. G., Nijboer, R., 2009, Astronomical Society of the Pacific Conference Series, 407, 384
Pankonin, V., Thomasson, P., Barsuhn, J., 1977, Astron Asphys. 54, 335
Payne, H. E., Anantharamaiah, K. R., Erickson, W. C., 1994, ApJ, 430, no. 2, pt. 1, 690-705
Pillai, T. et al. 2006a, A&A, 450, 569
Pillai, T. et al. 2006b, A&A, 447, 929
Pearson T. J., Readhead, A. C. S., 1984, ARA&A, 22, 97
Pearson C. P. et al., 2014, MNRAS, 444(1), 846-859
Persi, P., Palagi, F., & Felli, M., 1994, Astronomy & Astrophysics, 291(2), 577-594
Peterson, J. D, & Webber, W. R., 2002, ApJ, 575, 217-224
Pilbratt, G., et al., 2010, A&A, 518, L1
Pihlström, Y., 2006, 8th European VLBI Network Symposium Sep 26th-29th 2006, PoS(8thEVN)060
Pizzo, R. F. et al., LOFAR Imaging Cookbook: Manual data reduction with the imaging pipeline, Version 14.1 April 22, 2014
Prasad, P., Wijnholds, S.J., Huizinga, F. & Wijers, R.A.M.J., 2014, A&A, Astronomical instrumentation, 568, A48
Polychroni, D., Moore, T. J. T. & Allsopp, J. 2012, MNRAS, 422, 2992
Ptuskin, V. S., Soutoul, A., 1990, A&A, 237, 445- 453
Quireza, C., Rood, R.T., Balser, D. S., Bania, T. M., 2006, Astrophysical Journal Supplement Series, 165, 338-359
Rafferty D. A., Röttgering, H. J. A., Conway, J. E., Israel, F. P., Jarvis, M. J., Garrett, M. A., 2013, Astronomy & Astrophysics manuscript no. ms2, 'Constraints on the Low-Frequency Radio Properties of Starbursts' *in press*
Rathborne et al., 2005, ApJ, 630, L181
Reber, G., 1949, Galactic Radio Waves. Sky & Telescope, 8, 139
Rees, N., 1990, MNRAS, 244, 233
Refregier, A., 2003, MNRAS, 338, 35-47
Reich, W., 1994, eds Genzel R. & Harris A. I., The Nuclei of Normal Galaxies (Dordrecht: Kluwer), p. 55
Reich, P., Reich, W., 1988, Astronomy & Astrophysics Supplement Series, 74(1), 7-23
Reid, M., Wadsley, J., Petitclerc, N. et al., 2010, ApJ, 719, 561
Reipurth, B., Chini, R., Krügel, E., Kreysa, E., Sievers, A., 1993, Astron. Astrophys., 273, 221–238
Reipurth, B., Jewitt, D., Keil, K., 2007, 'Protostars & Planets V, Vol. 5' The University of Arizona space science series Space Science Series'
Reynolds, S. P., & Aller, H. D., 1988, ApJ, 327, 845
Reynolds, S. P., & Ellison, D. C., 1992, ApJ, 399, L75
Richardson, K. J., White, G. J., Sandell, G., Duncan, W. D., Krisciunas, K., 1989, Astronomy & Astrophysics, 221(1), 95-99
Rivera-Ingraham, A. et al., 2013 ApJ, 766, 85
Rivera-Ingraham, A., Martin, P. G., Polychroni, D., & Moore, T. J. T. 2011, ApJ, 743, 39
Rodríguez, L. F., Gómez, Y., López, J. A., García-Díaz, T. & Clark, D. M., 2010, Revista Mexicana de Astronoma y Astrofsica, 46, 29-35
Roelfsema, P. R., Goss, W. M., Wilson, T. L., 1987, A&A, 174, 232
Roelfsema, P. R., & Goss, W. M. 1991, A&AS, 87, 177
Roelfsema, P. R. & Goss, W. M., 1992, Astronomy & Astrophysics Review, 4(2), 161-214
Roger, R. S., Costain, C. H., & Bridle, A. H., 1973, AJ, 78, 1030
Roger, R. S., Costain, C. H., Landecker, T. L., Swerdlyk, C. M., 1999, Astronomy & Astrophysics

Supplement, 137, 7-19
Röttgering, H. et al., 2010, in ISKAF2010 Science Meeting
Röttgering, H., et al., 2011, Journal of Astrophysics & Astronomy, 32, 557-566
Röttgering, H., et al., 2012, A&A, 32, 557–566.
Routledge, D., Dewdney, P. E., Landecker, T. L., & Vaneldik, J. F., 1991, A&A, 247(2), 529-544
Rowan-Robinson M., 1979, ApJ 234, 111
Ruch G. T., Jones T. J., Woodward C. E., Polomski E. F., Gehrz R. D., Megeath, S. T., 2007, ApJ, 654, 338
Rybicki, G. B., Lightman, A. P., 1979, 'Radiative Processes In Astrophysics', Wiley-VCH, pp.88-96
Ryle, M., & Vonberg, D. D., 1946, Nature, 158, 339-340
Ryle, M. & Hewish, A., 1960, MNRAS, 120, 220
Ryle, M., Neville, A. C., 1962, MNRAS, 125, 39
Ryle, M., 1962, Nature, 194(4828), 517-518
Saraceno, P., André, P., Ceccarelli, C., Griffin, M., Molinari, S., 1996, Astron. Astrophys., 309, 827–839
Sargent A. I., 1977, ApJ, 218, 736
Salter, C. J., 1983, Bulletin of the Astronomical Society of India, 11, 1
Sault, R. J., 1994, Astronomy & Astrophysics Suppl. 107, 55-69
Sault, R. J. & Cornwell, T. J., 1999, Synthesis Imaging in Radio Astronomy II, eds. Taylor, G. B., Carilli, C. L., Perley, R. A., ASP Conference Series, 180, 65
Savage, R. S. & Oliver, S., 2007, ApJ, 661, 1339
Scaife, A. M. M., & Heald, G. H., 2012, MNRAS, 423, L30
Scaife, A. M. M., 2012, Astronomical Review, 7(4), 26-32
Scaife A. M. M., 2013, Advances in Astronomy, Vol. 2013, Article ID 390287, 25 pages
Sejnowski, T. J., Hjellming R. M., 1969, ApJ, 156, 915-925
Shain, C. A., Komesaroff, M. M., Higgins, C. S., 1961, Australian Journal of Physics, 14, 508
Shapiro, M. M., Stanev, T. & Wefel, J. P., 2001, Astrophysical Sources of High Energy Particles & Radiation (NATO Science Series). Kluwer Academic Publishers
Shaver, P. A., 1975, A&A, 43, 465
Shklovskii, I. S., 1953, Dokl. Akad. Nauk SSSR 91, 475−478
Shu, F. H., Adams, F. C., Lizano, S., 1987 Ann. Rev. Astron. Astrophys., 25, 23–81
Shu, F. H, 1991, 'The Physics of Astrophysics Vol. 1: Radiation', Published by University Science Books, ISBN 10: 0935702644
Shu, F. H., 1982, 'The Physical Universe: An Introduction to Astronomy', Published by University Science Books. pp. 44-47, ISBN 978-0-935702-05-7.
Shu, F. H., Adams, F. C. & Lizano, S., 1987, Annu. Rev. Astron. Astrophys., 25, 23–81
Simon et al. 2006a,ApJ, 639, 227
Simon et al. 2006b,ApJ, 653, 1325
Siparov, S., Samodurov, V., Laptev, G., 2012, A&A, 574, L2
Slane, P., Zimmerman, E. R., Hughes, J. P., Seward, F. D., Gaensler, B. M., & Clarke, M. J., 2004, ApJ, 601, 1045
Smirnov, O. M. & Noordam, J.E., 2006, Astronomical Data Analysis Software & Systems XV ASP Conference Series, 351, 355-359
Smirnov, O. M., 2011, A&A, 527, A108
Smirnov, O. M., 2011, A&A, 527, A107
Spitzer, L., 1998, 'Physical Processes in the Interstellar Medium', Publisher: John Wiley & Sons Ltd, Wiley-VCH
Stamatellos, D., Whitworth, A. P., 2004, eprint arXiv:astro-ph/0406549, Appears in the Proceedings of the Conference "The Young Local Universe", La Thuile (Italy), March 2004
Stecklum, B., Henning, T., Feldt, M., Hayward, T. L., Hoare, M. G., Hofner, P., Richter, S., 1998, Astronomical Journal, 115, 767
Stephenson, F. R., & Green, D. A., 1999, Astron. & Geophys., 40, 27
Stepkin, S. V., Konovalenko, A. A., Kantharia, N. G., & Shankar, N. U, 2007, MNRAS, 374, 852
Stepanov, R., Arshakian, T. G., Beck, R., Frick, P., & Krause, M., 2008, A&A, 480, 45
Stetson, P. B., 1987, Publications of the Astronomical Society of the Pacific, 99, 191-222

Sridharan et al., 2002, ApJ, 566, 931

Strobel, A., 1992, A&A, 253, 374

Subrahmanyan, R., Goss, W. M., Malin, D. F., 2001, Astron. J. 121, 399

Sung, H. & Lee, S.-W., 1995, Journal of the Korean Astronomical Society, 28(2), 119-137

Sunada et al., 2009, *in press*

Sutherland, W. & Saunders, W., 1992, MNRAS, 259, 413

Schwartz, P. R., Snell, R. L., Schloerb, F. P., 1989, Astrophysical Journal, Part 1, 336, 519-525

Taylor, G. B., Carilli, C. L., & Perley, R. A., 1999, 'Synthesis Imaging in Radio Astronomy II (VLA white book)' Astronomical society of the Pacific Conference Series, vol. 180, pp. 21-38

Tasse, C., Cohen, A. S., & Röttgering, H. J. A. et al., 2006, A&A, 456, 791

Tasse, C., van der Tol, S., van Zwieten, J., van Diepen, G., Bhatnagar, S., 2013, Astronomy & Astrophysics, 553, A105

Tasse, C., et al., 2012, LOFAR calibration & wide-field imaging Comptes Rendus Physique, 13(1), 28

Terzian, Y., Lebron, M., Churchwell, E., Deshpande, A., Bania, T. M., Araya, E., & Cersosimo, J. C., 2005, ALFA Radio Recombination Line Survey, http://www.naic.edu/alfa/galfa/docs/RRL_Whitepapers-31jan05.pdf

Terebey, S., Chandler, C.J., André, P., 1993, Astrophys. J., 414, 759–772

Terebey, S., Fich, M., Taylor, R., Cao, Y., Hancock, T., 2003, ApJ, 590, 906-916

Thompson, A. R., Moran, J. M, Swenson, G. W., 1991, 'Interferometry & Synthesis In Radio Astronomy, 2nd Edition', WILEY-VCH Verlag GmbH & Co. KGaA, 715 pages

Thompson, A. R., 1999, 'Fundamentals of Radio Interferometry', Synthesis Imaging in Radio Astronomy II, A Collection of Lectures from the Sixth NRAO/NMIMT Synthesis Imaging Summer School. Eds. Taylor, G. B., Carilli, C. L., Perley, R. A. ASP Conference Series, 180, 11-36

Thronson, H. A., Jr., Lada, C. J., & Hewagama, T., 1985, ApJ, 297, 662

Tieftrunk, A. R., Gaume, R. A., Claussen, M. J., Wilson, T. L., Johnston, K. J., 1997, A&A, 318, 931-946

Tian, W.W. & Leahy, D.A., 2005, A&A, 436, 187.

Tielens, A.G.G.M., 2005, 'The Physics & Chemistry of the Interstellar Medium', Cambridge University Press, Cambridge, UK, 510 pages

Tingay, S. J., De Kool, M., 2003, Astronomical Journal, 126, 723–733

Tingay, S. J., Jauncey, D. L., Reynolds, J. E., Tzioumis, A. K., King, E. A., Preston, R. A., Lovell, J. E. J., McCulloch, P. M., Costa, M. E., Nicolson, G., Koekemoer, A., Tornikoski, M., Kedziora-Chudczer, L., & Campbell-Wilson, D., 1997, Astronomical Journal, 113, 2025-2030.

Tomisaka, K., Habe, A., Ikeuchi, S., 1981, 78(2), 273-285

Urquhart et al. 2009, A&A, 507, 795

Urquhart et al. 2011, MNRAS, 418(3), 1689-1706

Uroševic, D., Pannuti, T. G., & Leahy, D., 2007, ApJ, 655, L41

Valdettaro et al., 2001,A&A, 368, 845

Vallee, J. P., Hughes, V. A., & Viner, M. R., 1979, A&A, 80, 186-200

van Bemmel , I. M., & Röttgering, H., 2007, "Ionospheric Limitations for SKA & LOFAR", Proceedings of Science, PoS(MRU)012

van Cappellen, W. A., Bregman, J. D. & Arts, M. J., 2005, Experimental Astronomy 17, 101-109

van der Kruit, P. C., 1971, Astron. Astrophys., 15: 1 10-22

van der Kruit, P. C., 1973, Astron. Astrophys., 29: 263-75

van Haarlem, M. P., Wise, M. W., Gunst, A. W., et al., 2013, A&A, 556, A2

van der Tol, S., Jeffs, B. D. & van der Veen, A.J., 2007, IEEE Trans. Signal Process, 55(9), 4497

van der Tak, F. F. S., Tuthill, P. G., & Danchi, W. C., 2005, A&A, 431, 993

van Weeren, R. J., Röttgering, H. J. A., & Rafferty, D. A. et al., 2012, A&A, 543, A43

van Weeren, R. J., Williams, W. L., Tasse, C. et al. 2014, ApJ, 793, 82

Vasyunina et al., 2009, A&A, 499, 149

Valtchanov, I., 2014, The Spectral & Photometric Imaging Receiver (SPIRE) Handbook Version 2.5

Vasilenko, N. M., 2007, Odessa Astronomical Publications, 20, 229.

Verschuur G. L. & Kellermann, K. I., 1974, 'Galactic & Extra-Galactic Radio Astronomy', Springer-Verlag, New York

Verkhodanova, O.V., Verkhodanovaa, N.V., Andernach, H., 2009, Astrophysical Bulletin, 64, 72–105

Vollmer, B., Davoust, E., Dubois, P. et al., 2005, A&A, 431, 1177
Vollmer, B., Gassmann, B., Derrière, S., et al., 2010, A&A, 511(A53), 11
Wang et al., 2006, ApJ, 651, L125
Ward-Thompson, D., Scott, P. F., Hills, R. E., André, P., 1994, MNRAS, 268, 276–290
Ward-Thompson, D., Motte, F., & André, P. 1999, MNRAS, 305, 143
Wilking, B. A., Claussen, M. J., Benson, P. J., Myers, P. C., Terebey, S., & Wootten, A., 1994, The Astrophysical Journal, 431(2), L119-L122
Wilking, B. A., 1996, in 'Planetary & Interstellar Processes Relevant to the Origins of Life', Whittet, D.C.B. 1997, Kluwer Academic Publishers
Weliachew L. N., Lucas R., 1988, Rep. Prog. Phys 51, 605
Weiler, K. W., 2013, The Promise of Long Wavelength Radio Astronomy, in Radio Astronomy at Long Wavelengths, eds. Stone, R. G., Weiler, K. W., Goldstein, M. L. & Bougeret, J. L., American Geophysical Union, Washington, D. C., doi: 10.1029/GM119p0243
Weiler, K. W., 1983, Observatory, 103, 85
Westerhout, G. H. 1958, BAN, 14, 215
West, J. L., 2003, Master's thesis, Univ. Manitoba
West, J. L., English, J., Normandeau, M., & Landecker, T. L. 2007, ApJ, 656, 914
Weinstein, A., 2009, Proceedings of the XLIVth Rencontres Demoriond Very High Energy Phenomena in the Universe, La Thuile, Aosta Valley Italy, 'Results of VERITAS Galactic Observations'
Walsh et al., 2008, PASA, 25, 105
Walsh et al., 2011 MNRAS, 416(3), 1764 - 1821
Wheelock, S., Gautier III, T. N., Chillemi, J., Kester, D., McCallon, H., Oken, C., White, J., Gregorich, D., Boulanger, F., Good, J., Chester, T., 1997, IRAS Sky Survey Atlas Explanatory Supplemen, (JPL 94-11; Pasadena: JPL)
White, G. J., 1979, MNRAS, 186(2), 377-381
White, G. J. & Macdonald, G. H., 1977, MNRAS, 188, 745
White, G. J., Tothill, N. F. H., Matthews, H. E., McCutcheon, W. H., Huldtgren, M., & McCaughrean, M. J., 1997, A&A, 323, 529-533
White, G. J., Rainey, R., Hayashi, S. S., & Kaifu, N., 1987, A&A, 173 (2), 337-346.
Whitney, B.A., Hartmann, L., 1993, ApJ, 402, 605–622
Whiting, M. T., 2012, MNRAS, 421, 3242-3256
Wielebinski, R., 2003, The Magnetized Interstellar Medium, Proceedings of the conference, held in Antalya, Turkey, September 8 - 12, eds. Uyaniker, B., Reich, W. & Wielebinski, R., Copernicus GmbH, Katlenburg-Lindau, 241-244
Wielebinski, R., 2005, in: R. Wielebinski, & R. Beck (eds.), Cosmic Magnetic Fields, Lecture Notes in Physics (Berlin: Springer) vol. 664
Whitworth, A., 1979, MNRAS, 186, 59-67
Wilson, T. L., Bieging, J., & Wilson, W. E. 1979, Astron Astrophys., 71, 205
Wilson, A. S. & Weiler, K. W., 1976, Astr, Astrophys. 49, 357
Wilking et al. 1994, ApJ, 431, L119
Wijnholds, S.J., 2007, 'LBA station configuration, LOFAR-ASTRON-MEM-214, 4 Dec. 2007'.
Wijnholds, S. J., & van der Veen, A. J, 2008, IEEE Jnl. on Sel. Areas of Sig. Proc., 2(5), 613–623
Wijnholds, S. J., 2010, 'Fish-eye observing with phased array radio telescopes.' Ph. D. thesis, Delft University of Technology, Delft, Printed in Netherlands, Wohrmann Print Service
Wijnholds, S. J., 2011a, 'Station Calibration Cookbook', Technical Report LOFAR-ASTRON-MAN-049, January 2011.
Wijnholds, S. J., 2011b, 'Overview of the Initial Production Version of the Station Calibration Pipeline', Technical Report LOFAR-ASTRON-MEM-263, January 2011
Wijnholds, S. J., Bregman, J. D. & van Ardenne, A., 2011, 'Calibratability & its impact on configuration design for the LOFAR & SKA phased array radio telescopes', Radio Sci., 46, RS0F07
Wright et al. 2010, The Astronomical Journal, Volume 140(6), 1868-1881
Wright, M. C. H., 1999, 'Image fidelity', BIMA Memo 73
Wynn-Williams, C. G., 1971, MNRAS, 151, 397 - 420
Yamamura, I., Makiuti, S., Ikeda, N., Fukuda, Y., Oyabu, S., Koga, T., White, G. J., 2010,

AKARI/FIS All-Sky Survey Bright Source Catalogue Version 1.0 Release Note
Yankulova, I. M., 1969, Soviet Astronomy, 13, 32-36
Yatawatta, S., 2008, LOFAR-ASTRON Memo 255. LOFAR beamshapes & their use in calibration & imaging, Tech. Rep., ASTRON
Yatawatta, S., Zaroubi, S., Bruyn, G., Koopmans L., Noordam, J., 2009, IEEE DSP, Marco Island, FL, 150-155, ISBN: 978-1-4244-3677-4
Yatawatta, S., 2010, 'Fundamental Limitations of Pixel Based Image Deconvolution in Radio Astronomy', Proc. IEEE Sensor Array & Multichannel Signal Processing Workshop (SAM), Israel, 69–72,
Yatawatta, S., 2011a, 'Radio astronomical image deconvolution using prolate spheroidal wave functions, 18th IEEE International Conference on Image Processing
Yatawatta, S. 2011b, 'Shapelets & related techniques in radio astronomical imaging", in Proc. URSI General Assembly, Istanbul, Turkey.
Young, C. H., Evans, N. J. II, 2005, ApJ, 627, 293
Yun, J. L., Moreira, M. C., Torrelles, J. M., Afonso, J. M., Santos, N. C., 1996, Astron. J., 111, 841–845
Zhang, X., Zheng Y., Chen H. et al., 1997, A&AS, 121, 59
Zinn, D., Bosch, J., Gertz, M., 2007, VLDB '07 Proceedings of the 33rd international conference on Very large data bases: 567-578
Zinnecker, H., & Yorke, H. W., 2007, ARA&A, 45, 481.
Zuckerman, B., & Evans, N. J., 1974, ApJ, 192, L149-L152

Appendix A

Symbols

θ	Angle of deviation from straight-line path
θ	Pitch angle between the uniform magnetic field $\boldsymbol{B}$ and the LOS
$\Delta\theta$	Opening angle of beamed synchrotron
θ_{PB}	Angular size of the synthesized beam
ϑ_x, ϑ_y	Source size
ϕ	Visibility phase
$\Delta\phi$	Phase variability
$d\Omega$	Unit solid angle
Ω	Solid angle of the source with respect to the observer
φ	Pitch angle between $\boldsymbol{V}$ and $\boldsymbol{B}$
σ	Sigma detection threshold above the local background RMS
σ_ν	The opacity
ζ(n)	Riemann zeta function of argument n
α	Spectral index
β	$\boldsymbol{V}/c$
γ	The Lorentz factor
A	Visibility amplitude
$\boldsymbol{B}$	Uniform magnetic field
$\boldsymbol{b}$	Impact parameter
B_ν	Spectral radiance of a black-body
c	Speed of light
d	Distance to the source
e	Elementary charge *1.60217657 x 10^{-19} C*
$\boldsymbol{E}$	Electrostatic field
E	Energy
dE	Change in energy
$E_{B\,tot}$	Total magnetic field energy
ε_{ff}	Total emissivity
$\varepsilon_{ij}(t)$	Additive noise
$f(\boldsymbol{V})$	Maxwellian probability distribution
$\boldsymbol{F}$	Force
F	Fraction of the source volume occupied by the magnetic field (filling factor)
$\mathbb{F}_\mathbf{0}$	Flux density of the emitting region at frequency v_0
FoV	Field of View
g_{ff}	Gaunt factor for free-free transitions
$g_i(t)$	Complex gain of antenna *i*
$g_j(t)$	Complex gain of antenna *j*
h	Planck's constant 6.62606957×10^{-34} joule.second

H	Specified height
dH	Thickness of ionosphere
H	Specified height of the ionosphere,
I_v	Synchrotron Volume Emissivity/ Intensity
J	*E*mission coefficient of free-free transitions
κ_v	Absorption coefficient
κ_{R}	Free-free absorption coefficient
K	Ratio of energy in the heavy particles to that in the electrons: CR proton/electron energy ratio, K
k	Boltzmann constant
l	Beam phase centre
L_{bol}	Bolometric luminosity
L_{H_2O}	Water maser luminosity
$L_{\mathrm{far-IR}}$	Luminosity at far-IR wavelengths
L_v	Luminosity
LOS	Line of Sight
ℓ	Path length through the emitting medium
m	Particle mass
m_P	Proton mass
m_e	Electron mass
n	Number of elements
n_B	Number of baselines
n_i	Number density of ions
n_e	Number density of free electrons
N	Total number of collisions
N_e	Thermal electron density
N_H	Total H column density
N_{H_2}	Total molecular H column density
p	*P*article (electron) exponent or spectral power law index
P	Total power
P'	Total power in particle's rest frame
q	Single point charge
R_C	Correlated signal of the cosine correlator
R_S	Correlated signal of the sine correlator
$\vec{s}$	Direction
s	Path length through the source in the line of sight (LOS)
S	Scale of ionospheric irregularities
S/N	Signal-to-noise
ds	Unit distance
T_g	Time delay of wavefront
τ_v	Optical depth
t	Time
t_B	Beamed time interval
T	Temperature
T_B	Brightness Temperature
T_{bol}	Bolometric Temperature
T_e	Electron Temperature
$\mathbb{T}$	Observed synchrotron pulse duration
TEC	Total Electron Content
dt	Unit time
Δt	Time interval from observers frame
Δt_L	Cyclotron period at the rest frame of the electron
u	Internal thermal energy density of a gas
U_{CR}	CR energy density
U_e	Energy density in electrons
U_p	Energy density in protons
U_B	Energy density in magnetic field

U_{tot}	Total energy density
V	Voltage of the signal
$\boldsymbol{V}$	Velocity
$\dot{\boldsymbol{V}}$	Acceleration
$\mathbb{V}$	Source volume
$d\mathbb{V}$	Unit volume
v	Frequency
v_c	Critical or turnover frequency
dv	Frequency interval
v_L	Cyclotron frequency
VF	Complex visibility function
$V_{ij}^{OBS}(t)$	Observed visibility between antennas *i* and *j*
$V_{ij}{}^{model}$	Initial approximate model of source visibilities
ω_L	Larmor frequency
ω_B	Gyration frequency of cyclotron when $\boldsymbol{V} \sim c$
ω_{Sync}	Synchrotron radiation
$\boldsymbol{X}$	Electron's position vector
$\mathbb{Z}$	Redshift
Z	Ion charge

Appendix B

A selection of sources with well determine polynomials

Decided Curvatures plotted to 4th polynomial:

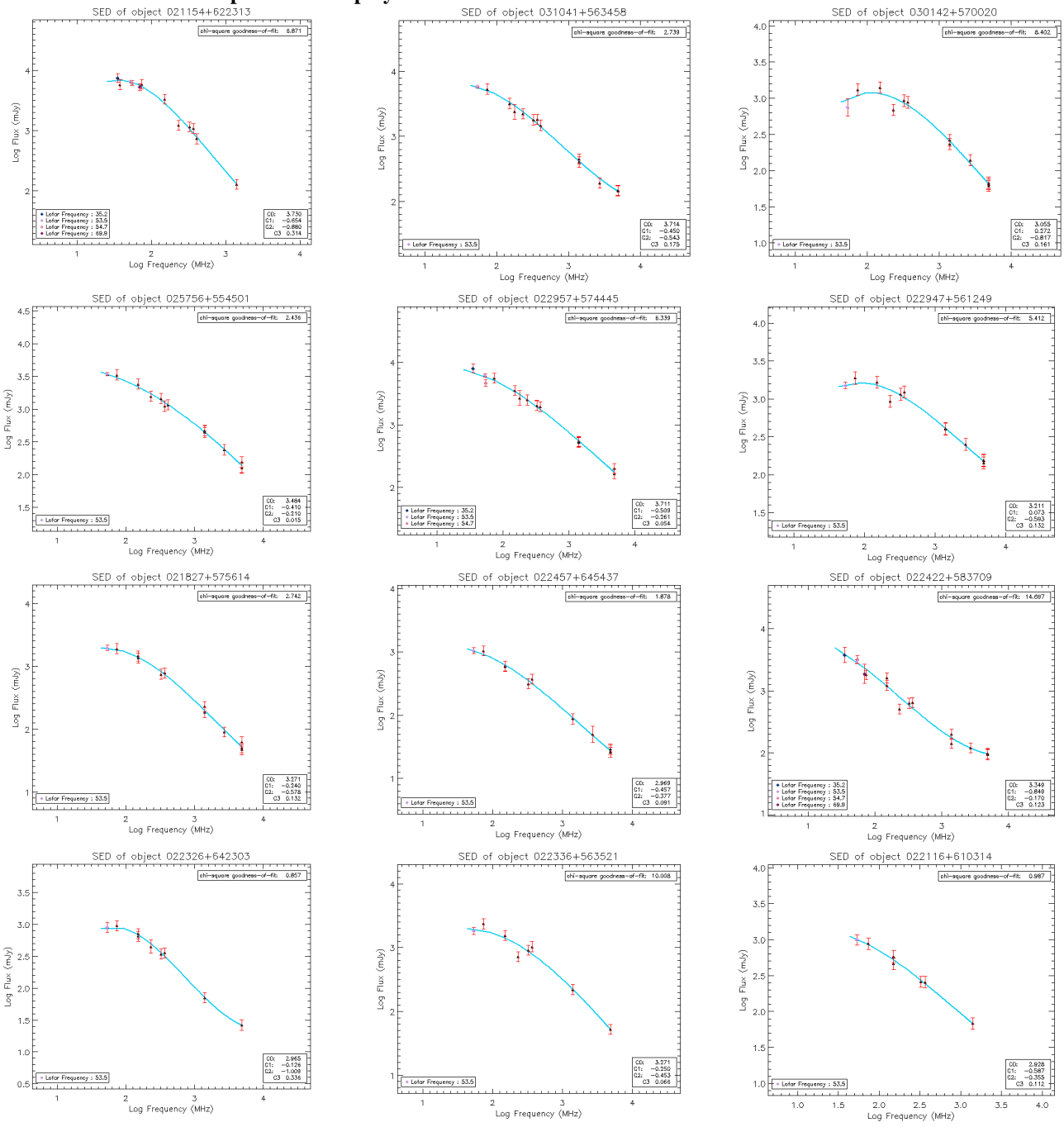

Decided Curvatures plotted to 3rd polynomial:

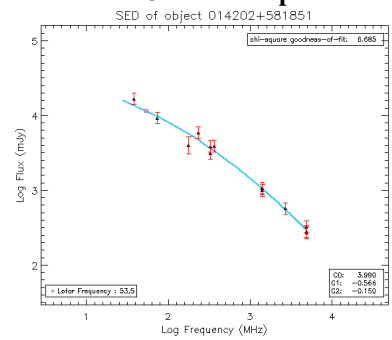

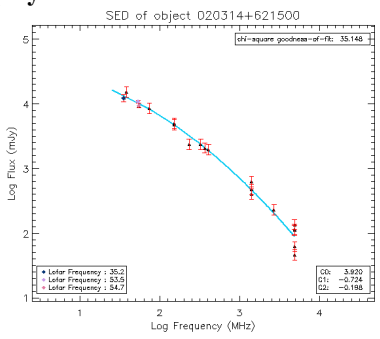

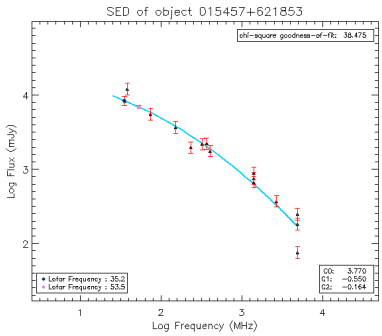

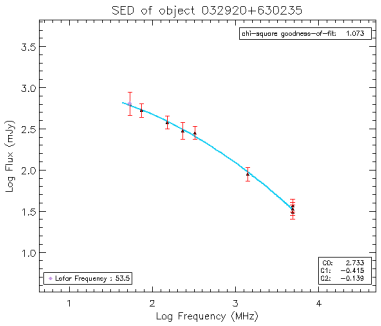

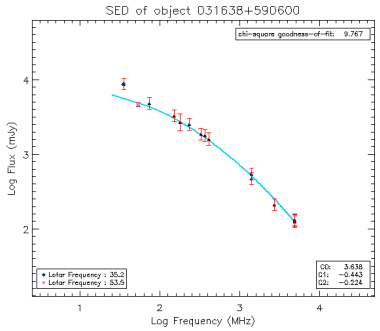

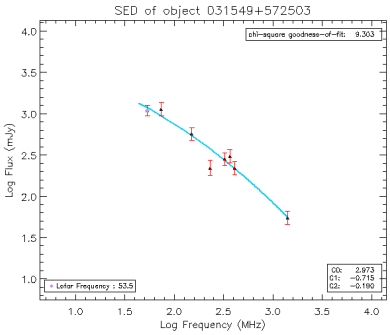

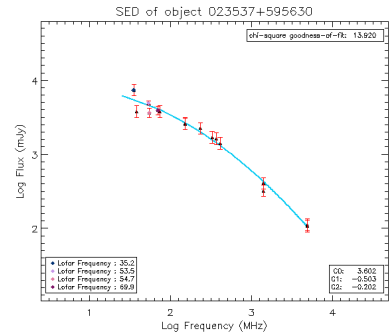

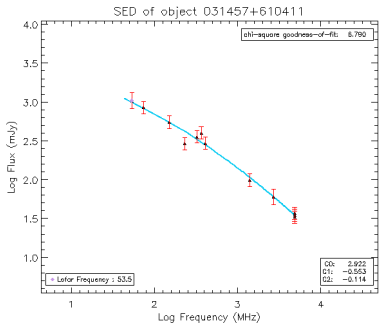

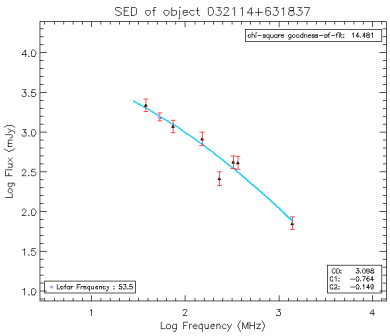

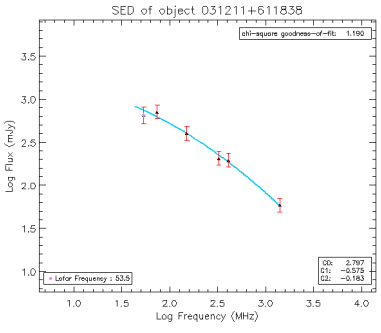

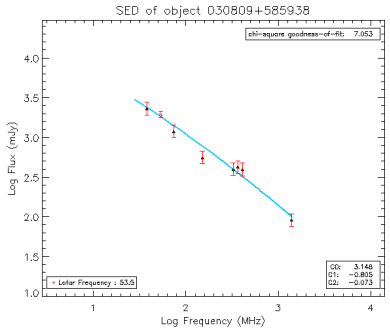

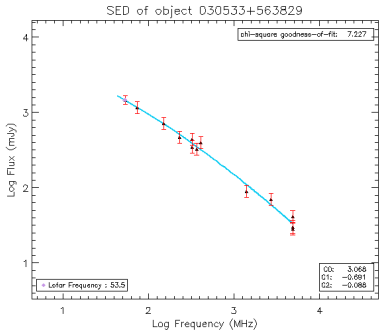

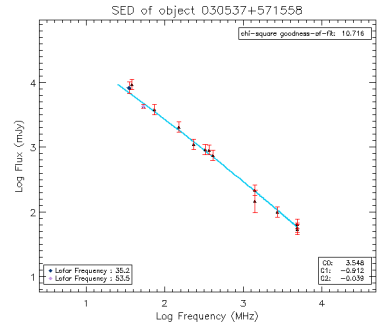

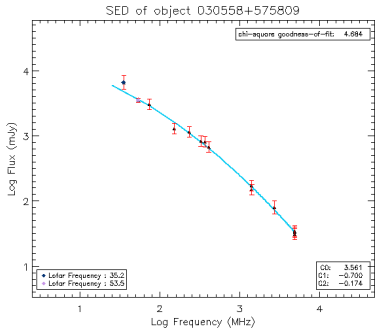

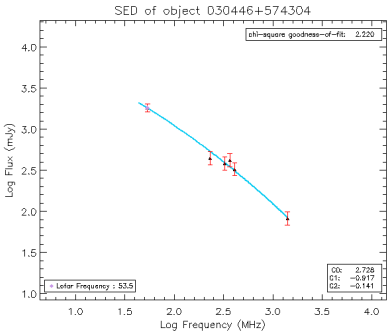

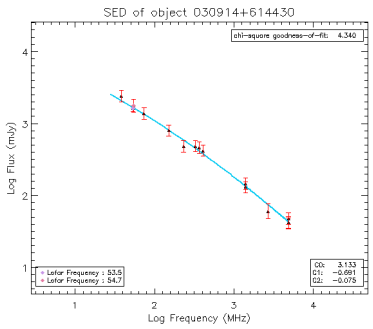
SED of object 030914+614430
chi-square goodness-of-fit: 4.340
Lofar Frequency : 53.5
Lofar Frequency : 54.7
C0: 3.133
C1: −0.691
C2: −0.075
Log Flux (mJy)
Log Frequency (MHz)

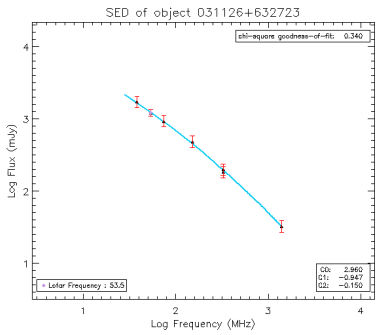
SED of object 031126+632723
chi-square goodness-of-fit: 0.340
Lofar Frequency : 53.5
C0: 2.960
C1: −0.847
C2: −0.150
Log Flux (mJy)
Log Frequency (MHz)

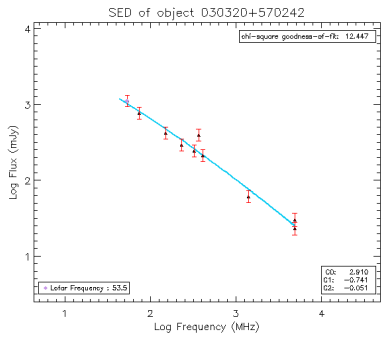
SED of object 030320+570242
chi-square goodness-of-fit: 12.447
Lofar Frequency : 53.5
C0: 2.910
C1: −0.741
C2: −0.051
Log Flux (mJy)
Log Frequency (MHz)

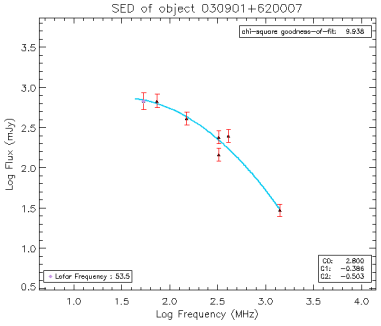
SED of object 030901+620007
chi-square goodness-of-fit: 9.938
Lofar Frequency : 53.5
C0: 2.800
C1: −0.386
C2: −0.503
Log Flux (mJy)
Log Frequency (MHz)

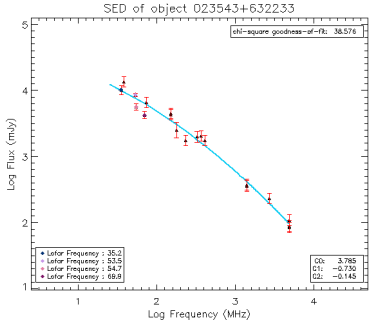
SED of object 023543+632233
chi-square goodness-of-fit: 38.576
Lofar Frequency : 35.2
Lofar Frequency : 53.5
Lofar Frequency : 54.7
Lofar Frequency : 69.8
C0: 3.785
C1: −0.730
C2: −0.145
Log Flux (mJy)
Log Frequency (MHz)

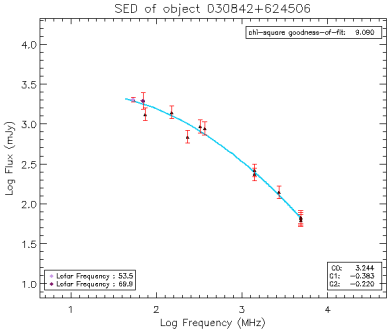
SED of object 030842+624506
chi-square goodness-of-fit: 9.090
Lofar Frequency : 53.5
Lofar Frequency : 69.8
C0: 3.244
C1: −0.383
C2: −0.220
Log Flux (mJy)
Log Frequency (MHz)

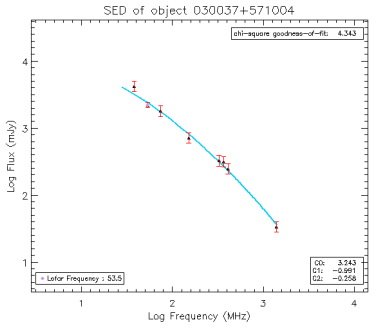
SED of object 030037+571004
chi-square goodness-of-fit: 4.343
Lofar Frequency : 53.5
C0: 3.243
C1: −0.991
C2: −0.256
Log Flux (mJy)
Log Frequency (MHz)

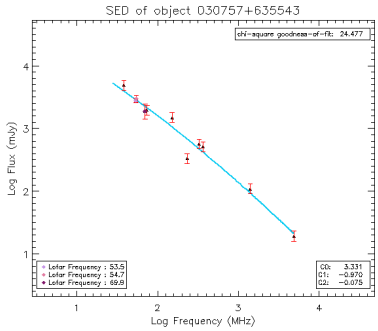
SED of object 030757+635543
chi-square goodness-of-fit: 24.477
Lofar Frequency : 53.5
Lofar Frequency : 54.7
Lofar Frequency : 69.8
C0: 3.331
C1: −0.970
C2: −0.075
Log Flux (mJy)
Log Frequency (MHz)

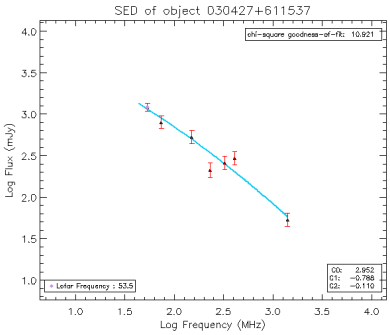
SED of object 030427+611537
chi-square goodness-of-fit: 10.921
Lofar Frequency : 53.5
C0: 2.952
C1: −0.788
C2: −0.110
Log Flux (mJy)
Log Frequency (MHz)

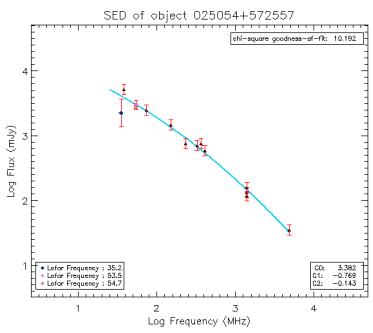
SED of object 025054+572557
chi-square goodness-of-fit: 10.192
Lofar Frequency : 35.2
Lofar Frequency : 53.5
Lofar Frequency : 54.7
C0: 3.382
C1: −0.763
C2: −0.143
Log Flux (mJy)
Log Frequency (MHz)

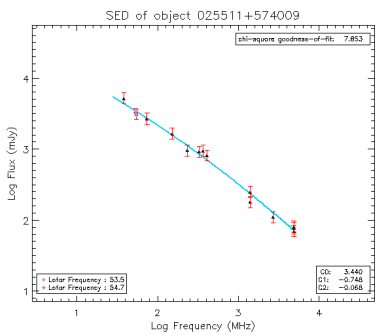
SED of object 025511+574009
chi-square goodness-of-fit: 7.853
Lofar Frequency : 53.5
Lofar Frequency : 54.7
C0: 3.440
C1: −0.748
C2: −0.068
Log Flux (mJy)
Log Frequency (MHz)

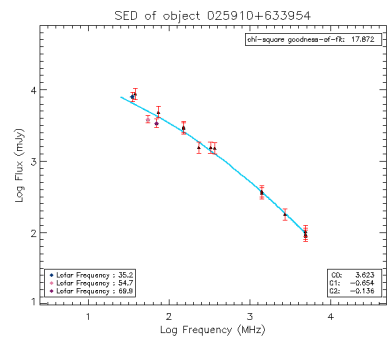
SED of object 025910+633954
chi-square goodness-of-fit: 17.872
Lofar Frequency : 35.2
Lofar Frequency : 54.7
Lofar Frequency : 69.8
C0: 3.623
C1: −0.654
C2: −0.136
Log Flux (mJy)
Log Frequency (MHz)

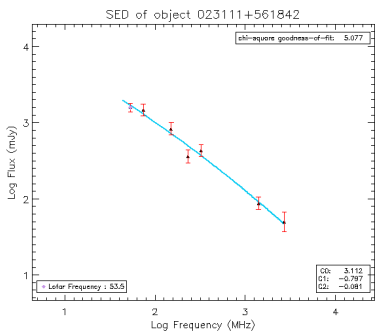
SED of object 023111+561842
chi-square goodness-of-fit: 5.077
Lofar Frequency : 53.5
C0: 3.112
C1: −0.797
C2: −0.081
Log Flux (mJy)
Log Frequency (MHz)

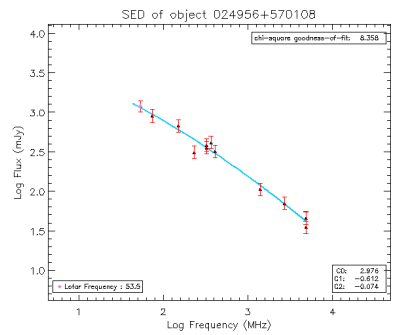
SED of object 024956+570108
chi-square goodness-of-fit: 8.358
Lofar Frequency : 53.5
C0: 2.976
C1: −0.612
C2: −0.074
Log Flux (mJy)
Log Frequency (MHz)

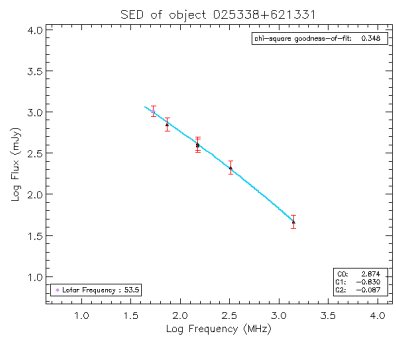
SED of object 025338+621331
chi-square goodness-of-fit: 0.348
Lofar Frequency : 53.5
C0: 2.874
C1: −0.830
C2: −0.087
Log Flux (mJy)
Log Frequency (MHz)

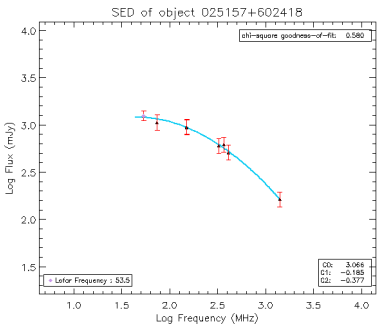
SED of object 025157+602418
chi-square goodness-of-fit: 0.580
Lofar Frequency : 53.5
C0: 3.066
C1: −0.185
C2: −0.377
Log Flux (mJy)
Log Frequency (MHz)

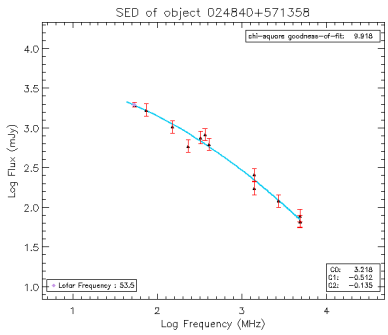
SED of object 024840+571358
chi-square goodness-of-fit: 9.918
Lofar Frequency : 53.5
C0: 3.218
C1: −0.512
C2: −0.135
Log Flux (mJy)
Log Frequency (MHz)

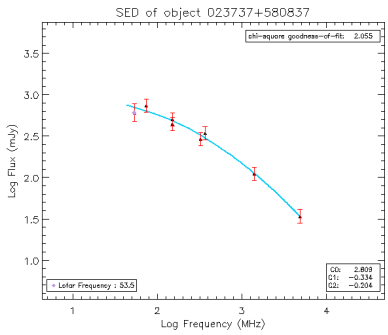
SED of object 023737+580837
chi-square goodness-of-fit: 2.055
Lofar Frequency : 53.5
C0: 2.809
C1: −0.334
C2: −0.204
Log Flux (mJy)
Log Frequency (MHz)

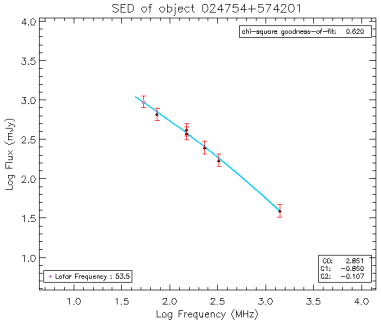
SED of object 024754+574201
chi-square goodness-of-fit: 0.620
Lofar Frequency : 53.5
C0: 2.851
C1: −0.850
C2: −0.107
Log Flux (mJy)
Log Frequency (MHz)

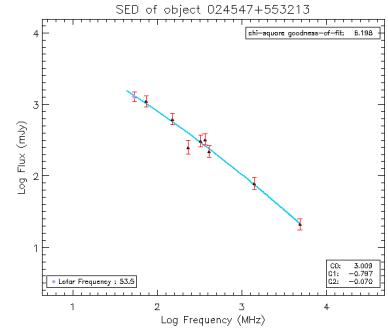
SED of object 024547+553213
chi-square goodness-of-fit: 6.198
Lofar Frequency : 53.5
C0: 3.009
C1: −0.797
C2: −0.070
Log Flux (mJy)
Log Frequency (MHz)

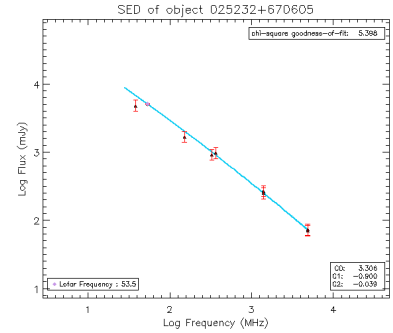
SED of object 025232+670605
chi-square goodness-of-fit: 5.368
Lofar Frequency : 53.5
C0: 3.306
C1: −0.900
C2: −0.039
Log Flux (mJy)
Log Frequency (MHz)

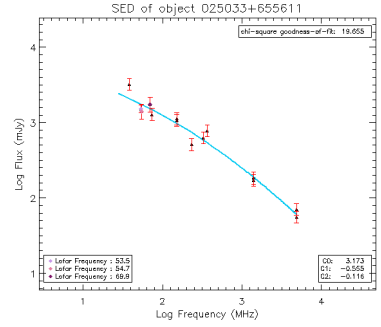
SED of object 025033+655611
chi-square goodness-of-fit: 19.655
Lofar Frequency : 53.5
Lofar Frequency : 54.7
Lofar Frequency : 69.8
C0: 3.173
C1: −0.555
C2: −0.116
Log Flux (mJy)
Log Frequency (MHz)

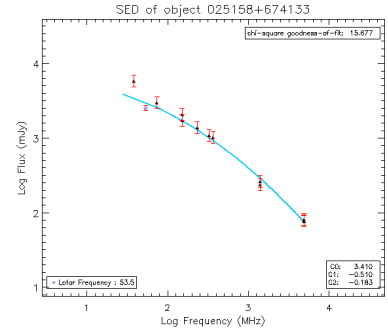
SED of object 025158+674133
chi-square goodness-of-fit: 15.677
Lofar Frequency : 53.5
C0: 3.410
C1: −0.510
C2: −0.183
Log Flux (mJy)
Log Frequency (MHz)

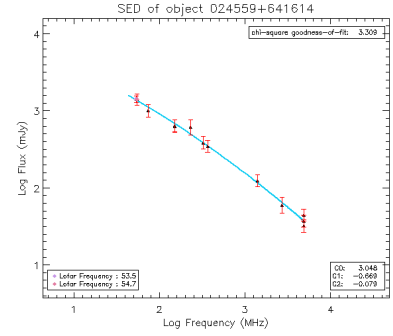
SED of object 024559+641614
chi-square goodness-of-fit: 3.309
Lofar Frequency : 53.5
Lofar Frequency : 54.7
C0: 3.048
C1: −0.669
C2: −0.079
Log Flux (mJy)
Log Frequency (MHz)

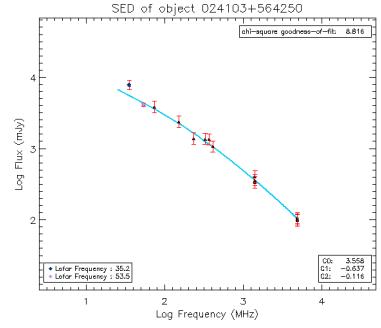
SED of object 024103+564250
chi-square goodness-of-fit: 8.816
Lofar Frequency : 35.2
Lofar Frequency : 53.5
C0: 3.558
C1: −0.637
C2: −0.116
Log Flux (mJy)
Log Frequency (MHz)

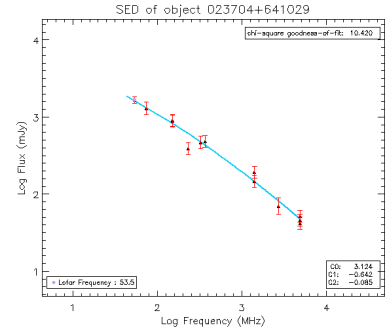
SED of object 023704+641029
chi-square goodness-of-fit: 10.420
Lofar Frequency : 53.5
C0: 3.124
C1: −0.640
C2: −0.085
Log Flux (mJy)
Log Frequency (MHz)

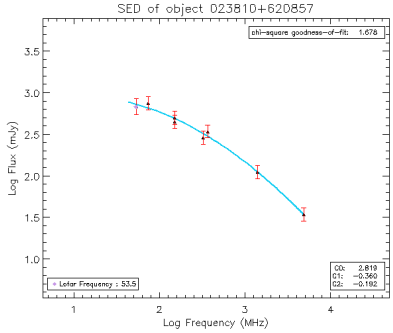
SED of object 023810+620857
chi-square goodness-of-fit: 1.678
Lofar Frequency : 53.5
C0: 2.819
C1: −0.360
C2: −0.192
Log Flux (mJy)
Log Frequency (MHz)

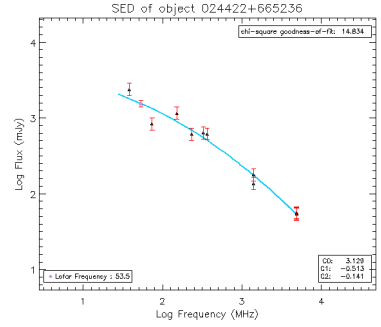
SED of object 024422+665236
chi-square goodness-of-fit: 14.834
Lofar Frequency : 53.5
C0: 3.129
C1: −0.513
C2: −0.141
Log Flux (mJy)
Log Frequency (MHz)

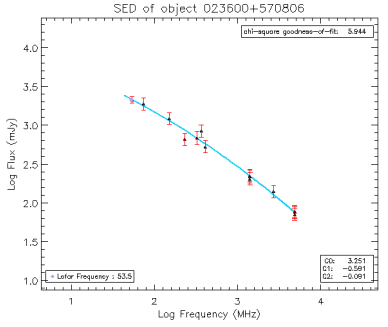
SED of object 023600+570806
chi-square goodness-of-fit: 5.944
Lofar Frequency : 53.5
C0: 3.351
C1: −0.591
C2: −0.091
Log Flux (mJy)
Log Frequency (MHz)

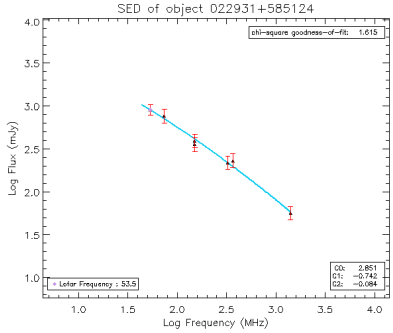
SED of object 022931+585124
chi-square goodness-of-fit: 1.615
Lofar Frequency : 53.5
C0: 2.851
C1: −0.742
C2: −0.084
Log Flux (mJy)
Log Frequency (MHz)

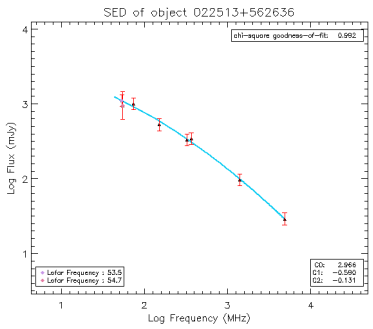
SED of object 022513+562636
chi-square goodness-of-fit: 0.992
Log Flux (mJy)
Log Frequency (MHz)
Lofar Frequency : 53.5
Lofar Frequency : 54.7
C0: 2.965
C1: -0.560
C2: -0.131

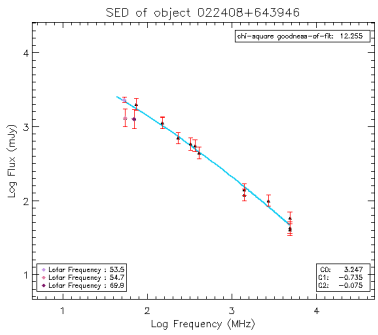
SED of object 022408+643946
chi-square goodness-of-fit: 12.255
Log Flux (mJy)
Log Frequency (MHz)
Lofar Frequency : 53.5
Lofar Frequency : 54.7
Lofar Frequency : 69.9
C0: 3.247
C1: -0.735
C2: -0.075

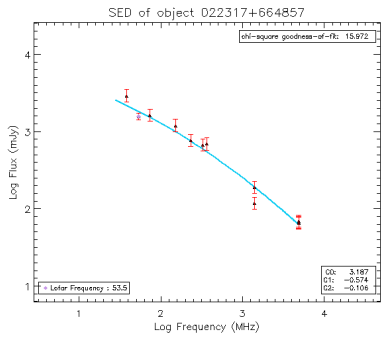
SED of object 022317+664857
chi-square goodness-of-fit: 15.972
Log Flux (mJy)
Log Frequency (MHz)
Lofar Frequency : 53.5
C0: 3.187
C1: -0.574
C2: -0.106

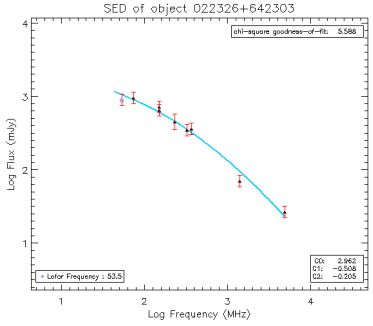
SED of object 022326+642303
chi-square goodness-of-fit: 5.588
Log Flux (mJy)
Log Frequency (MHz)
Lofar Frequency : 53.5
C0: 2.962
C1: -0.508
C2: -0.205

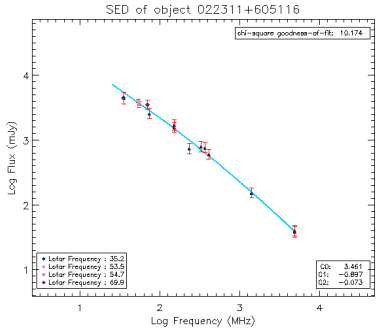
SED of object 022311+605116
chi-square goodness-of-fit: 10.174
Log Flux (mJy)
Log Frequency (MHz)
Lofar Frequency : 35.2
Lofar Frequency : 53.5
Lofar Frequency : 54.7
Lofar Frequency : 69.8
C0: 3.461
C1: -0.897
C2: -0.073

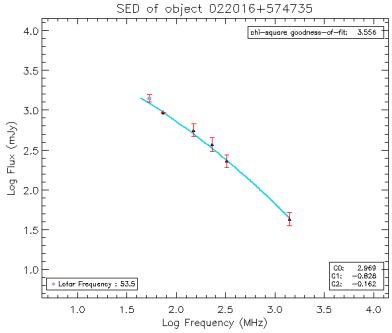
SED of object 022016+574735
chi-square goodness-of-fit: 3.556
Log Flux (mJy)
Log Frequency (MHz)
Lofar Frequency : 53.5
C0: 2.969
C1: -0.828
C2: -0.162

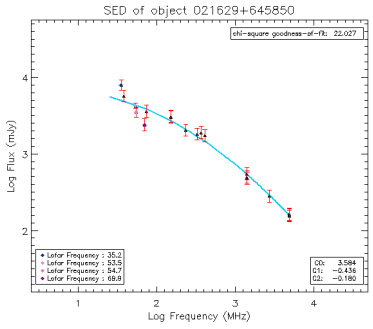
SED of object 021629+645850
chi-square goodness-of-fit: 22.027
Log Flux (mJy)
Log Frequency (MHz)
Lofar Frequency : 35.2
Lofar Frequency : 53.5
Lofar Frequency : 54.7
Lofar Frequency : 69.8
C0: 3.584
C1: -0.436
C2: -0.180

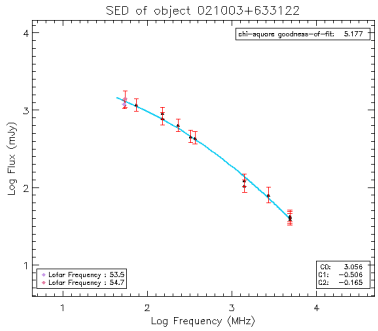
SED of object 021003+633122
chi-square goodness-of-fit: 5.177
Log Flux (mJy)
Log Frequency (MHz)
Lofar Frequency : 53.5
Lofar Frequency : 54.7
C0: 3.056
C1: -0.506
C2: -0.165

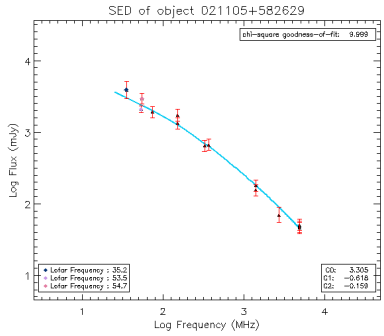
SED of object 021105+582629
chi-square goodness-of-fit: 9.999
Log Flux (mJy)
Log Frequency (MHz)
Lofar Frequency : 35.2
Lofar Frequency : 53.5
Lofar Frequency : 54.7
C0: 3.305
C1: -0.618
C2: -0.159

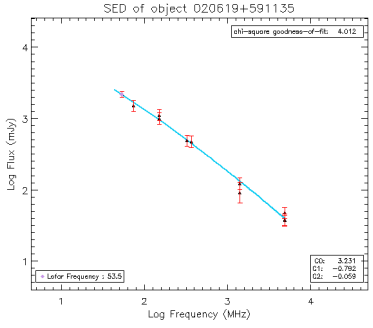
SED of object 020619+591135
chi-square goodness-of-fit: 4.012
Log Flux (mJy)
Log Frequency (MHz)
Lofar Frequency : 53.5
C0: 3.231
C1: -0.782
C2: -0.059

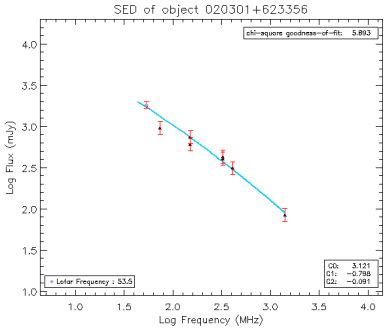
SED of object 020301+623356
chi-square goodness-of-fit: 5.893
Log Flux (mJy)
Log Frequency (MHz)
Lofar Frequency : 53.5
C0: 3.121
C1: -0.798
C2: -0.091

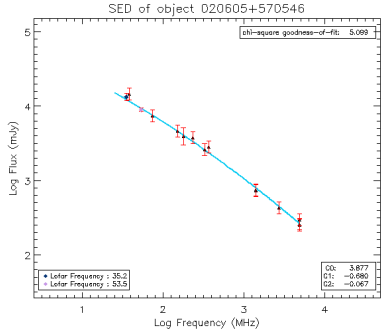
SED of object 020605+570546
chi-square goodness-of-fit: 5.099
Log Flux (mJy)
Log Frequency (MHz)
Lofar Frequency : 35.2
Lofar Frequency : 53.5
C0: 3.877
C1: -0.680
C2: -0.067

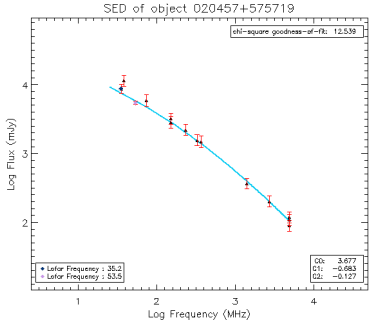
SED of object 020457+575719
chi-square goodness-of-fit: 12.539
Log Flux (mJy)
Log Frequency (MHz)
Lofar Frequency : 35.2
Lofar Frequency : 53.5
C0: 3.677
C1: -0.683
C2: -0.127

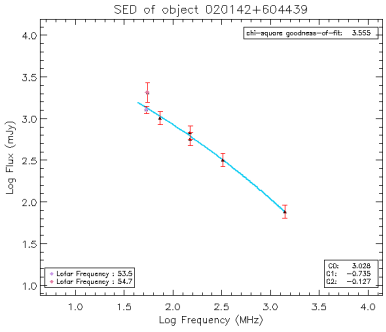
SED of object 020142+604439
chi-square goodness-of-fit: 3.555
Log Flux (mJy)
Log Frequency (MHz)
Lofar Frequency : 53.5
Lofar Frequency : 54.7
C0: 3.038
C1: -0.735
C2: -0.127

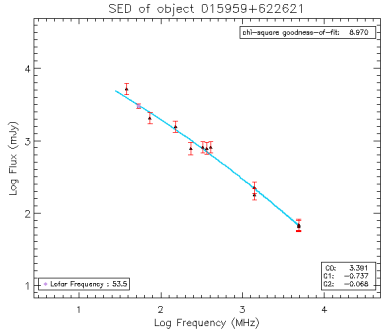
SED of object 015959+622621
chi-square goodness-of-fit: 8.970
Log Flux (mJy)
Log Frequency (MHz)
Lofar Frequency : 53.5
C0: 3.391
C1: -0.737
C2: -0.068

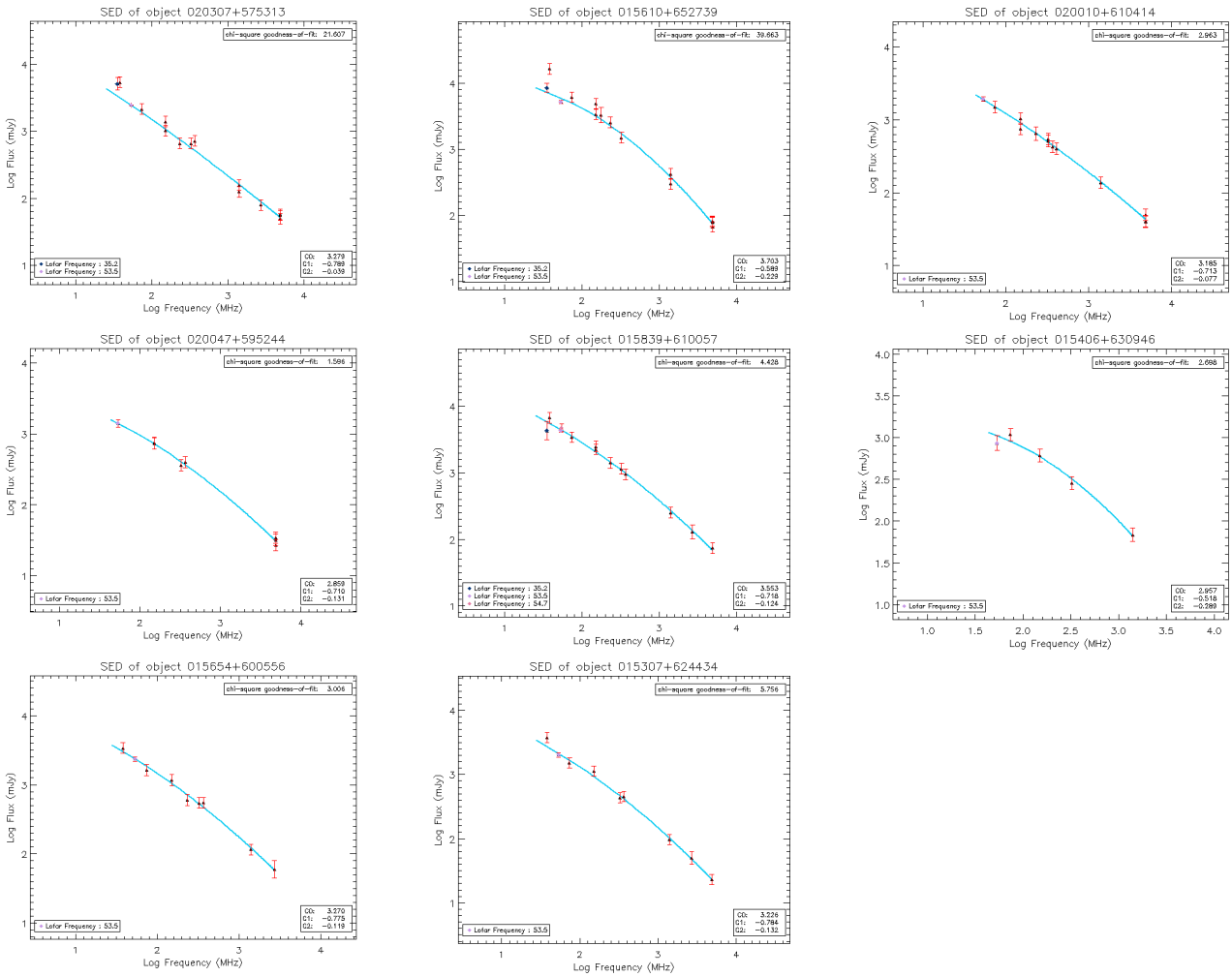

Decided Curvatures plotted to 2nd polynomial:

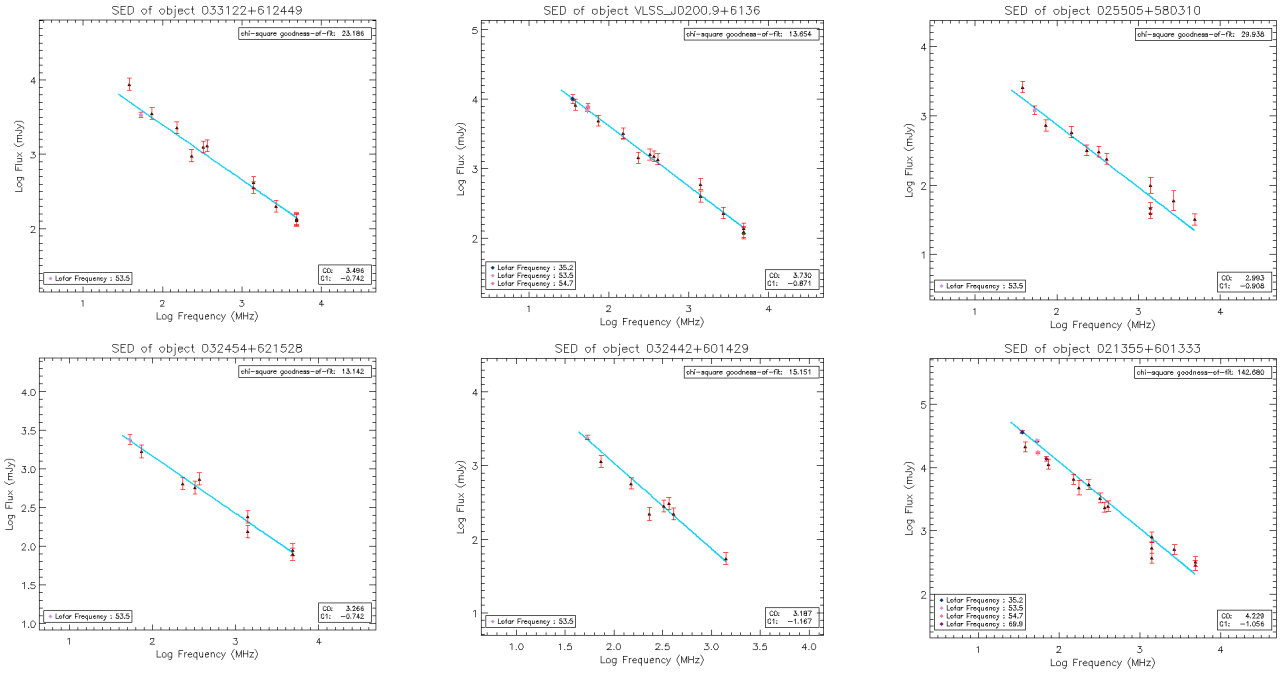

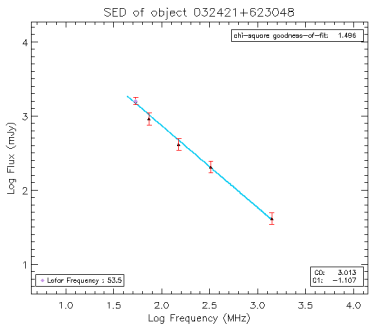
SED of object 032421+623048
chi-square goodness-of-fit: 1.496
Lofar Frequency : 53.5
C0: 3.013
C1: −1.107
Log Flux (mJy)
Log Frequency (MHz)

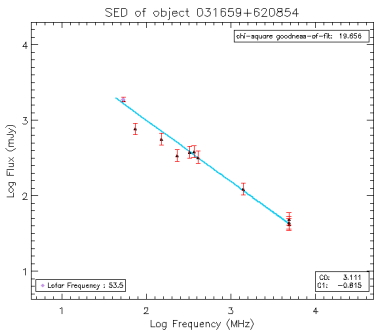
SED of object 031659+620854
chi-square goodness-of-fit: 19.656
Lofar Frequency : 53.5
C0: 3.111
C1: −0.815
Log Flux (mJy)
Log Frequency (MHz)

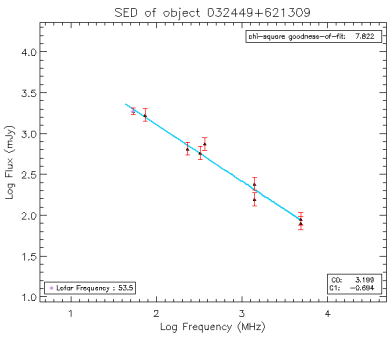
SED of object 032449+621309
chi-square goodness-of-fit: 7.822
Lofar Frequency : 53.5
C0: 3.199
C1: −0.694
Log Flux (mJy)
Log Frequency (MHz)

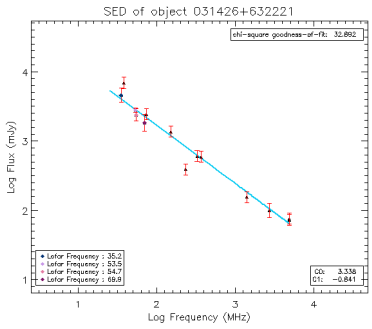
SED of object 031426+632221
chi-square goodness-of-fit: 32.892
Lofar Frequency : 35.2
Lofar Frequency : 53.5
Lofar Frequency : 54.7
Lofar Frequency : 69.8
C0: 3.338
C1: −0.841
Log Flux (mJy)
Log Frequency (MHz)

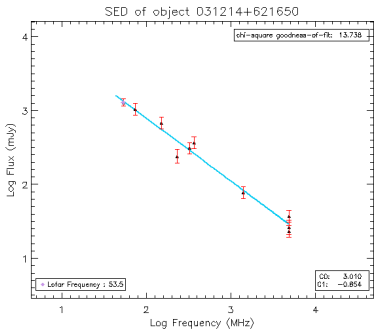
SED of object 031214+621650
chi-square goodness-of-fit: 13.738
Lofar Frequency : 53.5
C0: 3.010
C1: −0.854
Log Flux (mJy)
Log Frequency (MHz)

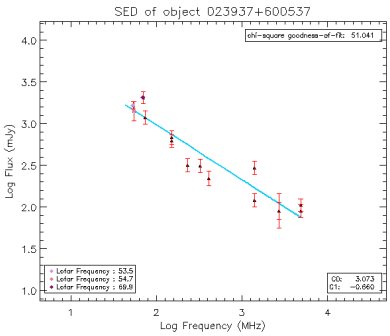
SED of object 023937+600537
chi-square goodness-of-fit: 51.041
Lofar Frequency : 53.5
Lofar Frequency : 54.7
Lofar Frequency : 69.8
C0: 3.073
C1: −0.660
Log Flux (mJy)
Log Frequency (MHz)

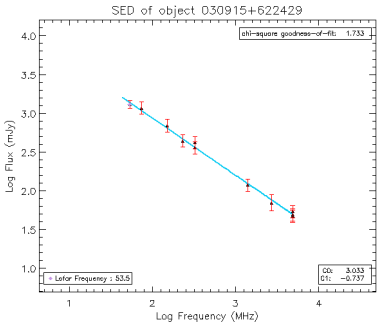
SED of object 030915+622429
chi-square goodness-of-fit: 1.733
Lofar Frequency : 53.5
C0: 3.033
C1: −0.737
Log Flux (mJy)
Log Frequency (MHz)

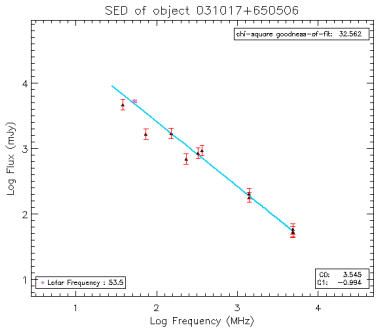
SED of object 031017+650506
chi-square goodness-of-fit: 32.562
Lofar Frequency : 53.5
C0: 3.545
C1: −0.994
Log Flux (mJy)
Log Frequency (MHz)

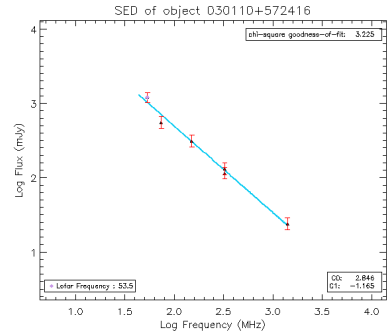
SED of object 030110+572416
chi-square goodness-of-fit: 3.225
Lofar Frequency : 53.5
C0: 2.846
C1: −1.165
Log Flux (mJy)
Log Frequency (MHz)

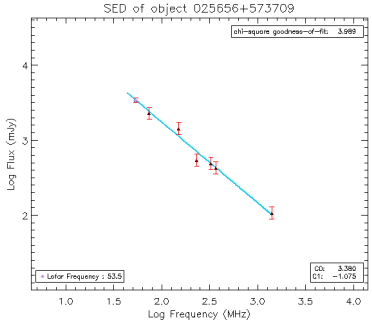
SED of object 025656+573709
chi-square goodness-of-fit: 3.989
Lofar Frequency : 53.5
C0: 3.360
C1: −1.075
Log Flux (mJy)
Log Frequency (MHz)

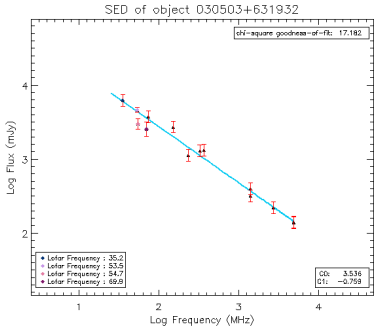
SED of object 030503+631932
chi-square goodness-of-fit: 17.182
Lofar Frequency : 35.2
Lofar Frequency : 53.5
Lofar Frequency : 54.7
Lofar Frequency : 69.8
C0: 3.536
C1: −0.758
Log Flux (mJy)
Log Frequency (MHz)

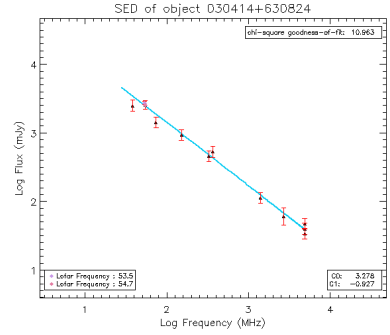
SED of object 030414+630824
chi-square goodness-of-fit: 10.963
Lofar Frequency : 53.5
Lofar Frequency : 54.7
C0: 3.378
C1: −0.927
Log Flux (mJy)
Log Frequency (MHz)

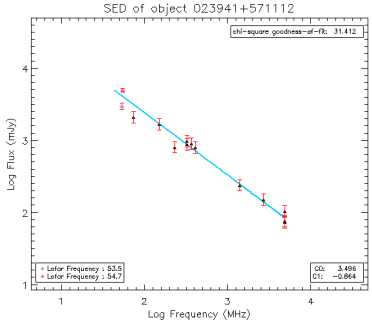
SED of object 023941+571112
chi-square goodness-of-fit: 31.412
Lofar Frequency : 53.5
Lofar Frequency : 54.7
C0: 3.496
C1: −0.864
Log Flux (mJy)
Log Frequency (MHz)

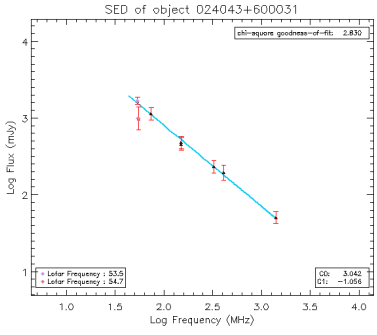
SED of object 024043+600031
chi-square goodness-of-fit: 2.830
Lofar Frequency : 53.5
Lofar Frequency : 54.7
C0: 3.042
C1: −1.056
Log Flux (mJy)
Log Frequency (MHz)

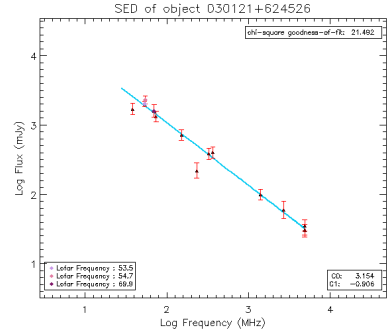
SED of object 030121+624526
chi-square goodness-of-fit: 21.492
Lofar Frequency : 53.5
Lofar Frequency : 54.7
Lofar Frequency : 69.8
C0: 3.154
C1: −0.906
Log Flux (mJy)
Log Frequency (MHz)

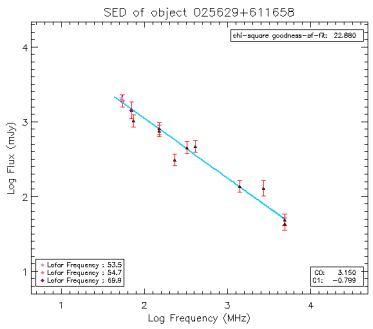
SED of object 025629+611658
chi-square goodness-of-fit: 22.880
Lofar Frequency : 53.5
Lofar Frequency : 54.7
Lofar Frequency : 69.8
C0: 3.150
C1: -0.799
Log Flux (mJy)
Log Frequency (MHz)

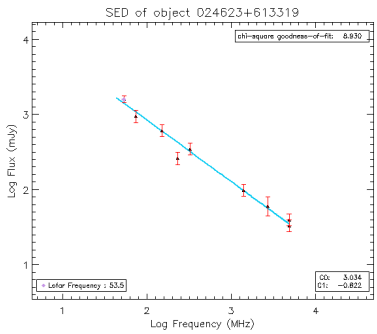
SED of object 024623+613319
chi-square goodness-of-fit: 6.930
Lofar Frequency : 53.5
C0: 3.034
C1: -0.822
Log Flux (mJy)
Log Frequency (MHz)

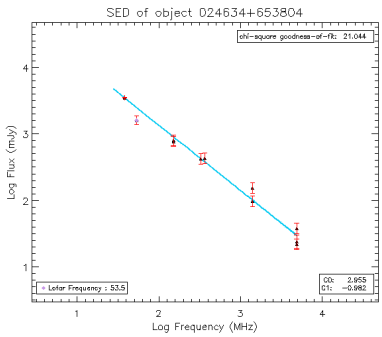
SED of object 024634+653804
chi-square goodness-of-fit: 21.044
Lofar Frequency : 53.5
C0: 2.955
C1: -0.982
Log Flux (mJy)
Log Frequency (MHz)

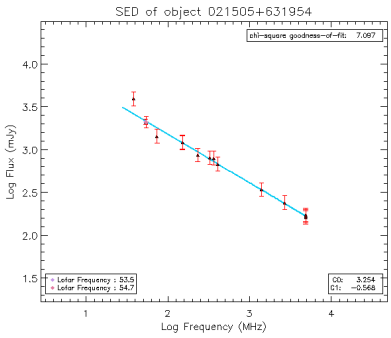
SED of object 021505+631954
chi-square goodness-of-fit: 7.097
Lofar Frequency : 53.5
Lofar Frequency : 54.7
C0: 3.254
C1: -0.568
Log Flux (mJy)
Log Frequency (MHz)

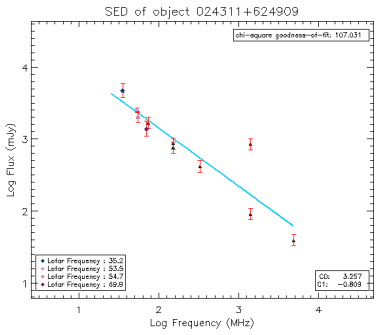
SED of object 024311+624909
chi-square goodness-of-fit: 107.031
Lofar Frequency : 35.2
Lofar Frequency : 53.5
Lofar Frequency : 54.7
Lofar Frequency : 69.8
C0: 3.257
C1: -0.808
Log Flux (mJy)
Log Frequency (MHz)

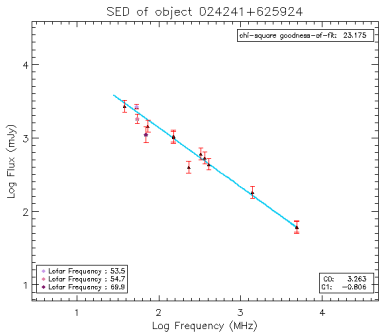
SED of object 024241+625924
chi-square goodness-of-fit: 23.175
Lofar Frequency : 53.5
Lofar Frequency : 54.7
Lofar Frequency : 69.8
C0: 3.263
C1: -0.806
Log Flux (mJy)
Log Frequency (MHz)

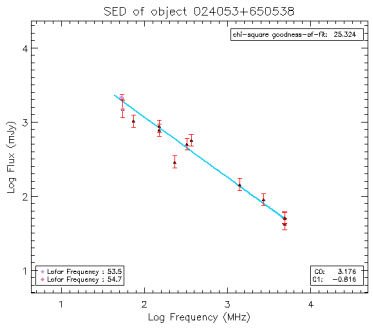
SED of object 024053+650538
chi-square goodness-of-fit: 25.324
Lofar Frequency : 53.5
Lofar Frequency : 54.7
C0: 3.176
C1: -0.816
Log Flux (mJy)
Log Frequency (MHz)

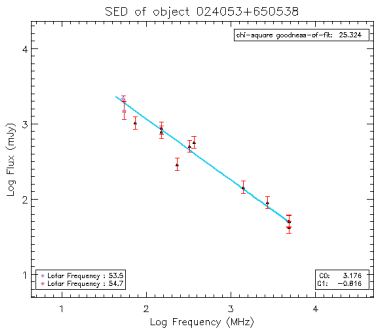
SED of object 024053+650538
chi-square goodness-of-fit: 25.324
Lofar Frequency : 53.5
Lofar Frequency : 54.7
C0: 3.176
C1: -0.816
Log Flux (mJy)
Log Frequency (MHz)

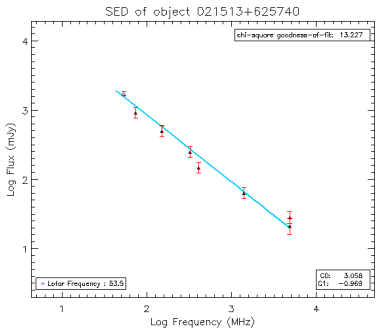
SED of object 021513+625740
chi-square goodness-of-fit: 13.227
Lofar Frequency : 53.5
C0: 3.058
C1: -0.969
Log Flux (mJy)
Log Frequency (MHz)

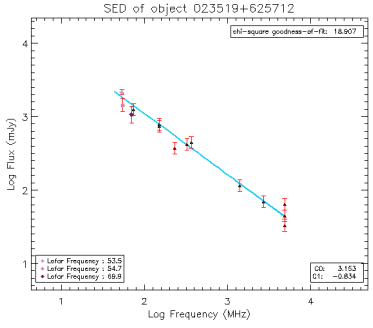
SED of object 023519+625712
chi-square goodness-of-fit: 18.907
Lofar Frequency : 53.5
Lofar Frequency : 54.7
Lofar Frequency : 69.8
C0: 3.153
C1: -0.834
Log Flux (mJy)
Log Frequency (MHz)

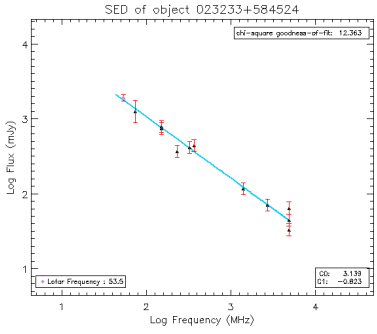
SED of object 023233+584524
chi-square goodness-of-fit: 12.363
Lofar Frequency : 53.5
C0: 3.139
C1: -0.823
Log Flux (mJy)
Log Frequency (MHz)

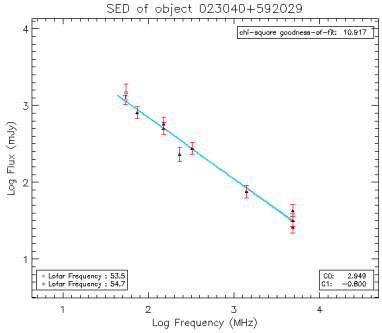
SED of object 023040+592029
chi-square goodness-of-fit: 10.917
Lofar Frequency : 53.5
Lofar Frequency : 54.7
C0: 2.949
C1: -0.800
Log Flux (mJy)
Log Frequency (MHz)

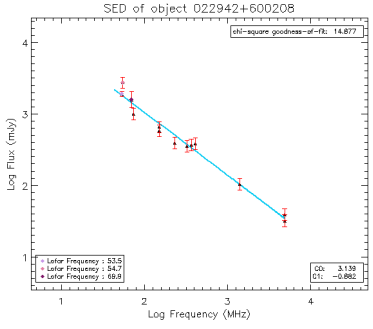
SED of object 022942+600208
chi-square goodness-of-fit: 14.877
Lofar Frequency : 53.5
Lofar Frequency : 54.7
Lofar Frequency : 69.8
C0: 3.139
C1: -0.862
Log Flux (mJy)
Log Frequency (MHz)

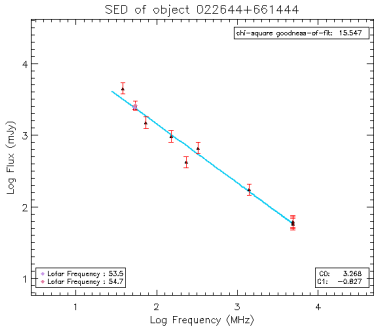
SED of object 022644+661444
chi-square goodness-of-fit: 15.547
Lofar Frequency : 53.5
Lofar Frequency : 54.7
C0: 3.268
C1: -0.827
Log Flux (mJy)
Log Frequency (MHz)

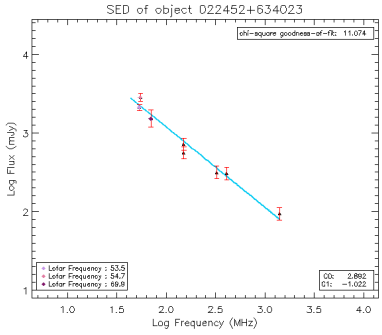
SED of object 022452+634023
chi-square goodness-of-fit: 11.074
Lofar Frequency : 53.5
Lofar Frequency : 54.7
Lofar Frequency : 69.8
C0: 2.892
C1: -1.022
Log Flux (mJy)
Log Frequency (MHz)

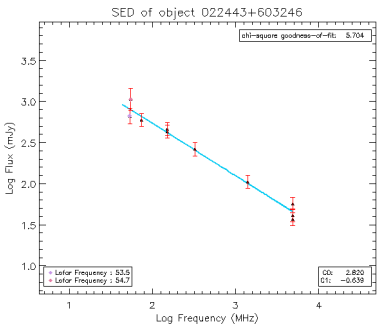
SED of object 022443+603246
chi-square goodness-of-fit: 5.704
Log Flux (mJy)
Log Frequency (MHz)
LoFar Frequency : 53.5
LoFar Frequency : 54.7
C0: 2.820
C1: −0.639

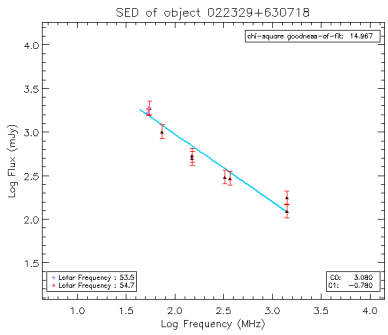
SED of object 022329+630718
chi-square goodness-of-fit: 14.967
Log Flux (mJy)
Log Frequency (MHz)
LoFar Frequency : 53.5
LoFar Frequency : 54.7
C0: 3.080
C1: −0.780

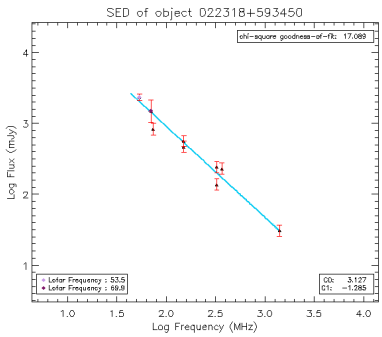
SED of object 022318+593450
chi-square goodness-of-fit: 17.089
Log Flux (mJy)
Log Frequency (MHz)
LoFar Frequency : 53.5
LoFar Frequency : 69.8
C0: 3.127
C1: −1.285

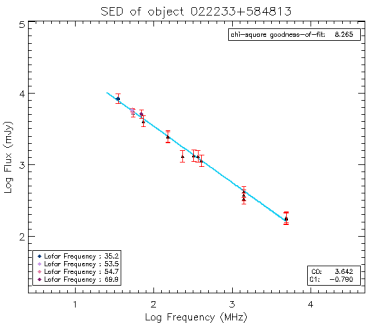
SED of object 022233+584813
chi-square goodness-of-fit: 8.265
Log Flux (mJy)
Log Frequency (MHz)
LoFar Frequency : 35.2
LoFar Frequency : 53.5
LoFar Frequency : 54.7
LoFar Frequency : 69.8
C0: 3.642
C1: −0.780

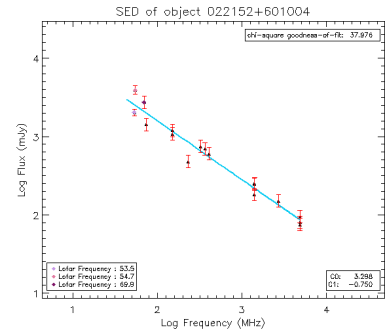
SED of object 022152+601004
chi-square goodness-of-fit: 37.976
Log Flux (mJy)
Log Frequency (MHz)
LoFar Frequency : 53.5
LoFar Frequency : 54.7
LoFar Frequency : 69.8
C0: 3.298
C1: −0.750

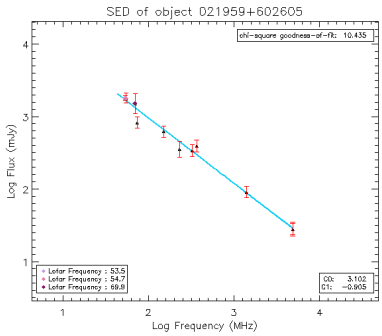
SED of object 021959+602605
chi-square goodness-of-fit: 10.435
Log Flux (mJy)
Log Frequency (MHz)
LoFar Frequency : 53.5
LoFar Frequency : 54.7
LoFar Frequency : 69.8
C0: 3.102
C1: −0.905

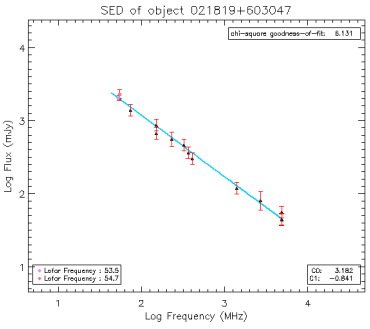
SED of object 021819+603047
chi-square goodness-of-fit: 8.131
Log Flux (mJy)
Log Frequency (MHz)
LoFar Frequency : 53.5
LoFar Frequency : 54.7
C0: 3.182
C1: −0.841

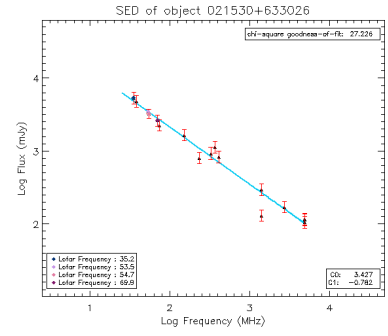
SED of object 021530+633026
chi-square goodness-of-fit: 27.226
Log Flux (mJy)
Log Frequency (MHz)
LoFar Frequency : 35.2
LoFar Frequency : 53.5
LoFar Frequency : 54.7
LoFar Frequency : 69.8
C0: 3.427
C1: −0.792

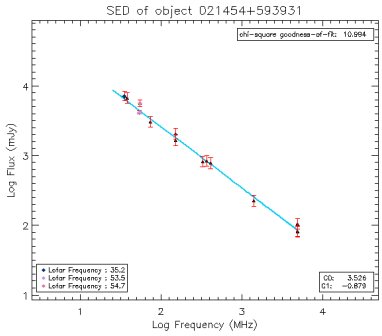
SED of object 021454+593931
chi-square goodness-of-fit: 10.994
Log Flux (mJy)
Log Frequency (MHz)
LoFar Frequency : 35.2
LoFar Frequency : 53.5
LoFar Frequency : 54.7
C0: 3.526
C1: −0.879

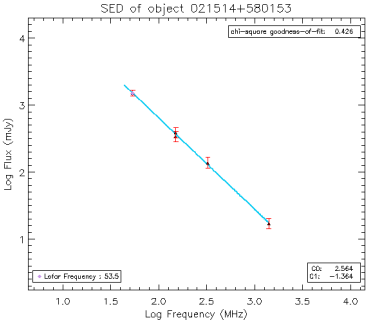
SED of object 021514+580153
chi-square goodness-of-fit: 0.426
Log Flux (mJy)
Log Frequency (MHz)
LoFar Frequency : 53.5
C0: 2.564
C1: −1.364

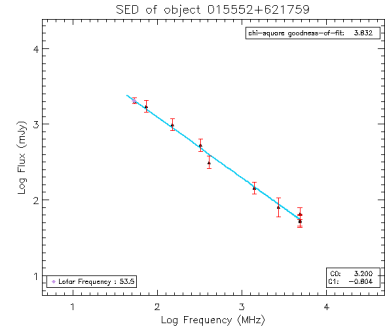
SED of object 015552+621759
chi-square goodness-of-fit: 3.832
Log Flux (mJy)
Log Frequency (MHz)
LoFar Frequency : 53.5
C0: 3.200
C1: −0.804

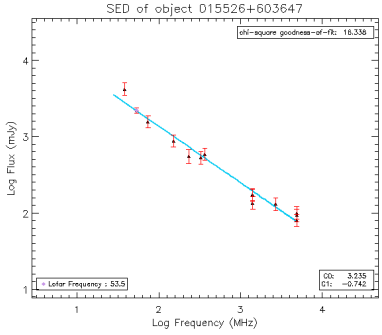
SED of object 015526+603647
chi-square goodness-of-fit: 16.338
Log Flux (mJy)
Log Frequency (MHz)
LoFar Frequency : 53.5
C0: 3.235
C1: −0.742

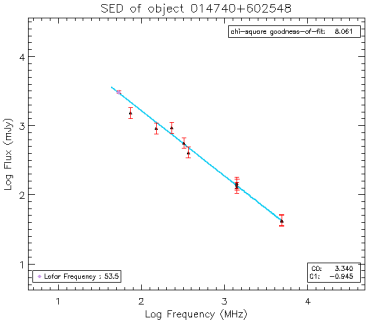
SED of object 014740+602548
chi-square goodness-of-fit: 8.061
Log Flux (mJy)
Log Frequency (MHz)
LoFar Frequency : 53.5
C0: 3.340
C1: −0.945

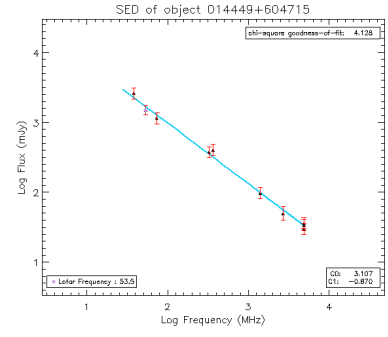
SED of object 014449+604715
chi-square goodness-of-fit: 4.128
Log Flux (mJy)
Log Frequency (MHz)
LoFar Frequency : 53.5
C0: 3.107
C1: −0.870

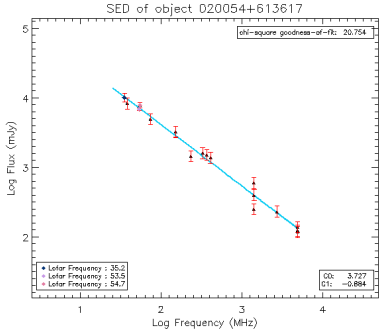
SED of object 020054+613617
chi-square goodness-of-fit: 20.754
Log Flux (mJy)
Log Frequency (MHz)
LoFar Frequency : 35.2
LoFar Frequency : 53.5
LoFar Frequency : 54.7
C0: 3.727
C1: −0.884

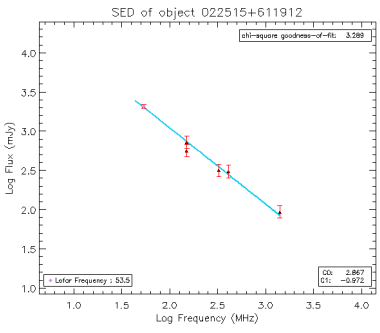
SED of object 022515+611912
chi-square goodness-of-fit: 3.289
+ Lofar Frequency : 53.5
C0: 2.867
C1: -0.972
Log Flux (mJy)
Log Frequency (MHz)

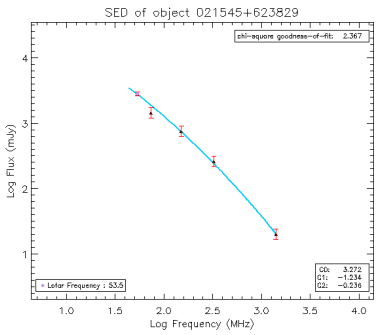
SED of object 021545+623829
chi-square goodness-of-fit: 2.367
+ Lofar Frequency : 53.5
C0: 3.272
C1: -1.334
C2: -0.236
Log Flux (mJy)
Log Frequency (MHz)

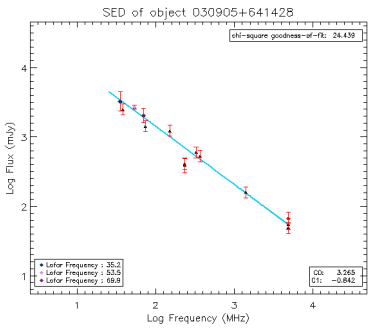
SED of object 030905+641428
chi-square goodness-of-fit: 24.439
+ Lofar Frequency : 35.2
+ Lofar Frequency : 53.5
+ Lofar Frequency : 69.8
C0: 3.265
C1: -0.842
Log Flux (mJy)
Log Frequency (MHz)

Appendix C:

List of targeted HERSCHEL Far-IR sources searched for H_2OMasers and corresponding spectra:

W3

w3_1 02:26:49.237 +61:57:47.85	w3_42 02:24:39.020 +61:25:23.27	w3_83 02:25:21.808 +61:33:27.06
w3_2 02:26:48.158 +62:03:33.80	w3_43 02:19:53.401 +61:02:04.93	w3_84 02:23:31.812 +61:51:13.55
w3_3 02:26:22.831 +61:54:01.18	w3_44 02:20:07.238 +61:01:20.29	w3_85 02:23:53.619 +61:51:59.04
w3_4 02:25:59.647 +61:58:21.45	w3_45 02:20:36.350 +60:55:45.05	w3_86 02:19:56.247 +61:11:51.17
w3_5 02:25:26.984 +61:56:22.93	w3_46 02:17:56.352 +61:24:22.40	w3_87 02:20:25.173 +61:10:42.69
w3_6 02:25:25.369 +61:58:28.03	w3_47 02:18:59.095 +61:28:19.62	w3_88 02:21:56.359 +61:06:45.92
w3_7 02:25:17.231 +62:00:25.19	w3_48 02:19:18.124 +61:29:40.87	w3_89 02:22:21.072 +61:07:15.75
w3_8 02:25:14.383 +62:02:01.18	w3_49 02:20:08.286 +61:10:23.03	w3_90 02:26:45.077 +61:32:17.84
w3_9 02:25:00.360 +62:05:09.43	w3_50 02:20:41.735 +61:09:56.36	w3_91 02:28:03.123 +61:24:34.46
w3_10 02:27:02.729 +61:36:44.37	w3_51 02:21:06.177 +61:06:00.37	w3_92 02:23:51.832 +61:57:58.40
w3_11 02:26:36.951 +61:41:17.84	w3_52 02:29:50.198 +61:45:03.42	w3_93 02:21:09.696 +61:51:49.06
w3_12 02:21:05.764 +61:27:26.99	w3_53 02:29:47.158 +61:49:59.88	w3_94 02:17:26.649 +61:58:04.45
w3_13 02:27:01.309 +61:39:22.87	w3_54 02:28:01.038 +61:45:08.22	w3_95 02:17:27.484 +62:03:08.78
w3_14 02:26:44.384 +61:29:45.41	w3_55 02:29:49.778 +61:32:20.82	w3_96 02:22:38.722 +61:58:51.33
w3_15 02:27:03.598 +61:29:47.58	w3_56 02:23:12.458 +62:09:52.13	w3_97 02:23:13.004 +61:54:45.68
w3_16 02:25:47.165 +61:20:56.99	w3_57 02:23:02.343 +62:10:37.96	w3_98 02:23:10.075 +62:07:48.98
w3_17 02:26:33.845 +61:39:42.30	w3_58 02:23:18.424 +62:12:38.76	w3_99 02:24:11.819 +61:49:32.25
w3_18 02:18:34.127 +61:54:35.13	w3_59 02:19:21.967 +62:16:54.04	w3_100 02:24:03.348 +62:01:08.30
w3_19 02:19:45.683 +61:36:51.94	w3_60 02:21:41.872 +62:00:40.53	w3_101 02:18:11.490 +61:54:55.05
w3_20 02:25:27.627 +61:15:20.84	w3_61 02:23:07.104 +61:58:28.85	w3_102 02:20:57.936 +62:02:36.90
w3_21 02:25:36.741 +61:13:44.40	w3_62 02:24:30.687 +62:03:27.26	w3_103 02:29:46.820 +60:57:23.32
w3_22 02:23:21.109 +61:12:34.51	w3_63 02:25:03.048 +62:08:59.12	w3_104 02:28:57.414 +60:53:13.56
w3_23 02:20:50.615 +61:12:01.10	w3_64 02:26:11.699 +62:11:41.13	w3_105 02:28:54.523 +60:59:16.54
w3_24 02:20:43.717 +61:26:52.32	w3_65 02:26:31.721 +62:14:59.37	w3_106 02:25:48.532 +61:07:45.90
w3_25 02:20:20.472 +61:26:50.67	w3_66 02:27:34.116 +62:09:15.25	w3_107 02:25:43.597 +61:10:41.26
w3_26 02:20:02.840 +61:28:50.09	w3_67 02:27:29.744 +62:07:48.27	w3_108 02:18:39.197 +60:40:34.62
w3_27 02:19:45.888 +61:29:34.43	w3_68 02:26:47.296 +62:15:31.21	w3_109 02:18:18.884 +60:47:24.43
w3_28 02:19:33.725 +61:34:08.30	w3_69 02:26:21.645 +62:04:26.96	w3_110 02:24:32.084 +61:09:13.57
w3_29 02:23:19.670 +61:56:23.65	w3_70 02:20:29.230 +62:05:40.70	w3_111 02:29:15.432 +61:12:33.16
w3_30 02:24:04.453 +61:34:22.12	w3_71 02:21:24.146 +62:10:39.75	w3_112 02:28:53.065 +61:10:06.83
w3_31 02:21:41.640 +61:05:44.40	w3_72 02:21:22.289 +62:01:33.86	w3_113 02:27:11.451 +61:26:06.53
w3_32 02:20:28.128 +61:05:11.08	w3_73 02:22:13.254 +62:00:16.52	w3_114 02:26:42.344 +61:25:36.26
w3_33 02:20:35.429 +61:07:16.60	w3_74 02:23:42.755 +62:07:46.86	w3_115 02:17:22.426 +60:38:03.67
w3_34 02:19:54.797 +61:05:16.71	w3_75 02:24:07.014 +62:04:38.85	w3_116 02:16:50.198 +60:37:45.75
w3_35 02:20:06.373 +61:04:23.55	w3_76 02:28:56.752 +61:25:45.70	w3_117 02:21:27.382 +61:05:25.45
w3_36 02:19:29.257 +61:07:31.79	w3_77 02:22:32.248 +61:24:54.26	w3_118 02:22:59.298 +61:09:12.72
w3_37 02:19:42.646 +61:11:22.26	w3_78 02:21:04.609 +61:24:30.26	w3_119 02:22:52.372 +61:11:30.18
w3_38 02:22:23.581 +61:06:10.65	w3_79 02:19:43.007 +61:06:20.80	w3_120 02:24:03.227 +61:09:57.84
w3_39 02:25:13.975 +61:18:29.01	w3_80 02:24:41.181 +61:14:19.18	w3_121 02:19:59.993 +61:33:33.36
w3_40 02:25:28.439 +61:18:28.12	w3_81 02:24:09.100 +61:21:50.32	w3_122 02:20:25.829 +61:31:34.58
w3_41 02:29:11.020 +61:05:36.36	w3_82 02:28:11.081 +61:12:49.13	w3_123 02:23:57.927 +61:32:09.11

W4

w4_1 02:52:36.033 +60:45:09.08
w4_2 02:45:28.207 +60:27:09.52
w4_3 02:51:53.738 +60:07:00.68
w4_4 02:52:17.105 +60:03:13.50
w4_5 02:36:36.898 +60:31:30.71
w4_6 02:53:39.748 +60:30:13.91
w4_7 02:46:18.462 +60:13:10.72
w4_8 03:07:24.120 +58:30:46.36
w4_9 03:14:05.913 +58:33:04.16
w4_10 03:14:42.131 +58:37:17.31
w4_11 03:15:11.554 +59:49:09.66
w4_12 03:13:38.073 +58:30:30.32
w4_13 03:20:43.601 +58:59:32.73
w4_14 03:21:20.114 +58:47:10.19
w4_15 03:15:30.252 +58:57:07.09
w4_16 03:23:04.629 +57:41:23.35
w4_17 03:27:46.994 +58:03:09.89
w4_18 03:27:30.864 +58:19:22.58
w4_19 03:27:23.768 +58:20:30.63
w4_20 03:33:50.455 +58:07:48.86
w4_21 03:39:12.998 +55:59:51.15
w4_22 03:48:48.555 +55:54:53.28
w4_23 03:38:12.684 +55:59:17.35
w4_24 03:39:11.596 +55:53:47.48
w4_25 03:38:53.044 +55:58:56.64
w4_26 03:47:35.352 +55:13:16.62
w4_27 03:56:58.222 +54:44:59.25
w4_26 04:01:55.689 +54:25:47.80
w4_29 04:10:12.152 +50:59:51.72
w4_30 04:11:05.082 +51:10:20.35
w4_31 04:11:10.895 +51:08:52.43
w4_32 04:07:10.912 +51:24:32.51
w4_33 04:07:11.558 +51:25:12.53
w4_34 04:10:55.197 +51:08:09.73
w4_35 04:02:18.109 +52:26:17.15
w4_40 03:56:15.551 +53:52:14.43
w4_43 03:55:38.181 +53:48:43.89
w4_49 03:27:38.494 +58:47:01.01
w4_50 03:27:24.141 +58:43:38.81
w4_56 04:22:26.728 +51:50:42.47
w4_57 04:22:32.872 +51:50:25.96

W5

w5_1 03:01:31.175 +60:29:16.32
w5_2 03:03:20.504 +60:28:07.27
w5_3 03:03:01.354 +60:28:20.60
w5_4 03:00:56.540 +60:40:18.31
w5_5 02:57:23.841 +60:40:41.05
w5_6 02:57:32.637 +60:38:24.59
w5_7 02:57:20.121 +60:38:48.12
w5_8 02:55:54.210 +60:37:33.52
w5_9 02:56:54.760 +60:45:37.36
w5_10 03:02:50.550 +60:25:42.67
w5_11 03:01:49.817 +60:35:35.43
w5_12 03:02:03.384 +60:34:49.49
w5_13 03:01:32.315 +60:25:56.35
w5_14 03:01:46.380 +60:24:12.19
w5_15 03:01:44.706 +60:28:47.17
w5_16 03:03:50.408 +60:20:14.85
w5_17 03:03:36.967 +60:20:44.80
w5_18 02:58:33.896 +60:43:34.88
w5_19 02:58:27.498 +60:45:05.97
w5_20 02:58:52.615 +60:43:53.07
w5_21 03:01:40.204 +60:41:50.38
w5_22 03:01:26.589 +60:41:04.52
w5_23 02:58:16.836 +60:43:45.84
w5_24 03:00:03.296 +60:50:37.28
w5_25 03:00:20.522 +60:47:34.70
w5_26 02:59:12.371 +60:45:34.49
w5_27 02:57:21.621 +60:53:10.66
w5_28 02:58:11.774 +60:48:36.96
w5_29 02:57:16.338 +60:50:02.56
w5_30 02:56:13.200 +60:39:08.16
w5_31 02:56:39.401 +60:41:58.63
w5_32 02:55:38.761 +60:38:25.15
w5_33 02:55:27.833 +60:36:18.29
w5_34 02:56:04.262 +60:35:05.12
w5_35 03:00:14.314 +60:59:22.57
w5_36 03:01:19.385 +60:24:12.11
w5_37 03:01:03.683 +60:21:41.92
w5_38 03:00:28.380 +60:19:23.55
w5_39 02:59:47.320 +60:21:14.29
w5_40 03:01:46.406 +60:30:56.31
w5_41 03:03:10.552 +60:20:08.60
w5_42 03:02:22.854 +60:45:43.22
w5_43 03:01:11.278 +60:40:39.38
w5_44 03:03:16.913 +60:57:46.23
w5_45 02:55:40.044 +60:00:12.98
w5_46 02:55:56.663 +60:03:44.10
w5_47 03:05:36.990 +60:11:11.77
w5_48 03:03:57.223 +60:22:39.74
w5_49 03:00:08.203 +60:17:00.63
w5_50 03:01:52.490 +60:26:04.15
w5_51 03:02:39.279 +60:28:12.50
w5_52 03:03:20.213 +60:24:13.47
w5_53 03:00:33.179 +60:07:26.56
w5_54 03:00:22.624 +60:06:23.71
w5_55 03:01:56.489 +60:32:44.07
w5_56 03:01:10.946 +60:18:09.04
w5_57 03:00:26.118 +60:17:26.31
w5_58 02:57:01.583 +60:33:03.65
w5_59 02:56:12.291 +60:10:14.11
w5_60 03:04:02.451 +59:08:53.63
w5_61 03:04:17.435 +59:13:31.68
w5_62 03:04:48.961 +59:31:24.02
w5_63 03:09:42.744 +59:52:48.89
w5_64 03:09:49.255 +59:54:31.58
w5_65 03:09:41.690 +59:55:19.17
w5_66 03:02:51.415 +60:24:09.14
w5_67 03:03:09.504 +60:26:09.28
w5_68 03:03:31.470 +60:26:20.73
w5_69 03:04:25.040 +60:55:47.44
w5_70 03:01:05.789 +60:41:56.29
w5_71 02:56:59.249 +60:43:30.80
w5_72 02:57:18.212 +60:41:53.20
w5_73 02:56:58.108 +60:39:37.34
w5_74 02:57:12.052 +60:45:24.92
w5_75 02:57:23.558 +60:44:23.82
w5_76 02:56:27.763 +60:45:02.29
w5_77 03:03:12.342 +60:29:57.97
w5_78 03:03:10.556 +60:27:57.23
w5_79 03:05:12.266 +60:48:38.40
w5_80 02:57:44.159 +60:47:54.47
w5_81 02:57:23.351 +60:28:42.21
w5_82 03:02:50.130 +60:39:37.90
w5_83 03:02:31.512 +60:42:54.23
w5_84 02:59:39.215 +60:46:57.30
w5_85 02:59:25.612 +60:46:10.68
w5_86 02:59:58.481 +60:48:29.93
w5_87 03:01:17.073 +60:47:46.35
w5_88 03:02:05.750 +60:27:34.02
w5_89 03:03:26.289 +60:16:49.87
w5_90 03:04:34.043 +60:28:58.68
w5_91 03:07:25.149 +60:49:40.30
w5_92 02:58:04.419 +60:50:01.56
w5_93 02:57:49.101 +60:49:26.65
w5_94 03:02:28.337 +60:29:38.60
w5_95 03:02:32.429 +60:34:55.13
w5_96 03:03:30.336 +60:38:54.54
w5_97 03:00:38.868 +60:49:54.75
w5_98 03:00:50.600 +60:59:17.36
w5_99 03:04:40.886 +60:54:06.19
w5_100 03:05:43.922 +60:33:14.31
w5_101 03:05:37.230 +60:38:35.87
w5_102 03:06:38.863 +60:19:22.31
w5_103 03:04:12.090 +60:22:12.06
w5_104 03:00:47.472 +60:47:50.01
w5_105 02:59:04.396 +60:55:27.44
w5_106 02:58:56.068 +60:59:20.09
w5_107 02:59:29.322 +60:58:44.85
w5_108 02:59:57.332 +60:59:32.17
w5_109 02:57:59.904 +60:54:40.20
w5_110 03:01:19.050 +60:21:44.12
w5_111 03:01:34.214 +60:22:30.04
w5_112 03:02:06.279 +60:25:04.03
w5_113 03:03:11.394 +60:33:47.15
w5_114 03:01:50.622 +60:41:39.85
w5_115 03:00:21.690 +60:23:26.97
w5_116 03:01:18.246 +60:44:34.74
w5_117 02:59:09.452 +60:49:12.90
w5_118 02:58:51.764 +60:49:32.43
w5_119 02:59:41.999 +60:29:06.80
w5_120 03:02:22.893 +60:38:23.64
w5_121 03:02:07.616 +60:39:38.89
w5_122 03:02:07.084 +60:42:04.70
w5_123 03:01:38.137 +60:44:51.51
w5_124 03:03:41.429 +60:35:04.80
w5_125 02:57:20.204 +60:22:39.33
w5_126 03:06:40.230 +60:39:17.95
w5_127 03:07:18.483 +60:47:23.87
w5_128 03:05:24.905 +60:39:48.03
w5_129 03:02:52.661 +60:31:34.56
w5_130 03:03:58.092 +60:30:49.65
w5_131 03:02:32.667 +60:22:58.54
w5_132 03:01:56.130 +60:22:38.31
w5_133 03:02:09.741 +60:30:33.11
w5_134 03:01:30.241 +60:31:14.97
w5_135 03:01:24.625 +60:27:25.80
w5_136 03:01:18.972 +60:29:26.57
w5_137 03:02:15.434 +60:33:19.66
w5_138 03:01:22.807 +60:42:50.64

w5_139 03:01:04.709 +60:38:48.81
w5_140 03:00:47.142 +60:38:52.62
w5_141 03:00:44.810 +60:41:14.20
w5_142 03:01:31.310 +60:46:23.14
w5_143 03:02:02.569 +60:44:09.72
w5_144 02:59:10.066 +60:19:00.68
w5_145 02:57:37.288 +60:25:23.84
w5_146 02:55:45.566 +60:33:15.78
w5_147 02:58:37.093 +60:41:57.17
w5_148 02:59:09.765 +60:52:32.87
w5_149 03:02:32.188 +60:46:51.66
w5_150 03:00:52.767 +60:16:47.90
w5_151 02:58:47.586 +60:51:41.24
w5_152 03:04:31.975 +59:58:23.37
w5_153 03:04:46.145 +59:43:47.12
w5_154 03:04:53.141 +59:53:25.68
w5_155 03:07:16.744 +60:01:02.68
w5_156 03:09:39.858 +59:50:34.84
w5_157 03:10:51.797 +59:30:45.93
w5_158 03:09:54.112 +59:38:55.49
w5_159 03:03:47.456 +59:05:04.30
w5_160 03:07:43.811 +59:02:35.46
w5_161 03:08:08.153 +59:08:29.38
w5_162 03:08:57.996 +59:13:36.16
w5_163 03:06:22.782 +59:17:56.39
w5_164 02:56:30.864 +59:34:04.30
w5_165 02:57:28.966 +59:51:58.78
w5_166 02:56:13.262 +59:54:43.47
w5_167 02:56:16.824 +59:56:40.70
w5_168 02:56:36.425 +59:59:49.29
w5_169 02:57:03.970 +60:05:30.58
w5_170 03:01:56.330 +59:51:34.19
w5_171 03:01:33.037 +60:10:44.24
w5_172 03:00:23.595 +60:15:26.23
w5_173 02:56:52.009 +60:03:28.14
w5_174 02:56:09.931 +59:58:46.99
w5_175 02:57:23.379 +60:19:09.71
w5_176 03:05:21.175 +59:45:36.73
w5_177 03:05:44.953 +59:41:36.57
w5_178 03:05:44.600 +59:47:43.30
w5_179 02:57:16.744 +60:07:49.71
w5_180 02:57:30.711 +60:16:32.24
w5_181 02:49:24.745 +60:46:54.77
w5_182 02:49:47.629 +60:42:12.26
w5_183 02:50:02.117 +60:41:41.95
w5_184 02:49:03.603 +60:43:17.41
w5_185 02:45:11.281 +60:49:39.31
w5_186 02:47:15.936 +60:30:46.59
w5_188 02:49:12.671 +61:00:40.00
w5_189 02:55:01.643 +60:35:41.27
w5_190 02:55:01.643 +60:35:41.27
w5_191 02:52:17.061 +60:03:13.32
w5_192 02:51:53.909 +60:07:02.23
w5_193 02:50:08.131 +61:59:51.57
w5_194 02:47:26.247 +61:56:50.57
w5_195 02:46:18.574 +60:13:10.77
w5_196 03:14:05.275 +58:33:07.89
w5_198 03:27:31.052 +58:19:18.93
w5_199 03:19:07.718 +57:51:52.60
w5_200 03:07:24.054 +58:30:45.71
w5_201 03:39:12.564 +55:59:48.99
w5_202 03:58:19.035 +54:39:39.93
w5_203 03:48:47.257 +55:54:08.46
w5_204 03:56:15.389 +53:52:12.38
w5_205 03:57:18.415 +54:10:45.96

Appendix D

The LOFAR point catalogue created in § 4.1.1. Please refer to the attached CD the catalogue in full for

- The LOFAR entire bandwidth point source catalogue centred at 53.5 MHz:

  LOFAR_ENTIRE_BW_53.5MHz_Point_Source_CAT_csv

- The LOFAR entire bandwidth point source catalogue centred at 35.2 MHz:

  LOFAR_NARROW_BW_35.2MHz_Point_Source_CAT_csv

- The LOFAR narrow bandwidth point source catalogue centred at 54.7 MHz:

  LOFAR_NARROW_BW_54.7MHz_Point_Source_CAT_csv

- The LOFAR narrow bandwidth point source catalogue centred at 69.9 MHz:

  LOFAR_NARROW_BW_69.9MHz_Point_Source_CAT_csv

Appendix E

A sample of the AKARI catalogue created in § 6. Please refer to the attached CD the catalogue in full.

- *AKARI_FULL_FAINT_SOURCE_CATALOGUE_csv*

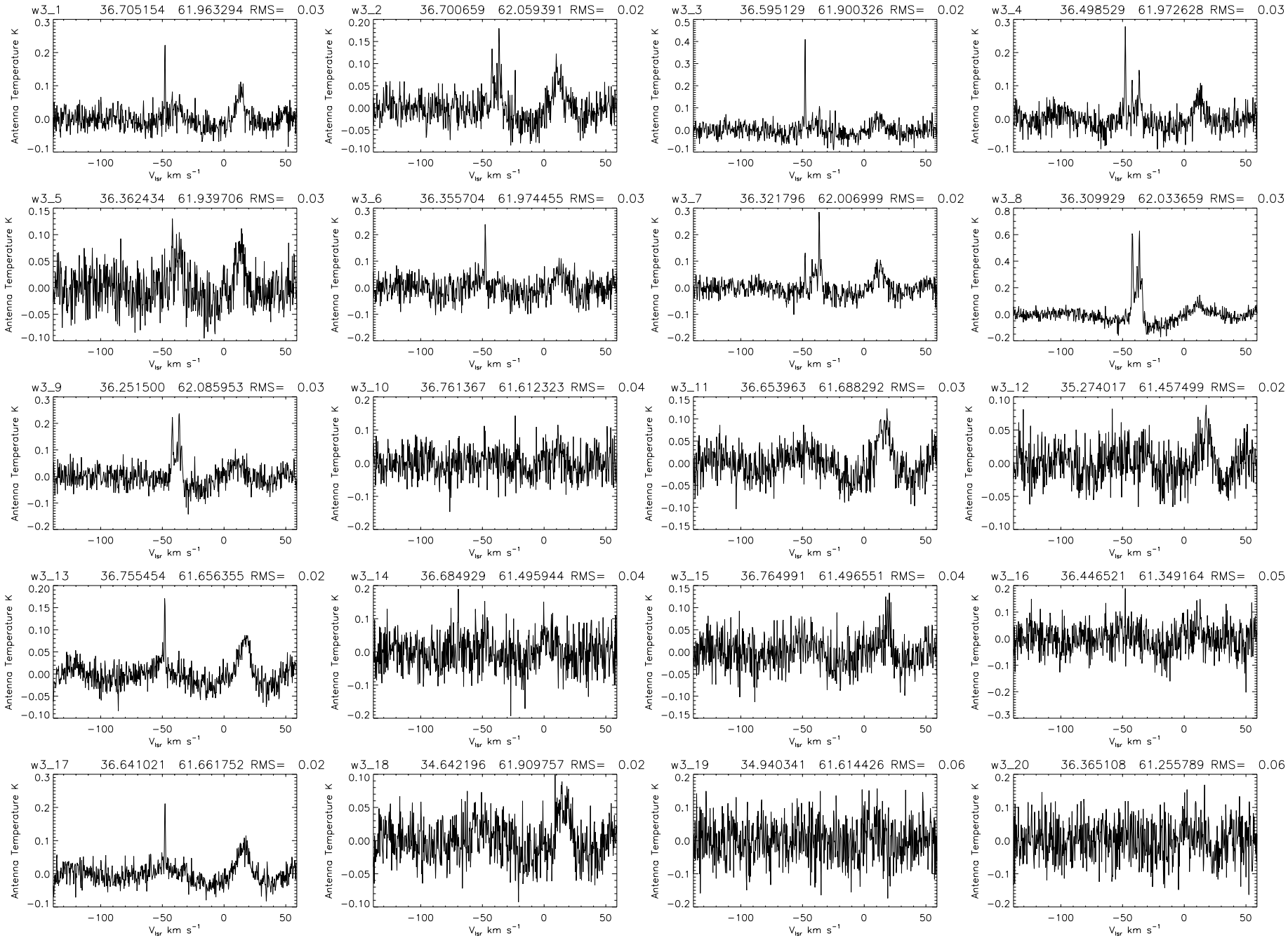
w3_1 36.705154 61.963294 RMS= 0.03
w3_2 36.700659 62.059391 RMS= 0.02
w3_3 36.595129 61.900326 RMS= 0.02
w3_4 36.498529 61.972628 RMS= 0.03
w3_5 36.362434 61.939706 RMS= 0.03
w3_6 36.355704 61.974455 RMS= 0.03
w3_7 36.321796 62.006999 RMS= 0.02
w3_8 36.309929 62.033659 RMS= 0.03
w3_9 36.251500 62.085953 RMS= 0.03
w3_10 36.761367 61.612323 RMS= 0.04
w3_11 36.653963 61.688292 RMS= 0.03
w3_12 35.274017 61.457499 RMS= 0.02
w3_13 36.755454 61.656355 RMS= 0.02
w3_14 36.684929 61.495944 RMS= 0.04
w3_15 36.764991 61.496551 RMS= 0.04
w3_16 36.446521 61.349164 RMS= 0.05
w3_17 36.641021 61.661752 RMS= 0.02
w3_18 34.642196 61.909757 RMS= 0.02
w3_19 34.940341 61.614426 RMS= 0.06
w3_20 36.365108 61.255789 RMS= 0.06
Antenna Temperature K
V_lsr km s^-1

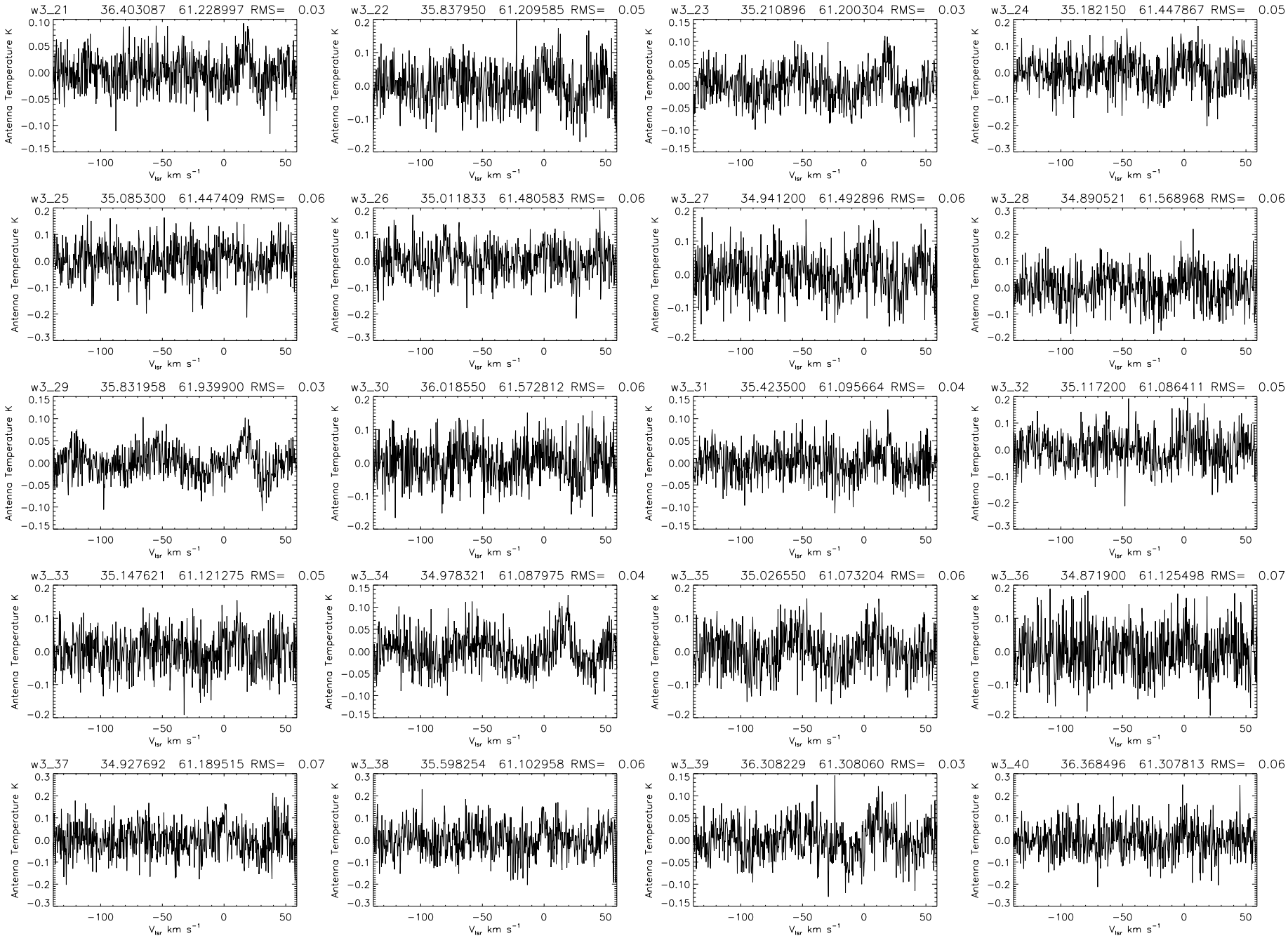
w3_21 36.403087 61.228997 RMS= 0.03
w3_22 35.837950 61.209585 RMS= 0.05
w3_23 35.210896 61.200304 RMS= 0.03
w3_24 35.182150 61.447867 RMS= 0.05
w3_25 35.085300 61.447409 RMS= 0.06
w3_26 35.011833 61.480583 RMS= 0.06
w3_27 34.941200 61.492896 RMS= 0.06
w3_28 34.890521 61.568968 RMS= 0.06
w3_29 35.831958 61.939900 RMS= 0.03
w3_30 36.018550 61.572812 RMS= 0.06
w3_31 35.423500 61.095664 RMS= 0.04
w3_32 35.117200 61.086411 RMS= 0.05
w3_33 35.147621 61.121275 RMS= 0.05
w3_34 34.978321 61.087975 RMS= 0.04
w3_35 35.026550 61.073204 RMS= 0.06
w3_36 34.871900 61.125498 RMS= 0.07
w3_37 34.927692 61.189515 RMS= 0.07
w3_38 35.598254 61.102958 RMS= 0.06
w3_39 36.308229 61.308060 RMS= 0.03
w3_40 36.368496 61.307813 RMS= 0.06
Antenna Temperature K
V_lsr km s^-1

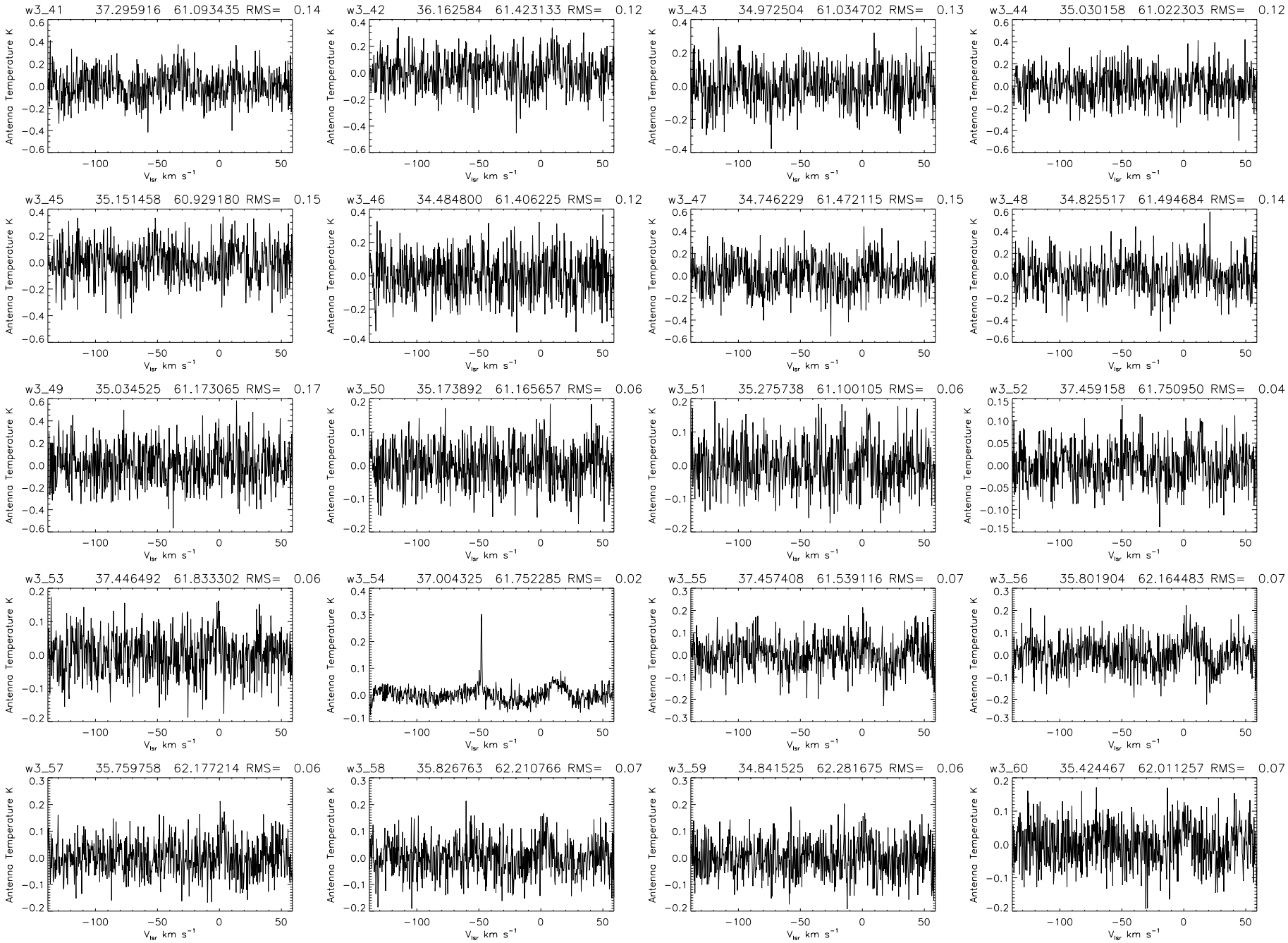
w3_41 37.295916 61.093435 RMS= 0.14
w3_42 36.162584 61.423133 RMS= 0.12
w3_43 34.972504 61.034702 RMS= 0.13
w3_44 35.030158 61.022303 RMS= 0.12
w3_45 35.151458 60.929180 RMS= 0.15
w3_46 34.484800 61.406225 RMS= 0.12
w3_47 34.746229 61.472115 RMS= 0.15
w3_48 34.825517 61.494684 RMS= 0.14
w3_49 35.034525 61.173065 RMS= 0.17
w3_50 35.173892 61.165657 RMS= 0.06
w3_51 35.275738 61.100105 RMS= 0.06
w3_52 37.459158 61.750950 RMS= 0.04
w3_53 37.446492 61.833302 RMS= 0.06
w3_54 37.004325 61.752285 RMS= 0.02
w3_55 37.457408 61.539116 RMS= 0.07
w3_56 35.801904 62.164483 RMS= 0.07
w3_57 35.759758 62.177214 RMS= 0.06
w3_58 35.826763 62.210766 RMS= 0.07
w3_59 34.841525 62.281675 RMS= 0.06
w3_60 35.424467 62.011257 RMS= 0.07
Antenna Temperature K
V_lsr km s^-1

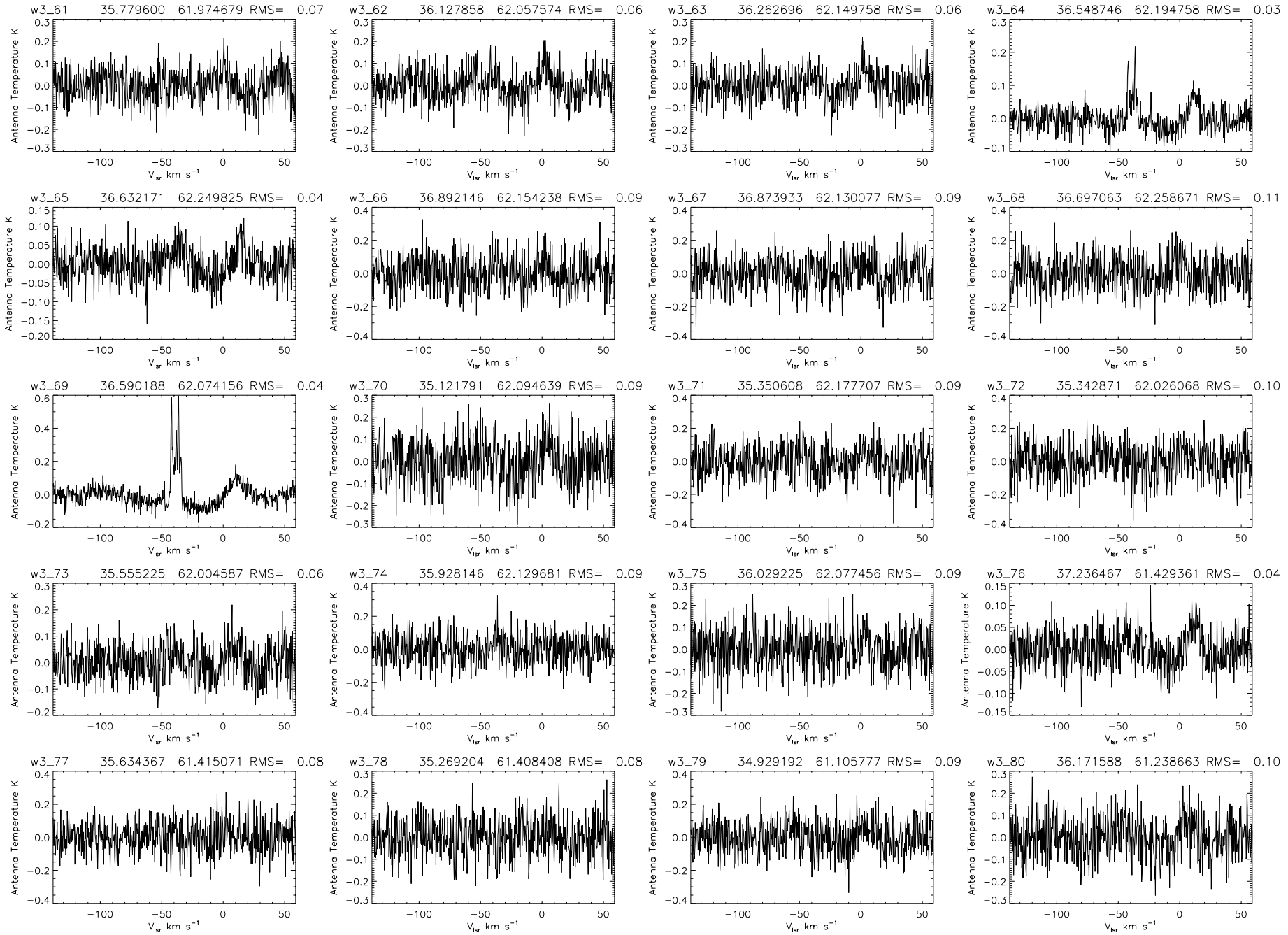
w3_61 35.779600 61.974679 RMS= 0.07
w3_62 36.127858 62.057574 RMS= 0.06
w3_63 36.262696 62.149758 RMS= 0.06
w3_64 36.548746 62.194758 RMS= 0.03
w3_65 36.632171 62.249825 RMS= 0.04
w3_66 36.892146 62.154238 RMS= 0.09
w3_67 36.873933 62.130077 RMS= 0.09
w3_68 36.697063 62.258671 RMS= 0.11
w3_69 36.590188 62.074156 RMS= 0.04
w3_70 35.121791 62.094639 RMS= 0.09
w3_71 35.350608 62.177707 RMS= 0.09
w3_72 35.342871 62.026068 RMS= 0.10
w3_73 35.555225 62.004587 RMS= 0.06
w3_74 35.928146 62.129681 RMS= 0.09
w3_75 36.029225 62.077456 RMS= 0.09
w3_76 37.236467 61.429361 RMS= 0.04
w3_77 35.634367 61.415071 RMS= 0.08
w3_78 35.269204 61.408408 RMS= 0.08
w3_79 34.929192 61.105777 RMS= 0.09
w3_80 36.171588 61.238663 RMS= 0.10
Antenna Temperature K
V_lsr km s^-1

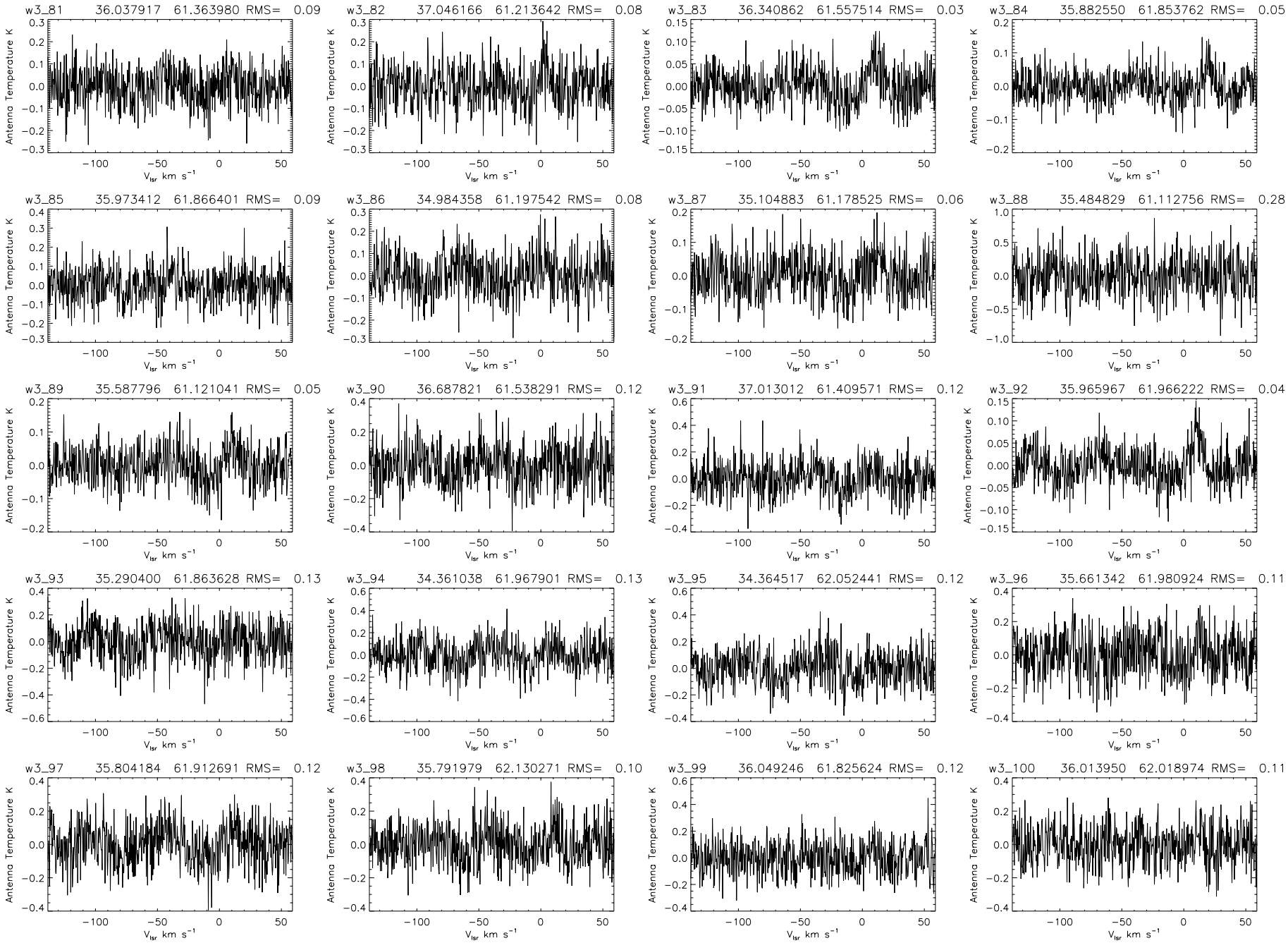
w3_81 36.037917 61.363980 RMS= 0.09
w3_82 37.046166 61.213642 RMS= 0.08
w3_83 36.340862 61.557514 RMS= 0.03
w3_84 35.882550 61.853762 RMS= 0.05
w3_85 35.973412 61.866401 RMS= 0.09
w3_86 34.984358 61.197542 RMS= 0.08
w3_87 35.104883 61.178525 RMS= 0.06
w3_88 35.484829 61.112756 RMS= 0.28
w3_89 35.587796 61.121041 RMS= 0.05
w3_90 36.687821 61.538291 RMS= 0.12
w3_91 37.013012 61.409571 RMS= 0.12
w3_92 35.965967 61.966222 RMS= 0.04
w3_93 35.290400 61.863628 RMS= 0.13
w3_94 34.361038 61.967901 RMS= 0.13
w3_95 34.364517 62.052441 RMS= 0.12
w3_96 35.661342 61.980924 RMS= 0.11
w3_97 35.804184 61.912691 RMS= 0.12
w3_98 35.791979 62.130271 RMS= 0.10
w3_99 36.049246 61.825624 RMS= 0.12
w3_100 36.013950 62.018974 RMS= 0.11
Antenna Temperature K
V_lsr km s^-1

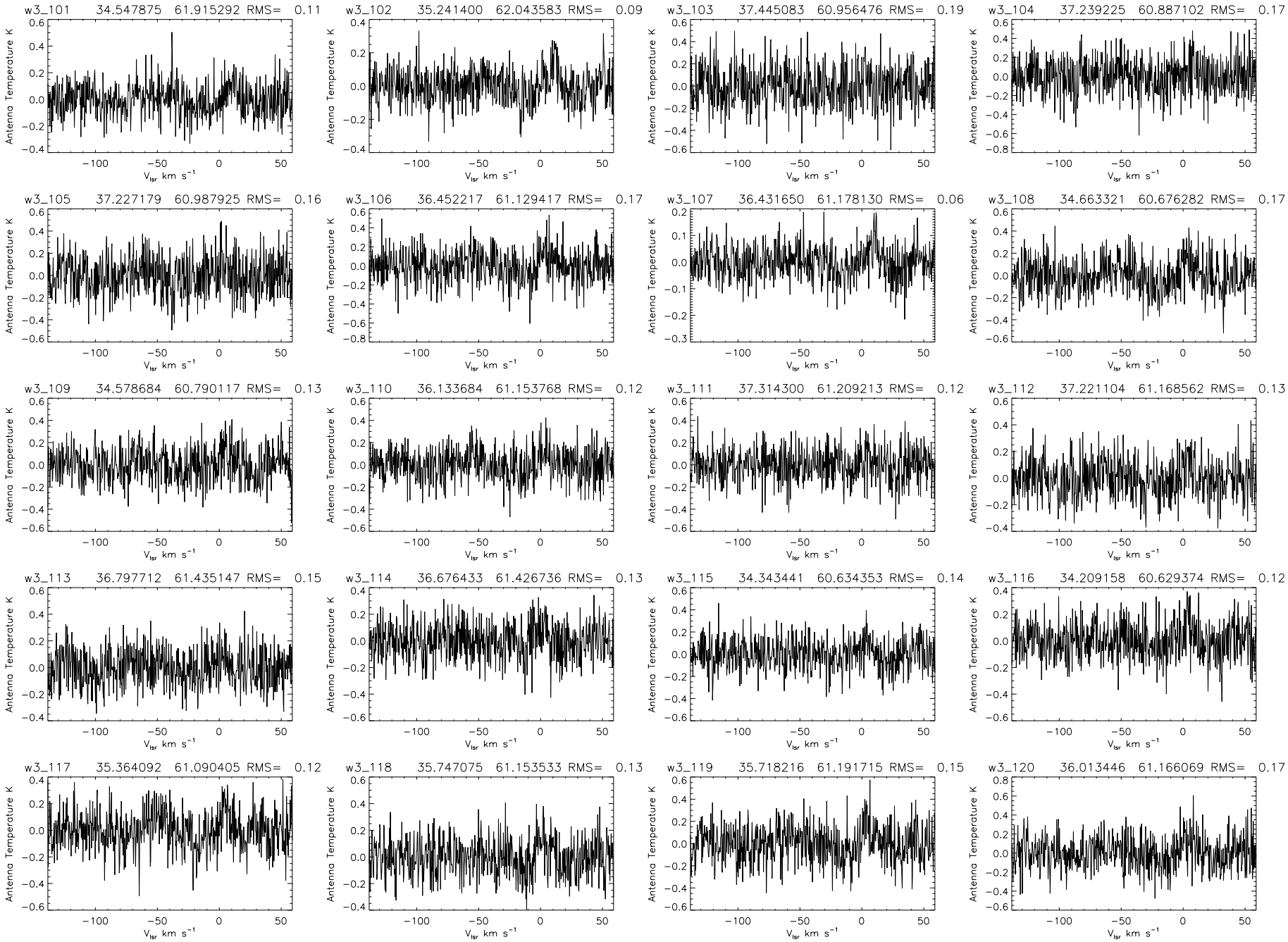
w3_101 34.547875 61.915292 RMS= 0.11
w3_102 35.241400 62.043583 RMS= 0.09
w3_103 37.445083 60.956476 RMS= 0.19
w3_104 37.239225 60.887102 RMS= 0.17
w3_105 37.227179 60.987925 RMS= 0.16
w3_106 36.452217 61.129417 RMS= 0.17
w3_107 36.431650 61.178130 RMS= 0.06
w3_108 34.663321 60.676282 RMS= 0.17
w3_109 34.578684 60.790117 RMS= 0.13
w3_110 36.133684 61.153768 RMS= 0.12
w3_111 37.314300 61.209213 RMS= 0.12
w3_112 37.221104 61.168562 RMS= 0.13
w3_113 36.797712 61.435147 RMS= 0.15
w3_114 36.676433 61.426736 RMS= 0.13
w3_115 34.343441 60.634353 RMS= 0.14
w3_116 34.209158 60.629374 RMS= 0.12
w3_117 35.364092 61.090405 RMS= 0.12
w3_118 35.747075 61.153533 RMS= 0.13
w3_119 35.718216 61.191715 RMS= 0.15
w3_120 36.013446 61.166069 RMS= 0.17
Antenna Temperature K
V_lsr km s^-1

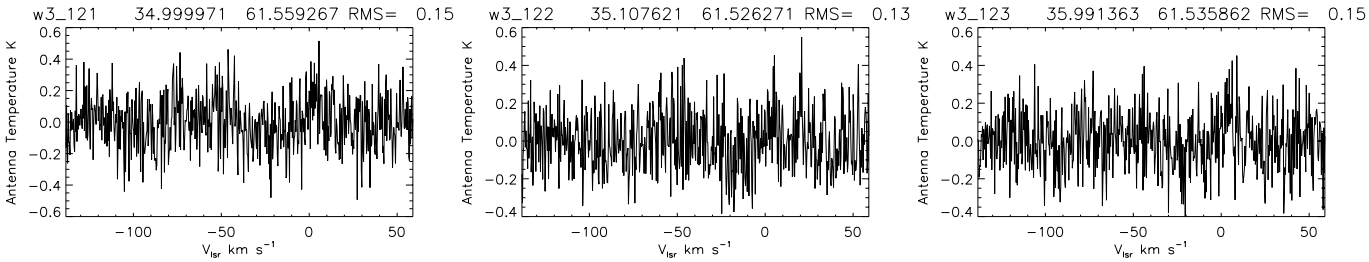
w3_121 34.999971 61.559267 RMS= 0.15
w3_122 35.107621 61.526271 RMS= 0.13
w3_123 35.991363 61.535862 RMS= 0.15
Antenna Temperature K
0.6
0.4
0.2
0.0
−0.2
−0.4
−0.6
−100
−50
0
50
V_lsr km s^-1

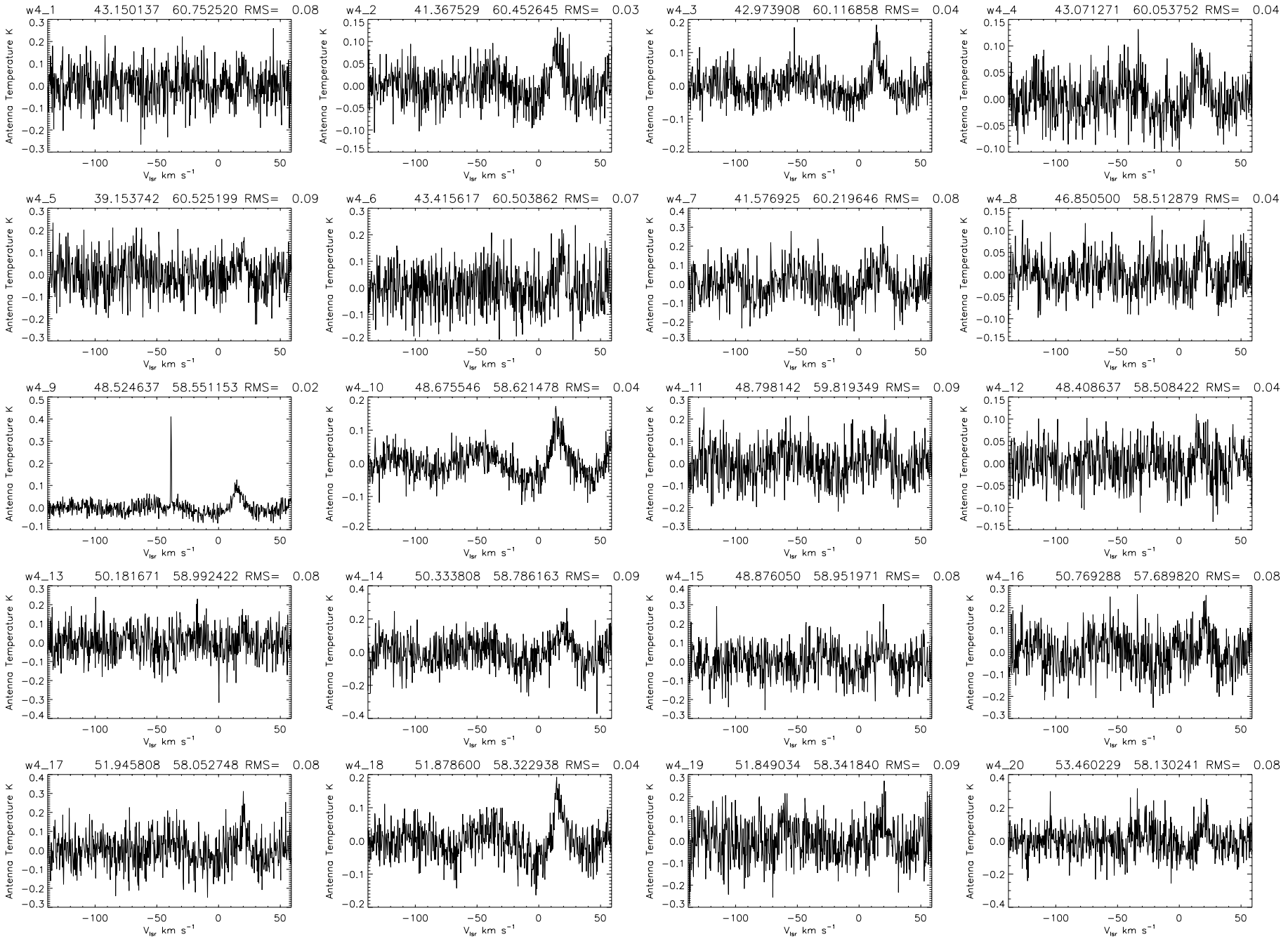
w4_1 43.150137 60.752520 RMS= 0.08
w4_2 41.367529 60.452645 RMS= 0.03
w4_3 42.973908 60.116858 RMS= 0.04
w4_4 43.071271 60.053752 RMS= 0.04
w4_5 39.153742 60.525199 RMS= 0.09
w4_6 43.415617 60.503862 RMS= 0.07
w4_7 41.576925 60.219646 RMS= 0.08
w4_8 46.850500 58.512879 RMS= 0.04
w4_9 48.524637 58.551153 RMS= 0.02
w4_10 48.675546 58.621478 RMS= 0.04
w4_11 48.798142 59.819349 RMS= 0.09
w4_12 48.408637 58.508422 RMS= 0.04
w4_13 50.181671 58.992422 RMS= 0.08
w4_14 50.333808 58.786163 RMS= 0.09
w4_15 48.876050 58.951971 RMS= 0.08
w4_16 50.769288 57.689820 RMS= 0.08
w4_17 51.945808 58.052748 RMS= 0.08
w4_18 51.878600 58.322938 RMS= 0.04
w4_19 51.849034 58.341840 RMS= 0.09
w4_20 53.460229 58.130241 RMS= 0.08
Antenna Temperature K
V_lsr km s^-1

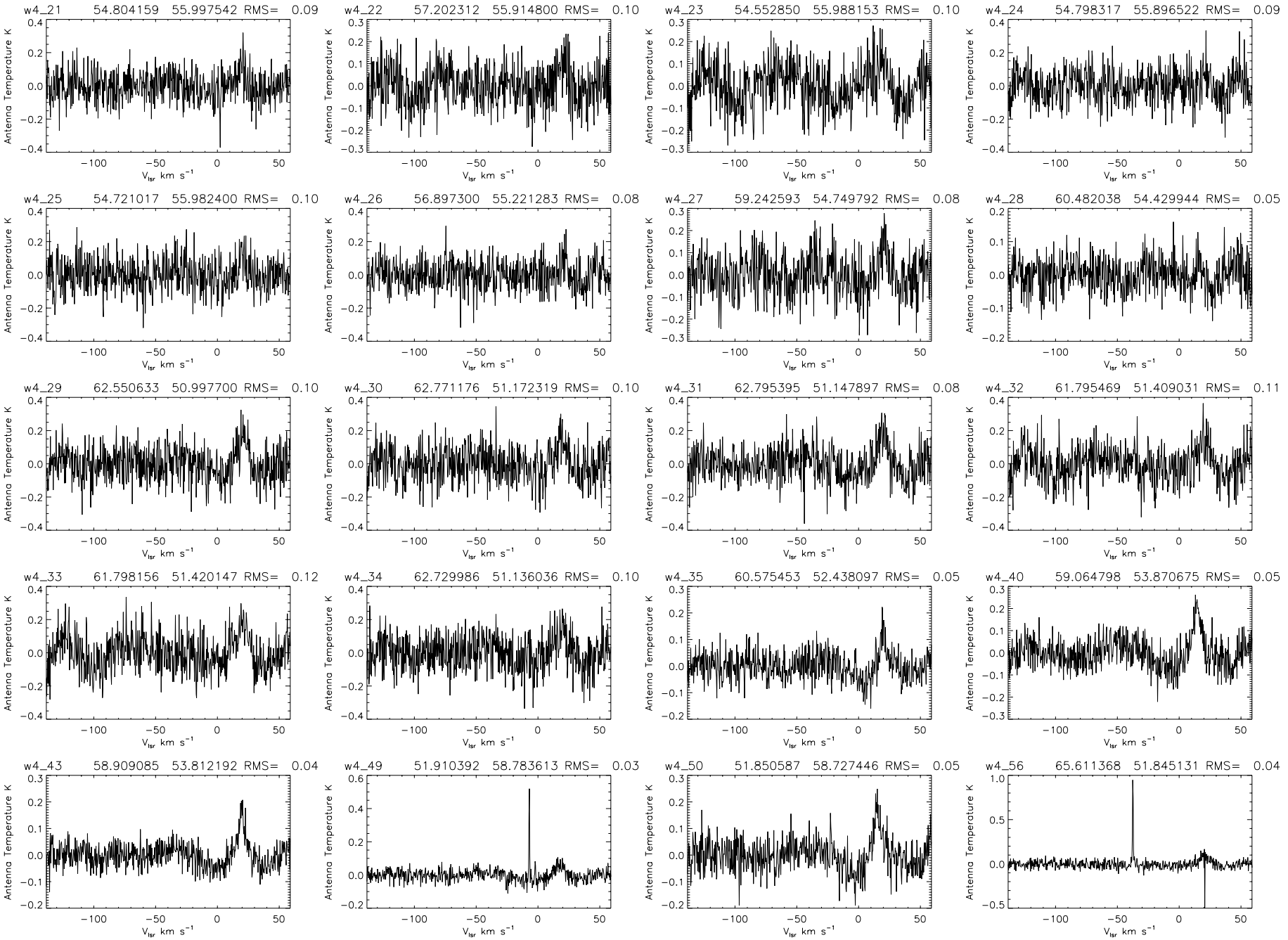
w4_21 54.804159 55.997542 RMS= 0.09
w4_22 57.202312 55.914800 RMS= 0.10
w4_23 54.552850 55.988153 RMS= 0.10
w4_24 54.798317 55.896522 RMS= 0.09
w4_25 54.721017 55.982400 RMS= 0.10
w4_26 56.897300 55.221283 RMS= 0.08
w4_27 59.242593 54.749792 RMS= 0.08
w4_28 60.482038 54.429944 RMS= 0.05
w4_29 62.550633 50.997700 RMS= 0.10
w4_30 62.771176 51.172319 RMS= 0.10
w4_31 62.795395 51.147897 RMS= 0.08
w4_32 61.795469 51.409031 RMS= 0.11
w4_33 61.798156 51.420147 RMS= 0.12
w4_34 62.729986 51.136036 RMS= 0.10
w4_35 60.575453 52.438097 RMS= 0.05
w4_40 59.064798 53.870675 RMS= 0.05
w4_43 58.909085 53.812192 RMS= 0.04
w4_49 51.910392 58.783613 RMS= 0.03
w4_50 51.850587 58.727446 RMS= 0.05
w4_56 65.611368 51.845131 RMS= 0.04
Antenna Temperature K
V_lsr km s^-1

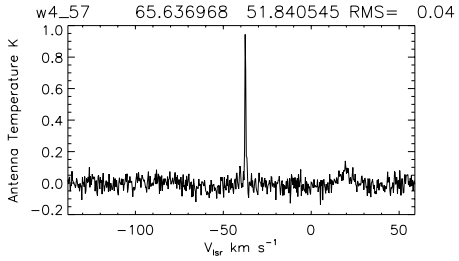
w4_57 65.636968 51.840545 RMS= 0.04
Antenna Temperature K
1.0
0.8
0.6
0.4
0.2
0.0
−0.2
−100
−50
0
50
V_lsr km s^-1

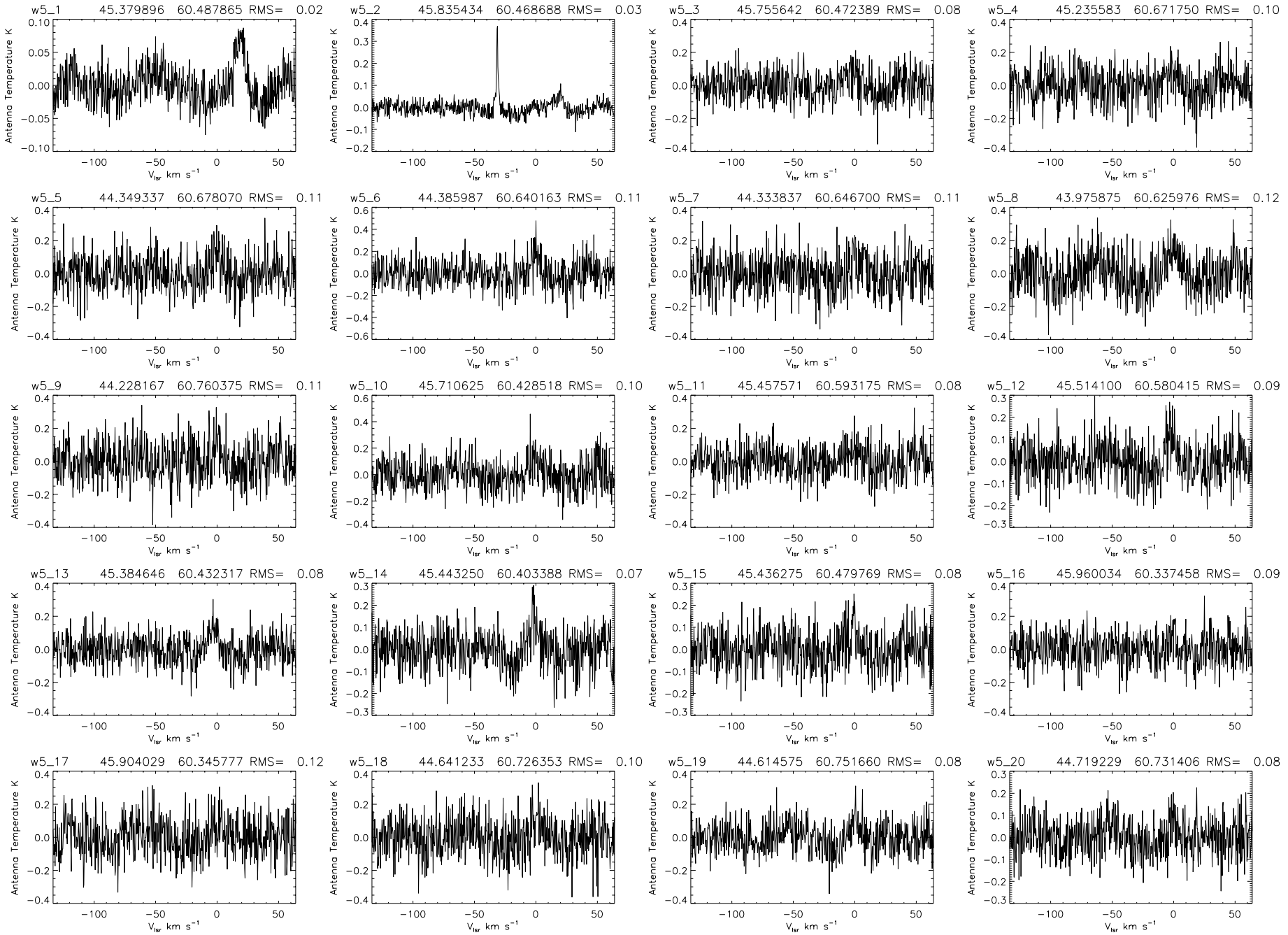
w5_1 45.379896 60.487865 RMS= 0.02
w5_2 45.835434 60.468688 RMS= 0.03
w5_3 45.755642 60.472389 RMS= 0.08
w5_4 45.235583 60.671750 RMS= 0.10
w5_5 44.349337 60.678070 RMS= 0.11
w5_6 44.385987 60.640163 RMS= 0.11
w5_7 44.333837 60.646700 RMS= 0.11
w5_8 43.975875 60.625976 RMS= 0.12
w5_9 44.228167 60.760375 RMS= 0.11
w5_10 45.710625 60.428518 RMS= 0.10
w5_11 45.457571 60.593175 RMS= 0.08
w5_12 45.514100 60.580415 RMS= 0.09
w5_13 45.384646 60.432317 RMS= 0.08
w5_14 45.443250 60.403388 RMS= 0.07
w5_15 45.436275 60.479769 RMS= 0.08
w5_16 45.960034 60.337458 RMS= 0.09
w5_17 45.904029 60.345777 RMS= 0.12
w5_18 44.641233 60.726353 RMS= 0.10
w5_19 44.614575 60.751660 RMS= 0.08
w5_20 44.719229 60.731406 RMS= 0.08
Antenna Temperature K
V_lsr km s^-1

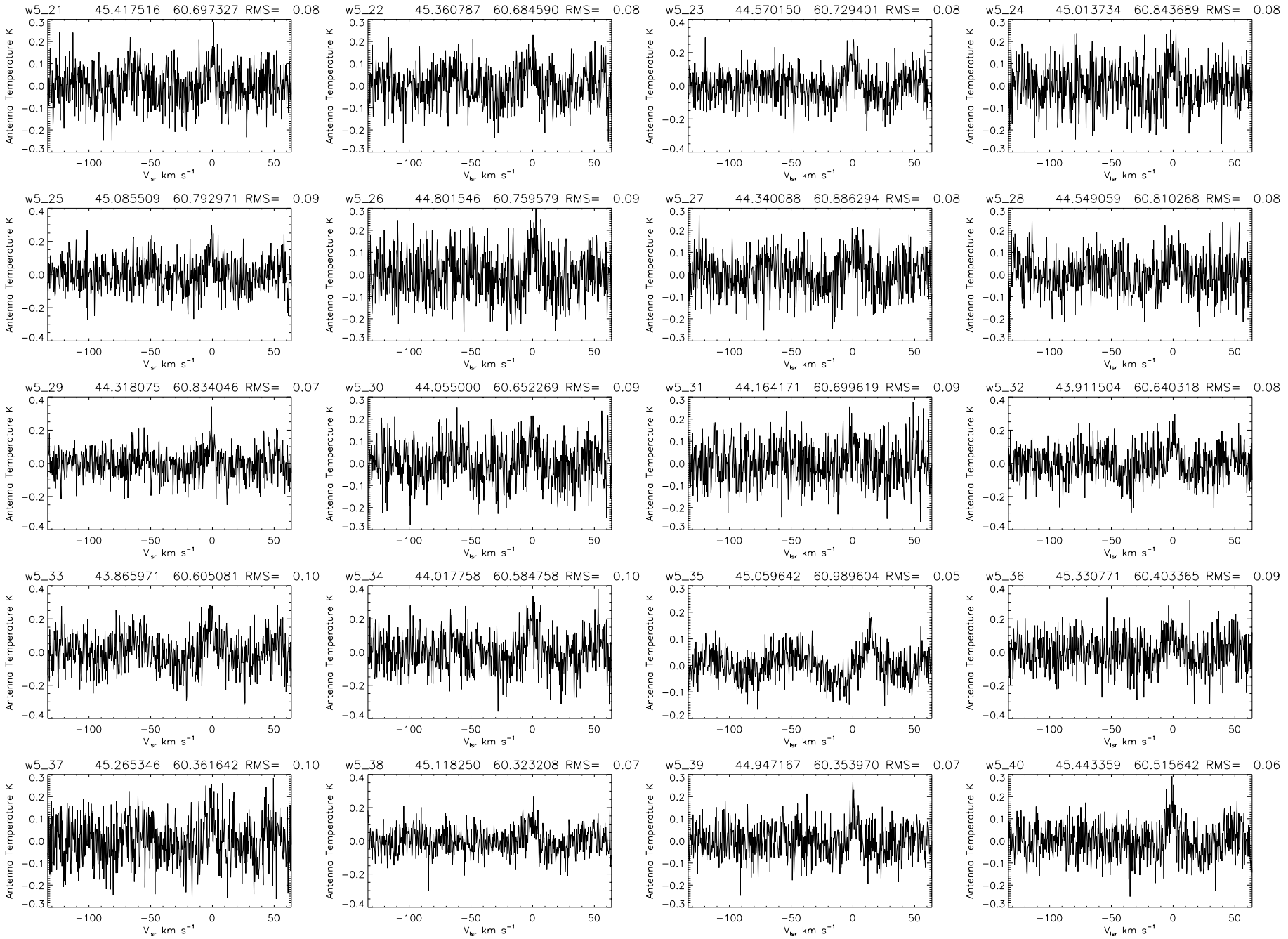
w5_21 45.417516 60.697327 RMS= 0.08
w5_22 45.360787 60.684590 RMS= 0.08
w5_23 44.570150 60.729401 RMS= 0.08
w5_24 45.013734 60.843689 RMS= 0.08
w5_25 45.085509 60.792971 RMS= 0.09
w5_26 44.801546 60.759579 RMS= 0.09
w5_27 44.340088 60.886294 RMS= 0.08
w5_28 44.549059 60.810268 RMS= 0.08
w5_29 44.318075 60.834046 RMS= 0.07
w5_30 44.055000 60.652269 RMS= 0.09
w5_31 44.164171 60.699619 RMS= 0.09
w5_32 43.911504 60.640318 RMS= 0.08
w5_33 43.865971 60.605081 RMS= 0.10
w5_34 44.017758 60.584758 RMS= 0.10
w5_35 45.059642 60.989604 RMS= 0.05
w5_36 45.330771 60.403365 RMS= 0.09
w5_37 45.265346 60.361642 RMS= 0.10
w5_38 45.118250 60.323208 RMS= 0.07
w5_39 44.947167 60.353970 RMS= 0.07
w5_40 45.443359 60.515642 RMS= 0.06
Antenna Temperature K
V_lsr km s^-1

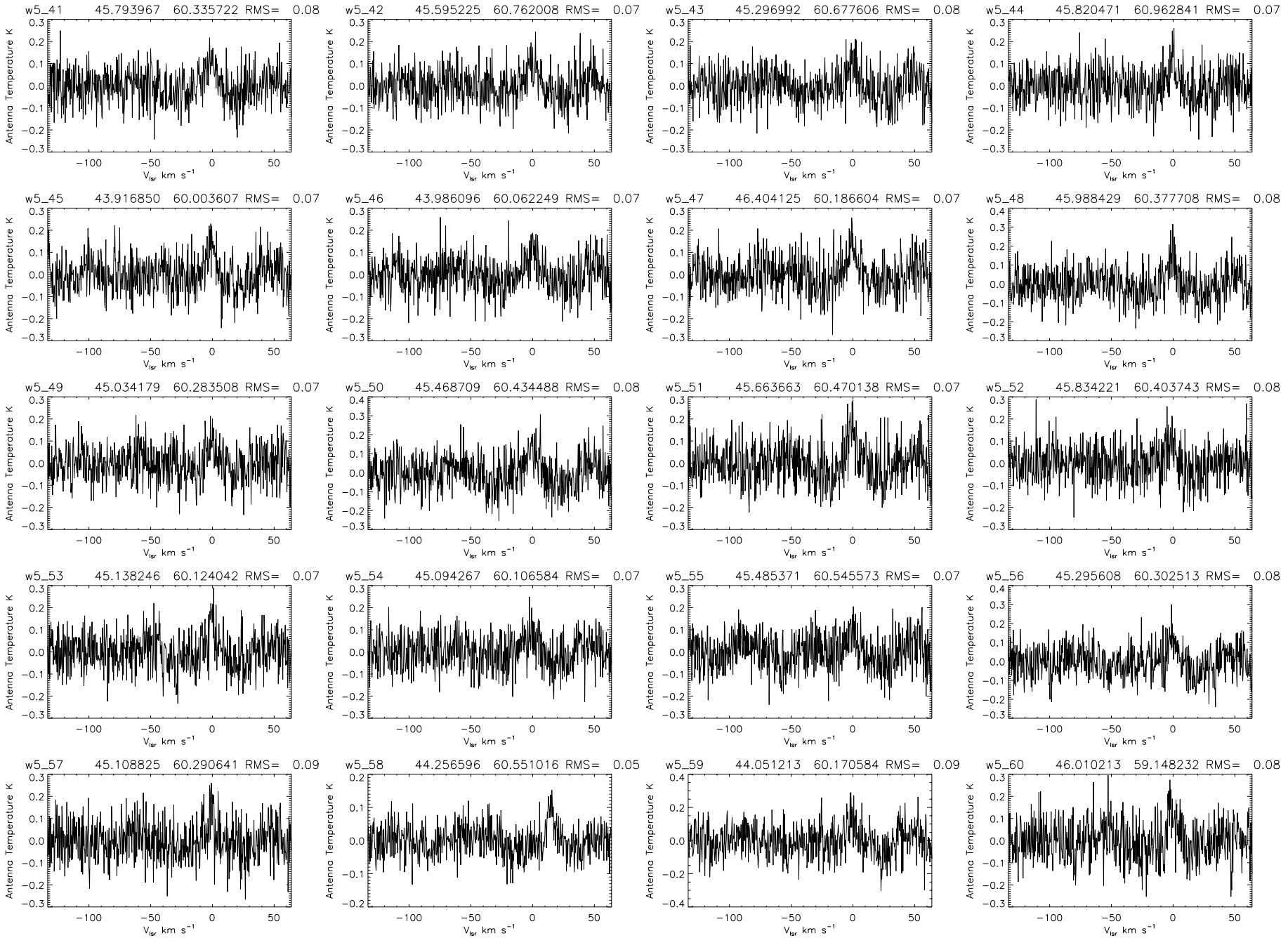
w5_41 45.793967 60.335722 RMS= 0.08
w5_42 45.595225 60.762008 RMS= 0.07
w5_43 45.296992 60.677606 RMS= 0.08
w5_44 45.820471 60.962841 RMS= 0.07
w5_45 43.916850 60.003607 RMS= 0.07
w5_46 43.986096 60.062249 RMS= 0.07
w5_47 46.404125 60.186604 RMS= 0.07
w5_48 45.988429 60.377708 RMS= 0.08
w5_49 45.034179 60.283508 RMS= 0.07
w5_50 45.468709 60.434488 RMS= 0.08
w5_51 45.663663 60.470138 RMS= 0.07
w5_52 45.834221 60.403743 RMS= 0.08
w5_53 45.138246 60.124042 RMS= 0.07
w5_54 45.094267 60.106584 RMS= 0.07
w5_55 45.485371 60.545573 RMS= 0.07
w5_56 45.295608 60.302513 RMS= 0.08
w5_57 45.108825 60.290641 RMS= 0.09
w5_58 44.256596 60.551016 RMS= 0.05
w5_59 44.051213 60.170584 RMS= 0.09
w5_60 46.010213 59.148232 RMS= 0.08
Antenna Temperature K
V_lsr km s^-1

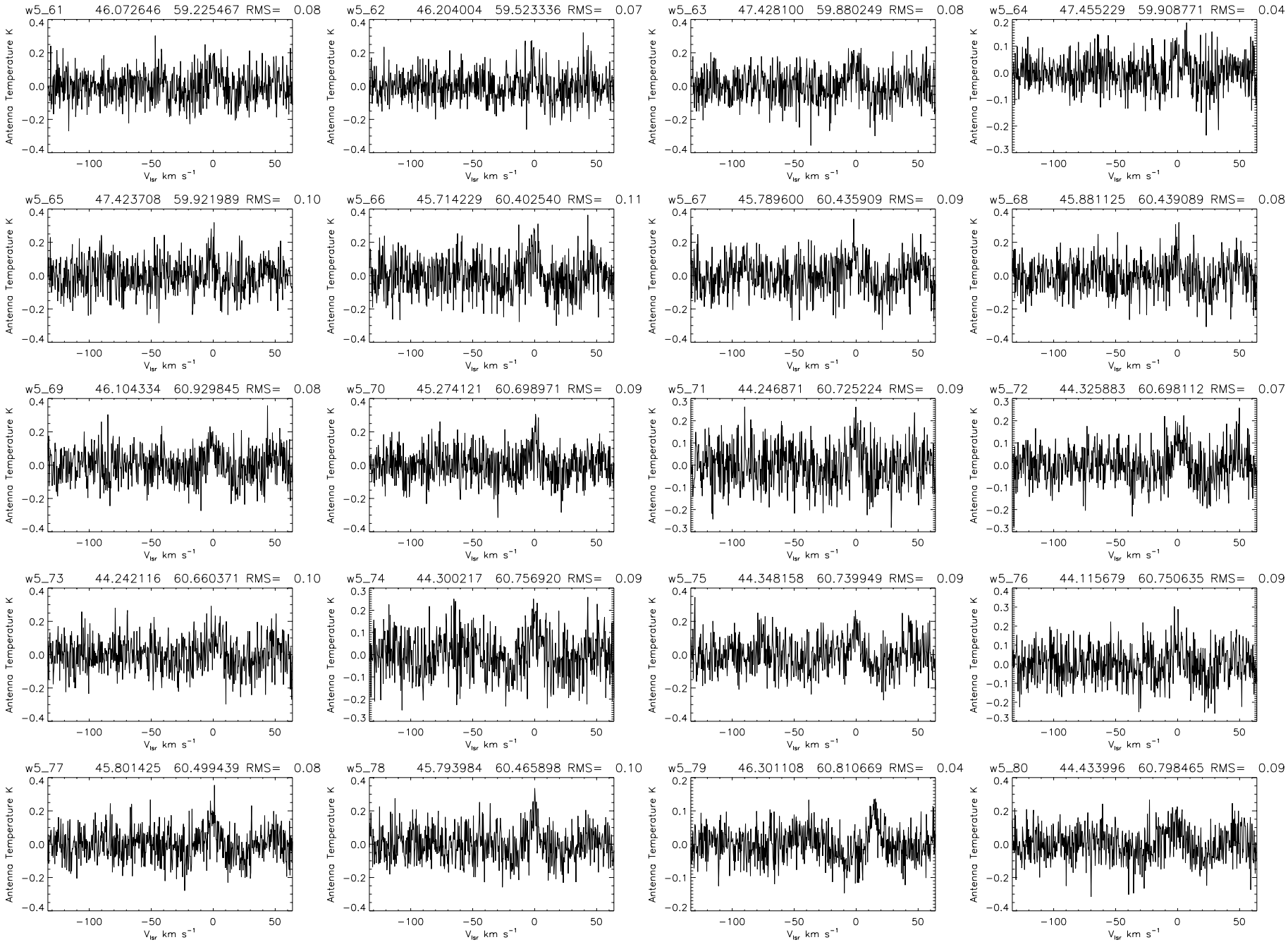
w5_61 46.072646 59.225467 RMS= 0.08
w5_62 46.204004 59.523336 RMS= 0.07
w5_63 47.428100 59.880249 RMS= 0.08
w5_64 47.455229 59.908771 RMS= 0.04
w5_65 47.423708 59.921989 RMS= 0.10
w5_66 45.714229 60.402540 RMS= 0.11
w5_67 45.789600 60.435909 RMS= 0.09
w5_68 45.881125 60.439089 RMS= 0.08
w5_69 46.104334 60.929845 RMS= 0.08
w5_70 45.274121 60.698971 RMS= 0.09
w5_71 44.246871 60.725224 RMS= 0.09
w5_72 44.325883 60.698112 RMS= 0.07
w5_73 44.242116 60.660371 RMS= 0.10
w5_74 44.300217 60.756920 RMS= 0.09
w5_75 44.348158 60.739949 RMS= 0.09
w5_76 44.115679 60.750635 RMS= 0.09
w5_77 45.801425 60.499439 RMS= 0.08
w5_78 45.793984 60.465898 RMS= 0.10
w5_79 46.301108 60.810669 RMS= 0.04
w5_80 44.433996 60.798465 RMS= 0.09
Antenna Temperature K
V_lsr km s^-1

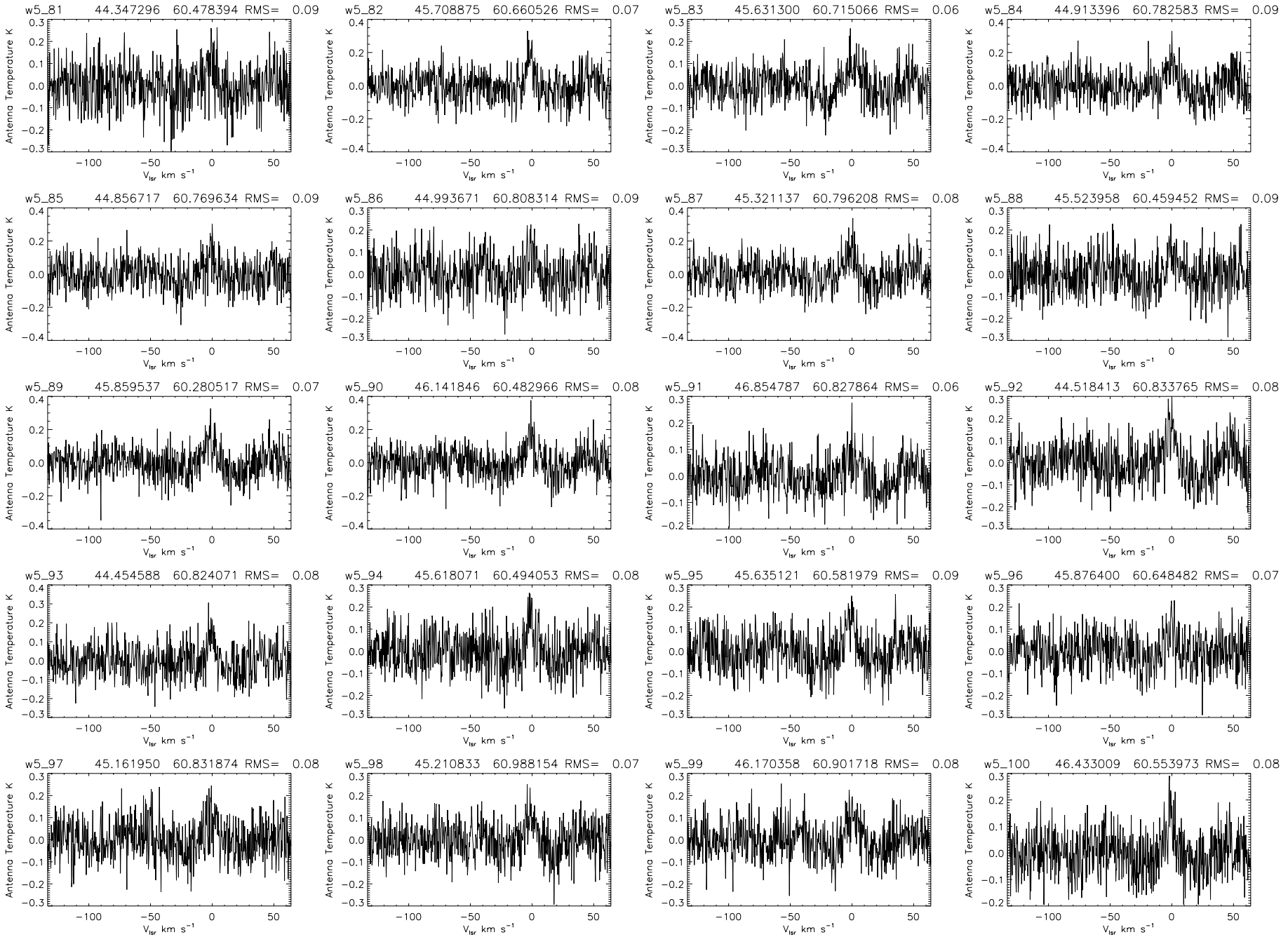
w5_81 44.347296 60.478394 RMS= 0.09
w5_82 45.708875 60.660526 RMS= 0.07
w5_83 45.631300 60.715066 RMS= 0.06
w5_84 44.913396 60.782583 RMS= 0.09
w5_85 44.856717 60.769634 RMS= 0.09
w5_86 44.993671 60.808314 RMS= 0.09
w5_87 45.321137 60.796208 RMS= 0.08
w5_88 45.523958 60.459452 RMS= 0.09
w5_89 45.859537 60.280517 RMS= 0.07
w5_90 46.141846 60.482966 RMS= 0.08
w5_91 46.854787 60.827864 RMS= 0.06
w5_92 44.518413 60.833765 RMS= 0.08
w5_93 44.454588 60.824071 RMS= 0.08
w5_94 45.618071 60.494053 RMS= 0.08
w5_95 45.635121 60.581979 RMS= 0.09
w5_96 45.876400 60.648482 RMS= 0.07
w5_97 45.161950 60.831874 RMS= 0.08
w5_98 45.210833 60.988154 RMS= 0.07
w5_99 46.170358 60.901718 RMS= 0.08
w5_100 46.433009 60.553973 RMS= 0.08
Antenna Temperature K
V_lsr km s^-1

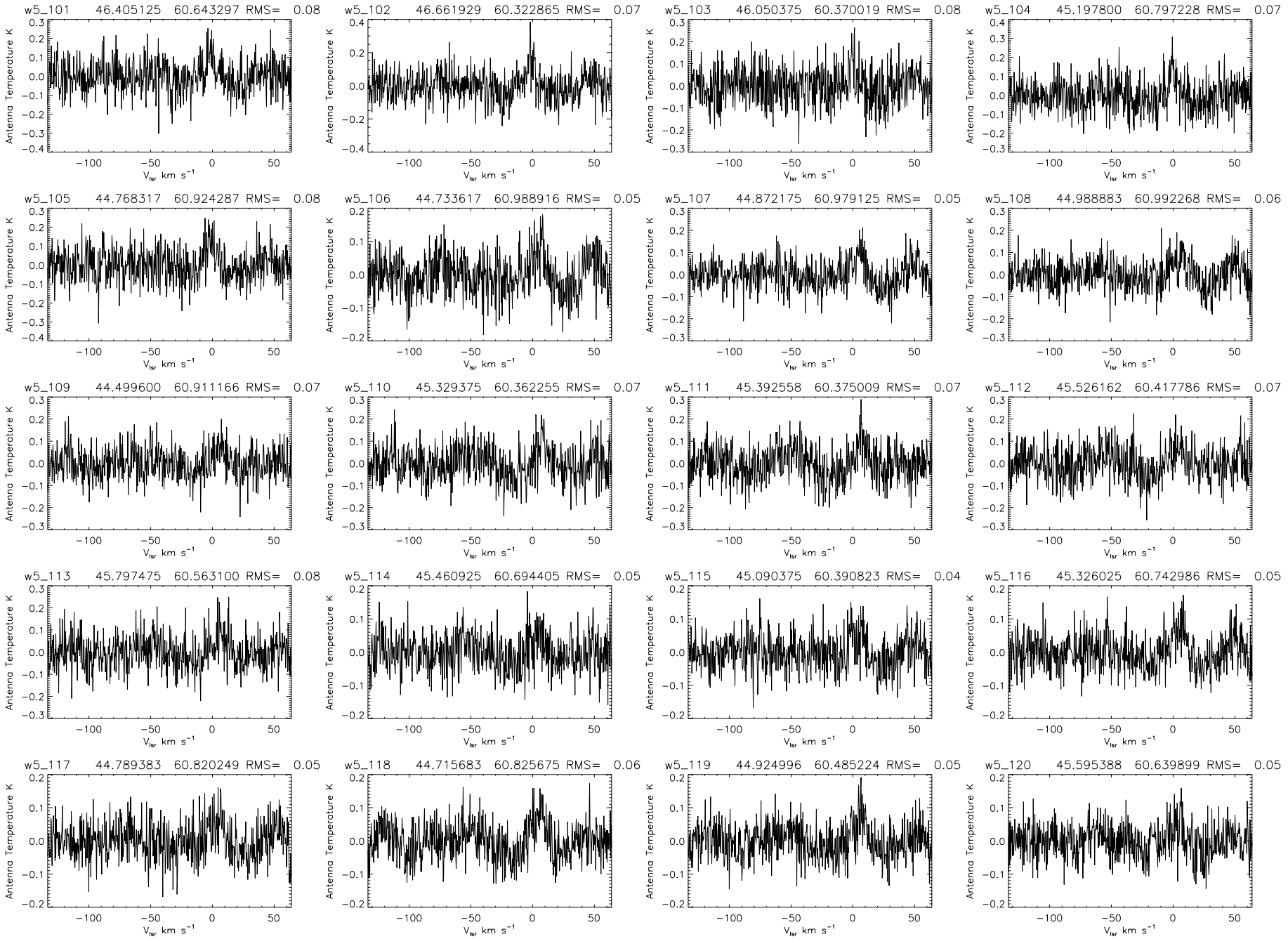
w5_101 46.405125 60.643297 RMS= 0.08
w5_102 46.661929 60.322865 RMS= 0.07
w5_103 46.050375 60.370019 RMS= 0.08
w5_104 45.197800 60.797228 RMS= 0.07
w5_105 44.768317 60.924287 RMS= 0.08
w5_106 44.733617 60.988916 RMS= 0.05
w5_107 44.872175 60.979125 RMS= 0.05
w5_108 44.988883 60.992268 RMS= 0.06
w5_109 44.499600 60.911166 RMS= 0.07
w5_110 45.329375 60.362255 RMS= 0.07
w5_111 45.392558 60.375009 RMS= 0.07
w5_112 45.526162 60.417786 RMS= 0.07
w5_113 45.797475 60.563100 RMS= 0.08
w5_114 45.460925 60.694405 RMS= 0.05
w5_115 45.090375 60.390823 RMS= 0.04
w5_116 45.326025 60.742986 RMS= 0.05
w5_117 44.789383 60.820249 RMS= 0.05
w5_118 44.715683 60.825675 RMS= 0.06
w5_119 44.924996 60.485224 RMS= 0.05
w5_120 45.595388 60.639899 RMS= 0.05
Antenna Temperature K
V_lsr km s^-1

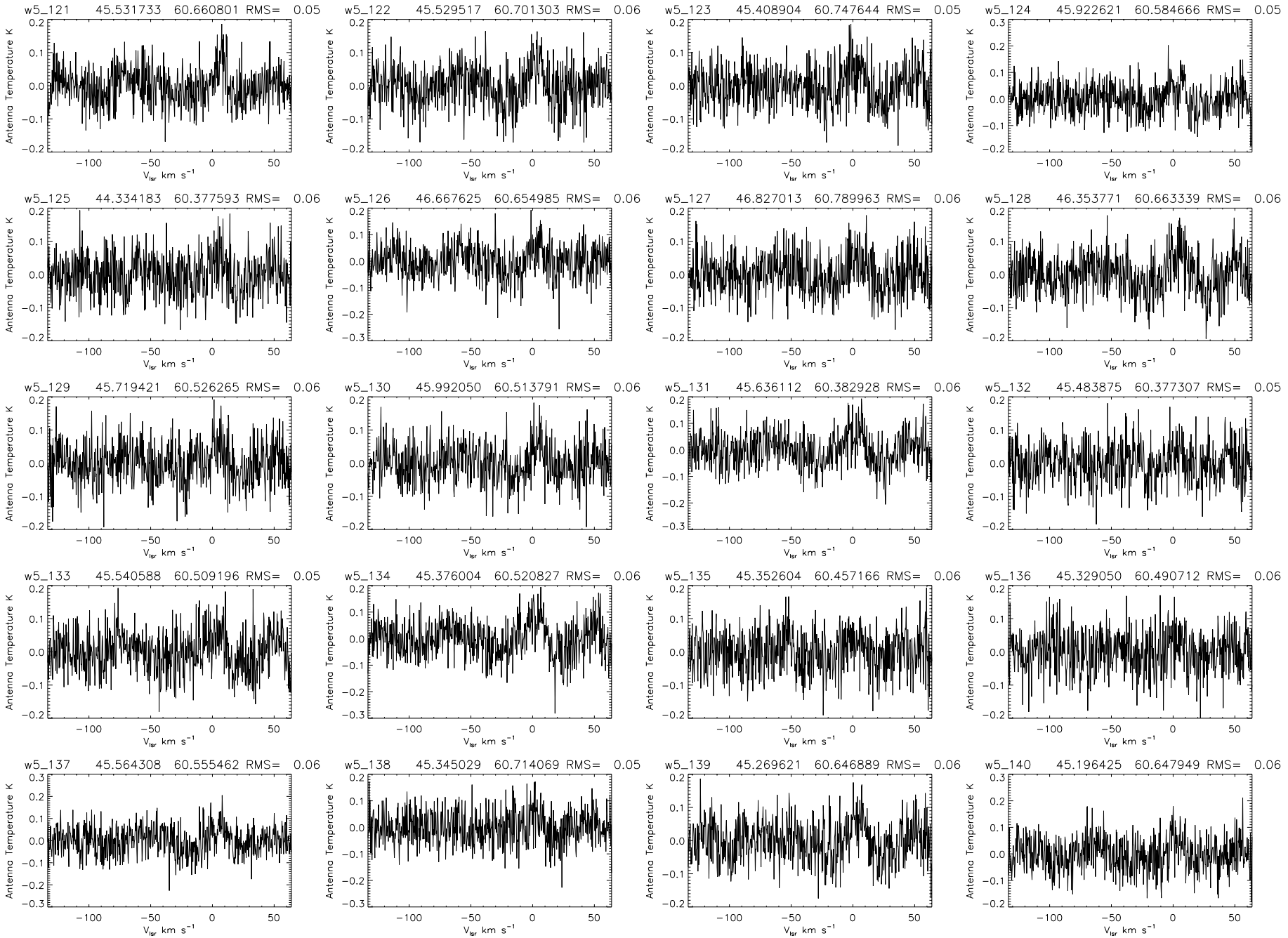
w5_121 45.531733 60.660801 RMS= 0.05
w5_122 45.529517 60.701303 RMS= 0.06
w5_123 45.408904 60.747644 RMS= 0.05
w5_124 45.922621 60.584666 RMS= 0.05
w5_125 44.334183 60.377593 RMS= 0.06
w5_126 46.667625 60.654985 RMS= 0.06
w5_127 46.827013 60.789963 RMS= 0.06
w5_128 46.353771 60.663339 RMS= 0.06
w5_129 45.719421 60.526265 RMS= 0.06
w5_130 45.992050 60.513791 RMS= 0.06
w5_131 45.636112 60.382928 RMS= 0.06
w5_132 45.483875 60.377307 RMS= 0.05
w5_133 45.540588 60.509196 RMS= 0.05
w5_134 45.376004 60.520827 RMS= 0.06
w5_135 45.352604 60.457166 RMS= 0.06
w5_136 45.329050 60.490712 RMS= 0.06
w5_137 45.564308 60.555462 RMS= 0.06
w5_138 45.345029 60.714069 RMS= 0.05
w5_139 45.269621 60.646889 RMS= 0.06
w5_140 45.196425 60.647949 RMS= 0.06
Antenna Temperature K
V_lsr km s^-1

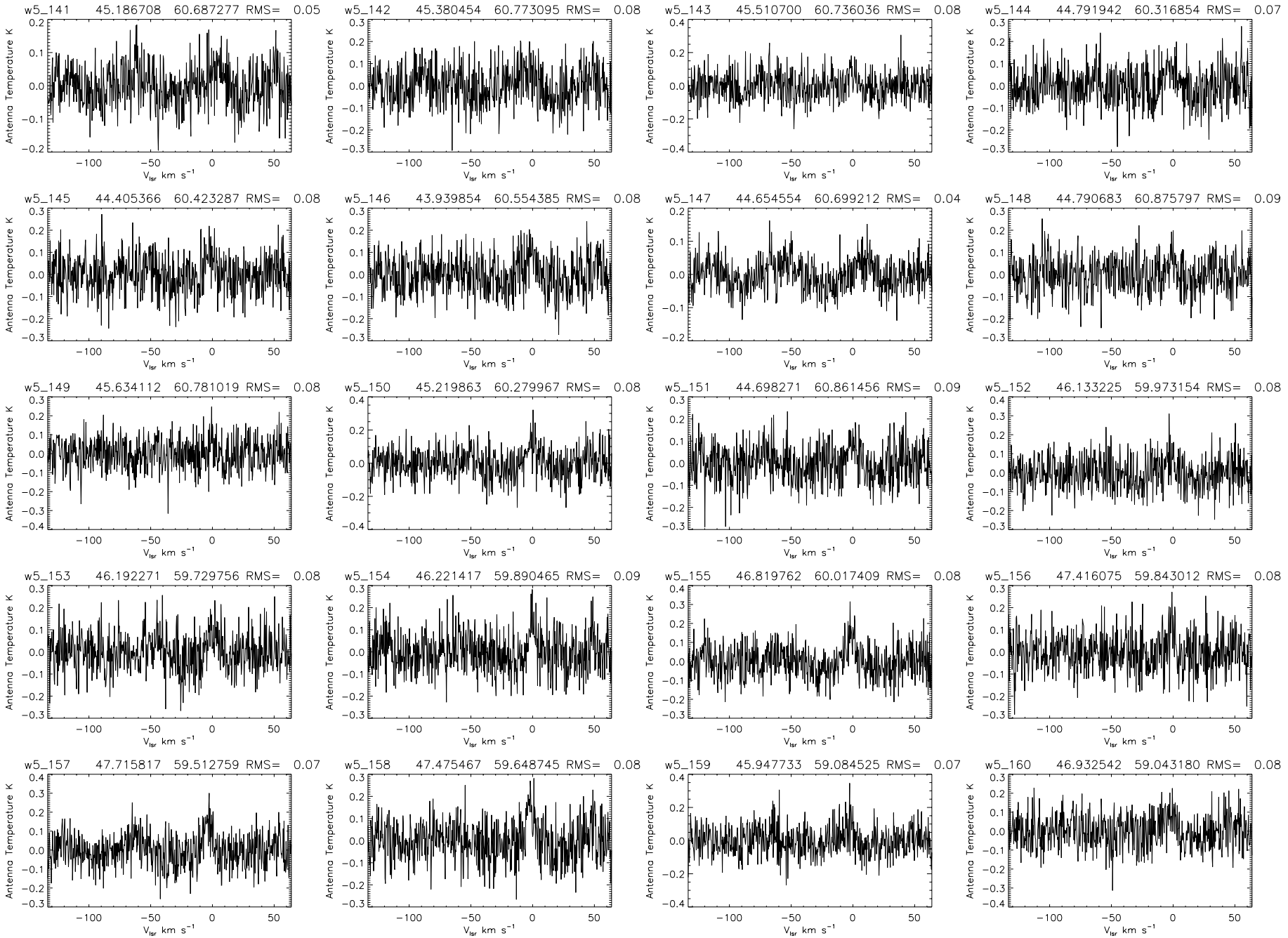
w5_141 45.186708 60.687277 RMS= 0.05
w5_142 45.380454 60.773095 RMS= 0.08
w5_143 45.510700 60.736036 RMS= 0.08
w5_144 44.791942 60.316854 RMS= 0.07
w5_145 44.405366 60.423287 RMS= 0.08
w5_146 43.939854 60.554385 RMS= 0.08
w5_147 44.654554 60.699212 RMS= 0.04
w5_148 44.790683 60.875797 RMS= 0.09
w5_149 45.634112 60.781019 RMS= 0.08
w5_150 45.219863 60.279967 RMS= 0.08
w5_151 44.698271 60.861456 RMS= 0.09
w5_152 46.133225 59.973154 RMS= 0.08
w5_153 46.192271 59.729756 RMS= 0.08
w5_154 46.221417 59.890465 RMS= 0.09
w5_155 46.819762 60.017409 RMS= 0.08
w5_156 47.416075 59.843012 RMS= 0.08
w5_157 47.715817 59.512759 RMS= 0.07
w5_158 47.475467 59.648745 RMS= 0.08
w5_159 45.947733 59.084525 RMS= 0.07
w5_160 46.932542 59.043180 RMS= 0.08
Antenna Temperature K
V_lsr km s^-1

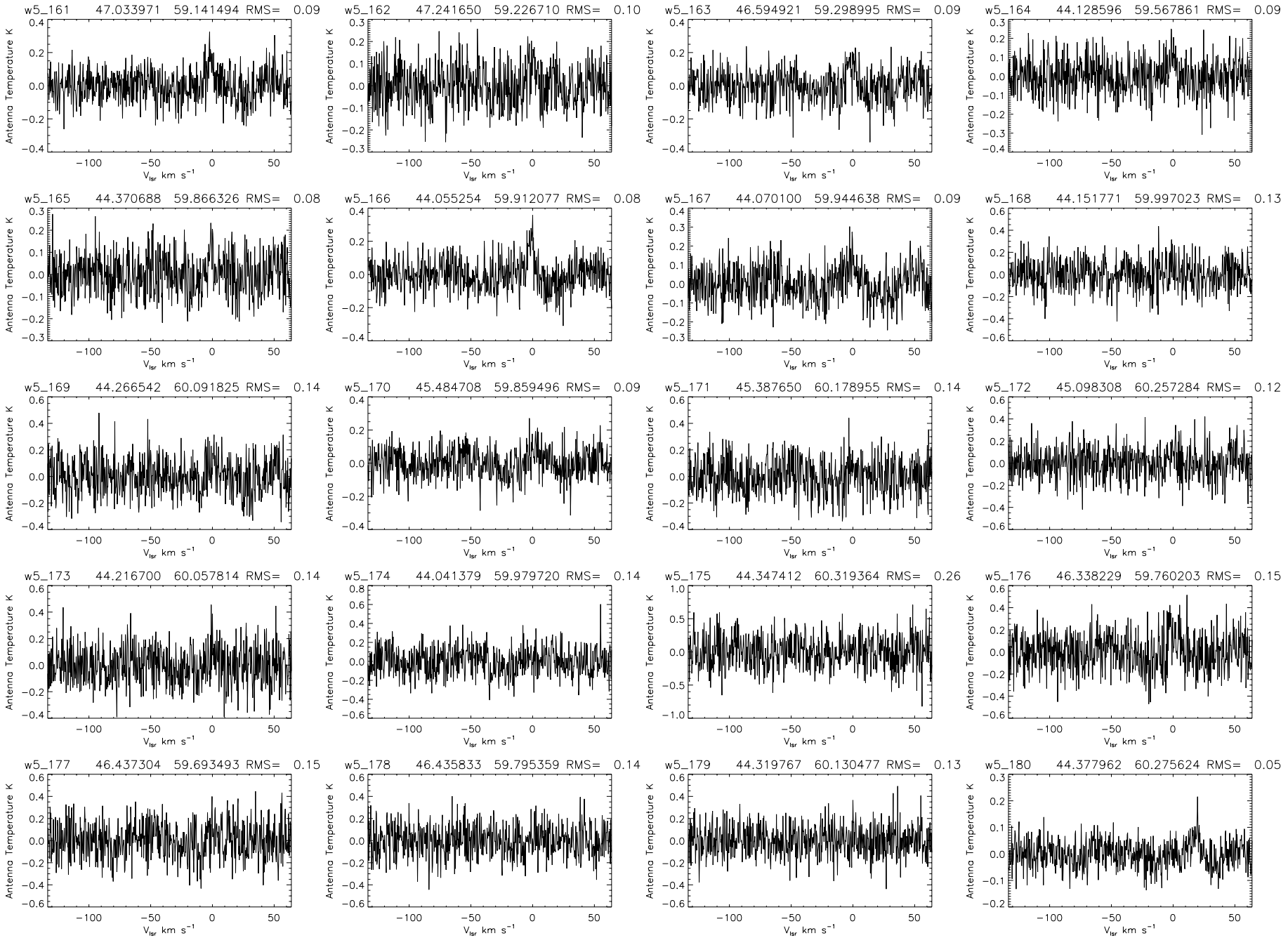
w5_161 47.033971 59.141494 RMS= 0.09
w5_162 47.241650 59.226710 RMS= 0.10
w5_163 46.594921 59.298995 RMS= 0.09
w5_164 44.128596 59.567861 RMS= 0.09
w5_165 44.370688 59.866326 RMS= 0.08
w5_166 44.055254 59.912077 RMS= 0.08
w5_167 44.070100 59.944638 RMS= 0.09
w5_168 44.151771 59.997023 RMS= 0.13
w5_169 44.266542 60.091825 RMS= 0.14
w5_170 45.484708 59.859496 RMS= 0.09
w5_171 45.387650 60.178955 RMS= 0.14
w5_172 45.098308 60.257284 RMS= 0.12
w5_173 44.216700 60.057814 RMS= 0.14
w5_174 44.041379 59.979720 RMS= 0.14
w5_175 44.347412 60.319364 RMS= 0.26
w5_176 46.338229 59.760203 RMS= 0.15
w5_177 46.437304 59.693493 RMS= 0.15
w5_178 46.435833 59.795359 RMS= 0.14
w5_179 44.319767 60.130477 RMS= 0.13
w5_180 44.377962 60.275624 RMS= 0.05
Antenna Temperature K
V_lsr km s^-1

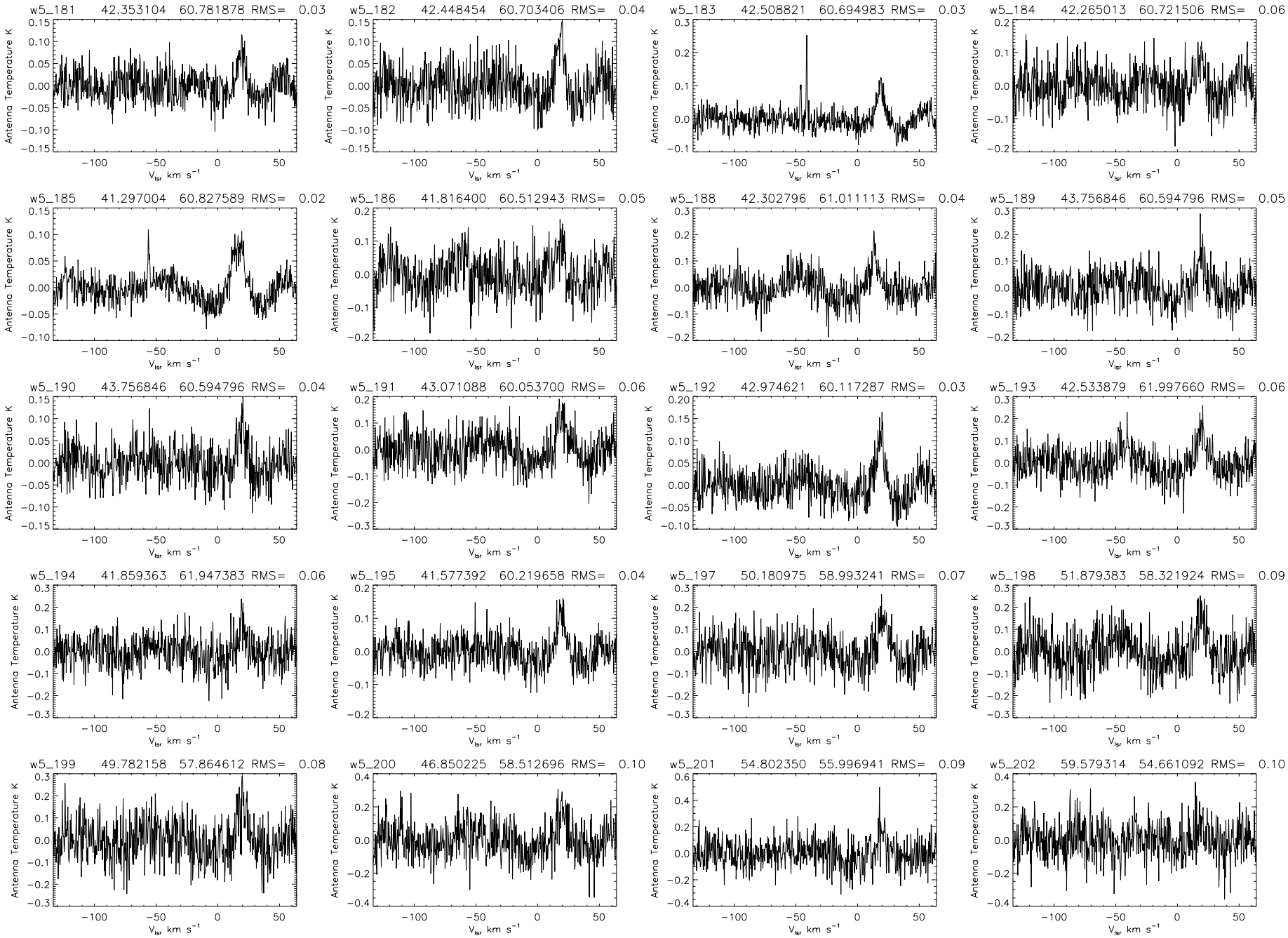
w5_181 42.353104 60.781878 RMS= 0.03
w5_182 42.448454 60.703406 RMS= 0.04
w5_183 42.508821 60.694983 RMS= 0.03
w5_184 42.265013 60.721506 RMS= 0.06
w5_185 41.297004 60.827589 RMS= 0.02
w5_186 41.816400 60.512943 RMS= 0.05
w5_188 42.302796 61.011113 RMS= 0.04
w5_189 43.756846 60.594796 RMS= 0.05
w5_190 43.756846 60.594796 RMS= 0.04
w5_191 43.071088 60.053700 RMS= 0.06
w5_192 42.974621 60.117287 RMS= 0.03
w5_193 42.533879 61.997660 RMS= 0.06
w5_194 41.859363 61.947383 RMS= 0.06
w5_195 41.577392 60.219658 RMS= 0.04
w5_197 50.180975 58.993241 RMS= 0.07
w5_198 51.879383 58.321924 RMS= 0.09
w5_199 49.782158 57.864612 RMS= 0.08
w5_200 46.850225 58.512696 RMS= 0.10
w5_201 54.802350 55.996941 RMS= 0.09
w5_202 59.579314 54.661092 RMS= 0.10
Antenna Temperature K
V_lsr km s^-1

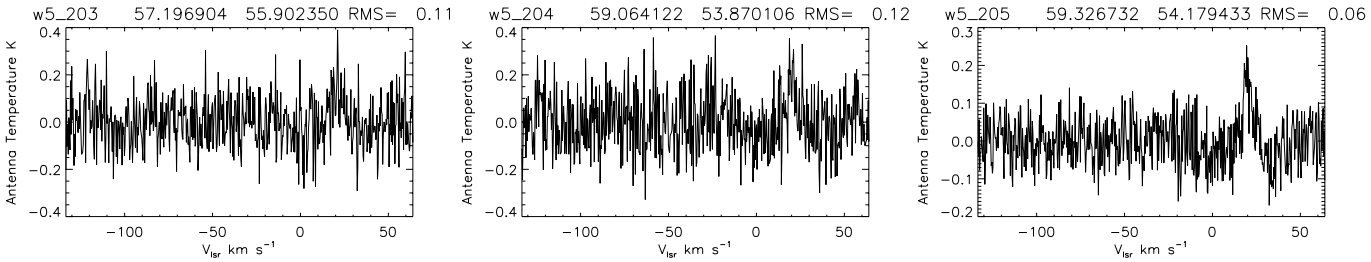
w5_203 57.196904 55.902350 RMS= 0.11
w5_204 59.064122 53.870106 RMS= 0.12
w5_205 59.326732 54.179433 RMS= 0.06
Antenna Temperature K
V_lsr km s^-1